

DISSERTATION

Synthese und *in situ* Untersuchungen von anorganisch-organischen Hybridverbindungen auf Basis von Metallphosphonaten und Bismutcarboxylaten

Verfasser

Mark Feyand

Zur Erlangung des Doktorgrades
der Mathematisch-Naturwissenschaftlichen Fakultät

Institut für Anorganische Chemie
Kiel, 2013

Erster Gutachter: Prof. Dr. Norbert Stock

Zweiter Gutachter: Prof. Dr. Wolfgang Bensch

Tag der mündlichen Prüfung: 27.05.2013

Zum Druck genehmigt: 27.05.2013

Gez. Prof. Dr. Wolfgang J. Duschl

Der Dekan

Meinen Eltern

Inhaltsverzeichnis

I. Allgemeiner Teil	9
1. Einleitung	11
2. Präparative Methoden	15
2.1. Solvothermalsynthese	15
2.2. Mikrowellenunterstützte Solvothermalreaktionen	16
2.3. Hochdurchsatzmethoden	17
2.4. Mikrowellenunterstützte Hochdurchsatzmethoden	19
3. Charakterisierungsmethoden	21
3.1. Röntgenbeugung	23
3.2. Einkristallstrukturanalyse	26
3.2.1. Direkte Methoden	27
3.2.2. Strukturverfeinerung	28
3.3. Röntgenpulverdiffraktometrie	29
3.4. Strukturlösung aus Pulverdaten	30
3.4.1. Indizierung und Raumgruppenbestimmung	31
3.4.2. Strukturlösung	31
3.4.3. Rietveld-Verfeinerung	33
3.4.4. Pawley- und Le-Bail-Verfeinerung	34
3.4.5. Experimentelle Methoden	35
3.4.6. Pulverdiffraktometrie an Synchrotronstrahlungsquellen	35
3.5. <i>In situ</i> Röntgenbeugung	38
3.6. Empirische Reaktionskinetik	39
3.6.1. Avrami Modell	39
3.6.2. Gualtieri Modell	42

II. Kumulativer Hauptteil	45
4. Polyfunktionalisierte Metallphosphonate	47
4.1. Metallphosphonate	47
4.2. Metallphosphonatosulfonate	48
4.3. Metallphosphonatocarboxylate	55
4.4. Aminofunktionalisierte Metallphosphonate	58
4.5. <i>In situ</i> Röntgenbeugung an anorganisch-organischen Hybridverbindungen	63
4.6. Ergebnisse	66
4.6.1. Systematic and <i>In Situ</i> Energy Dispersive X-ray Diffraction Investigations on the Formation of Lanthanide Phosphonatobutanesulfonates: $\text{Ln}(\text{O}_3\text{P}-\text{C}_4\text{H}_8-\text{SO}_3)(\text{H}_2\text{O})$ ($\text{Ln} = \text{La-Gd}$)	66
4.6.2. Copper Phosphonatoethanesulfonates: Temperature Dependent <i>in situ</i> Energy Dispersive X-ray Diffraction Study and Influence of the pH on the Crystal Structures	74
4.6.3. <i>In situ</i> Untersuchungen von Metallphosphonatocarboxylaten	83
4.6.4. High-throughput and <i>in situ</i> EDXRD Investigation on the Formation of Two New Metal Aminoethylphosphonates – $\text{Ca}(\text{O}_3\text{PC}_2\text{H}_4\text{NH}_2)$ and $\text{Ca}(\text{OH})(\text{O}_3\text{PC}_2\text{H}_4\text{NH}_3)\cdot 2\text{H}_2\text{O}$	94
4.6.5. Crystallisation Kinetics of Metal Organic Frameworks from <i>in situ</i> Time-Resolved X-ray Diffraction	101
4.6.6. High-Throughput Microwave Assisted Discovery of New Metal Phosphonates	126
5. Synthese und <i>in situ</i> Untersuchung von Bismutcarboxylaten	139
5.1. Bismutpyridincarboxylate	139
5.2. Bismutcarboxylate	141
5.3. Ergebnisse	144
5.3.1. Automated Diffraction Tomography for the Structure Elucidation of Twinned, Sub-micrometer Crystals of a Highly Porous, Catalytically Active Bismuth Metal–Organic Framework	144
5.3.2. High-throughput and <i>In situ</i> EDXRD Investigation of Bismuthcarboxylates	149

6. Strukturlösung von anorganisch-organischen Hybridverbindungen	161
6.1. Ergebnisse	161
6.1.1. CAU-3: A new family of porous MOFs with a novel Al-based brick: [Al ₂ (OCH ₃) ₄ (O ₂ C-X-CO ₂)] (X = aryl)	161
6.1.2. Fuel Purification, Lewis Acid and Aerobic Oxidation Catalysis Per- formed by a Microporous Co-BTT (BTT ³⁻ = 1,3,5-benzenetristetrazolate) Framework Having Coordinatively Unsaturated Sites	171
6.1.3. Systematic Investigation of Porous Inorganic-Organic Hybrid Com- pounds with Photo-Switchable Properties	183
6.1.4. [Zn(C ₃ H ₃ N ₂)(C ₃ H ₂ N ₂ -N=N-C ₆ H ₅)], a Mixed-Linker ZIF Containing a Photoswitchable Phenylazo Group	191
7. Zusammenfassung	199
7.1. Zusammenfassung der <i>in situ</i> Untersuchungen	199
7.2. Zusammenfassung der Strukturlösung von anorganisch-organischen Hybrid- verbindungen	201
7.3. Ausblick	205
 III. Anhang	 209

Synthese und *in situ* Untersuchungen von Metallphosphonaten und Bismutcarboxylaten

Die hier vorliegende Arbeit beschäftigt sich mit der Synthese und Charakterisierung von neuen anorganisch-organischen Hybridverbindungen und den *in situ* Untersuchungen ihrer Kristallisation. Den Hauptteil dieser Arbeit machten dabei die Untersuchung polyfunktionalisierter Metallphosphonate und Bismutcarboxylate aus. Die Kristallisationsprozesse wurden mittels energiedispersiver Röntgenbeugung (EDXRD) untersucht. Die Produktbildung von $[\text{Cu}_2(\text{O}_3\text{P}-\text{C}_2\text{H}_4-\text{SO}_3(\text{OH})(\text{H}_2\text{O})_2)] \cdot 3\text{H}_2\text{O}$ und $[\text{Cu}_2(\text{O}_3\text{P}-\text{C}_2\text{H}_4-\text{SO}_3(\text{OH})(\text{H}_2\text{O})_2)] \cdot 4\text{H}_2\text{O}$, während bei der Kristallisation von $\text{Ca}(\text{O}_3\text{P}-\text{C}_2\text{H}_4-\text{NH}_2)$ das Intermediat $[\text{Ca}(\text{OH})(\text{O}_3\text{P}-\text{C}_2\text{H}_4-\text{NH}_3)] \cdot 2\text{H}_2\text{O}$ beobachtet wird. Die Kristallstrukturen beider Intermediate und von $\text{Ca}(\text{O}_3\text{P}-\text{C}_2\text{H}_4-\text{NH}_2)$ wurden hierbei aus Röntgenpulverdaten bestimmt. EDXRD Untersuchungen der Bildung von $\text{M}(\text{HO}_3\text{P}-\text{CH}_2)_2-\text{NHCH}_2-\text{C}_6\text{H}_4-\text{COOH}$ ($\text{M} = \text{Mn}^{2+}, \text{Co}^{2+}, \text{Fe}^{2+}, \text{Ni}^{2+}$), zeigten verschiedene Reaktionszeiten und Intermediate in Abhängigkeit des Metallions. Die Kristallisation von $\text{Sm}(\text{O}_3\text{P}-\text{C}_4\text{H}_8-\text{SO}_3)(\text{H}_2\text{O})$, Co-CPO-27 und Ni-CPO-27 wurden *in situ* untersucht und unter Verwendung des Avrami bzw. Gualtieri Modells war es möglich die Geschwindigkeitskonstanten und Arrhenius-Aktivierungsenergien der Reaktionen sowohl unter mikrowellenunterstützten als auch konventionellen Synthesebedingungen zu bestimmen. Mikrowellenunterstützte Synthesemethoden konnten ebenfalls genutzt werden um die Verbindungen $[\text{Ni}(m-[(\text{HO}_3\text{PCH}_2)_2\text{NHCH}_2]_2\text{C}_6\text{H}_4)] \cdot \text{H}_2\text{O}$, $[\text{Cd}(p-[(\text{HO}_3\text{PCH}_2)_2\text{NHCH}_2]_2\text{C}_6\text{H}_4)]$ und $[\text{Zn}(p-[(\text{HO}_3\text{PCH}_2)_2\text{NHCH}_2]_2\text{C}_6\text{H}_4)\text{H}_2\text{O}]$ zu synthetisieren und ihre Kristallstrukturen konnten mittels Röntgenpulverbeugung bestimmt bzw. aus kristallographischen Zusammenhängen hergeleitet werden. Unter Verwendung von H_3BTB und $\text{Bi}(\text{NO}_3)_3 \cdot 5\text{H}_2\text{O}$ war es möglich das erste hoch poröse Bismutcarboxylat $\text{Bi}(\text{BTB})$ ($\text{H}_3\text{BTB} = 1,3,5\text{-Benzoltrisbenzoesäure}$) herzustellen, welches eine scheinbare spezifische Oberfläche von $1150 \text{ m}^2/\text{g}$ aufweist. Die Verbindung ist für die Hydroxymethylierung von Furan katalytisch aktiv. Die Kristallstruktur wurde aus einer Kombination von Elektronenbeugungsdaten, Rietveld-Verfeinerung und DFT Rechnungen bestimmt. Ebenso wurde zum ersten Mal die Kristallisation von Bismutcarboxylaten *in situ* untersucht. Es wurde gezeigt, dass in Abhängigkeit der verwendeten Linkermoleküle Pyromellitsäure (H_4Pyr), Trimellitsäure (H_3Tri) und Trimesinsäure (H_3BDC) unter ansonsten ähnlichen Reaktionsbedingungen isolierbare, nicht isolierbare oder gar keine Intermediate bei der Bildung von $\text{Bi}(\text{HPyr})$, $\text{Bi}(\text{Tri})(\text{H}_2\text{O})$ und

$(\text{Bi}_2(\text{O})(\text{OH})(\text{HBTC})(\text{NO}_3))$ entstehen.

Synthesis and *in situ* Investigation of Metalphosphonates and Bismuthcarboxylates

This thesis deals with the synthesis and characterization of new inorganic-organic hybrid compounds and the *in situ* investigations of their crystallization. The main part of this work deals with metalphosphonates and bismuthcarboxylates. The crystallization was investigated by *in situ* energy dispersive X-ray diffraction (EDXRD). The product formation of $[\text{Cu}_2(\text{O}_3\text{P}-\text{C}_2\text{H}_4-\text{SO}_3(\text{OH})(\text{H}_2\text{O})_2)] \cdot 3\text{H}_2\text{O}$ and $[\text{Cu}_2(\text{O}_3\text{P}-\text{C}_2\text{H}_4-\text{SO}_3(\text{OH})(\text{H}_2\text{O}))]$ proceeds through the metastable hydrated intermediate $[\text{Cu}_2(\text{O}_3\text{P}-\text{C}_2\text{H}_4-\text{SO}_3(\text{OH})(\text{H}_2\text{O})_2)] \cdot 4\text{H}_2\text{O}$, while in the crystallization of $\text{Ca}(\text{O}_3\text{P}-\text{C}_2\text{H}_4-\text{NH}_2)$ the intermediate $[\text{Ca}(\text{OH})(\text{O}_3\text{P}-\text{C}_2\text{H}_4-\text{NH}_3)] \cdot 2\text{H}_2\text{O}$ is observed. The crystal structure of both intermediates and $\text{Ca}(\text{O}_3\text{P}-\text{C}_2\text{H}_4-\text{NH}_2)$ were determined from X-ray powder diffraction data. *In situ* EDXRD investigations of the formation of $\text{M}(\text{HO}_3\text{P}-\text{CH}_2)_2\text{NHCH}_2-\text{C}_6\text{H}_4-\text{COOH}$ ($\text{M} = \text{Mn}^{2+}, \text{Co}^{2+}, \text{Fe}^{2+}, \text{Ni}^{2+}$), $\text{Ca}(\text{O}_3\text{P}-\text{C}_2\text{H}_4-\text{NH}_2)$ revealed different reaction times and intermediates depending on the metal ion used. The *in situ* investigation of the crystallization of $\text{Sm}(\text{O}_3\text{P}-\text{C}_4\text{H}_8-\text{SO}_3)(\text{H}_2\text{O})$, Co-CPO-27 and Ni-CPO-27 allowed the extraction of rate constants and Arrhenius activation energies for the crystallization under microwave-assisted as well as conventional syntheses methods using the model of Avrami and Gualtieri. Microwave-assisted heating was also used to synthesize the compounds $[\text{Ni}(m-[(\text{HO}_3\text{PCH}_2)_2\text{NHCH}_2]_2\text{C}_6\text{H}_4)] \cdot \text{H}_2\text{O}$, $[\text{Cd}(p-[(\text{HO}_3\text{PCH}_2)_2\text{NHCH}_2]_2\text{C}_6\text{H}_4)]$ and $[\text{Zn}(p-[(\text{HO}_3\text{PCH}_2)_2\text{NHCH}_2]_2\text{C}_6\text{H}_4)\text{H}_2\text{O}]$. Their crystal structures were determined from X-ray powder diffraction or derived from crystallographic relations.

The use of H_3BTB (1,3,5-benzenetrisbenzoic acid) and $\text{Bi}(\text{NO}_3)_3 \cdot 5\text{H}_2\text{O}$ allowed the synthesis of the first highly porous bismuth carboxylate $\text{Bi}(\text{BTB})$ with a specific surface area of $1150 \text{ m}^2/\text{g}$ (BET). The compound is catalytic active in the hydroxymethylation of furan. The crystal structure was determined by a combination of electron diffraction, Rietveld refinement and DFT calculations. In addition *in situ* EDXRD was employed to investigate the crystallization of bismuth carboxylates for the first time. Depending on the linker molecule pyromellitic acid (H_4Pyr), trimellitic acid (H_3Tri) and trimesic acid (H_3BDC) under similar reaction intermediates occur that were isolated and fully characterized.

Danksagung

Zuallererst möchte ich mich bei meinem Doktorvater Professor Stock für das Vertrauen, die Unterstützung und die Geduld beim Entstehen dieser Arbeit bedanken.

Mein weiterer Dank gilt dem gesamten Arbeitskreis Stock für die freundliche und hilfsbereite Atmosphäre. Ganz besonders möchte ich hierbei Felcitas Niekel und Dr. Helge Reinsch für die entspannte und freundschaftliche Atmosphäre im Labor und die hilfreichen Diskussionen danken.

Ebenso möchte ich der spektroskopischen Abteilung und allen Leuten die für mich Messungen durchgeführt haben danken. Dr. Antje Modrow und Nele Reimer sei insbesondere für die Sorptionsmessungen gedankt, sowie Inke Jess für die Geduld und dem Engagement das Beste aus den (zu kleinen) Kristallen herauszuholen. Weiterhin sei Allen gedankt die an den vielen Thermogravimetriemessungen beteiligt waren.

Prof. Bensch und Prof. Näther danke ich für die Bereitstellung der Instrumente und der Hilfestellung bei wissenschaftlichen Fragestellungen, Dr. Nicole Pienack, Dr. Beatrix Seidlhofer und Dr. Elena Antonova danke ich für die Unterstützung bei den *in situ* Experimenten.

Ebenfalls danken möchte ich allen Kooperationspartnern für die durchgeführten Messungen. Besonderer Dank gilt hierbei Dr. Enrico Mugnaioli und Dr. Ute Kolb, Dr. Johannes Dieterich, Frederik Vermoortele sowie Dr. Alexandra Lieb.

Henning Lühmann und Maren Rasmussen danke ich für die Durchführung der Messungen der magnetischen Eigenschaften.

Weiterhin danke ich allen F-Praktikanten und Bachelor Studenten für die Unterstützung bei dieser Arbeit. Besonderer Dank gilt hier Nele Hermer, Matthias Schulz, Annika Hübner und Milan Köppen.

Dr. Corinna Schmidt und Dr. Tim Ahnfeldt danke ich weiterhin für die angenehme Zeit am DESY und Dr. André Rothkirch für die intensive Betreuung an der Beamline F3, sowie

Dr. Casten Deiter für die Unterstützung an der Beamline P08.

Ganz besonders sei auch Britta Bahn gedankt für die unzähligen sichtbaren und auch für uns unsichtbaren bürokratischen Hilfestellungen.

Dr. Michael Wharmby sei für die hilfreichen Diskussionen gedankt.

Ebenso möchte ich meiner Familie danken, die mich immer unterstützt hat. Weiterhin danke ich Gerd Stute für die immerwährende Unterstützung während des Studiums und dieser Arbeit. Mein ganz besonderer Dank gilt Lydia ohne deren Unterstützung diese Arbeit nicht möglich gewesen wäre.

Abkürzungsverzeichnis

ADT	Automated Diffraction Tomography
bipy	4,4'-Bipyridin
H ₃ BTB	1,3,5-Benzoltrisbenzoesäure
H ₃ BTC	1,3,5-Benzoltricarbonsäure (Trimesinsäure)
DMA	Dimethylammonium
DMF	Dimethylformamid
DMSO	Dimethylsulfoxid
DTA	Differenz Thermoanalyse
EDX	energiedispersive Röntgenfluoreszenzspektroskopie
EDXRD	energiedispersive Röntgenbeugung
ESEM	environmental scanning electron microscope
FK	Festkörper
HIm	Imidazol
IR	Infrarot
MOF	Metal-Organic Framework
NMR	Kernresonanz
PD	Pulverdiffraktogramm
phen	1,10-Phenanthrolin
H ₂ PYDC	Pyridindicarbonsäure
H ₄ Pyr	1,2,4,5-Benzoltetracarbonsäure (Pyromellitsäure)
SAXS	Kleinwinkel-Röntgenstreuung
TEM	Transmissionselektronenmikroskop
TG	Thermogravimetrie
H ₃ Tri	1,2,4-Benzoltricarbonsäure (Trimellitsäure)
TU	Thioharnstoff
WAXS	Weitwinkel-Röntgenstreuung
XRD	Röntgenbeugung

Teil I.

Allgemeiner Teil

1 | Einleitung

Die gezielte Synthese von Verbindungen mit gewünschten Eigenschaften stellt heutzutage immer noch eine große Herausforderung dar, da die Einflüsse von Syntheseparametern auf die Produktbildung zu großen Teilen nicht verstanden sind. Es sind nur wenige Faustregeln bekannt und ein tiefer gehendes Verständnis der Nukleationsprozesse und des Kristallwachstums fehlen vollständig.^[1] Aus diesem Grund wurden eine Vielzahl an Charakterisierungsmethoden zur *in situ* Verfolgung von Reaktionen adaptiert, die meist jedoch das Arbeiten an Großforschungseinrichtungen voraussetzen. Vor allem Streumethoden wie Kleinwinkelstreuung,^[2-5] Röntgenabsorptionsspektroskopie,^[6,7] energiedispersive oder winkeldispersive Röntgenbeugung;^[8,9] spektroskopische Methoden wie Infrarot- und Raman-Spektroskopie^[10,11] NMR-Spektroskopie^[12,13] oder Massenspektromie^[14,15] sowie mikroskopische Methoden wie Röntgenmikroskopie,^[16] und Elektronenmikroskopie^[17,18] wurden angewendet. Hierdurch ist es möglich einen direkten Einblick in die Produktbildung zu gewinnen, kinetische Reaktionsparameter zu bestimmen oder metastabile Intermediate zu beobachten. Jede dieser spezifischen Methoden ist aufgrund ihrer lateralen und temporalen Beschränkungen nur in der Lage einen Teilbereich der Charakteristika einer Probe zu detektieren, welcher nur im idealen System Rückschlüsse auf die Gesamtheit der Probe erlaubt. Im realen System ist daher eine Kombination vielfältiger analytischer Ansätze nötig, um intrinsische und extrinsische Eigenschaften aufzuschlüsseln, ideal kristalline und fehlgeordnete Bereiche zu unterscheiden und im Idealfall Beziehungen zwischen atomaren, lokalen und makroskopischen Strukturen aufzudecken.^[1,6] Die neusten Generationen an Synchrotronstrahlungsquellen wie z.B. PETRA III oder das ESRF erlauben Zeitaufösungen und somit Informationen im Subsekunden Bereich. Diese Informationen sind nur teilweise durch *ex situ* Techniken zugänglich, da ein äußere Stimuli bei Abbruchexperimenten die Reaktionsbedingungen stark verändern und nicht gewährleistet ist, dass ein repräsentatives Bild des Kristallisationsprozess erhalten wird. Jedoch sind *in situ* Methoden apparativ und präparativ sehr aufwendig, sodass betreffende Studien immer noch rar sind. Viele der gewonnen Erkenntnisse sind meist nicht auf andere Verbindungsklassen übertragbar. Auf Grund dieser Schwierigkeiten und den dadurch bedingten geringen Kenntnisstands ist es nicht verwunderlich, dass Verbindungen mit herausragenden Eigen-

schaften von der Theorie vorhergesagt werden, jedoch nicht immer präparativ zugänglich sind.^[19,20]

Eine Verbindungsklasse, die solch herausragende Eigenschaften zeigt sind die sogenannten anorganisch-organischen Hybridverbindungen, die auch Koordinationspolymere oder Metal-Organic Frameworks genannt werden.^[21] Diese können, bedingt durch ihre Porosität und ihren modularen Aufbau, potentiell Anwendungen in der Gasspeicherung^[22–25], Katalyse,^[26] als medizinische Trägermaterialien^[27–29] bzw. als optische^[30] oder magnetische Materialien^[31] finden. Anorganisch-organischen Hybridverbindungen sind aus anorganischen Einheiten, die über organische Linkermoleküle verbrückt werden, aufgebaut. Als organische Linker kommen hierbei z.B. Carbonsäuren, Phosphonsäuren oder Sulfonsäuren in Frage.^[21,32]

Der modulare Aufbau bewirkt, das es möglich ist dieselben Netzwerktopologien zu erhalten, indem der organische Linker ersetzt wird, wodurch neue maßgeschneiderte Eigenschaften erzeugt werden. Dies wird als „isoretikuläre Synthese“ oder „Scale Chemistry“ bezeichnet.^[33,34] Werden hierbei zu große Hohlräume im Netzwerk erzeugt kann es zur Interpenetration kommen. Bei diesem Phänomenen durchdringen sich zwei unabhängige Netzwerke und wirken dadurch der Bildung von Poren entgegen. Dieses Konzept der „isoretikuläre Synthese“ oder „Scale Chemistry“ konnte für Metallcarboxylate eindrucksvoll aufgezeigt werden, ist jedoch in der Phosphonatchemie äußerst selten beschrieben.^[21,24] Dies liegt vor allem in der hohen Koordinationsflexibilität von Phosphonatgruppen begründet.

Obwohl eine riesige Anzahl an anorganisch-organischen Hybridverbindungen bekannt sind und die Anzahl an neuen Verbindungen fast exponentiell ansteigt, ist über die Synthese und die gezielte Syntheseplanung dieser Verbindungen sehr wenig bekannt. Es wurden bisher nur sehr wenige *in situ* Studien durchgeführt, die sich mit der Synthese von anorganisch-organischen Hybridverbindungen beschäftigen.^[35–42] Insbesondere bei der Kristallisation aus Lösungen können kristalline Intermediate beobachtet werden. Durch strukturelle Charakterisierung dieser können neue Erkenntnisse über die Kristallisationsmechanismen gewonnen werden, da die Intermediate hierbei ein lokales Minimum auf der Energiehyperfläche repräsentieren. Die Kenntnis der Kristallstruktur ist für das Verständnis des Bildungsmechanismus unabdingbar, wodurch die Strukturbestimmung dieser kristallinen Materialien zu einer der wichtigsten Charakterisierungsmethoden zählt.

Auf Grund der Metastabilität und des kurzen Stabilitätsfensters der Intermediate werden oft nur mikrokristalline Pulver erhalten, sodass die Kristallstrukturbestimmung rou-

tinemäßig nicht möglich ist. In jüngster Zeit können bei Nanometer großen Einkristallen Elektronenbeugungsdaten zur Kristallstrukturbestimmung genutzt werden, die z.B. mittels Automated Diffraction Tomography gewonnen werden.^[43,44] Diese Methode ist heute jedoch nur auf eine eng begrenzte Anzahl an Verbindungen anwendbar, da die Datensätze meisten sehr unvollständig sind oder die Proben auf Grund der Strahlungsempfindlichkeit erst gar nicht vermessen werden können. Besonders metastabile Verbindungen können sich durch eine lokale Erhitzung schnell in die thermodynamisch stabilere Phase umwandeln, was die Strukturbestimmung erschwert.^[45]

Bei mikrokristallinen Pulvern können Kristallstrukturen unter Umständen aus Röntgenpulverdaten bestimmt werden. Das dies überhaupt wegen des limitierten Informationsgehalts von Pulverdaten im Vergleich zu Einkristalldaten möglich ist, ist einer Vielzahl von Gründen zu verdanken. Ein Grund liegt in der technisch immer besser werdenden Instrumentierung. Neue Synchrotronstrahlungsquellen mit höherer Brillianz und niedriger Divergenz, neue fokussierende Röntgenoptiken und Detektorgenerationen wie Halbleiterdetektoren sind zugänglich. Ebenso tragen die immer besser werdende Computerleistung und Software zum Erfolg bei. Die Software wird immer weiter entwickelt, neue Software geschrieben oder alte an die Verwendung mit Röntgenpulverdaten angepasst. Vor allem die rasante Entwicklung von Realraummethoden,^[46,47] der Maximum Entropy Methode^[48,49] oder auch Charge Flipping,^[50-52] ermöglichen heutzutage die Strukturlösung auch wenn konventionelle direkte Methoden fehlschlagen. Trotz der vielen Bemühungen auf diesem Gebiet ist und bleibt die Strukturlösung aus Pulverdaten keine Standardmethode und ist keineswegs trivial.

Ziel dieser Arbeit war die systematische Untersuchung und Synthese neuer Metallphosphate und Bismutcarboxylate. Hierfür sollten große Ausschnitte aus dem Parameterraum systematisch mittels Hochdurchsatzmethoden untersucht werden. Die Kristallisation der neu erhaltenen Verbindungen sollte mittels *in situ* Methoden untersucht werden. Dabei sollte überprüft werden ob im Gebiet der Metallphosphonate und Bismutcarboxylate kristalline Intermediate während der Produktbildung auftreten.

2 | Präparative Methoden

2.1. Solvothermalsynthese

Eine geeignete und gut etablierte Methode zur Synthese von anorganisch-organischen Hybridverbindungen ist die Solvothermalsynthese. Hierbei werden in einem abgeschlossenen Reaktor die Edukte mit einem Lösungsmittel oberhalb dessen Siedepunktes erhitzt. Hierdurch baut sich ein autogener Druck auf, sodass sich die chemischen und physikalischen Eigenschaften des Lösungsmittels drastisch ändern.^[53] Wird Wasser als Lösungsmittel verwendet, nimmt mit steigender Temperatur und Druck, die Löslichkeit der Edukte im Allgemeinen zu, der pH-Wert ab, die Viskosität ab und die Dielektrizitätskonstante zu. Solvothermalsynthesen finden u.a. Anwendung um kinetisch stabile Produkte zu erhalten, die z.B. im Vergleich zu konventionellen Hochtemperatursynthesen nicht zugänglich sind. Ebenso werden ungewöhnliche Oxidationsstufen oder anders nicht zugängliche Tieftemperaturphasen erhalten. In der Arbeitsgruppe Stock stehen, wie in Abbildung 2.1 gezeigt, für die Solvothermalsynthese Teflonreaktoren in Stahlautoklaven oder Glasreaktoren zur Verfügung.



Abbildung 2.1.: Schematische Darstellung eines Stahlautoklaven mit Tefloneinsätzen (**links**), die im Arbeitskreis verwendeten Reaktoren (**mitte**) und die verwendeten Glasreaktoren (**rechts**).

Die Wahl der Reaktoren hängt von den Reaktionsbedingungen ab. So können z.B. in

Glasreaktoren keine fluoridhaltigen Lösungsmittel oder starke Basen eingesetzt werden, da der Reaktor angegriffen würde. Teflon hingegen kann nicht bei zu hohen Temperaturen (ca. 210 °C) verwendet werden, da Teflon oberhalb dieser Temperatur zu fließen beginnt.

2.2. Mikrowellenunterstützte Solvothermalreaktionen

In der organischen Chemie werden bereits seit Mitte der 80er Jahre mikrowellenunterstützte Reaktionen durchgeführt.^[54,55] Hierbei konnte gezeigt werden, dass höhere Ausbeuten und reinere Produkte erhalten werden. Während konventionelle Solvothermalsynthesen oft Stunden oder Tage benötigen, finden mikrowellenunterstützte Reaktionen in Sekunden oder Minuten statt. Daher werden mikrowellenunterstützte Reaktionen auch immer häufiger in der anorganischen Synthesechemie angewendet, wie z.B. in der Darstellung von Zeolithen, ZIFs, Metalloxiden oder Nanopartikeln.^[56-60]

Mikrowellenunterstützte Reaktionen beruhen auf der Wechselwirkung von Mikrowellenstrahlung (0.3 - 300 GHz) und mobilen elektrischen Ladungen wie z.B. polaren Lösungsmitteln oder Ionen. Die verschiedenen Wechselwirkungsmechanismen sind in Abbildung 2.2 gezeigt. In Lösung versuchen sich die polaren Lösungsmittelmoleküle entlang des elektrischen Feldes auszurichten. Da das Feld oszilliert kommt es zu einer kontinuierlichen Bewegung der Moleküle. Die damit verbundenen Stöße initiieren hierbei eine höhere kinetische Energie und als Folge dessen einen Anstieg der Temperatur in dem System.^[54]

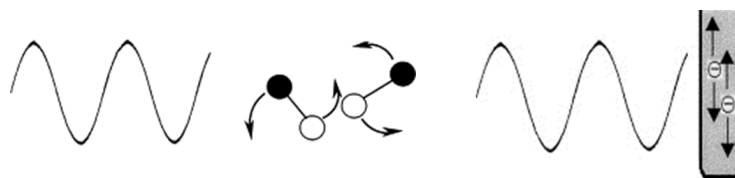


Abbildung 2.2.: Schematische Darstellung der verschiedenen Wirkungsweisen von Mikrowellenstrahlung auf polare Lösungsmittelmoleküle (**links**) und Ionen (**rechts**).^[54]

Durch die Wechselwirkungen wird das Lösungsmittel direkt und nicht über thermische Konvektion erwärmt, wodurch höhere Heizraten erreicht werden. Mikrowellenunterstützte Reaktionen wurden bereits an anorganisch-organischen Hybridverbindungen angewendet.^[61] Ziel hierbei war es, die Reaktion zu beschleunigen, Nanopartikel herzustellen oder die Ausbeute zu erhöhen.^[28,62-66] In der Arbeitsgruppe Stock wird der in Abbildung 2.3 gezeigte Mikrowellenreaktor Initiator der Fa. Biotage benutzt in den abgeschlossene Glasreaktionsgefäße mittels Roboterarm eingebracht werden können. Die Leistung wird hierbei an

die gewünschte Reaktionstemperatur angepasst. Diese wird mittels IR-Sensor durchgängig kontrolliert.

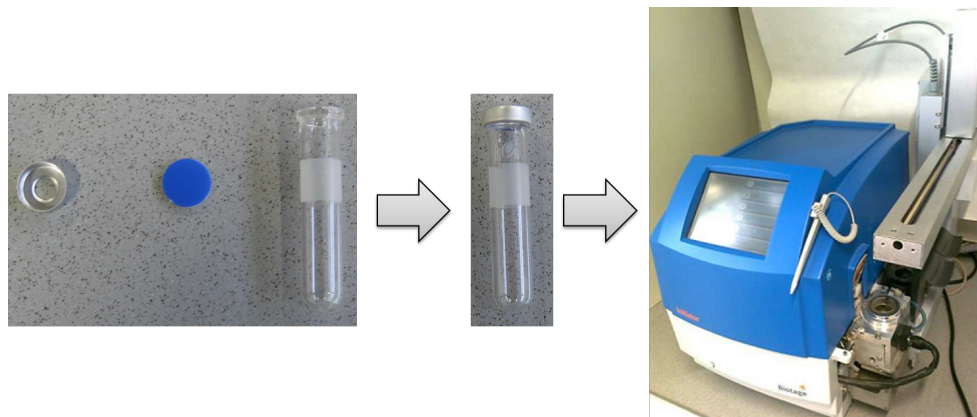


Abbildung 2.3.: Links: Reaktionsgefäß für mikrowellenunterstützte Reaktionen die mittels Septum verschlossen werden. Rechts: Verwendeter Mikrowellenreaktor des Typs Initiator der Fa. Biotage.

2.3. Hochdurchsatzmethoden

Die Synthese und Syntheseoptimierung neuer Verbindungen stellt eine große Herausforderung dar. Bei Kristallisationen aus Lösungen wie z.B. bei Solvothermalsynthesen, ist häufig ein enormer Aufwand an explorativer Arbeit nötig, um neue Verbindungen phasenrein und mit hoher Kristallinität zu erhalten, da Einflüsse der verschiedenen Syntheseparameter auf die Produktbildung nicht vorhersagbar sind. Dies hat neben einem hohen Zeitaufwand auch einen hohen Chemikalienverbrauch zur Folge.

Einen möglichen Ansatz zur Lösung dieses Problemes bieten Hochdurchsatzmethoden.^[67,68] Hierbei werden 24 oder 48 miniaturisierte Teflonreaktoren parallelisiert einem gemeinsamen Temperaturprogramm unterworfen. Die Arbeitsschritte wie Dosierung oder Charakterisierung werden hierbei möglichst automatisiert. Ein typischer Arbeitsablauf ist in Abbildung 2.4 gezeigt. Hochdurchsatzmethoden erlauben Ausschnitte aus dem komplexen Parameterraum gezielt und systematisch zu untersuchen. Dieses Wissen kann unter Umständen zur gezielten Synthese von neuen Verbindungen nutzbar sein.^[69-71]

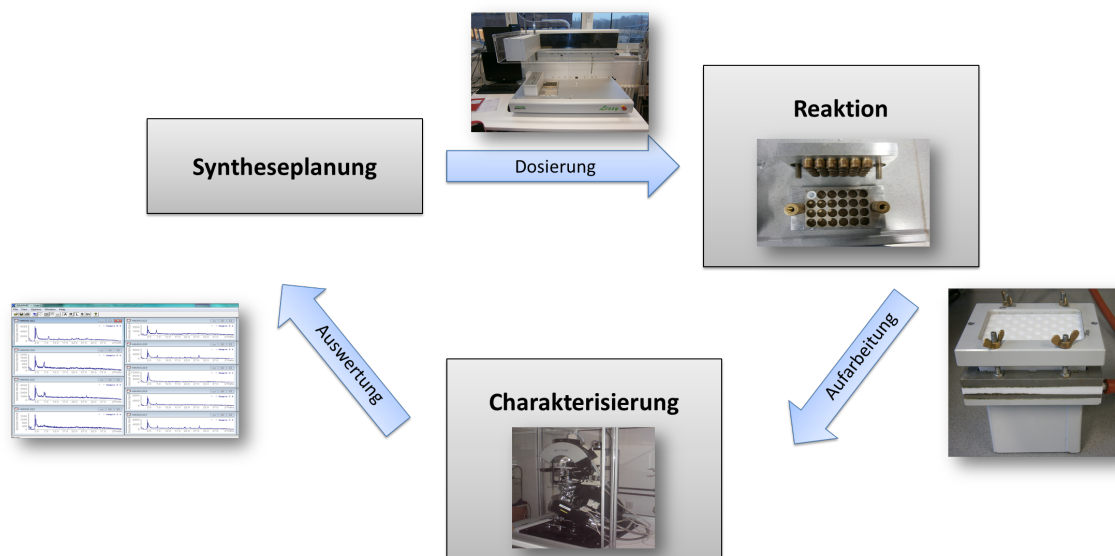


Abbildung 2.4.: Schematische Darstellung des Ablaufs der Hochdurchsatzmethodik.

Zu Beginn eines jeden Experiments steht die Syntheseplanung. Die Versuche werden im nächsten Schritt automatisiert mit einem Pipettierroboter in den Hochdurchsatzmultiklaven dosiert. Die Reaktoren werden anschließend, nach optionaler Alterung im Ofen einem gemeinsamen, definierten Temperaturprogramm unterworfen. Nach beendeter Synthese werden die Produkte in einer speziellen Filtriereinheit isoliert und zur Aufarbeitung gewaschen. Anschließend werden die Proben automatisch durch Röntgenpulverbeugung charakterisiert. Die Daten werden analysiert und die Ergebnisse fließen in die folgende Syntheseplanung wieder ein. Eine schematische Darstellung eines Reaktors und der Filtriereinheit ist in Abbildung 2.5 gezeigt.

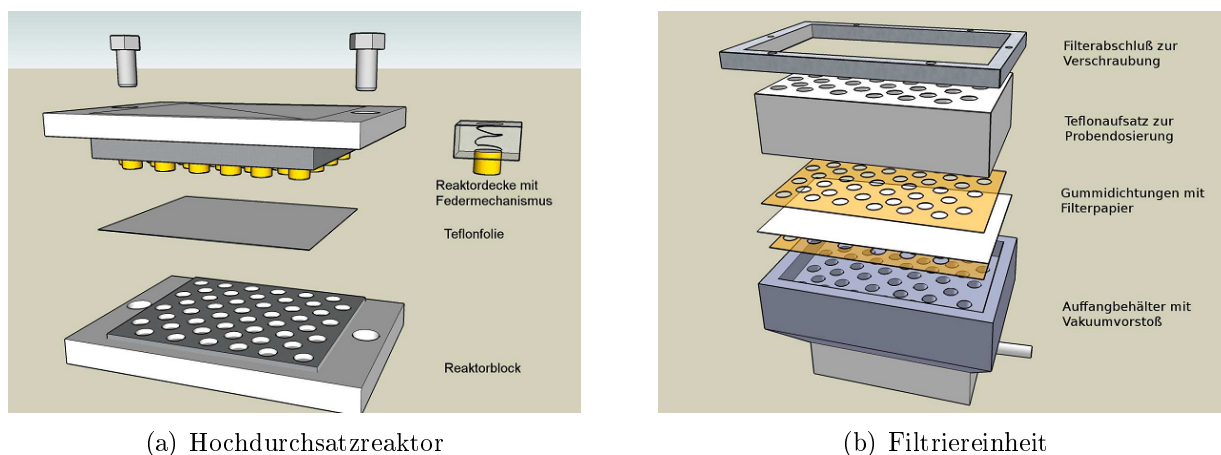


Abbildung 2.5.: Schematische Darstellung eines 48er Hochdurchsatzreaktors (links) und schematische Darstellung der in dieser Arbeit verwendeten Filtriereinheit (rechts).^[72]

In den letzten Jahren konnte mittels Hochdurchsatzmethoden eine Vielzahl an neuen Verbindungen synthetisiert werden. Im Bereich der anorganisch-organischen Hybridverbindungen wurde der Einfluss des Lösungsmittels,^[69] des pH-Wertes,^[73–76] der molaren Verhältnisse,^[71,73–76] der Temperatur,^[75,77] der Länge der organischen Einheit,^[71,76] des Ionenradiuses^[70,74] oder des Wassergehaltes auf die Produktbildung systematisch untersucht.^[67]

2.4. Mikrowellenunterstützte Hochdurchsatzmethoden

Ebenso wie konventionelles Heizen im Ofen hat sich in den letzten Jahren mikrowellenunterstütztes Heizen für Hochdurchsatzreaktionen etabliert.^[71,78] Der im Arbeitskreis Stock verwendete Hochdurchsatz Mikrowellen Reaktor ist in Abbildung 2.6 gezeigt.

2. Präparative Methoden



Abbildung 2.6.: Der Mikrowellen Reaktor Synthos 3000 der Firma Anton Paar (links), der Rotor (mitte) und die verwendeten Mikrowellenreaktoren (rechts).

Für die Synthesen werden, die in Abbildung 2.6 rechts gezeigten, Glasreaktoren verwendet. Diese werden mit einer Teflondichtung versehen und mit einer Schraubkappe verschlossen. Die Reaktoren erlauben ein Füllvolumen von 2 mL und werden in einen Siliciumcarbid-Reaktor passgenau eingesetzt. Die Reaktoren werden über den Siliciumcarbidblock nur indirekt geheizt. Der Block wiederum wird über ein Magnetron erhitzt und die Temperatur über einen IR-Sensor gemessen.

3 | Charakterisierungsmethoden

Die in dieser Arbeit verwendeten Charakterisierungsmethoden sind in Tabelle 3.1 zusammengefasst. Im Folgenden werden lediglich die Röntgenbeugungsmethoden näher erläutert, da diese den Hauptteil der Arbeit ausmachen.

3. Charakterisierungsmethoden

Tabelle 3.1.: In dieser Arbeit verwendete Charakterisierungsmethoden.

	<i>Gerät</i>	<i>Bemerkungen</i>
Einkristall- diffraktometrie	Stoe IPDS I / II	MoK $_{\alpha}$, Image Plate Detektor
	Bruker D8 3-circle diffractometer	MoK $_{\alpha}$, Apex II CCD Detektor
Pulver- diffraktometrie	Stoe Stadi P HT	CuK $_{\alpha 1}$, Phasenidentifizierung
	Stoe Stadi P	CuK $_{\alpha 1}$, PSD Detektor
	Panalytical Empyrean	CuK $_{\alpha 1/2}$, PixCell Detektor
	HASYLAB, Doris Beamline G3	Kapillarmessung, Transmission, Szitillationszähler
	HASYLAB, PETRA Beamline P08	Kapillarmessung, Transmission, Mythen Detektor
IR-Spektroskopie	Bruker Alpha P	ATR Einheit 4000-400 cm^{-1}
Raman- Spektroskopie	Bruker DSX Advance	0-3300 cm^{-1}
Elektronen- mikroskopie / EDX	Philips ESEM XL 30	Rasterelektronenmiroskopische Aufnahmen und EDX Analyse
	JEOL JSM-6500F	Rasterelektronenmiroskopische Aufnahmen
DTA / TG	Netsch STA-409CD	Luftrom 75 ml/min
<i>in situ</i> Röntgen- beugung	HASYLAB, Doris, F3	Energiedispersiv, Ge Halbleiter- detektor
ADT	FEI Tecnai F30	TEM 300 kV mit CCD Kamera
NMR-Spektroskopie	Bruker DRX 500	1H -NMR, ^{31}P -NMR in Lösungen
CHNS-Analyse	EuroEA3000	
Volumetrische Gas- sorption	BEL JAPAN INC. Belsorp $_{max}$	N $_2$, H $_2$, CO $_2$, H $_2$ O Gasadsorption bis 1 bar
Suszeptometer	Lake Shore Cryomatic AC Suszeptometer	AC und DC Messungen

3.1. Röntgenbeugung

Bei der Röntgenbeugung handelt es sich um ein elastisches Streuphänomen an Kristallen. Ein Kristall zeichnet sich durch eine dreidimensionale periodische und regelmäßige Anordnung von Atomen aus. Der Kristall und seine Kristallstruktur kann durch eine translationsperiodische Anordnung von Elementarzellen, in der sich die Atome befinden, beschrieben werden. Diese lässt sich durch die Zellparameter a, b, c und die Winkel α, β, γ definieren.

Wird eine kristalline Probe mit einem Röntgenstrahl bestrahlt, wird dieser an den Elektronenhüllen der Atome gebeugt. Der Kristall wirkt hierbei als ein dreidimensionales Beugungsgitter. Die austretenden Wellen durchlaufen je nach dem Ort im Kristall, an dem sie gebeugt werden verschiedene Wegstrecken. Die austretenden Strahlen interferieren miteinander und es resultiert aus ihrer Superposition ein für den Kristall und die Kristallstruktur charakteristisches Beugungsbild. Bragg nahm an, dass es sich bei dem Beugungsphänomen um Reflexion der Röntgenstrahlung an Netzebenen, die durch den Kristall verlaufen, handelt. Netzebenen sind fiktive Ebenen, die durch ihre Lage in der Elementarzelle des Kristalls fest definiert sind. Die Netzebenen werden meist nach den sogenannten Millerschen Indizes benannt, die sich aus den reziproken Schnittpunkten mit der Elementarzelle herleiten. In Abbildung 3.1 ist schematisch gezeigt, wie zwei Röntgenstrahlen auf zwei Netzebenen einer Netzebenenchar treffen.^[79]

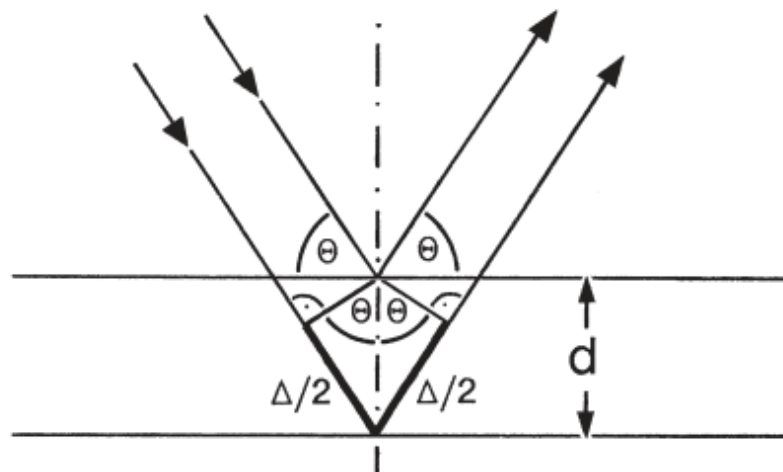


Abbildung 3.1.: Beugung an zwei Netzebenen. Hieraus resultiert der Gangunterschied Δ .^[79]

Beide Strahlen durchlaufen verschiedene Weglängen durch den Kristall. Je nach Gangunterschied kommt es zu konstruktiver oder destruktiver Interferenz. Durch Anwendung

3. Charakterisierungsmethoden

von trigonometrischen Zusammenhängen lässt sich die sogenannte Bragg'sche Gleichung aus Abbildung 3.1 herleiten (Gleichung 3.1)

$$n\lambda = 2d \sin \Theta \quad (3.1)$$

Hierbei ist n die Beugungsordnung, λ die Wellenlänge, d der Netzebenenabstand und Θ der Beugungswinkel. Ist der Gangunterschied Δ ein ganzzahliges Vielfaches der Wellenlänge, kommt es zur konstruktiven Interferenz. Ist der Gangunterschied ein halbes vielfaches der Wellenlänge, kommt es zur destruktiven Interferenz. Hieraus ergibt sich ein charakteristisches Beugungsbild für einen Kristall. Aus der Bragg'schen Gleichung ist ersichtlich, dass die Reflexposition von den Netzebenenabständen d abhängig ist, also nur von der Zellmetrik. Die Intensität eines Reflexes ist laut Gleichung 3.2 proportional zum Betragsquadrat des Strukturfaktors F . Die Intensitäten können durch Integration eines Reflexes aus einem Beugungsexperiment gewonnen werden.^[79]

$$I \propto |F_{hkl}|^2 \quad (3.2)$$

Der Strukturfaktor wiederum ist mit den Atomkoordinaten in der Elementarzelle über die sogenannte Strukturfaktorgleichung verknüpft (Gleichung 3.3).

$$F_{hkl} = \sum_{j=1}^N f_j \cdot \exp\left(-B \frac{\sin^2 \Theta}{\lambda^2}\right) \exp(2\pi i (hx_j + ky_j + lz_j)) \quad (3.3)$$

Hierbei ist f_j der Atomformfaktor, B der Temperaturfaktor, und x, y, z die Koordinaten der Atome in der Elementarzelle. Der Atomformfaktor ist eine atomspezifische Größe, die das Streuvermögen eines Atoms beschreibt. Er ist abhängig von der Elektronenzahl des jeweiligen Atoms und vom Beugungswinkel. Die typische Winkelabhängigkeit des Atomformfaktors für Wasserstoff, Kohlenstoff und Eisen ist in Abbildung 3.2 gezeigt.

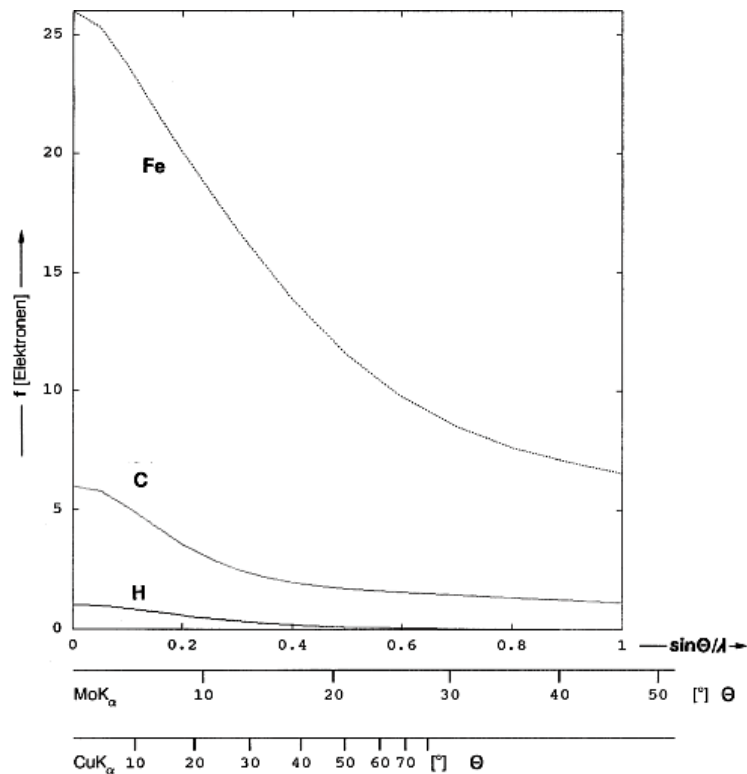


Abbildung 3.2.: Typischer Verlauf des Atomformfaktors für Wasserstoff, Kohlenstoff und Eisen. ^[79]

Aus Abbildung 3.2 wird ersichtlich, dass die Intensitäten von Reflexen mit zunehmenden Beugungswinkeln kleiner werden. Atomsorten, die im Periodensystem eng benachbart sind, können ebenso wie unterschiedliche Oxidationsstufen einer Atomsorte, mittels Röntgenstrukturanalyse nicht unterschieden werden. Die Abnahme der Intensität resultiert aus der endlichen Ausdehnung der Elektronendichte der Atome, an denen gebeugt wird. Mit zunehmendem Beugungswinkel wird der Anteil an destruktiver Interferenz immer größer und dadurch auch die Intensität des Reflexes geringer.

Der Temperaturfaktor B berücksichtigt die Schwingungen der Atome in der Elementarzelle. Dies muss berücksichtigt werden, da bei einem Röntgenbeugungsexperiment über einen Zeitraum von Minuten bis Tagen gemittelt wird. Das Atom selbst durchläuft dabei eine Vielzahl an Schwingungsperioden. Die Schwingung eines Atoms entlang einer imaginären Achse ist in Abbildung 3.3 zeigt. Als Ergebnis wird eine über die Schwingungsamplituden „verschmierte“ Elektronendichte erhalten. Im einfachsten Fall werden diese Ausdehnungen der Elektronendichte als isotrope Kugeln betrachtet. Eine bessere Näherung stellen jedoch Ellipsoide wie in Abbildung 3.4 gezeigt dar.

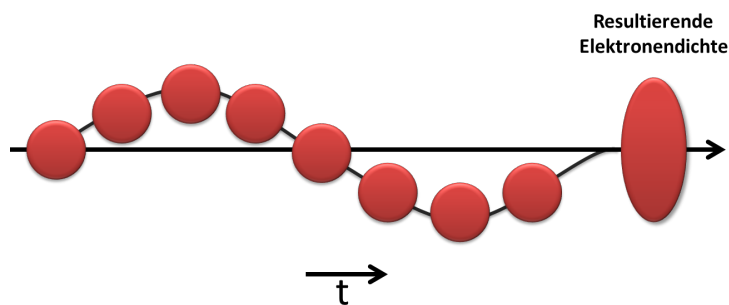


Abbildung 3.3.: Die Schwingung eines kugelförmigen Atoms. Die resultierende Elektronendichte ist rechts gezeigt.

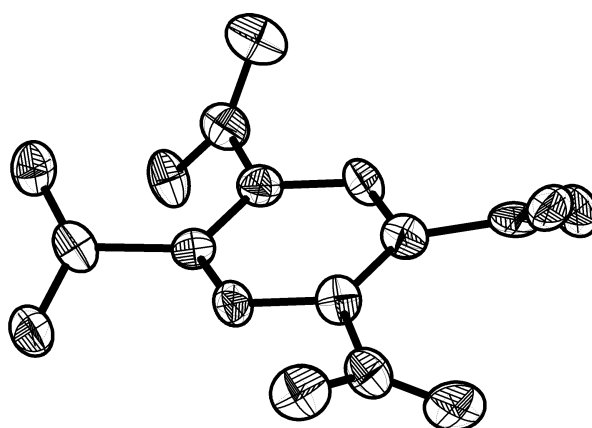


Abbildung 3.4.: Resultierende Schwingungsellipsoide des organischen Moleküls Pyromellitsäure mit 50% Aufenthaltswahrscheinlichkeit. Die Wasserstoffatome wurden zur besseren Übersicht weggelassen.

3.2. Einkristallstrukturanalyse

Wird ein Einkristall mit monochromatischer Röntgenstrahlung bestrahlt und der gebeugte Strahl detektiert, werden diskrete Beugungsmaxima (vgl. Abb. 3.5) beobachtet. Aus den Abständen der Reflexe können die Zellparameter bestimmt werden. Im Beugungsbild wird beobachtet, dass bestimmte Reflexe keine Intensität besitzen, d.h. ausgelöscht sind. Dieses ist auf Translationsymmetrien in der Elementarzelle zurückzuführen. Je nach Ursprung wird zwischen der integralen, der zonalen und der seriellen Auslöschung unterschieden, die alle für verschiedene Auslöschungen sorgen. Die integrale Auslöschung wird durch die Zen-

trierungen, also dem Bravais Gitter verursacht. Die zonale Auslöschung wird durch Gleit-
spiegelebenen und die serielle Auslöschung durch Drehspiegelachsen verursacht. Aus diesen
Auslöschungen wird eine vorläufige Raumgruppe bzw. Auslöschungsgruppe bestimmt. Die
Bestimmung der Raumgruppe wird weiterhin noch erschwert, da auch Reflexe durch die
Kristallstruktur bedingt eine niedrige bzw. keine messbare Intensität aufweisen.

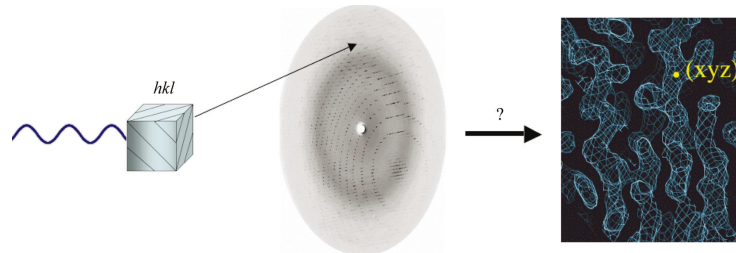


Abbildung 3.5.: Schematische Vorgehensweise einer Einkristallstrukturanalyse. Ein Einkristall wird Röntgenstrahlung ausgesetzt, die Beugungsmaxima werden vermessen und heraus eine Elektronendichtekarte bestimmt.^[80]

Sind die Elementarzelle und eine mögliche Raumgruppe bekannt, werden für die Strukturlösung noch die Strukturformfaktoren benötigt. Diese hängen nach Gleichung 3.2 mit der Intensität der Reflexe zusammen, die aus der Messung erhalten wurden. Der Strukturformfaktor ist eine Vektorgröße und setzt sich aus der Amplitude $|F_{hkl}|$ und einer Phase ϕ (Gleichung 3.4) zusammen.

$$I_{hkl} = |F_{hkl}|^2 e^{i\phi(hkl)} \quad (3.4)$$

Die Phaseninformation geht bei der Messung verloren und kann nicht experimentell bestimmt werden. Dies ist das sogenannte Phasenproblem. Zur Lösung des Phasenproblems können Patterson Methoden,^[81,82] direkte Methoden^[83] oder Charge Flipping^[84–86] verwendet werden. Unter Kenntnis der Amplituden und der Phase kann mittels Fouriertransformation eine Elektronendichtekarte nach Gleichung 3.5 bestimmt werden.

$$\rho(xyz) = \frac{1}{V} \sum_{hkl} |F_{hkl}|^2 e^{i\phi(hkl)} e^{-2\pi i(hx+kx+lx)} \quad (3.5)$$

Die erhaltene Elektronendichtekarte wird dann interpretiert und den Elektronendichten der Atome zugeordnet.

3.2.1. Direkte Methoden

Im Folgenden sollen nur die direkten Methoden näher erläutert werden, da diese in der Arbeit zur Einkristallstrukturanalyse verwendet wurden. Direkte Methoden finden in der

Literatur am häufigsten Anwendung um das Phasenproblem zu lösen. Sie beruhen auf statistischen Zusammenhängen zwischen den Amplituden und den Phasen des Strukturfaktors.^[87] Der erste Schritt besteht darin, die Amplituden auf Erwartungswerte zu normalisieren, um diese durch verschiedene Beugungswinkel und Streukraft der Atome untereinander vergleichbar zu machen. Hierzu werden die Atomformfaktoren aller Atome in der Zelle in die Statistik einbezogen. Die Summenformel sollte hierfür möglichst genau bekannt sein. Im zentrosymmetrischen Fall gibt es nach der Sayre-Gleichung sogenannte Triplett-Beziehungen zwischen den Vorzeichen der Phasen im zentrosymmetrischen Fall.

$$S(hkl) \approx S(h'k'l') \cdot S(h - h', k - k', l - l') \quad (3.6)$$

Die Triplett-Beziehung gilt besonders für sehr intensive Reflexe. Diesen werden willkürliche Phasen zugeordnet, die die Triplett Beziehung erfüllen. Hieraus kann nun eine erste Elektronendichtekarte berechnet werden. Wurden hinreichend viele Phasen richtig zugeordnet, können Atompositionen der schwersten Atome auf der Elektronendichtekarte lokalisiert werden.^[79] Die Strukturlösung der Röntgeneinkristallestrukturanalysen geschah in dieser Arbeit mit dem Programm ShelXS^[88] und die Lösung der aus Elektronenbeugung gewonnenen Einkristalldaten mit dem Programm Sir2011.^[89]

3.2.2. Strukturverfeinerung

Mit Hilfe direkter Methoden können meist nur wenige Atome lokalisiert werden. Daher werden nach der Strukturlösung in den nächsten Schritten mittels Differenz-Fourier-Analyse übriggebliebene Restelextronendichten zugeordnet. Je mehr Atome in der Zelle bekannt sind, desto mehr Phasen können korrekt berechnet werden.

$$\Delta\rho(xyz) = \frac{1}{V} \sum_{hkl} (F_{hkl}^{obs} - F_{hkl}^{calc}) e^{-2\pi i(hx+ky+lz)} \quad (3.7)$$

Dabei wird das aktuelle Strukturmodell gegen das kleinste Fehlerquadrat (vgl. Gleichung 3.8) verfeinert. Die Atomkoordinaten sowie thermische Auslenkungsparameter werden dann weiter verfeinert, wobei die Reflexe durch einen Wichtungsfaktors w gewichtet werden.

$$\Delta = \sum_{hkl} w \left(|F_{hkl}^{obs}| - |F_{hkl}^{calc}| \right)^2 \quad (3.8)$$

Nach jedem Verfeinerungszyklus wird eine neue Elektronendichtekarte erstellt und dieser Atome zugeordnet. Dies wird solange wiederholt bis das Strukturmodell vollständig ist. Im Anschluss wird eine Absorptionskorrektur durchgeführt. Durch die anisotrope Form des Kristalls durchläuft der Röntgenstrahl je nach Orientierung des Kristalls verschieden lange Strecken durch diesen und wird dabei auch verschieden stark durch Absorption abgeschwächt. Dadurch kommt es zu Fehlbestimmung von Intensitäten. Dies kann z.B. mit Hilfe einer numerischen Absorptionskorrektur korrigiert werden. Hierbei werden die Intensitäten von Symmetrieäquivalenten miteinander verglichen. Wurden die Intensitäten korrekt bestimmt müssen diese gleich sein. Die Differenz wird unter Zuhilfenahme eines Kristallmodells nun numerisch angepasst und die Intensitätsdifferenzen korrigiert. Die Verfeinerungen wurden in dieser Arbeit mit dem Programm ShelXL durchgeführt.^[88]

3.3. Röntgenpulverdiffraktometrie

Im Falle der Röntgenpulverbeugung wird nicht ein makroskopische Einkristall vermessen sondern im Idealfall eine unendliche Anzahl an mikrokristallinen Kristalliten. Hierbei werden im Beugungsbild keine diskreten und aufgelösten Reflexe beobachtet, sondern jeder einzelne Kristall verursacht eigene Reflexe, die jedoch anders zueinander im Raum orientiert sind (vgl. Abbildung 3.6). Im Idealfall werden nur noch die sogenannten Debye Scherrer Ringe beobachtet. Das eigentliche Pulverdiffraktogramm ist ein Schnitt durch diese Debye Scherrer Ringe. Als Folge dessen überlagern sich viele Reflexe, sodass der Informationsgehalt eines Pulverdiffraktogramms stark reduziert ist. Trotzdem ist Röntgenpulverdiffraktometrie eine unverzichtbare Standardmethode zur Phasenanalyse und -identifizierung.

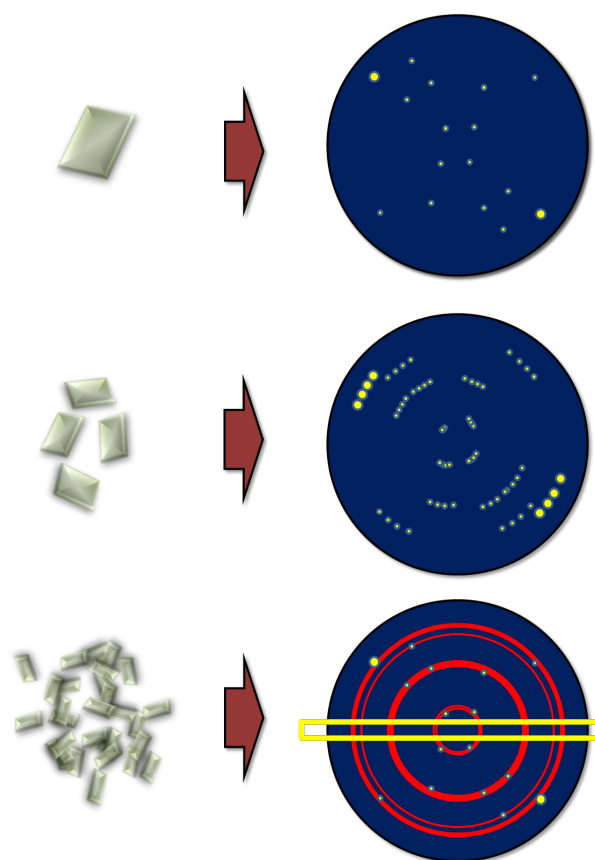


Abbildung 3.6.: Schematische Darstellung von Röntgenbeugung an einem Einkristall (oben), einer Vielzahl an Kristallen (mitte) und einem idealen Pulver (unten).

3.4. Strukturlösung aus Pulverdaten

Trotz des geringeren Informationsgehaltes ist es unter Umständen möglich Strukturen aus Röntgenpulverdaten zu lösen. Die Gründe hierfür sind vielseitig. Neue Generationen an Synchrotronstrahlungsquellen wie z.B. PETRA III und neue Detektorgenerationen wie Halbleiterdetektoren erlauben die Aufnahme von immer hoch aufgelösteren Pulverdiffraktogrammen. Die Verringerung der instrumentbedingten Reflexverbreiterung sorgt für besser aufgelöste Reflexe und die Intensitäten können genauer aus dem Pulverdiffraktogramm extrahiert werden. Die Software zur Auswertung von Pulverdiffraktogrammen wird seit Jahren stetig verbessert, was immer bessere Algorithmen zur Folge hat, wie z.B. in EXPO^[90-92] oder Fox^[47,93-95]. Sämtliche Schritte sind jedoch im Vergleich zur Einkristallstrukturanalyse mit mehr Fehlern behaftet. Die einzelnen Schritte einer Strukturlösung aus Pulverdaten sollen kurz im Folgenden erläutert werden.

3.4.1. Indizierung und Raumgruppenbestimmung

Für eine Strukturlösung ist die Kenntnis der Elementarzelle unabdingbar. Diese Information lässt sich indirekt aus einem Pulverdiffraktogramm erhalten. Hierzu werden die hkl -Werte der jeweiligen Netzebenenabstände bestimmt. Es lassen sich eine Vielzahl an möglichen Elementarzellen aus den Netzebenenabständen rekonstruieren und es wurden Konventionen für die richtige Wahl der Elementarzelle aufgestellt.^[79]

Im Falle eines Einkristalls ist eine Indizierung relativ eindeutig, da die Reflexe räumlich voneinander getrennt sind. Die exakte Lage eines Reflexes in einem Pulverdiffraktogramm ist meistens schwerer zu bestimmen, da die Reflexe stark überlappen und über eine Vielzahl von Kristalliten gemittelt wurden. Im Regelfall werden zunächst die Reflexpositionen grob bestimmt und anschließend das Pulverdiffraktogramm mit einer mathematischen Profifunktion angepasst. Dadurch können die Reflexpositionen verfeinert werden. Oft werden auch in diesem Schritt überlappende Reflexe oder Reflexe von Fremdphasen in der Differenzkurve erkannt. Dann erst wird mit den verfeinerten Reflexposition eine Indizierung unternommen. Dafür stehen Algorithmen wie ITO,^[96,97] DICVOL,^[98,99] TREOR^[100] oder auch ein in Topas implementierter least-square Algorithmus zur Verfügung.^[101]

Wurde die Elementarzelle bestimmt, muss im nächsten Schritt eine mögliche Raumgruppe oder Auslöschungsgruppe bestimmt werden. Für eine erfolgreiche Strukturlösung ist die Kenntnis der richtigen Raumgruppe nicht unabdingbar, jedoch kann eine falsche Raumgruppe die Strukturlösung verhindern. Die Raumgruppe wird meistens über einen Le-Bail- oder Pawley-Fit bestimmt (s.u.). Dies ist z.B. in das Programmpaket Expo2009 implementiert.^[91] Hierbei wird mittels einer Profifunktion und der Kenntnis der Zellparameter das gesamte Pulverdiffraktogramm ohne Annahme einer Symmetrie angepasst ($P1$). Alle Reflexe mit geringer oder ohne Intensität werden als ausgelöscht angenommen und hieraus mögliche Raumgruppen vorgeschlagen. Programme wie Topas berücksichtigen dies sofort nach der Indizierung und überprüfen, welche Reflexe für die Indizierung verwendet wurden. Aus fehlenden Reflexen wird direkt eine mögliche Raumgruppe vorgeschlagen.^[101]

3.4.2. Strukturlösung

Die Intensitäten der einzelnen Reflexe werden im nächsten Schritt mittels Le-Bail- oder Pawley-Methoden (s.u.) extrahiert. Dabei kommt es durch das Überlappen der Reflexe meist zu einer Fehlbestimmung von Intensitäten. Das heißt, dass für die Strukturlösung nicht nur die Phasen unbekannt sind, sondern zusätzlich noch Amplituden falsch bestimmt

3. Charakterisierungsmethoden

wurden. Dies erschwert die Strukturlösung mittels direkter Methoden oder macht sie ganz unmöglich. Wird ein Teil der Intensitäten richtig bestimmt, können Strukturen manchmal trotzdem mittels direkter Methoden gelöst werden. Dies ist z.B. mit dem Programm Expo möglich.^[91] Entscheidend ist hierbei die Qualität des Pulverdiffraktogramms.

Falls die Anwendung direkter Methoden fehlschlägt können z.B. globale Optimierungsmethoden im Realraum verwendet werden. Diese können nur bei bekanntem Zelleninhalt einer Verbindung verwendet werden. Dabei muss die Kristallstruktur sich in Fragmente unterteilen lassen. Ein typischer Ablauf ist in Abbildung 3.7 gezeigt.

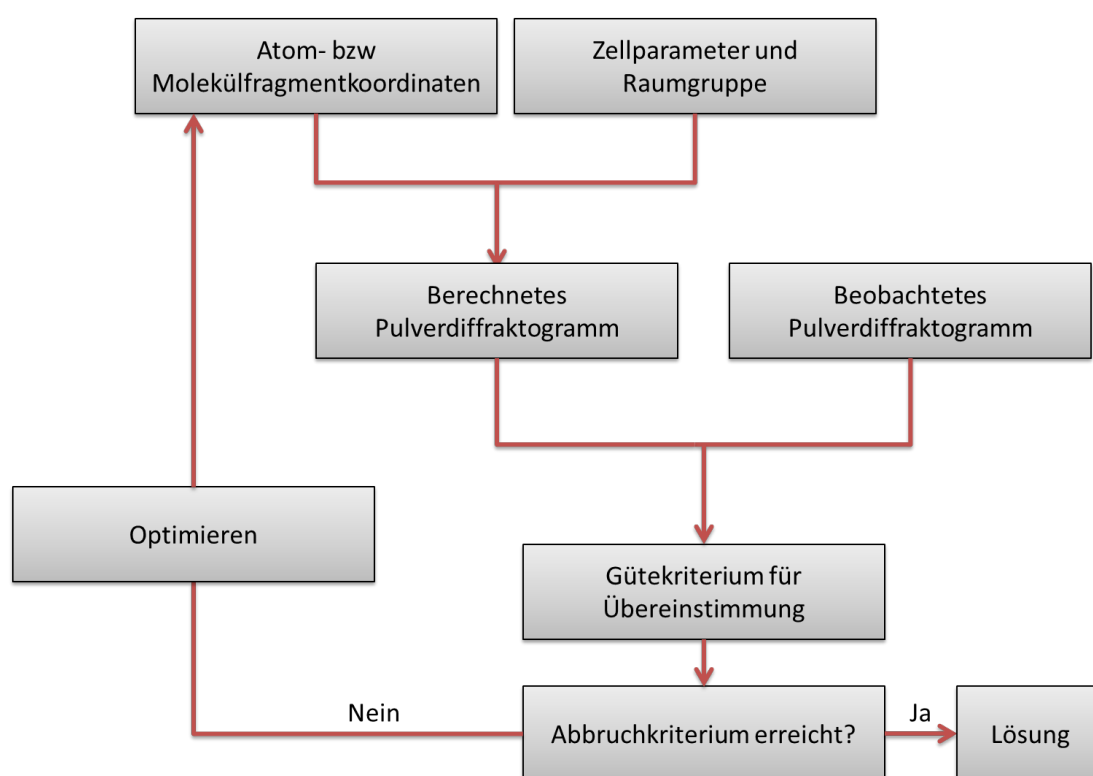


Abbildung 3.7.: Ablauf eines Optimierungsalgorithmus zur Kristallstrukturbestimmung aus Röntgenpulverdaten mittels Realraummethoden.^[102]

Die Zellparameter und die Raumgruppe müssen hierbei bekannt sein. Der Zelleninhalt wird zu Beginn an willkürliche Positionen in der Elementarzelle gelegt. Im nächsten Schritt wird ein Pulverdiffraktogramm berechnet, mit dem experimentellen verglichen und ein Gütekriterium für die Übereinstimmung abgefragt. Falls eine Konvergenz erreicht oder eine definierte Anzahl an Schritten durchgeführt worden ist, wird die Strukturlösung abgebrochen. Falls nicht, werden die Atom- oder Fragmentkoordinaten weiter in der Elementarzelle verschoben und danach erneut das experimentelle und berechnete Pulverdiffraktogramm

verglichen. Ziel des Vorgangs ist es das globale Minimum (gleichbedeutend mit der richtigen Struktur) (vgl. Abbildung 3.8) zu finden und nicht in einem lokalen Minimum zu enden. Hierbei werden Algorithmen wie Simulated Annealing oder Parallel Tempering in den Programmen FOX und Topas verwendet.^[103,104]

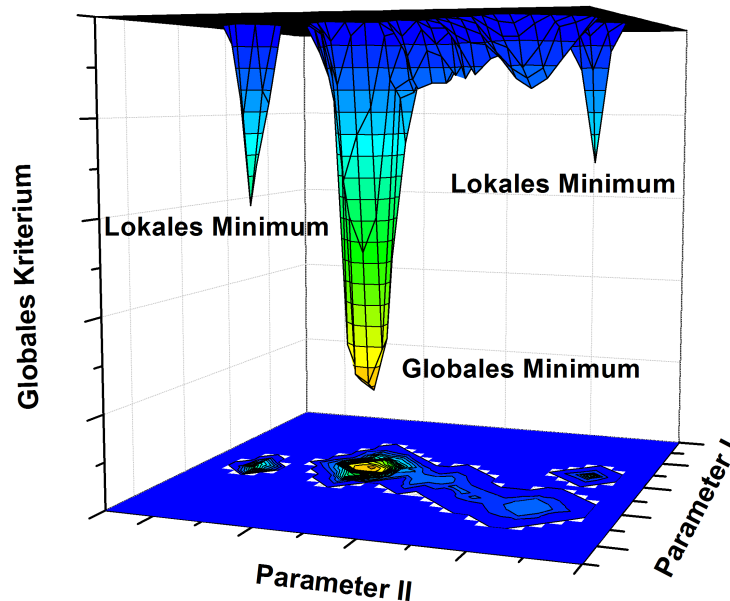


Abbildung 3.8.: Zweidimensionaler Schnitt durch einen x-dimensionalen Hyperraum.

Der Vorteil dieser Methode ist, dass sehr viel chemisches Wissen, wie die Kenntnis von Molekülfragmenten, in die Strukturlösung einfließen können und die Einzelintensitäten von überlappenden Reflexen nicht im voraus bestimmt werden müssen, sondern immer aus dem aktuellen Strukturmodell resultieren. Nachteile dieser Methoden sind jedoch der hohe Rechenaufwand und die damit verbundene hohe Rechenzeit.

3.4.3. Rietveld-Verfeinerung

Nachdem ein Strukturmodell erhalten worden ist, muss dieses noch verfeinert werden. Hierfür eignet sich bei Pulverdaten die Rietveld-Methode. Jeder Punkt im Pulverdiffraktogramm wird hierbei als Beobachtung gewertet. Dadurch ist es nicht mehr nötig die einzelnen Intensitäten von überlappenden Reflexen zu kennen, solange ein hinreichend gutes

Strukturmodell vorliegt. Jeder Punkt in einem Pulverdiffraktogramm ist gegeben durch:

$$I_i^{calc} = S_F \sum_{k=1}^{NReflexe} L_k |F_k|^2 \phi(2\Theta_i - 2\Theta_k) P_k A + bkg_i \quad (3.9)$$

Hierbei ist I_i^{calc} die Intensität des Messpunktes, S_F ein Skalierungsfaktor, L_k der Lorenzpolarisationsfaktor, $|F_k|^2$ der Strukturfaktor, P_k ein Korrekturfaktor für Vorzugsorientierungen, A ein Absorptionsfaktor und bkg_i der Korrekturterm für den Untergrund. Der Faktor $\phi(2\Theta_i - 2\Theta_k)$ ist hierbei die Profildfunktion, die die Reflexbreite und -form beschreibt. Die Intensitäten und Formen der Reflexe setzen sich hierbei zum Einen aus Anteilen der Struktur zusammen, zum Anderen aus Anteilen, die von dem verwendeten Pulverdiffraktometer verursacht werden. Ist das Instrument hinreichend gut beschrieben, beruht die Differenz allein auf Ungenauigkeiten in dem Strukturmodell und die strukturellen Parameter wie Atomkoordinaten und Temperaturfaktoren lassen sich iterativ nach der Methode des kleinsten Fehlerquadrats verfeinern. Am Ende der Verfeinerung sollte es keine Differenzen mehr zwischen dem beobachteten und dem berechneten Pulverdiffraktogramm geben.^[105]

3.4.4. Pawley- und Le-Bail-Verfeinerung

Die Pawley- und Le-Bail-Methoden sind Algorithmen zur Anpassung eines gesamten Pulverdiffraktogramms ohne Strukturmodell. Diese Methoden eignen sich zur Intensitätsextraktion für die Strukturlösung, Raumgruppenbestimmung und -überprüfung oder Zellparameterverfeinerung. Bei der Pawley-Verfeinerung werden eine Profildfunktion, die Zellparameter, der Untergrund und die Intensität eines jeden Reflexes als ein Parameter behandelt und simultan verfeinert.

Die Le-Bail-Methode führt im Prinzip eine Rietveld-Verfeinerung durch und verwendet Gleichung 3.9. Ohne ein Strukturmodell lässt sich jedoch kein Strukturfaktor berechnen. Daher werden zu Beginn alle Strukturfaktoren gleich gesetzt. Danach wird das gesamte Pulverdiffraktogramm iterativ angepasst. Die Le-Bail-Methode gilt im Vergleich zur Pawley-Methode als stabiler und schneller. Die Intensitäten von alleinstehenden Reflexen sind direkt nach dem ersten Schritt angepasst. Bei überlappenden Reflexen muss der Algorithmus die Strukturfaktoren schrittweise anpassen. Überlappen Reflexe komplett erhalten beide 50% der Intensität.^[106]

3.4.5. Experimentelle Methoden

Pulverdiffraktogramme zur Indizierung bzw. Strukturaufklärung wurden in dieser Arbeit im Labor an einem Stoe Stadi P oder einem Panalytical Empyrean Diffraktometer aufgenommen. Beide Diffraktometer sind mit einer Cu-Röntgenröhre ausgestattet und verwenden einen linear PSD bzw. einen PixCell-Halbleiter-Detektor. Hochaufgelöste Pulverdiffraktogramme wurden am DESY, Hamburg mittels Synchrotronstrahlung aufgenommen.

3.4.6. Pulverdiffraktometrie an Synchrotronstrahlungsquellen

Bewegen sich Elektronen oder Positronen mit annähernd Lichtgeschwindigkeit und werden auf eine Kreisbahn gezwungen, verlieren sie dabei Energie. Diese wird in Form von stark polarisierter, kohärenter und sehr intensiver Röntgenstrahlung frei. Sie kann für verschiedene Experimente, die besonders intensive und polarisierte Röntgenstrahlung verlangen, verwendet werden. Für Pulverdiffraktometrie standen die Beamlines G3 (DORIS) und P08 (PETRA) beide am HASYLAB, DESY zur Verfügung. Die Beamline G3 ist in Abbildung 3.9 gezeigt.

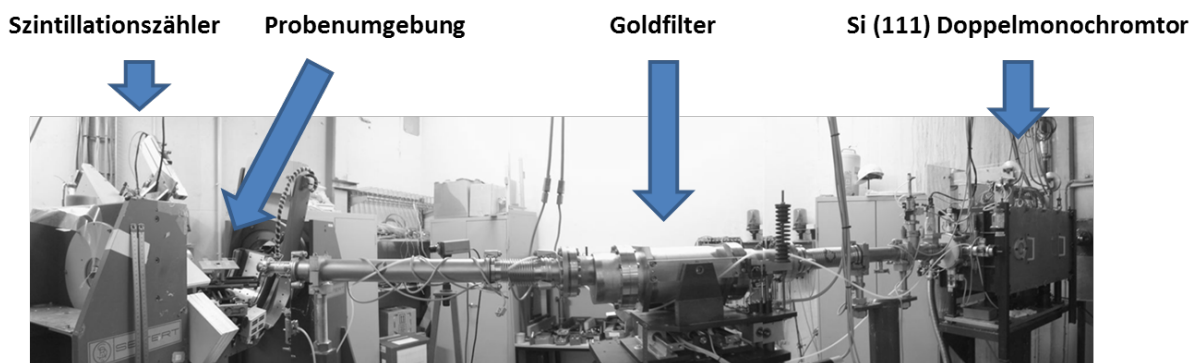


Abbildung 3.9.: Aufbau der Beamline G3, HASYLAB, DESY.

Der polychromatische Röntgenstrahl trifft auf einen Silicium Doppelmonochromator, der die Wellenlänge auf 1.54296 \AA monochromatisiert. Eine Goldfolie filtert hierbei höhere Beugungsordnungen heraus. Zur Probenjustage steht ein x, y, z Probentisch zur Verfügung, auf denen mit der zu untersuchenden Substanz gefüllte Kapillaren befestigt werden. Der gebeugte Strahl wird mit einem Szintillationszähler hinter einem Soller-Schlitz System zur Justage der Winkelakzeptanz detektiert.

Ebenso stand für die Messungen hochaufgelöster Pulverdiffraktogramme die Beamline P08 zur Verfügung. Diese ist in Abbildung 3.10 und 3.11 gezeigt.

3. Charakterisierungsmethoden

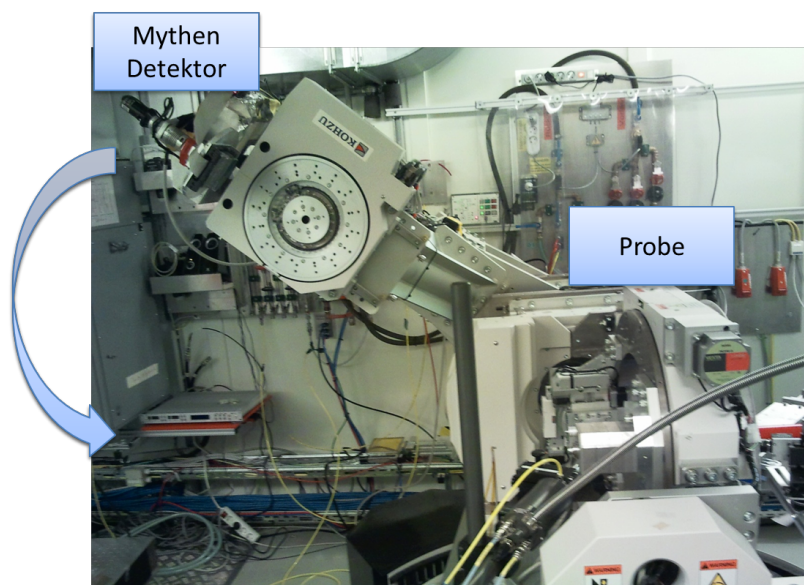


Abbildung 3.10.: Experimenteller Aufbau der Beamline P08, PETRA, HASYLAB. Der Pfeil zeigt die Bewegungsrichtung des Detektors.

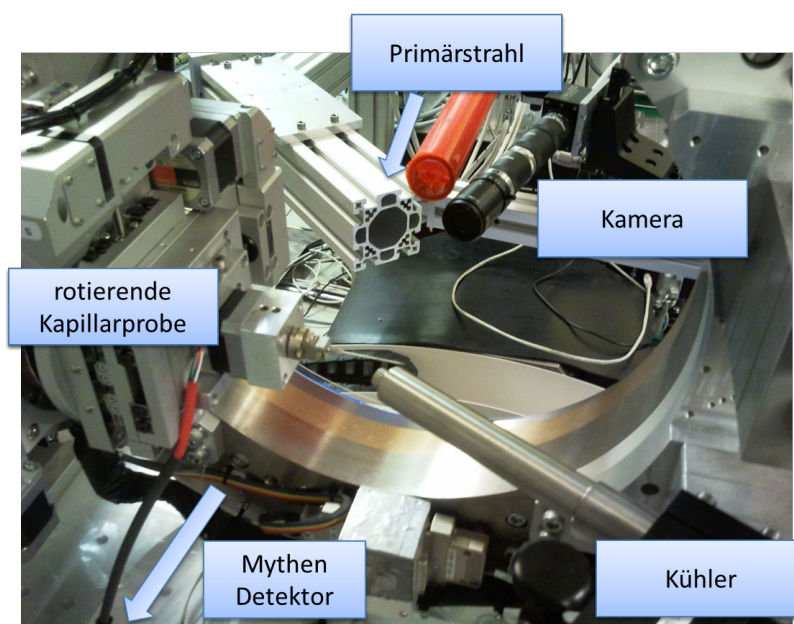


Abbildung 3.11.: Probenumgebung der Beamline P08, PETRA, HASYLAB mit Probenhalter, Probenkühler und Kamera zur Probenjustage.

Die weiße Röntgenstrahlung wird auf eine Wellenlänge von 0.824516 \AA mittels eines Silicium Doppelmonochromators monochromatisiert und auf die Probenumgebung fokussiert. Alle Proben wurden in Kapillaren auf einem rotierenden Probenhalter gemessen.

Die Proben können mit einem Oxford Cryostream gekühlt werden, um Strahlenschäden zu vermeiden und thermische Schwingungen der Atome zu minimieren. Der gebeugte Strahl wurde mit einem Mythen Halbleiterdetektor detektiert. Mit Hilfe eines Fast-Shutters war es möglich die Probe während der Bewegung des Detektorarms nicht der Röntgenstrahlung auszusetzen, um Strahlenschäden zu minimieren.

3.5. *In situ* Röntgenbeugung

Eine geeignete Methode Kristallisationen *in situ* zu verfolgen, ist die energiedispersive Röntgenbeugung (EDXRD). Für diese Experimente stand bis Oktober 2012 der Messplatz F3 DORIS, HASYLAB zur Verfügung. Dieser Messplatz ist in Abbildung 3.12 gezeigt.

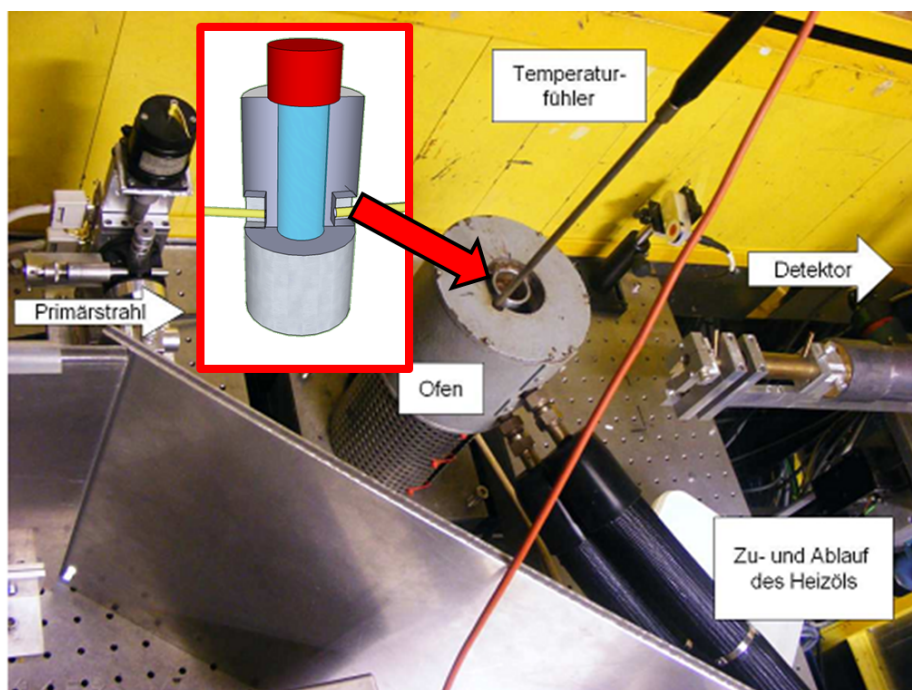


Abbildung 3.12.: Aufbau des Messplatzes F3 und schematische Darstellung des *in situ* Reaktors.

Hierbei wird weiße Röntgenstrahlung von einem Bending Magneten erzeugt. Der Röntgenstrahl wird kollimiert und unmonochromatisiert auf das Probengefäß fokussiert. Das Probengefäß wird von einem Aluminium-Autoklaven erhitzt, der indirekt von einem externen Ölthermostaten geheizt wird. Um ein konstantes Probenvolumen im Strahl zu gewährleisten wird das Reaktionsgemisch gerührt. Der gebeugte Strahl wird bei einem festen Winkel von einem Halbleiterdetektor detektiert. Ebenso wie für die winkeldispersive Röntgenbeugung gilt das Bragg'sche Gesetz. Jedoch werden hier nicht verschiedene Netzebenenabstände in Abhängigkeit des Beugungswinkels gemessen, sondern die Netzebenenabstände in Abhängigkeit der Wellenlänge, also der Energie. Für das Bragg'sche Gesetz ergibt sich somit:

$$E = \frac{hc}{2d\sin\theta} \quad (3.10)$$

Um nur ein kleines Streuvolumen innerhalb des Reaktionsgefäßes zu gewährleisten wird der

austretende Strahl durch ein Doppelspaltsystem vor dem Detektor kollimiert (vgl. Abbildung 3.13). Alle Energien treffen simultan auf den Halbleiterdetektor. Dieser kann zwischen den verschiedenen Energien auch bei einem festen Winkel unterscheiden.

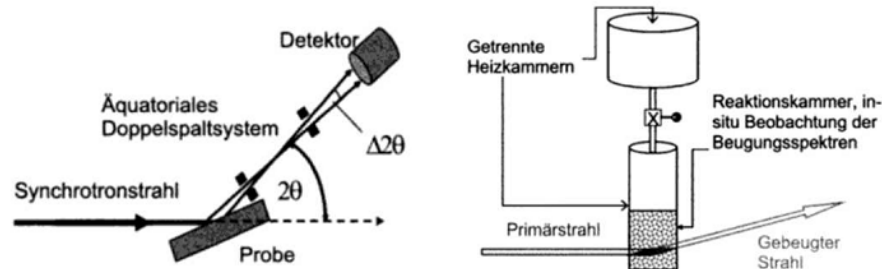


Abbildung 3.13.: Schematische Darstellung des Messaufbaus und des Prinzips der EDXRD. **Links:** Blick von oben auf die schematische Darstellung eines energiedispersiven Röntgenbeugungsexperiments mit Kollimatorblenden. **Rechts:** schematische Darstellung des experimentellen Aufbaus für Kristallisationsversuche aus Lösungen. ^[107]

Mit dieser Methode ist es nun möglich Reaktionen in konventionellen Reaktionsgefäßen zu untersuchen, da diese von dem intensiven weißen Strahl durchdrungen werden. Ebenso ist kein Abfahren des Winkels nötig sondern das gesamte Spektrum wird simultan gemessen.

3.6. Empirische Reaktionskinetik

Neben der Beobachtung von kristallinen Intermediaten und der rein qualitativen Beobachtung des Kristallisationsverlaufs können ebenfalls kinetische Studien durchgeführt werden. Am häufigsten werden dabei zur Auswertung der Messdaten die Modelle von Avrami und Gualtieri verwendet, die im Folgenden näher beschrieben werden.

3.6.1. Avrami Modell

Im Rahmen der Festkörperchemie wurde von Avrami und Eroféev ein Modell entwickelt um kinetische Auswertungen von Phasenumwandlungen durchzuführen. ^[108–110] Konventionelle Modelle galten oft nur für Gasphasenreaktionen oder machten zu viele Annahmen, die nicht auf Festkörperreaktionen übertragen werden konnten. In der Herleitung werden folgende Annahmen gemacht:

- Die Keimbildung findet zufällig und homogen statt.

3. Charakterisierungsmethoden

- Die Wachstumsgeschwindigkeit ist nicht von dem Fortschritt der Umwandlung abhängig.
- Die Keimbildung ist isotrop (sphärische Partikel).

Mit diesen Annahmen lässt sich die sogenannte Avrami-Erofëev Gleichung herleiten.

$$\alpha = 1 - [\exp(-kt_{red})^m] \quad (3.11)$$

Hierbei ist α der Reaktionsfortschritt, k die Geschwindigkeitskonstante, t_{red} die reduzierte Zeit und m der Avrami-Exponent. Im Falle der EDXRD Studien ist der Reaktionsfortschritt definiert als die Intensität zum Zeitpunkt t geteilt durch die Intensität zum Zeitpunkt $t = \infty$.

$$\alpha(t) = \frac{I(t)}{I_{t=\infty}} \quad (3.12)$$

Die Intensitäten werden hierbei aus dem Integral der Peaks bestimmt. Die reduzierte Zeit ist der Zeitpunkt an dem zum ersten Mal das Produkt auftritt. Im Falle der EDXRD Studien ist dies der Zeitpunkt an dem das kristalline Produkt zum ersten mal beobachtet wird, also dem ersten Auftreten eines Reflexes. Der Avrami-Exponent m war in der ursprünglichen Avrami-Gleichung gleichbedeutend mit der Dimensionalität des Kristallwachstums bei kontinuierlicher Nukleation (Dimensionalität = $m - 1$).

Die Avrami-Erofëev Gleichung lässt sich nach der Methode von Sharp und Hancock interpretieren.^[111] Hierfür wird sie durch Logarithmieren linearisiert.

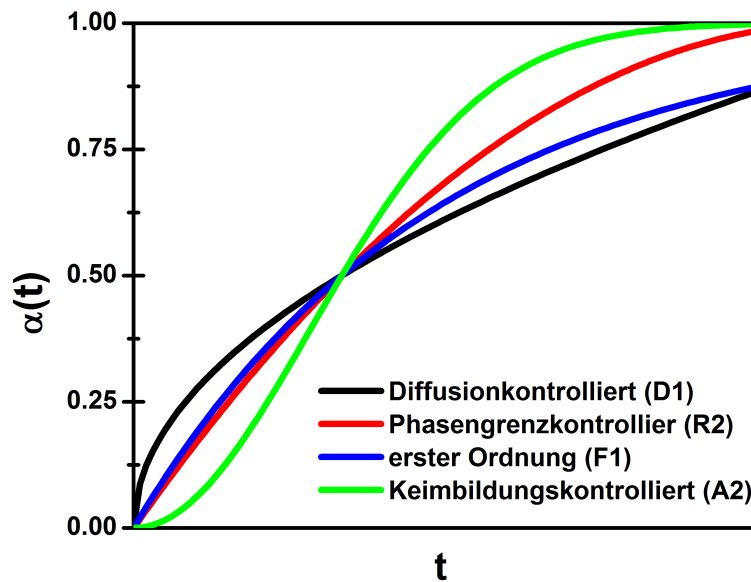
$$\ln[-\ln(1 - \alpha)] = m \cdot \ln(k) + m(\ln(t_{red})) \quad (3.13)$$

Eine Auftragung von $\ln[-\ln(1 - \alpha)]$ gegen $\ln(t_{red})$ der Messung ergibt für einen konstanten Reaktionsmechanismus eine Gerade. Werden verschiedene Steigungen beobachtet lässt dies auf einen Mechanismuswechsel schließen. Mittels linearer Regression können der Avrami-Exponent m und die Geschwindigkeitskonstante k bestimmt werden. Für Festkörperreaktionen gibt es eine Vielzahl an Modellen die auf die Avrami-Erofëev-Gleichung angewendet wurden. Je nach Modell und dem daraus resultierenden Mechanismus wird ein bestimmter Wert für m erwartet. Die theoretischen Modelle sind in Tabelle 3.2 zusammengefasst.^[111] Aus den Modellen ergeben sich ebenfalls theoretische Verläufe des Reaktionsfortschritts in Abhängigkeit der Reaktionszeit für die jeweiligen Modelle (vgl. Abbildung 3.14).

Neben der ursprünglichen Verwendung für Festkörperreaktionen wurde die Avrami-Erofëev-Gleichung und die Methode von Sharp und Hancock ebenfalls eingesetzt um Kristallisa-

Tabelle 3.2.: Zusammenhänge des Reaktionsfortschritts α von der Reaktionszeit t verschiedener Modelle für Festkörperreaktionen nach Sharp und Hancock.^[111]

Mechanismus	$f(\alpha) = kt$	m
<i>Diffusionskontrolle</i>		
D ₁	$\alpha^2 = 0.25 \left(\frac{t}{t_{1/2}} \right)$	0.62
D ₂	$(1 - \alpha) \ln(1 - \alpha) + \alpha = 0.1534 \left(\frac{t}{t_{1/2}} \right)$	0.57
D ₃	$\left[1 - (1 - \alpha)^{1/3} \right]^2 = 0.0425 \left(\frac{t}{t_{1/2}} \right)$	0.54
D ₄	$1 - \frac{2a}{3} - (1 - \alpha)^{2/3} + \alpha = 0.0367 \left(\frac{t}{t_{1/2}} \right)$	0.57
<i>Phasengrenzkontrolle</i>		
R ₂	$(1 - \alpha)^{1/2} = 0.2929 \left(\frac{t}{t_{1/2}} \right)$	1.11
R ₃	$(1 - \alpha)^{1/3} = 0.2063 \left(\frac{t}{t_{1/2}} \right)$	1.06
<i>Reaktion erster Ordnung</i>		
F ₁	$[-\ln(1 - \alpha)] = 0.6931 \left(\frac{t}{t_{1/2}} \right)$	1.00
<i>Keimbildungskontrolle</i>		
A ₂	$[-\ln(1 - \alpha)]^{1/2} = 0.8326 \left(\frac{t}{t_{1/2}} \right)$	2.00
A ₃	$[-\ln(1 - \alpha)]^{1/3} = 0.885 \left(\frac{t}{t_{1/2}} \right)$	3.00

**Abbildung 3.14.:** Auswahl von charakteristischen Verläufen des Reaktionsfortschritts $\alpha(t)$ in Abhängigkeit der Reaktionszeit t für verschiedene theoretische Modelle.^[111]

tionen von solvothermalen Synthesen,^[37,112,113] Sol-Gel Prozesse,^[114] Polymerkristallisationen^[115] oder sogar Interkalationsreaktionen^[116] kinetisch auszuwerten. Hierbei müssen die erhaltenen Ergebnisse sehr vorsichtig interpretiert werden und keinesfalls als Absolutwerte angesehen werden.^[117] Jedoch ist es mit dieser Methode möglich Geschwindigkeitskonstanten zu extrahieren, Mechanismuswechsel während der Reaktion zu beobachten oder aber Reaktionen untereinander zu vergleichen.

3.6.2. Gualtieri Modell

Seit 2001 wird außerdem das Gualtieri Modell auf Kristallisationen angewendet.^[118] Dieses wurde für die Kristallisation von Zeolithen entwickelt und trennt Nukleation und Kristallwachstum voneinander. Es werden folgende Annahmen gemacht:

- Die Geschwindigkeiten der Keimbildung und des Kristallwachstums sind nicht konstant, außer bei konstanter Übersättigung des Lösungsmittels. Als Folge der Abnahme der Übersättigung nehmen beide ab.
- Die Kristallisation kann ein-, zwei- oder drei-dimensional stattfinden.
- Die Nukleation kann homogen, heterogen oder autokatalytisch und in klaren Lösungen stattfinden.

Daraus wird erhalten:

$$\alpha(t) = \frac{1}{1 + \exp\left\{-\left(\frac{t-a}{b}\right)\right\}} \{1 - \exp[(-k_g t)^n]\} \quad (3.14)$$

Hierbei ist α der Reaktionsfortschritt, t die Reaktionszeit, k_g die Geschwindigkeitskonstante des Kristallwachstums und n die Dimensionalität des Wachstums. Diese kann z.B. aus mikroskopischen Aufnahmen bestimmt werden. a ist die reziproke Geschwindigkeitskonstante der Keimbildung und b gibt Aufschluss, ob die Kristallisation homogen ($b \approx 15$), heterogen ($b \approx 20$) oder autokatalysiert ($b \geq 20$) abläuft. Aus den Konstanten ergibt sich weiterhin eine Nukleationswahrscheinlichkeitsfunktion P_N :

$$P_N = \exp\left(-\frac{(t-a)^2}{2b^2}\right) \quad (3.15)$$

Um die Parameter k_g , a und b zu erhalten müssen die experimentellen Daten sorgfältig mittels eines least-square Algorithmus angepasst werden. In den letzten Jahren wurde

dieses Modell auf die Kristallisation von Zeolithen und Metal-Organic Frameworks angewendet.^[35,36,119]

Teil II.

Kumulativer Hauptteil

4 | Synthese und *in situ* Untersuchungen polyfunktionalisierter Metallphosphonate

Diese Arbeit beschäftigt sich mit der Synthese, Charakterisierung und *in situ* EDXRD Untersuchungen von polyfunktionalisierten Metallphosphonaten und Bismutcarboxylaten. Um den aktuellen Stand der Forschung darzulegen, soll im Folgenden eine Einführung in die Chemie der polyfunktionalisierten Metallphosphonate und in *in situ* Studien von anorganisch-organischen Hybridverbindungen gegeben werden. Der Fokus liegt hierbei auf Metallphosphonatosulfonaten, -phosphonatocarboxylaten und aminofunktionalisierten Metallphosphonaten, da diese den Hauptteil der Arbeit ausmachen. Anschließend werden die eigenen Arbeiten zu diesen Themen vorgestellt.

Der zweite Teil dieser Arbeit befasst sich mit der Synthese neuer Bismutcarboxylate und den *in situ* EDXRD Untersuchungen ihrer Kristallisation. Hierzu soll ebenso ein Überblick über die aktuellen Arbeiten auf diesem Gebiet gegeben werden, an den sich die eigenen Arbeiten anschließen.

4.1. Metallphosphonate

Phosphonsäuren bieten sich neben Carbonsäuren zum Aufbau von dreidimensionalen Gerüststrukturen an. Aktuelle Forschungsergebnisse haben gezeigt, dass Metallphosphonat basierende Hybridverbindungen potentielle Anwendung in der Gasspeicherung und -trennung,^[24,120] als optische Materialien,^[121,122] in der Katalyse^[123-125] oder als magnetische Materialien^[126-131] finden können. Durch die erhöhte Ladung und die höhere Anzahl an Ligandenatomen wird im Vergleich zu Carboxylaten eine höhere chemische Stabilität z.B. gegen Hydrolyse erwartet. Die stärkere C-P Bindung im Vergleich zur C-C Bindung in Metallcarboxylaten sollte beim Aufbau von Hybridverbindungen zu einer höheren thermischen Stabilität führen.^[132] Aus den selben Gründen neigen Metallphosphonate aber ebenso zu hoch kondensierten Netzwerken, die dichte Metallphosphonat Ketten oder Schichtstruk-

turen bilden. Die Chemie dieser Verbindungen zeichnet sich durch eine sehr flexible und komplexe Strukturchemie aus,^[132] die durch die Verwendung von polyfunktionalisierten Linker Molekülen sehr variabel gestaltet werden kann. Derartige Verbindungen sind jedoch erst in den letzten Jahren stärker systematisch untersucht worden und es ist vergleichsweise wenig über diese bekannt. Vor allem Phosphonosulfonsäuren, Phosphonocarbonsäuren aber auch aminofunktionalisierte Phosphonsäuren wurden untersucht und zeigten, dass neue und komplexere Struktur motive im Vergleich zu reinen Phosphonate erhalten werden können. Im Folgenden sollen typische Vertreter der Substanzklassen und ihre strukturellen Merkmale vorgestellt werden.

4.2. Metallphosphonatosulfonate

Seit langer Zeit werden Metallphosphonate und -sulfonate separat untersucht.^[32] Somit liegt auch der Schritt nahe beide funktionelle Gruppen in einem Linker zu kombinieren um neue Netzwerke zu erzeugen. Durch die erniedrigte Ladung der Sulfonate werden weniger stark kondensierte Netzwerke beobachtet, die häufig zusätzlich in Wasserstoffbrückenbindungen involviert sind.

Zur Synthese neuer Metallphosphonatosulfonate wurden zu Beginn der Untersuchungen die starren Linker *p*-Phosphonophenylsulfonsäure (H_3L^1) ($1,4-H_2O_3P-C_6H_3-SO_3H$) und *m*-Phosphonophenylsulfonsäure ($m-H_3L^2$) ($1,3-H_2O_3P-C_6H_3-SO_3H$) verwendet. Die literaturbekanntesten Verbindungen sind in Tabelle 4.1 und 4.2 zusammengefasst. Der Linker H_3L^1 wurde vor allem in Verbindung mit Cu^{2+} und Sn^{2+} in Hinblick auf die Synthese neuer Metallphosphonatosulfonate untersucht. Als Coliganden wurden weiterhin *1,10*-Phenanthrolin (phen) oder *4,4*-Bipyridin (bipy) in den Verbindungen $[Cu(L^1)(phen)] \cdot H_2O$, $[Cu(L^1)(bipy)] \cdot H_2O$ und $[Cu(L^1)(bipy)]$ genutzt. Die Verwendung von H_3L^1 führt oft zur Ausbildung von Kettenstrukturen, wie exemplarisch für die Verbindung $[Cu_2(L^1)(OH)(H_2O)]$ in Abbildung 4.1 gezeigt. Die Kristallstruktur ist aus zick-zack Ketten aus kantenverknüpften CuO_6 -Polyedern aufgebaut. Die Ketten werden untereinander über Phosphonat- und Sulfonatgruppen zu Schichten verbrückt. Diese Schichten werden durch die Phenyleinheiten verknüpft. In allen in Tabelle 4.1 zusammengefassten Verbindungen werden stark kondensierte anorganische Einheiten beobachtet, die sowohl über die Sulfonat als auch Phosphonatgruppen verknüpft sind. Die Sulfonatgruppen bilden zusätzlich Wasserstoffbrückenbindungen mit Wassermolekülen oder mit einer zweiten Sulfonsäure aus. Dies zeigt sich sehr deutlich in den Verbindungen $[Cu(L^1)(bipy)] \cdot H_2O$ und $[Cu(L^1)(bipy)]$. Durch Dehy-

Tabelle 4.1.: Literaturbekannte Verbindungen auf Basis von (1,4-H₂O₃P-C₆H₃-SO₃H) (H₃L¹) unter Verwendung von keinem, 1,10-Phenanthrolin (phen) oder 4,4-Bipyridin (bipy) als Coliganden.

Summenformel	M-O-M Strukturmotiv
[Cu(L ¹)(phen)] · H ₂ O	Dimere Einheiten ^[133]
[Cu _{1.5} (L ¹)(H ₂ O)]	Cluster ^[70]
[NaCu(L ¹)(H ₂ O) ₂]	Ketten ^[70]
[Cu ₂ (L ¹)(OH)(H ₂ O)]	Ketten ^[70]
[Cu ₃ (L ¹) ₂ (H ₂ O) ₂]	Ketten ^[70]
[Pb ₂ (L ¹)(OH)]	Ketten ^[70]
[Cu(L ¹)(bipy)] · H ₂ O	isoliert ^[134]
[Cu(L ¹)(bipy)]	isoliert ^[134]
[Sn ₂ (L ¹)(OH)]	Cluster ^[135]

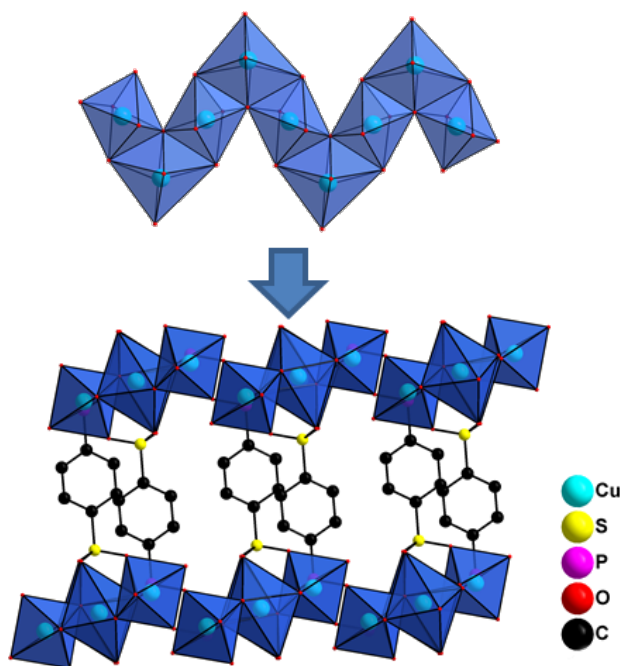


Abbildung 4.1.: Ketten aus CuO₆-Polyeder (oben) und Ausschnitt der Kristallstruktur von [Cu₂(L)(OH)(H₂O)]; Blick entlang der *a*-Achse der Verbindung.

dratisierung lassen sich strukturelle Änderungen erzeugen, welche durch unterschiedliche Jahn-Teller Verzerrungen verursacht werden.^[135]

Typischerweise werden bei der Synthese von Metallphosphonatosulfonaten Ketten- und Schichtstrukturen erhalten. Durch Absättigung der Koordinationsumgebung mit Coliganden können diese Bindungsmuster verhindert werden. Dies wurde von der Arbeitsgruppe um Mao am Beispiel von *m*-Phosphonophenylsulfonsäure (*m*-H₃L²) (1,3-H₂O₃P-C₆H₃-

4. Polyfunktionalisierte Metallphosphonate

SO₃H) gezeigt und in diesem Jahr auch von der Arbeitsgruppe Wang für H₃L¹.^[133] Alle bisher bekannten Verbindungen auf Basis von *m*-Phosphonophenylsulfonsäure sind in Tabelle 4.2 zusammengefasst.

Tabelle 4.2.: Tabelle der bisher veröffentlichten Verbindungen unter Einsatz von (*1,3*-H₂O₃P-C₆H₃-SO₃H) (H₃L²) unter Verwendung von *1,10*-Phenanthrolin (phen), *4,4*-Bipyridin (bipy) oder Piperidin(bismethylenphosphonsäure) (H₄L²) als Coliganden.

<i>Summenformel</i>	<i>M-O-M Strukturmotiv</i>
[La ₂ (L ²) ₂ (phen) ₄ (H ₂ O)] · 4.5H ₂ O	Cluster ^[130]
[La ₂ (L ²) ₂ (phen) ₂ (H ₂ O) ₅] · 3H ₂ O	Cluster ^[130]
[La ₂ (HL ²)(H ₂ L ²) ₂ (H ₂ O) ₄] · 8H ₂ O	1D-Ketten ^[130]
[Zn ₂ (phen) ₃] ₂ [Zn ₄ (L ²) ₄ (phen) ₄] · 20H ₂ O	Cluster ^[136]
[Zn ₆ (L ²) ₄ (phen) ₈] · 11H ₂ O	Cluster ^[136]
[Zn ₆ (L ²) ₄ (bipy) ₆ (H ₂ O) ₄] · 18H ₂ O	3D-Gerüst ^[136]
[Cd ₄ (L ²) ₂ (phen) ₆ (Cl) ₂ (H ₂ O) ₂] · 14H ₂ O	Cluster ^[137]
[Cd ₆ (L ²) ₄ (phen) ₈] · 14H ₂ O	Cluster ^[137]
[Cd ₃ (L ²) ₂ (phen) ₃ (H ₂ O) ₆] · 4H ₂ O	3D-Gerüst ^[137]
[Mn ₂ (HL ²) ₂ (phen) ₄] [Mn ₂ (HL ²) ₂ (phen) ₄ (H ₂ O)] · 6H ₂ O	Cluster ^[138]
[Mn ₄ (L ²) ₂ (phen) ₈ (H ₂ O) ₂] [ClO ₄] ₂ · 3H ₂ O	Cluster ^[138]
[Mn(phen)(H ₂ O) ₄] ₂ [Mn ₄ (L ²) ₄ (phen) ₄ (H ₂ O)] · 10H ₂ O	Cluster ^[138]
[Mn ₆ (L ²) ₄ (phen) ₈ (H ₂ O) ₂] · 4H ₂ O	Cluster ^[138]
[Mn ₆ (L ²) ₄ (phen) ₈ (H ₂ O) ₂] · 24H ₂ O	Cluster ^[138]
[Mn ₆ (L ²) ₄ (phen) ₆ (H ₂ O) ₄] · 5H ₂ O	1D-Ketten ^[138]
[Cu(HL ²)(bipy) ₆ (H ₂ O)] · xH ₂ O	3D-Gerüst ^[139]
[Pb ₃ (L ²) ₂ (H ₂ O) ₂] · 4H ₂ O	3D-Gerüst ^[140]
[Pb(HL ²)(phen)] · H ₂ O	Cluster ^[140]
[Pb ₆ (L ²) ₄ (phen) ₈] · 3H ₂ O	Cluster ^[140]
[Pb ₆ (L ²) ₄ (phen) ₁₀] · 2H ₂ O	Cluster ^[140]
[Pb ₆ (L ²) ₄ (bipy)(H ₂ O) ₂] · 2H ₂ O	3D-Gerüst ^[140]

In Abbildung 4.2 sind die Kristallstrukturen der zwei literaturbekannten Verbindungen [La₂(L²)₂(phen)₂(H₂O)₅] · 3H₂O und [Cu(L¹)(phen)] · H₂O gezeigt.^[130,133]

In der Verbindung [La₂(L²)₂(phen)₂(H₂O)₅] · 3H₂O werden durch die Absättigung der Koordinationsstellen mit *1,10*-Phenanthrolin vierkernige Cluster erhalten. Die Sulfonatgruppen ragen aus dem Cluster heraus und verbrücken diese über Wasserstoffbrücken.^[130] In der Kristallstruktur von [Cu(L¹)(phen)] · H₂O werden dimere Einheiten durch den Einsatz von *1,10*-Phenanthrolin beobachtet. Wieder sind die Sulfonatgruppen in Wasserstoffbrücken involviert, bilden jedoch zusätzlich Bindungen mit den Metallzentren aus.^[133]

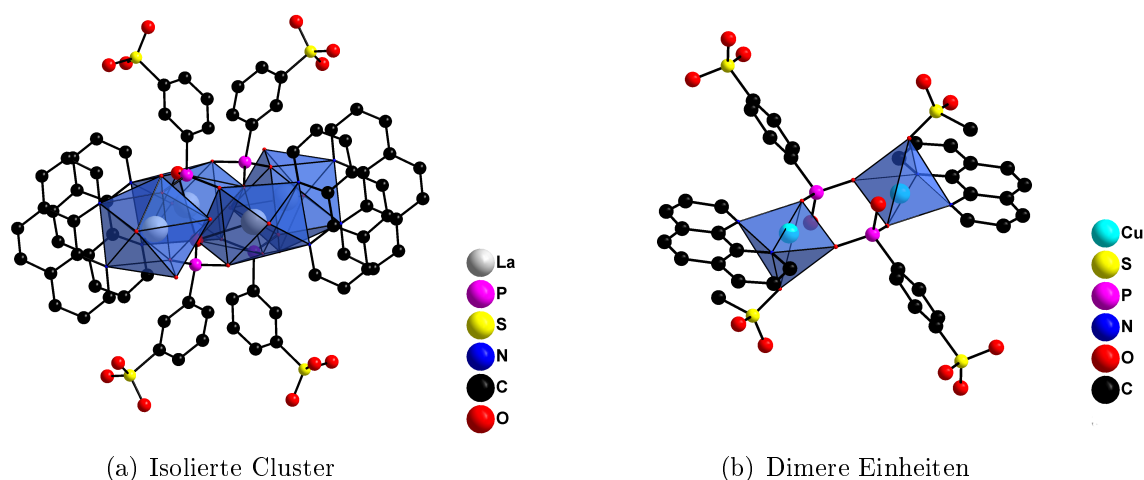


Abbildung 4.2.: Beispiele für den Einsatz von koordinationsabsättigenden Coliganden: Links am Beispiel der Verbindung $[\text{La}_2(\text{L}^2)_2(\text{phen})_2(\text{H}_2\text{O})_5] \cdot 3\text{H}_2\text{O}$ und rechts am Beispiel $[\text{Cu}(\text{L}^1)(\text{phen})] \cdot \text{H}_2\text{O}$.^[130,133]

Neben starren phenylbasierenden Linkern wurden auch flexible aliphatische Linker untersucht. Hierbei konnten 1,2-Phosphonoethansulfonsäure und 1,4-Phosphonobutansulfonsäure zur Synthese von Metallphosphonatosulfonaten mit den Metallen Ln^{3+} , Ba^{2+} , Sr^{2+} , Cu^{2+} und Ca^{2+} erfolgreich verwendet werden. Die bis heute bekannten Verbindungen mit den oben genannten Linkern sind in Tabelle 4.3 zusammengefasst.

In den Studien wurden systematisch Einflüsse, wie verschiedene molaren Verhältnisse von Metall zu Linker oder Reaktionstemperaturen auf die gebildeten Kristallstrukturen untersucht. Das System $\text{Cu}^{2+} / \text{H}_2\text{O}_3\text{P}-\text{C}_2\text{H}_4-\text{SO}_3\text{H} / \text{NaOH}$ in Wasser wurde mittels Hochdurchsatzmethoden bei sechs verschiedenen Temperaturen im Bereich von 90 bis 190 °C untersucht. Die Ergebnisse sind in Abbildung 4.3 zusammengefasst.

4. Polyfunktionalisierte Metallphosphonate

Tabelle 4.3.: Bekannte Verbindungen bei Einsatz von 1,2-Phosphonoethansulfonsäure und 1,4-Phosphonobutansulfonsäure.

1,2-Phosphonoethansulfonsäure	M-O-M Strukturmotiv
$\text{Ln}(\text{O}_3\text{P}-\text{C}_2\text{H}_4-\text{SO}_3)(\text{H}_2\text{O})$	Ketten ^[141]
$\text{Ln}(\text{O}_3\text{P}-\text{C}_2\text{H}_4-\text{SO}_3)$	Ketten ^[142]
$[\text{Er}(\text{O}_3\text{P}-\text{C}_2\text{H}_4-\text{SO}_3)(\text{OH})_3(\text{H}_2\text{O})] \cdot \text{H}_2\text{O}$	Schichten ^[143]
$\text{BaH}(\text{O}_3\text{P}-\text{C}_2\text{H}_4-\text{SO}_3)$	Ketten ^[144]
$\text{Sr}_3(\text{O}_3\text{P}-\text{C}_2\text{H}_4-\text{SO}_3)_2$	Schichten ^[145]
$[\text{Cu}_2(\text{O}_3\text{P}-\text{C}_2\text{H}_4-\text{SO}_3(\text{OH})(\text{H}_2\text{O}))]$	Ketten ^[146]
$[\text{Cu}_{2.5}(\text{O}_3\text{P}-\text{C}_2\text{H}_4-\text{SO}_3(\text{OH})_2)]$	Schichten ^[146]
$[\text{Cu}_2(\text{O}_3\text{P}-\text{C}_2\text{H}_4-\text{SO}_3(\text{OH})(\text{H}_2\text{O}))_2] \cdot 3\text{H}_2\text{O}$	Cluster ^[146]
$\text{Cu}_{1.5}(\text{O}_3\text{P}-\text{C}_2\text{H}_4-\text{SO}_3)(\text{H}_2\text{O})$	Ketten ^[147]
$\text{SrH}(\text{O}_3\text{P}-\text{C}_2\text{H}_4-\text{SO}_3)$	Ketten ^[148]
$\text{Ca}(\text{HO}_3\text{P}-\text{C}_2\text{H}_4-\text{SO}_3)(\text{H}_2\text{O})_2$	Ketten ^[148]
$\text{BaH}(\text{O}_3\text{P}-\text{C}_2\text{H}_4-\text{SO}_3)$	Schichten ^[148]
1,4-Phosphonobutansulfonsäure	
$[\text{Cu}_{1.5}(\text{O}_3\text{P}-\text{C}_2\text{H}_4-\text{SO}_3)] \cdot \text{H}_2\text{O}$	Cluster ^[149]
$\text{Cu}_{2.5}(\text{O}_3\text{P}-\text{C}_4\text{H}_8-\text{SO}_3)(\text{OH})_2$	Schichten ^[149]

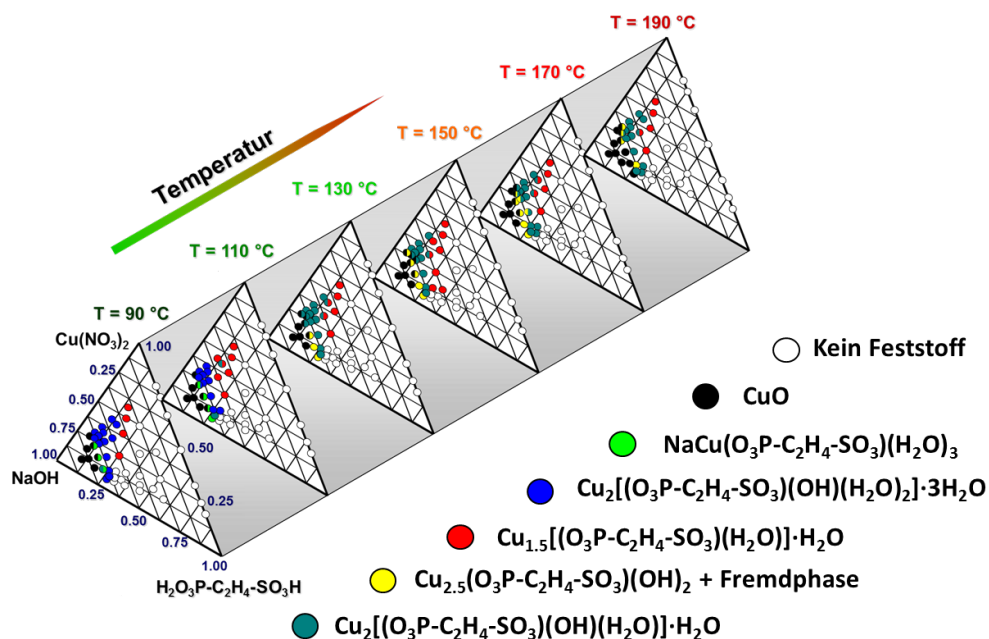
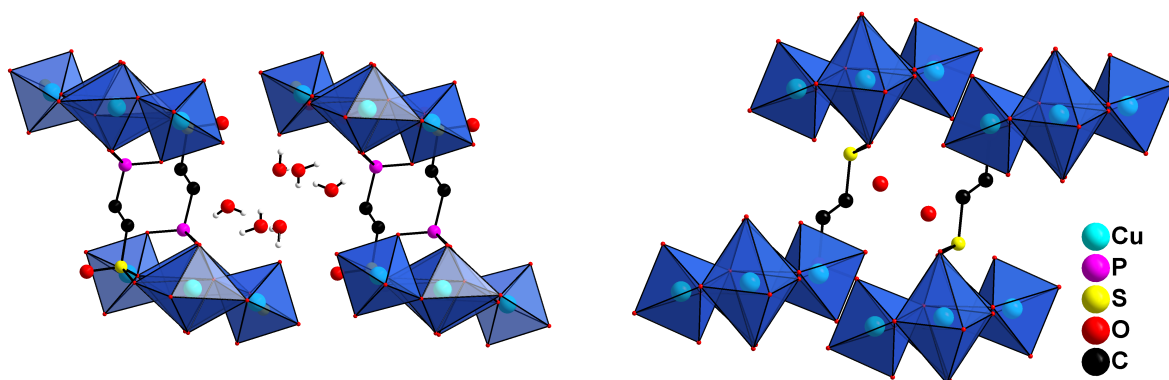


Abbildung 4.3.: Ergebnisse der temperaturlösten Hochdurchsatzexperimente.^[146]

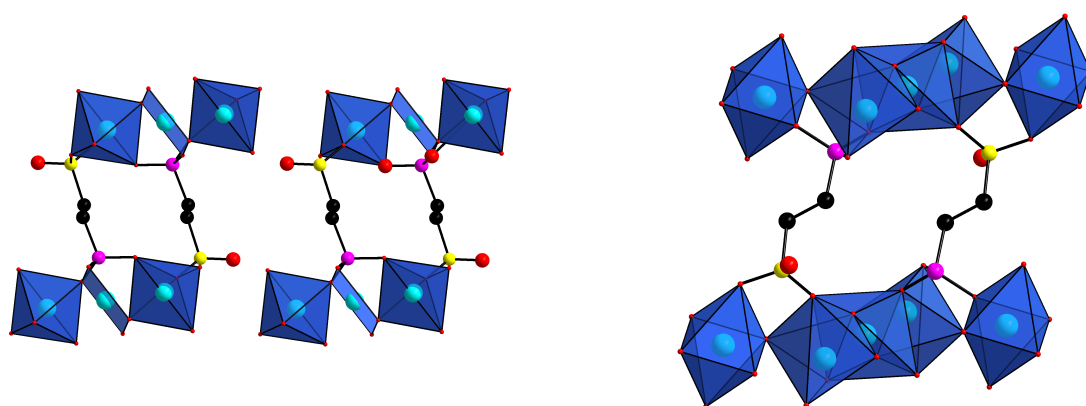
Bei den Untersuchungen konnten sechs Verbindungen erstmals entdeckt und vier Kristallstrukturen aufgeklärt werden. Diese sind in Abbildung 4.4 gezeigt. In den Verbindungen $[\text{Cu}_2(\text{O}_3\text{-C}_2\text{H}_4\text{-SO}_3)(\text{OH})(\text{H}_2\text{O})_2]$, $\text{Cu}_{2.5}(\text{O}_3\text{P-C}_2\text{H}_4\text{-SO}_3)(\text{OH})_2$ und $[\text{Cu}_2(\text{O}_3\text{P-C}_2\text{H}_4\text{-SO}_3)(\text{OH})(\text{H}_2\text{O})]\cdot\text{H}_2\text{O}$ wurden Ketten aus CuO_6 Polyedern beobachtet, die über die Linker zu 2D-Schichten verknüpft sind. Diese werden untereinander über Wasserstoffbrückenbindungen zusammengehalten. In der Verbindung $\text{Cu}_{1.5}(\text{H}_2\text{O}_3\text{P-C}_2\text{H}_4\text{-SO}_3\text{H})(\text{H}_2\text{O})$ werden im Gegensatz dazu Cu_3O_{12} Cluster beobachtet, die über die organische Baueinheit zu einer Schichtverbindung verknüpft werden.

4. Polyfunktionalisierte Metallphosphonate



(a) Ausschnitt der Kristallstruktur von $\text{Cu}_2(\text{O}_3\text{-C}_2\text{H}_4\text{-SO}_3)(\text{OH})(\text{H}_2\text{O})_2$ gezeigt entlang der b -Achse.

(b) Ausschnitt der Kristallstruktur von $[\text{Cu}_2(\text{O}_3\text{-C}_2\text{H}_4\text{-SO}_3(\text{OH})(\text{H}_2\text{O}))\cdot\text{H}_2\text{O}]$ gezeigt entlang der a -Achse.



(c) Ausschnitt der Kristallstruktur von $\text{Cu}_{1.5}(\text{H}_2\text{O}_3\text{P-C}_2\text{H}_4\text{-SO}_3\text{H})(\text{H}_2\text{O})$ gezeigt entlang der b -Achse.

(d) Ausschnitt der Kristallstruktur von $\text{Cu}_{2.5}(\text{O}_3\text{P-C}_2\text{H}_4\text{-SO}_3)(\text{OH})_2$ gezeigt entlang der a -Achse.

Abbildung 4.4.: Kristallstrukturen die in dem System $\text{Cu}^{2+} / \text{H}_2\text{O}_3\text{P-C}_2\text{H}_4\text{-SO}_3\text{H} / \text{NaOH}$ in Wasser als Lösungsmittel bestimmt werden konnten.

Von den Verbindungen, die sich bei niedrigen Temperaturen (90°C) bilden, konnten keine vermessbaren Einkristalle erhalten werden.

4.3. Metallphosphonatocarboxylate

Anorganisch-organische Hybridverbindungen auf Basis von Carboxylaten führen oft zu porösen Gerüststrukturen, während Metallphosphonate meistens zur Bildung von dichten Schichtstrukturen tendieren. Als Konsequenz sind auch polyfunktionalisierte Phosphonocarbonsäuren als möglicher Linker untersucht worden, um die strukturellen Eigenschaften von Metallphosphonatocarboxylaten zu untersuchen. Der Einsatz von 5-Phosphonobenzen-1,3-dicarbonsäure ($H_4\text{pbdc}$) in Verbindung mit Zink führt zu $[\text{Zn}_3(\text{pbdc})_2(\text{H}_2\text{O})]^{2-}$ -Solvens. In der Kristallstruktur ist Zink tetraedrisch von Sauerstoffatomen umgeben, die sowohl von Carboxylatgruppen als auch von Phosphonatgruppen stammen. Hierdurch bilden sich Polyederketten aus isolierten ZnO_4 -Polyedern, die zu einer offenen Gerüststruktur verknüpft werden. In den Poren befinden sich protonierte Amine die für den Ladungsausgleich sorgen.^[150] Die Kristallstruktur ist in Abbildung 4.5 gezeigt.

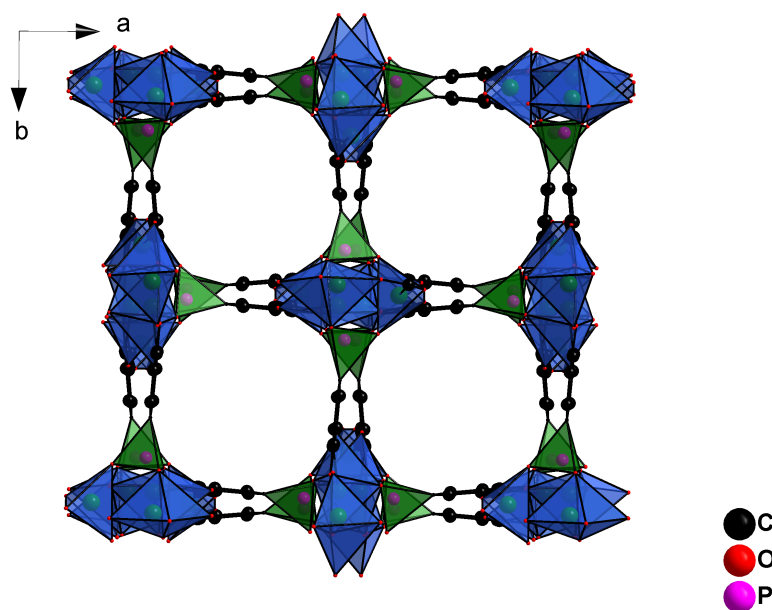


Abbildung 4.5.: Kristallstruktur von $[\text{Zn}_3(\text{pbdc})_2(\text{H}_2\text{O})] \cdot \text{Solvens}$. Die CPO_3 Polyeder sind in grün, die ZnO_4 Polyeder in blau dargestellt.^[150]

Auf Basis der, in dieser hier vorliegenden Arbeit, untersuchten Phosphonocarbonsäure $(\text{H}_3\text{OPCH}_2)_2\text{-N-CH}_2\text{-C}_6\text{H}_4\text{-COOH}$ (H_5L^3) wurden bereits Verbindungen mit La^{3+} , Sm^{3+} , Er^{3+} , Cd^{2+} , Zn^{2+} , Pb^{2+} , Co^{2+} und Ca^{2+} in der Literatur beschrieben. Die Summenformeln der Verbindungen und ihr struktureller Aufbau sind in Tabelle 4.4 zusammengefasst.

4. Polyfunktionalisierte Metallphosphonate

Tabelle 4.4.: Literaturbekannte Metallphosphonatocarboxylate auf Basis von $(\text{H}_3\text{OPCH}_2)_2\text{-N-CH}_2\text{-C}_6\text{H}_4\text{-COOH}$ (H_5L^3).

<i>Summenformel</i>	<i>M-O-M Einheit</i>	<i>Strukturmotiv</i>
$[\text{Ln}(\text{H}_4\text{L}^3)(\text{H}_3\text{L}^3)(\text{H}_2\text{O})] \cdot 2\text{H}_2\text{O}$	isolierte Polyeder	Ketten ^[121]
$\text{Er}(\text{H}_4\text{L}^3)(\text{H}_3\text{L}^3)$	isolierte Polyeder	Ketten ^[121]
$[\text{Cd}_3(\text{H}_2\text{O})_3(\text{H}_2\text{L})_2] \cdot 11\text{H}_2\text{O}$	isolierte Polyeder und Dimere	Schichten ^[151]
$[\text{Co}_3(\text{H}_2\text{L}^3)_2(\text{H}_2\text{O})_4(\text{bipy})]$	isolierte Polyeder	Schichten ^[152]
$[\text{Co}_2(\text{HL}^3)] \cdot \text{H}_2\text{O}$	Co_2O_{10} Cluster	Schichten ^[153]
$[\text{Co}(\text{HL}^3)]$	-	unbekannt ^[153]
$[\text{Co}_2(\text{HL}^3)] \cdot 3.5\text{H}_2\text{O}$	-	unbekannt ^[153]
$[\text{Cd}(\text{H}_4\text{L}^3)_2] \cdot 4\text{H}_2\text{O}$	isolierte Polyeder	Ketten ^[77]
$[\text{Cd}(\text{H}_4\text{L}^3)_2]$	isolierte Polyeder	Schichten ^[77]
$[\text{Cd}(\text{H}_3\text{L}^3)] \cdot \text{H}_2\text{O}$	Cd_2O_{10} Cluster	Schichten ^[77]
$[\text{Cd}_3(\text{H}_2\text{L}^3)_2] \cdot 14\text{H}_2\text{O}$	-	unbekannt ^[77]
$[\text{Cd}_2(\text{H}_1\text{L}^3)] \cdot 3\text{H}_2\text{O}$	-	unbekannt ^[77]
$[\text{Cd}_2(\text{H}_1\text{L}^3)] \cdot \text{H}_2\text{O}$	-	unbekannt ^[77]
$[\text{Sm}(\text{H}_2\text{L}^3)] \cdot \text{H}_2\text{O}$	Ketten	Schichten ^[73]
$[\text{Ca}(\text{H}_3\text{L}^3)] \cdot \text{H}_2\text{O}$	Ca_2O_{10} Cluster	Schichten ^[73]
$[\text{Ca}(\text{H}_4\text{L}^3)_2] \cdot 4\text{H}_2\text{O}$	isolierte Polyeder	Ketten ^[73]

In den Studien wurden die Einflüsse des pH-Wertes und der Temperatur auf die sich bildenden Kristallstrukturen untersucht. In allen Verbindungen wird eine -COOH-Gruppe beobachtet. Diese ist entweder in Wasserstoffbrückenbindungen mit einer zweiten Carbonsäuregruppe oder einer Phosphonsäuregruppe involviert. Die Phosphonsäuren hingegen liegen in verschiedenen Deprotonierungsgraden vor. Es werden nur wenige verschiedene anorganische Struktur motive erhalten, wodurch sich isostrukturelle Verbindungen ausbilden. Die häufigsten Struktur motive sind in Abbildung 4.6 gezeigt.

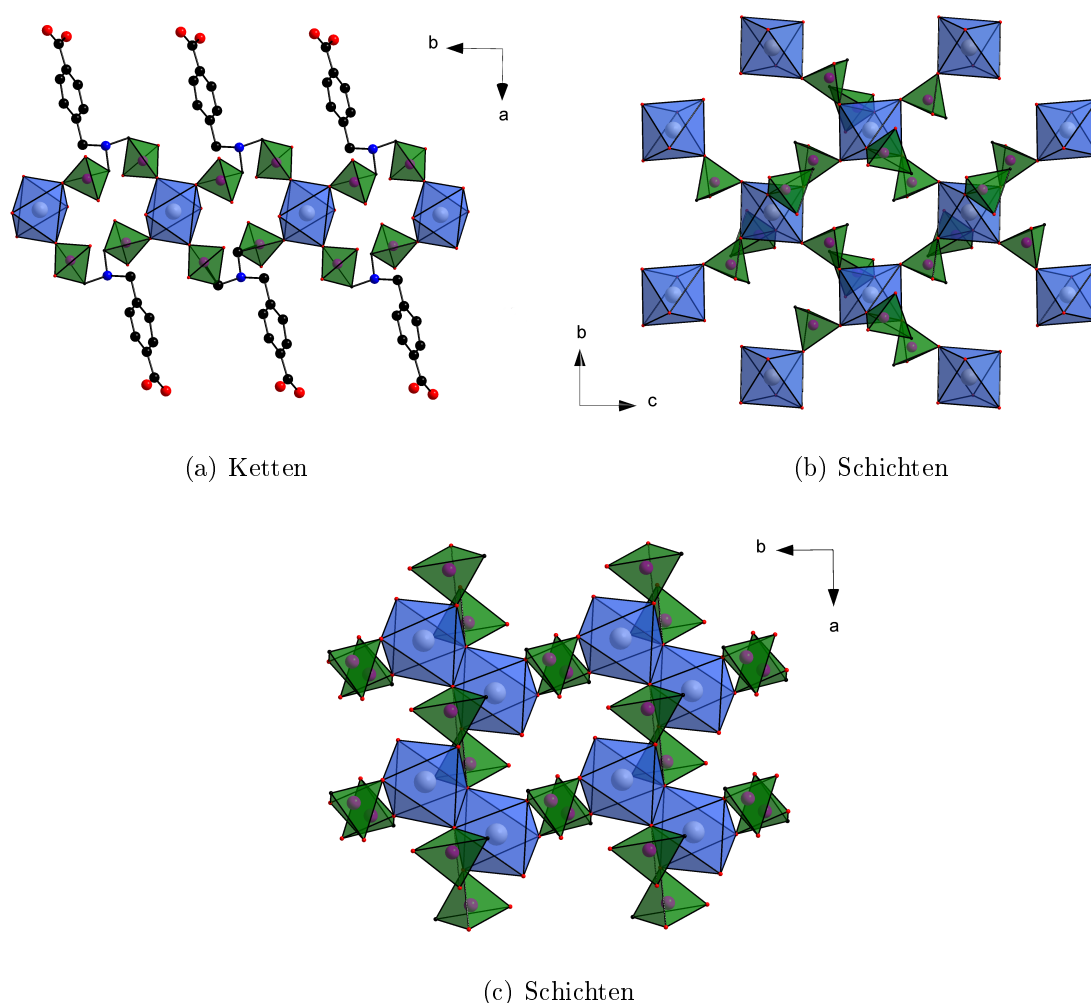


Abbildung 4.6.: **Oben links:** Ketten die in den Verbindungen der Zusammensetzung $[M(H_4L^3)]_2 \cdot 4H_2O$ ($M = Cd, Ca$) beobachtet werden, **Oben rechts:** Schichten aus isolierten MO_6 -Polyedern, die in den Verbindungen der Zusammensetzung $[M(H_4L^3)]_2$ ($M = Cd, Ca$) gebildet werden. **Unten:** Schichten aus dimeren M_2O_{12} -Clustern, wie sie in den Verbindungen der Zusammensetzung $[M(H_3L^3)] \cdot H_2O$ ($M = Cd, Ca, Co$) gefunden werden. Die Metallatome sind in grau, die Phosphoratome in lila, die Sauerstoffatome in rot, die Kohlenstoffatome in schwarz und die Stickstoffatome in blau dargestellt. Die CPO_3 Polyeder sind in grün, die MO_6 Polyeder in blau dargestellt.

In den Verbindungen der Zusammensetzung $[M(H_4L^3)]_2 \cdot 4H_2O$ und $[M(H_4L^3)]_2$ werden isolierte MO_6 -Polyeder beobachtet, die über die Methylphosphonsäuregruppen zu Ketten oder Schichten verknüpft sind. In der Verbindung der Zusammensetzung $[M(H_3L^3)] \cdot H_2O$ werden dimere M_2O_{10} Cluster beobachtet, die über Phosphonatgruppen zu Schichten verknüpft sind.

4.4. Aminofunktionalisierte Metallphosphonate

Neben sauren anionischen Gruppen lassen sich auch Amine mit Phosphonsäuren kombinieren. In der Vergangenheit wurden hierbei z.B. Aminoalkylphosphonsäuren verwendet.^[76,154–157] In allen Verbindungen koordinieren die Phosphonsäuren an die Metallzentren und bilden dadurch Schichten aus. Die Aminogruppen können sowohl in Wasserstoffbrückenbindungen untereinander gebunden sein, als auch an der Koordination an Metallionen beteiligt sein. Die Aminogruppen liegen in manchen Verbindungen protoniert vor. Hierdurch werden Wasserstoffbrückenbindungsmuster mit, z.B. in der Struktur eingebauten, Nitrationen beobachtet.

Aus dem sekundären zyklischen Amin Piperiazin lässt sich mittels einer „Mannichartigen“ Reaktion mit Formaldehyd und Phosphoriger Säure der Linker *N,N'*-Piperazinbismethylenphosphonsäure (H_4L^4) synthetisieren. In diesem Linker steht sowohl die Phosphonsäure als auch der Stickstoff für die Koordination an einem Metallzentrum zur Verfügung. Der Einsatz des Linkers führt zu der mikroporösen Verbindung STA-12 (STA= St Andrews) ($[M_2L^4] \cdot 8H_2O$, M= Mn, Co, Ni, Fe, Mg).^[120,158] Sie ist aus kantenverknüpften MO_5N Polyederketten aufgebaut. Der Linker verknüpft die Ketten zu einem sogenannten „Honigwaben“ Netzwerk und erzeugt so die offene Gerüststruktur, die in Abbildung 4.7 gezeigt ist.

Durch Verwendung von *N,N'*-4,4' Bipiperidinebis(methylenphosphonsäure) (H_4LL^4) wurden die isoretikulären Verbindungen (STA-16 = $[M_2LL^4] \cdot xH_2O$, M = Ni, Co) mit einer Erweiterung des Porendurchmessers von 8 Å auf 18 Å (vgl. Abbildung 4.7) erhalten.^[24]

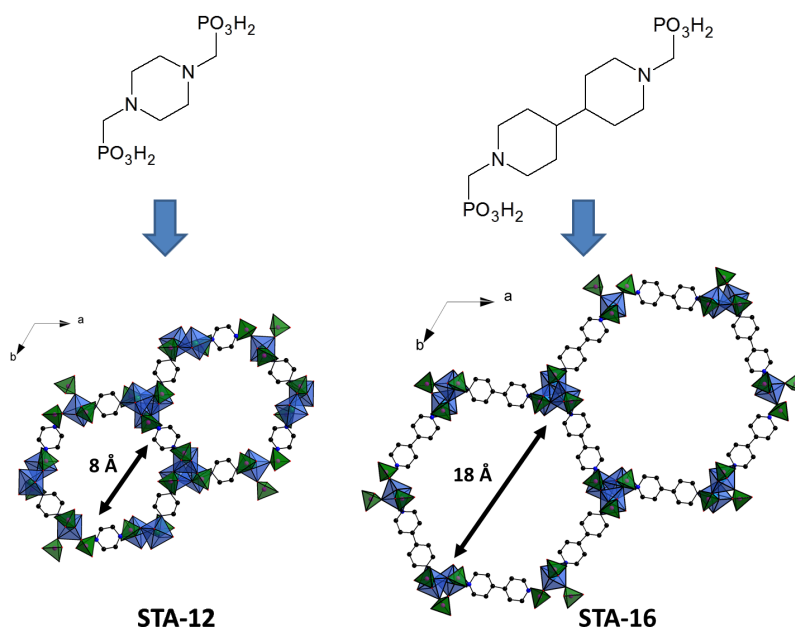


Abbildung 4.7.: Kristallstruktur von STA-12 und STA-16 mit den dazugehörigen Linkern. Die Metallatome sind in grau, die Phosphoratome in lila, die Sauerstoffatome in rot, die Kohlenstoffatome in schwarz und die Stickstoffatome in blau dargestellt. Die CPO_3 -Polyeder sind grün und die MO_5N -Polyeder sind blau dargestellt.

Ebenso können primäre Diamine zu Tetraphosphonsäuren umgesetzt werden. Aliphatische Gruppen wie 1,4-Diaminobutan wurden zur Erzeugung der Tetraphosphonsäuren $((\text{H}_2\text{O}_3\text{PCH}_2)_2\text{-NCH}_2)_2\text{-C}_4\text{H}_8 = \text{H}_8\text{L}^5$) genutzt und bereits in Kombination mit den zweiwertigen Metallionen $\text{M} = \text{Mn}^{2+}, \text{Ca}^{2+}, \text{Cd}^{2+}, \text{Co}^{2+}, \text{Fe}^{2+}, \text{Mg}^{2+}, \text{Zn}^{2+}$ und dreiwertigen Lanthanoiden ($\text{M} = \text{La}^{3+}, \text{Ce}^{3+}$) untersucht. Dies führte zu der Entdeckung von isostrukturellen Verbindungen mit der Zusammensetzung $\text{M}(\text{H}_6\text{L}^5)$ für die zweiwertigen Ionen.^[159] Die Verbindungen zeigen die in Abbildung 4.2b dargestellten isolierten MO_6 -Polyeder und bilden über Phosphonatgruppen verknüpfte Schichten aus. Die Phosphonsäuren sind jeweils einfach deprotoniert und die Stickstoffatome zur Ladungsneutralität protoniert. In den Lanthanoid-haltigen Verbindungen werden zusätzlich Oxalat- oder Sulfat-Ionen in die Struktur mit eingebaut und es werden Verbindungen mit den Zusammensetzungen $[\text{La}_2(\text{ox})_2(\text{H}_6\text{L})]$ und $[\text{La}_2(\text{ox})_2(\text{H}_6\text{L}^5)(\text{H}_2\text{O})_2] \cdot 4\text{H}_2\text{O}$ ^[160] bzw. $[\text{Ce}_2(\text{HSO}_4)_2(\text{H}_6\text{L}^5)(\text{H}_2\text{O})_6] \cdot 4\text{H}_2\text{O}$ und $[\text{Ce}_2(\text{HSO}_4)_2(\text{H}_6\text{L}^5)(\text{H}_2\text{O})_2] \cdot 2\text{H}_2\text{O}$ gebildet.^[161]

Studien, die sich mit starren aromatischen Tetraphosphonsäure Linkern beschäftigen sind sehr selten und daher sind auch nur wenige Kristallstrukturen bekannt. Auf Basis von *m*- $[(\text{H}_2\text{O}_3\text{PCH}_2)_2\text{-NCH}_2]_2\text{-C}_6\text{H}_4$ (H_8L^6) ist nur die Verbindung $[\text{Cu}_3(\text{H}_2\text{O})_5(\text{H}_2\text{L}^6)] \cdot 3\text{H}_2\text{O}$ bekannt.^[162] Sie ist aus Schichten, wie in Abbildung 4.8 gezeigt, aufgebaut die jeweils al-

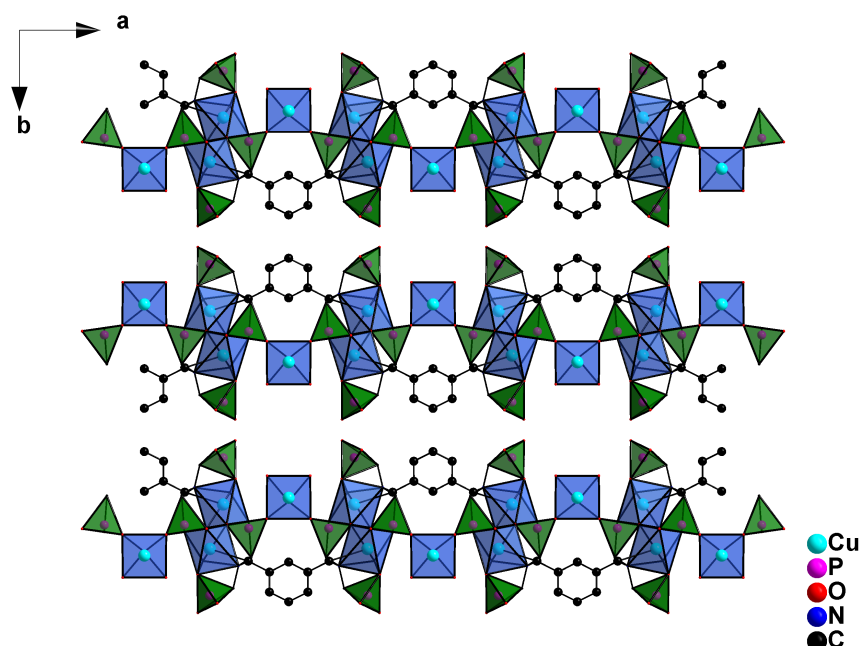


Abbildung 4.8.: Kristallstruktur von $[\text{Cu}_3(\text{H}_2\text{O})_5(\text{m}-\text{H}_2\text{L}^6)] \cdot 3\text{H}_2\text{O}$. Die CPO_3 -Polyeder sind grün die CuO_xN_y -Polyeder sind blau dargestellt.

ternierend von eckenverknüpften $\text{Cu}_2\text{O}_9\text{N}_2$ -Einheiten und CuO_5 -Einheiten gebildet werden. Diese werden über die Phosphonat-Einheiten miteinander verknüpft und von der organischen Baueinheit entlang der a -Achse verbrückt. Die Schichten sind untereinander über Wasserstoffbrückenbindungen verbunden.^[162]

Der Linker $p\text{-}[(\text{H}_2\text{O}_3\text{PCH}_2)_2\text{-NCH}_2]_2\text{-C}_6\text{H}_4$ (H_8L^7) führte bei der Reaktion mit Cu^{2+} -Ionen zu den Verbindungen $[\text{Cu}_2(\text{H}_2\text{O})_3(\text{H}_2\text{L}^7)] \cdot [\text{Cu}(\text{H}_2\text{O})_6] \cdot 2\text{H}_2\text{O}$ und mit Ca^{2+} -Ionen zu der Verbindung $[\text{Ca}(\text{H}_6\text{L}^7)] \cdot 2\text{H}_2\text{O}$.^[162,163]

Die Kristallstruktur von $[\text{Cu}_2(\text{H}_2\text{O})_3(\text{H}_2\text{L}^7)] \cdot [\text{Cu}(\text{H}_2\text{O})_6] \cdot 2\text{H}_2\text{O}$ ist in Abbildung 4.9 gezeigt. Sie ist aus kantenverknüpften $\text{Cu}_2\text{O}_9\text{N}_2$ -Dimeren aufgebaut, die von den Phosphonatgruppen zu Ketten entlang der b -Achse verknüpft sind. Die Ketten werden über die Phenylringe der Linkermoleküle verknüpft. Zwischen den so aufgespannten Schichten befinden sich $[\text{Cu}(\text{H}_2\text{O})_6]^{2+}$ -Ionen welche die Ladung kompensieren. Diese werden über Wasserstoffbrücken zwischen den Schichten gebunden.^[162]

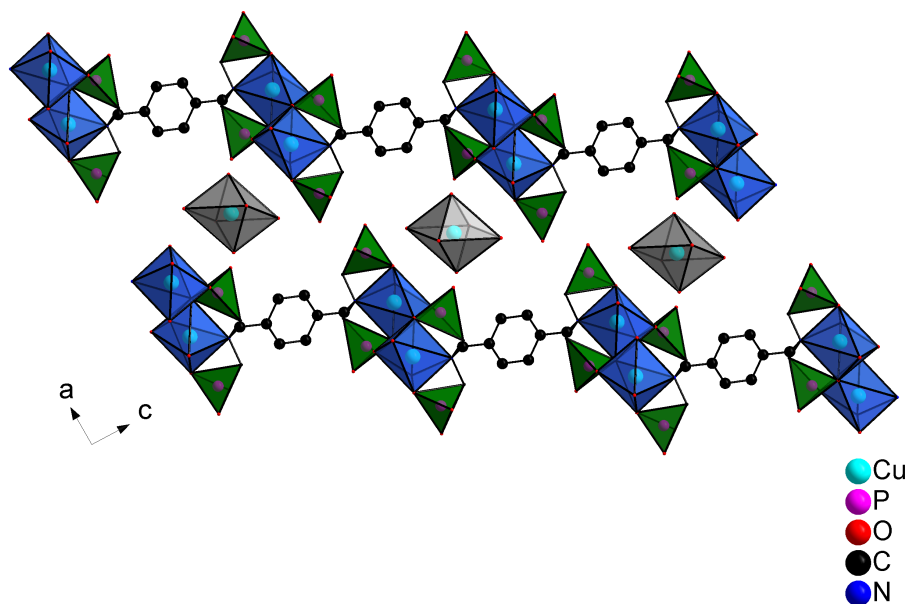


Abbildung 4.9.: Kristallstruktur von $[\text{Cu}_2(\text{H}_2\text{O})_3(\text{H}_2\text{L}^6)] \cdot [\text{Cu}(\text{H}_2\text{O})_6] \cdot 2\text{H}_2\text{O}$. Die CPO_3 -Polyeder sind grün, die $\text{Cu}_2\text{O}_9\text{N}_2$ -Polyeder sind blau dargestellt. $[\text{Cu}(\text{H}_2\text{O})_6]^{2+}$ -Ionen zwischen den Schichten sind grau dargestellt. ^[162]

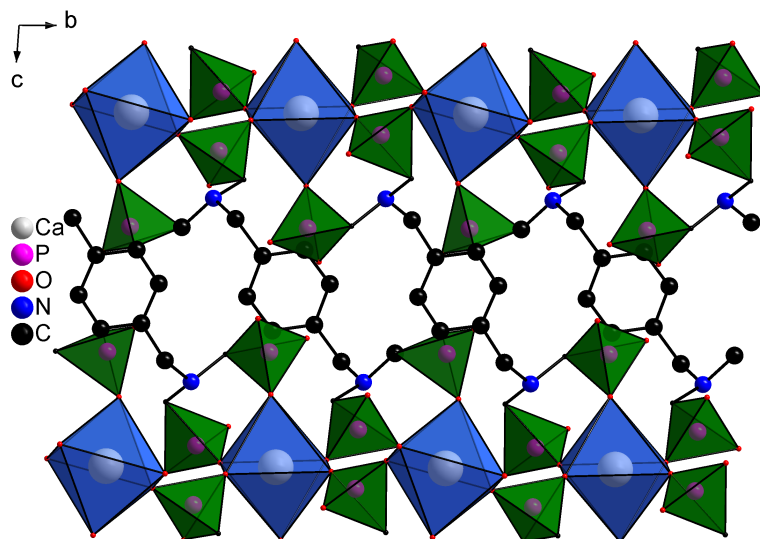


Abbildung 4.10.: Kristallstruktur von $[\text{Ca}(\text{H}_6\text{L}^7)] \cdot 2\text{H}_2\text{O}$. Die CPO_3 Polyeder sind grün, die CaO_6 -Polyeder sind blau dargestellt. Wassermoleküle wurden hier zur besseren Übersicht weggelassen. ^[163]

4. Polyfunktionalisierte Metallphosphonate

Die Kristallstruktur von $[\text{Ca}(\text{H}_6\text{L}^7)] \cdot 2\text{H}_2\text{O}$ ist in Abbildung 4.10 gezeigt. Diese ist aus CaO_6 -Polyedern aufgebaut, die über Phosphonatgruppen verknüpft sind. Dadurch bilden sich Schichten aus isolieren Polyedern, wie in Abbildung 4.2b gezeigt, aus. Die Schichten werden entlang der c -Achse über die Linker miteinander verknüpft.

4.5. *In situ* Röntgenbeugung an anorganisch-organischen Hybridverbindungen

In situ energiedispersive Röntgenbeugung (EDXRD) wurde in der Vergangenheit auf eine Vielzahl von Systemen angewendet. So wurden Kristallisationen von Thioantimonaten,^[6,164,165] Lithiumaluminiumdoppelhydroxiden,^[166] Alumophosphaten,^[167] Bismutmolybdaten,^[168] oder auch Zeolithen^[169] mittels EDXRD verfolgt. Erst seit 2010 werden *in situ* EDXRD-Untersuchungen an anorganisch-organischen Hybridverbindungen durchgeführt. Diese Studien und ihre Ergebnisse sind in Tabelle 4.5 zusammengefasst. Zusätzlich wurden noch eine winkeldispersive Röntgenbeugungsuntersuchung an MOFs durchgeführt, die zur Vollständigkeit mit aufgeführt ist.

Die ersten EDXRD Studien an anorganisch-organischen Hybridverbindungen untersuchten die Kristallisation von HKUST-1 ($[\text{Cu}_3(\text{BTC})_2] \cdot \text{Solvens}$) und wurden mittels Avrami Gleichung und der Methode von Sharp und Hancock im Temperaturbereich von 85-150 °C ausgewertet. Hierbei wurde eine Aktivierungsenergie von 73.3 kJ/mol erhalten. Dies ist in einer vergleichbaren Größenordnung mit Aktivierungsenergien der Kristallisation von Zeolithen.^[37]

Die Untersuchung der Kristallisation von Fe-MIL-53 ($[\text{Fe}(\text{OH})\text{BDC}] \cdot \text{Solvens}$) zeigte, dass bei 150 °C das kristalline Intermediat MOF-235 ($[\text{Fe}_3\text{O}(\text{BDC})_3(\text{DMF})_3][\text{FeCl}_4]$) als Zwischenstufe auftritt.^[37]

Ebenso wurden CAU-1-(OH)₂ ($[\text{Al}_8(\text{OH})_4(\text{OCH}_3)_8(\text{BDC}(\text{OH})_2)_6] \cdot x\text{H}_2\text{O}$) und CAU-1-NH₂ ($[\text{Al}_8(\text{OH})_4(\text{OCH}_3)_8(\text{BDC}(\text{NH}_2))_6] \cdot x\text{H}_2\text{O}$) mittels EDXRD untersucht. Ein Vergleich der mikrowellenunterstützten und konventionellen Synthese für die Kristallisation beider isoretikulärer Verbindungen führte zu kürzeren Reaktions- und Induktionszeiten für die mikrowellenunterstützten Reaktionen. Beide Verbindungen kristallisierten unter konventionellen Reaktionsbedingungen in ähnlichen Reaktionszeiten. Im Gegensatz dazu war die Reaktion von CAU-1-NH₂ bei mikrowellenunterstützten Synthesebedingungen signifikant schneller als die von CAU-1-(OH)₂.^[38,39]

Die Kombination aus SAXS- und WAXS-Messungen der Kristallisation von Al-MIL-53-NH₂ und Al-MIL-101-NH₂ in verschiedenen Lösungsmitteln zeigte, dass gebildete Intermediate stark abhängig vom Lösungsmittel bzw. einem Lösungsmittelgemisch sind. Die erhaltenen Ergebnisse sind in Abbildung 4.11 gezeigt.^[170] Wird die Reaktion in Wasser durchgeführt, bildet sich direkt Al-MIL-53-NH₂. In einem Lösungsmittelgemisch aus DMF und Wasser bildet sich zunächst Al-MOF-235-NH₂ als Intermediat und anschließend über

4. Polyfunktionalisierte Metallphosphonate

Tabelle 4.5.: Bisher durchgeführte Studien mittels Röntgenbeugung an anorganisch-organische Hybridverbindungen.

<i>Verbindung</i>	<i>Untersuchungen</i>
Metallcarboxylate	
HKUST-1	Kinetische Auswertung nach Avrami ^[37]
Fe-MIL-53	Qualitative Analyse, Beobachtung von Fe-MOF-235 als Intermediat ^[37]
CAU-1-(OH) ₂	Kinetische Auswertung nach Avrami für mikrowellenunterstütztes und konventionelles Heizen ^[38]
CAU-1-NH ₂	Kinetische Auswertung nach Avrami für mikrowellenunterstütztes und konventionelles Heizen ^[39]
Al-MIL-53-NH ₂ / Al-MIL-101-NH ₂	kombinierte SAXS- und WAXS-Messungen, kinetische Auswertung nach Gualtieri und Einfluss des Lösungsmittels ^[170]
Mn-MIL-100	Kinetische Auswertung nach Avrami und Gualtieri ^[171]
MOF-14	Kinetische Auswertung nach Gualtieri ^[36]
Li ₄ [C ₄ H ₂ S(CO ₂) ₂] ₂ [DMF] ₂	Kinetische Auswertung nach Gualtieri ^[35]
Fe-MIL-53	Untersuchung des Atmens von MIL-53 in Anwesenheit von verschiedenen Lösungsmitteln ^[172]
ZIF-8	Kinetische Auswertung der Synthese von Nanopartikeln nach Avrami und Gualtieri ^[119]
Metallphosphonate	
Zn ₂ (OH)(O ₃ P–C ₃ H ₆ –NH ₃) ₂ (NO ₃)	Kristallisation und pH-Wert induzierte Umwandlung ^[76]
[Zn(O ₃ P–C ₃ H ₆ –NH ₂)] · H ₂ O	Kristallisation ^[76]

einen Auflösungs-Rekristallisations-Mechanismus Al-MIL-53-NH₂. In reinem DMF wird ebenfalls Al-MOF-235-NH₂ als Intermediat beobachtet, das sich in MIL-101-NH₂ als weiteres Intermediat umwandelt. Dieses löst sich wieder auf und bildet Al-MIL-53-NH₂.^[170]

Die Kristallisation von Mn-MIL-100 ([Mn(μ₃-O)(OH)_x(H₂O)_y(BTC)₂]) wurde bei Temperaturen zwischen 125 und 145 °C mit EDXRD untersucht. Eine kinetische Auswertung wurde mittels Avrami und Gualtieri Modell durchgeführt und, obwohl beide Modelle von unterschiedlichen Annahmen ausgehen, ergeben sich Geschwindigkeitskonstanten in ähnlicher Größenordnung.^[171] Das Gualtieri Modell konnte ebenfalls erfolgreich auf die Kris-

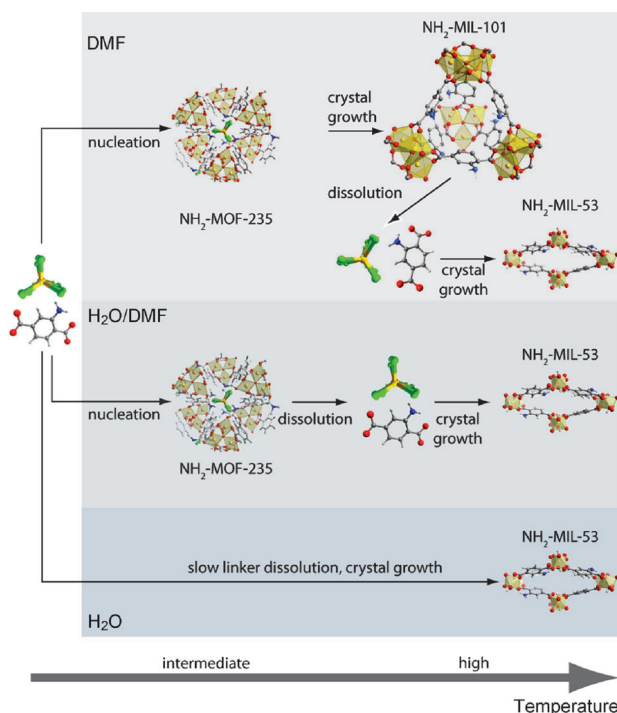


Abbildung 4.11.: Grafische Darstellung des Kristallisationsmechanismus bei verschiedenen Lösungsmitteln bzw. Lösungsmittelgemischen. Mit freundlicher Genehmigung von Wiley and Sons. ^[170]

tallisation des Kupfercarboxylat MOF-14 ($[\text{Cu}_3(\text{BTB})_2(\text{H}_2\text{O})_3] \cdot \text{Solvens}$), dem Lithiumcarboxylat $\text{Li}_4[\text{C}_4\text{H}_2\text{S}(\text{CO}_2)_2]_2[\text{DMF}]_2$ und ZIF-8 angewendet werden. Ebenso war es möglich das sogenannte „Atmen“ von Fe-MIL-53 zu untersuchen. Hierdurch konnten Informationen über die Geschwindigkeit von Lösungsmittelaufnahmen erhalten werden und Intermediate beobachtet werden. ^[172]

Im Bereich der Metallphosphonate wurden bisher nur sehr wenige EDXRD Studien unternommen. Es wurde die Kristallisation der Zinkaminophosphonate $\text{Zn}_2(\text{OH})(\text{O}_3\text{P-C}_3\text{H}_6\text{-NH}_3)_2(\text{NO}_3)$ und $[\text{Zn}(\text{O}_3\text{P-C}_3\text{H}_6\text{-NH}_2)] \cdot \text{H}_2\text{O}$ untersucht. Die Bildung beider Verbindungen wurde bei verschiedenen pH-Werten unter ansonsten ähnlichen Bedingungen untersucht. Zum Einen wurde die direkte Kristallisation der einzelnen Verbindungen beobachtet, zum Anderen die durch Zugabe von Natronlauge induzierte Phasenumwandlung von $\text{Zn}_2(\text{OH})(\text{O}_3\text{P-C}_3\text{H}_6\text{-NH}_3)_2(\text{NO}_3)$ in $[\text{Zn}(\text{O}_3\text{P-C}_3\text{H}_6\text{-NH}_2)] \cdot \text{H}_2\text{O}$. Hierbei wurden keine kristallinen Intermediate beobachtet. Gerade der Vergleich mit Metallcarboxylaten macht klar, dass noch sehr wenig über die Kristallisation von Metallphosphonaten oder polyfunktionalisierten Metallphosphonaten bekannt ist.

4.6. Ergebnisse der Synthesen und *in situ* Untersuchungen neuer polyfunktionalisierter Metallphosphonate

4.6.1. Systematic and *In Situ* Energy Dispersive X-ray Diffraction Investigations on the Formation of Lanthanide Phosphonatobutanesulfonates: $\text{Ln}(\text{O}_3\text{P-C}_4\text{H}_8\text{-SO}_3)(\text{H}_2\text{O})$ (Ln = La-Gd)

Dieser Artikel wurde in der Zeitschrift *Inorganic Chemistry* im Jahr 2010 veröffentlicht und beschäftigte sich mit der Synthese und *in situ* EDXRD Untersuchungen von neuen Lanthanoid Phosphonatobutansulfonaten (mit freundlicher Genehmigung der ACS).^[173] In vorherigen Arbeiten konnte gezeigt werden, dass es unter Verwendung von Cu^{2+} - und Zn^{2+} -Ionen möglich ist auch mit verschiedenen flexiblen Linker isoretikuläre Metallphosphonatoalkylsulfonate herzustellen.^[75,76,149] Lanthanoid-Ionen weisen eine noch höhere Koordinationszahl und dadurch auch eine höhere Koordinationsflexibilität auf, wodurch die Bildung von isoretikulären Netzwerken nicht selbstverständlich ist. Mittels Hochdurchsatzmethoden sollte überprüft werden, ob unter Verwendung des flexiblen polyfunktionalisierten Linkers 1,4-Phosphonobutansulfonsäure die Synthese isoretikulärer Verbindungen mit Lanthanoid-Ionen möglich ist.

Die Untersuchungen führten zu den neuen isostrukturellen Verbindungen $\text{Ln}(\text{O}_3\text{P-C}_4\text{H}_8\text{-SO}_3)(\text{H}_2\text{O})$ (Ln = La-Gd). Hochdurchsatzmethoden wurden eingesetzt um systematisch den Einfluss von molaren Verhältnis von $\text{Ln}^{3+}:\text{H}_3\text{L}$ und des pH-Wertes zu untersuchen. Die Kristallstrukturen von $\text{Sm}(\text{O}_3\text{P-C}_4\text{H}_8\text{-SO}_3)(\text{H}_2\text{O})$ und $\text{Pr}(\text{O}_3\text{P-C}_4\text{H}_8\text{-SO}_3)(\text{H}_2\text{O})$ konnten mittels Einkristallstrukturanalyse aufgeklärt werden. Die Verbindungen sind isoretikulär zu den bekannten Verbindungen $\text{Ln}(\text{O}_3\text{P-C}_2\text{H}_4\text{-SO}_3)(\text{H}_2\text{O})$.^[141] In der Studie wurde ebenso wie in dem System $\text{Ln}^{3+} / \text{H}_2\text{O}_3\text{P-C}_2\text{H}_4\text{-SO}_3\text{H} / \text{NaOH}$ nur eine Verbindung beobachtet. Die um zwei $-\text{CH}_2$ -Gruppen verlängerte Alkylkette und die dadurch höhere Flexibilität hat somit keinen Einfluss auf die gebildeten Kristallstrukturen.

Weiterhin war es Ziel dieser Arbeit erstmalig die Kristallisation von Metallphosphonaten mittels *in situ* EDXRD zu untersuchen, da über die Kristallisation solcher Verbindungen bis dato nichts bekannt war. Die Kristallisation der Verbindung $\text{Sm}(\text{O}_3\text{P-C}_4\text{H}_8\text{-SO}_3)(\text{H}_2\text{O})$ wurde sowohl mit konventionelle Heizmethoden als auch einem modifizierten Mikrowellen-

reaktor, der erstmals extra hierfür in den Versuchsaufbau an Beamline F3, DESY, Hamburg, eingebracht wurde, durchgeführt. Die Reaktion verläuft über zwei Stufen. Im ersten Schritt wird ein kristallines Intermediat beobachtet, das sich komplett in die Titelverbindung umwandelt. Das Intermediat konnte jedoch nicht isoliert werden. Die Temperaturen wurden jeweils für beide Synthesemethoden zwischen 110 und 150 °C variiert und die Methode von Sharp und Hancock verwendet, um die Kinetik der Kristallisation auszuwerten.^[111] Die unterschiedlichen Heizmethoden haben einen Einfluss auf die Reaktionsgeschwindigkeit, die Arrhenius Aktivierungsenergie und den präexponentiellen Faktor.

Systematic and In Situ Energy Dispersive X-ray Diffraction Investigations on the Formation of Lanthanide Phosphonatobutanesulfonates: $\text{Ln}(\text{O}_3\text{P-C}_4\text{H}_8\text{-SO}_3)(\text{H}_2\text{O})$ (Ln = La–Gd)Mark Feyand,[†] Christian Näther,[†] André Rothkirch,[‡] and Norbert Stock^{*†}[†]Institut für Anorganische Chemie, Christian-Albrechts-Universität, Max-Eyth Strasse 2, D 24118 Kiel, Germany, and [‡]HASYLAB, DESY Hamburg, Notkestrasse 85, 22607 Hamburg, Germany

Received September 1, 2010

Using the flexible linker $\text{H}_2\text{O}_3\text{P-C}_4\text{H}_8\text{-SO}_3\text{H}$ (H_3L) and rare earth ions Ln^{3+} (Ln = La, Ce, Pr, Nd, Sm, Eu, Gd) we were able to synthesize the new isostructural inorganic organic hybrid compounds $\text{Ln}(\text{O}_3\text{P-C}_4\text{H}_8\text{-SO}_3)(\text{H}_2\text{O})$. High-throughput experiments were employed to study the influence of the molar ratios Ln: H_3L and pH on the product formation. The crystal structure of the compounds $\text{Sm}(\text{O}_3\text{P-C}_4\text{H}_8\text{-SO}_3)(\text{H}_2\text{O})$ (**1**) and $\text{Pr}(\text{O}_3\text{P-C}_4\text{H}_8\text{-SO}_3)(\text{H}_2\text{O})$ (**2**) were determined by single crystal diffraction. The structures are built up from chains of edge-sharing LnO_8 -polyhedra that are connected by the phosphonate and sulfonate groups into layers. These layers are linked by the $-(\text{CH}_2)_4-$ group to form a three-dimensional framework. The synthesis of compound **1** was scaled up in a conventional oven as well as in a microwave reactor system. A modification of a microwave reactor system allowed its integration into the beamline F3 at HASYLAB, DESY, Hamburg. The crystallization was investigated in situ by means of energy dispersive X-ray diffraction using conventional as well as microwave heating methods applying temperatures varying from 110 to 150 °C. The formation of $\text{Sm}(\text{O}_3\text{P-C}_4\text{H}_8\text{-SO}_3)(\text{H}_2\text{O})$ takes place in two steps. In the first step a crystalline intermediate was observed, which transforms completely into compound **1**. The method by Sharp and Hancock was used to determine the rate constants, reaction exponents, and the Arrhenius activation energy for both reaction steps. Comparing both heating methods, microwave heating leads to fully crystallized reaction product after shorter reaction times, but neither the temperature nor the heating method has significant influence on the induction time.

Introduction

Inorganic–organic hybrid compounds are currently under intensive investigations because of their potential application in gas storage, catalysis, or charge storage materials.^{1,2} Most of these compounds are based on polycarboxylates, -phosphonates, or -sulfonates.^{3,4} Different polyfunctionalized organic building units containing two or more functional groups have been used less often. In the field of metal phosphonates these mainly include phosphonocarboxylic acids^{5–7} and

aminophosphonic acids.^{8,9} Very recently phosphonatosulfonic acids have also come into the focus of interest.^{10–14}

The majority of known metal phosphonatosulfonates are based on rigid organic building units, that is, *m*- and *p*-sulfo-phenylphosphonic acid. In combination with co-ligands often M–O-Clusters are obtained.^{15–20} Such compounds show a large structural variety ranging from isolated cluster,^{15,18,19} one-dimensional chains¹⁸ to three-dimensional frameworks.¹⁶ We are interested in the synthesis of hybrid compounds with flexible phosphonosulfonic acids and have therefore synthesized and

*To whom correspondence should be addressed. Phone: +49-431-880-1675. Fax: +49-431-880-1775. E-mail: stock@ac.uni-kiel.de.

- Clearfield, A. *Prog. Inorg. Chem.* **1998**, *47*, 371–510.
- Czaja, A. U.; Trukhan, N.; Müller, U. *Chem. Soc. Rev.* **2009**, *38*, 1284.
- Shimizu, G. K. H.; Vaidhyanathan, R.; Taylor, J. M. *Chem. Soc. Rev.* **2009**, *38*, 1430.
- Rowse, J. L. C.; Yaghi, O. M. *Microporous Mesoporous Mater.* **2004**, *73*, 3.
- Bauer, S.; Marrot, J.; Devic, T.; Férey, G.; Stock, N. *Inorg. Chem.* **2007**, *46*(23), 9998–10002.
- Bauer, S.; Bein, T.; Stock, N. *Solid State Sci.* **2008**, *10*(7), 837–846.
- Stock, N.; Frey, S. A.; Stucky, G. D.; Cheetham, A. K. *J. Chem. Soc., Dalton Trans.* **2000**, 4292–4296.
- Cao, G.; Hong, H. G.; Mallouk, T. E. *Acc. Chem. Res.* **1992**, *25*(9), 420–427.
- Casciola, M.; Costantino, U.; Peraio, A.; Rega, T. *Solid State Ionics* **1995**, *77*, 229–233.

- Sonnauer, A.; Stock, N. *Eur. J. Inorg. Chem.* **2008**, 5038.
- Sonnauer, A.; Feyand, M.; Stock, N. *Cryst. Growth Des.* **2008**, *9*(1), 586–592.
- Sonnauer, A.; Näther, C.; Höpfe, H. A.; Senker, J.; Stock, N. *Inorg. Chem.* **2007**, *46*(23), 9968–9974.
- Sonnauer, A.; Stock, N. *Inorg. Chem.* **2005**, *2007*(44), 5882.
- Sonnauer, A.; Stock, N. *J. Solid State Chem.* **2008**, *181*, 473.
- Du, Z.-Y.; Xu, H.-B.; Mao, J.-G. *Inorg. Chem.* **2006**, *45*, 9780.
- Du, Z.-Y.; Xu, H.-B.; Mao, J.-G. *Inorg. Chem.* **2006**, *45*, 6424.
- Du, Z.-Y.; Xie, Y.-R.; Wen, H. R. *Acta Crystallogr., Sect. E* **2007**, *E63*, M2766.
- Du, Z.-Y.; Prosvirin, V. A.; Mao, J.-G. *Inorg. Chem.* **2007**, *46*, 9884.
- Du, Z.-Y.; Li, X.-L.; Liu, Q.-Y.; Mao, J.-G. *Cryst. Growth Des.* **2007**, *7*, 1501.
- Du, Z.-Y.; Xu, H.-B.; Li, X.-L.; Mao, J.-G. *Eur. J. Inorg. Chem.* **2007**, 4520.

employed the phosphonosulfonic acids with different chain lengths $\text{H}_2\text{O}_3\text{P-C}_2\text{H}_4\text{-SO}_3\text{H}$ ^{10,12–14,21} and $\text{H}_2\text{O}_3\text{P-C}_4\text{H}_8\text{-SO}_3\text{H}$.¹¹

These metal phosphonosulfonates have been synthesized under solvothermal reaction conditions. Small variations in the reaction conditions often lead to new compounds resulting in complex crystallization diagrams. Mostly conventional heating methods have been used, and recently a study employing microwave assisted heating has been described.²¹ An acceleration of the product formation compared to conventional heating was observed. The influence of heating by microwave irradiation is discussed controversially in the literature.^{22,23} Some authors attribute the differences to thermal as well as non-thermal microwave effects.

To investigate the multiparameter space of such systems, high-throughput (HT) methods have been shown to accelerate the discovery of compounds and the synthesis optimization, as well as the determination of reaction trends.^{24–26} Thus, HT studies allow to systematically investigate the influence of different parameters such as the pH of the reaction mixture,²⁷ the reaction temperature,²⁸ the molar ratios of reactants,²⁹ and the nature of solvents.^{5,30} Although HT methods allow for effective study of reaction systems, they do not reveal information on the crystallization rate or mechanism.

The crystallization can be studied by energy dispersive X-ray diffraction (EDXRD) measurements.^{31–34} White beam synchrotron radiation is widely used to achieve a time resolution below one minute per spectrum. Employing this method, for example, the crystallization of zeolites,³⁴ thioantimonates,³² metal–organic frameworks (MOFs),³³ or the breathing effect of flexible MOFs³⁵ was investigated. EDXRD measurements allow the monitoring of the crystallization and thus offer the possibility to observe crystalline intermediate phases. These can either be isolated by quenching³³ or are only stable in the reaction mixture.^{33,36} Applying the Avrami–Erofeev equation and the method of Sharp and Hancock to the data, kinetic analyses yield the rate constants and information on the possible reaction mechanism.³⁷ This allows to study the influence of reaction temperatures and concentrations on the crystallization and the mechanism.³⁶ In case of temperature

dependent EDXRD studies, the Arrhenius activation energies can be calculated.^{31,32,36,38,39}

In this study we describe a systematic investigation of the rare earth phosphonosulfonates $\text{Ln}(\text{O}_3\text{P-C}_4\text{H}_8\text{-SO}_3)(\text{H}_2\text{O})$ ($\text{Ln} = \text{La–Gd}$) by HT methods and the first temperature dependent EDXRD on the formation of metal phosphonates. The influence of heating methods is studied by carrying out reactions under microwave as well as conventional heating which required the implementation of a microwave reactor system at beamline F3, HASYLAB, Hamburg.

Experimental Section

4-Phosphonobutanesulfonic acid $\text{H}_2\text{O}_3\text{P-C}_4\text{H}_8\text{-SO}_3\text{H}$ (H_3L) was synthesized as previously reported in the literature in a two step nucleophile substitution reaction of 1,4-dibromobutane with triethylphosphite and sodium sulfite.¹¹ All other reagents were of analytical grade (Fluka and Aldrich) and were used without further purification. HT-X-ray powder diffraction (XRPD) measurements were carried out on a Stoe Stadi P HT-diffractometer in transmission geometry with $\text{Cu K}\alpha_1$ radiation, equipped with an image plate detector. MIR spectra were recorded on an ATI Matheson Genesis in the spectral range $4000\text{–}400\text{ cm}^{-1}$ ($2.5\text{–}25\text{ }\mu\text{m}$) using the KBr disk method. For the thermogravimetric analysis under air a NETSCH STA 409 CD analyzer was used with a heating rate of 4 K/min (flow rate: 75 mL/min).

HT Experiments. The system $\text{SmCl}_3/\text{H}_3\text{L}/\text{NaOH}$ in water was investigated by using HT methods. All reagents were dispensed as aqueous solutions. The experiments were carried out to investigate the influence of the molar ratios $\text{H}_3\text{L}/\text{SmCl}_3$ and the pH on the product formation. A custom-made HT reactor containing 48 PTFE liners each with a maximum volume of $300\text{ }\mu\text{L}$ was used.⁴⁰ Different combinations of molar ratios $\text{SmCl}_3/\text{H}_3\text{L}/\text{NaOH}$ varying from 1–4:1–4:0–10 were investigated. The solutions were added to the PTFE inserts, homogenized by stirring, and heated in 15 h to $150\text{ }^\circ\text{C}$, held at that temperature for 48 h, and then cooled down to room temperature in 15 h. The products were filtered off, washed with water, dried in air and characterized by XRPD measurements. Details of the exact amounts employed and the reaction products are given in Supporting Information, Table S1. The pH values of all starting mixtures were measured using pH paper with an error range of ± 1 .

Scale-up Synthesis. Larger amounts of compound **1** were obtained using the optimized synthesis conditions as derived from the HT study. A $146\text{ }\mu\text{L}$ portion of an aqueous $4\text{ M H}_3\text{L}$ solution, $1560\text{ }\mu\text{L}$ of water, $146\text{ }\mu\text{L}$ of an aqueous 2 M SmCl_3 solution, and $292\text{ }\mu\text{L}$ of a 4 M NaOH solution were added into a Schott Duran glass culture tubes (Gl-14), mixed by shaking and heated in an oven for 15 h at $150\text{ }^\circ\text{C}$. The white solid was isolated and washed with water yielding an amount of 80.6 mg (72% based on H_3L).

Microwave Synthesis. Exactly the same amounts of base materials were used for the microwave assisted synthesis. The solutions of the base materials were mixed in a microwave tube (Biotage, 0.5–2 mL glass reactor), sealed with a septum, mixed by shaking, and heated in a microwave oven (Biotage Injector) for 4 h at $150\text{ }^\circ\text{C}$. The white solid was isolated by filtration and washed with water yielding an amount of 73.9 mg (66% based on H_3L).

Synthesis of $\text{Ln}(\text{O}_3\text{P-C}_4\text{H}_8\text{-SO}_3)(\text{H}_2\text{O})$ ($\text{Ln} = \text{La–Gd}$). Isostructural rare earth compounds were obtained applying the optimized synthesis conditions of the Sm compound as derived from the HT study. The HT reactors were used, and $15\text{ }\mu\text{L}$ of a $4\text{ M H}_3\text{L}$ solution, $156.0\text{ }\mu\text{L}$ of water, $15\text{ }\mu\text{L}$ of a 2 M LnX_3 ($\text{LnX}_3 = \text{La}(\text{NO}_3)_3$, $\text{Ce}(\text{NO}_3)_3$, $\text{Pr}(\text{NO}_3)_3$, $\text{Nd}(\text{NO}_3)_3$, $\text{Eu}(\text{NO}_3)_3$, $\text{Gd}(\text{CH}_3\text{CO}_2)_3$), and $15\text{ }\mu\text{L}$ of 4 M NaOH were mixed in the $300\text{ }\mu\text{L}$ PTFE inserts. The mixtures were homogenized by shaking and heated in an oven for

- (21) Sonnauer, A.; Stock, N. *J. Solid State Chem.* **2008**, *181*, 3065.
 (22) Hoz, A. d. I.; Diaz-Ortiz, A.; Moreno, A. *Chem. Soc. Rev.* **2005**, *34*, 164.
 (23) Obermayer, D.; Gutmann, B.; Kappe, C. O. *Angew. Chem., Int. Ed.* **2009**, *48*(44), 8321–8324.
 (24) Corma, A.; Diaz-Cabanas, M. J.; Jorda, J. L.; Martinez, C.; Moliner, M. *Nature* **2006**, *443*(7113), 842–845.
 (25) Banerjee, R.; Phan, A.; Wang, B.; Knobler, C.; Furukawa, H.; O’Keeffe, M.; Yaghi, O. M. *Science* **2008**, *319*, 939.
 (26) Stock, N. *Microporous Mesoporous Mater.* **2009**, *3*, 287.
 (27) Stock, N.; Bein, T. *Angew. Chem., Int. Ed.* **2004**, *43*(6), 767–770.
 (28) Bauer, S.; Stock, N. *Angew. Chem., Int. Ed.* **2007**, *46*(36), 6857–6860.
 (29) Stock, N.; Bein, T. *J. Mater. Chem.* **2005**, *15*, 1384.
 (30) Ahnfeldt, T.; Guillou, N.; Gunzelmann, D.; Margiolaki, I.; Loiseau, T.; Férey, G.; Senker, J.; Stock, N. *Angew. Chem., Int. Ed.* **2009**, *48*(28), 5163.
 (31) Engelke, L.; Schaefer, M.; Porsch, F.; Bensch, W. *Eur. J. Inorg. Chem.* **2003**, *2003*(3), 506–513.
 (32) Engelke, L.; Schäfer, M.; Schur, M.; Bensch, W. *Chem. Mater.* **2001**, *13*(4), 1383.
 (33) Millange, F.; Medina, M. I.; Guillou, N.; Férey, G.; Golden, K. M.; Walton, R. I. *Angew. Chem., Int. Ed.* **2010**, *49*(4), 763–766.
 (34) Walton, R. I.; O’Hare, D. *J. Phys. Chem. B.* **2001**, *105*(1), 91.
 (35) Millange, F.; Serre, C.; Guillou, N.; Férey, G.; Walton, R. I. *Angew. Chem., Int. Ed.* **2008**, *47*(22), 4100.
 (36) Kiebach, R.; Pienack, N.; Ordloff, M.-E.; Studt, F.; Bensch, W. *Chem. Mater.* **2006**, *18*(5), 1196–1205.
 (37) Sharp, J. D.; Hancock, J. H. *J. Am. Ceram. Soc.* **1972**, *55*, 74.
 (38) Finney, E. E.; Finke, R. G. *Chem. Mater.* **2009**, *21*(19), 4692–4705.
 (39) Francis, R. J.; Price, S. J.; Evans, J. S. O.; O’Brien, S.; O’Hare, D.; Clark, S. M. *Chem. Mater.* **1996**, *8*(8), 2102–2108.

(40) Stock, N. *Microporous Mesoporous Mater.* **2010**, *129*(3), 287.

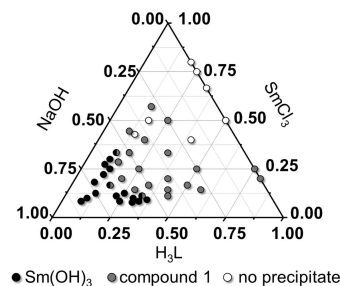
Table 1. Summary of Crystal Data, Intensity Measurement, and Structure Refinement Parameters for $\text{Sm}(\text{O}_3\text{P-C}_2\text{H}_4\text{-SO}_3)(\text{H}_2\text{O})$ (**1**) and $\text{Pr}(\text{O}_3\text{P-C}_2\text{H}_4\text{-SO}_3)(\text{H}_2\text{O})$ (**2**)

	compound 1	compound 2
formula	$\text{C}_4\text{H}_{10}\text{O}_7\text{PSSm}$	$\text{C}_4\text{H}_{10}\text{O}_7\text{PSPr}$
formula weight (g/mol)	383.52	374.05
crystal system	monoclinic	monoclinic
space group	$P2_1/c$ (No. 14)	$P2_1/c$ (No. 14)
<i>a</i> (pm)	1081.4(2)	1081.2(1)
<i>b</i> (pm)	1311.3(3)	1322.72(5)
<i>c</i> (pm)	710.58(14)	716.22(4)
β (deg)	104.51(3)	104.84(1)
<i>V</i> (10^6 pm^3)	975.5(4)	990.1(1)
<i>Z</i>	4	4
tot., uniq. data, R_{int}	8013, 1586, 0.050	7034, 1468, 0.063
observed data [$I > 2\sigma(I)$]	1303	1468
R1, wR2	0.0295, 0.0807	0.0285, 0.0837
GOF	0.98	1.16
Δe min./max. ($e/\text{\AA}^3$)	-1.17, 0.79	0.808, -0.828

48 h at 150 °C. The solids were filtered off and washed with water. The products were characterized by XRPD, patterns are shown in Supporting Information, Figure S2, and the refined cell parameters are given in Supporting Information, Table S2.

Structure Determination. Suitable crystals of the compounds $\text{Sm}(\text{O}_3\text{P-C}_2\text{H}_4\text{-SO}_3)(\text{H}_2\text{O})$ (**1**) and $\text{Pr}(\text{O}_3\text{P-C}_2\text{H}_4\text{-SO}_3)(\text{H}_2\text{O})$ (**2**) were carefully selected from the HT experiments using a polarizing microscope. X-ray diffraction measurements were performed on a STOE IPDS diffractometer equipped with a fine-focus sealed tube (Mo K_α radiation, $\lambda = 71.073 \text{ pm}$). For absorption correction the programs XRed and X-Shape were used.⁴¹ The crystal structures were solved by direct methods with SHELXS-97 and refined using SHELXL-97.⁴² For both compounds only non-merohedral twinned crystals were obtained. The reflections of both individuals were indexed separately using RECIPE, and integration of the intensities was performed using TWIN.⁴¹ By this procedure overlapping reflections were omitted. Experimental data and results of the structure determination of compounds **1** and **2** are given in Table 1. Selected bond lengths are given in Supporting Information, Table S3. For both compounds, the hydrogen atoms of the water molecule could be localized from the difference Fourier map. The hydrogen bond lengths and angles are given in the Supporting Information, Table S4, and the H-bonding scheme is given in the Supporting Information, Figure S3.

In Situ Experiments. EDXRD experiments were carried out at HASYLAB, beamline F3 at DESY, Hamburg, Germany. The white synchrotron radiation (4 to 55 KeV) was detected by a liquid nitrogen cooled germanium semiconductor detector system. The detector angle was set to approximately 1.9°. The best results were obtained by collimating the beam to $0.2 \times 0.2 \text{ mm}^2$. A microwave oven (Biotage Initiator) was modified to permit direct irradiation of the glass reactor (Supporting Information, Figure S6). One advantage of the microwave system is the online logging of the reaction conditions, that is, pressure, temperature, and stirring rates. For conventional heating a custom-made reactor system heated by an external thermostat (JULABO) was used.^{31,32} The spectra were recorded with acquisition times between 30 and 120 s to get the best resolution at the given reaction temperature. For both heating methods exactly the same amounts of starting materials were used: 148 μL of 2 M H_3L , 1500 μL of water, 148 μL of 2 M SmCl_3 , and 200 μL of 2 M NaOH solutions were mixed in a glass vessel and sealed. The reaction solutions were homogenized, and the first spectrum was taken directly after starting the heating. The reaction temperatures were set to 110, 120, 130, 140, and 150 °C.

**Figure 1.** Crystallization diagram of the system $\text{SmCl}_3/\text{H}_3\text{L}/\text{NaOH}$ at 150 °C.

Results and Discussion

HT Study. The results of this investigation, based on the XRPD measurements are shown in Figure 1. In the ternary crystallization diagram only two compounds can be observed. At the molar ratios of $\text{SmCl}_3/\text{H}_3\text{L}/\text{NaOH}$ 1–4:1–4:4–10 (pH > 10, Supporting Information, Table S1) only $\text{Sm}(\text{OH})_3$ was obtained. At the molar ratios of 1–5:1–4:1–4 (pH 2–9, Supporting Information, Table S1) the title compound **1** was obtained. No precipitate was observed at very acidic conditions for the molar ratios of 1–4:1–2:0–3 at a (pH 1–2, Supporting Information, Table S1). At the molar ratio $\text{SmCl}_3/\text{H}_3\text{L}/\text{NaOH} = 1:2:1$ a non-merohedral twinned crystal was isolated.

Substituting Sm by La, Ce, Pr, Nd, Eu, or Gd leads to the formation of the isostructural compounds. The title compound **2** was isolated from these experiments, which also form twinned crystals. The powder patterns as well as the refined cell parameters of the isostructural compounds $\text{Ln}(\text{O}_3\text{P-C}_4\text{H}_8\text{-SO}_3)(\text{H}_2\text{O})$ ($\text{Ln} = \text{La-Gd}$) are given in Supporting Information, Figure S2 and Table S2, respectively.

Crystal Structure of $\text{Sm}(\text{O}_3\text{P-C}_4\text{H}_8\text{-SO}_3)(\text{H}_2\text{O})$. Since all title compounds are isostructural, the description of the crystal structure is given using the example of $\text{Sm}(\text{O}_3\text{P-C}_4\text{H}_8\text{-SO}_3)(\text{H}_2\text{O})$ (**1**). It is not trivial to distinguish between phosphorus and sulfur employing X-ray scattering methods because of the similarity of the scattering factors. Both atoms have been differentiated by a comparison of the P–O and S–O bond lengths with bond length of lanthanide phosphonates and sulfonates as reported in the literature. For example the compounds $\text{Sm}[(\text{O}_3\text{PCH}_2)_2\text{N}(\text{H})\text{C}_6\text{H}_4\text{COOH}] \cdot \text{H}_2\text{O}$,⁴³ $\text{GdH}[\text{O}_3\text{P}(\text{CH}_2)_3\text{PO}_3]^{44}$, and $\text{La}(\text{O}_3\text{PC}_6\text{H}_5)(\text{HO}_3\text{-PC}_6\text{H}_5)^{45}$ show P–O bond lengths of 147(2)–155(1) pm whereas significantly shorter S–O bond lengths varying from 143(1) to 146(1) pm are observed for the compounds $\text{La}(\text{CH}_3\text{SO}_3)_3 \cdot 2\text{H}_2\text{O}$ ⁴⁶ and $(\text{C}_{10}\text{H}_7\text{SO}_3)[\text{Pr}(\text{C}_{10}\text{H}_7\text{SO}_3)_2(\text{H}_2\text{O})_6] \cdot \text{H}_2\text{O}$.⁴⁷ P–O bond lengths ranging from 149.0(1) to 155.2(4) pm and S–O bond lengths ranging from 145(1) and 147.3(4) pm were found for compounds **1** and **2** and agree very well with the literature data.

The three-dimensional structure is composed of Sm^{3+} and 4-phosphonatobutanesulfonate ($\text{O}_3\text{P-C}_4\text{H}_8\text{-SO}_3$)³⁻ ions as well as one water molecule. The Sm^{3+} ions are

(43) Bauer, S.; Bein, T.; Stock, N. *J. Solid State Chem.* **2005**, *179*, 145.(44) Serpaggi, F.; Férey, G. *J. Mater Chem.* **1998**, *8*, 2749.(45) Wang, R. C.; Zhang, Y.; Hu, H.; Frausto, R. R.; Clearfield, A. *Chem. Mater.* **1992**, *4*, 864.(46) Wickleder, M. *S. Z. Anorg. Allg. Chem.* **2001**, *627*, 1675.(47) Ohki, Y. S.; Y.; Nakamura, M.; Shimoi, M.; Ouchi, A. *Bull. Chem. Soc. Jpn.* **1985**, *58*, 2968.

(41) XRED version 1.19, X-Shape version 1.06, RECIPE, TWIN; Stoe & Cie GmbH: Darmstadt, Germany, 1999.

(42) Sheldrick, G. M. *SHELXTL-PLUS Crystallographic System*; Siemens Analytical X-ray Instruments Inc.: Madison, WI, 1992.

surrounded by eight oxygen atoms. Each rare earth ion is connected to six $\text{O}_3\text{P-C}_4\text{H}_8\text{-SO}_3^{3-}$ ions through five P–O–Sm and two S–O–Sm bonds. The full coordination sphere is completed by the H_2O molecule (Figure 2). The oxygen atoms act as end on (O1, O5, O6) as well as bridging ligand atoms (O2, O3). Thus, edge-sharing of the SmO_8 -polyhedra is observed that lead to the formation of chains along the *c*-axis. These chains are connected to layers by the phosphonate and sulfonate groups (Figure 3). The interconnection of the layers is accomplished through the $-(\text{CH}_2)_4-$ group and a three-dimensional framework is formed. The structure is further stabilized by hydrogen bonds between the oxygen atom O4 of the sulfonate group and the coordinated water molecule (OW1) (Supporting Information, Figure S3, Table S4).

The obtained compounds are isorecticular to the previously reported series $\text{Ln}(\text{O}_3\text{P-C}_2\text{H}_4\text{-SO}_3)(\text{H}_2\text{O})$ with Ln = La, Ce, Pr, Nd, Sm, Eu, Gd, Tb, Dy.¹² The extension of the organic linker from $-\text{C}_2\text{H}_4-$ with $-\text{C}_4\text{H}_8-$ led to the extension of the spacing from 832.6 to 1046.9 pm between the inorganic layers.

IR and Raman Spectroscopy Study. Compound **1** was studied by IR and Raman spectroscopy (Supporting Information, Figure S4). The bands between 1250 and 950 cm^{-1} can be assigned to the P–C, P–O, S–C, and S–O stretching vibrations of the tetrahedral CPO_3^- and CSO_3^- -groups. The broad band around 3421 cm^{-1} confirms the presence of water molecules that form H-bonds. The corresponding deformation band appears at 1662 cm^{-1} . Bands in the

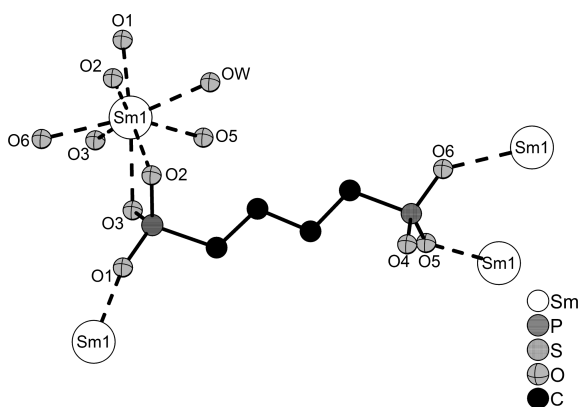


Figure 2. Coordination spheres of the Sm^{3+} ion in compound **1**.

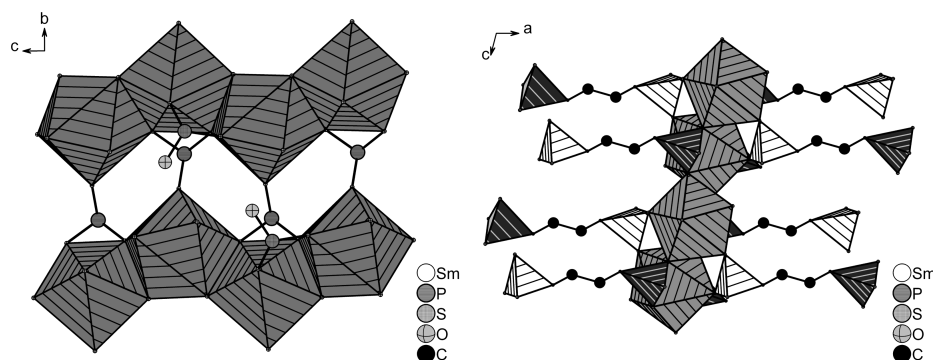


Figure 3. One-dimensional chains of edge-sharing SmO_8 -polyhedra along the *c*-axis are connected by the sulfonate- and phosphonate groups. SmO_8 -polyhedra are shaded in gray (left). The LaO_8 -polyhedra-sulfonate/phosphonate layers are interconnected by the $-(\text{CH}_2)_4-$ groups and form a three-dimensional network (right). The C-PO_3 tetrahedra are shaded dark gray and the C-SO_3 tetrahedra are shaded white.

region from 3000 to 2900 cm^{-1} are due to CH_2 stretching vibrations. The corresponding CH_2 -deformation vibration appears in the range of 1466 cm^{-1} .

Thermal Study. Thermogravimetric (TG) measurements were performed to gain deeper insight on the thermal stability of the title compound. The results of TG investigation (Supporting Information, Figure S5) show three steps of weight loss for $\text{Sm}(\text{O}_3\text{P-C}_2\text{H}_4\text{-SO}_3)(\text{H}_2\text{O})$. The loss of one water molecule per formula unit (observed, -5.1% ; calculated, -4.7%) is found up to a temperature of $360\text{ }^\circ\text{C}$. The dehydrated sample can be heated up to $400\text{ }^\circ\text{C}$ without any weight loss. Above this temperature the decomposition of the organic molecules takes place in two steps and leads to an X-ray amorphous residue. The dehydrated sample showed a poor crystallinity and could not be rehydrated with water.

In Situ X-ray Investigations. The formation of compound **1** was investigated by EDXRD measurement using conventional and microwave heating at 110 – $150\text{ }^\circ\text{C}$. The EDXRD spectra for the syntheses at $150\text{ }^\circ\text{C}$ are shown in Figure 4.

Qualitatively both crystallization processes are independent of the heating methods. Therefore, the results obtained by conventional heating are described. During the first 5 min a modulation of the background in the range of 30 – 40 keV is observed (compare Supporting Information, Figure S7). This indicates the presence of an X-ray amorphous side phase in the first step of the reaction. Furthermore after 1 min a crystalline intermediate phase is detected. This phase transforms completely into compound **1** during the first 7 min. The transformation is apparent from the peak shift in the range 31 – 34 keV (Figure 5). In quenching experiments it was not possible to isolate the intermediate phase in reasonable crystallinity. Unfortunately the most intensive peak of the intermediate phase and the peak corresponding to the 100 reflection of compound **1** overlap strongly (33.20 keV ($d = 1060\text{ pm}$) vs 32.76 keV ($d = 1027\text{ pm}$)). Hence, for a quantitative evaluation, a data deconvolution was carried out by a brute force method assuming the overlapping peaks as a superposition of two Gaussians. For this time-consuming calculation the free parameters like the half-width, standard derivation, and the peak position had to be restricted to certain value ranges. For given boundaries, all possible superpositions of the two Gaussians were tested to get the best description of the obtained spectra. The transformation of the intermediate phase and the resulting normalized integrals

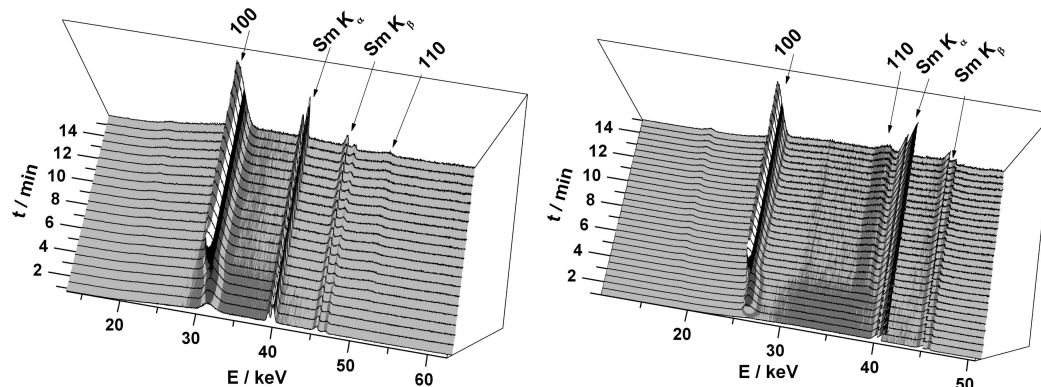


Figure 4. EDXRD patterns of the formation of compound **1** at 150 °C by conventional heating (left) and microwave heating (right).

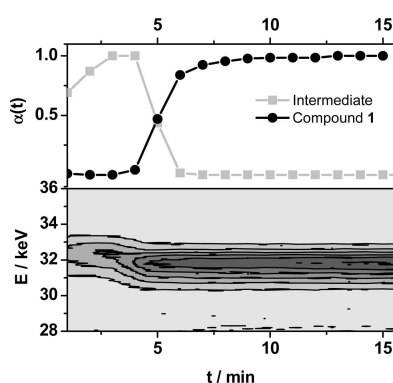


Figure 5. Surface plot of the transformation of the intermediate into compound **1** and reaction progress ($\alpha(t)$) for both phases (conventional heating, 150 °C).

$\alpha(t)$ (reaction progress) are shown in Figure 5. After the transformation ($t > 6$ min) process, the intensity of the 100 peak of compound **1** is slightly increasing which indicates that the reaction is not finished.

For the kinetic analyses the reactions were repeated at different temperatures (110, 120, 130, and 140 °C). Microwave as well as conventional heating was employed to study the temperature dependence and influence of the heating method on the reaction (Figure 6). Differences in the heating progress are clearly visible for different temperatures. The curves show for both heating methods, that higher temperatures lead to faster reactions and shorter induction times as one might expect. The intermediate phase is observed in all reactions. For both heating methods similar induction times were found, ranging from 3 to 8 min. The differences substantiate a closer look at the rate of reaction, which turns out higher for the microwave heating. This is seen by comparing the reactions at 110, 120, and 130 °C. While almost no changes in reaction time are found in microwave heating, a significant increase in reaction time with decreasing temperature is observed when applying conventional heating ($t(\alpha = 0.5, T = 130 \text{ °C}) \sim 7$ min and $t(\alpha = 0.5, T = 110 \text{ °C}) \sim 18$ min, Figure 6 (top)).

A quantitative evaluation of the crystallization was established using the Sharp–Hancock analysis.³⁷ The Sharp–Hancock equation $\ln[-\ln(1 - \alpha)] = m \cdot \ln(k) + m \cdot \ln(t_{\text{red}})$ yields by linear regression the reaction exponent m (Avrami

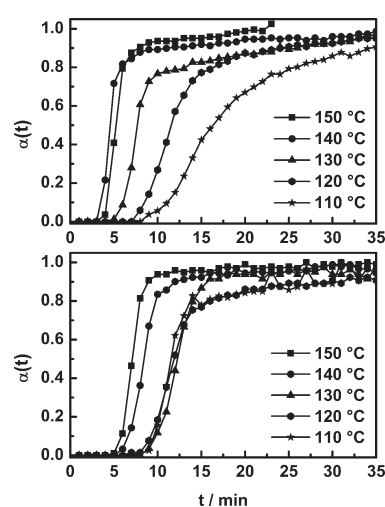


Figure 6. Normalized intensities of the 100 peak from the EDXRD measurements taken at different temperatures using conventional (top) and microwave heating (bottom). For clarity, the formation of the intermediate is not shown.

Table 2. Reaction Exponents m and Rate Constants Obtained from the Sharp–Hancock Analyses for the Early Reaction Step

T [°C]	k [s^{-1}]		m	
	microwave	microwave	conventional	conventional
110	2.9(1)	4.40×10^{-3} (4)	2.3(1)	2.49×10^{-3} (1)
120	2.0(2)	5.44×10^{-3} (4)	2.21(4)	3.34×10^{-3} (5)
130	2.80(1)	5.5×10^{-3} (1)	3.1(1)	5.40×10^{-3} (4)
140	2.2(2)	8.33×10^{-3} (5)	2.1(1)	4.70×10^{-3} (6)
150	2.11(7)	1.26×10^{-2} (4)	3.0(1)	9.9×10^{-3} (1)

exponent) and the rate constant k from the intercept $m \cdot \ln(k)$; α denotes the degree of crystallinity and t_{red} the aging time. All Sharp Hancock plots are given in the Supporting Information. The obtained reaction exponents and rate constants are summarized in Table 2 and 3.

Compound **1** is formed in two steps. In the early reaction stage, the transformation of the intermediate phase into compound **1** takes place. Here, reaction exponents varying from $m \sim 2.1$ to $m \sim 3.0$ were determined for both heating methods indicating a nucleation controlled reaction mechanism.³⁷ After the complete transformation into compound **1**, the reaction is still not finished, and the 100 peak increases

Table 3. Reaction Exponents m and Rate Constants Obtained from the Sharp–Hancock Analyses for the Late Reaction Step

T [°C]	k [s ⁻¹]		m	
	microwave	microwave	conventional	conventional
110	0.68(1)	1.97×10^{-3} (1)	0.29(1)	1.74×10^{-2} (5)
120	0.60(2)	4.74×10^{-3} (4)	0.3(1)	2.25×10^{-2} (4)
130	0.34(3)	1.08×10^{-3} (5)	0.3(1)	4.65×10^{-2} (3)
140	0.3(2)	9.05×10^{-2} (4)	0.31(4)	7.41×10^{-2} (5)
150	0.37(3)	5.02×10^{-2} (6)	0.23(7)	9.6×10^{-2} (1)

further. For the late reaction step, Avrami exponents between $m \sim 0.23$ and $m \sim 0.68$ were obtained which suggest a diffusion controlled mechanism. The model with the lowest Avrami exponent is a diffusion controlled reaction mechanism having a value of 0.62.³⁷ Smaller values have been reported previously and explained by hindered diffusion.^{48,49} It should be noted that the reaction mechanism models are empirical and have widely been applied to many reaction systems, even to crystallizations from sol–gels.³⁸ Furthermore, the models have previously been used for reactions where crystalline solids are formed directly from the reaction mixture, that is, without the formation of an intermediate. Nevertheless, this method allows to extract the rate constants and enables the comparison of reactions, for example, at different temperatures.

The obtained rate constants at different temperatures allow the determination of the Arrhenius activation energy and the pre-exponential factor for both heating methods (see Supporting Information). For the first reaction step an activation energy for the phase transition from the intermediate phase into compound **1** was determined as 34(7) kJ/mol with an pre-exponential factor of 3(1) for the microwave reaction and 41(9) kJ/mol with an pre-exponential factor of 4(1) for the conventional reaction. Within the precision of the measurement the values are independent of the heating methods. In the literature no values for the activation energy for the formation of phosphonates are given yet. A comparison with inorganic solids that form under nucleation controlled reaction mechanisms shows only slightly higher values. Thus, for the formation of zeolite A, barium titanate, or Mg–Al hydroxide an activation energy of 58, 55, and 41 kJ/mol was determined, respectively.^{50–52} For the second reaction step the observed activation energies differ significantly. For microwave and conventional heating activation energies of

62(6) kJ/mol and 128(27) kJ/mol were calculated. The pre-exponential factors were determined as 33(8) and 15(2) for microwave and conventional heating, respectively. This phenomenon has been previously observed. For the heating induced decomposition of sodium bicarbonate to sodium carbonate significant reduction of the activation energy was determined for the microwave heating method.⁵³ In another study on synthesis of titanium carbide the increase of the pre-exponential factor was observed for the microwave reactions. It was concluded that the mobility of molecules can be increased in presence of a microwave field.⁵⁴

Conclusion

HT methods help to discover new compounds and to establish their fields of formation. While normally reaction times in the range of days are used, the in situ study shows that in our case metal phosphonatosulfonates are formed in the range of minutes, and an intermediate phase is observed. From the in situ experiment it can be concluded that within the temperature range 110–150 °C the reaction proceeds in two steps for microwave as well as for conventional heating. While no influence on the phase transition between the intermediate and compound **1** is observed, differences are found for the ongoing crystallization after the transformation. At the late reaction step, conventional heating leads to significantly higher activation energies and lower pre-exponential factors than the microwave heating which could be due to a higher mobility of the ions under microwave irradiation. The study presented here shows that a combination of HT methods and in situ EDXRD measurement supports the efficient investigation of solvothermal reaction systems regarding the determination of fields of formation and the evaluation of crystallization processes.

Acknowledgment. We thank the HASYLAB, Hamburg for the beamtime and the DFG (project STO 643/2) for the financial support.

Supporting Information Available: Supporting Information with exact amounts used for the HT synthesis, XRPD patterns, selected bond distances, H-bonding figures, and results of the EDXRD study are available. This material is available free of charge via the Internet at <http://pubs.acs.org>. The Cambridge Crystallographic Data Center (CCDC) 790588–790589 contains the supplementary crystallographic data for this paper. These data can be obtained free of charge via the Internet at www.ccdc.cam.ac.uk/conts/retrieving.html (or from the CCDC, 12 Union Road, Cambridge CB2 1EZ, U.K.; fax, +44 1223 36033; e-mail, deposit@ccdc.ac.uk).

(48) Pradell, T.; Crespo, D.; Clavaguera, N.; Clavaguera-Mora, M. *J. Phys. Cond. Matter* **1998**, *10*, 3833.

(49) Kozlovsky, M. V. *Cryst. Res. Technol.* **2001**, No. 36, 1083.

(50) Davies, A. T.; Sankar, G.; Catlow, C. R. A.; Clark, S. M. *Phys. Chem. B* **1997**, *101*, 10115.

(51) Millange, F.; Walton, R. I.; O'Hare, D. *J. Mater. Chem.* **2000**, *10*, 1713.

(52) Walton, R. I.; Millange, F.; Smith, R. I.; Hansen, T. C.; O'Hare, D. *J. Am. Chem. Soc.* **2001**, *123*, 12547.

(53) Shibata, C.; Kashima, T.; Ohuchi, K. *J. Appl. Phys.* **1996**, *35*, 316.

(54) Binner, J. G. P.; Hassine, N. A.; Cross, T. E. *J. Mater. Sci.* **1995**, *30*, 5389.

4.6.2. Copper Phosphonatoethanesulfonates: Temperature Dependent *in situ* Energy Dispersive X-ray Diffraction Study and Influence of the pH on the Crystal Structures

Der folgende Artikel wurde 2012 in der Zeitschrift *Inorganic Chemistry* veröffentlicht und beschäftigte sich mit der *in situ* Untersuchung und Strukturaufklärung von Kupferphosphonatoalkylsulfonaten (mit freundlicher Genehmigung der ACS).^[174] Diese Arbeit knüpft an vorherige Arbeiten im Arbeitskreis Stock an.^[75] Das untersuchte System $\text{Cu}^{2+} / \text{H}_2\text{O}_3\text{P}-\text{C}_2\text{H}_4-\text{SO}_3\text{H} / \text{NaOH}$ hat sich darin als äußerst komplex erwiesen. In früheren Untersuchungen wurden in Abhängigkeit der Temperatur, des pH-Wertes und der molaren Verhältnisse sechs Verbindungen in Temperaturbereichen zwischen 90 und 190 °C gefunden. Zwei Verbindungen die bei 90°C entstehen konnten noch nicht strukturell charakterisiert werden. Ziel der Arbeit war es temperaturabhängige *in situ* EDXRD Untersuchungen in dem Reaktionssystem durchzuführen und die Kristallstrukturen der unbekanntenen Verbindungen aufzuklären.^[149]

Hierfür wurde die Kristallisation von $[\text{Cu}_2(\text{O}_3\text{P}-\text{C}_2\text{H}_4-\text{SO}_3)(\text{OH})(\text{H}_2\text{O})_2] \cdot 3\text{H}_2\text{O}$ *in situ* verfolgt, wobei ein vorher unbekanntes Intermediat $[\text{Cu}_2(\text{O}_3\text{P}-\text{C}_2\text{H}_4-\text{SO}_3)(\text{OH})(\text{H}_2\text{O})_2] \cdot 4\text{H}_2\text{O}$ beobachtet wurde. Das Intermediat konnte erfolgreich isoliert und die Kristallstruktur aus Röntgenpulverdaten bestimmt werden. Die temperaturinduzierte Phasenumwandlung von $[\text{Cu}_2(\text{O}_3\text{P}-\text{C}_2\text{H}_4-\text{SO}_3)(\text{OH})(\text{H}_2\text{O})_2] \cdot 3\text{H}_2\text{O}$ in $[\text{Cu}_2(\text{O}_3\text{P}-\text{C}_2\text{H}_4-\text{SO}_3)(\text{OH})(\text{H}_2\text{O})]$ konnte weiterhin bei 150 °C beobachtet werden. Durch den Vergleich der drei Strukturen wurde ein möglicher Reaktionspfad postuliert.

Zur Aufklärung der noch unbekanntenen Kristallstrukturen wurden mikrowellenunterstützte Synthesen durchgeführt, die zu vermessbaren Einkristallen führten. Dadurch konnte die Kristallstruktur der Verbindung $[\text{NaCu}(\text{O}_3\text{P}-\text{C}_2\text{H}_4-\text{SO}_3)(\text{H}_2\text{O})_2]$ bestimmt werden. Kraftfeldrechnungen ermöglichten weiterhin das Aufstellen eines Strukturmodells für die Verbindung $[\text{Cu}_{1.5}(\text{O}_3\text{P}-\text{C}_2\text{H}_4-\text{SO}_3)(\text{H}_2\text{O})_2]$ ausgehend von der literaturbekannten isoretikulären Verbindung. Das Modell konnte erfolgreich mittels Rietveld-Methode an Pulverdaten verfeinert werden. Hierdurch war es möglich den Einfluss des pH-Wertes auf die gebildete Kristallstruktur bei 90 °C zu extrahieren.

Copper Phosphonatoethanesulfonates: Temperature Dependent in Situ Energy Dispersive X-ray Diffraction Study and Influence of the pH on the Crystal Structures

Mark Feyand,[†] Annika Hübner,[†] André Rothkirch,[‡] David S. Wragg,[§] and Norbert Stock^{*†}

[†]Institut für Anorganische Chemie, Christian-Albrechts-Universität, Max-Eyth Straße 2, D 24118 Kiel, Germany

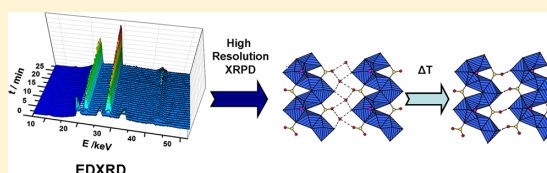
[‡]HASYLAB, DESY Hamburg, Notkestraße 85, 22607 Hamburg, Germany

[§]Centre for Materials Science and Nanotechnology/InGAP/Department of Chemistry, University of Oslo, Postbox 1033, Blindern, 0315 Oslo, Norway

Supporting Information

ABSTRACT: The system $\text{Cu}^{2+}/\text{H}_2\text{O}_3\text{P}-\text{C}_2\text{H}_4-\text{SO}_3\text{H}/\text{NaOH}$ was investigated using in situ energy dispersive X-ray diffraction (EDXRD) to study the formation and temperature induced phase transformation of previously described copper phosphonosulfonates. Thus, the formation of $[\text{Cu}_2(\text{O}_3\text{P}-\text{C}_2\text{H}_4-\text{SO}_3)(\text{OH})(\text{H}_2\text{O})]\cdot 3\text{H}_2\text{O}$ (4) at 90 °C is shown to proceed via a previously unknown intermediate $[\text{Cu}_2(\text{O}_3\text{P}-\text{C}_2\text{H}_4-\text{SO}_3)(\text{OH})(\text{H}_2\text{O})]\cdot 4\text{H}_2\text{O}$ (6), which could be structurally characterized from high resolution powder diffraction data.

Increase of the reaction temperature to 150 °C led to a rapid phase transformation to $[\text{Cu}_2(\text{O}_3\text{P}-\text{C}_2\text{H}_4-\text{SO}_3)(\text{OH})(\text{H}_2\text{O})]\cdot \text{H}_2\text{O}$ (1), which was also studied by in situ EDXRD. The comparison of the structures of 1, 4, and 6 allowed us to establish a possible reaction mechanism. In addition to the in situ crystallization studies, microwave assisted heating for the synthesis of the copper phosphonosulfonates was employed, which allowed the growth of larger crystals of $[\text{NaCu}(\text{O}_3\text{P}-\text{C}_2\text{H}_4-\text{SO}_3)(\text{H}_2\text{O})_2]$ (5) suitable for single crystal X-ray diffraction. Through the combination of force field calculations and Rietveld refinement we were able to determine the crystal structure of $[\text{Cu}_{1.5}(\text{O}_3\text{P}-\text{C}_2\text{H}_4-\text{SO}_3)]\cdot 2\text{H}_2\text{O}$ (3) and thus structurally characterize all compounds known up to now in this well investigated system. With the additional structural data we are now able to describe the influence of the pH on the structure formation.



INTRODUCTION

Inorganic–organic hybrid compounds are presently of great interest because of their potential prospects in gas storage, catalysis, and as nanoscale carriers for medical applications.^{1–3} Most of these compounds are based on polycarboxylates,⁴ -phosphonates,^{5–7} or -sulfonates.⁸ Inorganic–organic hybrid compounds based on polyfunctionalized linker molecules show a large structural variety depending on the reaction conditions such as reaction temperature and molar ratios of the starting materials.^{9–15} In the past polyfunctionalized, phosphonate-based organic building units such as phosphonocarboxylates,¹⁶ phosphonosulfonates,^{13,17–20} or aminophosphonates^{21–24} were investigated. Most of these compounds were obtained by crystallization from solutions or under solvothermal conditions, and these sealed reaction conditions make obtaining information about crystallization difficult. In principle numerous methods are available that allow study of the crystal formation,²⁵ but only a few studies dealing with the formation of inorganic–organic hybrid compounds have been reported. Among these, in situ EXAFS,²⁶ AFM,²⁷ in situ light scattering,^{28,29} in situ neutron diffraction,³⁰ and in situ energy dispersive X-ray diffraction (EDXRD)^{17,31–35} studies have been carried out.

In situ EDXRD has proven to be a valuable tool to investigate crystallization. In the past intercalation reactions,^{36,37} the crystallization of thioantimonates,³⁷ metal oxides,³⁸ metal–organic frameworks (MOFs)^{31,32,34} and the structural flexibility of MOFs³⁹ were investigated. There are only three studies up to now that have focused on the crystallization of metal phosphonates using EDXRD methods.^{17,40} In EDXRD studies extremely intense white beam synchrotron radiation is employed to achieve a good time resolution (less than a minute) while using conventional reaction vessels in the experiments. The white beam is sufficiently intense to penetrate steel autoclaves and thus reactions can be investigated without imposing an external influence on the reaction mixture if no beam sensitive solvents are used.⁴¹ In addition no scanning in 2θ is needed because of the fixed angle of the solid state detector. EDXRD experiments allow to extract kinetic parameters such as rate constants, Arrhenius activation energies, or to determine possible reaction mechanisms.^{17,37,42} In addition to quantitative analyses, it is possible to observe crystalline intermediates which may not be accessible by quenching or ex situ studies.^{17,31} Such

Received: September 10, 2012

Published: November 9, 2012

intermediates can give new insights into the crystallization process or even help to establish a possible reaction mechanism.³⁷

We are interested in the synthesis of inorganic–organic hybrid compounds based on polyfunctionalized linker molecules. Previously we have carried out a study of the reaction system $\text{Cu}^{2+}/\text{H}_2\text{O}_3\text{P}-\text{C}_2\text{H}_4-\text{SO}_3\text{H}/\text{NaOH}$ in water in the temperature range of 90 to 190 °C using high throughput methods.^{43,44} The systematic study allowed us to establish the fields of formation of five new hybrid compounds which are mainly defined by the reaction temperature range and the pH range of the reaction mixture (Figure 1). Structural trends

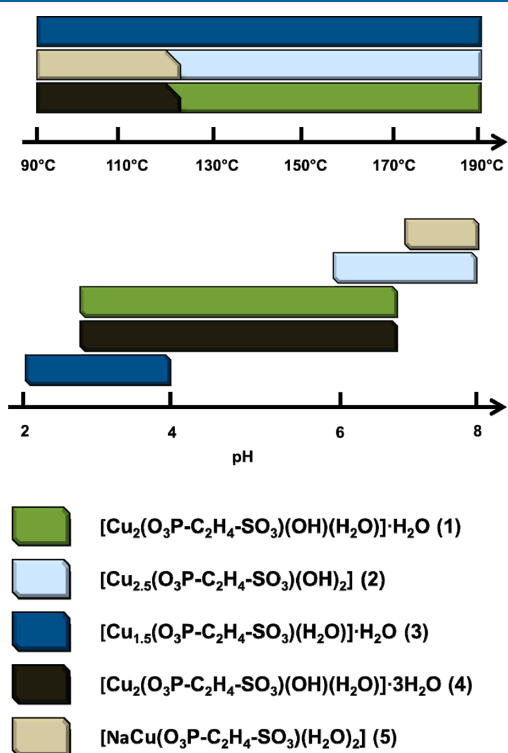


Figure 1. Reaction trends in the system $\text{Cu}^{2+}/\text{H}_2\text{O}_3\text{P}-\text{C}_2\text{H}_4-\text{SO}_3\text{H}/\text{NaOH}$ in water.⁴³ The structures of 3 and 5 (marked with *) are reported in this study.

could only be established for the phases formed at elevated temperatures ($[\text{Cu}_2(\text{O}_3\text{P}-\text{C}_2\text{H}_4-\text{SO}_3)(\text{OH})(\text{H}_2\text{O})]\cdot\text{H}_2\text{O}$ (1), $\text{Cu}_{2.5}(\text{O}_3\text{P}-\text{C}_2\text{H}_4-\text{SO}_3)(\text{OH})_2$ (2), $[\text{Cu}_2(\text{O}_3\text{P}-\text{C}_2\text{H}_4-\text{SO}_3)(\text{H}_2\text{O})_2(\text{OH})]\cdot 3\text{H}_2\text{O}$ (4)) which were structurally characterized.^{43,45}

Here we report the results of our in situ EDXRD study of the system $\text{Cu}^{2+}/\text{H}_2\text{O}_3\text{P}-\text{C}_2\text{H}_4-\text{SO}_3\text{H}/\text{NaOH}$ to investigate the temperature dependent formation of copper phosphonosulfonates. Furthermore, the influence of microwave assisted heating and the use of force field calculations in conjunction with Rietveld methods for the structure elucidation are presented. These approaches resulted in three new crystal structures and a reaction mechanism, and the synthesis-structure relationship of the whole system was established as well.

EXPERIMENTAL SECTION

4-Phosphonoethanesulfonic acid (H_3L) was synthesized in the literature in a two-step nucleophile substitution reaction starting from 1,2-dibromoethane and using triethylphosphite and sodium sulfite, as previously reported.⁹ All other reagents were of analytical grade (Fluka and Aldrich) and were used without further purification. XRPD measurements were carried out on a Stoe Stadi P diffractometer in transmission geometry with $\text{Cu}-\text{K}\alpha_1$ radiation, equipped with an image plate detector system or a linear PSD detector system for high resolution data. The MIR spectra were recorded on a Bruker ALPHA-P FT-IR spectrometer in the spectral range 4000–400 cm^{-1} . For the thermogravimetric analyses under air a NETSCH STA 409 CD analyzer was used with a heating rate of 4 K/min and an air flow rate of 75 mL/min. Electron microscopy and EDX analysis were carried out on a Phillips XL ESEM. High resolution powder XRD patterns were measured at beamline G3 at HASYLAB, DESY, Hamburg.⁴⁶ Single crystal measurement was carried out on a Bruker D8 3-circle diffractometer with an Apex II CCD detector. Syntheses were carried out under solvothermal conditions DURAN culture tubes 12 × 100 mm D50 GL 14 M.KAP, SCHOTT 261351155 for conventional heating, and an Anton Paar Synthos 3000 high-throughput microwave reactor system with custom-made Teflon inserts for microwave assisted heating.

In Situ Crystallization Experiments. EDXRD experiments were carried out at HASYLAB, beamline F3 at DESY, Hamburg, Germany. The white beam synchrotron radiation (4 to 55 keV) was detected by a liquid nitrogen cooled germanium semiconductor detector system. The detector angle was set to approximately 1.9°. The best results were obtained by collimating the beam to 0.2 × 0.2 mm^2 . To heat the samples a custom-made reactor system heated by an external thermostat (JULABO) was used. The reaction temperature of the reaction mixture is achieved within 2 min.⁴²

In Situ EDXRD Study of $[\text{Cu}_2(\text{O}_3\text{P}-\text{C}_2\text{H}_4-\text{SO}_3)(\text{H}_2\text{O})_2(\text{OH})]\cdot 3\text{H}_2\text{O}$ (4). The in situ experiments were carried out in Duran glass reactors. 2.0 M H_3L (263 μL , 0.53 mmol), 2.0 M $\text{Cu}(\text{NO}_3)_2$ (536 μL , 1.06 mmol), and 2.0 M NaOH (789 μL , 1.59 mmol) were combined, and H_2O was added to give the final volume (2500 μL).⁴³ The mixture was homogenized by shaking before transferring the vessel in the in situ reactor system. The reaction was carried out at 90 °C.

In Situ Transformation of 4 to $[\text{Cu}_2(\text{O}_3\text{P}-\text{C}_2\text{H}_4-\text{SO}_3)(\text{H}_2\text{O})_2(\text{OH})]\cdot\text{H}_2\text{O}$ (1).⁴³ The reaction mixture of the in situ experiment for the synthesis of 4 was temporarily removed from the in situ reactor. The reactor temperature was increased to 150 °C and the sample was reinserted into the in situ reactor.

Quenching Experiments of $[\text{Cu}_2(\text{O}_3\text{P}-\text{C}_2\text{H}_4-\text{SO}_3)(\text{H}_2\text{O})_2(\text{OH})]\cdot 4\text{H}_2\text{O}$ (6). 2.0 M H_3L (263 μL , 0.53 mmol), 2.0 M $\text{Cu}(\text{NO}_3)_2$ (536 μL , 1.06 mmol), and 2.0 M NaOH (789 μL , 1.59 mmol) were combined in a glass vessel and H_2O was added to give the final volume (2500 μL). The reaction mixture was stirred for 10 min at room temperature and the slightly blue solid was filtered and washed with water and immediately used for characterization.

Synthesis of $[\text{Cu}_{1.5}(\text{O}_3\text{P}-\text{C}_2\text{H}_4-\text{SO}_3)]\cdot 2\text{H}_2\text{O}$ (3). Twenty-six microliters of a 2 M H_3L , 79 μL H_2O , 79 μL of a 2 M $\text{Cu}(\text{NO}_3)_2$ solution, and 26 μL of a 2 M NaOH were added to a high-throughput Teflon reactor with a total volume of 250 μL .⁴⁴ The Teflon reactor was placed in a high-throughput steel reactor, sealed, and heated up in 6 h to 110 °C. The temperature was held for 48 h, and the reaction mixture was cooled down to room temperature in 6 h. The light blue product was filtered and washed with water. Larger amounts of the product were obtained by using five times the amount in a high-throughput reactor with a total volume of 2 mL (yield 77% and 89% based on H_3L).

Microwave-Assisted Synthesis of $\text{NaCu}(\text{O}_3\text{P}-\text{C}_2\text{H}_4-\text{SO}_3)(\text{H}_2\text{O})_2$ (5). Suitable single crystals of 5 were obtained by mixing 132 μL of a 2 M H_3L solution, 258 μL H_2O , 105 μL of a 2 M $\text{Cu}(\text{NO}_3)_2$ solution, and 105 μL of a 2 M NaOH solution in a 4 mL subsuming high-throughput Teflon reactor. The reaction mixture was heated for 6 h in an Anton Paar Synthos 3000 high-throughput microwave reactor. The product was filtered off and washed with

water. A mixture of blue plates (50–80 μm) and small amounts of a light blue powder were obtained.

Structure Determination. All crystal data, and structure refinement parameters of compound 3, 5, and 6 are summarized in Table 1.

Table 1. Summary of the Important Crystallographic Parameters of the Structure Determination and Refinement

	$[\text{Cu}_2(\text{O}_3\text{P}-\text{C}_2\text{H}_4-\text{SO}_3)(\text{H}_2\text{O})_2(\text{OH})]\cdot 4\text{H}_2\text{O}$ (6)	$[\text{Cu}_{1.5}(\text{O}_3\text{P}-\text{C}_2\text{H}_4-\text{SO}_3)(\text{H}_2\text{O})_2]$ (3)	$[\text{NaCu}(\text{O}_3\text{P}-\text{C}_2\text{H}_4-\text{SO}_3)(\text{H}_2\text{O})_2]$ (5)
structure determined from	powder data	powder data	single crystal data
formula sum	$\text{Cu}_2\text{C}_2\text{O}_{13}\text{PS}$	$\text{Cu}_{1.5}\text{C}_2\text{SPO}_8$	$\text{CuC}_2\text{H}_8\text{NaPSO}_8$
Z	4	2	4
crystal system	monoclinic	triclinic	monoclinic
<i>a</i> /Å	13.754(4)	5.0944(1)	14.757(3)
<i>b</i> /Å	7.1015(2)	8.4853(1)	7.690(1)
<i>c</i> /Å	13.491(4)	10.5077(2)	7.481(2)
α /deg	90	111.99(1)	90
β /deg	104.72(3)	93.07(1)	92.41(3)
γ /deg	90	101.29(1)	90
<i>V</i> /Å ³	1274.5(6)	408.9(1)	848.3(3)
space group	$P2_1/n$	$\bar{P}1$	$P2_1/c$
solution method	direct methods, Expo2009 ⁴⁷	force field calculation, Materials Studio 5.3 ⁴⁸	direct methods, ShelXS ⁴⁹
refinement method	least-squares Rietveld ⁵⁰	least-squares Rietveld ⁵⁰	least-squares ShelXL ⁴⁹
R_{wp} , R_{Bragg}	0.088, 0.034	0.085, 0.021	
$R_{\text{wp}}/R_{\text{exp}}$	5.29	1.39	
GOF			0.89
tot., uniq. data, R_{int}			7170, 2073, 0.094
Observed data [$I > 2\sigma(I)$]			1693
RI, wR2			0.0405, 0.1288
Δe min./max. ($e/\text{\AA}^3$)			-1.15, 1.92

Crystal Structure Determination of $\text{Cu}_2[(\text{O}_3\text{P}-\text{C}_2\text{H}_4-\text{SO}_3)(\text{H}_2\text{O})_2(\text{OH})]\cdot 4\text{H}_2\text{O}$ (6). The crystal structure of 6 was determined from high resolution powder diffraction data at beamline G3, HASYLAB, DESY. The sample was mounted in a 0.5 mm quartz capillary. The wavelength was set to 1.54296 Å by a double germanium (111) single crystal monochromator and calibrated with a LaB₆

standard. The diffracted beam was detected by a scintillation counter mounted behind a Soller slit system. The powder pattern was indexed and refined using Topas academics⁵⁰ ($a = 13.482(1)$, $b = 7.1077(7)$, and $c = 13.7609(8)$ Å, $\beta = 104.64(8)^\circ$, proposed space group $P2_1/n$, GOF = 27, which is related to the value of M20). The structure was solved by direct methods using EXPO 2009 in the space group $P2_1/n$.⁴⁷ The intensities were extracted in a 2θ -range from 7.8° to 70° (resolution 1.339 Å). It was possible to determine positions of the copper–oxygen polyhedra and the organic building unit. It is not possible to differentiate between the hydroxide and the water molecules, but the structure shows the same inorganic building unit as the literature known compound $\text{Cu}_2[(\text{O}_3\text{P}-\text{C}_2\text{H}_4-\text{SO}_3)(\text{H}_2\text{O})_2(\text{OH})]\cdot 3\text{H}_2\text{O}$ (4).⁴³ This model was employed in the Rietveld refinement using TOPAS academic⁵⁰ ($7.8^\circ \leq 2\theta \leq 80^\circ$). The profile was fitted using a simple axial model and a Thompson–Cox–Hastings profile function. The capillary absorption was corrected using the model by Sabine et al.⁵¹ Four additional water molecules were located between the layers from the difference Fourier map.

Structure Determination of $[\text{Cu}_{1.5}(\text{O}_3\text{P}-\text{C}_2\text{H}_4-\text{SO}_3)(\text{H}_2\text{O})_2]\cdot \text{H}_2\text{O}$ (3). The structural model of 3 was obtained from an isoreticular compound by force field calculations using Materials Studio 5.3,⁴⁸ and the structure was refined from laboratory X-ray powder diffraction data. The powder pattern was successfully indexed using Topas Academic⁵⁰ ($a = 5.094(2)$, $b = 8.483(2)$, $c = 10.499(2)$ Å, $\alpha = 115.59(1)$, $\beta = 66.64(1)$, $\gamma = 101.30(2)^\circ$, GOF = 48). The comparison of the lattice parameters with the ones of the literature known compound $[\text{Cu}_{1.5}(\text{O}_3\text{P}-\text{C}_4\text{H}_8-\text{SO}_3)(\text{H}_2\text{O})_2]\cdot 1.15\text{H}_2\text{O}$ ⁵² shows that the lattice parameters *a* and *c* corresponding to the inorganic layers are very similar ($a = 5.094(2)/5.1197(5)$ Å and $c = 10.499(2)/10.800(1)$ Å for the indexed and the literature known compounds, respectively). The *b* lattice parameter differs substantially $b = 8.483(2)/10.533(1)$ Å, which correlates with the exchange of a $-\text{C}_4\text{H}_8-$ by a $-\text{C}_2\text{H}_4-$ group. Starting from the literature known compound the $-\text{C}_4\text{H}_8-$ groups were replaced by $-\text{C}_2\text{H}_4-$ groups using Materials Studio 5.1.⁴⁸ The model was geometrically optimized using the universal force field implemented in Materials Studio and constraining the lattice parameters to the parameters obtained by indexing. The model was refined by the Rietveld technique using Topas academic 4.1.⁵⁰ The profile was fitted in the range $9-80^\circ$ (2θ) using a Thompson–Cox–Hastings profile function and a simple axial model. Because of the morphology (Supporting Information, Figure S6), a fourth order spherical harmonics series was used to model the preferred orientation induced by the needle like crystal shape.

Crystal Structure Determination of $[\text{NaCu}(\text{O}_3\text{P}-\text{C}_2\text{H}_4-\text{SO}_3)(\text{H}_2\text{O})_2]$ (5). The crystal structure of 5 was solved from single crystal X-ray diffraction data. X-ray diffraction measurements were performed on a Bruker D8 3-circle diffractometer with Apex II CCD detector using Mo *K* α radiation ($\lambda = 71.073$ pm). A hemisphere of diffraction data was collected, and the data were integrated using the program Saint (Bruker AXS, 2003). The data were scaled, and multiscan adsorption correction was applied using the program SADABS

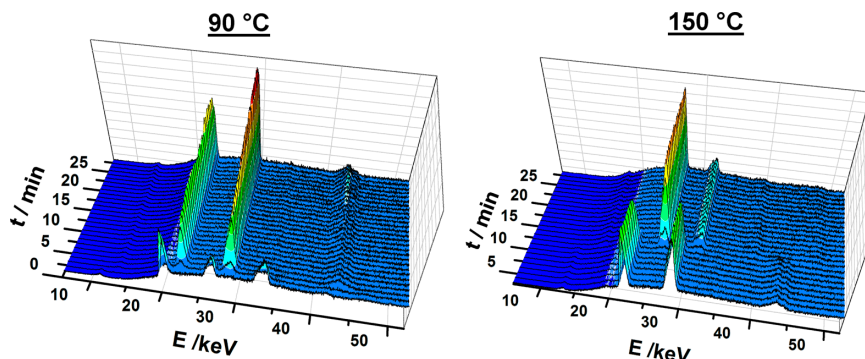


Figure 2. EDXRD spectra series of the crystallization of 4 (left) at 90 °C and its transformation into 1 (right) at 150 °C.

(Bruker (2003)). The crystal structures were solved by direct methods with SHELXS-97 and refined using SHELXL-97.⁴⁹ H-atoms connected to carbon atoms were placed onto calculated positions. H-atoms of the water molecules were localized in the difference Fourier map and refined as a riding model.

RESULTS AND DISCUSSION

In a previous study of the system $\text{Cu}^{2+}/\text{H}_2\text{O}_3\text{P}-\text{C}_2\text{H}_4-\text{SO}_3\text{H}/\text{NaOH}$ the field of formation of five new hybrid compounds had been obtained that allowed extraction of trends regarding temperature and pH dependence (Figure 1).⁴³ On the basis of the structural data of only three out of five hybrid compounds which were obtained at higher reaction temperatures (130 to 190 °C), we could establish synthesis-structure relationships. Thus, we were able to show that the degree of condensation of the inorganic building unit increases and the number of coordinating and noncoordinating water molecules decreases with increasing temperature.

The extended investigation of the system led to the following results: By using in situ EDXRD measurements, we were able to detect and characterize a previously unknown intermediate that transforms into **4** which itself transforms into **1** upon change of temperature. On the basis of these structures a possible reaction mechanism was deduced. In addition, microwave-assisted synthesis and force field calculations in conjunction with Rietveld methods for the structure elucidation allowed us to structurally characterize all known compounds in the investigated pH and temperature range.

Temperature Dependent In Situ EDXRD Investigation.

The crystallization of **4** was investigated at 90 °C. The EDXRD spectra as a function of reaction time are shown in Figure 2. After one minute the crystalline intermediate **6** was observed, which transforms completely into compound **4** during five minutes. Full crystallization is observed after 25 min. In addition, the temperature induced phase transformation of **4** into **1** was investigated (Figure 2, right). Therefore the reaction mixture was heated up to 150 °C and **4** began to transform into **1** after 12 min. The phase transformation is already completed after 15 min.

The intermediate phase **6**, which had not been observed previously, could also be obtained by quenching the reaction mixtures. To slow down the transformation the reaction was carried out at room temperature and after 15 min the intermediate could be obtained as a phase pure product. A comparison of the EDXRD spectrum and laboratory X-ray diffraction pattern is shown in the Supporting Information, Figure S4. The intermediate phase is kinetically stable under ambient conditions (in solution as well as the isolated microcrystalline powder) (Supporting Information, Figure S4). No single crystals could therefore be obtained, and the crystal structure had to be determined and refined from powder diffraction data. The final Rietveld plot is given in Figure 3.

The crystal structure of the intermediate phase **6** is built up from two crystallographically independent copper ions (Cu1, Cu2), one completely deprotonated $(\text{O}_3\text{P}-\text{C}_2\text{H}_4-\text{SO}_3)^{3-}$ molecule, one hydroxide ion, and five water molecules. Cu1 is coordinated by six oxygen atoms through two P–O–Cu, two S–O–Cu bonds, and two hydroxide ions (O7). Cu2 is surrounded by six oxygen atoms resulting from one P–O–Cu, two S–O–Cu bonds, two water molecules (Ow1 and Ow2), and one hydroxide ion (O7). The oxygen atoms O1, O2, O3 act as end on ligands and μ -O4 and μ -O5 as bridging atoms. The copper–oxygen polyhedra form zigzag chains along the *b*-

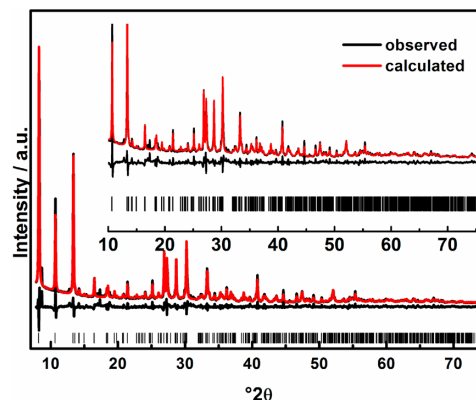


Figure 3. Final Rietveld plot of the structure refinement of **6**. The observed powder pattern is shown in black, the calculated powder pattern as an overlay in red, and the difference (observed-calculated) of both is given by the lower black line. The allowed positions of the Bragg peaks are given as tick marks.

axis (Figure 4) are connected by hydrogen bonds between the sulfonate groups and water molecules (Ow3, Ow4, Ow5, Ow6) along the *c*-axis. These layers are connected by $-\text{C}_2\text{H}_4-$ chains (Figure 4).

The complete reaction pathway based on the in situ EDXRD study is shown in Figure 5. After one minute the crystalline intermediate phase is observed at 90 °C which is built up from CuO_6 polyhedra chains. One water molecule (Ow3) is located between the chains and is involved in hydrogen bonds between uncoordinated oxygen atoms (O6) from sulfonate groups and a coordinated water molecule (Ow1) ($\text{O6}\cdots\text{Ow3} = 2.6946(5)$ Å and $\text{Ow3}\cdots\text{Ow1} = 2.7876(6)$ Å). Upon the transformation into **4** the noncoordinating water molecule Ow3 is released and the interchain distance decreases. A new hydrogen bond network is formed between the sulfonate oxygen atom (O6) and the coordinated water molecule (Ow1). After increasing the reaction temperature to 150 °C compound **1** is formed. The coordinating water molecule (OW1) is released, and the sulfonate group completes the coordination sphere of the Cu ion.

Thermogravimetric Analysis. The thermal stability of the intermediate was investigated by thermogravimetric (TG) analysis. The resulting TG curve is shown in Supporting Information, Figure S2. The compound shows two steps of weight loss. The first step can be assigned to the removal of six water molecules in the range of 25 to 120 °C (calc. 24.6%, obs. 26.2%), and the second step (obs. 24.0%) is due to the decomposition of the linker. The thermal decomposition leads to an X-ray amorphous residue, which contains copper and phosphorus in varying molar ratios as determined by energy dispersive X-ray analysis.

IR Spectroscopy. Compound **6** was studied by IR spectroscopy (Supporting Information, Figure S3). The broad bands between 3600 and 2900 cm^{-1} can be assigned to the uncoordinated and coordinated water molecules. The corresponding stretching vibrations appear at 1617 cm^{-1} . The bands between 1250 and 950 cm^{-1} can be assigned to the P–C, P–O, S–C, and S–O stretching vibrations of the tetrahedral CPO_3 - and CSO_3 -groups. Bands in the region from 3000 to 2900 cm^{-1} are due to CH_2 stretching vibrations. The corresponding CH_2 -

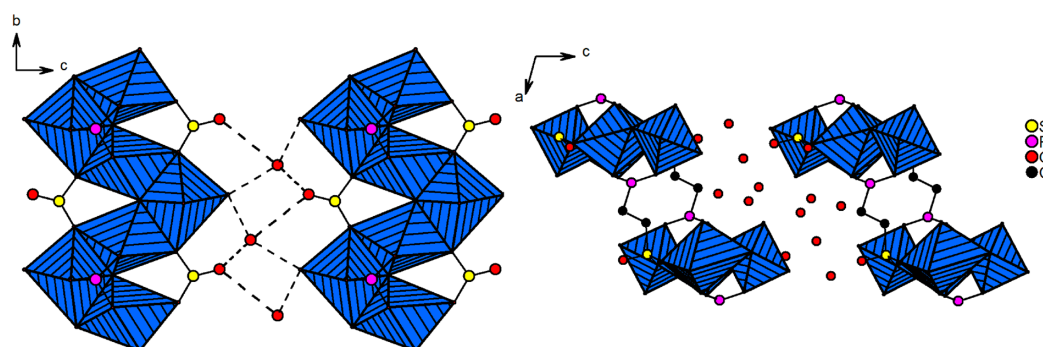


Figure 4. Crystal structure of the intermediate $\text{Cu}_2[(\text{O}_3\text{P}-\text{C}_2\text{H}_4-\text{SO}_3)(\text{H}_2\text{O})_2(\text{OH})]\cdot 4\text{H}_2\text{O}$ (6). View along the a -axis (left) and the b -axis (right). Dashed lines represent possible H-bonds.

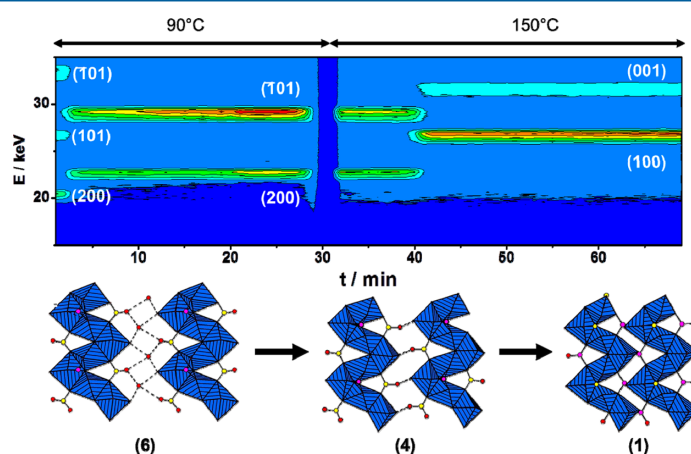


Figure 5. Illustration of the complete reaction pathway. The phase transformation at different temperatures is shown in the contour plot (top), and the correlated structural motifs of the copper oxygen chains are shown (bottom). The gap in the contour plot at ~ 30 min is due to the stage at which the specimen was removed from the vessel.

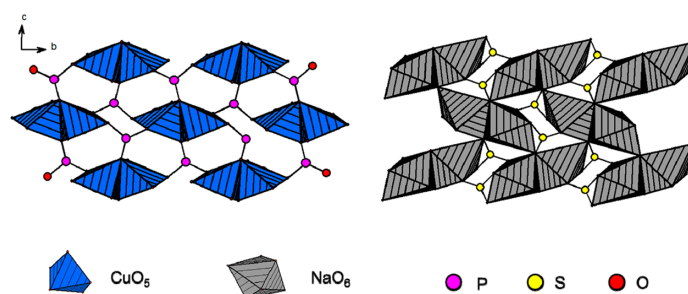


Figure 6. Section of the structure of **5**. Left: dimeric Cu_2O_8 units are connected by phosphonate groups to form layers in the b,c -plane; Right: Corner- and edge-sharing NaO_6 polyhedra are further connected by sulfonate groups to form layers in the of b,c -plane.

deformation vibration appears in the range of 1447 to 1388 cm^{-1} .

Influence of pH at a Reaction Temperature of 90 °C.

The influence of the pH in the system $\text{Cu}^{2+}/\text{H}_2\text{O}_3\text{P}-\text{C}_2\text{H}_4-\text{SO}_3\text{H}/$ on the structure formation was previously only established in the temperature range 130–190 °C. No information on the structures of the phases $[\text{Cu}_{1.5}(\text{O}_3\text{P}-\text{C}_2\text{H}_4-\text{SO}_3)(\text{H}_2\text{O})]\cdot \text{H}_2\text{O}$ (3) and $\text{NaCu}(\text{O}_3\text{P}-\text{C}_2\text{H}_4-\text{SO}_3)(\text{H}_2\text{O})_2$ (5) obtained at 90 °C were available. Therefore, two

different strategies were pursued: the use of microwave assisted heating and the ligand replacement strategy which has been extensively used in the structure determination of isoreticular MOFs.^{6,53–55}

Microwave-assisted heating has recently been incorporated in high-throughput methods.^{18,56} To obtain suitable single crystals of $\text{NaCu}(\text{O}_3\text{P}-\text{C}_2\text{H}_4-\text{SO}_3)(\text{H}_2\text{O})_2$ (5) 20 reactions were carried out, which resulted in about 50 μm large single crystals

of **5** (Supporting Information, Figure S8). These crystals were suitable for the structure determination.

Crystal Structure of $\text{NaCu}(\text{O}_3\text{P}-\text{C}_2\text{H}_4-\text{SO}_3)(\text{H}_2\text{O})_2$ (**5**).

The asymmetric unit is shown in the Supporting Information, Figure S7. The crystal structure is built up from one Cu^{2+} (Cu1), one Na^+ (Na1), one completely deprotonated $(\text{O}_3\text{P}-\text{C}_2\text{H}_4-\text{SO}_3)^{3-}$, and two water molecules. Cu1 is 5-fold coordinated by four oxygen atoms through P–O–Cu bonds (O1, O2, O3) and a single water molecule (Ow1). The oxygen atoms O1 and O2 act as end-on ligand atoms and O3 as a μ -O bridging atom, which connect the CuO_5 polyhedra to edge-sharing dimers (Figure 6). These Cu–O dimers are exclusively connected via the phosphonate groups along the *c*- and *b*-axis (Figure 6, left). Na1 is 6-fold coordinated by five S–O–Na bonds (O4, O5, O6) and one water molecule (Ow2). The oxygen atoms O5, O6, and O7 act as end-on, μ -O and μ_3 -O bridging atoms, respectively. The corner- and edge-sharing NaO_6 polyhedra are exclusively connected by the sulfonate groups, and layers in the *b,c*-plane are formed (Figure 6). Alternating layers are interconnected by the $-\text{C}_2\text{H}_4-$ organic building unit along the *a*-axis to form the final structure (Figure 7).

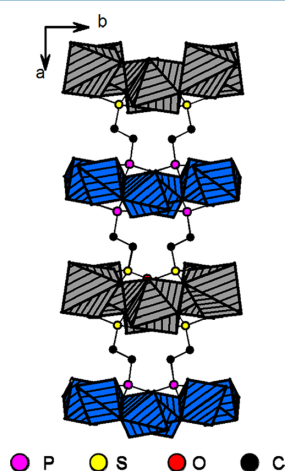


Figure 7. Section of the structure of **5**. Copper phosphonate and Sodium sulfonate layers are connected by the $-\text{C}_2\text{H}_4-$ groups (CuO_5 polyhedra blue, NaO_6 polyhedra gray).

The last of the known copper phosphonatoethylsulfonates which has not been structurally characterized so far is **3** ($[\text{Cu}_{1.5}(\text{O}_3\text{P}-\text{C}_2\text{H}_4-\text{SO}_3)(\text{H}_2\text{O})]\cdot\text{H}_2\text{O}$). The conventional and microwave assisted synthesis of **3** led only to a microcrystalline product of intergrown needles (20 to 30 μm in lengths, Supporting Information, Figure S6). Therefore the structure had to be determined from X-ray powder diffraction data. The combination of force field calculations and Rietveld refinement allowed us to establish the crystal structure of **3**. The structural model was set up using the ligand replacement strategy.^{53–55} Therefore, the powder pattern of **3** was indexed using TOPAS academic (Table 1). Comparing the lattice parameters with the ones of the previously reported compound $[\text{Cu}_{1.5}(\text{O}_3\text{P}-\text{C}_4\text{H}_8-\text{SO}_3)(\text{H}_2\text{O})]\cdot\text{H}_2\text{O}$ ⁵² one can expect that they form isorectangular structures ($a = 5.094(2)/5.1197(5)$ Å, $b = 8.483(2)/10.533(1)$ Å, $c = 10.499(2)/10.800(1)$ Å). The difference in the *b* lattice parameter was assumed to correlate

with the exchange of a $-\text{C}_4\text{H}_8-$ by a $-\text{C}_2\text{H}_4-$ group.⁵² The structural model was set up using Materials Studio 5.3, and the implemented Universal Force Field (UFF) was employed for the geometry optimization. The lattice parameters were fixed to the parameters obtained by indexing. The structural model obtained was refined by Rietveld methods using TOPAS academic. The final Rietveld plot is shown in Figure 8.

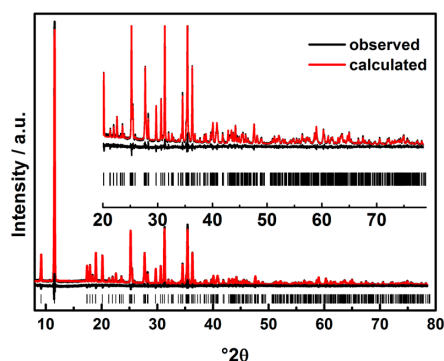


Figure 8. Final Rietveld plot of the structure refinement of compound **3**. The observed powder pattern is shown in black, the calculated powder pattern as an overlay in red, and the difference (observed-calculated) of both is given by the lower black line. The allowed positions of the Bragg peaks are given as tic marks.

Crystal Structure of $[\text{Cu}_{1.5}(\text{O}_3\text{P}-\text{C}_2\text{H}_4-\text{SO}_3)(\text{H}_2\text{O})]\cdot\text{H}_2\text{O}$ (**3**).

The framework contains two crystallographically independent Cu^{2+} ions (Cu1, Cu2) and one 2-phosphonatoethanesulfonate $(\text{O}_3\text{P}-\text{C}_2\text{H}_4-\text{SO}_3)^{3-}$ ion, as well as two water molecules (Ow1 coordinating and Ow2 noncoordinating). Cu1 is 6-fold coordinated by oxygen atoms through four P–O–Cu and two S–O–Cu bonds, whereas Cu2 is surrounded by five oxygen atoms through two S–O–Cu and two P–O–Cu bonds. The coordination sphere of Cu2 is completed by one coordinating water molecule (Ow1). The oxygen atoms act as end on (O1, O3, O4) as well as bridging ligand atoms (μ -O2, μ -O5), which connect the CuO_6 unit over two edges with two CuO_5 units to form Cu_3O_{12} clusters (Figure 9). These clusters are interconnected by the $-\text{C}_2\text{H}_4-$ group along the *b*-axis and by the phosphonate and sulfonate groups along the *a*-axis to form double layers, which are held together by hydrogen bonds between O6 and Ow2 (282(1) pm).

Synthesis-Structure Relationship. The structural characterization of the compounds which were obtained at 90 °C by varying the pH of the reaction mixture allows us to establish the synthesis-structure relationship.⁵⁷ The results are summarized in Figure 10. A low pH value between two and three leads to five and 6-fold coordinated face-sharing copper oxygen polyhedra. These polyhedra form isolated Cu_3O_{12} clusters which are connected by the phosphonate and sulfonate groups. Under less acidic conditions (pH = 3–7) edge-sharing zigzag chains of 6-fold coordinated CuO_6 polyhedra are found. This chain motif has already been observed for copper phosphonatosulfonates when $\text{H}_2\text{OP}-\text{C}_n\text{H}_{2n}-\text{SO}_3\text{H}$ ($n = 2, 4$) or p - $\text{H}_2\text{OP}-\text{C}_6\text{H}_4-\text{SO}_3\text{H}$ were employed.^{13,43,45} Under neutral to slightly basic conditions (pH = 7–8) 5-fold coordinated copper ions are observed which form dinuclear Cu_2O_{10} clusters. The molar ratio of $\text{Cu}^{2+}/\text{Na}^+$ of 1:1 leads to a mixed metal phosphonatosulfonate. Sodium shows a higher affinity toward

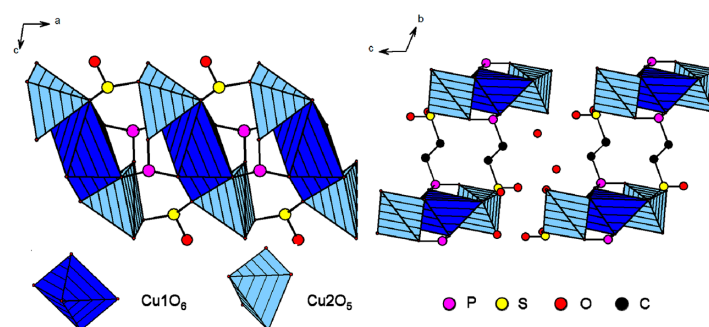


Figure 9. Sections of the crystal structure of **3**. Left: trimeric Cu–O building units are connected by sulfonate and phosphonate groups. Right: connection of the Cu phosphonate/sulfonate building units by the $-\text{C}_2\text{H}_4-$ groups. The CuO_6 polyhedra are shown as dark blue polyhedra, and the CuO_5 are shown as light blue polyhedra.

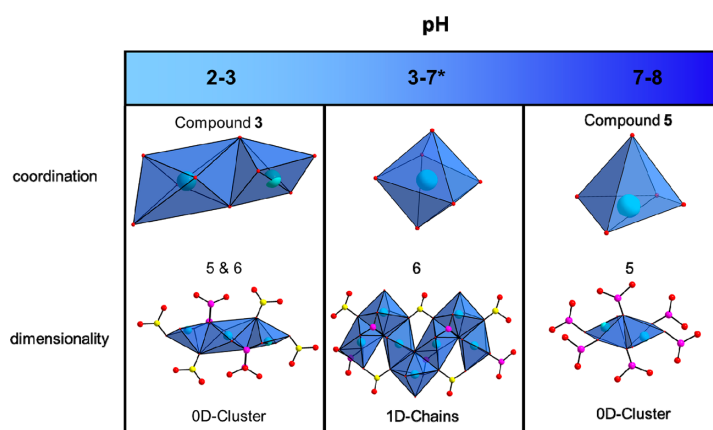


Figure 10. Influence of the pH on the coordination number and Cu–O building units formed at 90 °C (* structure reported previously).⁴⁵

the sulfonate group and copper a higher affinity toward the phosphonate groups. Thus, a three-dimensional structure of alternating Na–O–S and Cu–O–P layers interconnected by $-\text{C}_2\text{H}_4-$ groups was obtained. Although there is no structural data available on mixed metal phosphonatosulfonates, a few crystal structures of mixed Na/Cu phosphonates have been reported before.^{58–60} Using the 7-methyl-3,11-bis-(methylphosphonic) derivate of 3,7,11,17-tetraaza-bicyclo[11.3.1]heptadeca-1(17),13,15-triene leads to selective coordination of copper to nitrogen donor atoms and sodium to phosphonate ligands.⁵⁸ The methylenediphosphonate $\text{H}_2\text{O}_3\text{P}-\text{CH}_2-\text{PO}_3\text{H}_2$ in combination with Na^+ , Cu^{2+} , and V^{3+} leads to the coordination of all three metal species by the phosphonate group.⁵⁹ The polyfunctionalized linker $\text{HO}_2\text{C}-\text{CH}_2-\text{NH}-\text{CH}_2-\text{PO}_3\text{H}_2$ coordinates Cu^{2+} as well as Na^+ ions via the phosphonates group.⁶⁰

CONCLUSION

After HT methods allowed us to establish the fields of formation of the reaction system $\text{Cu}^{2+}/\text{H}_2\text{OP}-\text{C}_2\text{H}_4-\text{SO}_3\text{H}/\text{NaOH}$, only the combination of in situ EDXRD measurements and alternative synthesis methods (MW-assisted heating) and advanced structure-determination methods permitted us to get a detailed view on the formation of metal phosphonates and their synthesis-structure relationships. More in situ studies on the formation of metal phosphonates should be performed,

since these systems are feasible for finding crystalline intermediates that could allow a better understanding of crystallization processes.

ASSOCIATED CONTENT

Supporting Information

The asymmetric units of compound **3**, **5**, and **6**, selected bond lengths, and electron microscopic micrographs. This material is available free of charge via the Internet at <http://pubs.acs.org>.

AUTHOR INFORMATION

Corresponding Author

*Tel.: +49-431-880-1675. Fax: +49-431-880-1775. E-mail: stock@ac.uni-kiel.de.

Notes

The authors declare no competing financial interest.

ACKNOWLEDGMENTS

We thank the DFG (STO-643/2) for the financial support, DESY for beamtime, and Prof. Bensch (University of Kiel) and his group for the oven and the assistance at beamline F3.

REFERENCES

- Lee, J.; Farha, O. K.; Roberts, J.; Scheidt, K. A.; Nguyen, S. T.; Hupp, J. T. *Chem. Soc. Rev.* **2009**, *38* (5), 1450.

- (2) Li, J.-R.; Kuppler, R. J.; Zhou, H.-C. *Chem. Soc. Rev.* **2009**, 38 (5), 1477.
- (3) Horcajada, P.; Chalati, T.; Serre, C.; Gillet, B.; Sebrie, C.; Baati, T.; Eubank, J. F.; Heurtaux, D.; Clayette, P.; Kreuz, C.; Chang, J.-S.; Hwang, Y. K.; Marsaud, V.; Bories, P.-N.; Cynober, L.; Gil, S.; Férey, G.; Couvreur, P.; Gref, R. *Nat. Mater.* **2010**, 9 (2), 172.
- (4) Rowsell, J. L. C.; Yaghi, O. M. *Microporous Mesoporous Mater.* **2004**, 73 (1–2), 3.
- (5) Miller, S. R.; Pearce, G. M.; Wright, P. A.; Bonino, F.; Chavan, S.; Bordiga, S.; Margiolaki, I.; Guillou, N.; Férey, G. r.; Bourrelly, S.; Llewellyn, P. L. *J. Am. Chem. Soc.* **2008**, 130 (47), 15967.
- (6) Wharmby, M. T.; Mowat, J. P. S.; Thompson, S. P.; Wright, P. A. *J. Am. Chem. Soc.* **2011**, 133 (5), 1266.
- (7) Wharmby, M. T.; Miller, S. R.; Groves, J. A.; Margiolaki, I.; Ashbrook, S. E.; Wright, P. A. *Dalton Trans.* **2010**, 39 (28), 6389.
- (8) Shimizu, G. K. H.; Vaidyanathan, R.; Taylor, J. M. *Chem. Soc. Rev.* **2009**, 38 (5), 1430.
- (9) Sonnauer, A.; Stock, N. *J. Solid State Chem.* **2008**, 181 (3), 473.
- (10) Sonnauer, A.; Stock, N. *Acta Crystallogr., Sect. E: Struct. Rep. Online* **2008**, 64, M1433.
- (11) Sonnauer, A.; Stock, N. *J. Solid State Chem.* **2008**, 181 (11), 3065.
- (12) Sonnauer, A.; Stock, N. *Solid State Sci.* **2009**, 11 (2), 358.
- (13) Maniam, P.; Nather, C.; Stock, N. *Eur. J. Inorg. Chem.* **2010**, No. 24, 3866.
- (14) Du, Z. Y.; Li, X. L.; Liu, Q. Y.; Mao, J. G. *Cryst. Growth Des.* **2007**, 7 (8), 1501.
- (15) Du, Z. Y.; Xu, H. B.; Mao, J. G. *Inorg. Chem.* **2006**, 45 (24), 9780.
- (16) Bauer, S.; Stock, N. *Angew. Chem., Int. Ed.* **2007**, 46 (36), 6857.
- (17) Feyand, M.; Nather, C.; Rothkirch, A.; Stock, N. *Inorg. Chem.* **2010**, 49 (23), 11158.
- (18) Maniam, P.; Stock, N. *Inorg. Chem.* **2011**, 50 (11), 5085.
- (19) Maniam, P.; Stock, N. *Acta Crystallogr., Sect. C: Cryst. Struct. Commun.* **2011**, 67, E14.
- (20) Song, J. L.; Lei, C.; Sun, Y. Q.; Mao, J. G. *J. Solid State Chem.* **2004**, 177 (7), 2557.
- (21) Gemmill, W. R.; Smith, M. D.; Reisner, B. A. *J. Solid State Chem.* **2005**, 178 (9), 2658.
- (22) Fredouel, F.; Massiot, D.; Janvier, P.; Gingl, F.; Bujoli-Doeuff, M.; Evain, M.; Clearfield, A.; Bujoli, B. *Inorg. Chem.* **1999**, 38 (8), 1831.
- (23) Samanam, C. R.; Zamora, E. N.; Montchamp, J.-L.; Richards, A. F. *J. Solid State Chem.* **2008**, 181 (6), 1462.
- (24) Schmidt, C.; Feyand, M.; Rothkirch, A.; Stock, N. *J. Solid State Chem.* **2012**, 188 (0), 44.
- (25) Pienack, N.; Bensch, W. *Angew. Chem., Int. Ed.* **2011**, 50 (9), 2014.
- (26) Surble, S.; Millange, F.; Serre, C.; Férey, G.; Walton, R. I. *Chem. Commun. (Cambridge, U. K.)* **2006**, No. 14, 1518.
- (27) Shoaee, M.; Anderson, M. W.; Attfield, M. P. *Angew. Chem., Int. Ed.* **2008**, 47 (44), 8525.
- (28) Hermes, S.; Witte, T.; Hikov, T.; Zacher, D.; Bahnmüller, S.; Langstein, G.; Huber, K.; Fischer, R. A. *J. Am. Chem. Soc.* **2007**, 129 (17), 5324.
- (29) Juan-Alcañiz, J.; Goesten, M.; Martinez-Joaristi, A.; Stavitski, E.; Petukhov, A. V.; Gascon, J.; Kapteijn, F. *Chem. Commun. (Cambridge, U. K.)* **2011**, 47 (30), 8578.
- (30) Walton, R. I.; Smith, R. I.; O'Hare, D. *Microporous Mesoporous Mater.* **2001**, 48 (1–3), 79.
- (31) Millange, F.; Medina, M. I.; Guillou, N.; Férey, G.; Golden, K. M.; Walton, R. I. *Angew. Chem.* **2010**, 122 (4), 775.
- (32) Millange, F.; El Osta, R.; Medina, M. E.; Walton, R. I. *CrystEngComm* **2011**, 13 (1), 103.
- (33) Ahnfeldt, T.; Moellmer, J.; Guillerm, V.; Staudt, R.; Serre, C.; Stock, N. *Chem.—Eur. J.* **2011**, 17 (23), 6462.
- (34) Stavitski, E.; Goesten, M.; Juan-Alcañiz, J.; Martinez-Joaristi, A.; Serra-Crespo, P.; Petukhov, A. V.; Gascon, J.; Kapteijn, F. *Angew. Chem., Int. Ed.* **2011**, 50 (41), 9624.
- (35) Couck, S.; Gobechiya, E.; Kirschhock, C. E. A.; Serra-Crespo, P.; Juan-Alcañiz, J.; Martinez-Joaristi, A.; Stavitski, E.; Gascon, J.; Kapteijn, F.; Baron, G. V.; Denayer, J. F. M. *ChemSusChem* **2012**, 5 (4), 740.
- (36) O'Hare, D.; Evans, J. S. O.; Fogg, A.; O'Brien, S. *Polyhedron* **2000**, 19 (3), 297.
- (37) Behrens, M.; Kiebach, R.; Opehy, J.; Riemenschneider, O.; Bensch, W. *Chem.—Eur. J.* **2006**, 12 (24), 6348.
- (38) Kiebach, R.; Pienack, N.; Bensch, W.; Grunwaldt, J. D.; Michailovski, A.; Baiker, A.; Fox, T.; Zhou, Y.; Patzke, G. R. *Chem. Mater.* **2008**, 20 (9), 3022.
- (39) Millange, F.; Serre, C.; Guillou, N.; Férey, G.; Walton, R. I. *Angew. Chem., Int. Ed.* **2008**, 47 (22), 4100.
- (40) Schmidt, C.; Stock, N. *Inorg. Chem.* **2012**, 51 (5), 3108.
- (41) Wragg, D. S.; Byrne, P. J.; Giriat, G. t.; Ouay, B. L.; Gyepes, R. b.; Harrison, A.; Whittaker, A. G.; Morris, R. E. *J. Phys. Chem. C* **2009**, 113 (48), 20553.
- (42) Engelke, L.; Schaefer, M.; Schur, M.; Bensch, W. *Chem. Mater.* **2001**, 13 (4), 1383.
- (43) Sonnauer, A.; Stock, N. *Eur. J. Inorg. Chem.* **2008**, 2008 (32), 5038.
- (44) Stock, N. *Microporous Mesoporous Mater.* **2010**, 129 (3), 287.
- (45) Sonnauer, A.; Lieb, A.; Stock, N. *Acta Crystallogr., Sect. E: Struct. Rep. Online* **2008**, 64, M1417.
- (46) Wroblewski, T.; Clauß, O.; Crostack, H. A.; Ertel, A.; Fandrich, F.; Genzel, C.; Hradil, K.; Ternes, W.; Woldt, E. *Nucl. Instrum. Methods Phys. Res., Sect. A* **1999**, 428 (2–3), 570.
- (47) Altomare, A.; Camalli, M.; Cuocci, C.; Giacomazzo, C.; Moliterni, A.; Rizzi, R. *J. Appl. Crystallogr.* **2009**, 42 (6), 1197.
- (48) *Materials Studio*, 5.1; Accelrys: San Diego, CA, 2011.
- (49) Sheldrick, G. M. *SHELXTL-PLUS Crystallographic System*; Siemens Analytical X-ray Instruments Inc.: Madison, WI, 1992.
- (50) Coelho, A. *Topas Academic 4.1*; Coelho Software: Brisbane, Australia, 2007.
- (51) Sabine, T. M.; Hunter, B. A.; Sabine, W. R.; Ball, C. J. *J. Appl. Crystallogr.* **1998**, 31, 47.
- (52) Sonnauer, A.; Feyand, M.; Stock, N. *Cryst. Growth Des.* **2008**, 9 (1), 586.
- (53) Sonnauer, A.; Hoffmann, F.; Fröba, M.; Kienle, L.; Duppel, V.; Thommes, M.; Serre, C.; Férey, G.; Stock, N. *Angew. Chem., Int. Ed.* **2009**, 48 (21), 3791.
- (54) Senkovska, I.; Hoffmann, F.; Fröba, M.; Getzschmann, J.; Böhlmann, W.; Kaskel, S. *Microporous Mesoporous Mater.* **2009**, 122 (1–3), 93.
- (55) Reinsch, H.; Feyand, M.; Ahnfeldt, T.; Stock, N. *Dalton Trans.* **2012**, 41 (14), 4164.
- (56) Reimer, N.; Gil, B.; Marszalek, B.; Stock, N. *CrystEngComm* **2012**, 14 (12), 4119.
- (57) Forster, P. M.; Stock, N.; Cheetham, A. K. *Angew. Chem., Int. Ed.* **2005**, 44 (46), 7608.
- (58) Guerra, K. P.; Delgado, R.; Lima, L. M. P.; Drew, M. G. B.; Felix, V. *Dalton Trans.* **2004**, No. 12, 1812.
- (59) Yucasan, G.; Golub, V.; O'Connor, C. J.; Zubieta, J. *Inorg. Chim. Acta* **2006**, 359 (5), 1637.
- (60) Clarke, E. T.; Rudolf, P. R.; Martell, A. E.; Clearfield, A. *Inorg. Chim. Acta* **1989**, 164 (1), 59.

4.6.3. *In situ* Untersuchungen von Metallphosphonatocarboxylaten

Die vorhergehenden EDXRD Untersuchungen der Bildung von Metallphosphonatosulfonaten zeigten, dass Intermediate während der Kristallisation auftreten. Um zu untersuchen inwiefern diese Erkenntnisse auf andere polyfunktionalisierte Linker anwendbar sind wurden neue Metallphosphonatocarboxylate synthetisiert und die Kristallisation dieser Verbindungen *in situ* untersucht. Hierzu wurde der in Abbildung 4.12 gezeigte Linker 4-[Bis(phosphonomethyl)amino]methylbenzoesäure (H_5L^3) verwendet.

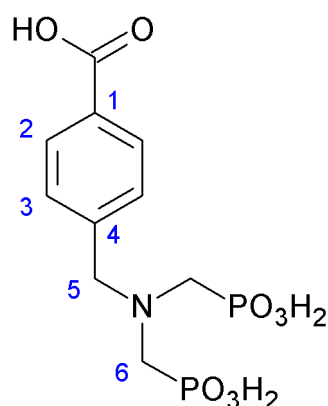


Abbildung 4.12.: Strukturformel des verwendeten Linkers H_5L^3 .

Aus einer leicht modifizierten, literaturbekannten Synthese konnte der Linker nach einer Mannich-artigen Reaktion hergestellt werden.^[175]

Synthese von H_5L^3 . 6.05 g (40 mmol) *p*-Aminomethylbenzoesäure und 6.56 g (80 mmol) phosphorige Säure wurden in 10 mL konz. HCl und 20 ml dest. Wasser gelöst. Die Reaktionsmischung wurde zum Sieden erhitzt und 8.1 mL (100 mmol) einer 38 %igen Formalin-Lösung langsam über den Zeitraum von 1 h hinzugegeben. Die Reaktionsmischung wurde für weitere 12 h unter Rückfluss erhitzt. Nach dem Abkühlen auf Raumtemperatur wurde das entstandene Produkt abfiltriert und mit 50 mL dest. Wasser gewaschen. Der weiße Feststoff wurde bei 80°C getrocknet und mittels 1H -NMR und ^{31}P -NMR Spektroskopie als H_5L^3 identifiziert.

1H -NMR(500MHz, NaOD/D₂O 10% TMS): δ = 7.56 (m, 2H, C2-H), 7.26 (m, 2H, C3-H), 3.68 (s, 2H, C5-H), 2.34 (dd, 4H, $^3J_{P-H}$ = 12.3 Hz, $^1J_{C-H}$ = 16.2 Hz, C6-H) ppm.

^{31}P -NMR(500MHz, NaOD/D₂O 10% H₃PO₄): δ = 17.00 ppm (s).

Durch Umsetzen des Linkers mit den zweiwertigen Übergangsmetallionen Mn^{2+} , Ni^{2+} , Co^{2+} und Fe^{2+} wurde die isostrukturelle Verbindung $[M((HO_3P-CH_2)_2-NHCH_2-C_6H_4-COOH)_2]$

($[M(H_4L^3)_2]$), $M = Mn, Co, Fe$ und Ni (**1-4**) erhalten.

Synthese von $[M((HO_3P-CH_2)_2-NHCH_2-C_6H_4-COOH)_2]$ ($[M(H_4L^3)_2]$) mit $M = Mn, Co, Fe$ und Ni (1-4**).** 40 mg H_5L^3 , 150 μL 2M wässrige MCl_2 Lösung ($M = Mn, Co, Ni$) bzw. 15.5 mg $FeCl_2 \cdot 4H_2O$ für $M = Fe$ und 2 ml dest. Wasser wurden in ein Duran Schott Kulturröhrchen gegeben, verschlossen und durch Schütteln homogenisiert. Die Reaktionsmischung wurde für 12 h auf 150 °C erhitzt, nach dem Abkühlen der entstandene Feststoff abfiltriert und mit dest. Wasser gewaschen.

Die Verbindungen sind isostrukturell mit der literaturbekannten Verbindung $[Cd((HO_3P-CH_2)_2-NHCH_2-C_6H_4-COOH)_2]$.^[77] Die Kristallstruktur wurde als Startmodell für weitere Rietveld-Verfeinerungen verwendet. Die finalen Ergebnisse der Rietveld-Verfeinerungen sind in Abbildung 4.13 gezeigt und die wichtigsten kristallographischen Parameter der Verfeinerungen sind in Tabelle 4.6 zusammengefasst. Die Messungen für $[Mn(H_4L^3)_2]$ wurden auf einem Stoe Stadi P mit linear PSD Detektor und die Messungen für $[Co(H_4L^3)_2]$, $[Fe(H_4L^3)_2]$ und $[Ni(H_4L^3)_2]$ wurden auf einem Panalytical Empyrean durchgeführt.

Tabelle 4.6.: Kristallographische Parameter und Gütekriterien der Verbindungen $[Mn(H_4L^3)_2]$ (**1**), $[Co(H_4L^3)_2]$ (**2**), $[Fe(H_4L^3)_2]$ (**3**) und $[Ni(H_4L^3)_2]$ (**4**).

	$[Mn(H_4L^3)_2]$ (1)	$[Co(H_4L^3)_2]$ (2)	$[Fe(H_4L^3)_2]$ (3)	$[Ni(H_4L^3)_2]$ (4)
a	14.9616(4)	15.0143(5)	15.040(5)	15.0587(2)
b	8.61317(18)	8.5735(2)	8.6071(2)	8.56024(12)
c	10.2432(2)	10.0301(2)	10.0618(3)	9.96992(16)
β	95.35(2)	95.06(3)	95.19(3)	94.90(2)
Raumgruppe	$P2_1/c$	$P2_1/c$	$P2_1/c$	$P2_1/c$
Zellvolumen	1314.25(5)	1286.09(6)	1297.23(7)	1280.48(3)
R_{wp}	3.34	3.23	5.12	6.42
R_{Bragg}	0.67	0.78	1.32	1.5
GOF	1.35	1.58	2.28	2.14

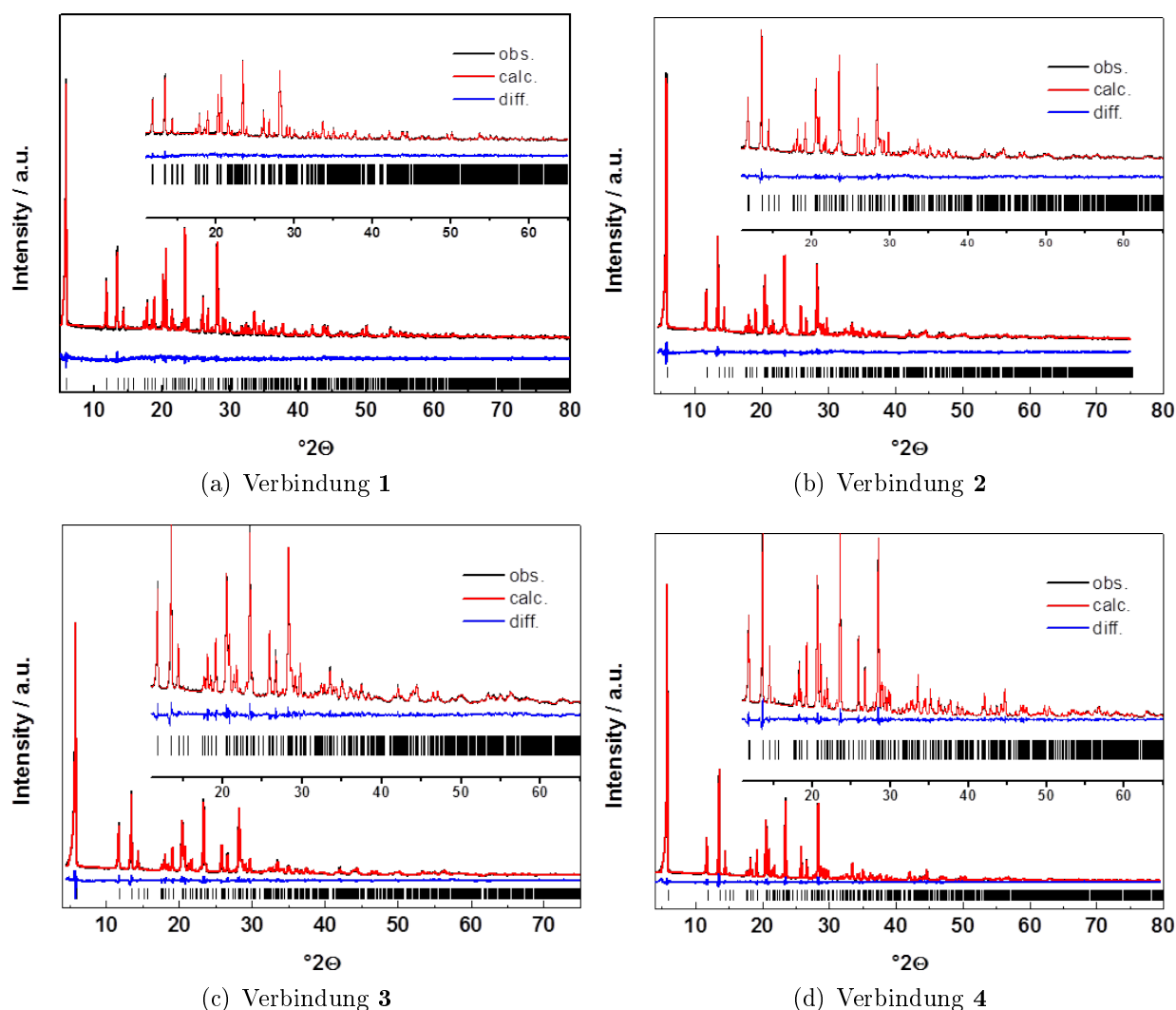


Abbildung 4.13.: Berechnetes, gemessenes Diffraktogramm und deren Differenz der finalen Rietveld-Verfeinerung der Verbindungen $[\text{Mn}(\text{H}_4\text{L}^3)_2]$ (**1**), $[\text{Co}(\text{H}_4\text{L}^3)_2]$ (**2**), $[\text{Fe}(\text{H}_4\text{L}^3)_2]$ (**3**) und $[\text{Ni}(\text{H}_4\text{L}^3)_2]$ (**4**). Das jeweils beobachtete Pulverdiffraktogramm ist schwarz gezeigt, das berechnete ist in rot gezeigt. Die Differenz der beiden ist in blau darunter dargestellt. Erlaubte Reflexpositionen sind als schwarze Balken angegeben.

Da alle Verbindungen isostrukturell kristallisieren wird nur die Kristallstruktur der Verbindung **1** repräsentativ erklärt. Die asymmetrische Einheit und die Koordinationsumgebung ist in Abbildung 4.14 gezeigt. Die Verbindung ist aus MnO_6 -Polyeder aufgebaut. Diese werden über Phosphonatgruppen zu einer Schicht in der b,c -Ebene, wie in Abbildung 4.15 a gezeigt, verknüpft. Die Linker ragen hierbei entlang der a -Achse in den Schichtzwischenraum und verknüpfen die Schichten über Wasserstoffbrückenbindungen, die zwischen den Carbonsäure-Gruppen und den Hydrogenphosphonat-Gruppen gebildet werden.

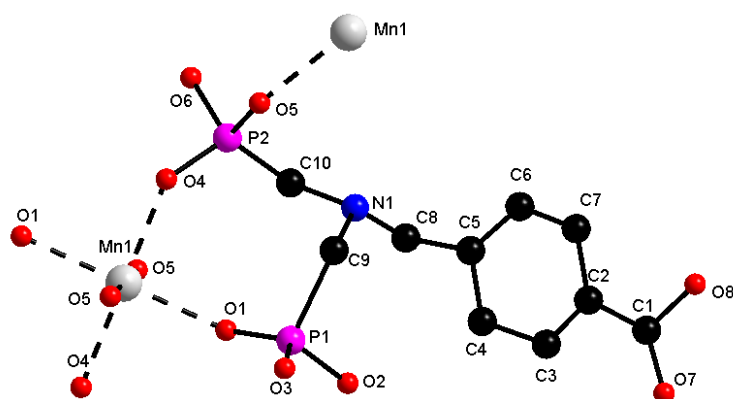


Abbildung 4.14.: Asymmetrische Einheit und Koordinationsumgebung des Mangans in der Verbindung **1**.

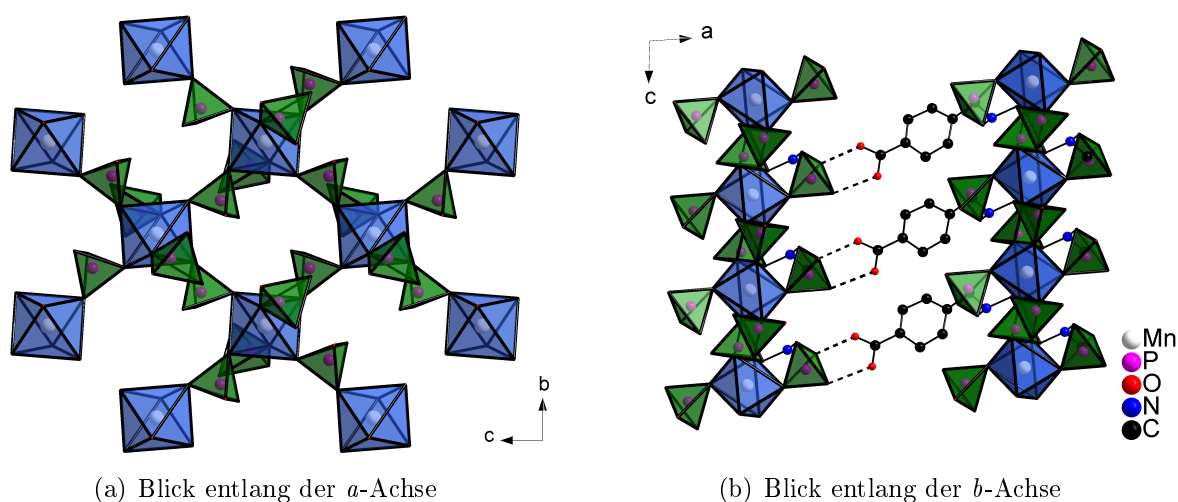


Abbildung 4.15.: Ausschnitt aus der Kristallstruktur von Verbindung **1**. Die MnO_6 -Polyeder sind in blau, die CPO_3 -Polyeder sind in grün gezeigt. Wasserstoffbrückenbindungen sind als gestrichelte Linien dargestellt.

Charakterisierung der Verbindung 1-4

Die Verbindungen **1-4** wurden mittels IR-Spektroskopie und thermogravimetrischer (TG) Analyse charakterisiert.

Die Ergebnisse der thermogravimetrischen Messungen sind in Abbildung 4.16 gezeigt. Die TG Messungen wurden unter Luftstrom im Temperaturbereich von 25 bis 900°C und mit einer Heizrate von 4 K/min durchgeführt. Alle vier Verbindungen zeigen einen unterschiedlichen mehrstufigen Gewichtsverlust zwischen 150 und 350 °C. Der Gewichtsverlust

kann der Zersetzung des Linkers zugeordnet werden. Die Zersetzung der Gerüste resultiert jedoch in glasartigen Rückständen, die nicht vom Tiegel entfernt werden konnten und somit konnten keine erwarteten Gewichtsverluste berechnet werden.

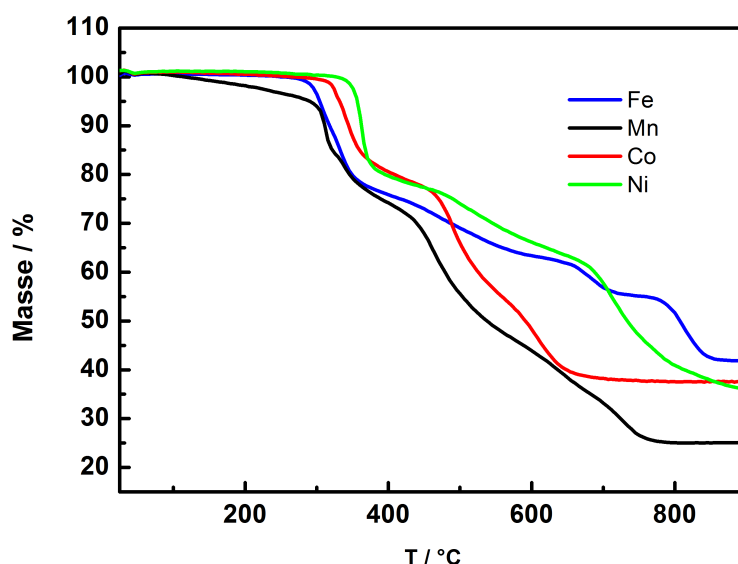


Abbildung 4.16.: Ergebnisse der thermogravimetrischen Analysen von $[\text{Mn}(\text{H}_4\text{L}^3)_2]$ (**1**), $[\text{Co}(\text{H}_4\text{L}^3)_2]$ (**2**), $[\text{Fe}(\text{H}_4\text{L}^3)_2]$ (**3**) und $[\text{Ni}(\text{H}_4\text{L}^3)_2]$ (**4**).

Die IR Spektren sind in Abbildung 4.17 gezeigt. Alle Spektren sind sehr ähnlich. Die Banden im Bereich von $3105\text{-}2905\text{ cm}^{-1}$ können den aromatischen und aliphatischen C-H Streckschwingungen zugeordnet werden. Die korrespondierenden Deformationsschwingungen werden im Bereich von $1465\text{-}1373\text{ cm}^{-1}$ beobachtet. Die in Wasserstoffbrückenbindungen involvierte C=O Schwingungen der Carbonsäuren liegen im Bereich von $1725\text{-}1695\text{ cm}^{-1}$, die C-P und P-O Streckschwingungen im Bereich von $1275\text{-}959\text{ cm}^{-1}$. Das IR-Spektrum von **2** zeigt hierbei auf Grund der geringeren Kristallinität breitere Peaks als die isotypen Verbindungen mit **1**, **3** und **4**.

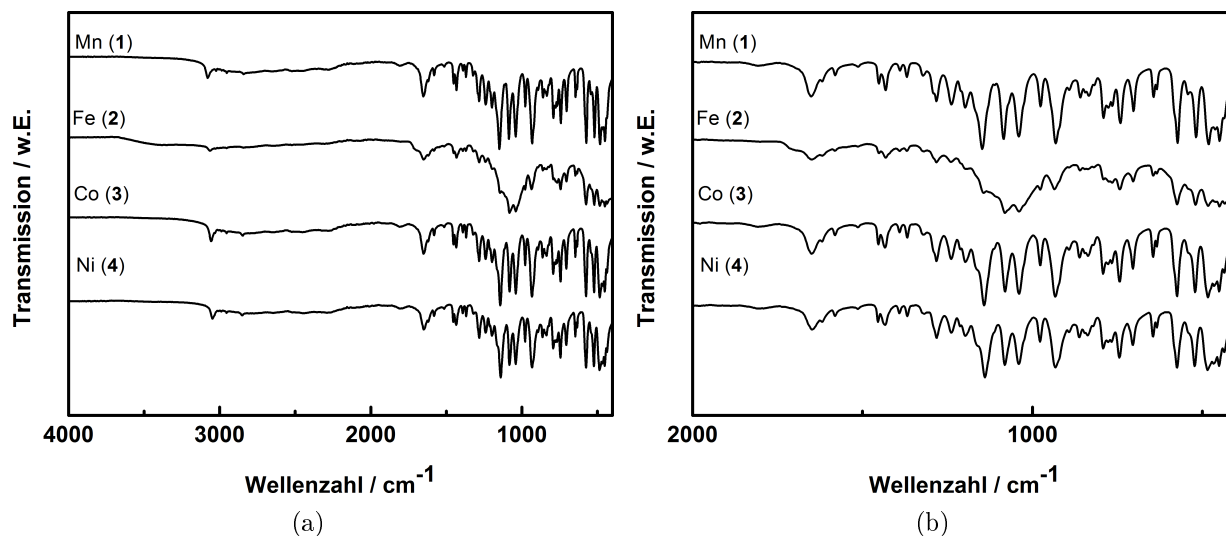


Abbildung 4.17.: IR-Spektren der Verbindungen $[\text{Mn}(\text{H}_4\text{L}^3)_2]$ (1), $[\text{Co}(\text{H}_4\text{L}^3)_2]$ (2), $[\text{Fe}(\text{H}_4\text{L}^3)_2]$ (3) und $[\text{Ni}(\text{H}_4\text{L}^3)_2]$ (4). **Links:** Die gesamten gemessenen Spektren. **Rechts:** Vergrößerte Ausschnitte im Bereich zwischen 2000 und 450 cm^{-1} .

In situ Untersuchungen zur Kristallisation der Verbindungen 1-4

Zur Untersuchung der Kristallisation wurden EDXRD Studien für die Verbindungen **1-4** durchgeführt. Die Reaktionen wurden bei 80 °C und ansonsten gleichen Reaktionsbedingungen durchgeführt. Die erhaltenen Spektren sind in Abbildung 4.18 gezeigt.

Bei der Kristallisation von Verbindung $[\text{Mn}(\text{H}_4\text{L}^3)_2]$ (1) wird bereits nach einer Minute ein kristallines Intermediat beobachtet. Dieses wandelt sich in den darauffolgenden sechs Minuten in Verbindung **1** um. Die Phasenumwandlung macht sich durch eine Verschiebung des Peaks von 13.21 keV ($d = 15.43 \text{ \AA}$) zu 13.79 keV ($d = 14.88 \text{ \AA}$) bemerkbar. Die vollständige Kristallisation ist nach ca. 20 Minuten abgeschlossen. Das Intermediat konnte allerdings nicht isoliert werden.

Die Verbindungen $[\text{Co}(\text{H}_4\text{L}^3)_2]$ (2) und $[\text{Fe}(\text{H}_4\text{L}^3)_2]$ (3) beginnen nach sechs bzw. zehn Minuten zu kristallisieren. In beiden Reaktionen wird kein kristallines Intermediat beobachtet. Die Kristallisationen sind nach 20 bzw. 35 Minuten beendet.

Die Kristallisation von $[\text{Ni}(\text{H}_4\text{L}^3)_2]$ (4) verläuft langsamer und komplexer als für die Verbindungen **1-3**. In den ersten 40 Minuten ist ein höherer Untergrund im Vergleich zu den späteren Spektren zu beobachten. Dies lässt auf eine mögliche röntgenamorphe Phase schließen, wie z.B. der noch nicht vollständig gelöste Linker. Nach 40 Minuten nimmt die Intensität dieses Untergrundes ab und die Reaktionslösung wird, wie aus *ex situ* Experimenten ersichtlich, klar. *Ex situ* Experimente zeigen, dass die Kristallisationen von **1-3** zu

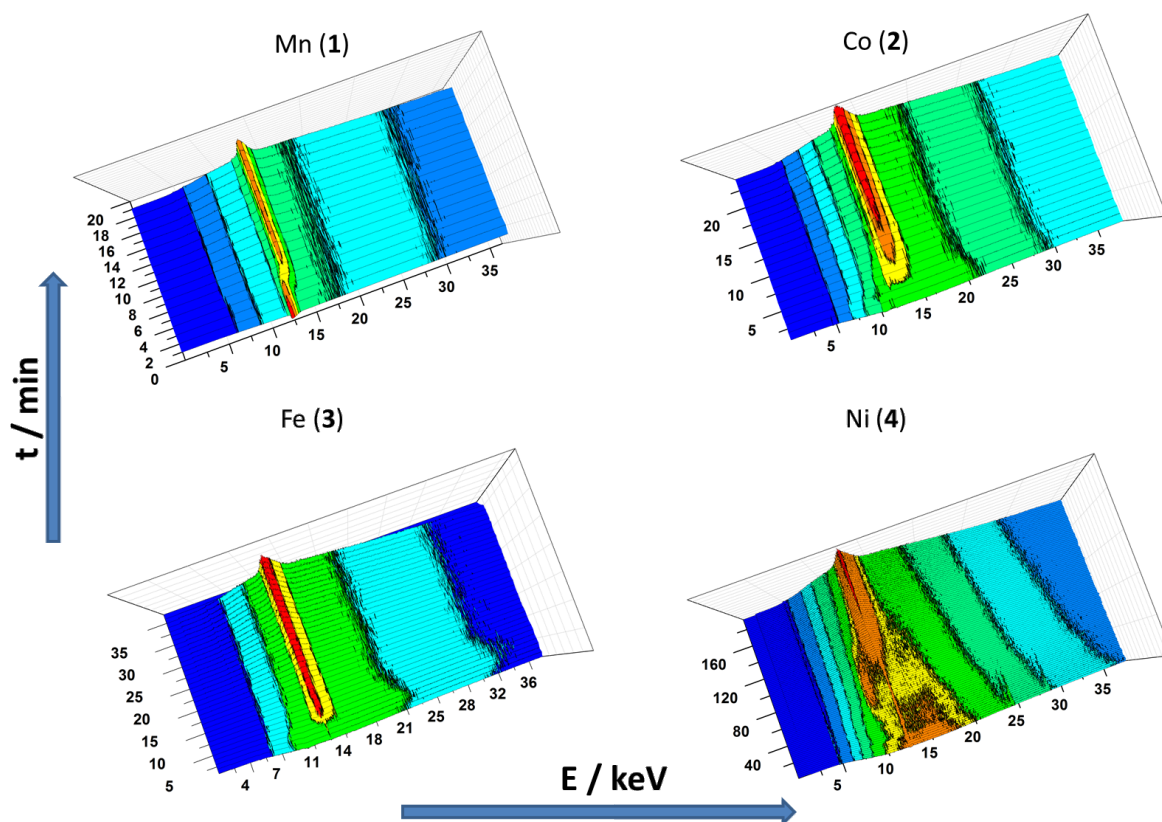


Abbildung 4.18.: EDXRD Spektren der Kristallisation von $[\text{Mn}(\text{H}_4\text{L}^3)_2]$ (1), $[\text{Co}(\text{H}_4\text{L}^3)_2]$ (2), $[\text{Fe}(\text{H}_4\text{L}^3)_2]$ (3) und $[\text{Ni}(\text{H}_4\text{L}^3)_2]$ (4).

keinem Zeitpunkt über eine klare Lösung verlaufen. Hierzu muss jedoch bemerkt werden, dass die Reaktionen bereits nach viel kürzeren Reaktionszeiten beendet sind. Nach ca. 60 Minuten bildet sich aus der klaren Lösung ein kristallines Intermediat, das sich nach 90 Minuten wieder langsam auflöst. Zeitgleich wächst der (100) Peak der Verbindung **4** an. Die Intermediate von **1** und **4** sind verschieden, wie an dem d -Wert von 15.43 \AA für das Intermediat von **1** und 16.23 \AA für das Intermediat von **4** zu erkennen ist. Die vollständige Kristallisation ist nach ca. 190 Minuten abgeschlossen. Das Intermediat ließ sich in Abbruchversuchen nicht isolieren.

Besonders die Kristallisation von **4** bedarf einer genaueren Untersuchung. Diese wurde mit einer *in situ* Zelle die in Abbildung 4.19 gezeigt ist, verfolgt. Die Kristallisationszelle ermöglicht das simultane Messen und Protokollieren von Temperatur, Druck, pH-Wert, Leitfähigkeit, Redoxpotential und IR Spektren während der Reaktion.^[176] Zeitgleich können Flüssigkeiten hinzu dosiert werden. Für Reaktionen stehen ein aus Edelstahl bestehender Druckreaktor und ein für drucklose Reaktionen geeigneter Glasreaktor zur Verfügung.



Abbildung 4.19.: *In situ* Kristallisationszelle. Links der Druckreaktor und rechts der Glasreaktor für Niedrigtemperatursynthesen.

Die Reaktionen wurden im Glasreaktor durchgeführt und ein zehnfacher Syntheseansatz verwendet. Zunächst wurden 400 mg Linker vorgelegt, dann aus der Dosiereinheit 20 ml Wasser hinzu dosiert. Die Reaktionsmischung wurde auf 80°C erhitzt und währenddessen IR Spektren, die Temperatur, das Redoxpotential und der pH-Wert gemessen. Die IR Spektren sollten Informationen über die erste amorphe Phase und der Spezies in Lösung geben. Das Redoxpotential wurde gemessen, da dieses abhängig von der Koordinationsumgebung des Metallions ist, und somit Rückschlüsse auf Änderungen in der der Koordinationsumgebung zulässt. Der pH-Wert lässt Rückschlüsse auf Protonierungen und Deprotonierungen des Linkers zu. Die IR Spektren wurden alle 30 s gemessen und die Temperatur, das Redoxpotential und der pH-Wert jede Sekunde. Nach Erreichen der Temperatur wurden 1.5 ml einer 2M NiCl₂ Lösung hinzugegeben. Dieser Zeitpunkt wurde als t=0 gesetzt. Die dreidimensionale Darstellung der IR-Spektren ist in Abbildung 4.20 gezeigt. Die gemessenen Parameter wie Temperatur, Redoxpotential, pH-Wert sowie die Intensitäten ausgewählter IR-Banden sind in Abbildung 4.21 zusammengefasst. Ein Ausschnitt der Intensitäten der

IR-Banden ist in Abbildung 4.22 vergrößert dargestellt.

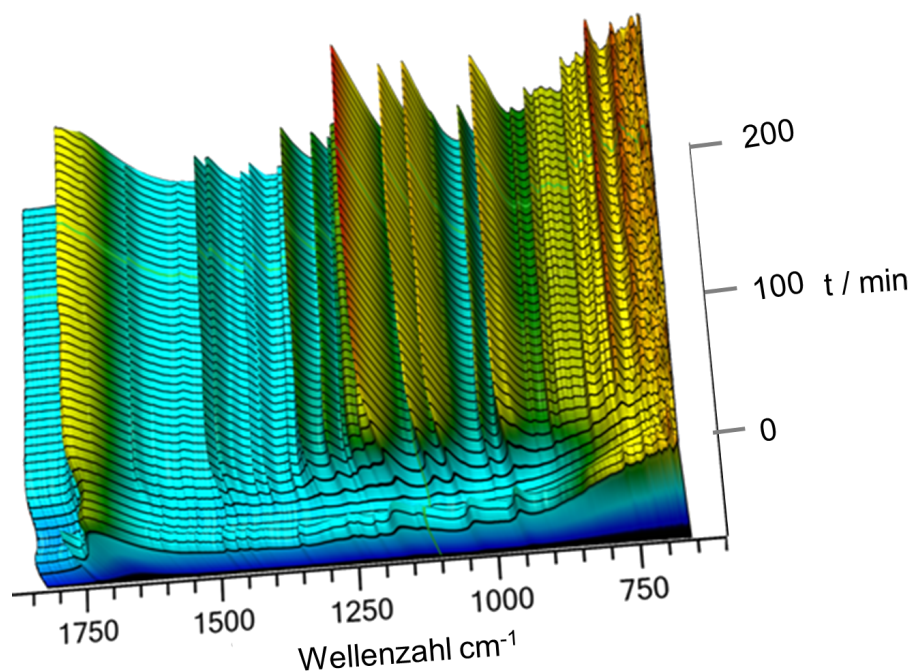


Abbildung 4.20.: Darstellung der gemessenen IR Spektren während der Synthese von 4.

Während des Aufheizens beginnt der Linker sich teilweise zu lösen. Dies hat während der Temperaturzunahme eine Erniedrigung des pH-Wertes zur Folge, da die Säure hierbei deprotoniert wird. Weiterhin wird eine Intensitätszunahme der Bande der C=O Streck-schwingung von freien Carbonsäuren (1741 cm^{-1}) und der P-O Steckschwingungen ($1341\text{--}1209\text{ cm}^{-1}$) beobachtet. Das Redoxpotential nimmt hierbei zunächst ab. Zum Zeitpunkt der Zugabe der Metallsalzlösung ($t = 0$) sinkt das Redoxpotential stark ab, steigt aber sofort wieder an. Die Intensitäten der Banden der freien Carbonsäure nehmen sofort innerhalb der nächsten Minute auf 0 ab. Die Intensitäten der P-O Schwingungen nehmen ab und steigen anschließend wieder an. Hierbei kommt es ebenso zu einer leichten Verschiebung des Bandenmaximums. Dies kann durch eine Reaktion der Nickelionen mit dem Linker zu einer neuen Verbindung erklärt werden. Dies ist auch in Übereinstimmung mit der zeitgleichen Abnahme des pH-Wertes, da die Phosphonsäure hierfür deprotoniert wird. Dieses Produkt lässt sich der röntgenamorphen Phase aus der EDXRD Studie zuordnen. Im Folgenden wird ein zweistufiger Anstieg des Redoxpotentials beobachtet, während der pH-Wert konstant bleibt. Im IR-Spektrum bleiben weiterhin die P-O Steckschwingungen beobachtet, jedoch verändern sich die Intensitäten in zwei Schritten. Die Banden der freien Carbonsäu-

re werden nicht wieder beobachtet. Dies ist ebenfalls in sehr guter Übereinstimmung mit den Ergebnissen der EDXRD Studie. Anhand beider Ergebnisse lässt sich schließen, dass in der klaren Lösung bereits eine Vororganisation der Nickel- und Linker-Ionen stattfindet und auf molekularer Ebene eine Verbindung entsteht die bereits alle im finalen Produkt enthaltenen Spezies enthält. Diese wandelt sich hiernach in das Intermediat um und dieses anschließend in das Produkt **4**. Da der pH-Wert konstant bleibt, kann man daraus schließen, dass alle Verbindungen mit dem selben Protonierungsgrad vorliegen.

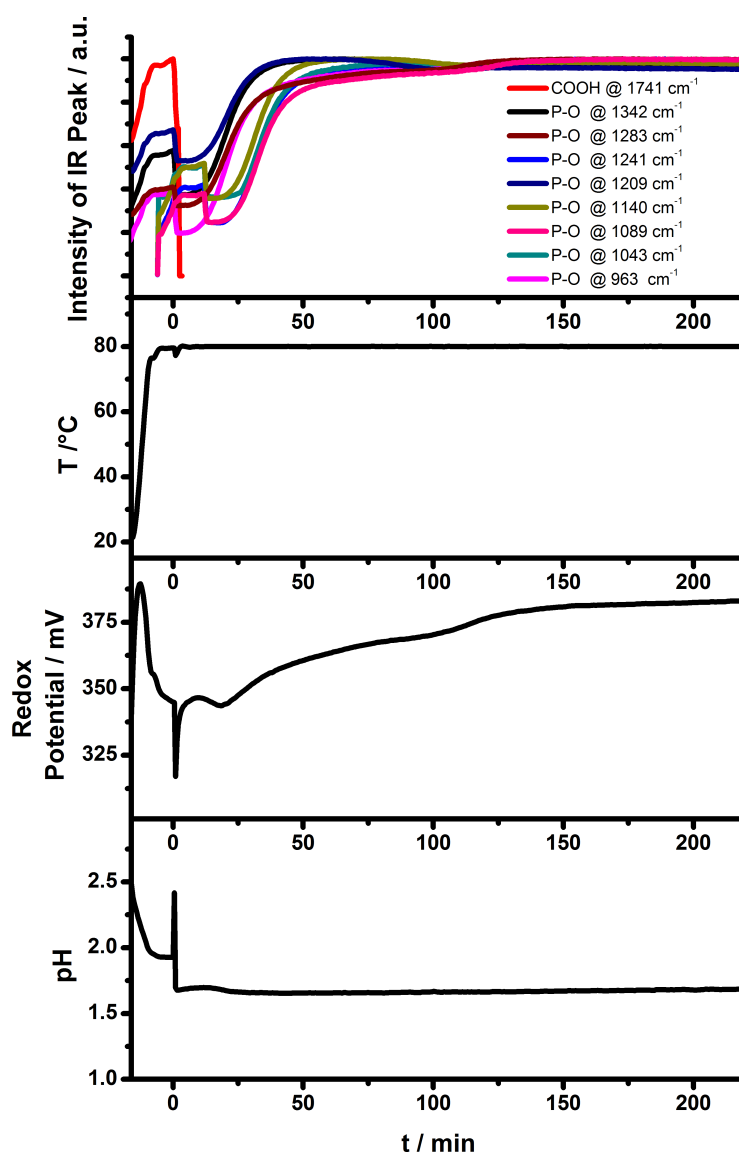


Abbildung 4.21.: Verlauf der Temperatur, des Redoxpotentials, pH Wertes und der Intensität von ausgewählten Banden bei der Synthese von **4**.

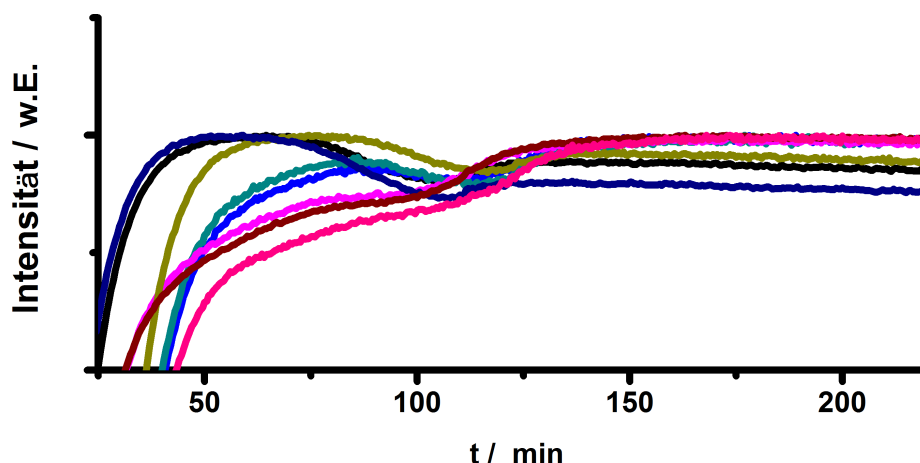


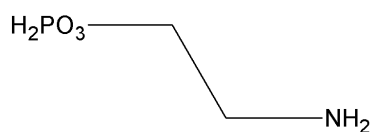
Abbildung 4.22.: Vergrößerter Ausschnitt der Intensitäten der IR-Banden aus den *in situ* Messung von **4**. Die Farben entsprechen den aus Abbildung 4.21.

Zusammenfassung und Ausblick

In dieser Studie konnte gezeigt werden, dass isostrukturelle Verbindungen von Übergangsmetallen mit sehr ähnlichen Eigenschaften und Ordnungszahlen auf sehr unterschiedlichen Wegen kristallisieren. Die Reaktionszeiten variieren hierbei zwischen 20 und 180 Minuten, wahrscheinlich aufgrund der verschiedenen Labilitäten der Ionen in Wasser gegenüber dem Linker.^[177] Es konnten keine kristallinen Intermediate für die Kristallisation von $[\text{Co}(\text{H}_4\text{L}^3)_2]$ (**2**) und $[\text{Fe}(\text{H}_4\text{L}^3)_2]$ (**3**) beobachtet werden, während $[\text{Mn}(\text{H}_4\text{L}^3)_2]$ (**1**) und Nickel $[\text{Ni}(\text{H}_4\text{L}^3)_2]$ (**4**) Intermediate zeigen. Besonders der Kristallisationsverlauf von $[\text{Ni}(\text{H}_4\text{L}^3)_2]$ (**4**) erwies sich als äußerst komplex. Die simultane Aufnahme von IR-Spektren, Redoxpotential und pH-Wert während *in situ* Röntgenbeugungsexperimenten würden besser vergleichbare und repräsentative Informationen über den Kristallisationsprozess geben und stellen den logischen nächsten Schritt da. Die gleichzeitige Aufnahme von hoch aufgelösten Pulverdiffraktogrammen könnte Einblicke in die Struktur der Intermediate geben, da diese *ex situ* nicht zugänglich sind. Information über die lokale Struktur und die amorphe Phase bei der Kristallisation von **4** könnten zusätzlich *in situ* EXAFS oder PDF Experimente liefern.

4.6.4. High-throughput and *in situ* EDXRD Investigation on the Formation of Two New Metal Aminoethylphosphonates – $\text{Ca}(\text{O}_3\text{PC}_2\text{H}_4\text{NH}_2)$ and $\text{Ca}(\text{OH})(\text{O}_3\text{PC}_2\text{H}_4\text{NH}_3)\cdot 2\text{H}_2\text{O}$

Der folgende Artikel wurde in der Zeitschrift *Journal of Solid State Chemistry* im Jahr 2012 veröffentlicht und behandelte die Hochdurchsatzsynthesen und *in situ* Untersuchungen von Calciumaminophosphonaten.^[178] Hierzu wurde 2-Aminoethylphosphonsäure (AEP), die in Abbildung 4.23 gezeigt ist, verwendet.



AEP

Abbildung 4.23.: Der verwendete Linker 2-Aminoethylphosphonsäure (AEP).

Hierbei stellte sich vor allem die Frage ob bei Aminophosphonaten Intermediate bei der Kristallisation auftreten.

Zur Synthese neuer Verbindungen wurde das Reaktionssystem $\text{Ca}^{2+} / \text{AEP} / \text{NaOH}$ systematisch mittels Hochdurchsatzmethoden untersucht und der pH-Wert und die molaren Verhältnisse von Metall zu Linker variiert. Die Synthesen führten zu der Verbindung $\text{Ca}(\text{O}_3\text{PC}_2\text{H}_4\text{NH}_2)$ und die Kristallstruktur konnte aus Röntgenpulverdaten bestimmt werden. Die Kristallisation der Verbindung wurde mittels *in situ* EDXRD untersucht und das kristalline Intermediat $[\text{Ca}(\text{OH})(\text{O}_3\text{PC}_2\text{H}_4\text{NH}_3)]\cdot 2\text{H}_2\text{O}$ beobachtet. Das Intermediat konnte erfolgreich isoliert werden und die Kristallstruktur aus Synchrotron Röntgenpulverdaten gelöst und verfeinert werden. Die Strukturen sind aus CaO_6 bzw. CaO_6N Polyedern aufgebaut, die kantenverknüpft sind und in $\text{Ca}(\text{O}_3\text{PC}_2\text{H}_4\text{NH}_2)$ Schichten und in $[\text{Ca}(\text{OH})(\text{O}_3\text{PC}_2\text{H}_4\text{NH}_3)]\cdot 2\text{H}_2\text{O}$ Ketten bilden. Diese werden über Wasserstoffbrückenbindungen oder Van-der-Waals Kräften in den Verbindung $[\text{Ca}(\text{OH})(\text{O}_3\text{PC}_2\text{H}_4\text{NH}_3)]\cdot 2\text{H}_2\text{O}$ bzw. $\text{Ca}(\text{O}_3\text{PC}_2\text{H}_4\text{NH}_2)$ zusammengehalten. Beide Verbindungen wurden mittels IR- und Raman spektroskopischen Untersuchungen, TG-Messungen und C,H,N-Elementaranalyse detailliert charakterisiert.



Contents lists available at SciVerse ScienceDirect

Journal of Solid State Chemistry

journal homepage: www.elsevier.com/locate/jssc

High-throughput and in situ EDXRD investigation on the formation of two new metal aminoethylphosphonates – $\text{Ca}(\text{O}_3\text{PC}_2\text{H}_4\text{NH}_2)$ and $\text{Ca}(\text{OH})(\text{O}_3\text{PC}_2\text{H}_4\text{NH}_3) \cdot 2\text{H}_2\text{O}$

Corinna Schmidt^a, Mark Feyand^a, André Rothkirch^b, Norbert Stock^{a,*}^a Institut für Anorganische Chemie, Christian-Albrechts-Universität, Max-Eyth Straße 2, D 24118 Kiel, Germany^b HASYLAB, DESY Hamburg, Notkestraße 85, 22607 Hamburg, Germany

ARTICLE INFO

Article history:

Received 2 November 2011

Received in revised form

15 January 2012

Accepted 22 January 2012

Available online 30 January 2012

Keywords:

Crystal growth

In situ EDXRD

Solvothermal

High-throughput

Crystal structure

ABSTRACT

The system Ca^{2+} /2-aminoethylphosphonic acid/ H_2O / NaOH was systematically investigated using high-throughput methods. The experiments led to one new compound $\text{Ca}(\text{O}_3\text{PC}_2\text{H}_4\text{NH}_2)$ (**1**) and the crystal structure was determined using in house X-ray powder diffraction data (monoclinic, $P2_1/c$, $a=9.7753(3)$, $b=6.4931(2)$, $c=8.4473(2)$ Å, $\beta=106.46(2)^\circ$, $V=514.20(2)$ Å³, $Z=4$). The formation of **1** was investigated by in situ energy dispersive X-ray diffraction measurements (EDXRD) at beamline F3 at HASYLAB (light source DORIS III), DESY, Hamburg. An intermediate, $\text{Ca}(\text{OH})(\text{O}_3\text{PC}_2\text{H}_4\text{NH}_3) \cdot 2\text{H}_2\text{O}$ (**2**), was observed and could be isolated from the reaction mixture at ambient temperatures by quenching the reaction. The crystal structure of **2** was determined from XRPD data using synchrotron radiation (monoclinic, $P2_1/m$, $a=11.2193(7)$, $b=7.1488(3)$, $c=5.0635(2)$ Å, $\beta=100.13(4)^\circ$, $V=399.78(3)$ Å³, $Z=2$).

© 2012 Elsevier Inc. All rights reserved.

1. Introduction

Inorganic–organic hybrid compounds have gained increased attention during the last years, due to their structural diversity and their potential application, for example in catalysis, gas storage or gas separation [1,2]. Most of these compounds contain polycarboxylate, -phosphonate or -sulfonate ions as linker molecules [3–5]. The use of polyfunctionalized linker molecules with different functionalities has also been investigated and various metal phosphonocarboxylates [6–9] and -phosphonosulfonates [10–12] have been described. Aminomethylphosphonic acid of secondary and tertiary amines have been successfully applied for various dense metal phosphonates [4,13] as well as porous compounds such as MIL-91 [14], STA-12 [15], and STA-16 [16]. The use of aminoalkylphosphonic acids of primary amines ($\text{H}_2\text{N}-\text{C}_n\text{H}_{2n}-\text{PO}_3\text{H}_2$) for the synthesis of inorganic–organic hybrid compounds is far less developed [17–24]. While various metal aminomethylphosphonates ($\text{M}=\text{Zn}^{2+}$, Cd^{2+} , Pb^{2+} , Hg^{2+} , Ag^+) [17] and metal aminoethylphosphonates ($\text{M}=\text{Zn}^{2+}$ [18], Cd^{2+} [19], Cu^{2+} [20], Co^{2+} [21], Cr^{2+} [22]) have been reported, the number of metal aminopropylphosphonates ($\text{M}=\text{Zr}^{4+}$ [23], Al^{3+} [24]) is rather limited. Although a variety of metal ions have been incorporated, these aminoalkylphosphonates crystallize exclusively in layered or pillared layered structures. In all cases, the phosphonate group is connected to the metal ions and the amino group either

coordinates to the metal ions, or it is protonated and protrudes into the interlayer space. In metal aminoethylphosphonates three structural motives are observed: (1) the coordination of the amino group to the metal ions result in pillared layered structures [18,19,21], (2) the protonation of the amino group results in layered structures, where chloride or sulfate ions are located between the layers [20,22], or (3) the amino group coordinates to the metal center within a metal phosphonate layer and simultaneously nitrate ions are located between the layers [20].

The discovery of new inorganic–organic hybrid compounds can be accelerated using high-throughput (HT) methods. The HT methodology enables an efficient and fast investigation of multi-parameter synthesis fields, thus the influence of the pH, the molar ratios of the starting materials, the reaction temperature and the solvents on the product formation can easily be determined [25–27]. Therefore, it allows us to rapidly discover new compounds, to optimize the synthesis conditions and to establish reaction trends.

Although the HT methodology enables an extensive investigation of large synthesis fields, no information on the formation of the compounds is obtained. Time resolved in situ EDXRD measurements are the method of choice to learn more about the crystallization process. This method has been employed to study the formation of zeolites [28], thioantimonates [29], and metal phosphonoalkylsulfonates [30], under solvothermal conditions. Recently, the studies were extended to inorganic–organic hybrid compounds, such as the metal organic frameworks, HKUST-1 ($[\text{Cu}_3(\text{BTC})_2] \cdot 3\text{H}_2\text{O}$ (BTC=1,3,5-benzenetricarboxylate)) [31], Fe-MIL-53 ($[\text{Fe}(\text{OH})(\text{O}_2\text{C}-\text{C}_6\text{H}_4-\text{CO}_2) \cdot \text{H}_2\text{O}]$) [31],

* Corresponding author. Fax: +49 431 880 1775.
E-mail address: stock@ac.uni-kiel.de (N. Stock).

[31], MOF-14 ($\text{Cu}_3(\text{BTB})_2(\text{H}_2\text{O})_3 \cdot (\text{DMF})_9(\text{H}_2\text{O})_2$, (BTB=4,4',4''-benzene-1,3,5-triyl-tribenzoic acid)) [32], Al-MIL-101- NH_2 ($\text{Al}_3\text{O}(\text{DMF})[(\text{OOC})_6\text{C}_6\text{H}_3\text{NH}_2(\text{COO})]_3 \cdot x\text{H}_2\text{O}$ [33], CAU-1-(OH) $_2$ ($[\text{Al}_8(\text{OH})_4(\text{OCH}_3)_8(\text{BDC}(\text{OH})_2)_6] \cdot x\text{H}_2\text{O}$ (BDC=1,4-benzenedicarboxylate)) [34] and CAU1- NH_2 ($[\text{Al}_8(\text{OH})_4(\text{OCH}_3)_8(\text{BDC}(\text{NH}_2)_2)_6] \cdot x\text{H}_2\text{O}$) [35]. In situ EDXRD measurements enable to monitor the crystallization process and therefore possible intermediates can also be observed. In some cases the intermediate can be isolated by quenching of the reaction mixture [31,33].

Although a number of metal ions have been investigated, there are no results on the use of alkaline earth metals for the formation of metal aminophosphonate hybrid compounds. Therefore, we have started a systematic investigation of these systems by carrying out a metal screening experiment. Based on these results, we have chosen Ca^{2+} as the metal ion of choice for more in depth studies. Here we present our results of the systematic HT investigation of the system $\text{Ca}^{2+}/\text{AEPA}/\text{H}_2\text{O}/\text{NaOH}$ (AEPA=2-aminoethylphosphonic acid) and the time resolved in situ EDXRD study of the synthesis of $\text{Ca}(\text{O}_3\text{PC}_2\text{H}_4\text{NH}_2)$.

2. Material and methods

The synthesis of 2-aminoethylphosphonic acid was performed based on reported procedures [36–38]. All reagents and solvents were purchased from commercial sources. They were of analytical grade and were used as obtained. HT X-ray powder diffraction (XRPD) measurements were performed on a Stoe Stadi P HT – diffractometer in transmission geometry with $\text{Cu } K_{\alpha 1}$ radiation and equipped with an image plate detector system. MIR spectra were collected on a Bruker Alpha spectrometer equipped with a diamond ATR unit in the spectral range of $4000\text{--}400\text{ cm}^{-1}$. Raman spectra were recorded using a Bruker FRA 106 Raman spectrometer. The thermogravimetric analysis was executed with a NETSCH STA 409 CD analyzer, under air (75 mL/min), with a heating rate of 2 K/min. Elemental analyses were carried out using a Eurovektor EuroEA Elemental Analyzer. The in situ EDXRD measurements were performed at beamline F3 at HASYLAB, DESY, Hamburg.

2.1. High-throughput experiments

Applying our HT method the system $\text{Ca}^{2+}/\text{AEPA}/\text{H}_2\text{O}/\text{NaOH}$ was investigated under solvothermal reaction conditions. All starting materials were applied as aqueous solutions. The reaction block was heated to $130\text{ }^\circ\text{C}$ in 2 h. After 48 h at the reaction temperature, the multiclave was cooled down within 12 h. A custom made HT reactor was employed containing 48 PTFE vessels each with a maximum volume of 300 μL . The molar ratios $\text{Ca}^{2+}:\text{AEPA}$ were varied from 0.17 to 6.5:1. The amount of NaOH was varied from 0.17 to 6:1 (NaOH:AEPA). The starting materials were added to the PTFE vessels in the following order: AEPA, $\text{Ca}(\text{NO}_3)_2 \cdot 4\text{H}_2\text{O}$, H_2O and NaOH. The reaction products were filtered off, washed with water and dried in air. All samples were characterized by XRPD measurements. The concentrations of the starting solutions and the exact amounts of the starting materials employed are given in Table S1 in the Supporting Information.

2.2. Synthesis of $\text{Ca}(\text{O}_3\text{PC}_2\text{H}_4\text{NH}_2)$ (1)

A single phase microcrystalline powder of **1** was obtained from the HT investigation by mixing 40 μL (40 μmol) of a 1 M aqueous solution of AEPA, 40 μL of a 2 M aqueous solution of $\text{Ca}(\text{NO}_3)_2 \cdot 4\text{H}_2\text{O}$, 90 μL H_2O and 30 μL of a 4 M aqueous solution of NaOH (molar ratio $\text{Ca}^{2+}:\text{AEPA}:\text{NaOH}=2:1:3$). Scale-up synthesis using Schott Duran glass culture tubes (5 mL) were

performed to get larger amounts of **1**. Therefore, the tenfold amount of the starting materials and the same temperature program were used. The purity was confirmed by the elemental analyses ((%) calcd. for $\text{CaPNC}_2 \cdot \text{H}_6\text{O}_3$: C: 14.73, N: 8.59, H: 3.71; found: C: 15.31, N: 8.23, H: 3.42) and the successful structure refinement of the XRPD data.

2.3. Synthesis of $\text{Ca}(\text{OH})(\text{O}_3\text{PC}_2\text{H}_4\text{NH}_3) \cdot 2\text{H}_2\text{O}$ (2)

Compound **2** was observed as an intermediate during the in situ EDXRD investigation. Based on these results the compound was obtained executing the scale up synthesis of **1** at room temperature under stirring and quenching the reaction mixture after 1 h by filtration. The synthesis resulted in a microcrystalline colorless powder. The purity was confirmed by the elemental analyses ((%) calcd. for $\text{CaPNC}_2\text{H}_{12}\text{O}_6$: C: 11.06, N: 6.45, H: 5.57; found: C: 10.85, N: 6.28, H: 3.95) and the successful structure refinement of the XRPD data.

2.4. In situ EDXRD investigation

The EDXRD investigation was performed at HASYLAB, beamline F3 using the light source DORIS III at DESY in Hamburg, Germany. White synchrotron radiation was used in combination with a germanium detector system cooled with liquid nitrogen. The detector angle was set to approximately 1.9° and the collimator to $0.2 \times 0.2\text{ mm}^2$. The reaction was carried out in Schott Duran glass culture tube (5 mL) placed in a custom-made reactor system heated by an external thermostat to $130\text{ }^\circ\text{C}$ [39]. To investigate the formation of **1** the optimized reaction conditions obtained from the HT investigation and the scale-up synthesis were used. The starting materials were employed as aqueous solutions (300 μL 1 M AEPA, 300 μL 2 M $\text{Ca}(\text{NO}_3)_2 \cdot 4\text{H}_2\text{O}$, 2.175 mL water and 225 μL 4 M NaOH ($\text{Ca}^{2+}:\text{AEPA}:\text{NaOH}=2:1:3$) which was stirred during the reaction. The exposure time for each EDXRD spectrum was 60 s.

2.5. Structure determination

The structure determination of $\text{Ca}(\text{O}_3\text{PC}_2\text{H}_4\text{NH}_2)$ (**1**) was accomplished using in house XRPD data. The XRPD measurement was performed on a STOE Stadi-P powder diffractometer in transmission geometry with $\text{Cu } K_{\alpha 1}$ radiation ($\lambda=154.0598\text{ pm}$) equipped with a position-sensitive detector. Indexing of the XRPD pattern of **1** was accomplished using the program EXPO2009 [40] and cell parameters were refined applying the program WinXPOW [41] (FOM: 36.4). The structure determination of $\text{Ca}(\text{OH})(\text{O}_3\text{PC}_2\text{H}_4\text{NH}_3) \cdot 2\text{H}_2\text{O}$ (**2**) was accomplished using synchrotron data. The synchrotron measurement was performed at HASYLAB, beamline G3 at DESY in Hamburg, Germany using monochromatic light ($\lambda=154.302\text{ pm}$) [42]. The powder pattern was indexed applying the program TOPAS [43] and cell parameters were refined using WinXPOW [41] (FOM: 37.5). Structure determinations were carried out with the program EXPO 2009 using direct methods. All atoms were observed in the structure solution and the atomic coordinates were set as the starting model for the Rietveld refinement applying the program TOPAS. The Rietveld refinement involved the following parameters for compound **1**: 4 cell parameters, 24 atomic coordinates (Table S2), 1 overall thermal factor, 1 scale factor, 1 zero point and 15 background parameters. For compound **2**: 4 cell parameters, 30 atomic coordinates (Table S3), 1 overall thermal factor, 1 scale factor, 1 zero point and 7 background parameters were used for the Rietveld refinement. Preferred orientation was modeled using spherical harmonics series. Restraints were applied to the P–O, P–C, C–C and C–N bond lengths and to the O–P–C and C–C–N

Table 1

Summary of crystal data and refined structure parameters for $\text{Ca}(\text{O}_3\text{PC}_2\text{H}_4\text{NH}_2)$ (**1**) and $\text{Ca}(\text{OH})(\text{O}_3\text{PC}_2\text{H}_4\text{NH}_3) \cdot 2\text{H}_2\text{O}$ (**2**).

	Compound 1	Compound 2
Formula	$\text{C}_2\text{H}_6\text{O}_3\text{PNCa}$	$\text{C}_2\text{H}_{12}\text{O}_6\text{PNCa}$
Weight (g/mol)	163.12	217.17
Crystal system	Monoclinic	Monoclinic
Space group	$P2_1/c$ (No. 14)	$P2_1/m$ (No. 11)
<i>a</i> (pm)	9.7753(3)	11.2193(7)
<i>b</i> (pm)	6.4931(2)	7.1488(3)
<i>c</i> (pm)	8.4473(2)	5.0635(2)
β (°)	106.46(2)	100.13(4)
<i>V</i> (Å ³)	514.20(2)	399.78(3)
<i>Z</i>	4	2
<i>R</i> _{wp}	0.0697	0.0502
<i>R</i> _{exp}	0.0397	0.0171
<i>R</i> _{Bragg}	0.0331	0.0221
G.O.F.	1.754	2.944

bond angles in both compounds. For compound **2** restraints were applied in addition to the O–O and O–N distances. The results of the final Rietveld refinements are shown in Figs. 2 and 5 for **1** and **2**, respectively. Results of the crystallographic work are summarized in Tables S4 and S5. Crystallographic data (excluding structure factors) for the structures in this paper have been deposited with the Cambridge Crystallographic Data Centre as supplementary publication nos. CCDC-847095 and 847096 for **1** and **2**, respectively. Copies of the data can be obtained, free of charge, on application to CCDC, 12 Union Road, Cambridge CB2 1EZ, UK (fax: +44 1223 336033 or email: deposit@ccdc.cam.ac.uk).

3. Results and discussion

The system $\text{Ca}^{2+}/\text{AEPA}/\text{H}_2\text{O}/\text{NaOH}$ was systematically investigated applying our high-throughput methodology. Therefore the molar ratio of the starting materials was varied stepwise. Based on the XRPD measurements of the resulting products a ternary crystallization diagram can be set up, which is shown in Fig. 1.

The HT experiment using 2-aminoethylphosphonic acid resulted in one new compound. Crystalline products of $\text{Ca}(\text{O}_3\text{PC}_2\text{H}_4\text{NH}_2)$ were obtained at molar ratios $\text{Ca}^{2+}:\text{AEPA}:\text{NaOH} = 0.5\text{--}6.5:1:1.5\text{--}4$, i.e., in the pH range $\sim 8 < \text{pH} < 13$. In a large field of formation, i.e., in the pH range $\sim 6 < \text{pH} < 7$ no precipitate was obtained. These results are marked in white in the ternary diagram. At pH=14 the experiment led to X-ray amorphous products (black points). The product obtained at a molar ratio $\text{Ca}^{2+}:\text{AEPA}:\text{NaOH} = 2:1:3$ was used for the structure determination.

3.1. Crystal structure of $\text{Ca}(\text{O}_3\text{PC}_2\text{H}_4\text{NH}_2)$ (**1**)

The crystal structure of **1** was determined from in house XRPD data. The final Rietveld plot is shown in Fig. 2.

Compound **1** contains one Ca^{2+} ion and one $(\text{O}_3\text{PC}_2\text{H}_4\text{NH}_2)^{2-}$ ion in the asymmetric unit. The coordination sphere of the calcium ion contains five linker molecules. The Ca^{2+} ion is surrounded by six oxygen atoms of the phosphonate groups and one nitrogen atom of the amino group which results in CaO_6N -polyhedra (Fig. 3, left). Each linker molecule is coordinated to five Ca^{2+} ions. While O3 and N1 act as monodentate ligands, O1 and O2 act as μ_2 and μ_3 bridging ligand atoms, respectively (Fig. 3, right).

Each CaO_6N -polyhedron is connected to three other CaO_6N -polyhedra via common edges. This leads to six-rings and layers are formed in the *b,c*-plane (Fig. 4, left). The $-\text{C}_2\text{H}_4-$ unit of the linker molecule is involved in the interconnection of the CaO_6N -

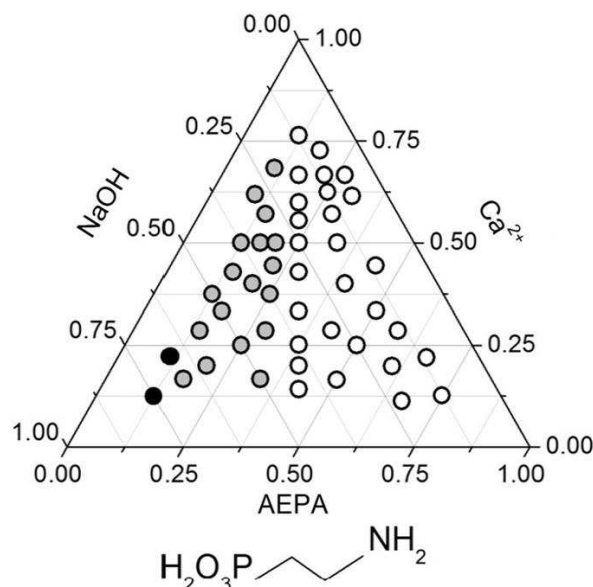


Fig. 1. Crystallization diagram of the system $\text{Ca}^{2+}/\text{AEPA}/\text{H}_2\text{O}/\text{NaOH}$. Title compound **1** ($\text{Ca}(\text{O}_3\text{PC}_2\text{H}_4\text{NH}_2)$) is marked in gray, X-ray amorphous products and no precipitate are marked in black and white, respectively.

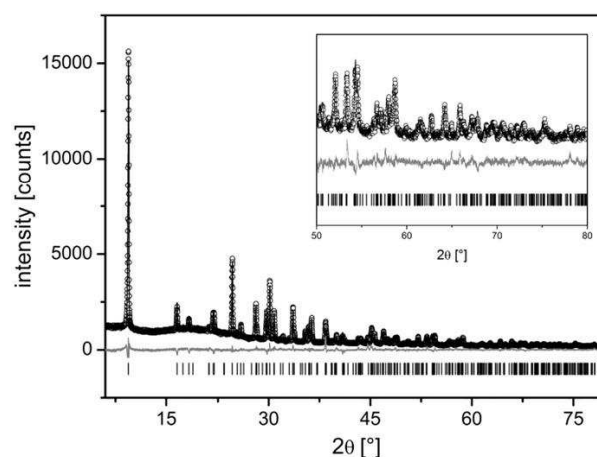


Fig. 2. Observed (○) and Rietveld refined XRPD pattern (black line) of compound **1**. The residual (difference plot of the measured vs. refined pattern) is presented by the gray line. The vertical lines below the patterns indicate the Bragg positions.

polyhedra within each layer. These layers are connected to each other through van der Waals interactions (Fig. 4, right).

3.2. Crystal structure of $\text{Ca}(\text{OH})(\text{O}_3\text{PC}_2\text{H}_4\text{NH}_3) \cdot 2\text{H}_2\text{O}$ (**2**)

The crystal structure of compound **2** was determined from synchrotron data. The final Rietveld plot is shown in Fig. 5.

The localization of the H-atoms is based on previously reported crystal structures of metal aminoethyl- and aminopropylphosphonates [18–24] in combination with the results of the IR spectroscopic and the thermogravimetric measurements. Thus, the crystal structure of **2** contains one Ca^{2+} ion, one linker molecule and one hydroxide ion as well as two water molecules per formula unit. The Ca^{2+} ion is surrounded by six oxygen atoms and CaO_6 -polyhedra are formed (Fig. 6, left). Each linker molecule is coordinated to four Ca^{2+} ions. While both oxygen atoms O1 are connected to one Ca^{2+} ion, the

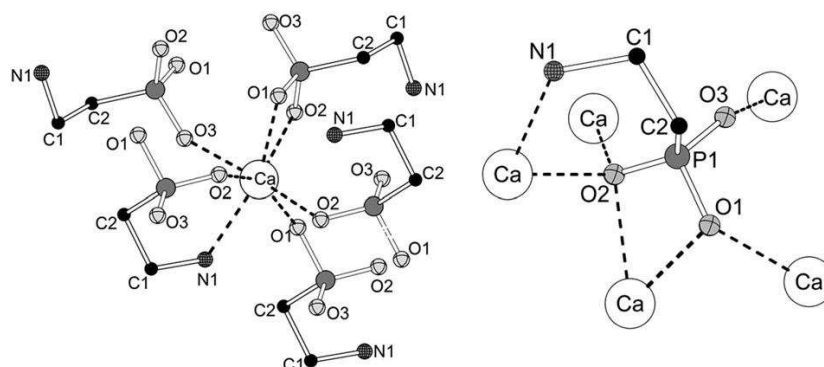


Fig. 3. Coordination sphere of the Ca^{2+} ion in $\text{Ca}(\text{O}_3\text{PC}_2\text{H}_4\text{NH}_2)$ (**1**) (left). Coordination scheme of the linker molecule to the Ca^{2+} ions (right).

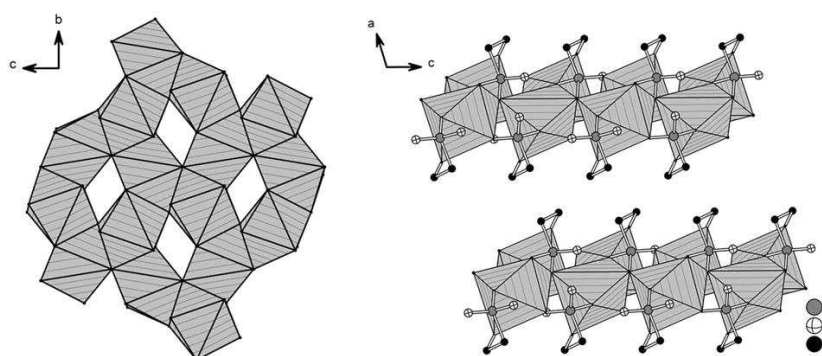


Fig. 4. Left: layer composed of edge-sharing CaO_6N -polyhedra in the b,c -plane. Right: layers in $\text{Ca}(\text{O}_3\text{PC}_2\text{H}_4\text{NH}_2)$ are interconnected by van der Waals interactions.

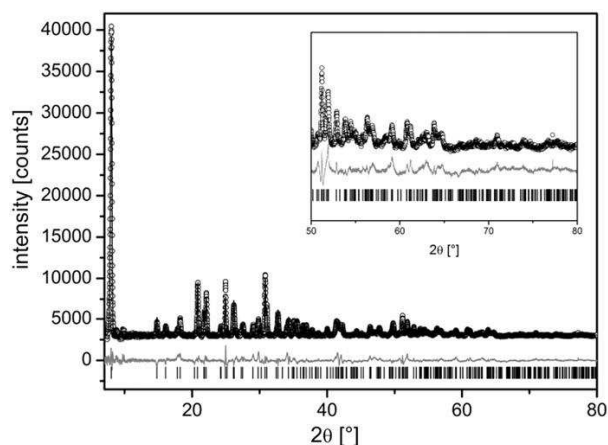


Fig. 5. Observed (○) and Rietveld refined XRPD pattern (black line) of compound **2**. The residual (difference plot of the measured vs. refined pattern) is presented by the gray line. The vertical lines below the patterns indicate the Bragg positions.

oxygen atom O2 acts as bridging atom. Edge-sharing of the CaO_6 -polyhedra through O2 and the hydroxide ions results in chains along the b -axis (Fig. 6, right). In the vicinity of the oxygen atoms O1 water molecules (OW1) are observed, which act as H-donors in hydrogen bonds to O1 ($D-A=236.7(5)$). The hydroxide ion OH is involved in hydrogen bonds to OW1 as the H-donor with a bond distance of $D-A=279.2(21)$ pm.

The Ca–O chains are connected via the phosphonate groups to build layers in the b,c -plane (Fig. 7, left). Although a hydroxide ion

is part of the structure, the amino group should be protonated due to the charge equalization. The presence of $-\text{NH}_3^+$ groups is supported by the fact that the $-\text{C}_2\text{H}_4\text{NH}_3^+$ units of the linker molecules point into the interlayer region where water molecules are located (OW2). The nitrogen atoms interact in hydrogen bonds as H-acceptor and N1-OW2 bond distances of 286.1(19) and 279.6(17) pm are observed (Fig. 7, right). In addition hydrogen bonds between OW2 and OW1 are found with a length of 261.6(9) pm. The anticipated hydrogen bonding scheme as well as the bond lengths and angles are given in the Supporting Information (Fig. S1, Tables S5 and S6).

Both compounds **1** and **2** are composed of layers. While edge-sharing of CaO_6N -polyhedra leads to six-rings in the layers of $\text{Ca}(\text{O}_3\text{PC}_2\text{H}_4\text{NH}_2)$ (**1**), the layers in $\text{Ca}(\text{OH})(\text{O}_3\text{PC}_2\text{H}_4\text{NH}_3) \cdot 2\text{H}_2\text{O}$ (**2**) contain of edge-sharing CaO_6 -polyhedra. In compound **2** hydroxide ions are involved in the connection of the Ca^{2+} ions. While the nitrogen atom in **1** is part of the coordination sphere of the Ca^{2+} ion, the amino groups in compound **2** are protonated and point into the interlayer space. The crystal structure of **2** is completed by two water molecules per formula unit. One water molecule (OW1) is located close to the Ca–O-layers and interacts in hydrogen bonds to the hydroxide ion, the phosphonate group and OW2. The second water molecule (OW2) is located in the interlayer space and there involved into hydrogen bonds with the nitrogen atoms.

3.3. Spectroscopic and thermal investigations

Compounds **1** and **2** were studied by infrared and Raman spectroscopy (Figs. S2 and S3). All compounds show the typical bands of the P–C and P–O stretching vibrations of the CPO_3 -group in the region $1130\text{--}950\text{ cm}^{-1}$. For compound **1**, the characteristic bands at

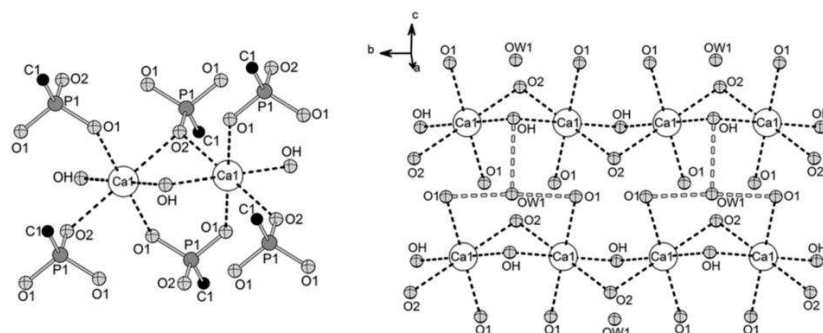


Fig. 6. Left: coordination sphere of the Ca^{2+} ions in $\text{Ca}(\text{OH})(\text{O}_3\text{PC}_2\text{H}_4\text{NH}_3) \cdot 2\text{H}_2\text{O}$ (**2**). Right: chain of edge-sharing CaO_6 -polyhedra along the b -axis. Hydrogen bonds between OW1, O1 and OH are observed (white dotted lines).

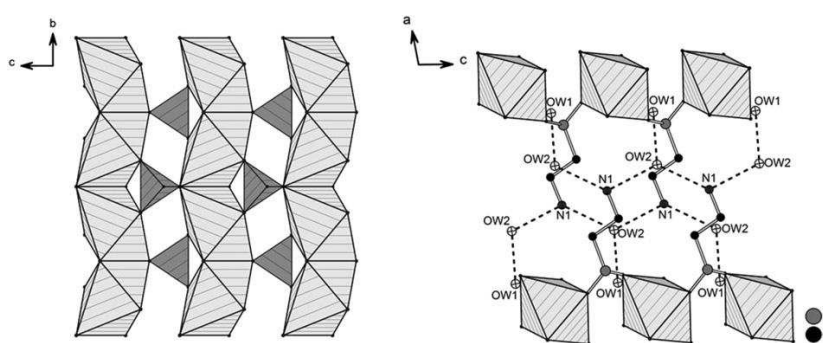


Fig. 7. Left: layer of chains of edge-sharing CaO_6 -polyhedra (shaded in light gray) and PO_3C -polyhedra (shaded in dark gray). OW1 and hydrogen bonds are omitted for clarity. Right: the $-\text{C}_2\text{H}_4\text{NH}_3$ units of the linker molecules point into the interlayer space. OW1 and hydrogen bonds (dotted lines) are observed between the water molecules OW1 and OW2 as well as OW2 and N1. Hydrogen bonds between OW1, O1 and OH are omitted for clarity.

$3358\text{--}3288\text{ cm}^{-1}$ and 1591 cm^{-1} for the stretching and deformation vibration of the amino group are observed, respectively. The vibration bands at $2900\text{--}2845\text{ cm}^{-1}$ and 1476 cm^{-1} correspond to the C–H stretching and deformation vibration of the CH_2 -group. The C–N stretching vibration results in a band at 1217 cm^{-1} . Compound **2** shows the characteristic vibration band at $3645\text{--}3600\text{ cm}^{-1}$ of bridging hydroxide ions. The bands for the stretching and deformation vibration of the protonated amino group are observed at $3331\text{--}3162\text{ cm}^{-1}$ and 1594 cm^{-1} . In comparison to the corresponding vibrations of compound **1** they are slightly weaker due to the protonation and the presence of hydrogen bonds. The bands at $2950\text{--}2890\text{ cm}^{-1}$ and 1475 cm^{-1} are related to the vibrations bands of the CH_2 -groups. The water molecules in the crystal structure lead to the broadening of the bands at 3250 cm^{-1} and 1590 cm^{-1} .

Thermogravimetric (TG) measurements up to $860\text{ }^\circ\text{C}$ for **1** and $900\text{ }^\circ\text{C}$ for **2** under air flow using a heating rate of 2 K/min were performed to gain deeper insight into the thermal stability of the compounds. The thermal degradation of compound **1** takes place in 3 steps in the range of $195\text{--}850\text{ }^\circ\text{C}$. A total weight loss of 25.6% is observed (calc.: 27.0%) which leads, based on XRPD measurements, to $\text{Ca}_2\text{P}_2\text{O}_7$. For compound **2** a multistep thermal degradation is observed. Up to $215\text{ }^\circ\text{C}$ a weight loss of 14.5% is observed which corresponds to the loss of two water molecules per formula unit (calc.: 16.5%). A total weight loss of 38.7% is measured up to $900\text{ }^\circ\text{C}$, which results in a X-ray amorphous product. The TG curves are presented in the Supporting Information (Figs. S4 and S5).

3.4. In situ EDXRD investigation

Although the HT experiment allows an efficient investigation of multiparameter fields and therefore the rapid discovery of new

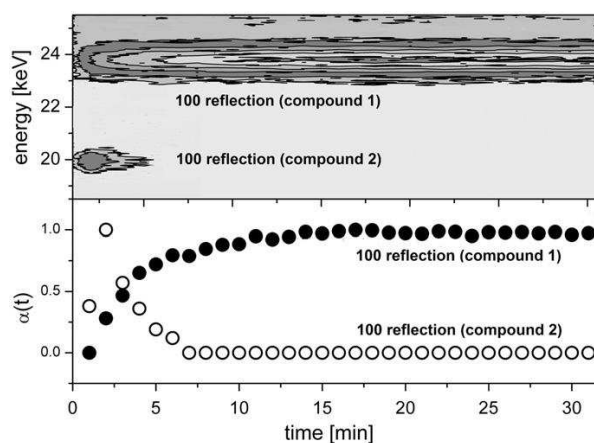


Fig. 8. Surface plot and normalized intensities of the 100 reflections of the formation of $\text{Ca}(\text{O}_3\text{PC}_2\text{H}_4\text{NH}_3)$ (**1**) and $\text{Ca}(\text{OH})(\text{O}_3\text{PC}_2\text{H}_4\text{NH}_3) \cdot 2\text{H}_2\text{O}$ (**2**).

compounds, no information about the crystallization itself or possible crystalline intermediates are obtained. Thus the formation of compound **1** was investigated by in situ EDXRD measurements at $130\text{ }^\circ\text{C}$ using conventional heating [39]. The reactants were employed as previously described. For an evaluation of the data, the reaction progress $\alpha(t) = I(t)/I(t_\infty)$ was determined, where I is the intensity at a given time t and at the end of the reaction t_∞ , respectively. The intensity I was obtained by integrating the 100 reflection of **1** and **2** (maximum error 6%). The surface plot and the reaction progress $\alpha(t)$ are shown in Fig. 8.

The surface plot shows two signals at 20 keV and 24 keV. This energy range corresponds under the given experimental settings to the 2θ range of 7 to 10.5° . The signal at 24 keV corresponds to the 100 reflection of compound **1** and is observed for the first time after 1 min. It reaches a maximum after 14 min. The second signal at 20 keV is immediately detected and reaches a maximum after 2 min. After 2 min the signal at 20 keV (marked in white) decreases and simultaneously the signal of the 100 reflection of $\text{Ca}(\text{O}_3\text{PC}_2\text{H}_4\text{NH}_2)$ (**1**) increases (marked in black). This reaction progress shows that the formation of compound **1** involves a formation of an intermediate. The curves of the reaction progress of **1** and **2** intersects at $\alpha(t)=0.5$. This suggests a direct transformation of the intermediate to the final product via a solid-solid transformation [44]. The intermediate was identified as $\text{Ca}(\text{O}-\text{H})(\text{O}_3\text{PC}_2\text{H}_4\text{NH}_3) \cdot 2\text{H}_2\text{O}$ (**2**) and the signal at 20 keV corresponds to the 100 reflection. The comparison of the EDXRD spectrum and the XRPD patterns of $\text{Ca}(\text{O}_3\text{PC}_2\text{H}_4\text{NH}_2)$ (**1**) and the intermediate $\text{Ca}(\text{OH})(\text{O}_3\text{PC}_2\text{H}_4\text{NH}_3) \cdot 2\text{H}_2\text{O}$ (**2**) is shown in the Supporting Informations (Fig. S6). The determined densities of the title compounds give a further indication for the formation of the intermediate as the kinetically stable product. While a density of $1.703(1) \text{ g cm}^{-3}$ was determined for compound **2** as the kinetically stable intermediate, the determination of the density led to $2.029(1) \text{ g cm}^{-3}$ for compound **1** as the thermodynamically stable product.

4. Conclusion

Using a combination of different synthesis and characterization tools such as high-throughput method as well as in situ EDXRD and high resolution XRPD measurements the reaction system $\text{Ca}^{2+}/\text{AEPA}/\text{H}_2\text{O}/\text{NaOH}$ was studied in detail. While the HT methods demonstrated the existence of the new compound $\text{Ca}(\text{O}_3\text{PC}_2\text{H}_4\text{NH}_2)$ in a large fraction of the crystallization diagram, the in situ EDXRD experiment showed that the crystallization is completed after 14 min at 130°C . In addition, the existence of a crystalline intermediate was observed. The high-resolution XRPD data using synchrotron radiation allowed us to determine its crystal structure.

Supporting information

Supporting Information with exact amounts used for the high-throughput syntheses, Atomic parameter for the Rietveld refinement, selected bond lengths and angles, IR spectrum and TG measurement, selected bond lengths and angles and the in situ study are available. This information is available free of charge via the Internet at <http://pubs.acs.org/>.

Acknowledgment

We thank the HASYLAB / DESY, Hamburg for the allocated beam time at the light source DORIS III (proposal number I-20100288), Ursula Cornelissen and Stephanie Pehlke for spectroscopic measurements, Beatrix Seidlhofer and Nicola Herzberg for TG/DTA measurements and the group of Prof. Dr. Wolfgang Bensch for the allocation of the reactor system for the in situ EDXRD studies.

Appendix A. Supporting materials

Supplementary data associated with this article can be found in the online version at doi:10.1016/j.jssc.2012.01.044.

References

- [1] K.K. Tanabe, S.M. Cohen, *Inorg. Chem.* 49 (2010) 6766.
- [2] A.U. Czaja, N. Trukhan, U. Müller, *Chem. Soc. Rev.* 38 (2009) 1284.
- [3] J.L. Rowsell, O.M. Yaghi, *Microporous Mesoporous Mater.* 73 (2004) 3.
- [4] G.K.H. Shimizu, R. Vaidhyanathan, J.M. Taylor, *Chem. Soc. Rev.* 38 (2009) 1430.
- [5] A. Clearfield, *Prog. Inorg. Chem.* 47 (1998) 371.
- [6] S. Bauer, T. Bein, N. Stock, *J. Solid State Chem.* 179 (2006) 145.
- [7] S. Bauer, T. Bein, N. Stock, *Inorg. Chem.* 44 (2005) 5882.
- [8] N. Stock, S.A. Frey, G.D. Stucky, A.K. Cheetham, *J. Chem. Soc., Dalton Trans.* (2000) 4292.
- [9] T.-B. Liao, Y. Ling, Z.-X. Chen, Y.-M. Zhou, L.-H. Weng, *Chem. Commun.* 46 (2010) 1100.
- [10] A. Sonnauer, M. Feyand, N. Stock, *Cryst. Growth Des.* 9 (2008) 586.
- [11] A. Sonnauer, N. Stock, *J. Solid State Chem.* 181 (2008) 473.
- [12] Z.-Y. Du, H.-B. Xu, X.-L. Li, J.-G. Mao, *Eur. J. Inorg. Chem.* (2007) 4520.
- [13] N. Stock, A. Stoll, T. Bein, *Microporous Mesoporous Mater.* 69 (2004) 65.
- [14] C. Serre, J.A. Groves, P. Lightfoot, A.M.Z. Slawin, P.A. Wright, N. Stock, T. Bein, M. Haouas, F. Taulelle, G. Férey, *Chem. Mater.* 18 (2006) 1451.
- [15] S.R. Miller, G.M. Pearce, P.A. Wright, F. Bonino, S. Chavan, S. Bordiga, I. Margiolaki, N. Guillou, G. Férey, S. Bourrelly, P.L. Llewellyn, *J. Am. Chem. Soc.* 130 (2008) 15967.
- [16] M.T. Wharmby, J.P.S. Mowat, S.P. Thompson, P.A. Wright, *J. Am. Chem. Soc.* 133 (2011) 1266.
- [17] C.R. Samanamu, E.N. Zamora, J.-L. Montchamp, A.F. Richards, *J. Solid State Chem.* 181 (2008) 1462.
- [18] S. Drumel, P. Janvier, D. Deniaud, B. Bujoli, *J. Chem. Soc., Chem. Commun.* (1995) 1051.
- [19] F. Fredoueil, D. Massiot, P. Janvier, F. Gingl, M. Bujoli-Doeuff, M. Evain, A. Clearfield, B. Bujoli, *Inorg. Chem.* 38 (1999) 1831.
- [20] S. Drumel, P. Janvier, M. Bujoli-Doeuff, B. Bujoli, *Inorg. Chem.* 35 (1996) 5786.
- [21] W.R. Gemmill, M.D. Smith, B.A. Reisner, *J. Solid State Chem.* 178 (2005) 2658.
- [22] E.M. Bauer, C. Bellitto, M. Colaoletto, G. Portalone, G. Righini, *Inorg. Chem.* 42 (2003) 6345.
- [23] G.L. Rosenthal, J. Caruso, *Inorg. Chem.* 31 (1992) 3104.
- [24] N. Zakowsky, P.S. Wheatley, I. Bull, M.P. Atfield, R.E. Morris, *Dalton Trans.* (2001) 2899.
- [25] N. Stock, T. Bein, *Angew. Chem. Int. Ed.* 116 (2004) 767.
- [26] S. Bauer, N. Stock, *Angew. Chem. Int. Ed.* 46 (2007) 6857.
- [27] N. Stock, T. Bein, *J. Mater. Chem.* 15 (2005) 1384.
- [28] R.I. Walton, F. Millange, D. O'Hare, A.T. Davies, G. Sankar, C.R.A. Catlow, *J. Phys. Chem. B* 105 (2001) 83.
- [29] R. Kiebach, N. Pienack, M.-E. Ordoñez, F. Studt, W. Bensch, *Chem. Mater.* 18 (2006) 1196.
- [30] M. Feyand, C. Näther, A. Rothkirch, N. Stock, *Inorg. Chem.* 49 (2010) 11158.
- [31] F. Millange, M.I. Medina, N. Guillou, G. Férey, K.M. Golden, R.I. Walton, *Angew. Chem. Int. Ed.* 49 (2010) 763.
- [32] F. Millange, R. El Osta, M.E. Medina, R.I. Walton, *Cryst. Eng. Commun.* 13 (2011) 103.
- [33] J. Juan-Alcañiz, M. Goesten, A. Martínez-Joaristi, E. Stavitski, A.V. Petukhov, J. Gascon, F. Kapteijn, *Chem. Commun.* 47 (2011) 8578.
- [34] T. Ahnfeldt, J. Moellmer, V. Guillermin, R. Staudt, C. Serre, N. Stock, *Chem. Eur. J.* 17 (2011) 6462.
- [35] T. Ahnfeldt, N. Stock, *CrystEngComm* (2011). doi:10.1039/C1CE05956D.
- [36] H. Becker, et al., *Organikum*, 22 Edition, Wiley-VCH, Weinheim, 2004, p. 600.
- [37] J. Barycki, P. Mastalerz, M. Soroka, *Tetrahedron Lett.* 36 (1970) 3147.
- [38] C. Wasielewski, M. Topolski, L. Dembkowski, *J. Prakt. Chem.* (1989) 507.
- [39] L. Engelke, M. Schäfer, M. Schur, W. Bensch, *Chem. Mater.* 13 (2001) 1383.
- [40] A. Altomare, M. Camalli, C. Cuocci, C. Giacovazzo, A. Moliterni, R. Rizzi, EXPO2009: structure solution by powder data in direct and reciprocal space, *J. Appl. Cryst.* 42 (2009) 1197.
- [41] WinXPow version 2.11, (2005), Stoe & Cie GmbH, Darmstadt, Germany.
- [42] T. Wroblewski, O. Clauf, H.-A. Crostack, A. Ertel, F. Fandrich, Ch. Genzel, K. Hradil, W. Ternes, E. Woldt, *Nucl. Instrum. Methods. A.* 428 (1999) 570.
- [43] A. Coelho, Topas V4.1, Academic version: General Profile and Structure Analysis Software for Powder Diffraction Data, Bruker AXS Ltd, (2004).
- [44] R. Kiebach, N. Pienack, W. Bensch, J.-D. Grunwaldt, A. Michailovskii, A. Baikar, T. Fox, Y. Zhou, G.R. Patzke, *Chem. Mater.* 20 (2008) 3022.

4.6.5. Crystallisation Kinetics of Metal Organic Frameworks from *in situ* Time-Resolved X-ray Diffraction

Das folgende Manuskript wurde bei der Zeitschrift *Powder Diffraction* eingereicht und wird momentan Begutachtet.

Es wurden die Kristallisation von CPO-27(Ni) und CPO-27(Co) ($[M_2BDC-(O)_2] \cdot 8H_2O$) unter solvothermalen Reaktionsbedingungen mittels *in situ* EDXRD untersucht. Die Kristallstruktur von CPO-27(Ni) ist in Abbildung 4.24 gezeigt. Die Verbindung ist aus 2,4-Dioxidoterephthalat-Ionen und M^{2+} -Ionen aufgebaut. Die Oxido und die Carboxylatgruppen koordinieren hierbei an das Nickel und bilden kantenveknüpfte NiO_6 Polyederketten aus. Diese werden von den Linkern zu einem Honigwaben-artigen Netzwerk verknüpft.

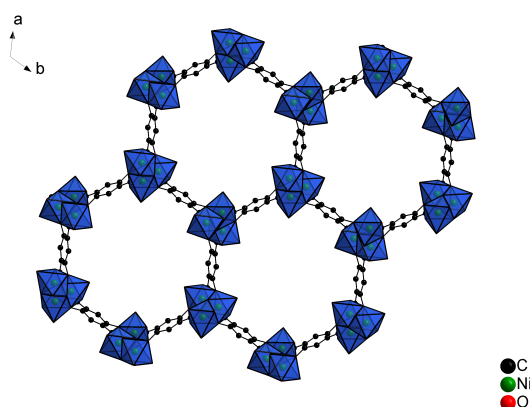


Abbildung 4.24.: Kristallstruktur von CPO-27(Ni). Die NiO_6 Polyeder sind blau dargestellt.

Ziel dieser Arbeit war es die Kristallisationskinetik beider Verbindungen bei Einsatz verschiedener Heizmethoden zu bestimmen. Hierzu wurden mikrowellenunterstützte Synthesemethoden und konventionelle Synthesemethoden verwendet. Die Kristallisation beider Verbindungen wurden im Temperaturbereich von 70 - 110 °C beginnend von einer klaren Lösung in einem THF/Wasser Gemisch (Volumenverhältnis 1/1) *in situ* verfolgt. Die Kinetik wurde mittels Gualtieri Modell ausgewertet.^[118] Aus den Studien wurden Geschwindigkeitskonstanten für die Nukleation und der Kristallwachstum bestimmt sowie aus den temperaturabhängigen Messungen die Arrhenius Aktivierungsenergie. Sowohl die Geschwindigkeitskonstanten für die Nukleation als auch für das Wachstum waren für Ni-CPO-27 größer als für Co-CPO-27. Mikrowellenunterstützte Synthesen führen zu höheren Reaktionsraten. Temperaturabhängige Messungen zeigten, dass die mikrowellenunterstützte Synthesen eine niedrigere Aktivierungsenergie besitzen.

Crystallisation Kinetics of Metal Organic Frameworks

From *in situ* Time-Resolved X-ray Diffraction

Racha El Osta¹, Mark Feyand,² Norbert Stock,² Franck Millange¹ and Richard I. Walton^{3*}

*author for correspondence, email: r.i.walton@warwick.ac.uk

1. Institut Lavoisier Versailles, Université de Versailles, UMR 8180, 78035 Versailles, France
2. Institut für Anorganische Chemie, Christian-Albrechts-Universität, Max-Eyth-Straße 2, D-24118 Kiel, Germany.
3. Department of Chemistry, University of Warwick, Coventry, CV4 7AL, UK

ABSTRACT

A time-resolved powder diffraction study of the crystallisation of porous metal organic framework materials with the CPO-27 structure ($[M_2(dhtp)(H_2O)_2] \cdot 8H_2O$ where, dhtp = 2,5-dihydroxyterephthalate) using the energy dispersive X-ray diffraction method is described. Crystallisation under solvothermal conditions is performed between 70 - 110 °C from clear solutions of metal salts ($M = Co^{2+}$ or Ni^{2+}) and 2,5-dihydroxyterephthalic acid in a mixture of THF-water in sealed reaction vessels, using both conventional and microwave heating. Integration of Bragg peak areas with time provides accurate crystallisation curves, which are modelled using the method of Gualtieri to determine rate constants for nucleation and for growth and then, by Arrhenius analysis, activation energies. Crystallisation is determined to be one-dimensional, consistent with the elongated morphology of the crystals produced in these reactions. With conventional heating the Co-containing CPO-27 crystallises more rapidly than the isostructural Ni-containing analogue and analysis of the kinetic parameters would suggest a complex multi-step crystallisation process. The effect of microwave heating is upon activation energies: the values for both nucleation and for crystal growth are lowered compared to reactions using conventional heating.

For submission to *Powder Diffraction* (Proceedings of EPDIC 13)

I. INTRODUCTION

Metal-organic framework (MOF) materials are a large, and growing, family of hybrid organic-inorganic solids that are the focus of intense investigation at present (Long and Yaghi, 2009; Kepert, 2010; MacGillivray, 2010; Farrusseng, 2011). The concept behind MOF structural chemistry is simple: the combination of metal ions, or clusters of metal ions, with polydentate ligands to yield extend structures whose topology is defined by the coordination preference of the metal and the connectivity, size and shape of the organic 'linkers' (Yaghi *et al.*, 2003). In many cases this approach yields open framework, three-dimensional structures that may possess considerable porosity, once any trapped solvent or unreacted ligand is removed. MOFs represent a new generation of porous solids that have the potential to extend the well-known applications of materials such as zeolites and mesoporous silicas (in separation, catalysis and sensing) into new directions (Czaja *et al.*, 2009). Despite their lower thermal stability compared to solely inorganic framework solids, of particular, fundamental interest is the use of MOFs for gas adsorption, making use of their exceptional porosity and the potential for strong interactions with coordinatively unsaturated framework metals or ligands of suitable design, in important applications such as hydrogen storage (Murray *et al.*, 2009) or CO₂ capture (Sumida *et al.*, 2012). MOFs are also attracting interest for a variety of other reasons, including for the storage and release of biologically active molecules (Horcajada *et al.*, 2012), for the realisation of chiral, porous hosts (Yoon *et al.*, 2012) and for the large structural flexibility that some exhibit (Férey and Serre, 2009).

In order to realise the potential of MOFs it is desirable to have some degree of predictability in their synthesis, and this requires the need for a detailed understanding of their crystallisation kinetics and mechanisms: i.e., the fundamental steps in the assembly of complex extended structures from dissolved precursors or reorganisation of gel phases mediated by solvent, and the relative rates of reaction of each step involved. This is a challenging problem, well-known from zeolite chemistry (Barrer, 1982; Cundy and Cox, 2003), where the observation of crystallisation in a sealed solvothermal reaction vessel requires the careful design of experiments that probe some change of physical property as reaction proceeds (Francis and O'Hare, 1998; Walton *et al.*, 1999a). Study of material

quenched from reaction at various times may give rudimentary information about the course of crystallisation, but makes the significant assumption that no irreversible change has occurred on removing the material; hence *in situ* studies are needed to follow properly the formation of product. There is probably no single experiment that allows chemical order over all lengths scales to be monitored simultaneously, and indeed both spectroscopic and diffraction methods have been applied to obtain the information required (Cheetham and Mellot, 1997; Walton and O'Hare, 2000; Pienack and Bensch, 2011).

In the case of MOFs only in the past few years have results from the *in situ* study of their crystallisation been reported; this includes *in situ* diffraction studies that have revealed the first quantitative information concerning the kinetics of crystallisation of some prototypical MOFs and the observation of metastable phases that have short lifetimes under solvothermal conditions (Millange *et al.*, 2010; Stavitski *et al.*, 2011). Other techniques that have been used to monitor MOF crystallisation include light scattering, which reveals information concerning the growth and decay of precrystallisation agglomerates in reaction solution (Zacher *et al.*, 2009), and atomic force microscopy that provides information about layer by layer surface growth of crystallites (Shoae *et al.*, 2008).

Herein we describe some new results obtained from an *in situ* powder X-ray diffraction study of the crystallisation of large-pore MOF materials with the CPO-27 structure. CPO-27, $[M_2(\text{dhtp})(\text{H}_2\text{O})_2] \cdot 8\text{H}_2\text{O}$, is constructed from M^{2+} centres connected by the multidentate linker 2,5-dihydroxyterephthlate (dhtp) to yield a three-dimensional structure with one-dimensional channels that have approximately circular openings of diameter $\sim 11 \text{ \AA}$ (Dietzel *et al.*, 2010), Figure 1. The metals are found in octahedral coordination, in edge-shared dimers further linked by shared corners, in which one of the vertices is terminally attached solvent (water or alcohol) that may be removed by thermal or vacuum treatment to yield coordinatively unsaturated metal sites. Isostructural frameworks are known for a variety of M^{2+} ions, including Ni, Fe, Mg, Co, Mn and Zn (in the latter case the framework is also known as MOF-74 (Rosi *et al.*, 2005)), and the materials have been studied for its useful properties in gas adsorption, for example, for dihydrogen (Dietzel *et al.*, 2010), H_2S (Allan *et al.*, 2012), selective binding of oxygen over nitrogen (Bloch *et al.*, 2011), and various toxic gases (Glover *et al.*, 2011). In this paper we describe an analysis of

the kinetics of crystallisation of two of these materials, CPO-27(Ni) and CPO-27(Co), and we compare the results with the so-far described kinetic studies of MOF crystallisation available in the literature. We have used the method of energy dispersive X-ray diffraction (EDXRD), which offers a convenient method of measuring powder diffraction patterns from within a sealed reaction vessel, due to the high intensity white X-ray beam, with fast data collection (of around 1 minute per diffraction pattern) because of the fixed-angle solid-state detector (Walton and O'Hare, 2000). EDXRD is a proven method for probing the crystallisation kinetics of a variety of materials under solvothermal conditions, from microporous zeotype materials (Munn *et al.*, 1992; Sankar *et al.*, 2007; Walton *et al.*, 1999b; Walton *et al.*, 2001) and open-framework phosphonates (Feyand *et al.*, 2010; Schmidt and Stock, 2012; Schmidt *et al.*, 2012; Feyand *et al.*, 2012), to metal oxides (Croker *et al.*, 2009; Kiebach *et al.*, 2008; Modeshia *et al.*, 2009) and metal sulfides (Francis *et al.*, 1996; Kiebach *et al.*, 2006), and also has been used to follow the intercalation of guest molecules into layered hosts (O'Hare *et al.*, 2000).

II. EXPERIMENTAL

In situ EDXRD data were recorded during the crystallisation of CPO-27 materials using Beamline F3 of the HASYLAB facility, Germany. This beamline received white-beam radiation with energy 13.5 – 65 keV and the incident X-ray beam on the sample was collimated to $20 \times 20 \mu\text{m}^2$. EDXRD patterns were accumulated using a fixed-angle solid-state germanium detector. Reactions were performed with 12 mm diameter DURAN® tubes fitted with PBT screw caps and PTFE-coated gaskets. 2 mL of the clear solution of reagents were placed into the reaction tube which was immediately transferred into a circulating oil heater equipped with a magnetic stirring device. Microwave assisted EDXRD studies were carried out in a Biotage Initiator microwave reactor system with custom modification to allow the beam to pass the microwave chamber and irradiate the glass vessel directly. The temperature within the microwave vial was measured by a IR sensor and the reactions were stirred continually through the study at a similar speed to the conventional heating experiments. The power of the microwave was controlled remotely to hold the desired temperature.

For the synthesis of CPO-27 materials, 0.937 g Ni acetate (or 0.938 g Co acetate) was dissolved in 25 ml of deionised water and separately 0.372 g 2,5-dihydroxyterephthalic acid was dissolved in 25 ml of tetrahydrofuran. In the reaction tube 1 ml of each solution was mixed to give a clear solution, which was immediately sealed and transferred to the heating device. EDXRD patterns were recorded in 120 s intervals using the Ge detector whose angle (2θ) was calibrated using the characteristic Bragg peaks of a pre-made solid sample of CPO-27(Ni). In the EDXRD experiment, each Bragg peak is characterised by an energy, E/keV , related to its d -spacing, $d/\text{\AA}$, according to Eq. 1.

$$E = \frac{6.1992}{d \sin \theta} \quad (1)$$

The raw EDXRD data were normalised to the incident beam intensity by using the logged synchrotron beam current, and Bragg peak integration was performed using the software f3tool (Rothkirch, 2009). The identification of the final solid product was also confirmed using *ex situ* high-resolution powder XRD. Each crystallisation run was repeated at least on three occasions during several visits to Beamline F3 to check for consistency in the data.

Kinetic analysis was performed using least-squares refinement to the equations derived by Gualtieri for the crystallisation of aluminosilicate zeolites under hydrothermal conditions (see below), within the software Origin (1991-2010). The products from the reactions studied *in situ* were recovered by suction filtration, dried and retained for later analysis using scanning electron microscopy. This was performed using a JEOL JSM-7001F FEG scanning electron microscope.

III. RESULTS AND DISCUSSION

Figure 2 shows a 3D contour plot of a typical CPO-27 crystallisation. In the energy window studied, two characteristic Bragg peaks are observed to form soon after starting the measurement, following only a short induction time, which is only apparent at the lowest temperatures used. Figure 3 shows crystallisation curves as a function of temperature for

Ni(II) and Co(II) containing CPO-27 determined by integration of the most intense (-120) Bragg peak of each phase. It is immediately apparent that the crystallisation of the Ni form of CPO-27 is retarded compared to the Co analogue, with, for example, the time for crystallisation to reach completion for CPO-27(Ni) at 110 °C being approximately the same for CPO-27(Co) at 90 °C. The induction times for crystallisation are very similar in each case, and crystallisation begins within a few minutes of heating. This is consistent with the previous observations of Haque and Jung who studied the crystallisation of the same materials from DMF-water mixtures and, by quenching and powder diffraction analysis of the products, derived approximate crystallisation curves (Haque and Jung, 2011). They proposed that the higher lability of $[\text{Co}(\text{H}_2\text{O})_6]^{2+}$ was responsible for its enhanced rate of reaction with the carboxylate ligand via increased solvent-ligand exchange kinetics.

For analysis of our new crystallisation curves, in order to obtain quantitative kinetic information concerning crystallisation, we have used the method of Gualtieri, who studied the crystallisation of aluminosilicate zeolites and derived an expression for the crystallisation kinetics (Gualtieri, 2001). This model provides a mathematical description based on nucleation-growth crystallisation and the advantage of using this model for simulating crystallisation is that it separates nucleation and growth into two processes, each with separate rate constants. We and others have recently applied the Gualtieri model to crystallisation data from a number of metal-organic frameworks (Cravillon *et al.*, 2012; El Osta *et al.*, 2012; Millange *et al.*, 2011; Reinsch and Stock, 2012), and this current study provides the opportunity to compare the calculated kinetic parameters between different MOF crystallisations to gain some greater physical insight into crystallisation.

The Gualtieri model describes crystallisation according to Eq. 2.

$$\alpha = \frac{1}{1 + \exp\left\{-\left(\frac{t-a}{b}\right)\right\}} \left[1 - \exp\left[-(k_g)^n\right]\right] \quad (2)$$

This expression shows how the extent of crystallisation (normalised from zero to one), α , is related to t , the time coordinate of the crystallisation, to the parameters k_g , the rate of crystal growth, a and b , constants that parameterise nucleation, and n the dimensionality of

crystal growth (which may be determined by independent observations, such as crystal morphology from electron microscopy and by consideration of the crystal symmetry of the material being studied). By fitting this expression against the experimentally determined extent of crystallisation, the probability of nucleation, P_N , can then be calculated using Eq. 3.

$$P_N = \exp\left\{-\frac{(t-a)^2}{2b^2}\right\} \quad (3)$$

The rate of nucleation, k_n , is then defined as $1/a$. The parameter b is believed to contain information about the crystal growth mechanism (see below).

Figures 4 and 5 show fits obtained by fitting of the Gualtieri model to the crystallisation data of CPO-27(Co) and CPO-27(Ni), respectively, using a least squares fitting procedure. It is important to note that in order to obtain a physically meaningful set of rate constants (increasing with reaction temperature) the value of n was required to be equal to 1 and hence was fixed to determine final refined values of the other parameters. This implies a one-dimensional crystal growth, which is entirely consistent with the needle-like crystals previously reported for CPO-27 materials (Haque and Jhung, 2011), and the SEM images recorded from our samples, Figure 6, that show a distinctive elongated morphology. Note that we have studied crystallisation curves derived from integration of the most intense (-120) Bragg peaks so this analysis may suggest that the long axis of the crystals lies in this direction.

Table I contains the fitted kinetic parameters. According to the Gualtieri model the parameter b contains information relating to the mechanism of crystal growth; in the original work the b value was compared to other kinetic models for crystallisation to distinguish between three types of crystallisation: homogeneous, heterogeneous and autocatalytic (Gualtieri, 2001). For values of b less than 15, it is suggested that crystallisation occurs via a heterogeneous pathway, meaning, for example, crystallisation take place at preformed aggregates in the reaction mixture. It is interesting to note that the b values, Table I, show a distinctive positive temperature dependence for both CPO-27(Ni) and CPO-27(Co). This would suggest that the crystallisation actually proceeds via at least two distinct

steps and the effect of temperature changes the limiting step, switching the dominant (i.e., rate determining) step.

In Table II we compare the activation energies for both crystal growth and nucleation, determined from Arrhenius plots, as shown in Figure 7, with values reported in the literature for other metal-organic framework materials whose solvothermal crystallisation has also been analysed using the Gualtieri model. It is interesting to observe that, while the activation energies of crystal growth for both CPO-27(Co) and CPO-27(Ni) are virtually the same ($\sim 90 \text{ kJ mol}^{-1}$), the activation energy for nucleation for the Ni material is approximately double that of the Co material. The CPO-27(Co) also shows a smaller activation energy for nucleation than for crystal growth. Both observations may reflect the greater lability of hydrated Co^{2+} over hydrated Ni^{2+} , such that the initial replacement of bound water by the ligand occurs rapidly to initiate the formation of nucleation sites for subsequent crystal growth. This would be consistent with the conclusions of the quenching studies of Haque and Jhung (Haque and Jhung, 2011). Our kinetic analysis also shows that the simulated nucleation curves do not extend far into the crystallisation period, suggesting that early formation of nucleation sites is followed by a longer period of crystallisation (note that the structure of CPO-27 contains edge shared metal-centred octahedral so the assembly of the structure is more complex than simply replacing the bound water by bridging ligands). The larger size of the CPO-27(Co) crystals that are formed confirms independently the observations from fitting the kinetic data; *i.e.*, since nucleation is more rapid than for the Ni analogue, a more extended period of crystal growth at the nucleation sites can take place.

Table II contains data from materials that show both one- and three-dimensional crystal growth and correspondingly yield crystals of elongated or isotropic form, respectively. The activation energies both for nucleation and for crystal growth all fall between 60 and 140 kJ mol^{-1} but the relative size within each pair of values for a given crystallisation varies quite noticeably. For the cases of three-dimensional crystal growth, leading to crystals with isotropic morphology, the two copper-containing MOFs MOF-14 and HKUST-1 show instantaneous nucleation (crystallisation commences as soon as the reagents are mixed), but nucleation controlled reactions (the activation energy for nucleation is

larger than for crystal growth and nucleation extends well into the crystallisation period) (Millange *et al.*, 2011). In the study of ZIF-8 crystallisation by Cravillon *et al.* (Cravillon *et al.*, 2012) where a short induction time for crystallisation was observed, the activation energies for nucleation and crystal growth are almost equal. It should be noted in that work that the addition of formate to the reagent mixture was used to accelerate nucleation, so this may be taken as a special case where the balance of nucleation and growth is being manipulated by a chemical interaction with an additional ligand that itself does not itself form part of the crystal structure of the product.

The cases of the materials that show one-dimensional crystal also shows some interesting trends. For the Li(TPDC)(DMF) (El Osta *et al.*, 2012) and CPO-27(Ni) MOFs their crystallisations are nucleation controlled, with high activation energies for nucleation compared to crystal growth. For the former case, however, nucleation does not extend far into the crystallisation, leading to larger needle-like crystals. For the latter case nucleation continues into the crystallisation period leading to smaller crystals since crystal growth occurs not only at the initially formed nucleation sites but in competition with those that continue to form.

Finally, we compare the kinetics of microwave heated reactions with those heated using conventional means. Table III shows activation energies obtained for the microwave reactions, which can be compared directly with the values in Tables I and II. The effect of microwave heating is apparent in a lowering of the activation energies of both crystal growth for both CPO-27(Co) and CPO-27(Ni) compared to the values seen in conventional heating studies. The effect of microwave heating is also apparent on the activation energy for nucleation: both materials now have more similar values. The advantage of microwave heating in solvothermal reactions is believed to be in the high heating rate and in application of homogeneous heating: for MOF crystallisation this generally results in shorter reaction times and the production of smaller crystals (Stock and Biswas, 2012). In a previous study of the formation of the aluminium dihydroxyterephthalate CAU-1-(OH)₂ using *in situ* EDXRD, it was found that microwave heating shortened both induction time and total time of crystallisation, compared to conventional heating, although activation energy (for crystallisation, determined using an Avrami-type model) was unchanged (Ahnfeldt *et al.*,

2011). Our new results for CPO-27 show different effects of microwave heating: first, a general lower of activation energies, and, second, a change to similar crystallisation kinetics for the Ni and Co versions of the material in that activation energies for nucleation and growth follow the same trend (in contrast to conventional heating), suggesting that the lower lability of solvated Ni²⁺ is overcome. Clearly more detailed studies must be undertaken from a range of materials to obtain a systematic view of the effect of microwave heating of MOF crystallisation, but our new results provide new reference kinetic data as a basis for this work.

IV. CONCLUSION

We have shown how the kinetics of crystallisation of an important porous MOF material under solvothermal conditions can effectively be monitored under both conventional and microwave heating conditions using time-resolved EDXRD. By use of a simple kinetic model, developed for zeolite crystallisation, we are able to compare the crystallisation kinetics of a variety of MOF materials reported in other studies. The results we have reported provide new kinetic data to describe the crystallisation of an important family of materials and will go towards a deeper understanding of their formation mechanisms. Ultimately this should lead to some control over crystal growth for the targeted preparation of materials with desired crystal structure and crystal form.

ACKNOWLEDGEMENTS

We thank DESY for provision of beamtime at HASYLAB and Professor Wolfgang Bensch (Kiel) for the loan of his heating device for the *in situ* crystallisation measurements. We are grateful to Professor Alessandro Gualtieri (Modena) for useful discussions. The research leading to these results has received funding from the European Community's Seventh Framework Programme (FP7/2007-2013) under grant agreement No. 228862.

Figure Captions

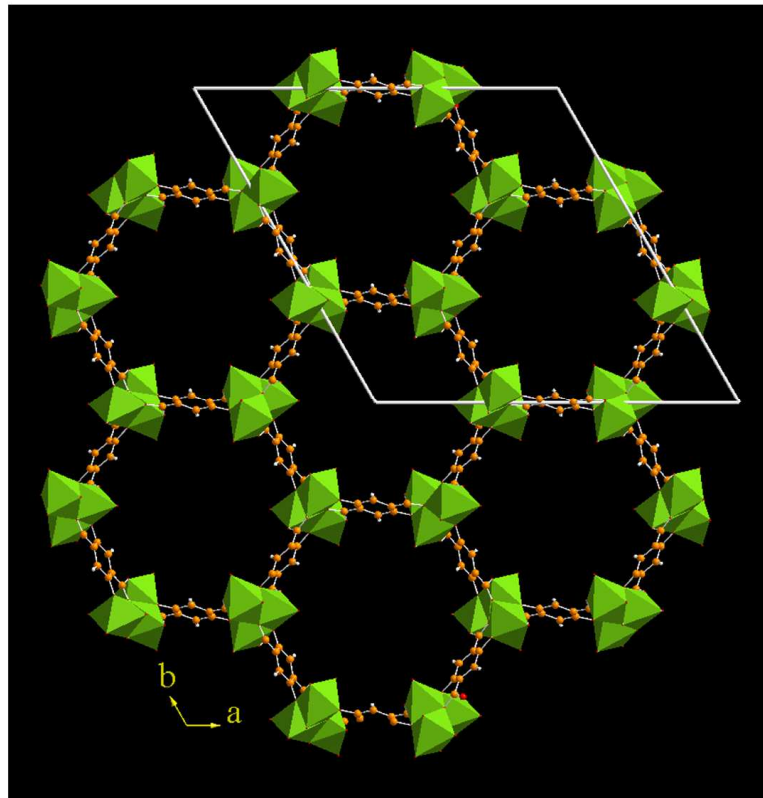


Figure 1: View of the structure of desolvated CPO-27 structure parallel to the 1D channels.

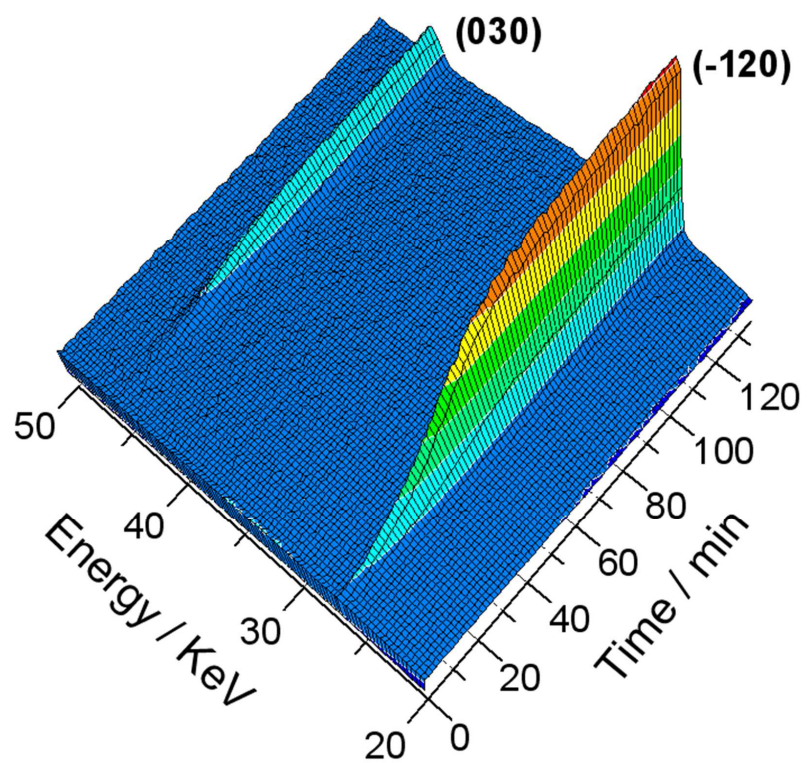


Figure 2: A 3D contour plot of the EDXRD data recorded during the crystallisation of CPO-27(Ni) at 90 °C.

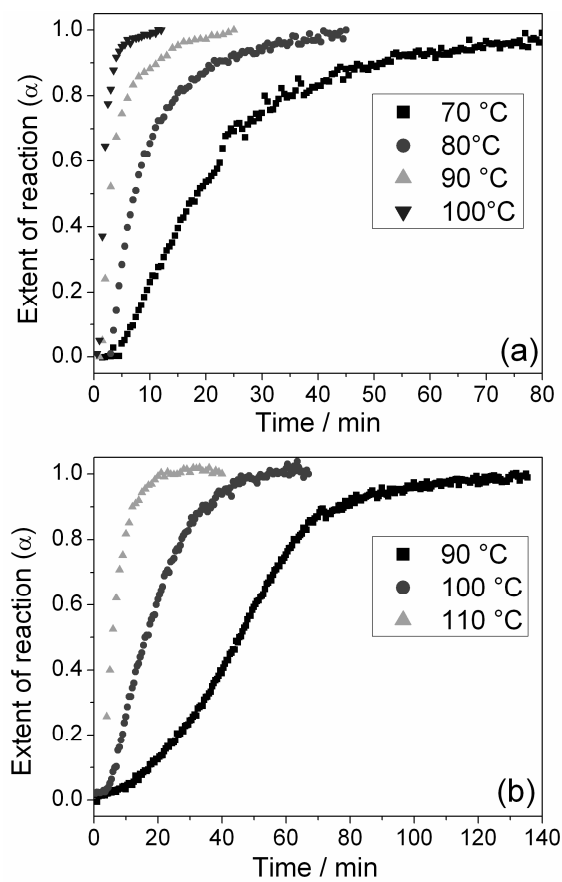


Figure 3: Crystallisation curves as a function of temperature for (a) CPO-27(Co) and (b) CPO-27(Ni) determined by integration of the (-120) Bragg peak of each phase.

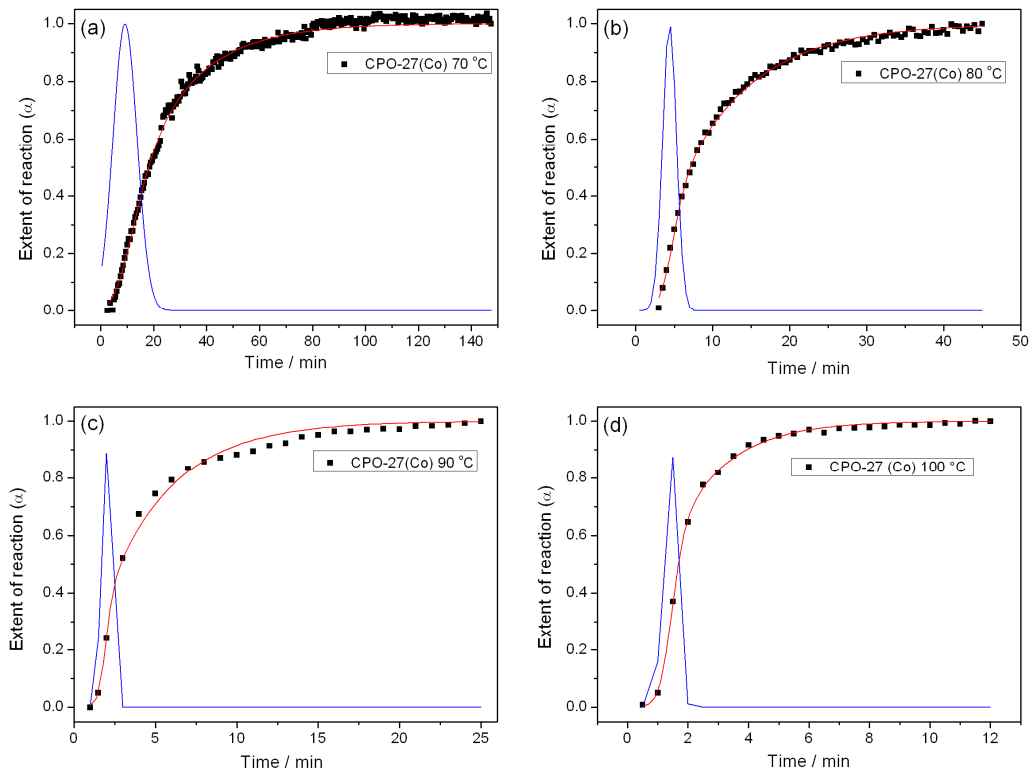


Figure 4: Fits obtained by fitting to the Gualtieri model to CPO-27 crystallisations for CPO-27(Co) at (a) 70 °C (b) 80 °C (c) 90 °C and (d) 100 °C.

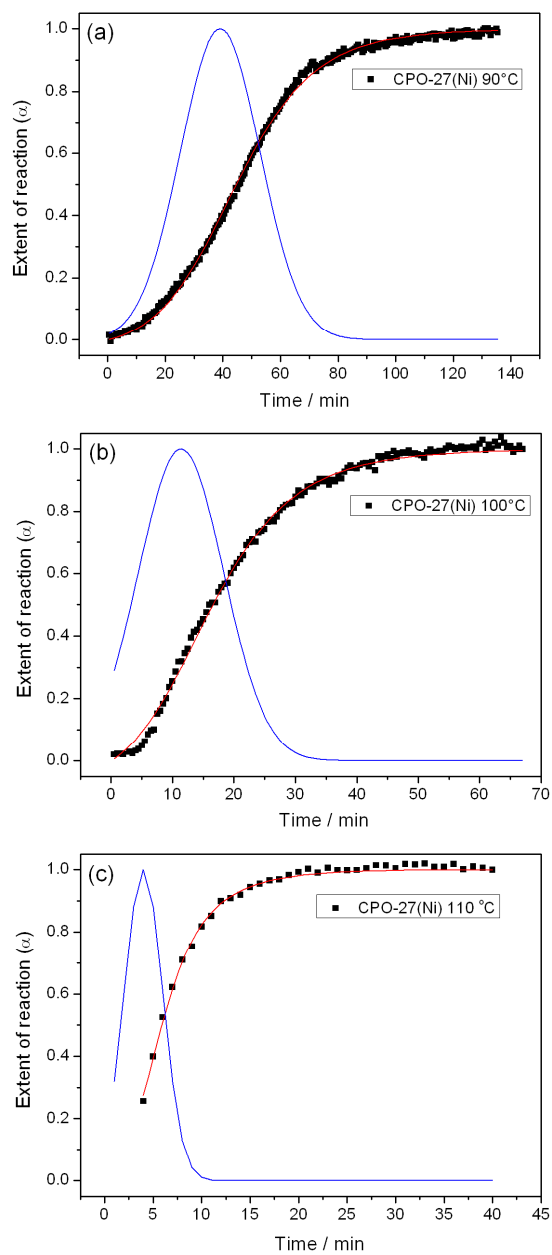


Figure 5: Fits obtained for fitting to the Gaultieri model to CPO-27 crystallisations for CPO-27(Ni) at (a)90 °C (b) 100 °C and (c) 110 °C.

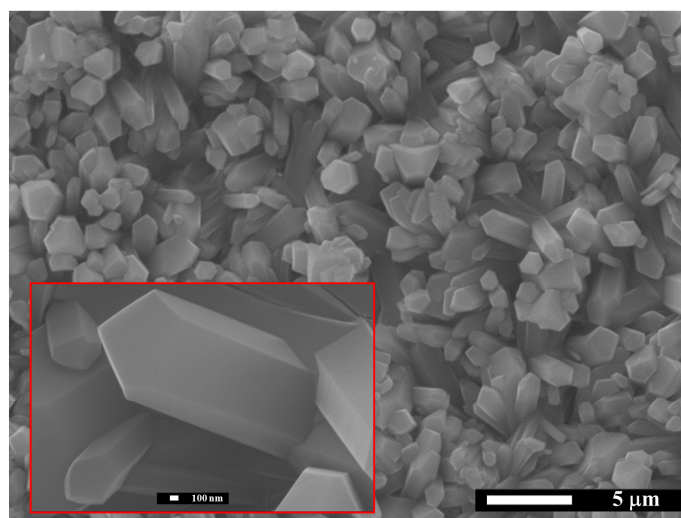
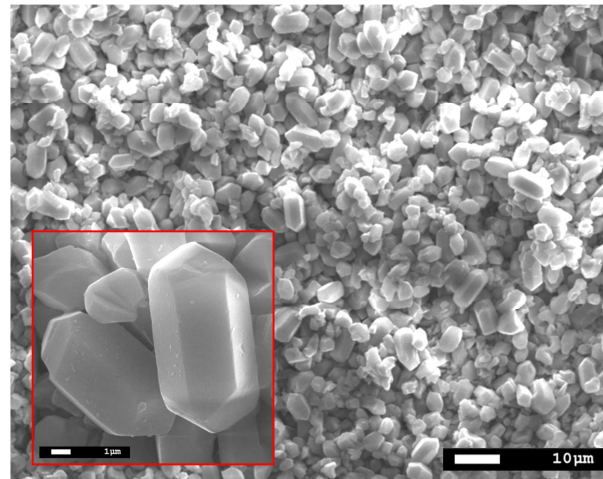


Figure 6: SEM images of typical samples of (a) CPO-27(Co) and (b) CPO-27(Ni) prepared using conventional heating.

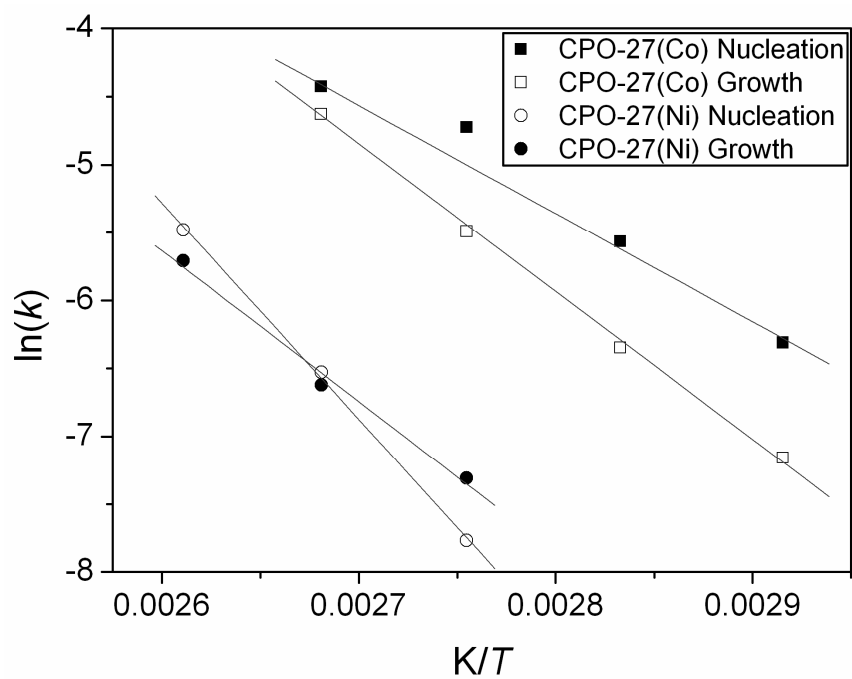


Figure 7: Arrhenius plots for nucleation and for growth obtained for the crystallisation of CPO-27(Co) and CPO-27(Ni). The lines are fits obtained by linear regression.

Table 1: Fitted kinetic parameters for crystallisation of CPO-27(Ni) and CPO-27(Co) from Gualtieri analysis of crystallisation curves. See Equations 2 and 3 in the text for definitions of the parameters.

Material	Temperature / °C	a / min	b / min	k_g	k_n
CPO-27(Ni)	90	30.04(34)	13.86(16)	0.041(1)	0.0333(4)
	100	11.38(34)	6.92(25)	0.080(3)	0.0879(26)
	110	4.00(13)	1.98(15)	0.199(7)	0.2500(81)
CPO-27(Co)	70	9.17(25)	4.52(23)	0.04673(4)	0.1091(30)
	80	4.37(6)	0.90(5)	0.1049(7)	0.2288(31)
	90	1.88(5)	0.23(6)	0.247(6)	0.532(14)
	100	1.394(15)	0.205(14)	0.586(8)	0.7174(77)

4. Polyfunktionalisierte Metallphosphonate

Table 2: Comparison of crystallisation data for various MOFs derived from Gualtieri fitting of crystallisation curves from *in situ* diffraction experiments (all time-resolved EDXRD studies with conventional heating). $E_a(\text{nuc})$ and $E_a(\text{gr})$ are activation energies for nucleation and growth, respectively.

Material	Nucleation	Crystal Morphology ^a	Crystal Size ^a	n^b	$E_a(\text{nuc})/\text{kJ mol}^{-1}$	$E_a(\text{gr})/\text{kJ mol}^{-1}$	Temperature Range / °C	Reference
CPO-27(Ni)	Induction time; extended nucleation	Elongated	up to 5 μm	1	132.3	92.3	$90 \leq T \leq 110$	This work
CPO-27(Co)	Instantaneous, short nucleation period	Elongated	$\sim 10 \mu\text{m}$	1	66.5	90.4	$70 \leq T \leq 100$	This work
Li(TPDC)(DMF) ^c	Induction time, short nucleation	Needle	$\sim 1 \text{ mm}$ in length	1	132.7	114.7	$160 \leq T \leq 180$	(El Osta <i>et al.</i> , 2012)
HKUST-1 (Cu)	Instantaneous and continuous	Octahedral	up to 20 μm	3	71.6	63.8	$85 \leq T \leq 125$	(Millange <i>et al.</i> , 2011)
MOF-14 (Cu)	Instantaneous and continuous	Cubic	up to 10 μm	3	113.9	82.8	$110 \leq T \leq 140$	(Millange <i>et al.</i> , 2011)
ZIF-8 (Zn) ^d	Short induction and continuous	Truncated cubic	greater than 20 μm	3	69.0	71.8	$120 \leq T \leq 140$	(Cravillon <i>et al.</i> , 2012)

a. Based on SEM observations of reactions allowed to reach completion; b. Dimensionality of crystal growth (see Equation 2); c. TPDC = 2,5-thiophenedicarboxylate and DMF = N,N'-dimethylformamide; d. Crystallisation was studied in the presence of formate as nucleation modifier.

Table 3: Crystallisation Kinetic Parameters Under Microwave Heating

Material	Nucleation	n	$E_a(\text{nuc})/$ kJ mol^{-1}	$E_a(\text{gr})/$ kJ mol^{-1}	Temperature Range / $^{\circ}\text{C}$
CPO-27(Ni)	Instantaneous, moderate nucleation period	1	72.8	63.8	$80 \leq T \leq 100$
CPO-27(Co)	Instantaneous, short nucleation period	1	83.6	48.4	$70 \leq T \leq 100$

REFERENCES

- Ahnfeldt, T., Moellmer, J., Guillerm, V., Staudt, R., Serre, C. and Stock, N. (2011) "High-throughput and time-resolved energy-dispersive X-ray diffraction (EDXRD) study of the formation of CAU-1-(OH)₂: microwave and conventional heating". *Chemistry - a European Journal*, **17**, 6462-6468.
- Allan, P. K., Wheatley, P. S., Aldous, D., Mohideen, M. I., Tang, C., Hriljac, J. A., Megson, I. L., Chapman, K. W., De Weireld, G., Vaesen, S. and Morris, R. E. (2012) "Metal-organic frameworks for the storage and delivery of biologically active hydrogen sulfide". *Dalton Trans.*, **41**, 4060-4066.
- Barrer, R. M. (1982) *Hydrothermal Chemistry of Zeolites*, Academic Press, London.
- Bloch, E. D., Murray, L. J., Queen, W. L., Chavan, S., Maximoff, S. N., Bigi, J. P., Krishna, R., Peterson, V. K., Grandjean, F., Long, G. J., Smit, B., Bordiga, S., Brown, C. M. and Long, J. R. (2011) "Selective binding of O₂ over N₂ in a redox-active metal-organic framework with open iron(II) coordination sites". *J. Amer. Chem. Soc.*, **133**, 14814-14822.
- Cheetham, A. K. and Mellot, C. F. (1997) "In situ studies of the sol-gel synthesis of materials". *Chem. Mat.*, **9**, 2269-2279.
- Cravillon, J., Schroder, C. A., Bux, H., Rothkirch, A., Caro, J. and Wiebcke, M. (2012) "Formate modulated solvothermal synthesis of ZIF-8 investigated using time-resolved in situ X-ray diffraction and scanning electron microscopy". *CrystEngComm*, **14**, 492-498.
- Crocker, D., Loan, M. and Hodnett, B. K. (2009) "Kinetics and mechanisms of the hydrothermal crystallization of calcium titanate species". *Cryst. Growth Des.*, **9**, 2207-2213.
- Cundy, C. S. and Cox, P. A. (2003) "The hydrothermal synthesis of zeolites: History and development from the earliest days to the present time". *Chem. Rev.*, **103**, 663-701.
- Czaja, A. U., Trukhan, N. and Müller, U. (2009) "Industrial applications of metal-organic frameworks". *Chem. Soc. Rev.*, **38**, 1284.
- Dietzel, P. D. C., Georgiev, P. A., Eckert, J., Blom, R., Strässle, T. and Unruh, T. (2010) "Interaction of hydrogen with accessible metal sites in the metal-organic frameworks M₂(dhtp) (CPO-27-M; M = Ni, Co, Mg)". *Chem. Commun.*, 4962-4964
- El Osta, R., Frigoli, M., Marrot, J., Medina, M. E., Walton, R. I. and Millange, F. (2012) "Synthesis, structure, and crystallization study of a layered lithium thiophene-dicarboxylate". *Cryst. Growth Des.*, **12**, 1531-1537.
- Farrusseng, D. (2011) *Metal-Organic Frameworks*, Wiley-VCH, Weinheim.
- Férey, G. and Serre, C. (2009) "Large breathing effects in three-dimensional porous hybrid matter: facts, analyses, rules and consequences". *Chemical Society Reviews*, **38**, 1380-1399.

- Feyand, M., Hübner, A., Rothkirch, A., Wragg, D. S. and Stock, N. (2012) "Copper phosphonatoethanesulfonates: temperature dependent in situ energy dispersive X-ray diffraction study and influence of the pH on the crystal structures". *Inorg. Chem.*, **51**, 12540-12547.
- Feyand, M., Näther, C., Rothkirch, A. and Stock, N. (2010) "Systematic and in situ energy dispersive X-ray diffraction investigations on the formation of lanthanide phosphonatobutanesulfonates: $\text{Ln}(\text{O}_3\text{P-C}_4\text{H}_8\text{-SO}_3)(\text{H}_2\text{O})$; (Ln = La-Gd)". *Inorg. Chem.*, **49**, 11158-11163.
- Francis, R. J. and O'Hare, D. (1998) "The kinetics and mechanisms of the crystallisation of microporous materials". *Journal of the Chemical Society-Dalton Transactions*, 3133-3148.
- Francis, R. J., Price, S. J., Evans, J. S. O., O'Brien, S., O'Hare, D. and Clark, S. M. (1996) "Hydrothermal synthesis of microporous tin sulfides studied by real-time in situ energy-dispersive X-ray diffraction". *Chem. Mater.*, **8**, 2102.
- Glover, T. G., Peterson, G. W., Schindler, B. J., Britt, D. and Yaghi, O. (2011) "MOF-74 building unit has a direct impact on toxic gas adsorption". *Chem. Eng. Sci.*, **66**, 163-170.
- Gualtieri, A. F. (2001) "Synthesis of sodium zeolites from a natural halloysite". *Phys. Chem. Miner.*, **28**, 719-728.
- Haque, E. and Jung, S. H. (2011) "Synthesis of isostructural metal-organic frameworks, CPO-27s, with ultrasound, microwave, and conventional heating: Effect of synthesis methods and metal ions". *Chemical Engineering Journal*, **173**, 866-872.
- Horcajada, P., Gref, R., Baati, T., Allan, P. K., Maurin, G., Couvreur, P., Ferey, G., Morris, R. E. and Serre, C. (2012) "Metal-organic frameworks in biomedicine". *Chem. Rev.*, **112**, 1232-1268.
- Kepert, C. J. (2010) *Metal-Organic Framework Materials*. In *Porous Materials* (Eds, Bruce, D. W., O'Hare, D. and Walton, R. I.) John Wiley and Sons, Chichester.
- Kiebach, R., Pienack, N., Bensch, W., Grunwaldt, J. D., Michailovski, A., Baiker, A., Fox, T., Zhou, Y. and Patzke, G. R. (2008) "Hydrothermal formation of W/Mo-Oxides: A multidisciplinary study of growth and shape". *Chem. Mater.*, **20**, 3022.
- Kiebach, R., Pienack, N., Ordolff, M. E., Studt, F. and Bensch, W. (2006) "Combined in situ EDXRD/EXAFS investigation of the crystal growth of $[\text{Co}(\text{C}_6\text{H}_{18}\text{N}_4)][\text{Sb}_2\text{S}_4]$ under solvothermal conditions: two different reaction pathways leading to the same product". *Chem. Mater.*, **18**, 1196.
- Long, J. R. and Yaghi, O. M. (2009) "The pervasive chemistry of metal-organic frameworks". *Chem. Soc. Rev.*, **38**, 1213-1214.
- MacGillivray, L. R. (2010) *Metal-Organic Frameworks Design and Application*, John Wiley and Sons, Hoboken.

4. Polyfunktionalisierte Metallphosphonate

- Millange, F., El Osta, R., Medina, M. E. and Walton, R. I. (2011) "A time-resolved diffraction study of a window of stability in the synthesis of a copper carboxylate metal-organic framework". *CrystEngComm*, **13**, 103-108.
- Millange, F., Medina, M., Guillou, N., Férey, G., Golden, K. M. and Walton, R. I. (2010) "Time-resolved in situ diffraction of the solvothermal crystallisation of some prototypical metal organic frameworks". *Angew. Chem. Int. Ed.*, **49**, 763-766.
- Modeshia, D. R., Darton, R. J., Ashbrook, S. E. and Walton, R. I. (2009) "Control of polymorphism in NaNbO_3 by hydrothermal synthesis". *Chem. Commun.*, 68-70.
- Munn, J., Barnes, P., Hausermann, D., Axon, S. A. and Klinowski, J. (1992) "In situ studies of the hydrothermal synthesis of zeolites using synchrotron energy-dispersive X-ray-diffraction". *Phase Transit.*, **39**, 129.
- Murray, L. J., Dinca, M. and Long, J. R. (2009) "Hydrogen storage in metal-organic frameworks". *Chemical Society Reviews*, **38**, 1294-1314.
- O'Hare, D., Evans, J. S. O., Fogg, A. and O'Brien, S. (2000) "Time-resolved, in situ X-ray diffraction studies of intercalation in lamellar hosts". *Polyhedron*, **19**, 297-305.
- OriginLabCorp (1991-2010) "OriginPro 8.1 SR3".
- Pienack, N. and Bensch, W. (2011) "In-situ monitoring of the formation of crystalline solids". *Angew. Chem.-Int. Edit.*, **50**, 2014-2034.
- Reinsch, H. and Stock, N. (2012) "Formation and characterization of Mn-MIL-100". *CrystEngComm*, in press, DOI: 10.1039/C1032CE26436F
- Rosi, N. L., Kim, J., Eddaoudi, M., Chen, B. L., O'Keeffe, M. and Yaghi, O. M. (2005) "Rod packings and metal-organic frameworks constructed from rod-shaped secondary building units". *Journal of the American Chemical Society*, **127**, 1504-1518.
- Rothkirch, A. (2009) f3tool version 0.3b (18.11.2009), Beamline F3, Hasylab (DESY).
- Sankar, G., Okubo, T., Fan, W. and Meneau, F. (2007) "New insights into the formation of microporous materials by in situ scattering techniques". *Faraday Discussions*, **136**, 157.
- Schmidt, C., Feyand, M., Rothkirch, A. and Stock, N. (2012) "High-throughput and in situ EDXRD investigation on the formation of two new metal aminoethylphosphonates - $\text{Ca}(\text{O}_3\text{PC}_2\text{H}_4\text{NH}_2)$ and $\text{Ca}(\text{OH})(\text{O}_3\text{PC}_2\text{H}_4\text{NH}_3) \cdot 2\text{H}_2\text{O}$ ". *Journal of Solid State Chemistry*, **188**, 44-49.
- Schmidt, C. and Stock, N. (2012) "Systematic investigation of zinc aminoalkylphosphonates: influence of the alkyl chain lengths on the structure formation". *Inorg. Chem.*, **51**, 3108--3118.
- Shoaei, M., Agger, J. R., Anderson, M. W. and Attfield, M. P. (2008) "Crystal form, defects and growth of the metal organic framework HKUST-1 revealed by atomic force microscopy". *CrystEngComm*, **10**, 646-648.

- Stavitski, E., Goesten, M., Juan-Alcaniz, J., Martinez-Joaristi, A., Serra-Crespo, P., Petukhov, A. V., Gascon, J. and Kapteijn, F. (2011) "Kinetic control of metal-organic framework crystallization investigated by time-resolved in situ X-ray scattering". *Angew. Chem.-Int. Edit.*, **50**, 9624-9628.
- Stock, N. and Biswas, S. (2012) "Synthesis of metal-organic frameworks (MOFs): routes to various MOF topologies, morphologies, and composites". *Chem. Rev.*, **112**, 933-969.
- Sumida, K., Rogow, D. L., Mason, J. A., McDonald, T. M., Bloch, E. D., Herm, Z. R., Bae, T. H. and Long, J. R. (2012) "Carbon dioxide capture in metal-organic frameworks". *Chem. Rev.*, **112**, 724-781.
- Walton, R. I., Francis, R. J., Halasyamani, P. S., O'Hare, D., Smith, R. I., Done, R. and Humphreys, R. J. (1999a) "Novel apparatus for the in situ study of hydrothermal crystallizations using time-resolved neutron diffraction". *Rev. Sci. Instrum.*, **70**, 3391-3396.
- Walton, R. I., Loiseau, T., O'Hare, D. and Férey, G. (1999b) "An in situ energy-dispersive X-ray diffraction study of the crystallisation of open-framework gallium oxyfluorophosphates with the ULM-3 and ULM-4 structure". *Chem. Mater.*, **11**, 3201.
- Walton, R. I., Millange, F., O'Hare, D., Davies, A. T., Sankar, G. and Catlow, C. R. A. (2001) "An in situ energy-dispersive X-ray diffraction study of the hydrothermal crystallisation of zeolite A. 1. influence of reaction conditions and transformation into sodalite". *J. Phys. Chem. B.*, **101**, 83.
- Walton, R. I. and O'Hare, D. (2000) "Watching solids crystallise using in situ powder diffraction". *Chem. Commun.*, 2283-2291.
- Yaghi, O. M., O'Keeffe, M., Ockwig, N. W., Chae, H. K., Eddaoudi, M. and Kim, J. (2003) "Reticular synthesis and the design of new materials". *Nature*, **423**, 705.
- Yoon, M., Srirambalaji, R. and Kim, K. (2012) "Homochiral metal-organic frameworks for asymmetric heterogeneous catalysis". *Chem. Rev.*, **112**, 1196-1231.
- Zacher, D., Liu, J. N., Huber, K. and Fischer, R. A. (2009) "Nanocrystals of $\text{Cu}_3(\text{btc})_2$ (HKUST-1): a combined time-resolved light scattering and scanning electron microscopy study". *Chem. Commun.*, 1031-1033.

4.6.6. High-Throughput Microwave Assisted Discovery of New Metal Phosphonates

Der folgende Artikel wurde in der Zeitschrift *Dalton Transactions* publiziert. Ziel dieser Arbeit war die Synthese und Strukturaufklärung neuer Metallphosphonate.

Die, in Abbildung 4.25 gezeigten, aromatischen Phosphonsäuren *m*- $[(\text{H}_2\text{O}_3\text{PCH}_2)_2\text{-NCH}_2]\text{C}_6\text{H}_4$ (H_8L^6) und *p*- $[(\text{H}_2\text{O}_3\text{PCH}_2)_2\text{-NCH}_2]\text{C}_6\text{H}_4$ (H_8L^7) wurden in Kombination mit den zweiwertigen Metallionen Ca^{2+} , Mn^{2+} , Ni^{2+} , Co^{2+} , Zn^{2+} und Cd^{2+} zur Darstellung von Metallphosphonaten verwendet. Hierbei wurde der Einfluss von verschiedenen Gegenionen wie NO_3^- und Cl^- überprüft.

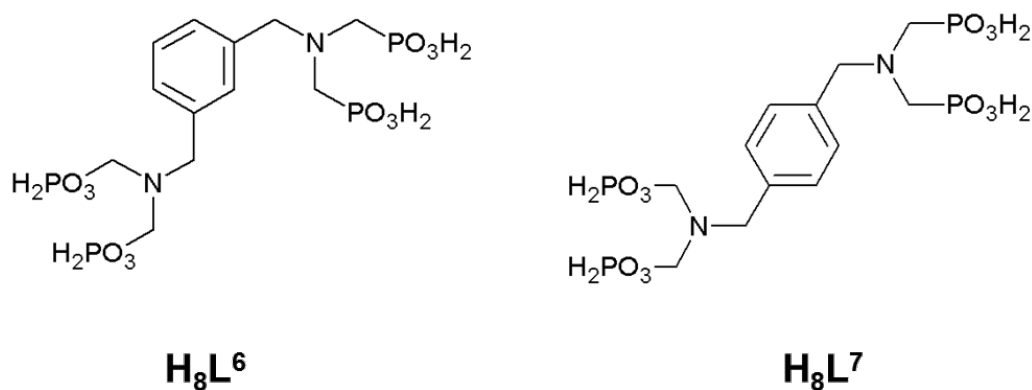


Abbildung 4.25.: Die verwendeten Linker (H_8L^6) und (H_8L^7).

In dieser Arbeit konnten zehn neue Verbindungen erhalten werden, die zum Teil isostrukturell zueinander sind und in drei verschiedenen Kristallstrukturen kristallisieren. Die Strukturen von $[\text{Ni}(\text{H}_8\text{L}^6)] \cdot \text{H}_2\text{O}$ und $\text{Cd}(\text{H}_6\text{L}^7)$ wurden aus Röntgenpulverdaten gelöst und verfeinert. Die Kristallstruktur von $[\text{M}(\text{H}_8\text{L}^7)\text{H}_2\text{O}]$ konnte anhand des Zellvolumens, aus den Ergebnissen der Indizierung, der möglichen Raumgruppe und der Summenformel hergeleitet werden und das so erhaltene Strukturmodell an Röntgenpulverdaten verfeinert werden. In den Verbindungen der Zusammensetzung $[\text{M}(\text{H}_8\text{L}^6)] \cdot \text{H}_2\text{O}$ ($\text{M} = \text{Ca}^{2+}$, Mn^{2+} , Ni^{2+} , Co^{2+} , Zn^{2+}) liegen MO_6 -Polyeder vor. Diese werden von Phosphonatgruppen zu Ketten verbrückt, die über die Phenylringe der Linker-Ionen zu einem dreidimensionalen Netzwerk verbunden sind. Die Verbindung $\text{Cd}(\text{H}_6\text{L}^7)$ bildet ebenso von Phosphonatgruppen verbrückte Ketten aus isolierten Polyedern. Diese Ketten werden über die Phenylringe der Linker zu einem dreidimensionalen Netzwerk verknüpft. Zwischen den Phosphonatgruppen bilden sich Wasserstoffbrückenbindungen aus. Die Verbindungen der Zusammensetzung

$[M(H_8L^7)H_2O]$ ($M = Mn^{2+}, Ni^{2+}, Co^{2+}, Zn^{2+}$) enthalten isolierte MO_6 -Polyeder, die über die Linker zu Ketten verknüpft sind. Diese werden nur über Wasserstoffbrückenbindungen zusammengehalten die sich zwischen dem koordinierten Wassermolekül und Phosphonatgruppen ausbilden. Die Verbindungen wurden mittels thermogravimetrischer Analyse, IR Spektroskopie und magnetischen Suszeptibilitätsmessungen charakterisiert.

High-throughput microwave-assisted discovery of new metal phosphonates†

Cite this: DOI: 10.1039/c3dt50413a

Mark Feyand,^a Christopher F. Seidler,^b Carsten Deiter,^c Andre Rothkirch,^c Alexandra Lieb,^d Michael Wark^b and Norbert Stock^{*a}

A systematic study was carried out to investigate the influence of linker geometry, metal ionic radius as well as the nature of the counter ions on the structure formation of metal tetraphosphonates. Two tetraphosphonic acids *p*- and *m*-(H₂O₃PCH₂)₂N-CH₂-C₆H₄-CH₂-N(CH₂PO₃H₂)₂, six metal ions (Ca²⁺, Mn²⁺, Co²⁺, Ni²⁺, Zn²⁺, and Cd²⁺) and two different counter ions (Cl⁻ and NO₃⁻) were employed using high throughput methods. Microwave (MW)-assisted heating led to the discovery of ten new metal-phosphonates which crystallize in three different crystal structures. The combination of direct methods and force field calculations allowed us to establish the crystal structures. The counter ion and the ionic radii of the metal ions have a profound influence on the crystallinity and the formed crystal structure. All compounds were characterized in detail by thermogravimetric analyses, IR spectroscopy and magnetic susceptibility measurements. The proton conductivity of two selected compounds is also reported.

Received 13th February 2013,
Accepted 12th April 2013

DOI: 10.1039/c3dt50413a

www.rsc.org/dalton

Introduction

Metal phosphonates are the focus of recent research activities due to their interesting properties such as magnetism, porosity,^{1,2} luminescence³ or catalysis.⁴ Metal phosphonates show a large structural variety depending on the linker molecule or the incorporated metal ion. The properties may change drastically upon variation of the constituents. The inorganic building units observed in metal phosphonates range from isolated clusters⁵ to chains^{2,6–8} or layers.^{8–10}

Suitable methods to synthesize metal phosphonates are solvothermal reactions. Recently, microwave assisted heating was applied to synthesize new metal phosphonates.^{7,11,12} Microwave (MW) assisted reactions have proven to lead to higher purities, high yields and much shorter reaction times.¹³ However, the sealed reaction conditions make obtaining information about crystallization difficult. In addition, the outcome of such reactions, *i.e.* the product formation, is not predictable and large variable parameters such as temperature, pH or molar ratio of reactants have to be studied exploratively.

High-throughput (HT) methods provide a combinatorial and more systematic approach.^{14,15} They allow researchers to investigate efficiently and in a fast manner important reaction parameters such as the reaction temperature,^{14,16} the concentration of reactants,¹⁷ ionic radii,¹⁸ the pH,^{10,16,17} or the length of the organic moiety.¹⁰ Recently HT MW assisted reactions were employed to establish the fields of formation of new metal-organic framework compounds. However, these methods have never been employed in metal phosphonate chemistry before.¹⁹

We are interested in the synthesis of new metal phosphonates and for the present study we have chosen the tetraphosphonic acids *p*- and *m*-(H₂O₃PCH₂)₂N-CH₂-C₆H₄-CH₂-N(CH₂PO₃H₂)₂. They have previously been shown to lead to three new compounds containing Ca²⁺ and Cu²⁺ ions.^{20,21}

Here we present the results of the systematic HT investigation of the synthesis of metal tetraphosphonates using MW-assisted heating and varying the linker geometry as well as the metal and counter ion. In addition, the crystal structures are determined from X-ray powder diffraction data and the detailed characterisation of the products is shown.

Experimental section

Materials and methods

All starting materials were obtained from Aldrich or ABCR and were used without further purification. The two tetraphosphonic acids were synthesized using a slightly modified Mannich-type procedure.²² XRPD measurements were carried out on a

^aInstitut für Anorganische Chemie, Christian-Albrechts-Universität, Max-Eyth Straße 2, D 24118 Kiel, Germany. E-mail: stock@ac.uni-kiel.de

^bLehrstuhl für Technische Chemie, Ruhr-Universität Bochum, Universitätsstr. 150, D44801 Bochum, Germany

^cHASYLAB, DESY Hamburg, Notkestraße 85, 22607 Hamburg, Germany

^dInstitut für Chemie, Otto-von-Guericke-Universität, Universitätsplatz 2, 39106

Magdeburg, Germany

† Electronic supplementary information (ESI) available: Assymmetric units, details about the structure determination, thermogravimetric measurements. See DOI: 10.1039/c3dt50413a

Stoe Stadi P diffractometer in transmission geometry with $\text{Cu-K}\alpha_1$ radiation, equipped with an image plate detector system or a linear PSD detector system for high resolution data. The MIR spectra were recorded on a Bruker ALPHA-P FT-IR spectrometer in the spectral range 4000–400 cm^{-1} . For the thermogravimetric analyses under air a NETZSCH STA 409 CD analyzer was used with a heating rate of 4 K min^{-1} and an air flow rate of 75 mL min^{-1} . High resolution powder XRD patterns were measured at beamline G3 (light source DORIS)²³ and beamline P08 (light source PETRA)²⁴ both at HASYLAB, DESY. Scaled up syntheses under conventional heating were carried out under solvothermal conditions using DURAN culture tubes D50 GL 14 M.KAP, SCHOTT. An Anton Paar Synthos 3000 microwave reactor was used for the high-throughput syntheses. Temperature dependent X-ray diffraction patterns were recorded on a Panalytical Empyrean diffractometer equipped with a PIXcell detector using a MRI TC radiation chamber with a Pt heater and Al_2O_3 crucibles.

Synthesis of $p\text{-(H}_2\text{O}_3\text{PCH}_2)_2\text{NCH}_2\text{-C}_6\text{H}_4\text{-CH}_2\text{N(CH}_2\text{PO}_3\text{H}_2)_2$ ($p\text{-H}_8\text{L}$). 5.00 g (36.7 mmol) p -xylenediamine and 12.0 g (147 mmol) phosphorous acid were added to 60 mL half concentrated hydrochloric acid.²² The mixture was heated to reflux and 13 mL (161 mmol) 37% formalin solution was slowly added. The reaction was then heated for 14 h and cooled to room temperature. The white precipitate was filtered and washed with deionized water. The product was identified as $p\text{-H}_8\text{L}$ by ^1H and ^{31}P -NMR spectroscopy (yield 45.17 g 60% based on p -xylenediamine) (see the ESI†).

Synthesis of $m\text{-(H}_2\text{O}_3\text{PCH}_2)_2\text{NCH}_2\text{-C}_6\text{H}_4\text{-CH}_2\text{N(CH}_2\text{PO}_3\text{H}_2)_2$ ($m\text{-H}_8\text{L}$). 10.00 g (73.4 mmol) m -xylenediamine and 24.0 g (294 mmol) phosphorous acid were added to 60 mL half concentrated hydrochloric acid.²² The mixture was heated to reflux and 26 mL (322 mmol) 37% formalin solution were slowly added. The reaction was then heated for 14 h and cooled to room temperature. The white precipitate was filtered and washed with deionized water. The product was identified as $m\text{-H}_8\text{L}$ by ^1H and ^{31}P -NMR spectroscopy (yield 67.76 g 45% based on m -xylenediamine) (see the ESI†).

HT microwave assisted reactions. The HT syntheses were carried out in 4 mL microwave glass vials in a 24 reactor setup using an Aton Parr HT reactor system. The reactions were carried out at 150 °C for 5 h using a power of 400 W. The molar ratio $\text{H}_8\text{L}:\text{M}^{2+}$ was kept at 1:1 and the concentration was fixed by using 25 mg of H_8L per reaction. To investigate the influence of the linker geometry 12 reactions per linker were carried out. To investigate different metal ion radii we studied Mn^{2+} , Ca^{2+} , Co^{2+} , Ni^{2+} , Zn^{2+} and Cd^{2+} using Cl^- and NO_3^- as counter ions. The obtained products were identified by X-ray powder diffraction. The results of the high-throughput investigation are summarized in Fig. 2. The exact reaction conditions are given in the ESI (Table S1†).

Scale-up synthesis of $\text{Cd}[p\text{-(HO}_3\text{PCH}_2)_2\text{N(H)-CH}_2\text{-C}_6\text{H}_4\text{-CH}_2\text{-N(H)(CH}_2\text{PO}_3\text{H)}_2]$ (1). 40 mg $p\text{-H}_8\text{L}$ (78 mmol), 117 μL (234 mmol) of a 2 M CdCl_2 solution and 3 mL deionized water were mixed in DURAN culture tubes, sealed and heated up to 150 °C for 12 h. The reaction mixture was filtered and washed

with water. Using pH paper pH = 2 was determined for the initial and final reaction solutions. The yield was 33 mg, 68% based on $p\text{-H}_8\text{L}$.

Scale-up syntheses of $\text{M}[p\text{-(HO}_3\text{PCH}_2)_2\text{N(H)-CH}_2\text{-C}_6\text{H}_4\text{-CH}_2\text{-N(H)(CH}_2\text{PO}_3\text{H)}_2(\text{H}_2\text{O})]$ ($\text{M} = \text{Mn, Co, Ni, Zn}$) (2). 40 mg $p\text{-H}_8\text{L}$ (78 mmol), 39 μL (78 mmol) of a 2 M $\text{M}(\text{NO}_3)_2$ solution and 3 mL deionized water were mixed in DURAN culture tubes, sealed and heated up to 150 °C for 12 h. The reaction mixture was filtered and washed with water. Using pH paper pH = 2 was determined for the initial and final reaction solution. The yields were 34, 13, 23, 26 mg, 70, 25, 45, 50% based on $p\text{-H}_8\text{L}$, for $\text{M} = \text{Mn, Co, Ni, Zn}$, respectively.

Scale-up syntheses of $\text{M}[m\text{-(HO}_3\text{PCH}_2)_2\text{N(H)-CH}_2\text{-C}_6\text{H}_4\text{-CH}_2\text{-N(H)(CH}_2\text{PO}_3\text{H)}_2]\cdot\text{H}_2\text{O}$ ($\text{M} = \text{Ca, Mn, Co, Ni, Zn}$) (3). 40 mg $m\text{-H}_8\text{L}$ (78 mmol), 39 μL (78 mmol) of a 2 M MCl_2 solution, 20 μL (39 mmol) of a 2 M NaOH solution and 3 mL deionized water were mixed in DURAN culture tubes, sealed and heated up to 150 °C for 12 h. The reaction mixture was filtered and washed with water. Using pH paper pH = 2 was determined for the initial and final reaction solutions. The yields were 38, 26, 40, 20, 21 mg (75, 50, 85, 42, 42% based on $m\text{-H}_8\text{L}$), for $\text{M} = \text{Ca, Mn, Co, Ni, Zn}$, respectively.

Crystal structure determination

All compounds were obtained as microcrystalline powders. Thus, the structures had to be determined from X-ray powder diffraction data. The important crystallographic parameters are given in Table 1.

Crystal structure determination of compound 1. High resolution XRPD data of compound 1 (Cd) were collected at beamline G3, HASYLAB, DESY, Hamburg using a wavelength of 1.54296(2) Å selected by a double silicon single crystal monochromator and determined with a LaB_6 standard. The diffracted beam was detected by a scintillation counter mounted behind a soller slit system. The sample was measured in a capillary (0.7 mm diameter). The powder pattern was successfully indexed using Topas Academic and the possible space group $P2_1/a$ was suggested.¹¹ The crystal structure was solved in $P2_1/a$ using direct methods implemented in EXPO2009. The heavy atom positions and the phosphonate groups could be located directly from the Fourier map. The structure model was completed using Materials Studio 5.3 applying force field calculations.²⁵ A universal force field was used as implemented in Materials Studio. The obtained model was further refined by Rietveld methods in the 2θ range of 9 to 80° using Topas Academic. The final Rietveld refinement included six background points, three Thompson–Cox–Hastings profile parameters, four lattice parameters, one scaling factor, a simple axial model, a fourth order spherical harmonics series, 45 atomic coordinates and three temperature factors (Cd, P, and C/N/O). The P–O and P–C distances were soft restrained. The final Rietveld plot is given in Fig. 3.

Crystal structure determination of compound 2. A high resolution XRPD pattern of compound 2 (Zn) was recorded at beamline P08, PETRA, DESY, Hamburg with a wavelength of 0.824516 Å. The powder pattern was successfully indexed using

Table 1 Crystallographic data of compounds **1**, **2** and **3** (SH = spherical harmonics series)

	Compound 1	Compound 2	Compound 3
Formula sum	C ₁₀ H ₁₈ N ₂ CdO ₁₂ P ₄	C ₁₀ H ₂₀ N ₂ ZnO ₁₃ P ₄	C ₁₀ H ₂₀ N ₂ NiO ₁₃ P ₄
Radiation source	Synchrotron	Synchrotron	Laboratory
Wavelengths/Å	1.54296	0.824516	CuKα ₁
<i>a</i> /Å	12.1198(4)	10.5960(3)	22.2633(4)
<i>b</i> /Å	15.1091(4)	7.5569(2)	8.5904(2)
<i>c</i> /Å	5.5632(1)	6.9120(2)	9.8834(2)
<i>α</i> /°	90	106.42(2)	90
<i>β</i> /°	97.28(2)	98.50(3)	90
<i>γ</i> /°	90	86.79(1)	90
Space group	<i>P2</i> ₁ / <i>a</i>	<i>P</i> $\bar{1}$	<i>Pm</i> <i>cn</i>
<i>R</i> _w	2.80	3.60	5.77
<i>R</i> _{Bragg} (without SH)	1.03(3.25)	0.79(4.25)	1.86(8.74)
GoF	1.42	1.97	1.81
Number of restraints	6	8	10
Number of parameters	80	85	78
Volume/Å ³	1010.62(5)	524.99(4)	1890.22(6)
<i>Z</i>	2	1	4

Topas Academic. Due to the small cell volume of 525(1) Å³ only one twofold deprotonated linker ion and one Zn²⁺ ion are present in the unit cell. A structure model was derived in the space group *P* $\bar{1}$ by molecular modeling using Materials Studio 5.3. Details are given in the ESI (Fig. S3†). The starting model was refined by Rietveld methods in the range of 4–40° 2θ using Topas Academic. The final Rietveld refinement included six background points, three Thompson–Cox–Hastings profile parameters, six lattice parameters, one scaling factor, a simple axial model, a fourth order spherical harmonics series, 48 atomic coordinates and three (Zn, P, and C/N) temperature factors. The P–O and P–C distances were soft restrained. The final Rietveld plot is given in Fig. 5.

Crystal structure determination of compound 3. The powder pattern of **3** (Ni) was collected on a Stoe Stadi P diffractometer equipped with a linear PSD detector. The structure was solved using direct methods implemented in EXPO2009. The inorganic building unit was directly located from the Fourier map and completed by force field calculations using Materials Studio 5.3. The structural model was refined by Rietveld methods in the range of 9 to 75° 2θ using Topas Academic. The final Rietveld refinement subsumed six background points, three Thompson–Cox–Hastings profile parameters, four lattice parameters, one scaling factor, a simple axial model, a fourth order spherical harmonics series, 45 atomic coordinates and three (Ni, P, and C/N/O) temperature factors. The P–O, P–C and some C–C distances were soft restrained. The final Rietveld plot is given in Fig. 7.

Proton conductivity

Proton conductivity was determined by impedance spectroscopy (IS).^{26,27} An oscillating voltage of 100 mV was applied over a frequency range from 1 to 10⁶ Hz using a Zahner Zennium electrochemical workstation. The powder samples were pressed into small pellets (diameter 8 mm, thickness 0.5–1.5 mm) and incorporated into a stack comprising the sample sandwiched between two graphitic slices. The stack was placed in a PTFE sample holder, and two sintered metal

electrodes were used to make electrical contact with the stack. The sample holder was placed in a gas-tight, temperature-controlled stainless steel chamber with an attached water reservoir.²⁸ The relative humidity (RH) in the cell was determined by the Clausius–Clapeyron relation and controlled by heating the water reservoir and the cell. Preceding each series of measurements, samples were equilibrated for 24 hours at 313 K and at 50% RH. The sample was equilibrated for 1 hour at the desired temperature and RH before measuring each data point. Each point was measured three times to determine reproducibility.

Results and discussion

To investigate the influence of the linker geometries the two tetraphosphonic acids *p*-(H₂O₃PCH₂)₂N-CH₂C₆H₄CH₂-N-(CH₂PO₃H₂)₂ (*p*-H₈L) and *m*-(H₂O₃PCH₂)₂N-CH₂C₆H₄CH₂-N-(CH₂PO₃H₂)₂ (*m*-H₈L) were synthesized (Fig. 1).

High throughput investigation

The influence of the geometry of tetraphosphonic acid on the formation of metal phosphonates was investigated using high-throughput methods.¹⁵ Thus six different metal ions with ionic radii between 0.74 and 1.14 Å (Mn²⁺, Ca²⁺, Co²⁺, Ni²⁺, Zn²⁺ and Cd²⁺) and different counter ions (NO₃⁻ and Cl⁻) were

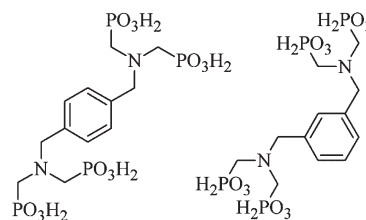


Fig. 1 Linker molecules used in this study. Left: *p*-(H₂O₃PCH₂)₂N-CH₂C₆H₄CH₂-N-(CH₂PO₃H₂)₂ (*p*-H₈L), right: *m*-(H₂O₃PCH₂)₂N-CH₂C₆H₄CH₂-N-(CH₂PO₃H₂)₂ (*m*-H₈L).

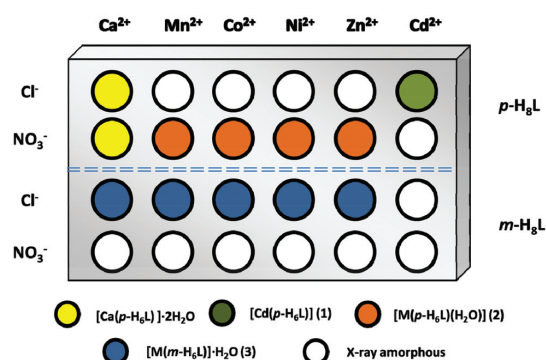


Fig. 2 Results of the high-throughput study. The compound $[\text{Ca}(p\text{-H}_8\text{L})]\cdot 2\text{H}_2\text{O}$ has already been reported before.²¹

used. 24 reactions were carried out under microwave assisted heating at 150 °C for 5 h and a molar ratio of $\text{H}_8\text{L}:\text{M}^{2+} = 1:1$ (details are given in Table S1†). The results of the study are presented in Fig. 2.

Using $p\text{-H}_8\text{L}$ and metal chlorides CdCl_2 leads to a highly crystalline compound of composition $[\text{Cd}(\text{HO}_3\text{PCH}_2)_2\text{NH}-\text{CH}_2\text{C}_6\text{H}_4\text{CH}_2\text{-NH}(\text{CH}_2\text{PO}_3\text{H})_2]$ (1). The use of metal nitrates instead of metal chlorides leads to the isostructural compounds $[\text{M}(\text{HO}_3\text{PCH}_2)_2\text{NH}-\text{CH}_2\text{C}_6\text{H}_4\text{CH}_2\text{-NH}(\text{CH}_2\text{PO}_3\text{H})_2(\text{H}_2\text{O})]$ (2) with $\text{M} = \text{Mn}^{2+}$, Co^{2+} , Ni^{2+} and Zn^{2+} , respectively. Using Cd^{2+} as the cation, only X-ray amorphous powders were obtained. Both Ca^{2+} salts lead to the literature known compound $[\text{Ca}(p\text{-H}_8\text{L})]\cdot 2\text{H}_2\text{O}$ in much shorter reaction times of 5 h compared to 48 h using conventional heating. In contrast, reactions of $m\text{-H}_8\text{L}$ with metal nitrates lead to X-ray amorphous compounds while reactions with metal chlorides result in crystalline compounds $[\text{M}(\text{HO}_3\text{PCH}_2)_2\text{NH}-\text{CH}_2\text{-C}_6\text{H}_4\text{-CH}_2\text{-NH}(\text{CH}_2\text{PO}_3\text{H})_2]\cdot(\text{H}_2\text{O})$ (3) for $\text{M} = \text{Mn}^{2+}$, Ca^{2+} , Co^{2+} , Ni^{2+} and Zn^{2+} and an X-ray amorphous product for $\text{M} = \text{Cd}^{2+}$.

Crystal structure of $[\text{Cd}(\text{HO}_3\text{PCH}_2)_2\text{NH}-\text{CH}_2\text{C}_6\text{H}_4\text{CH}_2\text{-NH}(\text{CH}_2\text{PO}_3\text{H})_2]$ (1). Using high resolution powder diffraction data the structure of 1 was determined by a combination of direct methods and molecular modeling. The final results of the structure refinement are given in Fig. 3.

The crystal structure of 1 is shown in Fig. 4 (and S4†). Each Cd^{2+} ion is six-fold coordinated with oxygen. These oxygen atoms derive from six different phosphonate groups. The formed polyhedra are connected by the phosphonate groups to one-dimensional chains along the c -axis. These chains are interconnected by the rest of the linker molecules to form a three dimensional network. The non-coordinating phosphonate groups are involved in hydrogen bonds which are shown in the ESI (Fig. S6†).

Crystal structure of $[\text{Zn}(\text{HO}_3\text{PCH}_2)_2\text{NH}-\text{CH}_2\text{C}_6\text{H}_4\text{CH}_2\text{-NH}(\text{CH}_2\text{PO}_3\text{H})_2(\text{H}_2\text{O})]$ (2 (Zn)). Taking into account the unit cell dimension, the space group symmetry and the unit cell content a structural model for 2 was derived by molecular modeling. The model was successfully refined using high resolution X-ray diffraction data (Fig. 5). The coordination

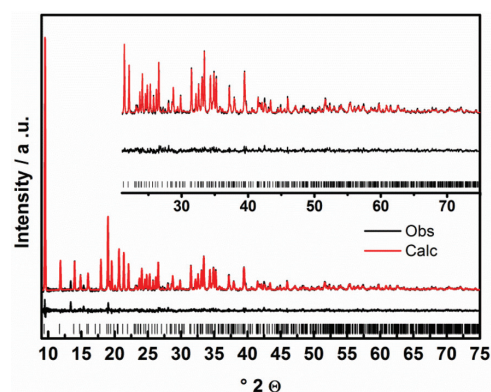


Fig. 3 Final Rietveld plot of 1. The observed powder pattern is shown in black, the calculated powder pattern as an overlay in red and the difference (observed – calculated) of both is given by the lower black line. The allowed positions of the Bragg peaks are given as ticks. The inset shows the higher 2θ range.

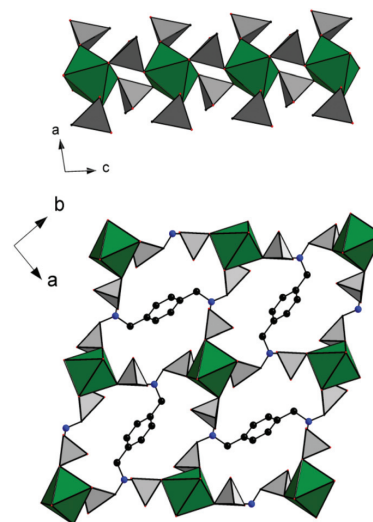


Fig. 4 Crystal structure of compound 1. Chains of corner-sharing CdO_6 and O_3PC polyhedra along the c -axis (top) and their connection to a three-dimensional network (bottom). MO_6 polyhedra are shown in green, O_3PC polyhedra in grey, and nitrogen and carbon atoms in blue and black, respectively.

environment of the Zn^{2+} ions and the interconnection of the metal ions by the linker molecules are shown in Fig. S7,† a section of the crystal structure in Fig. 6. The Zn^{2+} ions are sixfold coordinated by oxygen atoms of four different phosphonate groups and two water molecules. These ZnO_6 polyhedra are connected by the organic linker molecules along $[010]$ to form sheets (Fig. 6, middle), which are connected *via* two different kinds of hydrogen bonds ($\text{PO}-\text{H}\cdots\text{OP}$ and $\text{PO}-\text{H}\cdots\text{OH}$) as indicated by the donor-acceptor distances (Fig. S8†) between HO_3PC -groups phosphonate dimers.

The allowed positions of the Bragg peaks are given as ticks.

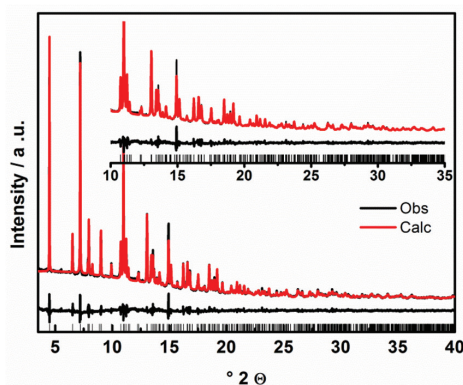


Fig. 5 Final Rietveld plot of **2** (Zn). The observed powder pattern is shown in black, the calculated powder pattern as an overlay in red and the difference (observed – calculated) of both is given by the lower black line. The allowed positions of the Bragg peaks are given as ticks. The inset shows the higher 2θ range.

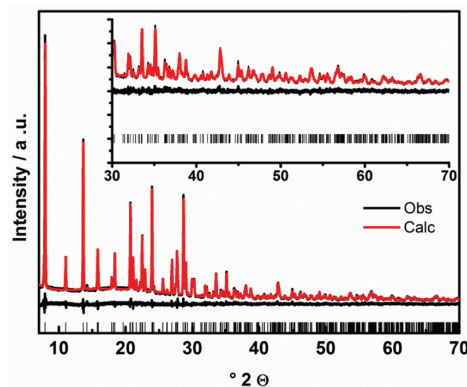


Fig. 7 Final Rietveld plot of **3** (Ni). The observed powder pattern is shown in black, the calculated powder pattern as an overlay in red and the difference (observed – calculated) of both is given by the lower black line. The allowed positions of the Bragg peaks are given as ticks. The inset shows the higher 2θ range.

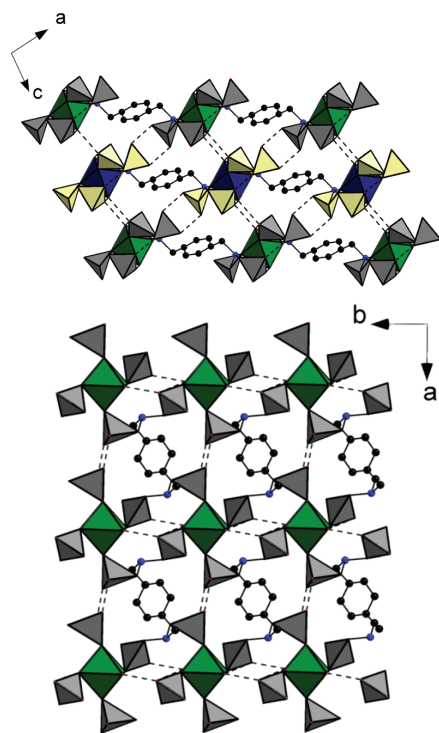


Fig. 6 Crystal structure of compound **2** (Zn). Connection of the Zn^{2+} ions by $p\text{-H}_6\text{L}^{2-}$ ions in the a,b -plane (bottom) and possible interconnection of the layers by postulated hydrogen bonds (top). MO_6 polyhedra are shown in green, O_3PC polyhedra in grey, and nitrogen and carbon atoms in blue and black, respectively. One layer is shown by blue MO_6 and yellow CPO_3 polyhedra.

Crystal structure of $[\text{Ni}(\text{HO}_3\text{PCH}_2)_2\text{NH-CH}_2\text{C}_6\text{H}_4\text{CH}_2\text{-NH}(\text{CH}_2\text{PO}_3\text{H})_2]\cdot\text{H}_2\text{O}$ (3** (Ni)).** In house XRPD data were used for the structure determination of **3** (Ni). Direct methods in

combination with difference Fourier calculations and molecular modeling led to a structural model that was successfully refined by Rietveld methods (Fig. 7). The coordination environment of the Ni^{2+} ions and the interconnection of the metal ions by the linker molecules are shown in Fig. S7† and the crystal structure is shown in Fig. 8. Each Ni^{2+} ion is sixfold coordinated by oxygen atoms of six different phosphonate groups and layers in the b,c -plane are formed. These layers are interconnected to a three dimensional network by the organic linker molecules. Based on $\text{P-O}\cdots\text{O-P}$ and $\text{P-O}\cdots\text{OH}_2$ distances between 2.50(2) and 3.06(2) Å hydrogen bonds can be postulated that further stabilize the structure (Fig. S9†).

Structural trends

As a result, from the crystal structures we can conclude that the ionic radius has a crucial influence on the crystal structure formation. Using $p\text{-H}_6\text{L}$ with Ca^{2+} ions with the largest ionic radius ($r_{\text{ionic}} = 1.14$ Å) leads to the literature known compound $[\text{Ca}(p\text{-H}_6\text{L})]\cdot 2\text{H}_2\text{O}$ ²¹ whereas the much smaller ions Mn^{2+} , Ni^{2+} , Co^{2+} , and Zn^{2+} ($r_{\text{ionic}} = 0.81, 0.79, 0.83, 0.88$ Å, respectively) form an isostructural compound. Cd^{2+} ions with an intermediate ionic radius of 1.09 Å crystallizes in a different crystal structure (compound **1**). All structures are pseudopolymorphic with **1** containing no, 2 one and $[\text{Ca}(p\text{-H}_6\text{L})]\cdot 2\text{H}_2\text{O}$ two water molecules per formula unit. Thus, the Cd^{2+} ions in **1** seem to have the right size to allow for the formation of a three dimensional coordination polymer. In contrast, layers are formed which are connected by hydrogen bonds for the structure of compound **2**. This leads to a higher flexibility of the network and can adjust to different ionic radii. In contrast the use of $m\text{-H}_6\text{L}$ leads to one isostructural compound for Mn^{2+} , Ni^{2+} , Co^{2+} , Ca^{2+} and Zn^{2+} .

IR spectroscopy

To learn more about the properties of the compounds we carried out IR spectroscopic and thermogravimetric

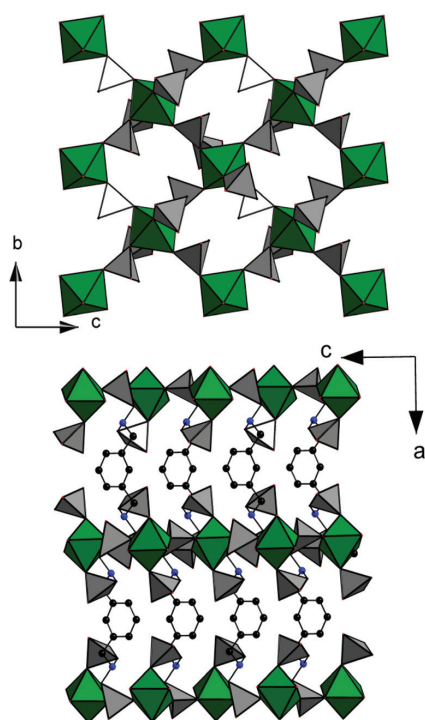


Fig. 8 Crystal structure of **3**. View along the *a*-axis (top) onto the layers and view along the layers connected by the organic linker molecules along the *b*-axis (bottom). Water molecules were omitted for clarity.

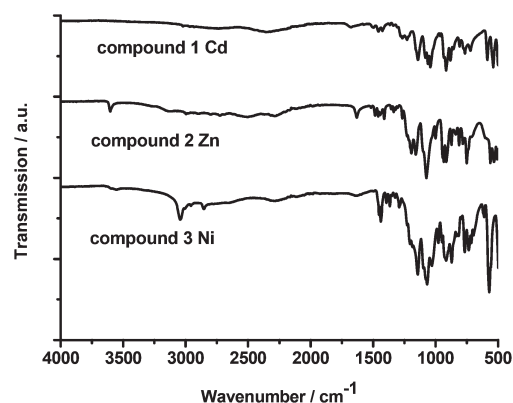


Fig. 9 IR-spectra of compounds **1**, **2** and **3**.

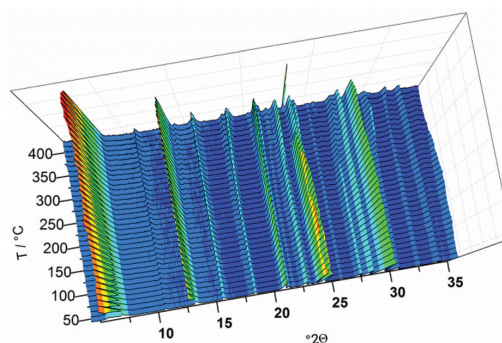


Fig. 10 Results of the temperature dependent XRPD measurements of compound **3** (Ni). The Bragg peak at $\sim 23.2^\circ$ 2θ is due to the sample holder.

measurements. The IR spectra of compound **1** (Cd), **2** (Zn) and **3** (Ni) are shown in Fig. 9. All other IR spectra are given in the ESI (Fig. S9 and S11[†]).

All three compounds show a very similar IR-spectrum. In the range between 1250 and 980 cm^{-1} the typical CPO_3 -bands are observed. The aromatic and aliphatic C–H stretching vibrations are observed in the region between 3098 and 2970 cm^{-1} and broad P–OH bands can be observed between 2840 and 2200 cm^{-1} . In accordance with the crystallographic data a broad band around 3600 cm^{-1} from the coordinated and uncoordinated water molecules of compound **2** and **3** is present.

Thermal stability

The thermal stability was investigated by thermogravimetric analyses (TG). The results of all TG measurements are given in the ESI (Fig. S12 and S13[†]). All compounds show different thermal stabilities. Compound **1** (Cd) is stable up to 300 °C and decomposes in a multiple step decomposition. As expected, compounds **2** (Zn) and **3** (Ni) show in addition to the decomposition in the range between 100 and 200 °C one step of weight loss which is due to the coordinated and uncoordinated water molecules. The removal of the uncoordinated water molecule in **3** (Ni) was further investigated by

temperature dependent XRPD in the range of 40–400 °C (Fig. 10).

The sample is stable up to at least 400 °C and shows slight shifts of the Bragg peaks and changes in the intensity above 200 °C. This can be explained by the loss of the water molecule. The lattice parameters of each pattern were extracted using parametric Pawley refinement methods as implemented in Topas academic¹¹ using the program Powder3D parametric.²⁹ The results are shown in Fig. 11. Up to 200 °C all lattice parameters and the cell volume are slightly increasing as expected due to the thermal expansion of the lattice. Above 200 °C the lattice parameters *a*- and *c*-axis as well as the cell volume are rapidly decreasing due to the loss of the water molecule while the *b*-axis length is further increasing. The cell volume is decreasing above 200 °C.

These lattice parameter changes with temperature can be explained by inspecting the crystal structure of **3** (Ni). Along [100] and [001] PO \cdots OP and PO \cdots Ow \cdots OP hydrogen bonds are observed (Fig. S9[†]). Removal of the water molecule (Ow) therefore results in a decrease of the *a*- and *c*-parameter. In contrast,

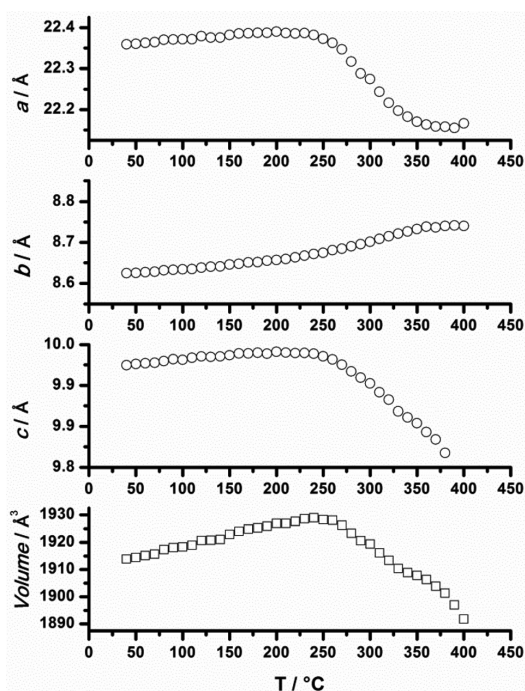


Fig. 11 Evolution of lattice parameters of compound 2. Parameters were obtained by parametric Pawley refinement.

along [010] no hydrogen bonds are observed which is reflected in the increase of the *b*-parameter with temperature.

Magnetic properties of 3 (Mn, Co and Ni)

Since compounds 2 (Mn, Co, Ni) decompose upon evacuation of the samples, only the compounds 3 (Mn, Co, Ni) were investigated for their magnetic properties. In that case, temperature and field dependent magnetic susceptibility measurements were performed.

Magnetic properties of [Mn(HO₃PCH₂)₂NH-CH₂C₆H₄CH₂-NH(CH₂PO₃H)₂]-H₂O. The temperature dependent magnetic susceptibility was measured in the temperature range of 300–2 K applying an external field of 0.1 T. The χ vs. *T* and $1/\chi$ vs. *T* plots for 3 (Mn) are given in Fig. 12. The compound shows a typical Curie–Weiss behavior in the temperature range of 300–9 K. Below this temperature regime the compound shows antiferromagnetic coupling. A least-square fit using the Curie–Weiss law leads to $C = 4.48 \text{ K cm}^3 \text{ mol}^{-1}$, and $\theta = -8.15 \text{ K}$, both in agreement with antiferromagnetic coupling. We observe a μ_{eff} of $5.98\mu_{\text{B}}$ which is in good agreement with the theoretical value of $5.92\mu_{\text{B}}$ for a high spin Mn²⁺ ion.

Magnetic properties of [Ni(HO₃PCH₂)₂NH-CH₂C₆H₄CH₂-NH(CH₂PO₃H)₂]-H₂O. The results of the temperature dependent magnetic susceptibility measurement of compound 3 (Ni) are shown in Fig. 13. The measurement was carried out in the temperature range of 300–2 K. The compound shows a

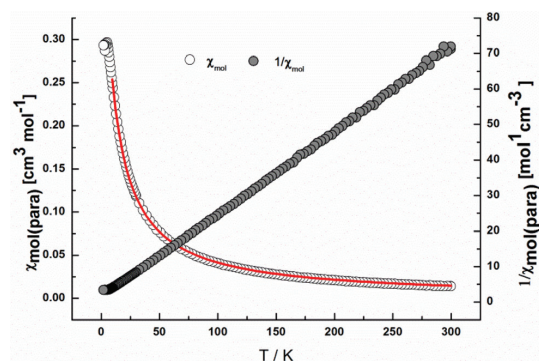


Fig. 12 Temperature dependent magnetic susceptibility of [Mn(HO₃PCH₂)₂NH-CH₂C₆H₄CH₂-NH(CH₂PO₃H)₂]-H₂O. The molar magnetic susceptibility is shown as white dots, the red line shows the Curie–Weiss fit and the reciprocal magnetic susceptibility is shown as grey dots.

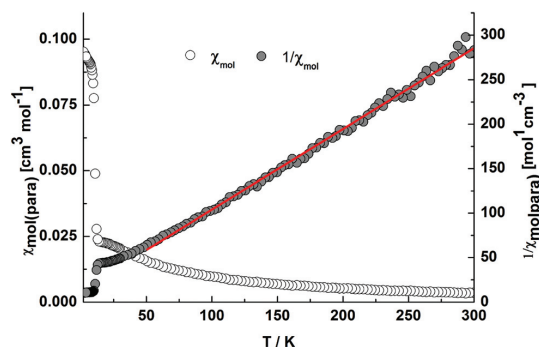


Fig. 13 Temperature dependent magnetic susceptibility of [Ni(HO₃PCH₂)₂NH-CH₂C₆H₄CH₂-NH(CH₂PO₃H)₂]-H₂O. The molar magnetic susceptibility is shown as white dots, the reciprocal magnetic susceptibility is shown as grey dots and the red line shows the linear fit of $1/\chi$ vs. *T*.

typical paramagnetic behavior between 300 and 50 K. Below 13.3 K ferromagnetic coupling is observed. Linear regression of the $1/\chi$ vs. *T* plot leads to values of $C = 1.10 \text{ K cm}^3 \text{ mol}^{-1}$ and $\theta = 13.26 \text{ K}$ which indicates ferromagnetic coupling. We observe a μ_{eff} of $2.98\mu_{\text{B}}$ which is in good agreement with the expected value for a Ni²⁺ ion of $2.83\mu_{\text{B}}$. To learn more about the ferromagnetic coupling a field dependent measurement at 4.2 K in the range of -9 T to 9 T was carried out. The obtained hysteresis loop is shown in Fig. 14. From that loop a magnetic reminiscence of $+M_{\text{r}} = 0.013N\beta \text{ mol}^{-1}$, $-M_{\text{r}} = -0.013N\beta \text{ mol}^{-1}$ and $H_{\text{c}} = 0.160 \text{ T}$, $-H_{\text{c}} = -0.159 \text{ T}$ was determined.

Magnetic properties of [Co(HO₃PCH₂)₂NH-CH₂C₆H₄CH₂-NH(CH₂PO₃H)₂]-H₂O. The temperature dependent magnetic susceptibility of compound 3 (Co) is shown in Fig. 15. The measurements were carried out in the temperature range of 300–2 K with zero field cooling (ZFC). The magnetic behavior is similar to the canted antiferromagnetic coupling observed in Co[HO₂C(CH₂)₃NH(CH₂PO₃H)₂]₂ which is built up

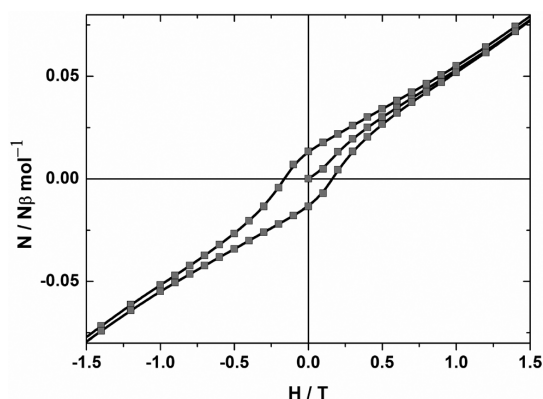


Fig. 14 Field dependent magnetic susceptibility measurement of **3** (Ni) at 4.2 K.

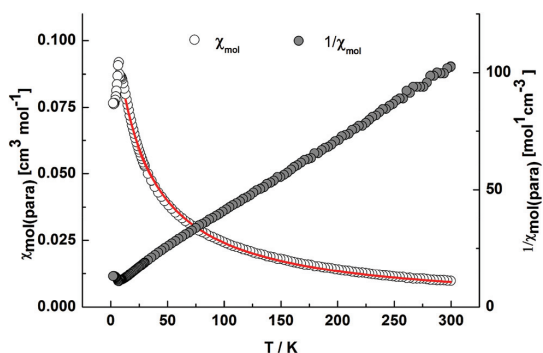


Fig. 15 Temperature dependent magnetic susceptibility of $[\text{Co}(\text{HO}_3\text{PCH}_2)_2\text{NH}-\text{CH}_2\text{C}_6\text{H}_4\text{CH}_2\text{NH}(\text{CH}_2\text{PO}_3\text{H})_2]\cdot\text{H}_2\text{O}$. The molar magnetic susceptibility is shown as white dots, the red line shows the Curie–Weiss fit and the reciprocal magnetic susceptibility is shown as grey dots.

from the same inorganic layered motif.³⁰ The temperature dependent measurement shows paramagnetic behavior in the temperature range between 300–13 K and antiferromagnetic coupling below 13 K. Nevertheless the susceptibility splits upon ZFC. A fit of the χ vs. T curve with the Curie–Weiss law leads to $C = 3.03 \text{ K cm}^3 \text{ mol}^{-1}$ and $\theta = -29.50 \text{ K}$. We observe a μ_{eff} of $5.02\mu_{\text{B}}$ which is much higher than the expected spin-only value of $\mu_{\text{eff}} = 3.87\mu_{\text{B}}$. However, this is in good agreement with the literature value of the canted antiferromagnet ($\mu_{\text{eff}} = 5.23\mu_{\text{B}}$) which can be explained by the spin orbital interactions of the Co^{2+} ions.

To understand the magnetic behaviour a field dependent initial curve and AC measurements were carried out (Fig. 16). The initial curve shows no step in the range of 0 to 9 T. Thus, a metamagnet can be excluded. The AC measurements show no shift in the maximum susceptibility. These results exclude the presence of spin glass or a ferromagnet. Thus, all results are in agreement with the presence of a canted antiferromagnet.

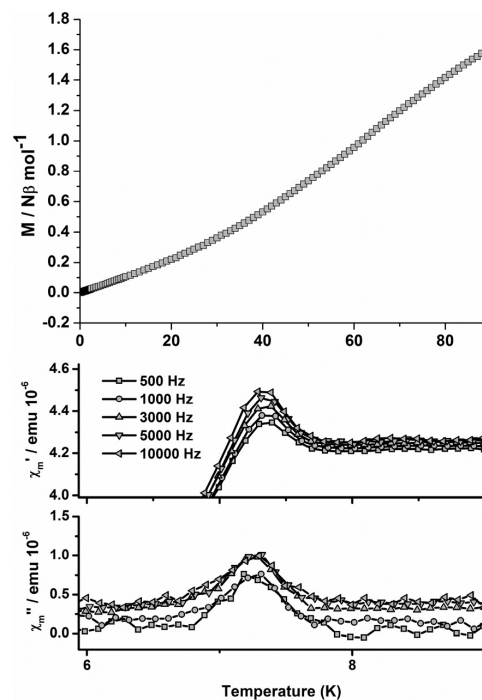


Fig. 16 Initial curve of the field dependent measurement of **3** (Co) at 4.2 K (top) and AC measurements of the susceptibility (bottom).

Proton conductivity

The compounds **2** (Zn) and **3** (Mn) were investigated for their proton conductivity properties because of their expected low toxicity and good crystallinity. While in **2** (Zn) one water molecule per formula unit is coordinated to the zinc ion in **3** (Mn) it is close to the $-\text{PO}_3\text{H}^-$ groups and is involved in hydrogen bonding. The proton conductivity was determined using eqn (1).²⁶

$$\sigma = \frac{1L}{RA} \quad (1)$$

where R : ohmic resistance, σ : proton conductivity, L : sample thickness, A : sample cross-section area.

The ohmic resistance was taken from the Bode phase plot of the impedance, which shows the impedance phase shift versus frequency. The impedance corresponding to the phase shift closest to zero is approximately equal to the ohmic resistance of the sample.^{26,27} Each impedance value was measured three times, and the arithmetic mean was used in the analyses.

Both metal phosphonates exhibit proton conductivity (Fig. 17); however, the proton conductivity at 413 K and 100% RH of compound **3** (Mn) ($1.53 \times 10^{-3} \text{ S cm}^{-1}$) is not only 35 times higher than that of **2** (Zn) ($4.26 \times 10^{-5} \text{ S cm}^{-1}$), but also much more reproducible (rep.). The proton conductivity of **3** (Mn) is in the same order of magnitude as observed for the compound $[\text{Mg}((\text{HO}_3\text{PCH}_2)_2\text{NH}-\text{C}_8\text{H}_{16}-\text{NH}(\text{CH}_2\text{PO}_3\text{H})_2)]\cdot 6\text{H}_2\text{O}$, which exhibits a value of $1.6 \times 10^{-3} \text{ S cm}^{-1}$ at 298 K.³¹ As

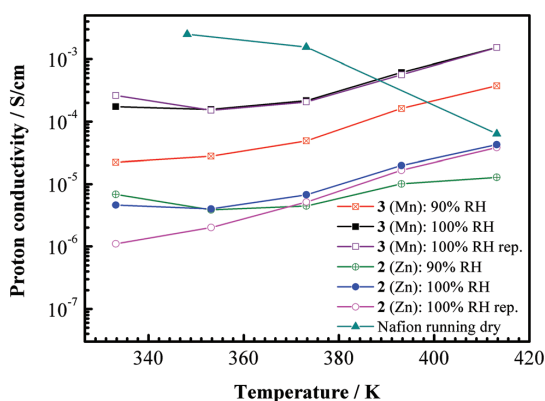


Fig. 17 Proton conductivity of the two phosphonates ($[\text{Zn}(\text{HO}_3\text{PCH}_2)_2\text{NH}-\text{CH}_2\text{C}_6\text{H}_4\text{CH}_2\text{-NH}(\text{CH}_2\text{PO}_3\text{H})_2(\text{H}_2\text{O})]$ – **2** (Zn) and $[\text{Mn}(\text{HO}_3\text{PCH}_2)_2\text{NH}-\text{CH}_2\text{C}_6\text{H}_4\text{-CH}_2\text{-NH}(\text{CH}_2\text{PO}_3\text{H})_2(\text{H}_2\text{O})]$ – **3** (Mn)) at different temperatures and relative humidities (90% RH and 100% RH), compared to the polymer Nafion® at 100% RH.³²

expected, relative humidity has a strong influence on the proton conductivity of the investigated phosphonates: for example, a 10% decrease of RH at 413 K results in a 5-fold decrease in the proton conductivity of **3** (Mn).

At temperatures above 393 K, the proton conductivity of **3** (Mn) exceeds that of Nafion®, which is the most widely used polymer as membrane in Proton Exchange Membrane Fuel Cells (PEMFC). In contrast to Nafion® for which the loss in conductivity at these high temperatures is well-documented due to dehydration of the membrane,³³ the metal ions and the phosphonate groups seem to interact well enough with the water molecules under the measurement conditions to keep water molecules in the structures.

Thus, the metal phosphonates are comparable to oxide nanoparticles or functionalized ordered mesoporous oxides being widely discussed as additives for PEMFCs in order to avoid the shortcomings of Nafion® at high temperatures and low relative humidities.³⁴ Since especially sulfonic acid functionalized variants of MCM-41, obtained by co-condensation, exhibit very high proton conductivities up to 0.2 S cm^{-1} ,³² new metal sulfonates with defined porosity might be an even more prospective class of materials.

XRD measurements reveal that during the impedance spectroscopy measurement (Fig. S14 and S15†), **2** (Zn) is in part transformed into a new crystalline product whose structure is unknown. The structural change causes conductivity losses and corresponding irreproducibility observed in the **2** (Zn) impedance spectra. In contrast, the second metal phosphonate, **3** (Mn), shows no significant changes in the XRD pattern after IS, and thus features reproducible impedance data.

Conclusion

High-throughput methods employing microwave-assisted heating were shown to be an excellent tool for the rapid

discovery of metal phosphonates. Although the counter ions of the metal salts employed are not incorporated into the structure, they have a distinct influence on the crystallinity of the resulting compound. Thus the systematic investigation using different counter ions of metal salts is important.

Since all compounds in this study are obtained as microcrystalline powders, the structure determination had to be carried out from X-ray powder diffraction data. Here, the combined approach of direct methods and force field calculations to establish a structural model has proven to be very valuable. Subsequent Rietveld refinements could be carried out to obtain the crystal structures. Here the results observed for reactions with *p*-H₈L are especially interesting. Depending on the ionic radii of the metal ions three different crystal structures are formed. This suggests that systematic studies on the influence of ionic radii are important for the discovery of new structures.

Finally the isostructural compounds **3** (Mn, Ni and Co) show magnetic properties ranging from antiferromagnetic, to ferromagnetic and canted antiferromagnetic interactions.

Acknowledgements

Portions of the research were carried out at the light source DORIS III and PETRA III at DESY, a member of the Helmholtz Association (HGF). We thank Katrin Pflaum (DESY) for assistance at the beamline, Prof. Bensch (CAU Kiel), Henning Lüthmann (CAU Kiel) and the Bensch group for the TG measurements and the DFG (STO-643/2 and WA 1116/17-2) for financial support.

Notes and references

- M. T. Wharmby, S. R. Miller, J. A. Groves, I. Margiolaki, S. E. Ashbrook and P. A. Wright, *Dalton Trans.*, 2010, **39**, 6389–6391.
- M. T. Wharmby, J. P. S. Mowat, S. P. Thompson and P. A. Wright, *J. Am. Chem. Soc.*, 2011, **133**, 1266–1269.
- S. F. Tang, J. L. Song and J. G. Mao, *Eur. J. Inorg. Chem.*, 2006, 2011–2019; J.-G. Mao, *Coord. Chem. Rev.*, 2007, **251**, 1493–1520; A. Sonnauer, C. Nather, H. A. Hoppe, J. Senker and N. Stock, *Inorg. Chem.*, 2007, **46**, 9968–9974; Y. Zhu, Z. Sun, Y. Zhao, J. Zhang, X. Lu, N. Zhang, L. Liu and F. Tong, *New J. Chem.*, 2009, **33**, 119–124.
- Y. Ji, X. Ma, X. Wu, N. Wang, Q. Wang and X. Zhou, *Catal. Lett.*, 2007, **118**, 187–194; X.-J. Zhang, T.-Y. Ma and Z.-Y. Yuan, *J. Mater. Chem.*, 2008, **18**, 2003–2010; M. Deng, Y. Ling, B. Xia, Z. Chen, Y. Zhou, X. Liu, B. Yue and H. He, *Chem.-Eur. J.*, 2011, **17**, 10323–10328; M. J. Beier, W. Kleist, M. T. Wharmby, R. Kissner, B. Kimmerle, P. A. Wright, J.-D. Grunwaldt and A. Baiker, *Chem.-Eur. J.*, 2012, **18**, 887–898; C. Queffelec, M. Petit, P. Janvier, D. A. Knight and B. Bujoli, *Chem. Rev.*, 2012, **112**, 3777–3807; K. J. Gagnon, H. P. Perry and A. Clearfield, *Chem. Rev.*, 2011, **111**, 1034–1054.

- 5 V. Chandrasekhar, P. Sasikumar, R. Boomishankar and G. Anantharamian, *Inorg. Chem.*, 2006, **45**, 3344–3351; Z. Y. Du, H. B. Xu and J. G. Mao, *Inorg. Chem.*, 2006, **45**, 9780–9788; D. Kong, J. Zon, J. McBee and A. Clearfield, *Inorg. Chem.*, 2006, **45**, 977–986; Z.-Y. Du, X.-L. Li, Q.-Y. Liu and J.-G. Mao, *Cryst. Growth Des.*, 2007, **7**, 1501–1507; Z.-Y. Du, A. V. Prosvirin and J.-G. Mao, *Inorg. Chem.*, 2007, **46**, 9884–9894.
- 6 A. Sonnauer, M. Feyand and N. Stock, *Cryst. Growth Des.*, 2009, **9**, 586–592.
- 7 M. Feyand, C. Nather, A. Rothkirch and N. Stock, *Inorg. Chem.*, 2010, **49**, 11158–11163.
- 8 M. Feyand, A. Hübner, A. Rothkirch, D. S. Wragg and N. Stock, *Inorg. Chem.*, 2012, **51**, 12540–12547.
- 9 R. C. Wang, Y. P. Zhang, H. L. Hu, R. R. Frausto and A. Clearfield, *Chem. Mater.*, 1992, **4**, 864–871; J. G. Mao, Z. K. Wang and A. Clearfield, *Inorg. Chem.*, 2002, **41**, 6106–6111; D. M. Poojary, B. L. Zhang and A. Clearfield, *J. Am. Chem. Soc.*, 1997, **119**, 12550–12559.
- 10 C. Schmidt, M. Feyand, A. Rothkirch and N. Stock, *J. Solid State Chem.*, 2012, **188**, 44–49.
- 11 Y.-F. Yang, Y.-S. Ma, S.-S. Bao and L.-M. Zheng, *Dalton Trans.*, 2007, 4222–4226.
- 12 A. Sonnauer and N. Stock, *J. Solid State Chem.*, 2008, **181**, 3065–3070.
- 13 K. J. Rao, B. Vaidhyanathan, M. Ganguli and P. A. Ramakrishnan, *Chem. Mater.*, 1999, **11**, 882–895.
- 14 S. Bauer and N. Stock, *Chem. Unserer Zeit*, 2007, **41**, 390–398.
- 15 N. Stock, *Microporous Mesoporous Mater.*, 2010, **129**, 287–295.
- 16 A. Sonnauer and N. Stock, *Eur. J. Inorg. Chem.*, 2008, **2008**, 5038–5045.
- 17 P. M. Forster, N. Stock and A. K. Cheetham, *Angew. Chem., Int. Ed.*, 2005, **44**, 7608–7611.
- 18 P. Maniam, C. Näther and N. Stock, *Eur. J. Inorg. Chem.*, 2010, **2010**, 3866–3874.
- 19 P. Maniam and N. Stock, *Inorg. Chem.*, 2011, **50**, 5085–5097; N. Reimer, B. Gil, B. Marszalek and N. Stock, *Cryst. EngComm*, 2012, **14**, 4119–4125.
- 20 F. Costantino, T. Bataille, N. Audebrand, E. Le Fur and C. Sangregorio, *Cryst. Growth Des.*, 2007, **7**, 1881–1888.
- 21 N. Stock, A. Stoll and T. Bein, *Microporous Mesoporous Mater.*, 2004, **69**, 65–69.
- 22 K. Moedritzer and R. R. Irani, *J. Org. Chem.*, 1966, **31**, 1603–1607.
- 23 T. Wroblewski, O. Clauß, H. A. Crostack, A. Ertel, F. Fandrich, C. Genzel, K. Hradil, W. Ternes and E. Woldt, *Nucl. Instrum. Methods Phys. Res., Sect. A*, 1999, **428**, 570–582.
- 24 O. H. Seeck, C. Deiter, K. Pflaum, F. Bertam, A. Beerlink, H. Franz, J. Horbach, H. Schulte-Schrepping, B. M. Murphy, M. Greve and O. Magnussen, *J. Synchrotron Radiat.*, 2012, **19**, 30–38.
- 25 Accelrys, *Materials Studio 5.5*, (2011).
- 26 J. Grehn and J. Krause, *Metzler Physik*, Schroedel Verlag, Hannover, 3rd edn, 1998.
- 27 E. Barsoukov and J. R. MacDonald, *Impedance spectroscopy*, Wiley & Sons, New Jersey, 2nd edn, 2005.
- 28 G. Alberti, M. Casciola, L. Massinelli and B. Bauer, *J. Membr. Sci.*, 2001, **185**, 73–81.
- 29 P. Rajiv, R. E. Dinnebier and M. Jansen, *Mater. Sci. Forum*, 2010, 97.
- 30 B.-P. Yang, A. V. Prosvirin, Y.-Q. Guo and J.-G. Mao, *Inorg. Chem.*, 2008, **47**, 1453–1459.
- 31 R. M. P. Colodrero, P. Olivera-Pastor, E. R. Losilla, D. Hernández-Alonso, M. A. G. Aranda, L. Leon-Reina, J. Rius, K. D. Demadis, B. Moreau, D. Villemin, M. Palomino, F. Rey and A. Cabeza, *Inorg. Chem.*, 2012, **51**, 7689–7698.
- 32 R. Marschall, J. Rathouský and M. Wark, *Chem. Mater.*, 2007, **19**, 6401–6407.
- 33 L. Carrette, K. A. Friedrich and U. Stimming, *Fuel Cells*, 2001, **1**, 5–39; M. N. T. A. Zawodzinsky, L. O. Sillerud and S. Gottesfeld, *J. Phys. Chem.*, 1991, **95**, 6040–6044.
- 34 C. Laberty-Robert, K. Valle, F. Pereira and C. Sanchez, *Chem. Soc. Rev.*, 2011, **40**, 961–1005; P. Tolle, C. Kohler, R. Marschall, M. Sharifi, M. Wark and T. Frauenheim, *Chem. Soc. Rev.*, 2012, **41**, 5143–5159.

5 | Synthese und *in situ* Untersuchung von Bismutcarboxylaten

Seit Beginn der Erforschung poröser Metall-organischen Gerüstverbindungen wurden fast alle Metalle des Periodensystems zur Synthese neuer Gerüstverbindungen verwendet. Die Anzahl an Untersuchungen, die sich mit der Synthese neuer Bismutcarboxylate beschäftigen sind vergleichsweise immer noch sehr gering. Dies ist sehr verwunderlich, da Bismut-basierende Gerüstverbindungen eine Vielzahl von interessanten Eigenschaften aufweisen könnten. Bereits einfache Salze wie BiCl_3 können in der Katalyse eingesetzt werden.^[179,180] Die Gründe hierfür liegen zum Einen an dem freien Elektronenpaar, das in katalytische Prozesse eingreifen kann und zum Anderen an der schlechten Abschirmung der f-Orbitale. Hierdurch ist Bismut Lewis-sauer.^[179,180] Es konnte Beispielsweise gezeigt werden, dass Bismutchlorid die Friedel-Crafts-Acylierung von Carbonsäurechloriden an Anisol katalysieren kann.^[179] Werden solche katalytischen Eigenschaften in MOFs eingebracht, können stereo- oder regioselektive Katalysatoren erhalten werden.^[181] Bismut gilt zusätzlich als nicht giftig, was es für potentielle Anwendungen interessant macht. Die geringe Toxizität ist vor allem im Vergleich zu seinen direkten Nachbarn im Periodensystem, wie Blei, Antimon, Polonium oder Tellur überraschend.^[179,180] MOFs die auf tri- oder tetravalenten Metallionen basieren, zeigen oft eine hohe chemische und thermische Stabilität, daher sollte dies ebenso auf Bismutcarboxylate zutreffen.^[69,182,183]

5.1. Bismutpyridincarboxylate

In der Vergangenheit wurden Bismut-Monocarboxylate wie -acetate, -salicylate oder auch -benzoate auf Grund ihrer Anwendung als Medikament^[184] oder Katalysator intensiv untersucht. Hierbei wurde eine Vielzahl anorganischer Struktur motive wie Bi_xO_y -Ketten oder -Cluster beobachtet, die potentiell geeignet sind, um auch poröse Gerüststrukturen durch deren Verknüpfung mit Polycarboxylaten zu erzeugen.^[185-188] Die ersten Bismutpolycarboxylate wurden auf Basis von 2,5- und 2,6-Pyridindicarbonsäure hergestellt. Eine Auswahl bekannter Bismutpyridincarboxylate ist in Tabelle 5.1 zusammengefasst.

5. Synthese und *in situ* Untersuchung von Bismutcarboxylaten

Tabelle 5.1.: Literaturbekannte Bismutpyridincarboxylate und ihre strukturellen Eigenschaften.

Linker	Summenformel	M-O-M Strukturmotiv
2,5-Pyridin-dicarbonsäure	$[\text{Bi}(\text{PYDC})_2] \cdot (\text{H}_3\text{O})(\text{H}_2\text{O})_{0,83}$	isolierte Schichten, (Kagome Netzwerk) ^[189]
	$\text{Bi}(\text{PYDC})(\text{HPYDC})(\text{H}_2\text{O})$ $[\text{K}_4\text{Bi}(\text{PYDC})_3(\text{HPYDC})] \cdot (\text{H}_2\text{O})_{3,3}$	Ketten ^[190] anionische Schichtverbindung ^[190]
	$(\text{DMA})_3\text{Bi}(\text{PYDC})_2(\text{HPYDC})_2$	Ketten, anionisches Gerüst ^[190]
2,6-Pyridin-dicarbonsäure	$[\text{Bi}_6(\text{PYDC})_8(\text{HPYDC})_2(\text{TU})_8]$	Cluster, TU = Thioharnstoff ^[191]
	$[\text{Bi}_2(\text{PYDC})_3(\text{TSC})(\text{H}_2\text{O})_2] \cdot \text{H}_2\text{O}$	Ketten, TSC = Thiosemicarbazid ^[191]
	$[\text{Ni}(\text{H}_2\text{O})_6][\text{Bi}_2(\text{PYDC})_4] \cdot 2\text{H}_2\text{O}$	anionische Ketten, NiO_6^{2+} Kationen ^[192]
	$[\text{Co}(\text{H}_2\text{O})_6][\text{Bi}_2(\text{PYDC})_4] \cdot 2\text{H}_2\text{O}$	anionische Ketten, CoO_6^{2+} Kationen ^[192]
	$[\text{H}_2\text{PYDA}][\text{Bi}_2(\text{PYDC})_4]$	anionische Cluster, PYDA = 2,6-pyridindiamin ^[193]
	$[(\text{Hphen})_2][\text{Bi}(\text{PYDC})_2(\text{H}_2\text{O})_2] \cdot 5\text{H}_2\text{O}$ $[\text{BiCl}(\text{H}_2\text{O})_8(\text{PYDC})]$	anionische Cluster ^[194] Ketten ^[195]
	$[(\text{HPYDA}^2)_2][\text{Bi}_2(\text{PYDC})_4(\text{H}_2\text{O})_2] \cdot 4\text{H}_2\text{O}$	dimere Einheiten, PYDA^2 = 2,3-pyridindiamin ^[196]
	$[\text{Bi}(\text{PYDC})(\text{HPYDC})] \cdot \text{H}_2\text{O}$	dimere Einheiten zu Ketten verknüpft ^[197]
	$[\text{Bi}(\text{PYDC})] \cdot 3\text{DMA}$	monomerer Komplex, DMA = dimethylammonium ^[198]
	$\text{Bi}(\text{PYDC}) \cdot 3\text{DMA} \cdot 2\text{H}_2\text{O}$	monomerer Komplex, DMA = dimethylammonium ^[198]
	$[\text{Bi}(\text{PYDC})(\text{DMF})] \cdot \text{DMA}$	dimere Cluster, DMA = dimethylammonium ^[198]
	$\text{Bi}(\text{PYDC})(\text{PDCME})(\text{MeOH})$	dimere Cluster, DMA = dimethylammonium, PDCME = 6-methyloxycarbonylpyridin-2-carboxylat ^[198]
	$[\text{LiBi}(\text{PYDC})_3(\text{H}_2\text{O})] \cdot 2\text{DMA}$	dimere Einheiten, von Li^+ verbrückt, DMA = dimethylammonium ^[198]
$\text{Li}_5\text{Bi}(\text{PYDC})_4(\text{H}_2\text{O})_2$	monomere Einheiten, von Li^+ verbrückt ^[198]	

In allen Verbindungen koordinieren sowohl das Stickstoffatom als auch die Carboxylatgruppen. Die Verwendung von 2,6-Pyridindicarbonsäure führt häufig zur Ausbildung von dimeren anionischen $[\text{Bi}_2\text{O}_{14}]^{2-}$ Einheiten, wie sie exemplarisch in Abbildung 5.1 Mitte gezeigt sind. Hierbei ist die grün markierte Stelle in der Einheit variabel und kann durch unterschiedliche Liganden besetzt werden. Die Koordination von Wasser führt zur Ausbildung von Clustern.^[196] Das Wasser kann ebenso gegen andere Lösungsmittelmoleküle wie DMF^[198] oder Thioharnstoff^[191] ausgetauscht werden. Hierdurch ergeben sich neue Wasserstoffbrückenbindungsmuster. Der Austausch des Wassermoleküls gegen eine Carboxylatgruppe einer weiteren dimeren Einheit führt zur Bildung von polymeren Ketten der Einheiten.^[197]

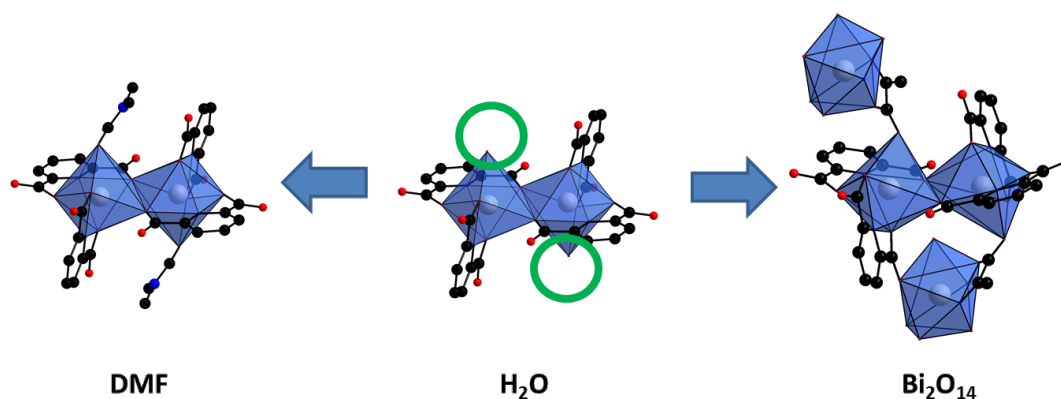


Abbildung 5.1.: Dimere Bi_2O_{14} Einheiten. Die variable Koordinationsstelle ist grün markiert. **Links:** Dimere Einheit mit koordinieren DMF Molekülen.^[198] **Mitte:** Dimere Einheit mit Wassermolekülen.^[196] **Rechts:** Verbrücken der Einheit mit weiteren dimeren Einheiten über die Pyridindicarbonsäure.^[197]

5.2. Bismutcarboxylate

Ebenso, aber weniger intensiv, wurde die Verwendung monofunktionalisierter Carbonsäuren als Linker zur Synthese neuer Bismutcarboxylate untersucht. Die literaturbekannten Verbindungen sind in Tabelle 5.2 zusammengefasst.

Der Einsatz von Natriumhydroxid in Kombination mit Polycarboxylaten führte zur Bildung von Mischmetallverbindungen, wie z.B. in Abbildung an der Verbindung 5.2 an $[\text{NaBi}(\text{BDC})_2(\text{DMF})_2]$ gezeigt. Die Kristallstruktur ist aus Bi-O-Na Ketten aufgebaut, die von Terephthalationen verbrückt werden und so eine offene Gerüststruktur bilden. DMF Moleküle vervollständigen die Koordinationsumgebung der Bi^{3+} -Ionen und ragen in die

5. Synthese und *in situ* Untersuchung von Bismutcarboxylaten

Tabelle 5.2.: Literaturbekannte Bismutcarboxylate unter Verwendung von Dicarbonsäuren 1,4-Benzoldicarbonsäure(H₂BDC), 1,3-Benzoldicarbonsäure (H₂ITA) und Tricarbonsäuren 1,3,5-Benzentriscarbonsäure (H₃BTC) (DMF = Dimethylformamid, DMA = Dimethylammonium, HIm = Imidazol, 2,2-bipy = 2,2-Bipyridin, EtOH = Ethanol, DMSO = Dimethylsulfoxid).

Linker	Summenformel	M-O-M Struktur
Dicarbonsäuren	[NaBi(BDC) ₂ (DMF) ₂]	Na-O-Bi Ketten ^[199]
	[NaBi(BDC) ₂ (DMF)(H ₂ O)] · DMF	Na-O-Bi Ketten ^[199]
	[NaBi(ITA) ₂ (DMF)]	Na-O-Bi Schichten ^[199]
	[NaBi(ITA) ₂ (EtOH)]	Na-O-Bi Schichten ^[199]
	DMA[Bi(BDC) ₂ (DMF)] · 2DMF	Ketten, Schichten ^[200]
	DMA[Bi(BDC) ₂] · DMF	Ketten, 3D-Netzwerk ^[200]
	(DMA) ₂ [Bi ₄ (BDC) ₇ (HIm)] · 2DMF	Ketten, 3D-Netzwerk, ^[200]
	DMA[Bi(BDC) ₂] ·	Ketten, 3D-Netzwerk ^[200]
Tricarbonsäuren	[Bi(BTC)(NO ₃)(2,2-bipy)(DMSO)] · DMSO	Isolierte Einheiten, Ketten bipy = Bipyridin ^[201]

potentiell zugänglichen Poren. Diese Gastmoleküle konnten allerdings bisher nicht unter Erhalt der kristallinen Struktur entfernt werden.

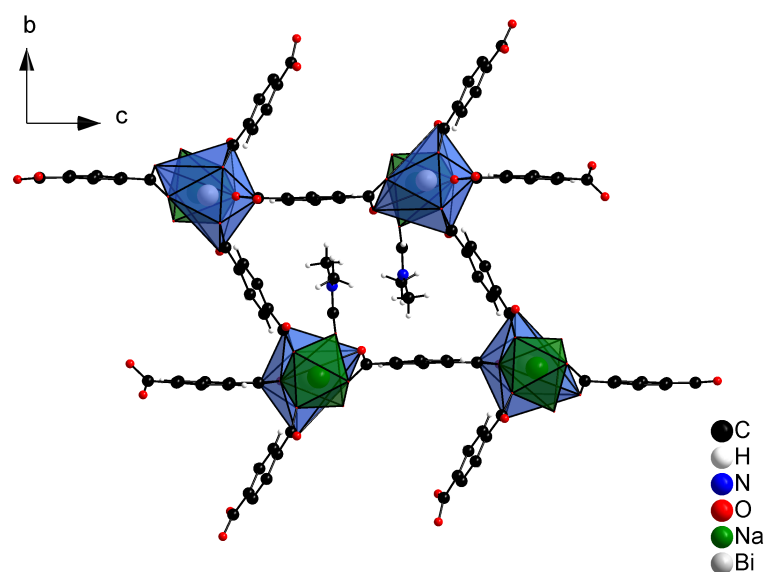


Abbildung 5.2.: Ausschnitt aus der Kristallstruktur von [NaBi(BDC)₂(DMF)₂].

Oft verhindern auch die geladenen Gerüststrukturen die Zugänglichkeit der Poren. Die Kristallstruktur der Verbindung DMA $[\text{Bi}(\text{BDC})_2]$ (DMA = Dimethyammonium) ist in Abbildung 5.3 gezeigt und hat theoretisch zugängliche Poren. In diesen liegen DMA Ionen als Gegenionen vor. Diese konnten nicht entfernt oder ausgetauscht werden ohne das Gerüst zu zerstören.

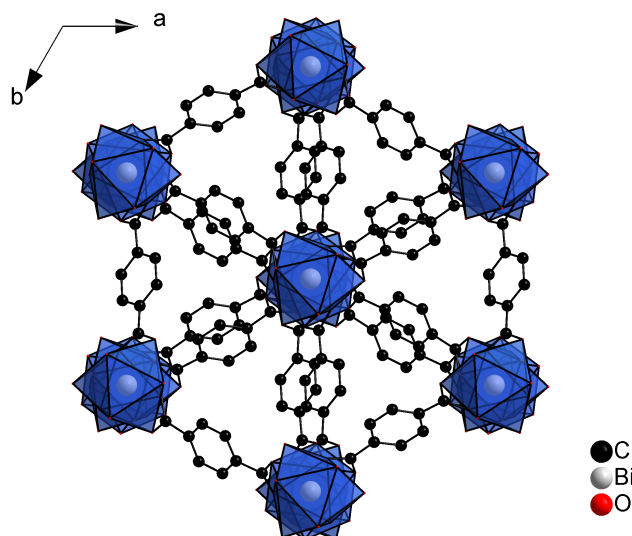


Abbildung 5.3.: Kristallstruktur der Verbindung DMA $[\text{Bi}(\text{BDC})_2]$. Die DMA Moleküle wurden zur Übersichtlichkeit weggelassen.

Weit weniger intensiv wurden tripodale Liganden untersucht. Unter Verwendung von Trimesinsäure und 2,2-Bipyridin in DMSO (Dimethylsulfoxid) wurde die Verbindung $[\text{Bi}(\text{BTC})(\text{NO}_3)(2,2\text{-bipy})(\text{DMSO})] \cdot \text{DMSO}$ erhalten. Die Verbindung ist aus isolierten BiO_9 -Polyedern aufgebaut, die über Carboxylat-Ionen zu Ketten verknüpft sind.^[201]

Keine der hier vorgestellten Verbindungen zeigte eine signifikante Porosität, da das kristalline Netzwerk während der Aktivierung zerstört wird. Vor allem könnte das hohe bestreben der Bi^{3+} -Ionen hoch kondensierte BiO_x -Polyederketten und -schichten zu bilden, den Aufbau einer offenen Gerüststruktur verhindern.

5.3. Ergebnisse der Synthesen neuer Bismutcarboxylate und deren *in situ* Untersuchungen.

5.3.1. Automated Diffraction Tomography for the Structure Elucidation of Twinned, Sub-micrometer Crystals of a Highly Porous, Catalytically Active Bismuth Metal–Organic Framework

Der folgende Artikel wurde in der Zeitschrift *Angewandte Chemie* im Jahre 2012 veröffentlicht und behandelt die Synthese und Strukturbestimmung eines neuen porösen Bismutcarboxylats.^[202] Im Vorfeld zu dieser Arbeit wurden in den veröffentlichten Synthesen hauptsächlich Wasser, DMSO und DMF als Lösungsmittel zur Synthese von Bismutcarboxylaten verwendet. Für aluminiumbasierende MOFs hat sich in der Vergangenheit Methanol als Lösungsmittel bewährt und wurde auch aus diesem Grund zur Darstellung von Bismutcarboxylaten verwendet.^[38,39,69] Der sterisch anspruchsvolle Linker H₃BTB (H₃BTB = 1,3,5-Benzoltrisbenzoesäure) sollte die Ausbildung von hochkondensierten Ketten oder Schichten verhindern und so die Bildung einer offenen Gerüststruktur ermöglichen.

Das neue Bismutcarboxylat CAU-7 (Bi(BTB)) (CAU = Christian-Albrechts Universität) wurde aus Methanol durch Einsatz von Bi(NO₃)₃ · 5H₂O und H₃BTB gewonnen. Die Verbindung konnte nur als nanokristallines Pulver erhalten werden. Die Kristallstruktur wurde mittels ADT (Automated Diffraction Tomographie) aus Elektronenbeugungsdaten gelöst und mit einer Kombination aus Rietveld-Methode und DFT Rechnungen verfeinert. Die Verbindung zeigt eine hohe thermische Stabilität (bis 380 °C) und Stickstoffsorptionsmessungen ergaben eine scheinbare spezifische Oberfläche nach BET von 1150 m²/g. Das Material katalysiert die Hydroxymethylierung von Methylfuran (vgl. Abbildung 5.4).

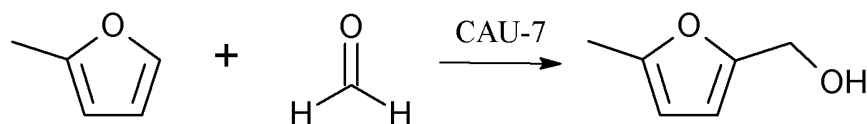


Abbildung 5.4.: Hydroxymethylierung von Methylfuran.

Automated Diffraction Tomography for the Structure Elucidation of Twinned, Sub-micrometer Crystals of a Highly Porous, Catalytically Active Bismuth Metal–Organic Framework**

Mark Feyand, Enrico Mugnaioli, Frederik Vermoortele, Bart Bueken, Johannes M. Dieterich, Tim Reimer, Ute Kolb,* Dirk de Vos, and Norbert Stock*

The number of metal–organic framework (MOF) compounds has increased almost exponentially over the last decade as a consequence of their fascinating structures and potential applications.^[1] They are composed of inorganic building units, such as metal ions or clusters, which are connected through organic linker molecules to form a porous three-dimensional network. Most of the MOFs are based on rigid polycarboxylate linker molecules,^[2] but a large variety of metal ions, mainly transition-metal ions, have also been incorporated.^[2c,3] The chemical and thermal stability of metal carboxylate based MOFs is crucial for potential applications and depends on the metal ions incorporated.^[4] In general, metal ions in higher oxidation states lead to more stable structures.

While the use of divalent metal ions often results in the formation of single crystals, whose structures can be routinely determined by single-crystal X-ray diffraction,^[2c,3c] tri- and tetravalent metal carboxylates are mostly obtained as microcrystalline powders and the determination of their structures poses immense challenges.^[2a,3a,4c,5] Direct methods have been successfully employed, but complicated structures with large unit cells necessitate the use of nonstandard approaches. Thus, computational assisted structure determination, namely, the AASBU^[4c] approach (assembling of secondary building units), the ligand-replacement strategy,^[2a,6] and

DFT^[7] calculations have been applied. Recently automated diffraction tomography (ADT) has been introduced as a new method for collecting three-dimensional electron diffraction data from single nanosized crystals,^[8] thus allowing single-crystal analysis even for porous and organic sub-microcrystalline samples.

A trivalent metal that exhibits interesting catalytic properties is bismuth. It is nontoxic, noncarcinogenic, and for a rare metal relatively inexpensive, and thus bismuth compounds are used as green catalysts.^[9] Despite these characteristics, the number of bismuth-based MOFs is rather limited and only a few compounds with limited porosity have been described.^[10] This is in contrast to the many known bismuth-oxo clusters, which could possibly be used for the construction of new MOFs.^[11]

Here, we present the synthesis of the first highly crystalline, porous, and catalytically active bismuth-based MOF Bi(BTB) (BTB = 1,3,5-benzenetrisbenzoate), whose structure was elucidated by a combination of electron diffraction, Rietveld refinement, and DFT calculations.

Bi(BTB), denoted as CAU-7 (CAU = Christian-Albrechts-Universität) was synthesized by using conventional as well as microwave (MW) assisted heating. The reaction of Bi(NO₃)₃·5H₂O with H₃BTB in methanol at 120 °C led to phase-pure CAU-7 (for a detailed synthesis procedure see the Supporting Information). The reaction time can be reduced from 12 h to 20 min by using MW-assisted instead of conventional heating, but this leads to the formation of 10–20 μm large agglomerates of strongly intergrown elongated crystals of about 100 nm (see Figures S2–S4 in the Supporting Information). The addition of DMF in the conventional synthesis results in the formation of larger rodlike crystals ranging from 200 to 300 nm in length. Transmission electron microscopy confirmed that isolated CAU-7 crystals have a typical rodlike shape with different length/diameter ratios (see Figure S5 in the Supporting Information). Such isolated rods were used to collect electron diffraction data by automated diffraction tomography (ATD).

Single-crystal ADT electron diffraction datasets were collected using a cryo holder cooled to 120 K and mild illumination conditions. To prevent beam damage and improve the signal intensity, the diffraction data were acquired in the precession mode.^[12] The three-dimensional diffraction space reconstruction leads to lattice parameters $a = 32 \text{ \AA}$, $b = 28 \text{ \AA}$, $c = 4 \text{ \AA}$, $\alpha = \beta = \gamma = 90^\circ$, and extinction group $Pb-a$. The reconstructed reciprocal space is shown in Figure 1.

[*] M. Feyand, T. Reimer, Prof. Dr. N. Stock
Institut für Anorganische Chemie
Christian Albrechts Universität zu Kiel
Max-Eyth Strasse 2, 24118 Kiel (Germany)
E-mail: stock@ac.uni-kiel.de

Dr. E. Mugnaioli, Dr. U. Kolb
Institut für Physikalische Chemie
Johannes Gutenberg-Universität Mainz
Welderweg 11, 55099 Mainz (Germany)

Dr. J. M. Dieterich
Institut für Physikalische Chemie
Georg-August-Universität Göttingen
Tammannstrasse 6, 37077 Göttingen (Germany)

F. Vermoortele, B. Bueken, Prof. Dr. D. de Vos
Centre for Surface Chemistry and Catalysis
Kasteelpark Arenberg 23, 3001 Heverlee (Belgium)

[**] We thank Steffen Schmidt (LMU München) for the SEM micrographs, Michael T. Wharmby for his assistance in preparing the graphics, and the DFG for financial support (SPP 1362, grant agreement no. STO 643/5-2). This work has also been supported by the Stiftung Rheinland-Pfalz für Innovation and the state Schleswig Holstein.

Supporting information for this article is available on the WWW under <http://dx.doi.org/10.1002/anie.201204963>.

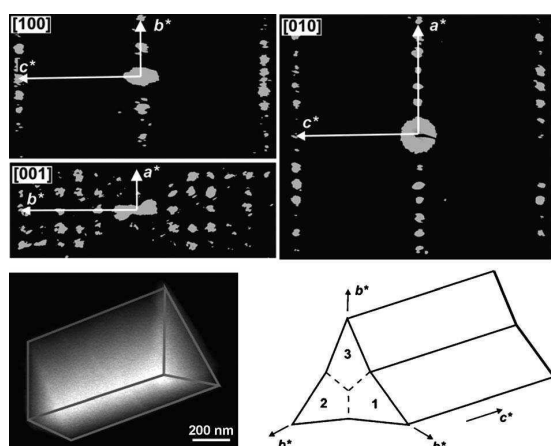


Figure 1. Reconstructed three-dimensional diffraction space of CAU-7 projected along the main directions (top), a rod tilted to expose the triangular base (bottom left), and a sketch of the trilling arrangement (bottom right).

The ADT data also showed that each rod is in fact a twin aggregate composed of three individuals that grow following the pseudo-hexagonal symmetry of the structure (Figure 1), and thus a trilling is formed (see Figures S6 and S7 in the Supporting Information). The three individuals share the same [001] direction, which is also the main growth direction of the rod. The [010] directions are rotated by 120° , and are parallel to the “almost” equivalent $[2-10]$ and $[-2-10]$ directions of the other domains.

The structure of CAU-7 was determined on the basis of electron diffraction data collected on two single domains. Simulated annealing (SA) routines were used as implemented in SIR2011.^[13] The structure was finally solved in the space group $Pb2_1a$ with one independent bismuth atom and one independent BTB^{3-} molecule in the unit cell. All six torsion angles of the BTB^{3-} molecule were kept free to rotate during the solving process. The crystal structure was refined from X-ray powder diffraction data using Topas Academics 4.1.^[14] More details are given in the Supporting Information.

DFT-based calculations on the CAU-7 crystal structure were carried out to further support the experimental observations. A plane-wave approach, as implemented in the CPMD program package was employed, using the PBE functional together with Goedecker–Teter–Hutter pseudopotentials and a final wavefunction cutoff of 100 Rydberg (density cutoff: 400 Ry) and the experimental lattice parameters.^[15] The calculated Bi–O distances are between 2.336 and 3.221 Å for the optimized structure, which is in good agreement with the experimentally obtained values (2.16(1)–3.38(1) Å). More details of the DFT calculations are given in the Supporting Information.

In the crystal structure of CAU-7, the Bi^{3+} ions are ninefold coordinated by oxygen atoms of the BTB^{3-} ions, thereby forming threefold capped trigonal prisms. Face sharing of the BiO_9 polyhedra leads to chains along the c -axis (Figure 2). Such polyhedra are already known for the bismuth benzoate $Bi(O_2C_6H_5)_3$, which shows very similar

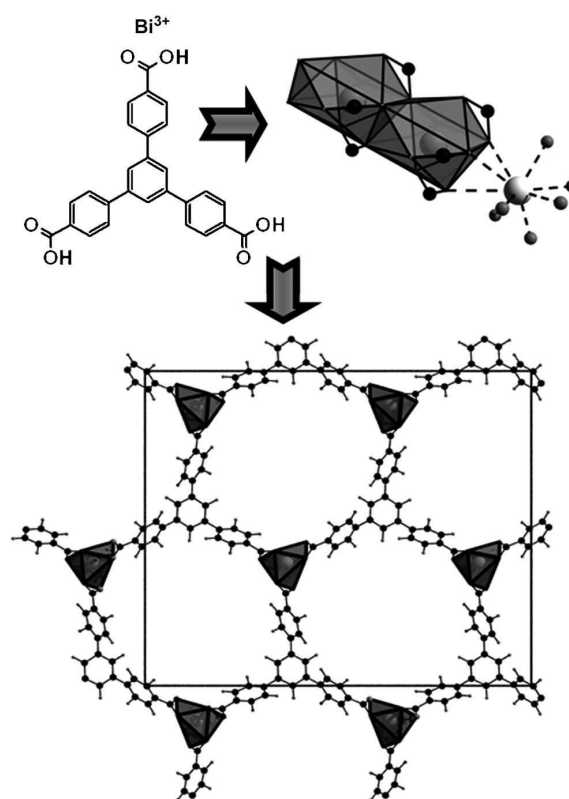


Figure 2. Crystal structure of CAU-7. The connection of 1,3,5-benzenetricarboxylate (BTB^{3-}) and Bi^{3+} ions (top left) leads to face-sharing BiO_9 polyhedra which form chains along the [001] direction (top right). These chains are interconnected into a honeycomb network (bottom).

bond lengths that range from 2.250(6) to 3.110(6) Å.^[16] The BTB^{3-} linkers connect the chains into a slightly distorted honeycomb network with approximately 1 nm wide, one-dimensional channels, as determined with PLATON.^[15b,17] Each carboxylate group of the linker molecule contains one μ - and one end-on-linked oxygen atom.

The thermal stability of CAU-7 was investigated by thermogravimetric (TG) analysis and temperature-dependent X-ray powder diffraction (TD-XRPD) measurements. The as-synthesized product, which contains noncoordinating H_3BTB molecules (see Figure S17 in the Supporting Information for the IR spectra), was treated with DMF and methanol. This was followed by ultrasonication in methanol for 30 min. The TG curve (see Figure S15 in the Supporting Information) shows a weight loss of 14.2% as a result of the loss of solvent molecules from the pores between 25 and 80°C. Above 350°C, the loss of one BTB molecule is observed, which results at 1000°C in Bi_2O_3 (found: 52.1%, calcd: 51.1%). The TD-XRPD measurements (see Figure S16 in the Supporting Information) confirm the stability of the crystalline framework up to 380°C. Above this temperature, decomposition takes place and results in an X-ray amorphous phase at 400°C.

Prior to the sorption experiments CAU-7 was thermally activated at 160 °C for 12 h under vacuum. The elemental analysis of the activated sample confirms the complete removal of the H₃BTB and DMF molecules.^[15e] The BET evaluation of the type 1 N₂ sorption curve of CAU-7 results in a specific surface of $A_{\text{BET}} = 1150 \text{ m}^2 \text{ g}^{-1}$ and a micropore volume of $V_{\text{m}} = 0.43 \text{ cm}^3 \text{ g}^{-1}$ ($V_{\text{m}}(\text{calcd}) = 0.43 \text{ cm}^3 \text{ g}^{-1}$ ^[17]). These values are comparable to other BTB-based MOFs with honeycomb networks, such as CAU-4 (Al(BTB): $A_{\text{BET}} = 1520 \text{ m}^2 \text{ g}^{-1}$, $V_{\text{m}} = 0.61 \text{ cm}^3 \text{ g}^{-1}$ ^[18]) and MIL-103 (Tb(H₂O)(BTB): $A_{\text{BET}} = 700 \text{ m}^2 \text{ g}^{-1}$).^[19] Isolated AlO₆ and edge-sharing TbO₉ polyhedra are observed in these structurally related compounds. The sorption behavior towards H₂, H₂O, and CO₂ shows the expected results for a hydrophobic MOF (see Figures S11–S14 in the Supporting Information). Thus, an uptake of 1.07, 2.62, and 4.31 wt% is observed for H₂ (77 K), H₂O (298 K), and CO₂ (298 K), respectively, at 1 bar.

The catalytic activity of CAU-7 was demonstrated in the solvent-free hydroxymethylation of hemicellulose-derived 2-methylfuran to 5-methylfurfuryl alcohol (see the Supporting Information).

This reaction requires Lewis or Brønsted acid sites of well-defined strength.^[20] If the acidity is too strong, consecutive condensations and polymerization result; the optimum catalyst should give high yields at high conversions. CAU-7 was compared to other MOFs with reported Lewis or Brønsted acidity, such as the Zr-terephthalate UiO-66^[21] and the Ga-terephthalate MIL-53(Ga).^[22] In contrast with these, CAU-7 gives high yields at high conversions, thus avoiding consecutive condensation reactions. CAU-7 possesses mild Lewis acid sites, as demonstrated by the chemisorption of acetonitrile (see Figure S4 in the Supporting Information). The hydrophobic nature of the material facilitates fast desorption of the alcohol reaction product. The heterogeneity of the catalyst was confirmed.

In conclusion, we have discovered the first permanently porous, highly crystalline bismuth-based MOF that also exhibits catalytic activity. The incorporation of other potentially interesting metals into MOF structures should also be possible. Moreover, the potential of the ADT method for the investigation of crystalline features and structure–property relationships of nanosized crystals has been shown. ADT revealed the twinning law and the orientation of CAU-7 crystals in the rodlike aggregates, and, coupled with the SA method, resulted in an efficient method for the structure determination of beam-sensitive materials.

Received: June 25, 2012

Published online: September 13, 2012

Keywords: bismuth · heterogeneous catalysis · metal–organic frameworks · structure elucidation

- [1] a) L. Ma, C. Abney, W. Lin, *Chem. Soc. Rev.* **2009**, *38*, 1248–1256; b) L. J. Murray, M. Dinca, J. R. Long, *Chem. Soc. Rev.* **2009**, *38*, 1294–1314; c) P. Horcajada, C. Serre, M. Vallet-Regi, M. Sebban, F. Taulelle, G. Férey, *Angew. Chem.* **2006**, *118*, 6120–6124; *Angew. Chem. Int. Ed.* **2006**, *45*, 5974–5978; d) P. Horcajada, C. Serre, G. Maurin, N. A. Ramsahye, F. Balas, M.

- Vallet-Regi, M. Sebban, F. Taulelle, G. Férey, *J. Am. Chem. Soc.* **2008**, *130*, 6774–6780; e) J. S. Seo, D. Whang, H. Lee, S. I. Jun, J. Oh, Y. J. Jeon, K. Kim, *Nature* **2000**, *404*, 982–986.
- [2] a) A. Sonnauer, F. Hoffmann, M. Froeba, L. Kienle, V. Duppel, M. Thommes, C. Serre, G. Férey, N. Stock, *Angew. Chem.* **2009**, *121*, 3849–3852; *Angew. Chem. Int. Ed.* **2009**, *48*, 3791–3794; b) S. Bauer, C. Serre, T. Devic, P. Horcajada, J. Marrot, G. Férey, N. Stock, *Inorg. Chem.* **2008**, *47*, 7568–7576; c) J. L. C. Rowsell, O. M. Yaghi, *Microporous Mesoporous Mater.* **2004**, *73*, 3–14; d) S. Kitagawa, R. Matsuda, *Coord. Chem. Rev.* **2007**, *251*, 2490–2509; e) N. Klein, I. Senkovska, K. Gedrich, U. Stoeck, A. Henschel, U. Mueller, S. Kaskel, *Angew. Chem.* **2009**, *121*, 10139–10142; *Angew. Chem. Int. Ed.* **2009**, *48*, 9954–9957.
- [3] a) T. Ahnfeldt, N. Guillou, D. Gunzelmann, I. Margiolaki, T. Loiseau, G. Férey, J. Senker, N. Stock, *Angew. Chem.* **2009**, *121*, 5265–5268; *Angew. Chem. Int. Ed.* **2009**, *48*, 5163–5166; b) B. Chen, M. Eddaoudi, S. T. Hyde, M. O’Keeffe, O. M. Yaghi, *Science* **2001**, *291*, 1021–1023.
- [4] a) M. Dan-Hardi, C. Serre, T. O. Frot, L. Rozes, G. Maurin, C. M. Sanchez, G. R. Férey, *J. Am. Chem. Soc.* **2009**, *131*, 10857–10859; b) J. H. Cavka, S. Jakobsen, U. Olsbye, N. Guillou, C. Lamberti, S. Bordiga, K. P. Lillerud, *J. Am. Chem. Soc.* **2008**, *130*, 13850–13851; c) G. Férey, C. Mellot-Draznieks, C. Serre, F. Millange, J. Dutour, S. Surblé, I. Margiolaki, *Science* **2005**, *309*, 2040–2042.
- [5] a) T. R. Whitfield, X. Wang, L. Liu, A. J. Jacobson, *Solid State Sci.* **2005**, *7*, 1096–1103; b) H. Reinsch, M. Feyand, T. Ahnfeldt, N. Stock, *Dalton Trans.* **2012**, *41*, 4164–4171.
- [6] I. Senkovska, F. Hoffmann, M. Fröba, J. Getzschmann, W. Böhlmann, S. Kaskel, *Microporous Mesoporous Mater.* **2009**, *122*, 93–98.
- [7] F. Salles, G. Maurin, C. Serre, P. L. Llewellyn, C. Knöfel, H. J. Choi, Y. Filinchuk, L. Oliviero, A. Vimont, J. R. Long, G. R. Férey, *J. Am. Chem. Soc.* **2010**, *132*, 13782–13788.
- [8] a) U. Kolb, T. Gorelik, M. T. Otten, *Ultramicroscopy* **2008**, *108*, 763–772; b) U. Kolb, T. Gorelik, C. Kübel, M. T. Otten, D. Hubert, *Ultramicroscopy* **2007**, *107*, 507–513; c) S. J. Sedlmaier, E. Mugnaioli, O. Oeckler, U. Kolb, W. Schnick, *Chem. Eur. J.* **2011**, *17*, 11258–11265; d) E. Mugnaioli, T. Gorelik, U. Kolb, *Ultramicroscopy* **2009**, *109*, 758–765; e) D. Denysenko, M. Grzywa, M. Tonigold, B. Streppel, I. Krkljus, M. Hirscher, E. Mugnaioli, U. Kolb, J. Hanss, D. Volkmer, *Chem. Eur. J.* **2011**, *17*, 1837–1848; f) U. Kolb, T. Gorelik, E. Mugnaioli, A. Stewart, *Polym. Rev.* **2010**, *50*, 385–409; g) J. Jiang, J. L. Jorda, J. Yu, L. A. Baumes, E. Mugnaioli, M. J. Diaz-Cabanas, U. Kolb, A. Corma, *Science* **2011**, *333*, 1131–1134.
- [9] a) N. M. Leonard, L. C. Wieland, R. S. Mohan, *Tetrahedron* **2002**, *58*, 8373–8397; b) J. M. Bothwell, S. W. Krabbe, R. S. Mohan, *Chem. Soc. Rev.* **2011**, *40*, 4649–4707.
- [10] a) A. Thirumurugan, W. Li, A. K. Cheetham, *Dalton Trans.* **2012**, *41*, 4126–4134; b) A. C. Wibowo, M. D. Smith, H.-C. zur Loye, *CrystEngComm* **2011**, *13*, 426–429; c) A. C. Wibowo, M. D. Smith, H. C. zur Loye, *Chem. Commun.* **2011**, *47*, 7371–7373; d) A. C. Wibowo, M. D. Smith, H.-C. zur Loye, *CrystEngComm* **2011**, *13*, 426–429; e) D. T. Tran, D. Chu, A. G. Oliver, S. R. J. Oliver, *Inorg. Chem. Commun.* **2009**, *12*, 1081–1084; f) A. Thirumurugan, J.-C. Tan, A. K. Cheetham, *Cryst. Growth Des.* **2010**, *10*, 1736–1741; g) A. Thirumurugan, A. K. Cheetham, *Eur. J. Inorg. Chem.* **2010**, 3823–3828; h) S. Busch, I. Stein, U. Ruschewitz, *Z. Anorg. Allg. Chem.* **2012**, DOI: 10.1002/zaac.201200006.
- [11] a) D. Mansfeld, L. Miersch, T. Rueffer, D. Schaarschmidt, H. Lang, T. Boehle, R. W. Troff, C. A. Schalley, J. Mueller, M. Mehring, *Chem. Eur. J.* **2011**, *17*, 14805–14810; b) L. Miersch, T. Rueffer, H. Lang, S. Schulze, M. Hietschold, D. Zahn, M. Mehring, *Eur. J. Inorg. Chem.* **2010**, 4763–4769; c) L. Miersch, T. Rueffer, M. Mehring, *Chem. Commun.* **2011**, *47*, 6353–6355;

- d) L. Miersch, M. Schlesinger, R. W. Troff, C. A. Schalley, T. Rueffer, H. Lang, D. Zahn, M. Mehring, *Chem. Eur. J.* **2011**, *17*, 6985–6990; e) K. Wojcik, T. Rueffer, H. Lang, A. A. Auer, M. Mehring, *J. Organomet. Chem.* **2011**, *696*, 1647–1651; f) L. Miersch, T. Ruffer, M. Mehring, *Chem. Commun.* **2011**, *47*, 6353–6355.
- [12] A. Kverneland, V. Hansen, R. Vincent, K. Gjønnnes, J. Gjønnnes, *Ultramicroscopy* **2006**, *106*, 492–502.
- [13] a) M. Camalli, B. Carrozzini, G. L. Cascarano, C. Giacomazzo, *Cryst. Res. Technol.* **2011**, *46*, 555–560; b) M. C. Burla, R. Caliandro, M. Camalli, B. Carrozzini, G. L. Cascarano, C. Giacomazzo, M. Mallamo, A. Mazzone, G. Polidori, R. Spagna, *J. Appl. Crystallogr.* **2012**, *45*, 357–361; c) A. T. Brunger, *Annu. Rev. Phys. Chem.* **1991**, *42*, 197–223; d) A. Altomare, R. Caliandro, C. Cuocci, C. Giacomazzo, A. G. G. Moliterni, R. Rizzi, C. Platteau, *J. Appl. Crystallogr.* **2008**, *41*, 56–61.
- [14] A. Coelho, *TOPAS-Academic V4.1* **2007**.
- [15] a) CPMD v3.15.1, <http://www.cpmc.org>, Copyright IBM Corp., Copyright MPI fuer Festkoerperforschung 1990–2008; b) S. Goedecker, M. Teter, J. Hutter, *Phys. Rev. B* **1996**, *54*, 1703–1710; c) J. P. Perdew, K. Burke, M. Ernzerhof, *Phys. Rev. Lett.* **1996**, *77*, 3865–3868; d) C. Hartwigsen, S. Goedecker, J. Hutter, *Phys. Rev. B* **1998**, *58*, 3641–3662; e) M. Krack, *Theor. Chim. Acta* **2005**, *114*, 145–152.
- [16] N. A. Tumanov, E. V. Timakova, E. V. Boldyreva, *Acta Crystallogr. Sect. E* **2010**, *66*, m1248.
- [17] A. L. Spek, *Acta Crystallogr. Sect. D* **2009**, *65*, 148–155.
- [18] H. Reinsch, M. Krüger, J. Wack, J. Senke, F. Salles, G. Maurin, N. Stock, *Micropor. Mesopor. Mater.*, **2012**, *157*, 50–55.
- [19] a) T. Devic, C. Serre, N. Audebrand, J. Marrot, G. Férey, *J. Am. Chem. Soc.* **2005**, *127*, 12788–12789; b) T. Devic, V. Wagner, N. Guillou, A. Vimont, M. Haouas, M. Pascolini, C. Serre, J. Marrot, M. Daturi, F. Taulelle, G. Férey, *Microporous Mesoporous Mater.* **2011**, *140*, 25–33.
- [20] I. Iovel, E. Lukevics, *Chem. Heterocycl. Compd.* **1998**, *34*, 1–12.
- [21] F. Vermoortele, R. Ameloot, A. Vimont, C. Serre, D. De Vos, *Chem. Commun.* **2011**, *47*, 1521–1523.
- [22] U. Ravon, G. Chaplais, C. Chizallet, B. Seyyedi, F. Bonino, S. Bordiga, N. Bats, D. Farrusseng, *ChemCatChem* **2010**, *2*, 1235–1238.

5.3.2. High-throughput and *In situ* EDXRD Investigation of Bismuthcarboxylates

Der folgende Artikel wurde bei der Zeitschrift *Chemistry- A European Journal* zur Veröffentlichung angenommen und behandelt die Hochdurchsatzuntersuchung und die *in situ* EDXRD Untersuchung von Bismutcarboxylaten. Auf Basis von Trimesinsäure (H_3BTC), Pyromellitsäure (H_4Pyr) und Trimellitsäure (H_3Tri) (Abbildung 5.5) wurden fünf neue Bismutcarboxylate $Bi_2(O)(Pyr)(H_2O)$, $Bi(HPyr)$, $Bi(Tri)(H_2O)$, $Bi_2(O)(OH)(HBTC)(NO_3)$ und $Bi_6O_5(BTC)_2 (HBTC)_4$ synthetisiert und ihre Kristallstruktur aus Röntgen-Einkristallbeugungsdaten bestimmt.

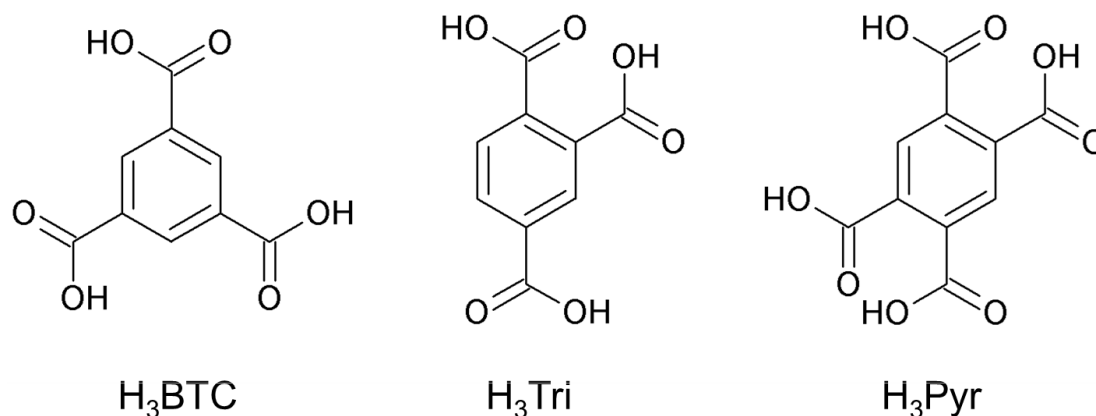


Abbildung 5.5.: Hydroxymethylierung von Methylfuran.

Um ein tiefergehendes Verständnis über die Bildungsmechanismen von Bismutcarboxylaten zu erhalten wurden *in situ* EDXRD Untersuchungen der Bildung von $Bi(HPyr)$, $Bi(Tri)(H_2O)$ und $Bi_2(O)(OH)(HBTC)(NO_3)$ durchgeführt. In Kombination mit *ex situ* Untersuchungen konnte hierbei gezeigt werden, dass bei der Kristallisation von $Bi(HPyr)$ anfangs das Intermediat $Bi_2(O)(Pyr)(H_2O)$ entsteht und dieses sich anschließend in das Intermediat $Bi(HPyr)$ umwandelt. Dieses wandelt sich letztendlich in das polymorphe Endprodukt um. Bei der Kristallisation von $Bi(Tri)(H_2O)$ wurden keine kristallinen Intermediate beobachtet. Die EDXRD Untersuchungen zur Bildung von $Bi_2(O)(OH)(HBTC)(NO_3)$ zeigten, dass sich das Intermediat $[(Bi(BTC)(H_2O)] \cdot H_2O$ bildet, dieses sich in die Verbindung $Bi_6O_5(BTC)_2(HBTC)_4$ umwandelt und sich $Bi_2(O)(OH)(HBTC)(NO_3)$ beim Abkühlen der Reaktionsmischung bildet. Die Verbindung $Bi_2(O)(Pyr)(H_2O)$ und die beiden Polymorphe $Bi(HPyr)$ wurden auf ihre Lumineszenz-Eigenschaften untersucht.

Systematic Investigations on Bismuth Tri- and Tetraarylcboxylates: Crystal Structures - *in situ* X-ray Diffraction - Intermediates - Luminescence

Mark Feyand,^[a] Milan Köppen^[a], Gernot Friedrichs^[b] and Norbert Stock^[a]

Abstract: The systematic investigation of the systems Bi³⁺/ carboxylic acid / HNO₃ using the tri- and tetracarboxylic acids pyromellitic (H₄Pyr), trimellitic (H₃Tri) and trimesic (H₃BTC) acid led to the discovery of five new bismuth carboxylates. The structural characterisation allows the establishment of the influence of the linker geometry and the Bi³⁺ : linker molar ratio in the starting solution on the crystal structure. The crystallization of three selected compounds was

investigated by *in situ* energy dispersive X-ray diffraction. Three new crystalline intermediates were observed within minutes and two of them could be isolated by quenching of the reaction mixture. Their crystal structures were determined from laboratory and synchrotron X-ray powder diffraction data which allowed us to establish a possible reaction pathway. In depth characterisation of the luminescence properties of the three bismuth pyromellate compounds was carried out.

Fluorescence and phosphorescence could be assigned to (mainly) ligand and metal based transitions. The polymorphs BiHPyr exhibit different luminescence properties although their structures are very similar. Surprisingly, doping of the three host structures with Eu³⁺ and Tb³⁺ ions was only successful for one of the polymorphs.

Keywords: Bismuth, inorganic-organic hybrid compounds, EDXRD, *in situ*, crystallization.

Introduction

Inorganic-organic hybrid compounds are in the focus of recent research activities due to their interesting sorption,^[1-2] optical,^[3-6] catalytic,^[7-8] or magnetic properties.^[9] While over the last decade most metal ions have been incorporated in this class of materials, only in the last few years bismuth carboxylate based compounds have been reported.^[10-15] These show interesting optical^[10-13, 15] or catalytic properties^[14] and it is surprising that studies dealing with the synthesis of new bismuth carboxylates are very scarce.

Since the synthesis of metal carboxylates from reactants of low solubility can successfully be carried out under solvothermal conditions, leading to a great variety of different products, this method has also been applied to synthesize bismuth carboxylates.^[10-11, 14-16] The reactions are carried out in sealed reactors under autogenous pressure at elevated temperatures above the boiling point of the solvent. It is well known that the synthesis parameters such as temperature, pH or molar ratio of the starting materials have a strong influence on the product formation. The inter-relationship of these parameters is very complex and thus structure prediction is rarely possible. Hence, extensive explorative synthetic work is necessary to obtain highly crystalline and pure compounds. High-throughput (HT) methods have been proven to allow the systematic and efficient investigation of parts of this complex parameter space.^[17-18] Thus, these methods have been used for the systematic study of the influence of the pH,^[19-22] temperature,^[23-24] linker geometry and size,^[25-26] concentration^[21-22] or ionic radii.^[27] In addition to the discovery of new compounds, the systematic

variation of synthesis parameters allowed the establishment synthesis-structure relationships. Although HT methods are very valuable in finding new compounds, no information about the crystallization is obtained and thus a deeper understanding of the processes leading to the final product is not possible.

Recently, numerous methods have been developed to gain more information about the solvothermal crystallization mechanisms of materials.^[28-29] The detection and structural characterization of crystalline intermediates is especially important because their crystal structures represent a local minimum on the energy hypersurface. These minima represent one step of the reaction mechanism and will

[a] M. Feyand, M. Köppen, Prof. N. Stock
Institut für Anorganische Chemie
Christian-Albrechts-Universität zu Kiel
Max-Eyth Straße 2, 24118 Kiel (Germany)
Fax: (+49) 4318801775
E-mail: stock@ac.uni-kiel.de

[b] G. Friedrichs
Institut für Physikalische Chemie
Christian-Albrechts-Universität zu Kiel
Max-Eyth Straße 1, 24118 Kiel (Germany)

Supporting information for this article is available on the WWW under <http://www.chemeurj.org/> or from the author.

help to understand the crystallization. Energy dispersive X-ray diffraction (EDXRD) has widely been applied to follow the crystallization of zeolites, metal phosphonates, metal-organic frameworks or thioantimonates under solvothermal reaction conditions.^[26, 30-35] Thus, it was possible to extract kinetic parameters,^[20, 34, 36] detect crystalline intermediates^[26, 37] or observe phase transformations.^[19, 26, 36]

Here we present the systematic high-throughput investigation of the synthesis of new bismuth carboxylates using pyromellitic, trimellitic and trimesic acid. To obtain a deeper understanding of the crystallisation processes, *in situ* EDXRD studies on three new bismuth carboxylates were carried out.

Results and Discussion

Results of the high-throughput experiments.

In a systematic high-throughput study the three linker molecules pyromellitic acid (H_4Pyr , 1,2,4,5-benzenetetracarboxylic acid), trimellitic acid (H_3Tri , 1,2,4-benzenetricarboxylic acid) and trimesic acid (H_3BTC , 1,3,5-benzenetricarboxylic acid) were used in combination with $Bi(NO_3)_3 \cdot 5H_2O$ to synthesize new bismuth carboxylates. The Bi^{3+} : linker molar ratios were varied from 2:1-0.5:1 with and without the addition of 5 mol equivalent of HNO_3 . All the ratios are based on the amount of the linker, which was kept constant (15 mg). The results of the HT experiment and the results which are based on X-ray powder diffraction measurements, are shown in Fig. 1 and the important inorganic building units are shown in Fig. 2. The use of pyromellitic acid leads to two new compounds. At the molar ratio of 2:1 the compound $Bi_2(O)(Pyr)(H_2O)$ (**1**) is formed while at the lower ratio of 0.5:1 the compound $Bi(HPyr)$ (**3**) is observed. The addition of HNO_3 has no influence on the phases formed. At intermediate molar ratios a mixture of both compounds is observed. The use of trimellitic acid leads to the new compound $Bi(Tri)(H_2O)$ (**4**). The Bi^{3+} : H_3Tri molar

ratio has no influence on the formed product. While in the absence of HNO_3 an unknown impurity with low crystallinity is observed, the addition of 5 mol equivalents of HNO_3 leads to the phase-pure compound **4**. Changing the linker to trimesic acid, the new compound $Bi_2(O)(OH)(HBTC)(NO_3)$ (**8**) is formed as a phase-pure product at the Bi^{3+} : H_3BTC molar ratios of 2:1 in the absence of HNO_3 and 2:1-1:1 with additional HNO_3 . In the absence of additional acid and at molar ratios 1.5-0.5:1 the compound $Bi_6O_5(BTC)_2(HBTC)$ (**7**) is formed as a side-product.

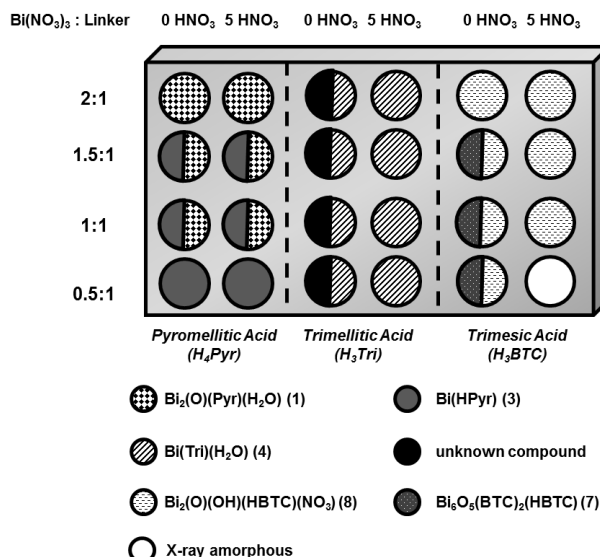


Fig. 1. of the HT experiment derived from X-ray powder diffraction using pyromellitic acid (H_4Pyr , 1,2,4,5-benzenetetracarboxylic acid), trimellitic acid (H_3Tri , 1,2,4-benzenetricarboxylic acid) and trimesic acid (H_3BTC , 1,3,5-benzenetricarboxylic acid) in combination with $Bi(NO_3)_3 \cdot 5H_2O$.

The syntheses of all compounds except of **7** were successfully scaled-up and the crystal structures could be determined by single

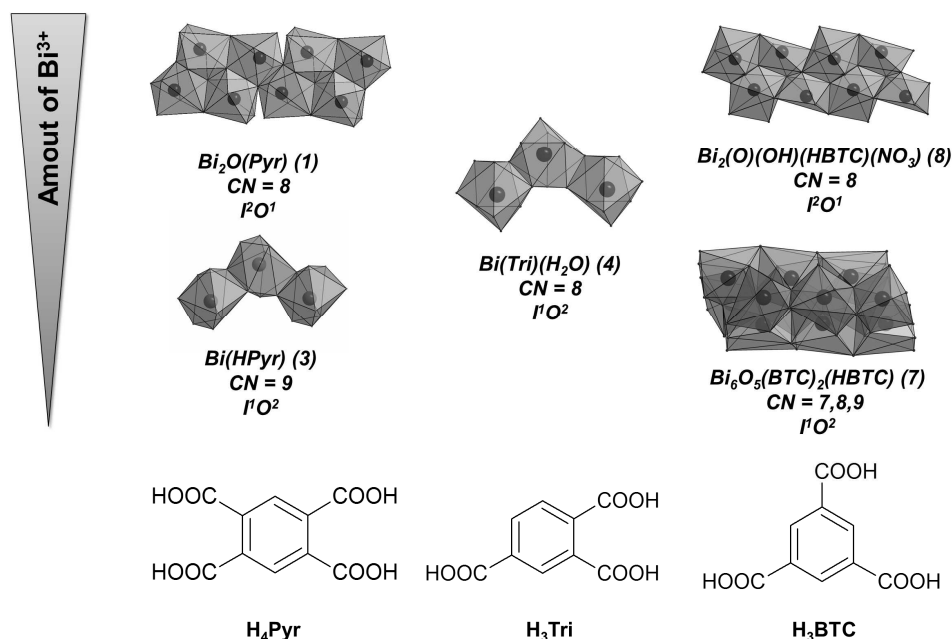


Fig.2 Inorganic structural motifs of compounds **1**, **3**, **4**, **7** and **8** derived from single crystal X-ray diffraction. The crystal structures have been notated as suggested by Cheetham *et al.*^[37]

crystal X-ray diffraction. Suitable crystals were isolated from the HT experiments or the scale-up syntheses. All compounds were characterized by thermogravimetric (TG) analysis, IR-spectroscopy, elemental analysis and X-ray powder diffraction. Details about the structure determination and the crystal structures are given in the experimental section and the supporting information, respectively.

Structural trends and results of the HT experiments

Using H_4Pyr or H_3BTC as the linker molecules and molar ratios of Bi^{3+} : linker $\geq 2 : 1$ lead to structures containing Bi-O-layers (compounds **1** and **8**), while at Bi^{3+} : linker molar ratios $< 2 : 1$ chains of BiO_x -polyhedra are observed (compounds **3** and **7**). A similar inorganic chain of edge-sharing BiO_8 -polyhedra is observed when the linker H_3Tri is employed (compound **4**). Thus, the higher molar ratios lead to the incorporation of more Bi^{3+} ions in the crystal structure. This is also reflected in the higher densities of 4.140 and 3.275 g/cm^3 for **1** and **3** and 4.021 and 3.568 g/cm^3 for **8** and **7**, while compound **4** exhibits a density of 3.174 g/cm^3 (calculated from the crystal structures).

In situ EDXRD studies

To get a better understanding of product formation the crystallization of compounds **3**, **4** and **8** was investigated by EDXRD at 150 °C. For all reactions water was used as the solvent without the addition of HNO_3 . More details about the reaction conditions are given in the experimental section. In EDXRD studies intense white beam synchrotron radiation is employed to achieve a good time resolution (≤ 1 minute) while using conventional reaction vessels in the experiments. The white beam is sufficiently intense to penetrate steel autoclaves and thus reactions can be investigated without imposing an external influence on the reaction mixture provided no beam sensitive solvents are used.^[39] In addition no scanning is needed due to the fixed angle of the solid state detector. For all experiments detector angles of about 2° were used. More details about identification of the phases observed in the EDXRD experiments are given in Table S8. A more quantitative evaluation of the EDXRD measurements including integration of the peaks in order to obtain crystallization curves or to determine kinetic parameter could not be carried out due to the high reaction rates and the overlap of the Bragg peaks of different compounds.

$\text{Bi}(\text{NO}_3)_3$ / pyromellitic acid / H_2O (compound **3**)

The reaction system was investigated at 150 °C by *in situ* EDXRD using a molar ratio Bi^{3+} : H_4Pyr = 1:2. The obtained spectra are represented as a three-dimensional plot in Figure 3. The homogenisation of the reaction mixture leads to an X-ray amorphous precipitate. Immediate upon heating, **1** is observed in the EDXRD spectra. The intensity of the most strongest signal (at 29.54 keV) starts to decrease after 10 minutes and two peaks at 38.12 and 48.64 keV are detected. This transformation is completed after 60 minutes without any further changes during the investigated 8 h of reaction time. *Ex situ* experiments for the synthesis of compound **2** resulted in a highly crystalline phase-pure sample of $\text{Bi}(\text{HPyr})$ (**2**). As an additional result of the study, we were able to isolate the polymorphic compound **3** after a reaction time of 18 - 60 h. *Ex situ* studies showed that without an excess of the linker H_4Pyr , i.e. Bi^{3+} : $\text{H}_4\text{Pyr} < 2 : 1$, compound **1** is the final product after a reaction time of one week.

The crystal structures of **1** and **3** were determined from X-ray single crystal diffraction, but only a microcrystalline product of **2** could be obtained. Thus, the crystal structure had to be determined from X-ray powder diffraction data. The crystal structure determination was accomplished using real space methods as implemented in the program FOX^[40] and the structure was refined by the Rietveld method using Topas Academic.^[41] The final Rietveld plot is shown in Figure 4. Details about the structure determination and refinement are given in the experimental section and in the supporting information.

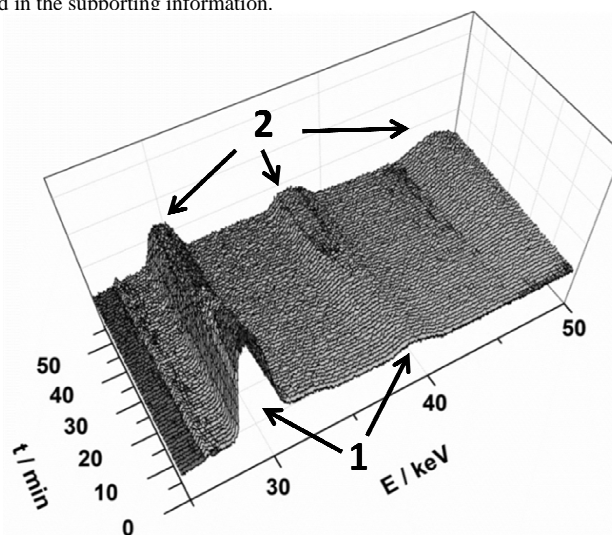


Fig. 3. Three-dimensional representation of the crystallization of **3** in the reaction system $\text{Bi}(\text{NO}_3)_3$ / pyromellitic acid / H_2O at 150 °C. While **3** is only obtained after 16 h, the intermediate phases **1** and **2** are formed in shorter reaction times. See Table S8 in the supporting information for the indexing of the signals.

The inorganic building units of the three compounds obtained during the crystallization experiments are shown in Fig. 5 whilst the crystal structures of the two polymorphs are shown in Fig. 6. More details of the crystal structures are given in the supporting information. $\text{Bi}_2(\text{O})(\text{Pyr})(\text{H}_2\text{O})$ (**1**) (Fig. S1) crystallizes immediately upon heating. The crystal structure of **1** is built-up from face-sharing BiO_8 polyhedra which form Bi_4O_{12} tetrameric units. Edge-sharing of these units by the oxygen atoms of carboxylate groups lead to the formation of layers. The presence of additional linker (H_4Pyr) in the reaction mixture allows the transformation from **1** to $\text{Bi}(\text{HPyr})$ (**2**) to take place. After 18 h the polymorphic compound $\text{Bi}(\text{HPyr})$ (**3**) is observed. The structures of compound **2** and **3** (Fig. S3-S5 and Fig. S7-S9, respectively) contain both chains of face-sharing BiO_8 polyhedra. These chains are connected by the aromatic rings of the pyromellate ions to form a three-dimensional network, while one carboxylate group is protonated and forms $\text{CO}-\text{H}\cdots\text{OC}$ hydrogen bonds. The Bi-O-chains in **2** and **3** differ in the angle of the interconnection of the polyhedra.

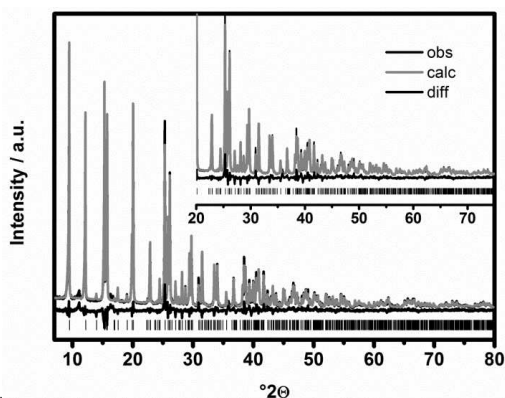


Fig. 4. Final Rietveld plot of the structure refinement of Bi(HPyr) (**2**). The observed powder pattern is shown in black, the calculated powder pattern as an overlay in grey and the difference (observed-calculated) of both is given by the lower black line. The allowed positions of the Bragg peaks are given as tick marks. A wavelength of 1.5406 Å was used.

The density of the **1**, **2** and **3** increases from 2.749 to 3.207 and 3.275 g/cm^3 , respectively, while the space group symmetry decreases from $C2/c$ to $P2_1/a$ and $P-1$. According to Ostwald's step rule compound **3** should be the thermodynamically most stable product. Compound **1** with an I^2O^1 connectivity^[38], which contains a more condensed inorganic building unit than compound **2** and **3** (I^1O^2 connectivity), is less stable under these reaction conditions and transforms into **2**.^[38] In contrast, the transformation from a less to a higher condensed inorganic building unit has been observed for open-framework zinc phosphates.^[42] The transformation of **1** into **2** may occur due to the release of H_2O from the structure on reaction with the ligand, leading to an entropy gain for the system due to the increased degrees of freedom of the H_2O molecule in the solution.

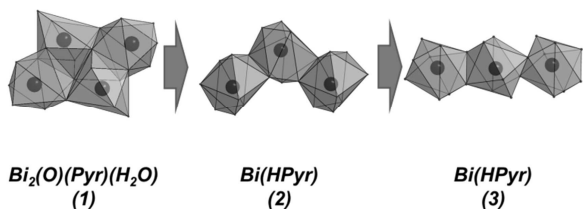


Fig. 5. Inorganic building units of the compounds obtained in the time dependent formation of **3**.

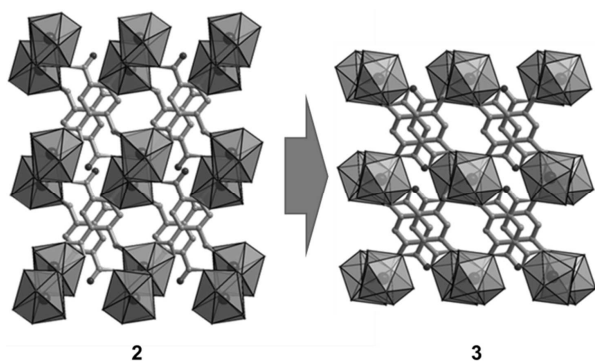


Fig. 6. Crystal structure of the polymorphic compounds **2** and **3**. View along the b -axis. The carbon and oxygen atoms are shown as grey and black spheres, respectively. The BiO_8 polyhedra are given in grey.

$\text{Bi(NO}_3)_3$ / trimellitic acid / H_2O (compound **4**)

The crystallization of $\text{Bi(Tri)(H}_2\text{O)}$ (**4**) was investigated at 150 °C by *in situ* EDXRD (Fig. 7). Compound **4** starts to crystallize after 10 minutes and the reaction is already completed after about 20 minutes. During the first 10 minutes a slightly higher background compared to the final spectra in the region of 35–40 keV is observed that could be explained by the presence of an X-ray amorphous intermediate or precursor. This observation correlates well with the fact that in *ex situ* experiments a white X-ray amorphous precipitate is formed upon mixing of the starting materials at room temperature. Compound **4** persists as the final product even after one week of reaction time.

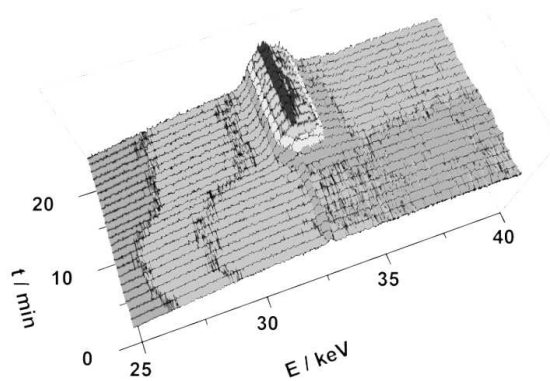


Fig. 7. Three-dimensional representation of the crystallization of $\text{Bi(Tri)(H}_2\text{O)}$ (**4**) at 150 °C.

Dehydration properties

The crystal structure of **4** was determined by single crystal X-ray diffraction. One molecule of water per formula unit is observed (Fig. S17-S19), which coordinates in a terminal manner to the Bi^{3+} ion in the structure. Thermogravimetric measurements (Fig. S23) demonstrate that the water can be removed at 150 °C. The irreversible dehydration at 200 °C for 12 h results in the crystalline compound Bi(Tri) (**5**). The powder pattern (Fig. S21) was successfully indexed using Topas academics and the lattice parameters were refined using the Pawley method ($a = 6.7135(6)$, $b = 19.558(2)$, $c = 6.4222(4)$ Å and $\alpha = 90$, $\beta = 90.23(2)$, $\gamma = 90$ °, chosen space group $P2_1$).^[41] The Pawley fit is shown in the supporting information (Fig. S22). The structure could not be solved from X-ray powder diffraction data.

$\text{Bi(NO}_3)_3$ / trimesic acid / H_2O (compound **8**)

The three-dimensional representation of the crystallization of **8** as studied by EDXRD at a reaction temperature of 150 °C is shown in Figure 8. Already after one minute a crystalline intermediate $[\text{Bi(BTC)(H}_2\text{O)}] \cdot \text{H}_2\text{O}$ (**6**) (I^1O^2 , chains of corner-sharing BiO_8 polyhedra) is observed. Compound **6** transforms after 10 minutes into a second intermediate which could not be isolated. This compound is further transformed after 20 minutes into $\text{Bi}_6\text{O}_5(\text{BTC})_2(\text{HBTC})$ (**7**) (I^1O^2 , chains of corner- and face-sharing

BiO_x polyhedra, x = 7-9) which was previously isolated from HT experiments. No further transformation to compound **8** was detected during the *in situ* EDXRD study. Surprisingly quenching of the reaction mixture led to phase-pure product of **8** (I²O¹, layers of XXX corner- and face-sharing BiO_x polyhedra, x = 6, 8). Apparently upon cooling, **7** transforms into **8** under these reaction conditions.

Intermediate **6** was successfully isolated by quenching of the reaction mixture while similar experiments for the second intermediate exclusively resulted in yet another new phase in mixtures with compound **6** or **8**. The crystal structure of the [Bi(BTC)(H₂O)]·H₂O (**6**) was determined from high resolution X-ray powder diffraction data measured at beamline P08 at PETRA, HASYLAB, DESY. The structure determination was accomplished by using real space methods as implemented in the program FOX.^[40] The crystal structure was refined by the Rietveld method as implemented in Topas Academics.^[41] The final Rietveld plot is shown in Fig. 9 and detailed structural description of compounds **6**, **7** and **8** are given in the supporting information in the Figures S25-S27, S28-S30 and S32-S34, respectively. The inorganic building units of **6** - **8** are given in Fig. 10.

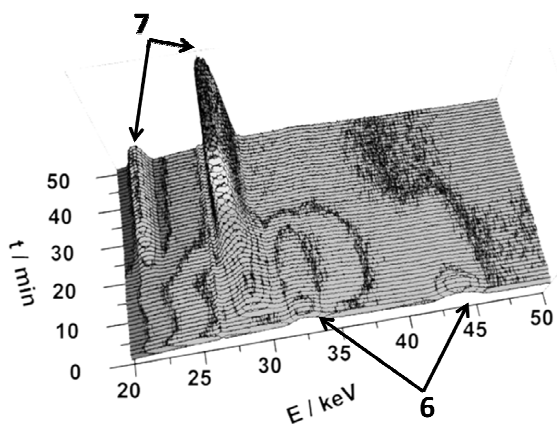


Fig. 8. Three-dimensional representation of the crystallization in the system Bi(NO₃)₃ / H₃BTC / H₂O at 150 °C. See Table S8 in the supporting information for the indexing of the signals.

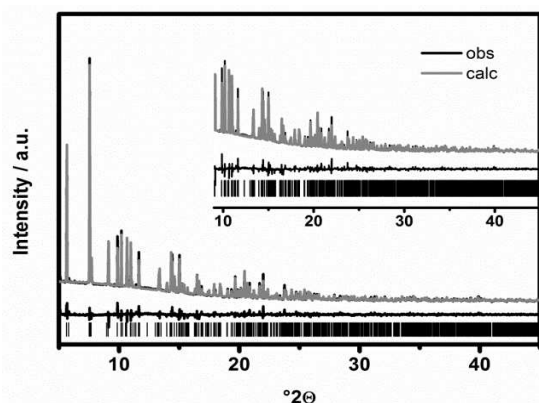


Fig. 9. Final Rietveld plot of compound [Bi(BTC)H₂O]·H₂O (**6**). The observed powder pattern is shown in black, the calculated powder pattern as an overlay in grey and the difference (observed-calculated) of both is given by the lower black line. The allowed

positions of the Bragg peaks are given as tick marks. A wavelength of 0.825986 Å was

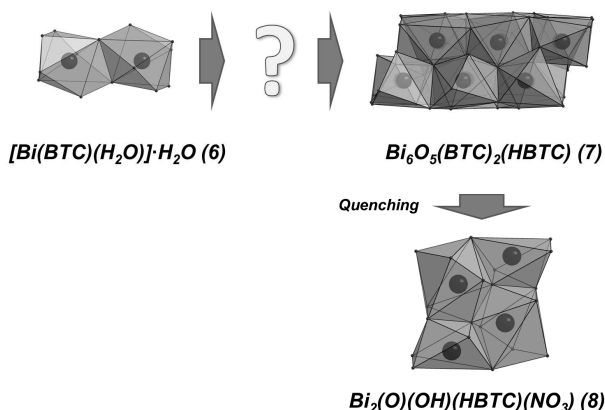


Fig. 10. Reaction pathway derived from the *in situ* and *ex situ* experiments.

Summary of the *in situ* experiments

The *in situ* EDXRD experiments have shown that bismuth carboxylates crystallize with very short reaction times. In addition, crystalline intermediates are often observed. Our results suggest that due to the long reaction times - usually days, up to a week - commonly used in the synthesis of bismuth carboxylates, metastable intermediates have been overlooked. Re-investigation of these systems should therefore be undertaken.

Characterization of compound 1-8

In order to learn more about the thermal stability, TG analyses were carried out. The TG measurements and their interpretation for compound **1-4**, **6-8** are given in the supporting information (Fig. S11-S13, S23 and S36-S37). The observed weight losses are summarized in Table 1. All compounds containing water molecules show a weight loss at temperatures between 40 °C and 200 °C and all compounds start to decompose between 340 °C and 380 °C.

Table 1. Weight losses observed during the thermogravimetric analyses of compound **1-4** and **7, 8**.

compound	loss of water	decomposition of the framework
1	40-180 °C	350 °C
2	-	360 °C
3	-	380 °C
4	150-200 °C	340 °C
6	80-150 °C	380 °C
7	40-120 °C	360 °C
8		300 °C

All compounds were also characterized by IR-spectroscopy. The IR-spectra and their interpretation are given in the supporting information (Fig. S14-S16, S24 and S38-S39). All compounds show characteristic broad bands in the region of 2500-3400 cm^{-1} which can be assigned to O-H vibrations of the water molecules. Between 1550 to 1560 cm^{-1} the asymmetric stretching vibrations of the carboxylate groups and in the range of 1400-1480 cm^{-1} the symmetric stretching vibration are observed. The aromatic C-C stretching vibrations are observed in the range of 1480-1500 cm^{-1} and the symmetric and asymmetric aromatic C-H deformation vibrations are observed in the range between 760-870 cm^{-1} .

Luminescence properties and doping experiments of 1 - 3

Bi^{3+} containing solids are well known as materials with distinct luminescence properties. The physical reasons for the large Stokes shifts that are highly dependent on the crystal structure and the composition of the host lattice, the unique temperature dependences of the emission lifetimes, typically on the order of 10^{-3} s at low and 10^{-7} - 10^{-5} s at high temperatures, as well as the spectroscopic assignment of the two distinct often observed emission bands in the visible luminescence spectra have been thoroughly discussed in the literature.^[43-47] Usually, the spectroscopy of Bi^{3+} with s^2 in the ground and sp configuration in the first excited state is discussed in terms of Russell-Saunders type electronic energy terms. The energetically lowest possible $^3\text{P}_0 \leftarrow ^1\text{S}_0$ excitation is strongly forbidden. Therefore, the $^3\text{P}_1 \leftarrow ^1\text{S}_0$ transition, which is possible due to spin-orbit coupling of the $^3\text{P}_1$ and $^1\text{P}_1$ states, is observed as the so-called A band. Following absorption, fast non-radiative relaxation and equilibration of the Bi^{3+} system into the $^3\text{P}_0$ and $^3\text{P}_1$ levels is assumed with the $^3\text{P}_0$ level acting as a metastable trapping state.^[43, 48] The ratio of the population of both states strongly depends on the temperature, and emission from both states is possible. Typically, at high temperatures the fast $^3\text{P}_1 \rightarrow ^1\text{S}_0$ emission dominates, however, at lower temperatures the observed excited state lifetimes steadily increase and reach plateau values on the order of 10^{-3} s. The corresponding slow emission component can be assigned to the highly forbidden $^3\text{P}_0 \rightarrow ^1\text{S}_0$ transition. In most cases, due to broad bands and the rather small $^3\text{P}_0$ - $^3\text{P}_1$ energy splitting, the two emission bands are not resolved in the spectra. Nevertheless two separate luminescence bands are often observed. These two bands exhibit similar luminescence decay behaviour and have been frequently ascribed to result from rather complex Jahn-Teller effects.^[45, 48-50]

The three pyromellitic acid based compounds **1-3** were selected for the detailed investigation of their photoluminescence characteristics in order to study the influence of the crystal structure. Especially the properties of **2** and **3** in comparison with **1** were of interest since the former two compounds are polymorphs with very similar crystal structures. Therefore, excitation and emission spectra of the observed short-lived (as of now termed fluorescence) and long-lived (as of now termed phosphorescence) spectral components have been recorded. Upon excitation with a standard UV lamp at a wavelength of 254/366 nm, **1** and **2** show strong blue luminescence colour and **3** a pale green. The resolved luminescence spectra are illustrated in Figures 11-13.

In all three cases, a short-lived fluorescence band centred at 430-470 nm and a second red-shifted long-lived phosphorescence band centred at 490-530 nm was observed. The splitting will be discussed below. The respective, markedly different fluorescence and phosphorescence excitation spectra of **1** and **2** suggest that two

different emission centres are responsible for the two luminescence components. Note that the maxima of the two excitation spectra are shifted by approximately 20 nm for **1** and that the two-peak phosphorescence excitation feature of **2** can in fact be explained by a single broad absorption band of the one luminescent centre peaking around 340 nm with a pronounced intensity reduction arising from the strongly interfering absorption of the other luminescent centre at 330 nm. Due to the overall lower luminescence of **3** and the much stronger spectral overlap of the fluorescence and phosphorescence band, the temporal and spectral separation of the bands was experimentally more demanding and the interpretation of the obtained spectra is less clear. Both fluorescence and phosphorescence excitation spectra are very similar, nevertheless a good quality phosphorescence spectrum could be obtained by excitation at 275 nm and detection at 560 nm.

The phosphorescence bands have been further analyzed by recording intensity decay curves (see Figures S40-S44 in the supporting information) and luminescence lifetimes have been extracted by fitting biexponential functions. The fast decay component with lifetimes of 49-113 μs were close to the time resolution of the applied spectrophotometer and may be ascribed to residual signal from the underlying fluorescence band. The long decay components yielded lifetimes of $\tau = 1.1$ ms, 0.84 ms and 1.80 ms for **1**, **2** and **3**, respectively.

We attribute the short-lived components peaking at 430-470 nm to intraligand luminescence from ($\pi^* \rightarrow \pi$) or ($n \rightarrow \pi^*$) transitions of the pyromellate ions. Both the maxima of the fluorescence excitation spectra at 320-340 nm and the observed Stokes shifts of 110-130 nm are consistent with the 320 nm maximum and 115 nm Stokes shift measured for alkaline aqueous solutions of the pure pyromellitic acid (Fig. S45). Bi^{3+} ions give rise to the second luminescent centre causing the long-lived luminescence peaking at 490-530 nm. Again, both the maxima of the phosphorescence excitation spectra at 320-360 nm (A band absorption) and the large observed Stokes shifts of 170-190 nm are consistent with observations in other Bi^{3+} containing systems.^[43, 47-48, 51] According to the literature, the measured long luminescence decay times on the order of $\tau_{\text{slow}} = 1$ ms reflect

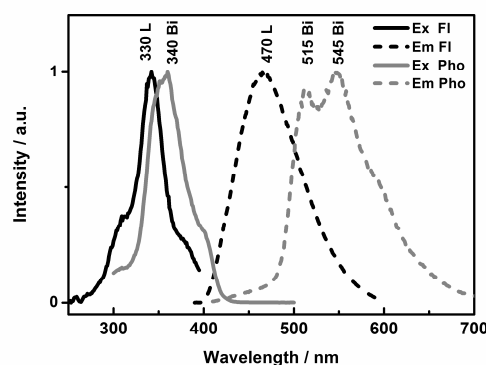


Figure 11. Luminescence spectra of compound **1**. The fluorescence (fl) excitation and emission spectra were measured with $\lambda_{\text{excitation}} = 310$ nm and $\lambda_{\text{emission}} = 460$ nm, respectively. The phosphorescence excitation and emission spectra were measured with $\lambda_{\text{excitation}} = 360$ nm and $\lambda_{\text{emission}} = 515$ nm, respectively. L refers to the luminescence of the linker ion.

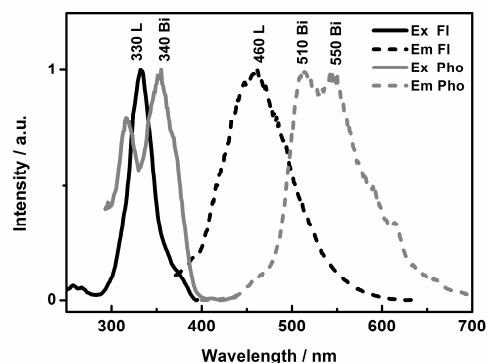


Figure 12. Luminescence spectra of compound **2**. The fluorescence excitation and emission spectra were measured with $\lambda_{\text{excitation}} = 330$ nm and $\lambda_{\text{emission}} = 460$ nm, respectively. The phosphorescence excitation and emission spectra were measured with $\lambda_{\text{excitation}} = 355$ nm and $\lambda_{\text{emission}} = 515$ nm, respectively. L refers to the luminescence of the linker ion.

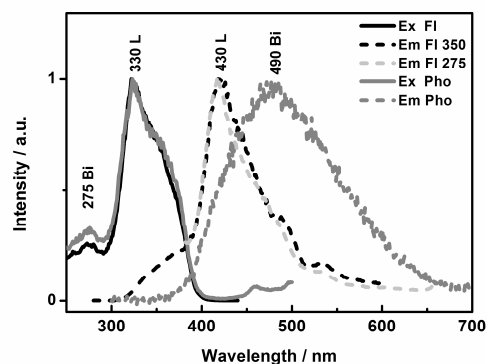


Figure 13. Luminescence spectra of compound **3**. The fluorescence excitation and emission spectra were measured with $\lambda_{\text{excitation}} = 275$ or 350 nm and $\lambda_{\text{emission}} = 430$ nm, respectively. The phosphorescence excitation and emission spectra were measured with $\lambda_{\text{excitation}} = 275$ nm and $\lambda_{\text{emission}} = 560$ nm, respectively. L refers to the luminescence of the linker ion.

the lifetime of the 3P_0 state. However, to the best of our knowledge, such long decay times have as yet only been reported at very low temperatures. Typically, at room temperature the population of and equilibration with the 3P_1 state is significant and hence much shorter decay times are observed. Thus, the high τ_{slow} values obtained in this work may reflect a larger energetic 3P_1 - 3P_0 separation or a slow equilibration of both states by non-radiative processes. Within uncertainty limits, the decay times observed at both maxima of the double-peak feature observed for **1** and **2** are identical and it may be speculated whether the two bands, which are separated by 30-40 nm, arise from simultaneous 3P_1 - 1S_0 and 3P_0 - 1S_0 emission. In this case, the ratio of the two peaks should show significant temperature dependence. However, test measurements performed by heating the samples up to 80°C did not change the ratios and therefore we conclude that the splitting is more likely due to the presence of the above-mentioned Jahn-Teller distortions. In summary the very similar compounds **2** and **3** show different luminescence properties whereas the compounds **1** and **2** with no obvious relations between their crystal structures yield similar spectra.

Bismuth-containing materials are known to be good hosts for lanthanide ions inducing sensitized luminescence.^[10-11, 15] We were

only able to dope compound **3** using 2 mol% of Eu^{3+} and Tb^{3+} . Only short reaction times of 12 h (compared to 92h) lead to the incorporation of lanthanide ions in the crystal structure. The amount of Eu^{3+} and Tb^{3+} ions was determined by EDX analyses by comparison of $\text{Eu}_L / \text{Bi}_L$ lines yielding an amount of 4 % Eu^{3+} and Tb^{3+} . The luminescence spectra of the doped compound **3** are shown in Figure 14. The Tb^{3+} doped compound shows the characteristic $^5D_4 \rightarrow ^7F_J$ transitions and the Eu^{3+} doped compound the typical $^5D_0 \rightarrow ^7F_J$ transitions that are responsible for the observed green and red luminescence. Very similar results have been observed for other Tb^{3+} - and Eu^{3+} -doped bismuth carboxylates.^[10-11, 15]

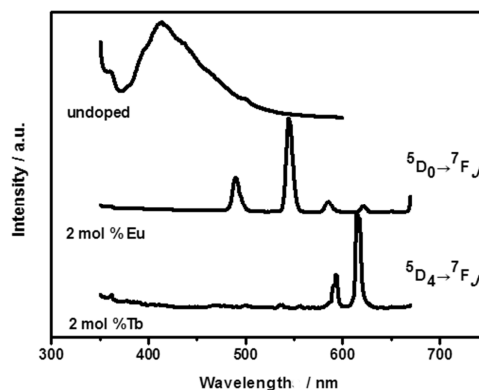


Figure 14. Luminescence spectra ($\lambda_{\text{excitation}} = 320$ nm) of the doped and undoped compound **3**.

Conclusion

High-throughput experiments allowed the rapid and efficient discovery of five new bismuth carboxylates. The reaction conditions as the molar ratio of metal : linker plays a crucial role in determining which compound is stable. In combination, *in situ* EDXRD allowed us to get a deeper insight in the crystallization of bismuth carboxylates, including the identification and characterization of crystalline intermediates. The crystallization of bismuth carboxylates shows that intermediates might be present that can be isolated by quenching or are only stable in solution. The different crystallization mechanisms proceed without intermediate (**4**) or through two intermediates (**3,7**), showing that even for very similar reaction systems no predictions can be made. A better understanding of the crystallization processes requires more *in situ* studies, including the characterization of metastable intermediates. For intermediates that are only stable in the reaction mixture high resolution PXRD data must be collected *in situ* for structure determination. The luminescence properties of bismuth carboxylates are dominated by a combination of a short-lived linker luminescence and a long-lived Bi^{3+} luminescence. Exceptionally long Bi^{3+} emission decay times of about 1 ms have been observed at room temperature.

Experimental Section

All chemicals were obtained by Aldrich or ABCR and were used without further purification. XRPD measurements were carried out on a Stoe Stadi P diffractometer in transmission geometry with $\text{Cu-K}\alpha_1$ radiation, equipped with an image plate detector. The MIR spectra were recorded on a Bruker ALPHA-P FT-IR spectrometer in the spectral range 4000 - 400 cm^{-1} . For the thermogravimetric analyses under air a NETSCH

STA 409 CD analyzer was used with a heating rate of 4 K/min and an air flow rate of 75 ml/min. Electron microscopy was carried out on a Phillips XL ESEM. High resolution powder XRD patterns were measured at beamline P08 PETRA at HASYLAB, DESY, Hamburg. Syntheses were carried out under solvothermal conditions using DURAN culture tubes D50 GL 14 M.KAP, SCHOTT 261351155. Elemental Analyses were carried out on a Eurovektor EA.

High-throughput (HT) experiments: The system $\text{Bi}^{3+} / \text{L} / \text{HNO}_3$ with $\text{L} =$ pyromellitic acid or trimellitic acid or trimesic acid in water was investigated by using HT methods. A custom-made HT reactor containing 24 PTFE liners, each with a maximum volume of 2 mL, was used.^[17, 52] The amount of the respective organic linker molecule was fixed at 15 mg each. Eight reactions with different molar ratios of $\text{Bi}^{3+} / \text{L}$ were carried out for each linker with and without the addition of 5 mol equiv. of 2 M HNO_3 solution. The solids were added to the reactors and 1 ml of water and the HNO_3 solution were added to the reaction mixture, homogenized by shaking, and heated in 1 h to 150 °C, held at that temperature for 18 h, and then cooled down to room temperature in 6 h. The products were filtered off, washed with water, and DMF (DMF = N,N-dimethylformamide) dried in air and characterized by XRPD measurements. Details of the exact amounts used are given in supporting information Table S1.

In situ crystallization experiments: EDXRD experiments were carried out at HASYLAB, beamline F3 at DESY, Hamburg, Germany. The white beam synchrotron radiation (4 to 55 keV) was detected by a liquid nitrogen cooled germanium semiconductor detector system. The detector angle was set to approximately 1.9°. The best results were obtained by collimating the beam to 0.2 x 0.2 mm². To heat the samples a custom made reactor system heated by an external thermostat (JULABO) was used. The reaction temperature of the reaction mixture is achieved within 2 minutes.^[50] The reaction conditions for the *in situ* experiments were derived from the high-throughput experiments.

In situ EDXRD of the system $\text{Bi}(\text{NO}_3)_3 / \text{pyromellitic acid} / \text{H}_2\text{O}$: 50 mg (0.197 mmol) pyromellitic acid (H_2Pyr) and 47.7 mg (0.0983 mmol) ground $\text{Bi}(\text{NO}_3)_3 \cdot 5\text{H}_2\text{O}$ were combined with 2 ml of distilled water in a Schott Duran glass reactor. The reaction was carried out in a preheated custom made reactor system under stirring at 150 °C.^[30]

In situ EDXRD of the system $\text{Bi}(\text{NO}_3)_3 / \text{trimellitic acid} / \text{H}_2\text{O}$: 30 mg (0.142 mmol) trimellitic acid (H_3Tri) and 34.6 mg (0.071 mmol) ground $\text{Bi}(\text{NO}_3)_3 \cdot 5\text{H}_2\text{O}$ were combined with 2 ml of distilled water in a Schott Duran glass reactor. The reaction was carried out in a preheated custom made reactor system under stirring at 150 °C.^[30]

In situ EDXRD of the system $\text{Bi}(\text{NO}_3)_3 / \text{trimesic acid} / \text{H}_2\text{O}$: 30 mg (0.142 mmol) trimellitic acid (H_3BTC) and 69.2 mg (0.142 mmol) ground $\text{Bi}(\text{NO}_3)_3 \cdot 5\text{H}_2\text{O}$ were combined with 2 ml of distilled water in a Schott Duran glass reactor. The reaction was carried out in a preheated custom made reactor system under stirring at 150 °C.^[30]

Luminescence Measurements: Luminescence measurements were recorded on Xenon flash lamp based Varian/Agilent CARY Eclipse fluorescence spectrophotometer with a spectral resolution of about 5 nm. Time-resolved emission spectra were measured by sequentially off-setting the gate time of the detector relative to the flash lamp. Mainly determined by the minimum gate width, the time resolution was limited to about 40 μs . Time-delayed emission spectra (phosphorescence) were measured with a preset delay and gate time of 0.2 and 5 ms, respectively. All reported spectra are corrected for instrumental spectral response and are normalized with respect to the occurring maximum intensity.

Synthesis of $\text{Bi}_2(\text{O})(\text{Pyr})(\text{H}_2\text{O})$ (1) The amounts of the starting materials used in the *in situ* experiments of the system $\text{Bi}(\text{NO}_3)_3 / \text{pyromellitic Acid} / \text{H}_2\text{O}$, i.e. a molar ratio $\text{Bi}(\text{NO}_3)_3 : \text{pyr} = 2:1$, were used in Duran Schott culture tubes in a custom made aluminium autoclave placed on a heated stirrer at 150 °C. The reactions mixture was quenched after 2 minutes by immersing the glass vessel into ice water. The white microcrystalline precipitate was filtered and washed with DMF and water. Suitable single crystals of **1** can be obtained by mixing 20.0 mg (0.79 mmol) pyromellitic acid and 76.3 mg (0.157 mmol) $\text{Bi}(\text{NO}_3)_3 \cdot 5\text{H}_2\text{O}$ ($\text{Bi}(\text{NO}_3)_3 : \text{pyr} = 2:1$) and 1 ml of water in a 2 ml high-throughput Teflon vessel. The reaction was heated up to 150 °C in 14 h, the temperature was held for 60 h and the reaction mixture was cooled down to room temperature in 48 h. The product was filtered and washed with 1 ml of DMF and 1 ml of water. White single crystals were obtained. Phase-purity was confirmed by X-ray diffraction (Fig. S2) and elemental analyses. (obs. C 16.91 %, H 0.90 %, calc. based on $\text{Bi}_2\text{O}(\text{C}_{10}\text{H}_2\text{O}_8)(\text{H}_2\text{O})$ C 16.27 %, H 1.09 %)

Synthesis of $\text{Bi}(\text{HPyr})$ (2): 50 mg (0.197 mmol) pyromellitic acid (H_2Pyr) and 47.7 mg (0.0983 mmol) ground $\text{Bi}(\text{NO}_3)_3 \cdot 5\text{H}_2\text{O}$ were combined with 2 ml of distilled water in a Schott Duran glass reactor. The mixture was heated up to 150 °C in a custom made aluminium autoclave placed on a heated stirrer. The reaction was quenched after 50 min by putting the glass vessel into ice water. The product was filtered off and washed with DMF and water. A white microcrystalline powder was obtained. Phase-purity was confirmed by X-ray powder diffraction (Fig. S6) and elemental analyses (obs. C

26.20 %, H 0.63 %, calc. based on $\text{Bi}(\text{C}_{10}\text{H}_2\text{O}_8)$ C 26.10 %, H 0.66 % (yield 28.9 mg (32 %, based on H_2Pyr)).

Synthesis of $\text{Bi}(\text{HPyr})$ (3): 250 mg (0.984 mmol) pyromellitic acid (H_2Pyr) and 954 mg (1.96 mmol) of $\text{Bi}(\text{NO}_3)_3 \cdot 5\text{H}_2\text{O}$ were combined in a 23 ml Teflon lined steel reactor and 9.5 ml of distilled water were added. The mixture was heated up to 150 °C in 1 h, the temperature was held for 48 h and subsequently cooled down to room temperature in 12 h. The product was filtered and washed with 10 ml of DMF and 10 ml of water. A white powder was obtained with a yield of 577 mg 79 % based on H_2Pyr . The phase-purity was confirmed by elemental analyses (Obs. C 26.49 %, H 0.54 %, calc. based on $\text{Bi}(\text{C}_{10}\text{H}_2\text{O}_8)$ C 26.10 %, H 0.66 %) and X-ray powder diffraction (Fig. S10).

Synthesis of $\text{Bi}(\text{Tri})(\text{H}_2\text{O})$ (4): 150 mg (0.714 mmol) 1,3,5-benzenetricarboxylic acid (H_3BTC) and 346.2 mg (0.714 mmol) of $\text{Bi}(\text{NO}_3)_3 \cdot 5\text{H}_2\text{O}$ were added to a 23 ml Teflon lined steel reactor. 8.21 ml distilled water and 1.79 ml 2M HNO_3 were added and the reactor was sealed. The reaction mixture was heated to 150 °C and kept at this temperature for 12 h. After cooling to room temperature the resulting product was filtered and washed with DMF and water. 237.5 mg of a white powder were obtained yield 76.6% based on H_3BTC . The phase-purity was confirmed by X-ray powder diffraction (Fig. S20) and elemental analysis (obs. C 24.90 %, H 1.16 % calc. based on $\text{Bi}(\text{C}_9\text{H}_3\text{O}_6)(\text{H}_2\text{O})$ C 25.26 %, H 1.16 %).

Synthesis of $\text{Bi}(\text{Tri})$ (5): Compound **5** was obtained by heating compound **4** at 200 °C for 15 h. A comparison of the powder patterns of **4** and **5** is given in the supporting information in Fig. S21.

Synthesis of $(\text{Bi}(\text{BTC})(\text{H}_2\text{O})) \cdot \text{H}_2\text{O}$ (6): Compound **6** was obtained by quenching the reaction mixture of the *in situ* experiments of the system $\text{Bi}(\text{NO}_3)_3 / \text{trimesic Acid} / \text{H}_2\text{O}$ after 5 minutes at 150 °C. The precipitate was filtered off and washed with DMF and water.

Synthesis of $\text{Bi}_6\text{O}_5(\text{BTC})_2(\text{HBTC})$ (7): 150 mg (0.714 mmol) 1,3,5-benzenetricarboxylic acid (H_3BTC) and 346.2 mg (0.714 mmol) $\text{Bi}(\text{NO}_3)_3 \cdot 5\text{H}_2\text{O}$ were combined in a 23 ml Teflon lined steel reactor with 9.64 ml of distilled water and 0.357 ml 2 M NaOH. The reactor was sealed and the mixture was heated up to 150 °C in 24 h, the temperature was held for 60 h and the reaction mixture was cooled down to room temperature in 48 h. The product was filtered off and washed with 10 ml of DMF and 10 ml of water. 239.7 mg of a white powder was obtained. The product was identified as compound **6** with the presence of a unknown impurity (Fig. S31).

Synthesis of $(\text{Bi}_2(\text{O})(\text{OH})(\text{HBTC})(\text{NO}_3))$ (8): Larger amounts of **8** could be obtained by using 150 mg (0.714 mmol) 1,3,5-benzenetricarboxylic acid (H_3BTC) and 692 mg (1.43 mmol) $\text{Bi}(\text{NO}_3)_3 \cdot 5\text{H}_2\text{O}$ in 10 ml water in a 23 ml Teflon lined steel reactor. The reaction mixture was heated up to 150 °C in 24 h. The temperature was held for 48 h and the reaction mixture was cooled to room temperature in 12 h. The precipitate was filtered off and washed with DMF and water. Phase-purity was confirmed by XRPD (Fig. S35) and elemental analyses. (obs. C 14.99 %, H 0.70 %, N 1.94 % calc. based on $\text{Bi}_2\text{O}(\text{OH})(\text{C}_9\text{H}_3\text{O}_6)(\text{NO}_3)$ C 15.23 %, H 0.60 %, N 2.03 %) The compound could also be obtained quenching the reaction mixture of the *in situ* experiments of the system $\text{Bi}(\text{NO}_3)_3 / \text{trimesic acid} / \text{H}_2\text{O}$ after 20 minutes.

Synthesis of the doped compound **3.** 250 mg (0.984 mmol) pyromellitic acid (H_2Pyr), 233.8 mg (1.96 mmol) of $\text{Bi}(\text{NO}_3)_3 \cdot 5\text{H}_2\text{O}$ and 98 μL of 0.1 M $\text{Tb}(\text{NO}_3)_3$ or $\text{Eu}(\text{NO}_3)_3$ solution were combined in a 23 ml Teflon lined steel reactor and 9.9 ml of distilled water were added. The mixture was heated at 150 °C for 12 h. The product was filtered and washed with 10 ml of DMF and 10 ml of water.

Crystal structure determination

The crystal structures of **1**, **3**, **4**, **7**, **8** were determined from single crystal X-ray diffraction data. X-ray diffraction measurements were performed on a Stoe IPDS diffractometer equipped with and image plate detector using Mo $K\alpha$ radiation ($\lambda = 71.073$ pm). The crystal structures were solved by direct methods with the program SHELXS-97 and refined using the program SHELXL-97.^[54] H-atoms connected to carbon atoms were placed onto calculated positions. H-atoms of the water molecules could not be localized in the difference Fourier maps. The OH^- and O^{2-} ions were distinguished by comparison of the bond geometry and the bond lengths with the literature known crystal structure of the basic bismuth nitrate ($[\text{Bi}_6(\text{H}_2\text{O})(\text{NO}_3)_4(\text{OH})_4](\text{NO}_3)_5$).^[55] For all compounds numerical absorption correction were carried out using XShape and XRed.^[56] The crystals of compound **4** and **7** were merohedrally twinned and were refined using the BASF and TWIN command implemented in ShelXL.^[54] The crystal structures of **2** and **6** were determined from X-ray powder diffraction data. The powder patterns were measured on a Panalytical empyrean diffractometer equipped with a PixCell detector system using $\text{Cu } K\alpha_{1,2}$ radiation and at beamline P08, PETRA, DESY, Hamburg with a wavelength of 0.825986 Å using a Mythen detector. The powder patterns were indexed using Topas

academic.^[41] The crystal structures were solved using FOX starting with one independent bismuth atom and one linker molecule for compound **2** and an additional water molecule for compound **6**.^[40] The crystal structures were refined by the Rietveld method using Topas academic.^[41] The final Rietveld plots are given in Fig. 4 and 9. The important crystallographic parameters are summarized in the supporting information. The Cambridge Crystallographic Data Center (CCDC) 930908 – 930913 and 930927 contains the supplementary crystallographic data for this paper. These data can be obtained free of charge via the Internet at www.ccdc.cam.ac.uk/conts/retrieving.html (or from the CCDC, 12 Union Road, Cambridge CB2 1EZ, U.K; fax,+ 44 1223 36033; e-mail, deposit@ccdc.ac.uk).

Acknowledgements

We thank Dr. Michael Wharmby for the assistance with the powder data analyses and revision of the manuscript, Dr Christian Näther and Inke Jess for the single crystal X-ray diffraction measurements and the helpful discussions, Prof. Bensch and group for the support in the *in situ* experiments, the Ralph Norwid Schindler Stiftung for making available the fluorescence spectrophotometer, the Land Schleswig-Holstein and the SPP 1415 "Kristalline Nichtgleichgewichtsphasen" for the financial support.

- [1] J.-R. Li, R. J. Kuppler, H.-C. Zhou, *Chem. Soc. Rev.* **2009**, *38*, 1477-1504.
- [2] N. L. Rosi, J. Eckert, M. Eddaoudi, D. T. Vodak, J. Kim, M. O'Keeffe, O. M. Yaghi, *Science* **2003**, *300*, 1127-1129.
- [3] Y. Cui, Y. Yue, G. Qian, B. Chen, *Chem. Rev.* **2011**, *112*, 1126-1162.
- [4] M. D. Allendorf, C. A. Bauer, R. K. Bhakta, R. J. T. Houk, *Chem. Soc. Rev.* **2009**, *38*, 1330-1352.
- [5] M. Maes, F. Vermoortele, L. Alaerts, S. Couck, C. E. A. Kirschhock, J. F. M. Denayer, D. E. De Vos, *J. Am. Chem. Soc.* **2010**, *132*, 15277-15285.
- [6] P. Horcajada, T. Chalati, C. Serre, B. Gillet, C. Sebrie, T. Baati, J. F. Eubank, D. Heurtaux, P. Clayette, C. Kreuz, J.-S. Chang, Y. K. Hwang, V. Marsaud, P.-N. Bories, L. Cynober, S. Gil, G. Férey, P. Couvreur, R. Gref, *Nature Mater.* **2010**, *9*, 172-178.
- [7] D. Farrusseng, S. Aguado, C. Pinel, *Angew. Chem. Int. Ed.* **2009**, *48*, 7502-7513.
- [8] J. Lee, O. K. Farha, J. Roberts, K. A. Scheidt, S. T. Nguyen, J. T. Hupp, *Chem. Soc. Rev.* **2009**, *38*, 1450-1459.
- [9] M. Kurmoo, *Chem. Soc. Rev.* **2009**, *38*, 1353-1379.
- [10] A. Thirumurugan, A. K. Cheetham, *Eur. J. Inorg. Chem.* **2010**, *2010*, 3823-3828.
- [11] A. Thirumurugan, J.-C. Tan, A. K. Cheetham, *Cryst. Growth Des.* **2009**, *10*, 1736-1741.
- [12] A. C. Wibowo, S. A. Vaughn, M. D. Smith, H.-C. zur Loye, *Inorg. Chem.* **2010**, *49*, 11001-11008.
- [13] A. C. Wibowo, M. D. Smith, H.-C. zur Loye, *CrystEngComm* **2011**, *13*, 426-429.
- [14] M. Feyand, E. Mugnaioli, F. Vermoortele, B. Bueken, J. M. Dieterich, T. Reimer, U. Kolb, D. de Vos, N. Stock, *Angew. Chem.* **2012**, *124*, 10519-10522.
- [15] A. Thirumurugan, W. Li, A. K. Cheetham, *Dalton Trans.* **2012**, *41*, 4126-4134.
- [16] A. T. Davies, G. Sankar, C. R. A. Catlow, S. M. Clark, *J. Phys. Chem. B* **1997**, *101*, 10115-10120.
- [17] H. Reinsch, N. Stock, *Micropor. Mesopor. Mater.*
- [18] E. Biemmi, S. Christian, N. Stock, T. Bein, *Micropor. Mesopor. Mater.* **2009**, *117*, 111-117.
- [19] C. Schmidt, M. Feyand, A. Rothkirch, N. Stock, *J. Solid State Chem.* **2012**, *188*, 44-49.
- [20] C. Schmidt, N. Stock, *Cryst. Growth Des.* **2011**, *11*, 5682-5687.
- [21] N. Stock, T. Bein, *Angew. Chem.* **2004**, *116*, 767-770.
- [22] P. M. Forster, N. Stock, A. K. Cheetham, *Angew. Chem.* **2005**, *117*, 7780-7784.
- [23] S. Bauer, N. Stock, *Angew. Chem.* **2007**, *119*, 6981-6984.
- [24] A. Sonnauer, N. Stock, *Eur. J. Inorg. Chem.* **2008**, *2008*, 5038-5045.
- [25] P. Maniam, N. Stock, *Inorg. Chem.* **2011**, *50*, 5085-5097.
- [26] C. Schmidt, M. Feyand, A. Rothkirch, N. Stock, *J. Solid State Chem.* **2012**, *188*, 44-49.
- [27] P. Maniam, C. Näther, N. Stock, *Eur. J. Inorg. Chem.* **2010**, *2010*, 3866-3874.
- [28] N. Pienack, W. Bensch, *Angew. Chem. Int. Ed.* **2011**, *50*, 2014-2034.
- [29] M. P. Attfield, P. Cubillas, *Dalton Trans.* **2012**, *41*, 3869-3878.
- [30] L. Engelke, M. Schaefer, M. Schur, W. Bensch, *Chem. Mat.* **2001**, *13*, 1383-1390.
- [31] R. Kiebach, N. Pienack, W. Bensch, J. D. Grunwaldt, A. Michailovski, A. Baiker, T. Fox, Y. Zhou, G. R. Patzke, *Chem. Mat.* **2008**, *20*, 3022-3033.
- [32] B. Seidlhofer, E. Antonova, J. Wang, D. Schinkel, W. Bensch, *Z. Anorg. Allg. Chem.* **2012**, *638*, 2555-2564.
- [33] R. El Osta, M. Frigoli, J. Marrot, M. E. Medina, R. I. Walton, F. Millange, *Cryst. Growth Des.* **2012**, *12*, 1531-1537.
- [34] F. Millange, R. El Osta, M. E. Medina, R. I. Walton, *CrystEngComm* **2011**, *13*, 103-108.
- [35] F. Millange, M. I. Medina, N. Guillou, G. Férey, K. M. Golden, R. I. Walton, *Angew. Chem.* **2010**, *122*, 775-778.
- [36] M. Feyand, C. Nather, A. Rothkirch, N. Stock, *Inorg. Chem.* **2010**, *49*, 11158-11163.
- [37] M. Feyand, A. Hübner, A. Rothkirch, D. S. Wragg, N. Stock, *Inorg. Chem.* **2012**, *51*, 12540-12547.
- [38] A. K. Cheetham, C. N. R. Rao, R. K. Feller, *Chem. Comm.* **2006**, *0*, 4780-4795.
- [39] D. S. Wragg, P. J. Byrne, G. Giriat, B. L. Ouay, R. Gyepes, A. Harrison, A. G. Whittaker, R. E. Morris, *J. Phys. Chem. C* **2009**, *113*, 20553-20558.
- [40] V. Favre-Nicolin, R. Cerny, *J. Appl. Crystallogr.* **2002**, *35*, 734-743.
- [41] A. Coelho, Coelho Software **2007**.
- [42] R. I. Walton, A. J. Norquist, S. Neeraj, S. Natarajan, C. N. R. Rao, D. O'Hare, *Chem. Comm.* **2001**, *0*, 1990-1991.
- [43] G. Boulon, B. Moine, J. C. Bourcet, R. Reisfeld, Y. Kalisky, *J. Luminescence* **1979**, *18/19*, 924-928.
- [44] G. Boulon, C. K. Jørgensen, R. Reisfeld, *Chem. Phys. Lett.* **1980**, *75*, 24-26.
- [45] D. M. A. Ranfagni, M. Bacci, G. Viliiani, P. Fontana, *Adv. Phys.* **1983**, *32*, 823-905.
- [46] A. A. Setlur, A. M. Srivastava, *Opt. Mater.* **2006**, *29*, 410-415.
- [47] C. W. M. Timmermanns, G. Blasse, *J. Solid State Chem.* **1984**, *52*, 222-232.
- [48] J.-G. Kang, H.-M. Yoon, G.-M. Chun, Y.-D. Kim, T. Tsuboi, *J. Phys. Condens. Matter* **1994**, *6*, 2101-2116.
- [49] A. Fukuda, *Phys. Rev. B* **1970**, *1*, 4161-4178.
- [50] G. Blasse, *Mater. Chem. Phys.* **1987**, *16*, 201-236.
- [51] K. Polák, E. Miháková, *Opt. Mater.* **2010**, *32*, 1280-1282.
- [52] N. Stock, *Micropor. Mesopor. Mater.* **2010**, *129*, 287-295.
- [53] A. Sonnauer, F. Hoffmann, M. Fröba, L. Kienle, V. Duppel, M. Thommes, C. Serre, G. Férey, N. Stock, *Angew. Chem. Int. Ed.* **2009**, *48*, 3791-3794.
- [54] G. M. Sheldrick, Siemens Analytical X-ray Instruments Inc.: Madison, WI, **1992**.
- [55] F. Lazarini, *Acta Crystallogr. Sect. B* **1979**, *35*, 448-450.
- [56] XShape and XRed, Stoe and Cie, Darmstadt, Germany, **1998**.

6 | Strukturlösung von anorganisch-organischen Hybridverbindungen

Die im Folgenden vorgestellten Ergebnisse behandelten die Kristallstrukturbestimmung von anorganisch-organischen Hybridverbindungen auf Basis von Metallcarboxylaten, Metalltetrazolaten und Zinkimidazolaten. Hierfür wurden sowohl Röntgen-Einkristallstrukturanalysen, Strukturlösungen aus Röntgenpulverdaten, Kraftfeldrechnungen, sowie Rietveld-Verfeinerungen verwendet.

6.1. Ergebnisse der Strukturlösungen von anorganisch-organischen Hybridverbindungen

6.1.1. CAU-3: A new family of porous MOFs with a novel Al-based brick: $[\text{Al}_2(\text{OCH}_3)_4(\text{O}_2\text{C-X-CO}_2)]$ (X = aryl)

Der folgende Artikel wurde in der Zeitschrift *Dalton Transaction* im Jahr 2012 veröffentlicht und behandelte die Synthese und Strukturlösung einer neuen "Familie" (genannt CAU-3) an Metall-organischen Gerüstverbindungen (reproduced with permission from RSC, *Dalton Trans.*, **2012**, 41, 4164-4171).^[203]

Es wurden drei neue isoretikuläre Verbindungen in dem System Al^{3+} / Aryldicarbonsäure / NaOH / Methanol unter Verwendung von den Linkern Aminoterephthalsäure ($\text{H}_2\text{BDC-NH}_2$), Terephthalsäure (H_2BDC) und Naphthalindicarbonsäure (H_2NDC) synthetisiert. Die Synthesen der Verbindungen wurden mittels Hochdurchsatzmethoden optimiert und die Verbindungen mittels Thermogravimetrie, IR- und Raman-Spektroskopie und Sorptionsmessungen charakterisiert. Die Kristallstruktur der Verbindung $[\text{Al}_2(\text{OCH}_3)_4\text{BDC}]$ wurde aus Pulverdaten gelöst und verfeinert. Die Struktur konnte in der rhomboedrischen Raumgruppe $R\bar{3}m$ mittels direkter Methoden gelöst, mittels Kraftfeldrechnungen komplettiert und mit der Rietveld-Methode verfeinert werden. Die Strukturen der Verbindungen $[\text{Al}_2(\text{OCH}_3)_4\text{NDC}]$ und $[\text{Al}_2(\text{OCH}_3)_4\text{BDC-NH}_2]$ wurden mittels Kraftfeldrechnungen aus

dem vorher erhaltenen Strukturmodell modelliert und mit der Rietveld-Methode erfolgreich verfeinert. Hierbei erniedrigt sich die Symmetrie der Struktur von CAU-3-NDC zu $R\bar{3}$, da die Symmetrie des Naphthalindicarboxylat-Ions nicht mit der Spiegelebene in der Elementarzelle zu vereinbaren ist. Die CAU-3 Verbindungen sind aus $[Al_{12}(OCH_3)_{24}]^{12+}$ Clustern aufgebaut und werden durch die jeweiligen Aryldicarboxylationen zu dem **fcu** Netzwerk verknüpft.

CAU-3: A new family of porous MOFs with a novel Al-based brick: [Al₂(OCH₃)₄(O₂C-X-CO₂)] (X = aryl)[†]

Helge Reinsch, Mark Feyand, Tim Ahnfeldt and Norbert Stock*

Received 21st October 2011, Accepted 7th December 2011

DOI: 10.1039/c2dt12005d

A new family of Al-based MOFs denoted as CAU-3 (CAU = Christian-Albrechts-Universität) was discovered in the solvothermal system Al³⁺/aryldicarboxylic acid/NaOH/methanol by applying high-throughput-methods. The three compounds reported in this article [Al₂(OCH₃)₄BDC], [Al₂(OCH₃)₄BDC-NH₂] and [Al₂(OCH₃)₄NDC] (BDC = 1,4-benzenedicarboxylate; NDC = 2,6-naphthalenedicarboxylate) are all based on the same unprecedented inorganic building unit [Al₁₂(OCH₃)₂₄]¹²⁺, which is a dodecameric cyclic aluminium-methanolate-cluster. The material CAU-3-NDC was found to exhibit the highest surface area as well as the highest micropore volume of all Al-based MOFs reported until now.

Introduction

During the past few years, the research on highly porous MOFs with tailored properties has become a main objective for scientists in the field of porous materials.^{1–5} This relatively new class of materials is built up from inorganic vertices, most often metal ions or cationic metal-oxo-clusters, which are connected to each other using polytopic organic linker-molecules. These organic parts of the network usually consist of organic anions often bearing carboxylate- or phosphonate-groups. To create pores by separating the inorganic vertices from each another, the linker molecule is often based on a rigid aromatic unit like benzene or naphthalene. Once the reaction conditions for the formation of such a hybrid compound are known, similar reaction parameters should in principle allow the incorporation of further functionalized and also larger organic molecules into the structure, while keeping the inorganic brick unchanged. This approach towards the synthesis of new compounds is commonly referred to as isorecticular synthesis.⁶ There are only few examples for the synthesis of isorecticular families of MOFs, consisting of more than two materials based on the same inorganic building unit.^{7–12} An example is the MIL-88-series, which is based on dicarboxylate ions but contains trimeric M(III)₃-μ₃O⁷⁺-clusters, where M(III) stands for a Cr³⁺ or Fe³⁺. These compounds exhibit enormous changes in their lattice parameters, depending not only upon the metal ion (Fe³⁺, Cr³⁺) and the dicarboxylate-molecule, but also

on the presence and the nature of guest molecules inside the pores.⁹ Another example was reported for the Zr⁴⁺-based MOFs called UiO-66, -67, and 68.^{10,11} In this case, Zr₆O₄(OH)₄¹²⁺-clusters are twelvefold connected by linear dicarboxylate ions to form a **fcu**-net, which corresponds to a fcc-packing of inorganic building blocks. Due to their outstanding chemical stability, the functionalized analogues of the UiO-66 (based on 1,4-benzenedicarboxylate) have shown to be ideal candidates for further post-synthetic modification reactions.¹²

One reason for this limited number of examples is due to the complexity of solvothermal reactions. Small changes of the organic linker molecule have often a strong influence on the solubility as well as the acid–base and the coordination properties. Thus, the reaction conditions have to be established and optimized for each organic linker molecule separately. In this context, high-throughput-methods have proven to be a highly valuable tool for the intentional synthesis of MOFs.^{13,14} Applying this methodology, we were recently able to synthesize the amino-functionalized Al-MIL-53,¹⁵ a MOF with lozenge-shaped channels bearing NH₂-groups which can be further chemically modified, and Cr-MIL-101-NDC,¹⁶ which exhibits giant pores with a diameter of 4.6 nm. The miniaturization of the reaction vessels, the parallelization of the synthesis and the automated characterization open the opportunity to screen even complex reaction systems with large parameter-spaces. Therefore, chemical trends can be easily identified, and synthesis parameters can be rapidly optimized with a rather low consumption of starting materials.

Recently we have started a systematic high-throughput investigation on the role of the solvent in the synthesis of Al-based MOFs. In contrast to MOFs based on divalent cations, only few Al-based MOFs have been reported in the literature since mostly very small μm-sized crystals have been obtained, which complicates the structure determination. The frameworks of these known porous Al-MOF structures contain only six different

Christian-Albrechts-Universität zu Kiel, Institut für Anorganische Chemie, Max-Eyth-Str. 2, 24118 Kiel, Germany. E-mail: stock@ac.uni-kiel.de; Fax: +49 431 8801775; Tel: +49 431 8801675

[†]Electronic supplementary information (ESI) available: Crystallographic data, details of the Rietveld refinements and further XRPD data, selected bond lengths, TG curves. CCDC reference numbers 799242–799244 for CAU-3-NDC, CAU-3-BDC, and CAU-3-BDC-NH₂, respectively. For ESI and crystallographic data in CIF or other electronic format see DOI: 10.1039/c2dt12005d

Al–O bricks.^{17–23} This rather limited number of structures is in sharp contrast to the diversity of polynuclear species that are known from the solvolysis reactions of aluminium salts.^{24,25} For this reason, the field of Al³⁺-based MOFs still is a promising chemical system for the discovery of new materials. Due to the high thermal and chemical stability of the known Al-based MOFs, as well as to the cost-effective availability of the usually nontoxic starting materials, these yet unknown compounds could be of high interest for commercial applications.

Especially linear dicarboxylic acids have shown to be useful for the synthesis of isoreticular compounds, not only but also due to the commercial availability of a variety of dicarboxylic acids with different size and functionalization. In combination with one-dimensional chains of corner-sharing AlO₆-octahedra, several porous compounds based on the MIL-53 structure are known, showing interesting sorption behaviour as well as high thermal stabilities.^{26–30} Another example for a dicarboxylate-based Al-MOF is CAU-1, which contains twelvefold connected octanuclear Al-oxo-clusters.^{23,31} Herein we report the synthesis and characterization of a new family of porous MOFs based on linear aryldicarboxylate ions, which contain the novel dodecameric Al-based brick [Al₁₂(OCH₃)₂₄]¹²⁺.

Experimental

Materials and methods

Chemicals. AlCl₃·6H₂O (Riedel-de Haen, ≥99%), Al(NO₃)₃·9H₂O (Merck, ≥99%), H₂BDC (Aldrich, ≥98%), H₂BDC-NH₂ (Fluka, ≥98%), NaOH (Baker, ≥97%), methanol (BASF, purum), and *N,N*-dimethyl-formamide (BASF, tech.) were used as purchased. 2,6-Naphthalenedicarboxylic acid was synthesized by hydrolysis of dimethyl 2,6-naphthalenedicarboxylate (Aldrich, 98%).

Methods. Most reactions were carried out using our 24-high-throughput reactor system.³² The upscaled synthesis was performed in custom made Teflon inserts in steel autoclaves with a volume of 30 mL. The high-throughput X-ray analyses were performed in transmission geometry using a STOE HT powder diffractometer equipped with a xy-stage and an image plate detector (IPDS) system (Cu-Kα1 radiation). Temperature dependent X-ray powder diffraction (XRPD) data was measured on a STOE Stadi-P diffractometer in transmission geometry equipped with an image plate detector (IPDS) using Cu-Kα1 radiation. High-precision X-ray powder diffraction data for the structure solution was collected on a STOE Stadi-P powder diffractometer equipped with a linear position sensitive detector (PSD) system (monochromated Cu-Kα1 radiation) in transmission geometry. XRPD data for the structure refinement was recorded on a Panalytical X-pert Highscore diffractometer in reflection-geometry. MIR spectra were recorded on an ATI Matheson Genesis spectrometer in the spectral range of 4000–400 cm⁻¹ using the KBr disk method. FT-Raman spectra were recorded on a Bruker IFS 66 FRA 106 in the range of 0–3300 cm⁻¹ using a Nd/YAG-Laser (1064 nm). The thermogravimetric analyses were recorded using an NETZSCH STA 409 CD analyzer. The samples were heated in Al₂O₃ crucibles at a rate of 4 K min⁻¹ under a flow of air (25 ml min⁻¹). The TG data were corrected for buoyancy and

current effects. The molecular modelling software used was Materials Studio 5.0.³³ Sorption experiments were performed using a BEL JAPAN INC. Belsorp_{max}.

Synthesis and high-throughput-investigations

Discovery and synthesis optimisation of CAU-3-BDC, [Al₂(OCH₃)₄BDC]. The compound CAU-3-BDC (**1**) was discovered in a high throughput-experiment using AlCl₃·6H₂O, terephthalic acid (H₂BDC), methanol and 2 M methanolic NaOH as starting materials. After the reaction at 125 °C for 5 h, the tendencies in the product formation shown in Fig. 1 could be observed. Exact amounts of starting materials can be found in Table S5.† The molar ratio Al³⁺:H₂BDC was kept constant at 4, the absolute amount of starting material was increased from row to row and from column to column, the amount of base was raised.

The compound was obtained from a highly diluted basic solution. Under more acidic and more concentrated conditions the well known compounds CAU-1 and MIL-53 are formed. Furthermore an unknown product of very low crystallinity was observed. Although the material obtained under these conditions already exhibited a remarkable porosity (apparent specific surface area of A_{BET} ~1200 m² g⁻¹), the crystallinity of the sample was rather low. A detailed high-throughput-investigation (~200 reactions) led to an improved synthesis procedure for CAU-3-BDC and the crystallinity was improved substantially. Therefore, the Al³⁺-source was varied (nitrate, chloride and perchlorate), as well as the molar ratios and the absolute amounts of starting materials. We also investigated the influence of H₂O on the product formation. While the use of Al(ClO₄)₃·9H₂O or the addition of small amounts of water led to the formation of X-ray amorphous products or Al₂O₃, we observed highest crystallinity only for very small concentrations of H₂BDC and large excess of Al(NO₃)₃·9H₂O and NaOH. To achieve an optimum of crystallinity we also varied the heating program. The progress during this synthesis optimization is visualized in Fig. 2.

The optimized synthesis procedure of **1** in the 24 reactor system is as follows: a mixture of Al(NO₃)₃·9H₂O (45.2 mg, 0.120 mmol), terephthalic acid (H₂BDC; 2.5 mg, 0.015 mmol) and a solution of NaOH in methanol (2 M, 60 μL, 0.120 mmol) was suspended in methanol (1.340 mL). The reactor was heated up to 125 °C in 12 h. The temperature was held for 5 h and the reactor was allowed to cool down to room temperature in 4 h.

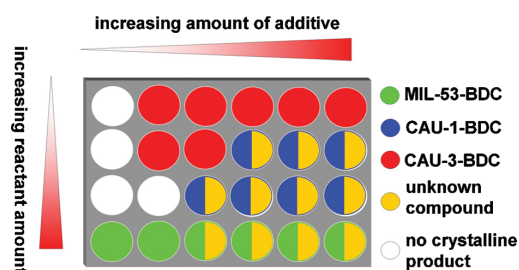


Fig. 1 Results of the high-throughput investigation for the discovery of CAU-3-BDC.

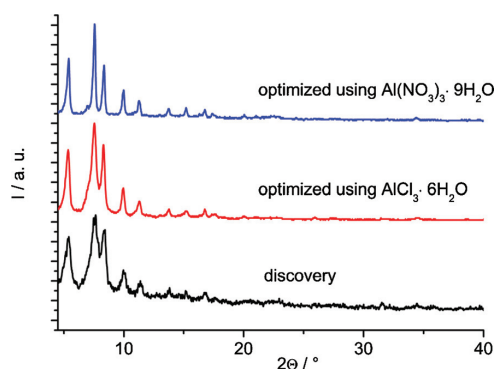


Fig. 2 Improvement of the crystallinity of the products during the HT-assisted synthesis optimization.

Scale-up of the reaction was performed in a 30 mL custom-made autoclave with Teflon insert. For this synthesis, the reaction parameters were stepwise adjusted to the larger reactor.

$\text{Al}(\text{NO}_3)_3 \cdot 9\text{H}_2\text{O}$ (540 mg, 1.44 mmol), H_2BDC (40 mg, 0.240 mmol) and a solution of NaOH in methanol (2 M, 720 μL , 1.44 mmol) were suspended in methanol (16.0 mL). The reactor was heated up to 125 °C in 12 h. The temperature was held for 3 h and the reactor was allowed to cool down to room temperature in 1 h.

After the filtration, a white microcrystalline powder was obtained. Thermogravimetric analysis and TEM-images revealed, that a large amount of an X-ray amorphous byproduct was formed. To remove this byproduct, 100 mg of the reaction product were treated with 10 mL of DMF in a microwave oven (Biotage Initiator) at 150 °C for 1 h under stirring. To remove the DMF, the filtrated solid was treated with 10 mL methanol and heated up in the microwave oven to 100 °C for 1 h. The product was dried at room temperature in air, and further activated under vacuum for the sorption experiments (160 °C/12 h/0.1 mbar). Since the crystallinity slightly decreases during this process (Fig. S1), the structure solution and refinement were performed using the XRPD measurements of the “as synthesized” compound. All other analytical data was measured for the activated product stored under ambient conditions prior to the measurements.

Elemental analysis on an activated sample: found: C: 35.43%, H: 4.07%. Calculated values, based on the deduced formula $[\text{Al}_2(\text{OCH}_3)_4(\text{O}_2\text{CC}_6\text{H}_4\text{CO}_2)] \cdot 3.6\text{H}_2\text{O}$: C: 35.4%, H: 5.7%.

Discovery and synthesis optimisation of CAU-3-BDC-NH₂, $[\text{Al}_2(\text{OCH}_3)_4\text{BDC-NH}_2]$. Starting from the optimized reaction conditions for **1**, the synthesis of the amino-functionalized analogue CAU-3-BDC-NH₂ (**2**) was attempted. Surprisingly, the reaction conditions are very similar. For the optimized synthesis of **2** in the multiclave, a mixture of $\text{Al}(\text{NO}_3)_3 \cdot 9\text{H}_2\text{O}$ (52 mg, 0.139 mmol), 2-aminoterephthalic acid ($\text{H}_2\text{BDC-NH}_2$, 2.5 mg, 0.014 mmol) and a 2 M solution of NaOH in methanol (69 μL , 0.138 mmol) were suspended in methanol (1.330 mL). The reactor was heated up to 125 °C in 8 h. The temperature was held for 6 h and the reactor was allowed to cool down to room temperature in 1 h.

For the up-scaling of the reaction we used again our 30 mL custom-made autoclave with a Teflon insert. For this synthesis, $\text{Al}(\text{NO}_3)_3 \cdot 9\text{H}_2\text{O}$ (540 mg, 1.44 mmol), $\text{H}_2\text{BDC-NH}_2$ (40 mg, 0.220 mmol) and a solution of NaOH in methanol (2 M, 720 μL , 1.44 mmol) were suspended in methanol (16.0 mL). The reactor was heated up to 125 °C in 12 h. The temperature was held for 3 h and the reactor was allowed to cool down to room temperature in 1 h.

After the filtration, a yellow microcrystalline product was obtained. Thermogravimetric measurements revealed the presence of an X-ray amorphous byproduct, which was removed by applying the same procedure as for CAU-3-BDC. The crystallinity of CAU-3-BDC-NH₂ decreased slightly during this treatment (Fig. S2†). Therefore, XRPD data of the as-synthesized product was used for the structure refinement while all other analytical data was measured for the activated material. Elemental analysis on an activated sample (160 °C/12 h/0.1 mbar) stored under ambient conditions: found: C: 31.02%, H: 3.81%, N: 1.96%; These values differ from the assumed formula $[\text{Al}_2(\text{OCH}_3)_4(\text{O}_2\text{C-C}_6\text{H}_3\text{NH}_2\text{-CO}_2)] \cdot 3.6\text{H}_2\text{O}$ which are calculated to be: C: 34.1%, H: 5.7%, N: 3.3%. After dissolution in $\text{D}_2\text{O}/\text{NaOD}$ we observed in the NMR-spectrum, that CAU-3-NH₂ not only contains aminoterephthalate ions, but also terephthalate anions and N-methylated aminoterephthalate ions. We attribute the discrepancy between the experimental values and the ideal formula to this *in situ* conversion of the linker and to small amounts of X-ray amorphous Al-species (see also TG-measurement). Further investigations of this phenomenon are in progress.

Discovery and synthesis optimisation of CAU-3-NDC, $[\text{Al}_2(\text{OCH}_3)_4\text{NDC}]$. The synthesis of CAU-3-NDC (**3**) needed much more effort, since it is highly sensitive to every single parameter during the synthesis, and every small change leads to the formation of crystalline byproducts, whose structures and compositions are a subject of current research. Without the use of high-throughput-methods, optimization of the synthesis conditions (~800 reactions) would have been hardly possible. Due to the large number of reactions that were performed, a detailed description of the HT-investigations is not given. The varied parameters comprise the Al^{3+} -source (nitrate, chloride and perchlorate) and the molar ratios and absolute amounts of starting materials. Due to the sensitivity of the reaction towards the thermal process, the chemical composition of the starting mixture had to be screened using different heating programs. This finally led to the optimized synthesis of **3** in the 24 reactor system, which is as follows: a mixture of $\text{AlCl}_3 \cdot 6\text{H}_2\text{O}$ (29.3 mg, 0.12 mmol), 2,6-naphthalenedicarboxylic acid (H_2NDC ; 7.5 mg, 0.03 mmol) and a 2 M solution of NaOH (52 μL , 0.1 mmol) in methanol was suspended in methanol (448 μL) and heated to 130 °C in 1 h. The temperature was kept for 4 h and the reactor was allowed to cool down in 1 h. The white, as-synthesized product contains traces of sodium chloride (see also structure refinement) and X-ray amorphous byproducts like residual linker molecules in the pores. EDX measurements showed molar ratios of Al: Cl ranging from 2.5 to 3. IR-spectroscopy proved the presence of residual naphthalene dicarboxylic acid. Elemental analysis on a thermally activated sample (160 °C/12 h/0.1 mbar) stored under ambient conditions prior to the measurement:

found: C: 47.97%, H: 3.81%. Calculated values, based on the ideal formula $[\text{Al}_2(\text{OCH}_3)_4(\text{O}_2\text{CC}_{10}\text{H}_6\text{CO}_2)]$: C: 48.9%, H: 4.6%. Although these values are in quite good agreement, the described material still contains the mentioned byproducts.

All measurements were performed with the as-synthesized microcrystalline product. The only activation step for the sorption measurements was heating under vacuum, which hardly influences the crystallinity (Fig. S3†). Several attempts were made, to perform a scale-up of the synthesis and to further activate the as-synthesized compound. The products of the synthesis in larger reactors exhibit a much lower specific surface area, although, based on the XRPD measurements, no differences were observed. Further activation steps were attempted in several solvents, but the raw material decomposes in water, DMF and even ethanol. The solvent treatment in methanol led only to a reduction of the amount of chloride ions.

The absolute amounts synthesized are in all three cases quite low. In the case of CAU-3-BDC and CAU-3-BDC-NH₂, we usually obtain ~25 mg of fully activated sample from one up-scaled reaction. One reason is the low overall concentration of the linker molecule that is necessary to obtain the title compounds. The other reason is the elaborate activation procedure to remove the X-ray amorphous byproducts. In the case of CAU-3-NDC, around 8 mg are obtained from one HT-reaction.

Structure determination and refinement

The experimental XRPD pattern of CAU-3-BDC was successfully indexed with Topas Academics³⁴ as a hexagonal crystal system with the lattice parameters $a = 21.0480(4)$ Å and $c = 34.8305(7)$ Å with a goodness of fit of 23. Based on the extinction conditions, the rhombohedral space group $R\bar{3}m$ was suggested by the program. The structure solution was carried out successfully with the Expo2004³⁵ software package using Direct Methods. Starting from the space group $R\bar{3}m$, the positions of the aluminum based brick were determined. By recycling these fragments in a new intensity extraction, in addition parts of the BDC²⁻ ion were localized. This starting model was completed by force field calculations with the software package Forcite implemented in Materials Studio 5.0.³³ For the calculations, the universal force field was used without an optimization of the cell parameters. The completed model was refined with Rietveld techniques using Topas Academics.³⁴ The final Rietveld refinement involved 15 background parameters, 15 atomic parameters, 4 temperature factors, 1 scale factor and 2 cell parameters. The peak shape was modeled using a Pearson VII function and anisotropic peak broadening effects were taken into account using a spherical harmonics series. The C–C distances and the C–O distances of the methoxy groups were restrained. The final Rietveld plot shown in Fig. 3 led to satisfying structural model indicators ($R_{\text{Bragg}} = 0.4\%$, $R_{\text{wp}} = 4.76\%$ and $\text{GoF} = 1.64$). Selected bond lengths and the asymmetric unit can be found in the supporting informations in Fig. S4 and Table S1,† respectively.

The structural model of CAU-3-BDC was used for the Rietveld refinement of CAU-3-BDC-NH₂. The difference Fourier calculations showed electron densities at a distance of 1.5 Å from the lateral carbon atoms of the phenyl ring. Assigning these electron densities to a nitrogen atom with a site occupation of 0.25 led to a significant lowering of the R -values R_{bragg} and R_{wp}

by 1 and 0.5%. The results of the final Rietveld refinement are shown in Fig. S5.† The C–C distances, C–O distances of the methoxy groups as well as the C–N distances were restrained and an overall temperature factor was used. The refinement led to good structure indicators of $R_{\text{Bragg}} = 0.59\%$, $R_{\text{wp}} = 4.17\%$ and $\text{GoF} = 1.71$. Selected bond lengths are given in Table S2.†

The indexing and lattice parameter refinement of the experimental powder pattern of **3** was carried out with the Stoe WinXPow software package.³⁶ The hexagonal cell parameters $a = 23.1533(5)$ Å and $c = 40.4120(9)$ Å were obtained. For the construction of a model of CAU-3-NDC, we started from the structure of CAU-3-BDC. The space group was converted to $P1$ and the terephthalate ions were replaced by naphthalene dicarboxylate ions after adjusting the cell parameters to the ones obtained from the indexing process, using Materials Studio 5.0. The model was submitted to a full energy minimization without an optimization of the unit cell constants with the universal force field (UFF) implemented in the software. For this simulation, the aluminum atoms were replaced by iron due to their very similar ionic radii (0.67 vs. 0.69) and the missing parameters for octahedrally coordinated aluminum in the parameter set. Van der Waals interactions were represented by a classical 12-6 Lennard Jones potential. The convergence criteria were set to 1.0×10^{-4} kcal mol⁻¹ and 0.005 kcal mol⁻¹ Å⁻¹ and 5.0×10^{-5} Å (displacement) respectively. The obtained structural model possesses lower symmetry than the parent-structure CAU-3-BDC and exhibits the space group $R\bar{3}$, due to the break of the symmetry caused by the naphthalene dicarboxylate ions (atomic coordinates and a simulated powder pattern of this model can be found in Table S3 and Fig. S6†). This structural model was used to carry out the Rietveld refinement. Due to the lower crystallinity and the two-fold number of atomic parameters caused by the lower symmetry, the atomic positions of the NDC²⁻ ions were restrained and an overall temperature factor was used. The final refinement leads to satisfying structure indicators ($R_{\text{Bragg}} = 4.47\%$, $R_{\text{wp}} = 9.41\%$ and $\text{GoF} = 4.80$). The final Rietveld plot is shown in Figure S7† and selected bond lengths are given in Table S4.† Two reflections at 32.62° and 45.42° are observed which are due to NaCl as an impurity. The final parameters of all three refinements are summarized in Table 1.

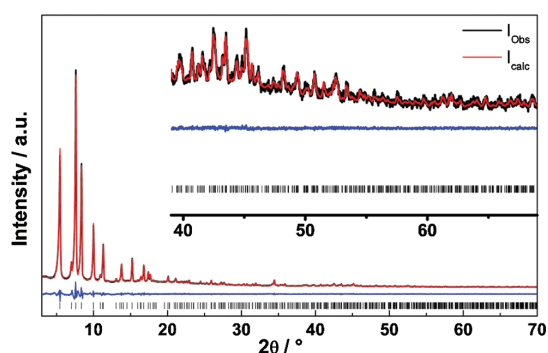
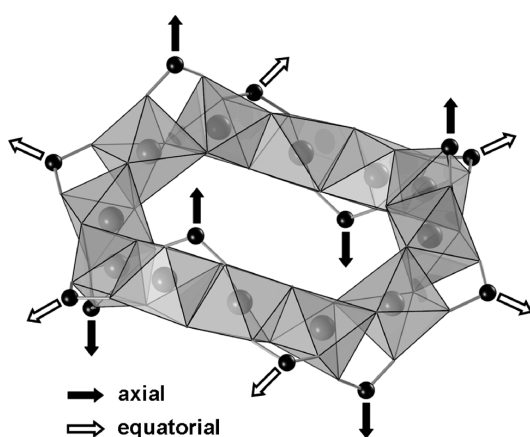


Fig. 3 Final Rietveld-plot for **1**. Measured intensities are in black, calculated intensities are in red, the difference plot is blue. The vertical bars mark the Bragg-positions.

Table 1 Final parameters obtained from the Rietveld-refinements

	CAU-3-BDC	CAU-3-BDC-NH ₂	CAU-3-NDC
Empirical formula	Al ₂ O ₈ C ₁₂ H ₁₆	Al ₂ O ₈ C ₁₂ N ₁ H ₁₇	Al ₂ O ₈ C ₁₆ H ₁₈
M g mol ⁻¹	342.21	357.23	368.25
Crystal system	Rhombohedral	Rhombohedral	Rhombohedral
Space group	<i>R</i> 3̄ <i>m</i>	<i>R</i> 3̄ <i>m</i>	<i>R</i> 3̄
<i>a</i> /pm	2110.51(5)	2093.5(1)	2320.56(2)
<i>c</i> /pm	3488.8(1)	3481.3(2)	4063.51(4)
<i>V</i> /10 ⁶ pm ³	13458.1(8)	13214(1)	18950.(3)
<i>Z</i>	18	18	18
<i>R</i> _{wp} /%	4.76	4.17	9.41
<i>R</i> _{Bragg} /%	0.4	0.59	4.47
GoF	1.64	1.71	4.8
weighted Durbin-Watson statistic	0.594	0.312	0.120

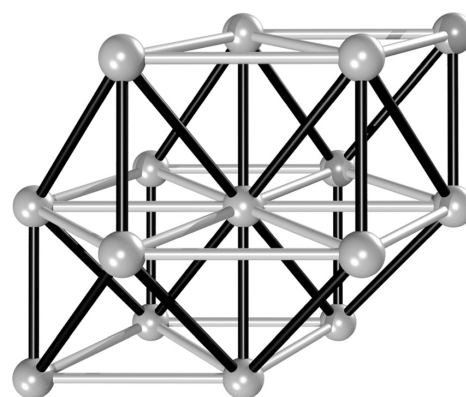
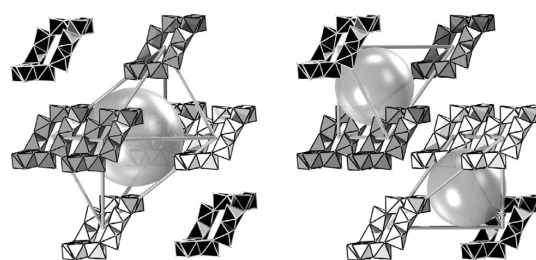
**Fig. 4** Dodecameric building unit and its connectivity mode in the framework of CAU-3-BDC. Methyl-groups are omitted for clarity.

Results and discussion

Structural description

The structure of CAU-3-BDC is based on dodecameric [Al₁₂(OCH₃)₂₄]¹²⁺ cations, to which twelve carboxylate moieties are coordinated, each one bridging two Al-ions (Fig. 4).

Thus, the inorganic units are composed of twelve edge-sharing AlO₆-polyhedra. The edge-sharing oxygen atoms are part of methanolate ions, while the other oxygen-atoms result from the coordination of the bridging carboxylate-groups. Similar dodecameric clusters have been only observed twice in molecular complexes containing the transition metals Fe³⁺ and Mn³⁺/Cr³⁺ ions.^{37,38} To the best of our knowledge this is the first time, that this cluster has been observed in Al chemistry as well as in the chemistry of MOFs. Recently, the Mn³⁺/Cr³⁺ building block was proposed as a possible brick for the formation of new metal-organic frameworks.³⁹ Besides the octanuclear cyclic cluster incorporated in the framework of CAU-1,²³ this building unit is the second example of an wheel-shaped aluminium carboxylate, whose occurrence is again strictly limited to the incorporation into a metal-organic framework.

**Fig. 5** Schematic representation of a part of the distorted *fcu*-net. The white bonds represent the connectivity in the *xy*-plane of the inorganic brick, the black ones the connectivity along the *z*-axis.**Fig. 6** The two different types of cavities in the *fcu*-framework. Different colours emphasize the ABC stacking of the of the Al-based bricks [Al₁₂(OCH₃)₂₄]¹²⁺.

The twelvefold connectivity by dicarboxylate units leads to the formation of a *fcu*-net (Fig. 5).

This high connectivity is remarkable, since only few examples of such MOFs have been reported. Besides the well known UiO-66,¹⁰ for example the frameworks of CAU-1²³ and its Ti-analogue MIL-125⁴⁰ exhibit this connectivity mode. While the latter two MOFs show a distorted pseudo-bcc packing of clusters, the assembly in CAU-3 leads to a fcc-packing like in UiO-66. Due to the anisotropic shape of the cluster a strongly distorted packing is observed (Fig. S7†).

Accordingly, the [Al₁₂(OCH₃)₂₄]¹²⁺ clusters are connected sixfold in their *xy*-plane and sixfold alternating in both directions along the *z*-axis of the cyclic cluster. The resulting network contains tetrahedral and octahedral cavities which are strongly distorted due to the anisotropic shape of the Al-containing brick (Fig. 6).

Assuming a spherical shape, the diameters of the tetrahedral and octahedral cavities are approximately 10 and 11 Å (calculated based on van-der-Waals radii), respectively. In reality larger molecules could be accommodated and based on the estimated available free space, the incorporation of rod-shaped guests with maximum length of 27 Å should be possible. The triangular apertures of these cavities differ only slightly in size and should be accessible for molecules up to a diameter of 7 Å.

The dimensionality and shape of the pores differ only slightly for compound **2**, since the amino-group is statistically distributed over the four possible positions of the aromatic ring. The larger linker molecule in **3** leads to an extended, non-interpenetrating framework containing distorted tetrahedral and octahedral cavities of ~ 14 Å and ~ 15 Å in diameter, assuming a spherical guest. Based on the structure, rod-shaped guests with maximum length of 38 Å should fit into the octahedral cavities.

Spectroscopic and thermal properties

The vibrational spectra (Fig. 7) of the three title compounds are very similar. The characteristic bands for the carboxylate vibrations around 1580 cm^{-1} and 1420 cm^{-1} clearly show the presence of the dicarboxylate ions coordinating to the Al^{3+} -ions. The aliphatic C–H vibrations at 2950 cm^{-1} and 2840 cm^{-1} are due to the bridging methanolate ions in the Al-based brick. In the case of as synthesized CAU-3-NDC, the absorption band around 1700 cm^{-1} is attributed to residual naphthalene dicarboxylic acid molecules occluded in the pores.

The band at 1250 cm^{-1} (C–N-vibration) in the spectrum of CAU-3-BDC-NH₂ proves the incorporation of aminoterephthalic acid, although the characteristic NH₂-bands around 3450 cm^{-1} are not observed, probably due to the presence of hydrogen-bonded water inside the pores. In the Raman-spectra, especially the aromatic C–C-vibrations between 1640 cm^{-1} and 1380 cm^{-1} are well resolved.

The thermal stability of all three MOFs was investigated in air atmosphere up to at least $800\text{ }^\circ\text{C}$ with a heating rate of 4 K

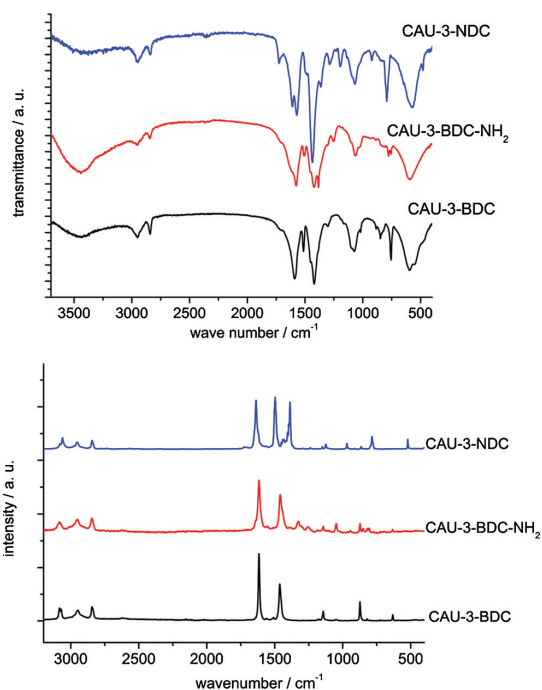


Fig. 7 IR- (top) and Raman-spectra (bottom) of the different CAU-3 MOFs.

min^{-1} (Fig. S9, S10 and S11†). For **1**, the first weight loss of -16.5% corresponds to the removal of incorporated solvent molecules. At higher temperatures ($\sim 200\text{ }^\circ\text{C}$), the decomposition of the frameworks and thus the structural collapse proceeds in two steps (calc.: 58.7% , obs.: 60.9%). The product formed in the end is weakly crystalline Al_2O_3 . In the case of CAU-3-BDC, we were also able to prove the structural rigidity of the framework during the activation process. Temperature-dependent XRPD data (Fig. 8) demonstrates, that no uncommon cell parameter shifts can be observed.

While the chemical decomposition of **1** shows a stepwise mechanism in the TG curve, the structure of the framework collapses directly during the second weight loss. The increased stability during the TDXRPD experiment compared to the TG-data is attributed to the different experimental set ups.

The decomposition of CAU-3-BDC-NH₂ (**2**) is similar to that of **1**. Like for CAU-3-BDC, the decomposition starts after the removal of adsorbed solvent (10.3%) at a temperature of $\sim 180\text{ }^\circ\text{C}$. The two last weight losses correspond quite well to the decomposition of **2** (calc.: 66.4% , obs.: 62.4%), although the difference could be attributed to a small amount of X-ray-amorphous Al-oxo-species.

The decomposition of **3** during the TG-experiment shows a similar stability ($\sim 180\text{ }^\circ\text{C}$), but due to the observed byproducts, we did not attribute the weight losses to defined steps of decomposition.

Sorption properties

For the sorption measurements, the samples were activated in vacuum (10^{-2} mbar) at $160\text{ }^\circ\text{C}$ for 12 h. The XRPD patterns of the samples after the sorption experiments can be found in the supporting information (Fig. S1–S3). The nitrogen isotherms (Fig. 9) were measured at 77 K . The BET-method was applied to calculate the apparent surface area and the micropore volumes were calculated from the amount adsorbed at $p/p_0 = 0.5$.

The sorption experiments confirm the tendencies that we expected. The incorporation of the amino-group leads to a decrease of micropore volume as well as apparent surface area,

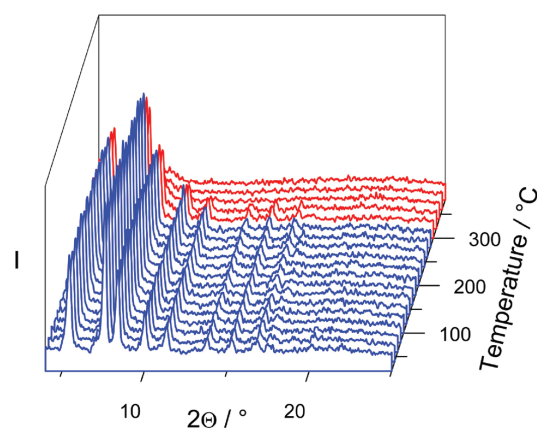


Fig. 8 Temperature-dependent XRPD patterns of CAU-3-BDC (**1**), measured under air.

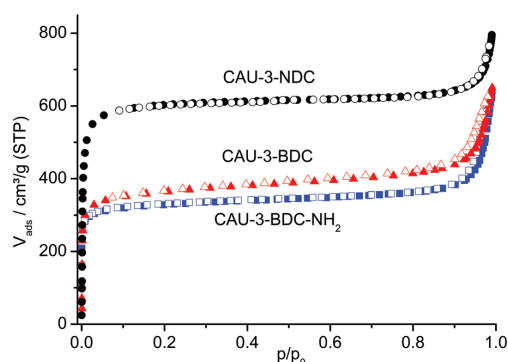


Fig. 9 N₂-Sorption isotherms for 1, 2 and 3 measured at 77 K.

Table 2 Apparent specific surface areas and V_{mic} values of the CAU-3-MOFs

Compound	A_{BET} m ² g ⁻¹	$A_{Langmuir}$ m ² g ⁻¹	V_{mic} cm ³ g ⁻¹
CAU-3-BDC	1550	1920	0.64
CAU-3-BDC-NH ₂	1250	1520	0.53
CAU-3-NDC	2320	2750	0.95

while the enlargement of the linker molecule results in a drastically increased uptake. The BET-surfaces as well as the micropore volumes are summarized in Table 2.

The apparent specific surface areas and the micropore volume measured for CAU-3-NDC 3 are to the best of our knowledge the highest reported so far for any literature known Al-MOF. Changing the adsorbate from N₂ to H₂O, the influence of the functional group is clearly visible (Fig. 10). The use of H₂O vapour leads to strong hysteresis. The absolute amount of adsorbed water is similar for both CAU-3-BDC and CAU-3-BDC-NH₂, but due to the presence of the polar amino group, the adsorbed amount of water vapour at lower partial pressures is higher in CAU-3-NH₂.

Although this is a purely qualitative sorption study, the influence of the amino group with its ability for hydrogen bonding is obvious.

Conclusion

Summarizing our results, we have synthesized three new Al-containing MOFs by applying our high-throughput-methods and characterized them in detail. This new family of MOFs contains an unprecedented brick, [Al₁₂(OCH₃)₂₄]¹²⁺, which is twelvefold connected by dicarboxylate molecules to form a **fcu**-net. This inorganic unit is the second example for the occurrence of a wheel-shaped aluminium cluster in a metal-organic framework. All three compounds of the CAU-3-family are highly porous and exhibit BET-surface areas larger than 1200 m² g⁻¹ and micropore volumes higher than 0.5 cm³ g⁻¹. They are thermally stable up to at least 180 °C in air. The sorption properties are altered upon incorporation of a functional group or a larger linker molecule, respectively.

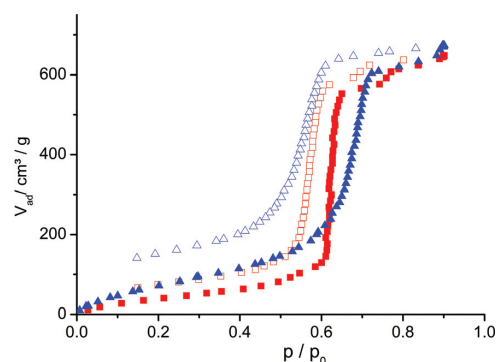


Fig. 10 Water vapour isotherms for 1 and 2 measured at 25 °C. Blue triangles for the NH₂-functionalized compound 2, red squares for 1. Empty symbols represent the desorption-, filled symbols represent the adsorption-branch.

Acknowledgements

This work has been financially supported by the DFG (SPP 1362). The research leading to these results has received funding from the European Community's Seventh Framework Programme (FP7/2007–2013) under grant agreement n° 228862'.

Notes and references

- G. Férey, *Chem. Soc. Rev.*, 2008, **37**, 191.
- Z. Wang and S. M. Cohen, *Chem. Soc. Rev.*, 2009, **38**, 1315.
- S. Kitagawa, R. Kitaura and S. Noro, *Angew. Chem., Int. Ed.*, 2004, **43**, 2334.
- C. Janiak, *Dalton Trans.*, 2003, 2781.
- R. Long and O. M. Yaghi, *Chem. Soc. Rev.*, 2009, **38**, 1213.
- O. M. Yaghi, M. O'Keeffe, N. W. Ockwig, H. K. Chae, M. Eddaoudi and J. Kim, *Nature*, 2003, **423**, 705.
- T. Devic, P. Horcajada, C. Serre, F. Salles, G. Maurin, B. Moulin, D. Heurtaux, G. Clet, A. Vimont, J.-M. Grenèche, B. Le Ouay, F. Moreau, E. Magnier, Y. Filinchuk, J. Marrot, J.-C. Lavalley, M. Daturi and G. Férey, *J. Am. Chem. Soc.*, 2010, **132**, 1127.
- M. Eddaoudi, J. Kim, N. Rosi, D. Vodak, J. Wachter, M. O'Keeffe and O. M. Yaghi, *Science*, 2002, **295**, 469.
- C. Serre, C. Mellot-Draznieks, S. Surblé, N. Audebrand, Y. Filinchuk and G. Férey, *Science*, 2007, **315**, 1828.
- J. H. Cavka, S. Jakobsen, U. Olsbye, N. Guillou, C. Lamberti, S. Bordiga and K. P. Lillerud, *J. Am. Chem. Soc.*, 2008, **130**, 13850.
- A. Schaate, P. Roy, A. Godt, J. Lippke, F. Waltz, M. Wiebcke and P. Behrens, *Chem.–Eur. J.*, 2011, **17**, 6643.
- M. Kandiah, S. Usseglio, S. Svelle, U. Olsbye, K. P. Lillerud and M. Tilset, *J. Mater. Chem.*, 2010, **20**, 9848.
- S. Bauer, C. Serre, T. Devic, P. Horcajada, J. Marrot, G. Férey and N. Stock, *Inorg. Chem.*, 2008, **47**, 7568.
- P. Maniam and N. Stock, *Inorg. Chem.*, 2011, **50**, 5085.
- T. Ahnfeldt, D. Gunzelmann, T. Loiseau, D. Hirsemann, G. Férey, J. Senker and N. Stock, *Inorg. Chem.*, 2009, **48**, 3057.
- A. Sonnauer, F. Hoffmann, M. Fröba, L. Kienle, V. Duppel, M. Thommes, C. Serre, G. Férey and N. Stock, *Angew. Chem., Int. Ed.*, 2009, **48**, 3791.
- C. Volkringer, D. Popov, T. Loiseau, G. Férey, M. Burghammer, C. Riekkel, M. Haouas and F. Taulelle, *Chem. Mater.*, 2009, **21**, 5695.
- C. Volkringer, D. Popov, T. Loiseau, N. Guillou, G. Férey, M. Haouas, F. Taulelle, C. Mellot-Draznieks, M. Burghammer and C. Riekkel, *Nat. Mater.*, 2007, **6**, 760.
- C. Volkringer, T. Loiseau, N. Guillou, G. Férey, M. Haouas, F. Taulelle, N. Audebrand, I. Margiolaki, D. Popov, M. Burghammer and C. Riekkel, *Cryst. Growth Des.*, 2009, **9**, 2927.
- C. Volkringer, T. Loiseau, M. Haouas, F. Taulelle, D. Popov, M. Burghammer, C. Riekkel, C. Zlotea, F. Cuevas, M. Latroche,

6. Strukturlösung von anorganisch-organischen Hybridverbindungen

- D. Phanon, C. Knöfel, P. L. Llewellyn and G. Férey, *Chem. Mater.*, 2009, **21**, 5783.
- 21 C. Volkringer, T. Loiseau, N. Guillou, G. Férey, M. Haouas, F. Taulelle, E. Elkaim and N. Stock, *Inorg. Chem.*, 2010, **49**, 9852.
- 22 C. Volkringer, T. Loiseau, N. Guillou, G. Férey and E. Elkaim, *Solid State Sci.*, 2009, **11**, 1507.
- 23 T. Ahnfeldt, N. Guillou, D. Gunzelmann, I. Margiolaki, T. Loiseau, G. Férey, J. Senker and N. Stock, *Angew. Chem., Int. Ed.*, 2009, **48**, 5163.
- 24 W. Schmitt, E. Baissa, A. Mandel, C. E. Anson and A. K. Powell, *Angew. Chem., Int. Ed.*, 2001, **40**, 3577.
- 25 E. A. Mainicheva, O. A. Gerasko, L. A. Sheludyakova, D. Y. Naumov, M. I. Naumova and V. P. Fedin, *Russ. Chem. Bull.*, 2006, **55**, 267.
- 26 T. Loiseau, C. Serre, C. Huguenard, G. Fink, F. Taulelle, M. Henry, T. Bataille and G. Férey, *Chem.-Eur. J.*, 2004, **10**, 1373.
- 27 I. Senkowska, F. Hoffmann, M. Fröba, J. Getzschmann, W. Böhlmann and S. Kaskel, *Microporous Mesoporous Mater.*, 2009, **122**, 93.
- 28 A. Comotti, S. Bracco, P. Sozzani, S. Horike, R. Matsuda, J. Chen, M. Takata, Y. Kubota and S. Kitagawa, *J. Am. Chem. Soc.*, 2008, **130**, 13664.
- 29 J. Gascon, U. Aktay, M. D. Hernandez-Alonso, G. P. M. Van Klink and F. Kapteijn, *J. Catal.*, 2009, **261**, 75.
- 30 S. Couck, J. F. Denayer, G. V. Baron, T. Remy, J. Gascon and F. Kapteijn, *J. Am. Chem. Soc.*, 2009, **131**, 6326.
- 31 T. Ahnfeldt, J. Moellmer, V. Guillermin, R. Staudt, C. Serre and N. Stock, *Chem.-Eur. J.*, 2011, **17**, 6462.
- 32 E. Biemmi, S. Christian, N. Stock and T. Bein, *Microporous Mesoporous Mater.*, 2009, **117**, 111.
- 33 Materials Studio Version 5.0, Accelrys Inc., San Diego, CA, 2009.
- 34 Topas Academics 4.2, Coelho Software, 2007.
- 35 A. Altomare, M. Cavalli, R. Calandro, C. Cuocci, C. Giacovazzo, A. Gagliardi, A. G. G. Moliterni and R. Rizzi, EXPO2004. Program for Solving Crystal Structures from Powder Data by direct Methods, 2004.
- 36 STOE WinXPOW version 2.11, Stoe & Cie GmbH, 2005, Darmstadt, Germany.
- 37 T. C. Stamatatos, A. G. Christou, C. M. Jones, B. J. O'Callaghan, K. A. Abboud, T. A. O'Brien and G. Christou, *J. Am. Chem. Soc.*, 2007, **129**, 9840.
- 38 M. Helliwell, A. A. Smith, S. J. Teat and R. E. P. Winpenny, *Inorg. Chim. Acta*, 2003, **354**, 49.
- 39 D. J. Tranchemontagne, J. L. Mendoza-Cortes, M. O'Keeffe and O. M. Yaghi, *Chem. Soc. Rev.*, 2009, **38**, 1257.
- 40 M. Dan-Hardi, C. Serre, T. Frot, L. Rozes, G. Maurin, C. Sanchez and G. Férey, *J. Am. Chem. Soc.*, 2009, **131**, 10857.

6.1.2. Fuel Purification, Lewis Acid and Aerobic Oxidation Catalysis Performed by a Microporous Co-BTT (BTT³⁻ = 1,3,5-benzenetristetrazolate) Framework Having Coordinatively Unsaturated Sites

Der folgende Artikel wurde in der Zeitschrift *Journal of Materials Chemistry* veröffentlicht und behandelte die Synthese und Charakterisierung von Metalltetrazolaten (reproduced with permission from RSC, *J. Mater. Chem.*, 2012, 22, 10200).^[204] Hierzu wurde der in Abbildung 6.1 Linker 1,3,5-Benzoltristetrazol (H₃BTT) verwendet.

Der Linker führt in Synthesen mit Co²⁺- und Cd²⁺-Ionen zu den zwei isostrukturellen mikroporösen Verbindungen der Zusammensetzung [Co(DMA)₆]₃[(Co₄Cl)₃(BTT)₈(H₂O)₁₂]₂ · 12H₂O und [Cd(DMF)₆]₃[(Cd₄Cl)₃(BTT)₈(H₂O)₁₂]₂ · 14H₂O · 4DMF (DMF = Dimethylformamid, DMA = Dimethylacetamid), die unter solvothermalen Bedingungen in DMA bzw. DMF hergestellt wurden. Die Kristallstrukturen konnten mittels Einkristallstrukturanalysen bestimmt werden. Die Verbindungen sind aus quadratisch planaren [M₄Cl]⁷⁺ Einheiten aufgebaut, die von den BTT³⁻-Ionen zu einem (3,8) verknüpften sogenannten „Moravia“ Netz verbrückt sind. Das Gerüst ist hierbei anionisch geladen und die Ladung wird durch [M(Solvens)₆]²⁺ Gegenionen in den Poren ausgeglichen.

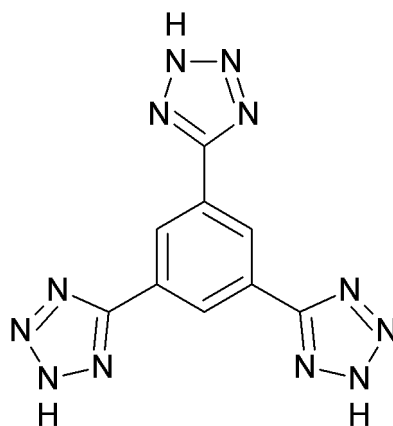


Abbildung 6.1.: Strukturformel von 1,3,5-Benzoltristetrazol (H₃BTT).

Die Verbindungen wurden mittels Röntgenpulvermessungen, IR-Spektroskopie, Thermogravimetrie und Sorptionsmessungen charakterisiert. Die koordinierten Lösungsmittelmoleküle können thermisch entfernt werden, wodurch freie Lewis-saure Zentren erzeugt werden. Diese sollten für Anwendungen in der Gastrennungen oder Katalyse von Interesse sein. Um die Zugänglichkeit und Aktivität der Lewis-saure Zentren zu demonstrieren wurden

die Verbindung $[\text{Co}(\text{DMA})_6]_3[(\text{Co}_4\text{Cl})_3(\text{BTT})_8(\text{H}_2\text{O})_{12}]_2 \cdot 12\text{H}_2\text{O}$ thermisch aktiviert und auf katalytische Eigenschaften sowie die Adsorption von schwefelhaltigen Verbindungen untersucht. Die durch Lewis-saure Zentren katalysierte Ringöffnung von Styroloxid zu 2-Methoxy-2-phenylethanol in Anwesenheit von Methanol wurde untersucht und mit der katalytischen Aktivität von $\text{Co}(\text{NO}_3)_2 \cdot 6\text{H}_2\text{O}$ verglichen. Hierbei zeigte sich, dass nach 29 h eine Ausbeute von 67 und 40 % für $[\text{Co}(\text{DMA})_6]_3[(\text{Co}_4\text{Cl})_3(\text{BTT})_8(\text{H}_2\text{O})_{12}]_2 \cdot 12\text{H}_2\text{O}$ bzw. für $\text{Co}(\text{NO}_3)_2 \cdot 6\text{H}_2\text{O}$ erhalten wurde. Des Weiteren wurde die Verbindung auf in der katalytischen aeroben Oxidation von Cycloalkanen und Benzylkomponenten in Anwesenheit von N-Hydroxyphthalimid untersucht für die ansonsten Cobalt(II)salze verwendet werden.^[205] Die Verbindung zeigt eine ähnliche hohe Umwandlung wie das kommerziell erhältliche Fe(BTC), zeigt aber eine höhere Selektivität. Zur Überprüfung der Eignung als Sorbens von schwefelhaltigen Molekülen wurden die Adsorption von Thiophen, Benzothiophen und Dibenzothiophen aus einem Gemisch von n-Heptan / Toluol (80 / 20) überprüft, und zeigten die selektive Aufnahme der schwefelhaltigen Moleküle.

Fuel purification, Lewis acid and aerobic oxidation catalysis performed by a microporous Co-BTT (BTT³⁻ = 1,3,5-benzenetristetrazolate) framework having coordinatively unsaturated sites†Shyam Biswas,^a Michael Maes,^b Amarajothi Dhakshinamoorthy,^c Mark Feyand,^a Dirk E. De Vos,^b Hermenegildo Garcia^c and Norbert Stock^{*a}

Received 1st November 2011, Accepted 23rd December 2011

DOI: 10.1039/c2jm15592c

Two isostructural microporous metal–organic frameworks [Co(DMA)₆]₃[(Co₄Cl)₃-(BTT)₈(H₂O)₁₂]₂·12H₂O (BTT³⁻ = 1,3,5-benzenetristetrazolate; DMA = *N,N'*-dimethylacetamide) (1) and [Cd(DMF)₆]₃[(Cd₄Cl)₃(BTT)₈(H₂O)₁₂]₂·14H₂O·4DMF (DMF = *N,N'*-dimethylformamide) (2) were synthesized under solvothermal conditions. The structures of both compounds were determined by single-crystal X-ray diffraction data. Each compound adopts a porous three-dimensional framework consisting of square-planar [M₄Cl]⁷⁺ (M²⁺ = Co, 1; Cd, 2) units interconnected by triangular tritopic BTT³⁻ bridging ligands to give an anionic (3,8)-connected “Moravia” net. Phase purity of the compounds was confirmed by X-ray powder diffraction (XRPD), IR spectroscopy, thermogravimetric (TG) and elemental analysis. TGA and temperature-dependent XRPD (TDXRPD) experiments indicate a moderate thermal stability up to 350 and 300 °C, respectively. Guest exchange followed by heating led to microporous solids with coordinatively unsaturated metal sites. These unsaturated metal sites create opportunities in adsorptive and catalytic applications. These have been probed by the selective removal of sulfur compounds from fuel feeds as well as the catalytic ring opening of styrene oxide and the oxidation of several cycloalkanes and benzyl compounds.

1 Introduction

Metal–organic frameworks (MOFs),¹ which are constructed from metal ions or clusters interconnected by polytopic organic linkers, have generated a great deal of interest in recent years because of their structures, diverse topologies and potential applications in areas such as gas or liquid phase adsorption and separation,² or catalysis.³ The exceptionally high pore volume and surface area of MOFs allow the facile access of substrates to the catalytically active sites, either integrated at metal nodes^{3,4} or located on the organic ligands.⁵ The pores of MOFs can be tuned in a systematic way and hence optimized to a specific catalytic application. Besides a high density of catalytically active sites in

MOFs, one of their major advantages is that all active sites are identical, because of the highly crystalline nature of the material.^{4a,b} Compared to homogeneous transition metal catalysts, the heterogeneous MOF catalysts would simplify the work-up procedure by allowing simple filtration, facilitating product separation and catalyst regeneration.⁶ However, some disadvantages might hamper application of MOFs in catalysis. As MOFs are synthesized under relatively mild conditions of temperature and pressure, they are mostly unstable above 600 K.^{4a} Moreover, some MOFs seem to be unstable towards water in solvent concentrations, or even to atmospheric moisture.⁷ The reactions catalyzed at low temperature, such as liquid phase transformations, seem to be more promising for MOFs as compared to high temperature gas phase reactions. Thus, organic synthesis and, more specifically, synthesis of fine chemicals requiring low temperature can be accomplished employing MOFs as catalysts.^{1a,3b} For optimal catalytic activity, the catalytic sites must be oriented towards the pore interior and be freely accessible to substrate molecules.^{4a} However, in many MOFs the metal ions are integral parts of the framework, and therefore they are completely saturated by coordination to the organic ligands.⁸ Despite these drawbacks, there is an increasing number of reports showing the potentiality of MOFs in catalysis.^{3,4}

In favorable cases, the removal of solvent molecules by thermal activation leads to coordinatively unsaturated metal

^aInstitut für Anorganische Chemie, Christian-Albrechts-Universität, Max-Eyth-Strasse 2, 24118 Kiel, Germany. E-mail: stock@ac.uni-kiel.de; Fax: +49-4318801775; Tel: +49-4318801675

^bCentre for Surface Chemistry and Catalysis, Katholieke Universiteit Leuven, Kasteelpark Arenberg 23, 3001 Leuven, Belgium

^cInstituto Universitario de Tecnología Química CSIC-UPV and Departamento de Química, Universidad Politécnica de Valencia, Av. De los Naranjos s/n, 46022 Valencia, Spain

† Electronic supplementary information (ESI) available: View of topological nets, XRPD patterns, TG and elemental analyses, IR, fluorescence and UV-Vis spectra, digital photos, bond lengths, reusability test for ring opening of epoxide. CCDC reference numbers 851169 and 851168. For ESI and crystallographic data in CIF or other electronic format see DOI: 10.1039/c2jm15592c

sites (CUSs) which are very beneficial since CUSs can strongly interact with guest molecules such as gases and organic molecules in adsorption and catalysis. The generation of CUSs on the inner pore surface is a fundamental strategy for improving the room temperature hydrogen storage performance of MOFs.^{9,10} MOFs with CUSs are also useful as potential separation materials for the capture of CO₂ from flowing gas mixtures.¹¹ Recently, several liquid phase separations were described like the separation of alkylaromatics and a steam cracker's C₅-cut.¹² Furthermore, the presence of CUSs was demonstrated to play a decisive role in the selective removal of *N*-heterocyclic aromatic contaminants from fuels.¹³ Crude oil naturally contains sulfur compounds, which are undesirable since they cause SO_x exhaust gases. Currently, fuel feeds contain as low as 10 ppmw S and it can be expected that these levels are to be lowered further. Therefore, the complete removal of these sulfur compounds by adsorption might be an interesting application for MOFs. CUSs can be considered as Lewis acid sites. Intermediate Lewis acid sites like Co²⁺, Cu²⁺ and Zn²⁺ have been reported to be able to interact with soft bases like typical sulfur compounds like thiophene, benzothiophene and dibenzothiophene.¹⁴ CUS can offer a promising tool in catalysis because regular arrangements and well-defined environments of metal centers in the pore channels induce regioselectivity and shape- or size-selectivity towards guest molecules or reaction intermediates.^{16,15} In the case of Lewis acid catalyzed reactions, the availability of CUSs is a key requirement. Several MOFs having CUSs such as Cu-BTC (BTC³⁻ = benzene-1,3,5-tricarboxylate),¹⁶ Mn-BTT (BTT³⁻ = 1,3,5-benzenetriazolate),¹⁷ Fe-MIL-100 (MIL = Materials of Institute Lavoisier)^{4f} and Cr-MIL-101¹⁸ have been shown to catalyze a wide variety of organic reactions including cyanosilylation,^{4a,d,19} aerobic oxidation,²⁰ peroxodative oxidation,^{20d,21} epoxide ring opening,²² hydrogenation,²³ acetalization,²⁴ *N*-methylation,²⁵ sulfoxidation,²⁶ Mukaiyama-aldol reaction,¹⁹ Friedel-Crafts alkylation,^{4f} Knoevenagel condensation,²⁷ Heck coupling,²⁷ Claisen-Schmidt condensation,²⁸ etc.²⁹ It is still necessary to expand the reaction types that can be catalyzed by MOFs, trying to demonstrate the advantages and limitations of these materials as catalysts, especially *versus* other common solid catalysts such as zeolites and clays.

Inspired by the above mentioned advantages, we have synthesized and fully characterized two isostructural microporous MOFs possessing CUSs, namely [Co(DMA)₆]₃[(Co₄Cl)₃(BTT)₈(H₂O)₁₂]₂·12H₂O (DMA = *N,N'*-dimethylacetamide) (**1** or Co-BTT) and [Cd(DMF)₆]₃[(Cd₄Cl)₃(BTT)₈(H₂O)₁₂]₂·14H₂O·4DMF (DMF = *N,N'*-dimethylformamide) (**2** or Cd-BTT). Each compound, being isotopic with the previously reported M-BTT (M²⁺ = Mn,¹⁷ Cu,³⁰ or Fe³¹) materials, adopts a porous three-dimensional (3D) framework constructed of square-planar [M₄Cl]⁷⁺ (M²⁺ = Co, **1**; Cd, **2**) units interconnected by triangular tritopic BTT³⁻ bridging ligands to give an anionic (3,8)-connected "Moravia" net. During the preparation of the manuscript, a compound having similar chemical composition and identical framework topology as **2** has been reported.³² However, our synthetic method is different and we have been able to prove the permanent porosity of the compound. Compound **1** bears redox-active Co sites, in addition to the CUSs possessed by both compounds. Due to the partial decomposition of the framework of **2** after thermal activation, its catalytic and

adsorptive features were not investigated. Compound **1**, which has a higher thermal stability, was found to catalyze the ring opening of styrene oxide, and the aerobic oxidation of several cycloalkanes and benzylic compounds. It is noteworthy that the ring opening of epoxides is an important synthetic tool for the preparation of 1,2-diols and β-alkoxyalcohols.³³ Moreover, the oxidation of C–H bonds with molecular oxygen has been a target for producing oxygenated compounds such as alcohols and ketones.³⁴ Furthermore, the potential of compound **1** for the selective removal of sulfur from fuel feeds has been probed by single compound adsorption isotherms.

2 Experimental

2.1 Materials and general methods

The H₃BTT ligand was synthesized according to a previously published procedure.¹⁷ All other starting materials were of reagent grade and used as received from the commercial supplier. Fourier transform infrared (FTIR) spectra in the range 4000–400 cm⁻¹ were recorded on an ATI Matheson Genesis FT-IR spectrometer from KBr pellets or an ALPHA-ST-IR Bruker spectrometer with an ATR unit. UV-Vis diffuse reflectance spectra (DRS) were recorded on a Varian Cary 5000 UV-Vis-NIR spectrophotometer in the range of 300–1100 nm and converted into normal absorption spectra with the Kubelka-Munk function.³⁵ Elemental analyses (C, H, N) were carried out on a Eurovector EuroEA Elemental Analyzer. Thermogravimetric analysis (TGA) was performed with a Netzsch STA-409CD thermal analyzer in a temperature range of 25–800 °C under air atmosphere at a heating rate of 4 °C min⁻¹. Ambient temperature X-ray powder diffraction (XRPD) patterns were measured using CuKα radiation (λ = 1.5406 Å) with a STOE STADI P diffractometer equipped with a linear position-sensitive detector (LPSD). Temperature-dependent X-ray powder diffraction (TDXRPD) experiments were performed under air atmosphere with a STOE STADI P diffractometer equipped with an image-plate position-sensitive detector (IPPSD) and a STOE capillary furnace (version 0.65.1) using CuKα radiation. The simulated powder patterns were calculated using data from single-crystal X-ray diffraction. The solid-state fluorescence emission spectra were collected on a Varian Cary Eclipse spectrofluorometer in the 320–550 nm region at room temperature using an excitation wavelength of 300 nm. The nitrogen, carbon dioxide and hydrogen sorption isotherms up to 1 bar were measured using a Belsorp Max apparatus at –196, 25 and –196 °C, respectively. The samples were heated at 135 °C under dynamic vacuum for 24 h prior to sorption and catalytic experiments.

Safety note! *Metal azides and tetrazolate compounds are potentially explosive, and caution should be exercised when dealing with such materials.* However, the small quantities used in this study were not found to present a hazard.

2.2 Synthesis

Elemental analyses of the compounds in different forms are presented in Table S1 (ESI†).

[Co(DMA)₆]₃[(Co₄Cl)₃(BTT)₈(H₂O)₁₂]₂·12H₂O (**1**). A mixture of CoCl₂·6H₂O (68 mg, 0.29 mmol) and H₃BTT (40 mg,

0.14 mmol) in 4 mL of DMA was acidified with 8 drops of HCl (2 M). The resulting solution was placed in a glass tube (10 mL). The tube was sealed and heated in a programmable oven to 130 °C at a rate of 1.8 °C min⁻¹, held at this temperature for 24 h, then cooled to room temperature at a rate of 1.8 °C min⁻¹. The supernatant was removed and the remaining red cubic crystals of **1** were washed with DMA (3 × 1 mL) and dried in air to yield 115 mg (0.01 mmol, 48%).

[Cd(DMF)₆]₃(Cd₄Cl)₃(BTT)₈(H₂O)₁₂·14H₂O·4DMF (2). A mixture of Cd(NO₃)₂·4H₂O (88 mg, 0.29 mmol) and H₃BTT (40 mg, 0.14 mmol) in 4 mL of DMF was acidified with 3 drops of HCl (2 M). The resulting solution was placed in a glass tube (10 mL). The tube was sealed and heated in a programmable oven to 70 °C at a rate of 0.8 °C min⁻¹, held at this temperature for 24 h, then cooled to room temperature at a rate of 0.8 °C min⁻¹. The resulting colorless cubic crystals of **2** were collected by filtration, washed with DMF (3 × 1 mL) and dried in air to yield 105 g (0.01 mmol, 37%).

2.3 Activation of **1** and **2**

Each (0.5 g) of the as-synthesized samples of **1** and **2** was first soaked in methanol (4 × 50 mL) for 96 h, during which period, the solvent was discarded and fresh solvent was added after each 24 h. Thus, the non-coordinated and coordinated solvent molecules in **1** and **2** were exchanged with methanol molecules. In the second step, the methanol-exchanged solids were heated at 135 °C under dynamic vacuum for 24 h to remove the occluded and bound methanol molecules. After cooling to room temperature, the thermally activated compounds adsorb water from air (denoted as “hydrated form” hereafter).

2.4 Single-crystal X-ray diffraction

Structures of **1** and **2** were determined from single-crystal X-ray diffraction data. Single-crystal X-ray diffraction intensities of **1** and **2** were collected on a STOE IPDS diffractometer employing monochromated MoK α radiation ($\lambda = 0.71073 \text{ \AA}$) at 293 and 200 K, respectively. Initial structures were solved by direct methods and refined by full-matrix least-squares techniques based on F^2 using the SHELXL-97 program.³⁶ Details of single-crystal data collection and refinement of **1** and **2** are summarized in Table 1.

2.5 Catalytic experiments

Preparation of the *N*-hydroxyphthalimide (NHPI)/I catalyst. NHPI (200 mg) (1 wt%) was dissolved in 7 mL of dichloromethane and 3 mL of methanol. To this solution, 1 g of solid **1** (corresponding to a 5 wt% of NHPI) was added and the resulting suspension was heated at 40 °C for 4 h. After the required time, the mixture was cooled and the solvent was removed by rotary evaporation. The resulting solid was dried at 80 °C for 2 h.

Typical experimental procedure. Styrene oxide (0.1 mL) in methanol (5 mL), cyclooctane (2 mL) or the benzylic compounds (2 mL) and the corresponding catalyst (20 or 50 mg for methanolysis or aerobic oxidation, respectively) were placed in a two-necked flask (10 mL). For aerobic oxidation, the flask was

equipped with a balloon filled with molecular oxygen. The mixture was stirred at 50 °C (methanolysis of styrene oxide), 100 °C (toluene oxidation) or 120 °C (cyclooctane and rest of benzylic oxidations) for the required time as mentioned in Table 3. Blank reactions at these temperatures showed no catalytic conversions of the substrates. The course of the oxidation was followed by analyzing four aliquots (2 μ L) of the reaction mixture collected with a microsyringe. At the end of the reaction, the heterogeneous mixture was cooled, diluted with acetonitrile and methanol, and filtered. The liquid phase was dried over anhydrous MgSO₄. The conversion, purity and yield of the final products were determined using a Hewlett Packard 5890 series II gas chromatograph with a FID detector and high purity helium as carrier gas. The products were identified by comparing their retention times in GC with authentic samples and with GC-MS Hewlett Packard 6890 series. Quantification was performed using *n*-dodecane as GC external standard. To a known aliquot of the sample, a given amount of *n*-dodecane was added and the solution was injected in the GC to determine the degree of conversion and selectivity. The corresponding response factors of the substrates and products were used to transform relative peak areas into molar ratios. Under the present experimental conditions, oxidation of the external standard was not observed. The identity of the products was confirmed by GC-MS and also by co-injection of authentic samples. Personal safety items have to be used to minimize the risks when using mixtures of alkanes and oxygen. For most of the alkanes studied in the present work, the boiling point is higher than the working temperature. All the reactions were performed in a sealed glass reactor fitted with a condenser. The reactions were carried out under an oxygen saturated atmosphere.

Detection of octanedioic acid. Aerobic oxidation reaction of cyclooctane was carried out as described in the previous section. After 24 h, the reaction mixture was diluted with acetonitrile and methanol, and the catalyst was filtered off. The filtrate was subjected under reduced pressure to remove all the volatile compounds. To the resulting residue (pale yellow oil), 1 mL *N*, *O*-bis(trimethylsilyl)trifluoroacetamide with trimethylchlorosilane was added and the resulting solution was heated at 80 °C for 6 h. The reaction mixture was diluted with acetonitrile and injected in GC-MS. The formation of the disilylated product of dicarboxylic acid (7%) was observed.

To confirm that most of the octanedioic acid can be quantified using this procedure, a known quantity of adipic acid (100 mg, 5 wt%) was added to the cyclooctane (2 mL) suspension of the NHPI/I catalyst and the suspension was heated at 120 °C for 6 h under inert atmosphere. After this time, the reaction mixture was diluted with acetonitrile and methanol and filtered off. After removing the solvent and cyclooctane under reduced pressure, 95% of the initial amount of adipic acid was quantified.

Experimental procedure for reusability. The reusability of NHPI/I was tested for oxidation of cyclooctane. At the end of the reaction, the reaction mixture was diluted with acetonitrile and methanol, and filtered off. The filtered catalyst was dried at 60 °C for 2 h and reused directly without further purification for the second run.

Table 1 Single-crystal X-ray data and structure refinement parameters for **1** and **2**. The reported compositions of the compounds are based on the crystal structure refinement. The final structural model was refined without the guest molecules in the pores by using the SQUEEZE option implemented in the program PLATON⁴³

Compound	1	2
Formula	C ₂₄ H ₈ ClCo ₄ N ₃₂ O ₄	C ₂₄ H ₈ Cd ₄ ClN ₃₂ O ₄
Formula mass	1079.79	1293.71
<i>T</i> /K	293(2)	200(2)
λ /Å	0.71073	0.71073
Crystal dimensions/mm	0.10 × 0.10 × 0.10	0.07 × 0.07 × 0.07
Crystal system	Cubic	Cubic
Space group	<i>Pm</i> $\bar{3}$ <i>m</i>	<i>Pm</i> $\bar{3}$ <i>m</i>
<i>a</i> /Å	18.739(2)	19.357(2)
<i>V</i> /Å ³	6580.0(13)	7252.5(14)
<i>Z</i>	3	3
<i>D_c</i> /g cm ⁻³	0.817	0.889
μ /mm ⁻¹	0.810	0.928
<i>F</i> (000)	1599	1851
θ Range/°	1.54–28.03	2.10–26.00
Measured reflections	65 999	31 576
Independent reflections/ <i>R</i> _{int}	1619/0.0579	1474/0.1063
Data/restraints/parameters	1619/0/47	1474/0/47
<i>R</i> ₁ (<i>I</i> > 2 σ (<i>I</i>)) ^a	0.0782	0.0406
<i>wR</i> ₂ (all data) ^b	0.2379	0.1058
Goodness-of-fit on <i>F</i> ²	1.251	1.142
$\Delta\rho_{\text{max,min}}$ /eÅ ⁻³	1.106, -1.090	1.072, -0.924

^a $R_1 = \sum ||F_o| - |F_c|| / \sum |F_o|$. ^b $wR_2 = \{ \sum [w(F_o^2 - F_c^2)]^2 / \sum [w(F_o^2)] \}^{1/2}$.

2.6 Adsorption experiments

Liquid phase batch adsorption experiments were carried out in 1.8 mL glass vials filled with 0.025 g of activated compound **1** and a solution of heptane : toluene in a volumetric ratio of 80 : 20 contaminated with sulfur compounds at 25 °C following a literature procedure.^{12a,37} Uptakes were directly calculated from GC output data.

3 Results and discussion

3.1 Synthesis

In order to check the generality of formation of the M-BTT framework structures, reactions analogous to those employed in forming Cu-BTT and Mn-BTT were attempted using either chloride salts, or a combination of dilute hydrochloric acid and nitrate salts of a series of first-row transition-metal ions (Fe²⁺–Zn²⁺) and Cd²⁺ ion. The amide solvents used included DMF, *N,N*-diethylformamide (DEF), DMA, *N*-methyl-2-pyrrolidone (NMP) and the reaction temperatures used ranged from 60 °C to 140 °C. In addition to previously reported M-BTT (M²⁺ = Mn, Cu, and Fe) materials,^{17,30,31} highly crystalline solids have been achieved with Co²⁺ and Cd²⁺ salts. It is worthy to mention that the guest Mn²⁺ ions in the methanol-exchanged form of Mn-BTT Mn₃[(Mn₄Cl)₃(BTT)₈(CH₃OH)₁₀]₂ have been formerly exchanged with cations such as Li⁺, Cu⁺, Fe²⁺, Co²⁺, Ni²⁺, Cu²⁺ and Zn²⁺ to produce a wide variety of isostructural bimetallic framework solids.³⁸

3.2 Structure description

The single-crystal X-ray diffraction studies reveal that the framework topologies of both **1** and **2** are identical, and they correspond to the M-BTT (M²⁺ = Mn, Cu or Fe)^{17,30,31} structure

previously reported by the Long group. As displayed in Fig. 1, the cubic (space group: *Pm* $\bar{3}$ *m*) structures are built of chloride-centered square-planar [M₄Cl]⁷⁺ (M²⁺ = Co, **1**; Cd, **2**) units which are interconnected with triangular planar BTT³⁻ ligands to form an anionic, 3D framework. The M²⁺ ions of the [M₄Cl]⁷⁺ squares are bridged by tetrazolate rings from eight BTT ligands *via* their N² and N³ donor atoms. Similarly, each BTT ligand is connected with three [M₄Cl]⁷⁺ units. Thus, six [M₄Cl]⁷⁺ units and eight BTT ligands, each of which is coordinated with six adjacent M²⁺ ions, describe the square and hexagonal faces of a truncated octahedron, respectively. The truncated octahedron resembles a sodalite cage. Each sodalite-like cage is connected with six adjacent cages through its square faces, thus constructing a network closely related to that of sodalite. However, the topological connectivity of the network is completely different from that of sodalite. The trigonal planar BTT linkers and the square-planar [M₄Cl]⁷⁺ units surrounded by eight tetrazolates can be considered as 3- and 8-connected nodes, respectively, to construct a 3D (3,8)-connected framework (Fig. S1†). In TOPOS³⁹ and RCSR⁴⁰ databases, this unique topological connectivity has been named as the “Moravia” net, which was recently predicted to exist.⁴¹ Five metal–tetrazolate (M = Mn, Fe, Cu)^{17,30,31} frameworks isostructural to **1** and **2**, along with three metal–carboxylate (M = Fe, Co, Cu)⁴² networks, have yet been reported to adopt this topological net. Notably, the report of the carboxylate-based framework H₆[(Co₄O)₃(TATB)₈] (H₃TATB = 4,4′,4′′-s-triazine-2,4,6-triyltribenzoic acid)^{42a} having the same “Moravia” topology affirms the similarities between tetrazolate- and carboxylate-based bridging linkers. Both frameworks are anionic having formula [(M₄Cl)₃(BTT)₈(H₂O)₁₂]³⁻. The sixth coordination site of each octahedrally coordinated M²⁺ ion is provided by water molecules. For both compounds, [M(solvent)₆]²⁺ ions situated inside the sodalite-like cages balance the charge so that the overall compounds appear as electrostatically neutral.

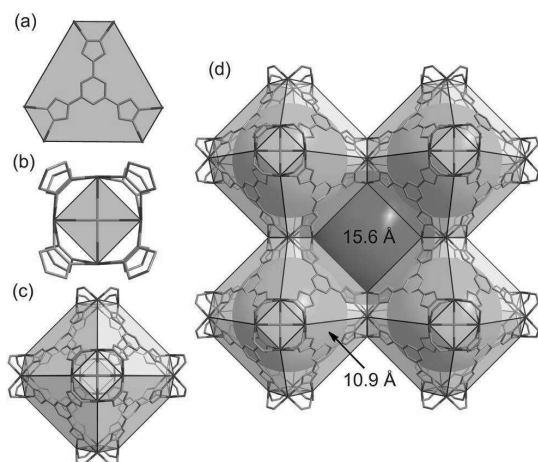


Fig. 1 Views of the frameworks of **1** and **2** in wire representation (color codes: N, light blue; Co or Cd, dark blue; C, grey, Cl, green). (a) BTT ligand connected with six neighbouring M^{2+} ions constructing the 3-connected node and hexagonal face. (b) Four M^{2+} ions bridged by eight tetrazolate rings forming the 8-connected node and square face. (c) A sodalite-like cage constructed from six $[M_4Cl]^{7+}$ units and eight BTT linkers located at its square and hexagonal faces, respectively. (d) A cube of eight cages, each of which is connected with six adjacent cages through its square faces. The void cavity inside the cages and the one formed by connecting eight such cages are displayed as cyan and magenta spheres, respectively. For clarity, hydrogen atoms and coordinated water molecules have been removed from all structural plots.

Taking the van der Waals radii of C atoms (1.75 Å) into account, imaginary spheres with diameters of 10.9 and 15.6 Å could fit into the sodalite-like cages and the larger cages formed by eight sodalite-like cages, respectively. The nearly circular cage window between the larger cages would admit the passage of an imaginary sphere with a diameter of 10.2 Å, taking the van der Waals radii of N atoms (1.55 Å) into account. The M–N distances of **1** and **2** are 2.098(3) and 2.329(3) Å, respectively. The M–O distances observed in **1** and **2** are 2.082(7) and 2.301(8) Å, respectively. The solvent accessible volumes of **1** and **2** estimated by the program PLATON⁴³ are 4384.2 and 4934.9 Å³, respectively, which are 66.6% and 68.0% of the respective unit cell volumes (6580.0 Å³, **1**; 7252.5 Å³, **2**). The counter ions or solvent molecules inside the pores could not be refined owing to the severe thermal disorder, and they were characterized by the IR spectroscopy, TGA and elemental analysis. The final structural model was refined without the counter ions or solvent molecules by using the SQUEEZE option implemented in the program PLATON.⁴³

4 TGA and XRPD

Phase purity of **1** and **2** was examined using XRPD patterns recorded from as-synthesized **1** and **2** at ambient conditions. The experimental XRPD patterns of **1** and **2** (Fig. S2 and S3†) are consistent with the simulated ones as gleaned from the single-crystal X-ray diffraction data. The compounds retain their crystallinity upon soaking in methanol and consequent heating

at 135 °C for 24 h under dynamic vacuum (*i.e.*, activation), as verified by the XRPD patterns of the corresponding samples (Fig. S4 and S5†). Moreover, TGA and temperature-dependent XRPD (TDXRPD) experiments were performed to examine the thermal stability of both compounds. It is observed that as-synthesized **1** and **2** decompose above 350 and 300 °C, respectively.

In the TG curve of as-synthesized **1** (Fig. 2a), the first weight loss of 8.3% in the range 25–120 °C is attributed to the removal of 12 guest water molecules per formula unit (calc. 7.6%). The second weight loss of 16.5% in the range of 120–270 °C is due to the removal of 18 DMA molecules per formula unit (calc. 18.5%). After that the framework starts to decompose leading to the formation of an X-ray amorphous material. Below the decomposition temperature, the first weight loss steps of 29.5 and 22.9% are assigned to the removal of 82 methanol and 104 water molecules for methanol-exchanged and hydrated **1** (Fig. S8 and S9†), respectively (calc. 29.5 and 23.0%).

TDXRPD analysis (Fig. 2b) shows that as-synthesized **1** is stable up to 350 °C. After that the compound starts to decompose and becomes completely amorphous at 400 °C.

In the TG curve of as-synthesized **2** (Fig. 3a), the first weight loss of 7.8% in the range 25–120 °C is assigned to the loss of 14 non-coordinated water molecules per formula unit (calc. 6.8%). The second weight loss of 16.2% in the range of 120–270 °C is due to the removal of 22 molecules of occluded DMF molecules per formula unit (calc. 16.0%). After that decomposition of the compound occurs resulting in the formation of CdO. Below the decomposition temperature, the first weight loss steps of 25.4 and 18.6% are assigned to the removal of 82 methanol and 98 water molecules for methanol-exchanged and hydrated **2** (Fig. S10 and S11†), respectively (calc. 25.4 and 18.6%).

From the TDXRPD patterns (Fig. 3b), it becomes obvious that as-synthesized **2** is stable up to 300 °C. After that the material starts to decompose and becomes completely amorphous at 300 °C.

5 FT-IR, luminescence and UV-Vis spectroscopy

The FT-IR spectra of the as-synthesized, methanol-exchanged and thermally activated samples of isostructural **1** and **2** (Fig. S6 and S7†) are almost identical, as expected. The characteristic

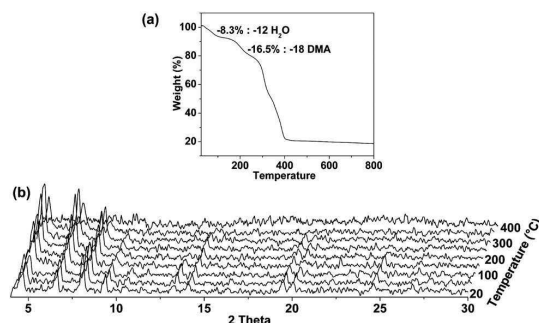


Fig. 2 (a) TG analysis of as-synthesized **1** under air atmosphere. (b) TDXRPD plots of as-synthesized **1** in the range of 20–400 °C.

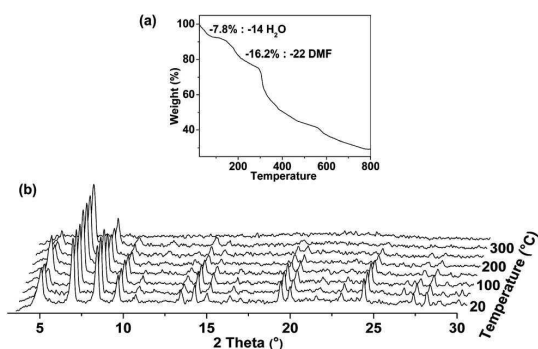


Fig. 3 (a) TG analysis of as-synthesized **2** under air atmosphere. (b) TDXRPD plots of as-synthesized **2** in the range of 20–350 °C.

strong absorption bands assignable to carbonyl groups of occluded DMA and DMF molecules appear at 1613 and 1658 cm^{-1} in the IR spectra of as-synthesized **1** and **2**, respectively.⁴⁴ In the IR spectra of methanol-exchanged **1** and **2**, the carbonyl stretching bands of amide solvent molecules are absent, and a new absorption band attributable to the C–O stretching frequency of the methanol molecule is present at 1019 cm^{-1} .^{17,30,31} These changes indicate that the amide solvent molecules are completely exchanged by the methanol molecules. The absence of the strong bands at 1019 cm^{-1} in the IR spectra of thermally activated **1** and **2** suggests that methanol molecules have been removed from methanol-exchanged **1** and **2**.

Inspired by the strong fluorescence emissions of previously reported coordination polymers containing tetrazolate ligands and d^{10} metal ions,⁴⁵ we investigated the luminescent properties of the as-synthesized sample of Cd-based **2**. Upon excitation at a wavelength of 300 nm, free H_3BTT ligand exhibits a sharp, strong emission band at 350 nm and a weak, broad band centered at 415 nm (Fig. S12†). Because the sharp emission band of as-synthesized **2** occurs at the similar position (340 nm) to that of the free H_3BTT ligand, it should be assigned to the intraligand $\pi-\pi^*$ transition of the BTT ligand.

The solid-state UV-Vis spectra of as-synthesized **1** (Fig. S13†) display three absorption peaks at 1030, 500 and 450 nm in the visible region, which can be attributed to the spin-allowed transitions ${}^4\text{T}_{1g}(\text{F}) \rightarrow {}^4\text{T}_{2g}(\text{F})$ (ν_1), ${}^4\text{T}_{1g}(\text{P})$ (ν_2), and ${}^4\text{A}_{2g}(\nu_3)$, respectively.⁴⁶ The calculated values of Dq (1110 cm^{-1}) and B (925 cm^{-1}) from these transitions are comparable to those of other compounds with octahedrally coordinated Co^{2+} ions.⁴⁶ The absorption band at 450 nm is very weak for thermally activated **1** due to the change of the coordination environment of Co^{2+} ions from octahedral to square-pyramidal as a result of removal of coordinated methanol molecules. The coordination transition of Co^{2+} ions is also verified by the change of color of as-synthesized **1** from red to grayish pink after thermal activation (Fig. S14†).

6 Gas sorption properties

N_2 , CO_2 and H_2 sorption studies were performed on thermally activated **1** and **2**. The results of the sorption analysis are presented in Table 2. The sorption capacities of the present

compounds are comparable with the previously reported Mn-BTT,¹⁷ Cu-BTT³⁰ and Fe-BTT³¹ compounds.

The N_2 adsorption and desorption measurements carried out with thermally activated **1** and **2** revealed reversible type-I isotherms (Fig. 4) with a small hysteresis loop in the pp_0 region of 0.5–1.0 at -196 °C.

The CO_2 adsorption properties of thermally activated **1** and **2** were investigated at 25 °C up to 1 bar. As shown in Fig. 5, the CO_2 adsorption isotherms of both compounds follow type-I behavior in the pressure range from 0 to 1 bar. The lower CO_2 uptake of **2** (Table 2) can be attributed to the partial decomposition of the framework after thermal activation leading to the significant loss of crystallinity of the material, as verified by X-ray powder diffractometry (Fig. S5†).

The hydrogen adsorption isotherms of thermally activated **1** and **2** follow reversible type-I behavior (Fig. 6) at -196 °C up to 1 bar.

7 Selective removal of sulfur compounds from fuel feeds

The smaller sodalite-like cages of compound **1** are likely inaccessible to larger organic molecules since the cage windows between the smaller and the larger cages are too small. However, the cage windows between the larger cages have a diameter of 10.2 Å and are thus sufficiently large to allow larger organic molecules, as typically encountered in the liquid phase, to diffuse through. Since these large cages contain CUSs, the potential of compound **1** for the selective removal of sulfur compounds from fuel feeds has been probed by measuring the single compound adsorption isotherms of thiophene, benzothiophene and dibenzothiophene out of a synthetic mixture of heptane : toluene in a volumetric ratio 80 : 20 (H/T 80/20), a mixture that simulates an actual fuel feed composition (Fig. 7).

Single compound isotherms reveal the selective uptake of all three sulfur compounds tested. Thiophene is adsorbed up to 2 wt%, while benzothiophene and dibenzothiophene reach saturation levels of 7 and 11 wt%, respectively. These results correspond to an uptake of 2.5 molecules of thiophene per unit cell, 4 molecules of benzothiophene and even 4.5 molecules of dibenzothiophene per unit cell. A unit cell comprises half a large supercage and 1 complete sodalite-type cage and it contains 8 CUSs per half a large supercage.

It has been reported that toluene, abundantly present as solvent molecules, co-adsorbs in MOFs with CUSs on the less specific adsorption sites like the aromatic rings in the pore walls.¹³ Therefore, adsorption of these sulfur compounds can be assumed to occur mainly on the CUSs. Co^{2+} can be considered as an intermediate Lewis acid site and will be able to interact with weak bases like sulfur compounds and toluene molecules. The uptake of thiophene is relatively low, with approximately one out of three CUS occupied. Thiophene is smaller than (di)benzothiophene and will thus only be able to interact with the CUSs. Since the aromatic ring of toluene molecules will also be able to interact with these CUSs, not all of these sites will be occupied by thiophene, resulting in a fairly low uptake.

In the case of benzothiophene and dibenzothiophene, up to 4.5 molecules can be adsorbed in the unit cell of compound **1**. In addition to their sulfur atoms, these compounds can interact by

Table 2 Results of sorption analysis for the M-BTT ($M^{2+} = \text{Co, Cd, Mn, Cu, Fe}$) solids

Compound	BET surface area ^a /m ² g ⁻¹	Langmuir surface area ^a /m ² g ⁻¹	Micropore volume ^a at $p/p_0 = 0.5$ (cm ³ g ⁻¹)	H ₂ uptake at 1 bar (wt%)	CO ₂ uptake at 1 bar (wt%)
Co-BTT	1749	1993	0.67	1.5	13.7
Cd-BTT	1415	1635	0.58	1.4	6.2
Mn-BTT ¹⁷	2100	—	—	2.3	—
Cu-BTT ³⁰	1710	1770	—	2.4	—
Fe-BTT ³¹	2010	2200	—	2.3	13.5

^a The specific surface areas and micropore volumes have been calculated from the N₂ adsorption isotherms.

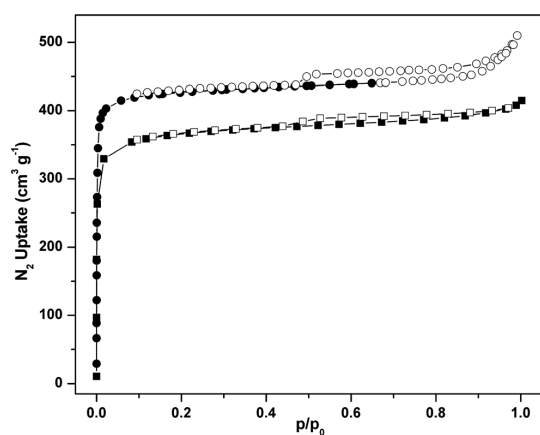


Fig. 4 Low pressure N₂ adsorption (solid symbols) and desorption (empty symbols) isotherms of thermally activated **1** (circles) and **2** (squares) measured at -196 °C.

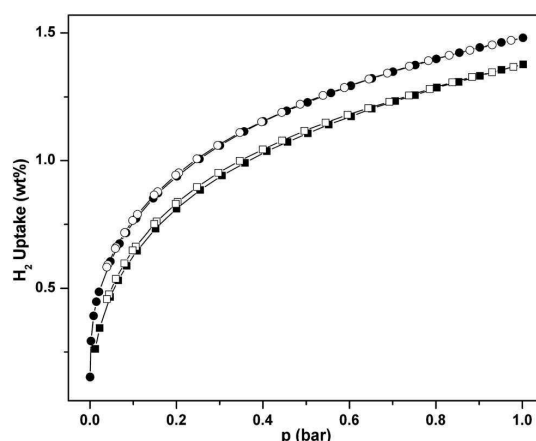


Fig. 6 Low pressure H₂ adsorption (solid symbols) and desorption (empty symbols) isotherms of thermally activated **1** (circles) and **2** (squares) measured at -196 °C.

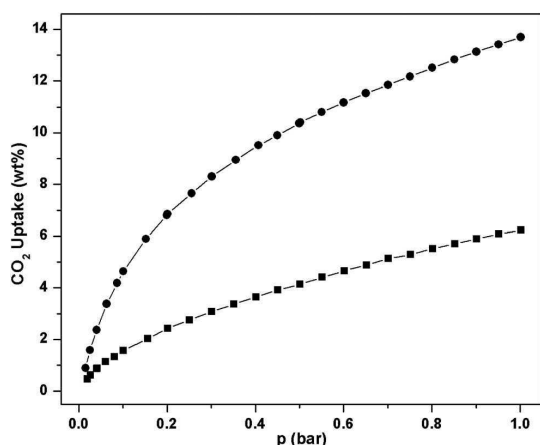


Fig. 5 CO₂ adsorption isotherms of thermally activated **1** (circles) and **2** (squares) measured at 25 °C.

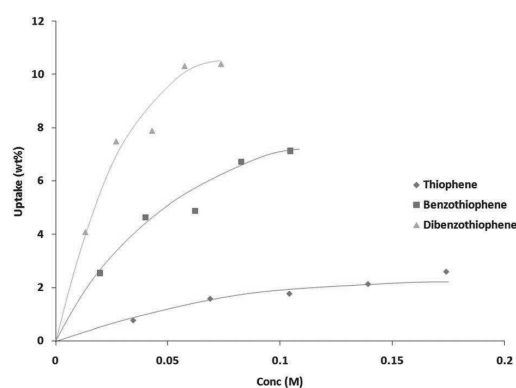


Fig. 7 Single compound adsorption isotherms measured in the batch mode: uptake (wt%) of thiophene, benzothiophene or dibenzothiophene out of a mixture of H/T 80/20 as a function of equilibrium concentration (M). Experiments were performed at room temperature (25 °C).

means of their own aromatic rings with, for example, the organic linker in the pore walls. π - π interactions between the aromatic rings of adsorbate molecules and organic linkers of the host have been extensively reported.⁴⁷ This additional interaction leads to a more pronounced uptake of these aromatic ring containing

sulfur compounds compared to thiophene. The fact that not all free ligation sites are occupied can be explained by the cage dimensions. It is logic to assume that these larger molecules can only be adsorbed in limited amounts before the cages are completely saturated. In addition to this, the adsorption of

(di)benzothiophene on one free metal site might sterically hinder the adsorption on a nearby free metal site. In this case, these metal sites will likely be occupied by smaller toluene solvent molecules.

8 Catalytic properties

Encouraged by the availability of both Lewis acidic and potentially redox-active Co sites in thermally activated **1**, we have investigated its catalytic performance in the ring opening of styrene epoxide and in the aerobic oxidation of different cycloalkanes and benzylic compounds.

8.1 Ring opening of styrene oxide

The previously reported Mn-BTT compound, which is isostructural to **1**, was shown to exhibit size-selective Lewis acid catalysis in the cyanosilylation of carbonyl substrates and in the Mukaiyama-aldol reaction.¹⁹ Selecting ring opening of epoxide as the model reaction, we have screened the methanolysis of styrene oxide in the presence of thermally activated **1**. The time-conversion plot for the transformation of styrene oxide with methanol as a nucleophile to 2-methoxy-2-phenylethanol is shown in Fig. 8. The conversions of the substrate to the product were 67 and 40% after 29 h in the presence of thermally activated **1** and $\text{Co}(\text{NO}_3)_2 \cdot 6\text{H}_2\text{O}$ (Fig. 8a and c), respectively. This fact confirms the higher efficiency of thermally activated **1** compared to the homogeneous catalyst.

To verify whether the catalysis of ring opening of styrene oxide with methanol is truly heterogeneous or is due to some leached Co^{2+} ions present in the liquid phase, the reaction was carried out under the optimized conditions at 50 °C using thermally activated **1** as catalyst. Then, the solid was filtered in hot from the reaction mixture after 9 h at 30% formation of 2-methoxy-2-phenylethanol. After removal of catalyst **1**, the solution in the absence of solid was again stirred at 50 °C. After 29 h, no further product formation was observed in the absence of solid (Fig. 8b).

Reusability of **1** as a heterogeneous catalyst for the ring opening of styrene oxide was investigated under optimized conditions at 50 °C. After the reaction time, the solid catalyst was filtered, washed with methanol, heated at 135 °C for 24 h under vacuum, and used for another consecutive run without further treatment. The catalyst exhibited very minor decrease in percentage conversions upon reuse for the second and third runs (Fig. S15†). A comparison of the XRD patterns of the fresh and thrice-used sample of **1** (Fig. S4†) verifies the structural integrity of thermally activated **1** under the catalytic conditions.

8.2 Aerobic oxidation of cycloalkanes and benzylic compounds

Besides as solid Lewis acid, we also studied the activity of solid **1** to promote the aerobic oxidation of C–H bonds in combination with *N*-hydroxyphthalimide (NHPI) as radical initiator. It is well documented in the literature that NHPI in combination with Co^{2+} salts is a powerful homogeneous catalyst for the aerobic oxidation of alkanes, alcohols and other organic compounds.⁴⁸ We have recently shown that NHPI adsorbed within the pores of commercial Fe(BTC) is an efficient catalyst for the selective oxidation of cycloalkanes.⁴⁹ It can be assumed that other MOFs,

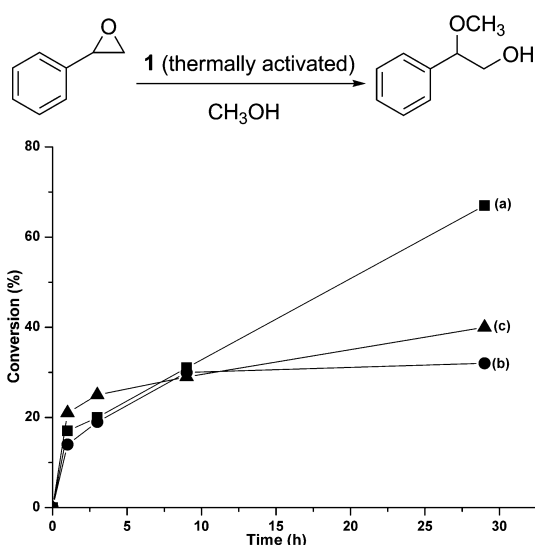


Fig. 8 Time conversion plot for the ring opening of styrene oxide in methanol with: (a) thermally activated **1**, (b) removal of the catalyst, and (c) $\text{Co}(\text{NO}_3)_2 \cdot 6\text{H}_2\text{O}$. Reaction conditions: (a) styrene oxide (0.1 mL), thermally activated **1** (20 mg), methanol (5 mL), 50 °C; (b) same as conditions given in "a" with removal of the catalyst after 9 h; (c) styrene oxide (0.1 mL), $\text{Co}(\text{NO}_3)_2 \cdot 6\text{H}_2\text{O}$ (34 mg), methanol (5 mL), 50 °C. The scheme for the reaction is shown on the top.

Table 3 Aerobic oxidation of cycloalkanes and benzylic compounds using NHPI/**1**^a

Run	Substrate	Time/h	Conversion (%) ^b	Selectivity (%) ^b	
				ol/one	Others
1		1	—	—	—
2		4	3	99 ^c	—
3		9	7	99 ^c	—
4		24	—	—	—
5		1	5	99 ^c	—
6		4	10	99 ^c	—
7		9	14	99 ^c	—
8		29	20	99 ^c	—
9		1	3	98	—
10		4	13	98	—
11		9	34	95	5 ^d
12		29	41	93	7 ^d
13		1	1.3	98	2
14		4	13	97	3
15		9	25	96	4
16		29	48	78	22 ^e

^a Reaction conditions: substrate (2 mL), NHPI/**1** (50 mg, having 5 wt% loading of NHPI), 120 °C, oxygen purged; in the case of toluene at 100 °C. ^b Determined by GC. ^c Selectivity corresponds to ketone. ^d Small percentage of tetralin hydroperoxide, 1-naphthol and 1,4-benzoquinone was also formed. ^e This number corresponds to the combined selectivity of cyclooctylhydroperoxide, cyclooctanediol, cyclooctanedione, octanedioic acid.

particularly those containing Co^{2+} , having NHPI incorporated inside the pores, can also act similarly.

The aerobic oxidation of several cycloalkanes and benzylic compounds in the presence of solid **1** containing NHPI was examined. The results of the catalytic activity are presented in Table 3.

Comparison of the results achieved using NHPI/**1** with those recently reported for the analogous NHPI/Fe(BTC) system indicates that **1** as host exhibits lower activity, but a higher selectivity towards ol/one at the same conversion level. Considering that selectivity is the key issue in aerobic oxidations, it seems that solid **1** containing Co^{2+} should be a preferable catalyst than Fe(BTC).

9 Conclusions

Summarizing, we have discovered two new microporous MOFs: Co-BTT (**1**) and Cd-BTT (**2**) using 1,3,5-benzenetris-tetrazole (H_3BTT) as linker and a solvothermal approach in two different amide solvents (DMA for **1**; DMF for **2**). The successful synthesis and characterization of these two compounds generalize the feasibility of synthesizing microporous M-BTT frameworks with most of the 3d (Mn, Fe, Co, Cu) along with a 4d (Cd) transition metal(II) ion. Both compounds are highly porous and promising for gas phase adsorption and storage applications. The availability of CUSs reveals the compounds potential for the purification of fuel feeds and these CUSs as well as redox-active Co sites enabled the thermally activated Co-BTT solid as a heterogeneous catalyst in the ring opening of styrene oxide, and in the aerobic oxidation of several cycloalkanes and benzylic compounds.

Acknowledgements

The Deutsche Forschungsgemeinschaft (DFG, SPP 1362 "Porous Metal–Organic Frameworks" under the grant STO 643/5-2) is gratefully acknowledged for the financial support. The research leading to these results has received funding from the European Community's Seventh Framework Programme (FP7/2007-2013) under grant agreement no. 228862.

References

- (a) G. Férey, *Chem. Soc. Rev.*, 2008, **37**, 191; (b) S. Kitagawa, R. Kitaura and S. Noro, *Angew. Chem., Int. Ed.*, 2004, **43**, 2334; (c) O. M. Yaghi, M. O'Keeffe, N. W. Ockwig, H. K. Chae, M. Eddaoudi and J. Kim, *Nature*, 2003, **423**, 705.
- (a) L. J. Murray, M. Dinca and J. R. Long, *Chem. Soc. Rev.*, 2009, **38**, 1294; (b) J.-R. Li, R. J. Kuppler and H.-C. Zhou, *Chem. Soc. Rev.*, 2009, **38**, 1477; (c) L. Hamon, P. L. Llewellyn, T. Devic, A. Ghoufi, G. Clet, V. Guillerm, G. D. Pirngruber, G. Maurin, C. Serre, G. Driver, W. van Beek, E. Jolmaitre, A. Vimont, M. Daturi and G. Férey, *J. Am. Chem. Soc.*, 2009, **131**, 17490.
- (a) A. Corma, H. Garcia and F. X. Llabres i Xamena, *Chem. Rev.*, 2010, **110**, 4606; (b) D. Farrusseng, S. Aguado and C. Pinel, *Angew. Chem., Int. Ed.*, 2009, **48**, 7502; (c) J. Y. Lee, O. K. Farha, J. Roberts, K. A. Scheidt, S. T. Nguyen and J. T. Hupp, *Chem. Soc. Rev.*, 2009, **38**, 1450; (d) Z. Wang, G. Chen and K. Ding, *Chem. Rev.*, 2009, **109**, 322; (e) L. Ma, C. Abney and W. Lin, *Chem. Soc. Rev.*, 2009, **38**, 1248.
- (a) K. Schlichte, T. Kratzke and S. Kaskel, *Microporous Mesoporous Mater.*, 2004, **73**, 81; (b) C. Janiak, *Dalton Trans.*, 2003, 2781; (c) L. Alaerts, E. Seguin, H. Poelman, F. Thibault-Starzyk, P. A. Jacobs and D. E. De Vos, *Chem.–Eur. J.*, 2006, **12**, 7353; (d) A. Henschel, K. Gedrich, R. Kraehnert and S. Kaskel, *Chem. Commun.*, 2008, 4192; (e) J. W. Han and C. L. Hill, *J. Am. Chem. Soc.*, 2007, **129**, 15094; (f) P. Horcajada, S. Surblé, C. Serre, D. Y. Hong, Y. K. Seo, J. S. Chang, J. M. Greneche, I. Margiolaki and G. Férey, *Chem. Commun.*, 2007, 2820.
- (a) S. Hasegawa, S. Horike, R. Matsuda, S. Furukawa, K. Mochizuki, Y. Kinoshita and S. Kitagawa, *J. Am. Chem. Soc.*, 2007, **129**, 2607; (b) C. Wu, A. Hu, L. Zhang and W. Lin, *J. Am. Chem. Soc.*, 2005, **127**, 8940; (c) Y. K. Hwang, D.-Y. Hong, J.-S. Chang, S. H. Jung, Y.-K. Seo, J. Kim, A. Vimont, M. Daturi, C. Serre and G. Férey, *Angew. Chem., Int. Ed.*, 2008, **47**, 4144; (d) M. J. Ingleson, J. P. Barrio, J. Bacsá, C. Dickinson, H. Park and M. J. Rosseinsky, *Chem. Commun.*, 2008, 1287; (e) K. S. Suslick, P. Bhyrappa, J. H. Chou, M. E. Kosal, S. Nakagaki, D. W. Smithenry and S. R. Wilson, *Acc. Chem. Res.*, 2005, **38**, 283; (f) S. H. Cho, B. Ma, S. T. Nguyen, J. T. Hupp and T. E. Albrecht-Schmitt, *Chem. Commun.*, 2006, 2563; (g) A. M. Shultz, O. K. Farha, J. T. Hupp and S. T. Nguyen, *J. Am. Chem. Soc.*, 2009, **131**, 4204; (h) J. S. Seo, D. Whang, H. Lee, S. I. Jun, J. Oh, Y. J. Jeon and K. Kim, *Nature*, 2000, **404**, 982; (i) O. R. Evans, H. L. Ngo and W. Lin, *J. Am. Chem. Soc.*, 2001, **123**, 10395; (j) A. G. Hu, H. L. Ngo and W. Lin, *J. Am. Chem. Soc.*, 2003, **125**, 11490; (k) A. Hu, H. L. Ngo and W. Lin, *Angew. Chem., Int. Ed.*, 2003, **42**, 6000; (l) D. N. Dybtsev, A. L. Nuzhdin, H. Chun, K. P. Bryliakov, E. P. Talsi, V. P. Fedin and K. Kim, *Angew. Chem., Int. Ed.*, 2006, **45**, 916.
- A. Chesney, *Green Chem.*, 1999, **1**, 209.
- (a) L. Huang, H. Wang, J. Chen, Z. Wang, J. Sun, D. Zhao and Y. Yan, *Microporous Mesoporous Mater.*, 2003, **58**, 105; (b) C. Lin, S. Chui, S. Lo, F. Shek, M. Wu, K. Suwinska, J. Lipkowski and I. Williams, *Chem. Commun.*, 2002, 1642; (c) J. A. Greathouse and M. D. Allendorf, *J. Am. Chem. Soc.*, 2006, **128**, 10678.
- (a) S. Kitagawa, R. Kitaura and S. Noro, *Angew. Chem., Int. Ed.*, 2004, **43**, 2334; (b) M. Rosseinsky, *Microporous Mesoporous Mater.*, 2004, **73**, 15; (c) O. Yaghi, C. Davis, G. Li and H. Li, *J. Am. Chem. Soc.*, 1997, **119**, 2861.
- (a) P. D. C. Dietzel, Y. Morita, R. Blom and H. Fjellvåg, *Angew. Chem., Int. Ed.*, 2005, **44**, 6354; (b) M. Dinca and J. R. Long, *J. Am. Chem. Soc.*, 2005, **127**, 9376; (c) N. L. Rosi, J. Kim, M. Eddaoudi, B. Chen, M. O'Keeffe and O. M. Yaghi, *J. Am. Chem. Soc.*, 2005, **127**, 1504; (d) A. Vimont, J.-M. Goupil, J.-C. Lavalley, M. Daturi, S. Surblé, C. Serre, F. Millange, G. Férey and N. Audebrand, *J. Am. Chem. Soc.*, 2006, **128**, 3218; (e) H. R. Moon, N. Kobayashi and M. P. Suh, *Inorg. Chem.*, 2006, **45**, 8672; (f) M. Dinca, A. Dailly, Y. Liu, C. M. Brown, D. A. Neumann and J. R. Long, *J. Am. Chem. Soc.*, 2006, **128**, 16876; (g) P. D. C. Dietzel, B. Panella, M. Hirscher, R. Blom and H. Fjellvåg, *Chem. Commun.*, 2006, 959; (h) M. Dinca, W. S. Han, Y. Liu, A. Dailly, C. M. Brown and J. R. Long, *Angew. Chem., Int. Ed.*, 2007, **46**, 1419; (i) M. Dinca and J. R. Long, *Angew. Chem., Int. Ed.*, 2008, **47**, 6766; (j) S. R. Caskey, A. G. Wong-Foy and A. J. Matzger, *J. Am. Chem. Soc.*, 2008, **130**, 10870; (k) P. D. C. Dietzel, R. Blom and H. Fjellvåg, *Eur. J. Inorg. Chem.*, 2008, 3624; (l) Y. Liu, H. Kabbour, C. M. Brown, D. A. Neumann and C. C. Ahn, *Langmuir*, 2008, **24**, 4772.
- Unsaturated metal sites within inorganic and hybrid materials have formerly been shown to improve hydrogen adsorption (a) P. M. Forster, J. Eckert, J.-S. Chang, S.-E. Park, G. Férey and A. K. Cheetham, *J. Am. Chem. Soc.*, 2003, **125**, 1309; (b) M. R. Hartman, V. K. Peterson, Y. Liu, S. S. Kaye and J. R. Long, *Chem. Mater.*, 2006, **18**, 3221; (c) P. M. Forster, J. Eckert, B. D. Heiken, J. B. Parise, J. W. Yoon, S. H. Jung, J.-S. Chang and A. K. Cheetham, *J. Am. Chem. Soc.*, 2006, **128**, 16846.
- (a) S. R. Caskey, A. G. Wong-Foy and A. J. Matzger, *J. Am. Chem. Soc.*, 2008, **130**, 10870; (b) P. D. C. Dietzel, R. E. Johnsen, H. Fjellvåg, S. Bordiga, E. Groppo, S. Chavan and R. Blom, *Chem. Commun.*, 2008, 5125; (c) P. D. C. Dietzel, V. Besikiotis and R. Blom, *J. Mater. Chem.*, 2009, **19**, 7362; (d) D. Britt, H. Furukawa, B. Wang, T. G. Glover and O. M. Yaghi, *Proc. Natl. Acad. Sci. U. S. A.*, 2009, **106**, 20637.
- (a) L. Alaerts, C. Kirschhock, M. Maes, M. van der Veen, V. Finsy, A. Depla, J. Martens, G. Baron, P. Jacobs, J. Denayer and D. E. De Vos, *Angew. Chem., Int. Ed.*, 2007, **46**, 4372; (b) M. Maes, L. Alaerts, F. Vermoortele, R. Ameloot, S. Couck, V. Finsy, J. Denayer and D. E. De Vos, *J. Am. Chem. Soc.*, 2010, **132**, 2284.

- 13 M. Maes, M. Trekels, M. Boulhout, S. Schouteden, F. Vermoortele, L. Alaerts, D. Heurtaux, Y.-K. Seo, Y. K. Hwang, J.-S. Chang, I. Beurroies, R. Denoyel, K. Temst, A. Vantomme, P. Horcajada, C. Serre and D. E. De Vos, *Angew. Chem., Int. Ed.*, 2011, **50**, 4210.
- 14 K. Cychosz, A. Wong-Foy and A. Matzger, *J. Am. Chem. Soc.*, 2008, **130**, 6938.
- 15 B. Kesanli and W. Lin, *Coord. Chem. Rev.*, 2003, **246**, 305.
- 16 S. S. Y. Chui, S. M. F. Lo, J. P. H. Charmant, A. G. Orpen and I. D. Williams, *Science*, 1999, **283**, 1148.
- 17 M. Dincă, A. Dailly, Y. Liu, C. M. Brown, D. A. Neumann and J. R. Long, *J. Am. Chem. Soc.*, 2006, **128**, 16876.
- 18 G. Férey, C. Mellot-Draznieks, C. Serre, F. Millange, J. Dutour, S. Surblé and I. Margiolaki, *Science*, 2005, **309**, 2040.
- 19 S. Horike, M. Dincă, K. Tamaki and J. R. Long, *J. Am. Chem. Soc.*, 2008, **130**, 5854.
- 20 (a) A. Dhakshinamoorthy, M. Alvaro and H. Garcia, *ACS Catal.*, 2011, **1**, 48; (b) A. Dhakshinamoorthy, M. Alvaro and H. Garcia, *ChemCatChem*, 2010, **2**, 1438; (c) A. Dhakshinamoorthy, M. Alvaro and H. Garcia, *Chem. Commun.*, 2010, **46**, 6476; (d) J. Kim, S. Bhattacharjee, K.-E. Jeong, S.-Y. Jeong and W.-S. Ahn, *Chem. Commun.*, 2009, 3904.
- 21 A. Dhakshinamoorthy, M. Alvaro and H. Garcia, *J. Catal.*, 2009, **267**, 1.
- 22 A. Dhakshinamoorthy, M. Alvaro and H. Garcia, *Chem.–Eur. J.*, 2010, **16**, 8530.
- 23 A. Dhakshinamoorthy, M. Alvaro and H. Garcia, *Adv. Synth. Catal.*, 2009, **351**, 2271.
- 24 A. Dhakshinamoorthy, M. Alvaro and H. Garcia, *Adv. Synth. Catal.*, 2010, **352**, 3022.
- 25 A. Dhakshinamoorthy, M. Alvaro and H. Garcia, *Appl. Catal., A*, 2010, **378**, 19.
- 26 Y. K. Hwang, D.-Y. Hong, J.-S. Chang, H. Seo, M. Yoon, J. Kim, S. H. Jung, C. Serre and G. Férey, *Appl. Catal., A*, 2009, **358**, 249.
- 27 Y. K. Hwang, D.-Y. Hong, J.-S. Chang, S. H. Jung, Y.-K. Seo, J. Kim, A. Vimont, M. Daturi, C. Serre and G. Férey, *Angew. Chem., Int. Ed.*, 2008, **47**, 4144.
- 28 A. Dhakshinamoorthy, M. Alvaro and H. Garcia, *Adv. Synth. Catal.*, 2010, **352**, 711.
- 29 L. Alaerts, E. Séguin, H. Poelman, F. Thibault-Starzyk, P. A. Jacobs and D. E. De Vos, *Chem.–Eur. J.*, 2006, **12**, 7353.
- 30 M. Dincă, W. S. Han, Y. Liu, A. Dailly, C. M. Brown and J. R. Long, *Angew. Chem., Int. Ed.*, 2007, **46**, 1419.
- 31 K. Sumida, S. Horike, S. S. Kaye, Z. R. Herm, W. L. Queen, C. M. Brown, F. Grandjean, G. J. Long, A. Dailly and J. R. Long, *Chem. Sci.*, 2010, **1**, 184.
- 32 W. Ouellette, K. Darling, A. Prosvirin, K. Whitenack, K. R. Dunbar and J. Zubietta, *Dalton Trans.*, 2011, **40**, 12288.
- 33 (a) J. Huang, T. Akita, J. Faye, T. Fujitani, T. Takei and M. Haruta, *Angew. Chem., Int. Ed.*, 2009, **48**, 7862; (b) A. K. Sinha, S. Seelan, S. Tsubota and M. Haruta, *Angew. Chem., Int. Ed.*, 2004, **43**, 1546.
- 34 (a) N. Komiya, T. Naota, Y. Oda and S. I. Murahashi, *J. Mol. Catal. A: Chem.*, 1997, **117**, 21; (b) A. Boettcher, M. W. Grinstaff, J. A. Labinger and H. B. Gray, *J. Mol. Catal. A: Chem.*, 1996, **113**, 191.
- 35 W. W. Wendlandt and H. G. Hecht, *Reflectance Spectroscopy*, Interscience Publishers/JohnWiley & Sons, New York, 1966.
- 36 (a) G. M. Sheldrick, *SHELXTL Version 5.1*, Bruker Analytical X-ray Instruments Inc., Madison, Wisconsin, USA, 1998; (b) G. M. Sheldrick, *SHELX-97 PC Version*, University of Göttingen, Germany, 1997.
- 37 L. Alaerts, M. Maes, M. van der Veen, P. Jacobs and D. E. De Vos, *Phys. Chem. Chem. Phys.*, 2009, **11**, 2903.
- 38 M. Dincă and J. Long, *J. Am. Chem. Soc.*, 2007, **129**, 11172.
- 39 V. A. Blatov, *IUCr CompComm Newsletter*, 2006, **7**, 4.
- 40 Reticular Chemistry Structure Resource, (<http://okeeffews1.la.asu.edu/RCSR/home.htm>).
- 41 M. J. Bucknum and E. A. Castro, *Cent. Eur. J. Chem.*, 2005, **3**, 169.
- 42 (a) S. Ma and H.-C. Zhou, *J. Am. Chem. Soc.*, 2006, **128**, 11734; (b) S. B. Choi, M. J. Seo, M. Cho, Y. Kim, M. K. Jin, D.-Y. Jung, J.-S. Choi, W.-S. Ahn, J. L. C. Rowsell and J. Kim, *Cryst. Growth Des.*, 2007, **7**, 2290; (c) Y.-X. Tan, Y.-P. He and J. Zhang, *Chem. Commun.*, 2011, **47**, 10747.
- 43 A. L. Spek, *J. Appl. Crystallogr.*, 2003, **36**, 7.
- 44 T. J. Markley, B. H. Toby, R. M. Pearlstein and D. Ramprasad, *Inorg. Chem.*, 1997, **36**, 3376.
- 45 (a) J.-Y. Zhang, Y.-Q. Yang, H.-Q. Peng, A.-L. Cheng and E.-Q. Gao, *Struct. Chem.*, 2008, **19**, 535; (b) T. Jiang, Y.-F. Zhao and X.-M. Zhang, *Inorg. Chem. Commun.*, 2007, **10**, 1194; (c) W.-C. Song, J.-R. Li, P.-C. Song, Y. Tao, Q. Yu, X.-L. Tong and X.-H. Bu, *Inorg. Chem.*, 2009, **48**, 3792; (d) Y. Li, X. H. Zhong, F.-K. Zheng, M.-F. Wu, Z. F. Liu and G.-C. Guo, *Inorg. Chem. Commun.*, 2011, **14**, 407; (e) Y. Li, G. Xu, W.-Q. Zou, M.-S. Wang, F.-K. Zheng, M.-F. Wu, H.-Y. Zeng, G.-C. Guo and J.-S. Huang, *Inorg. Chem.*, 2008, **47**, 7945.
- 46 (a) A. B. P. Lever, *Inorganic Electronic Spectroscopy*, Elsevier Publishing Company, Amsterdam, 1968, ch. 9; (b) The *Dq* and *B* values were estimated by using the transition energy ratio diagrams in pp. 393–400 of the same book as in ref. 46a.
- 47 (a) X. Wang, L. Liu and A. Jacobsen, *Angew. Chem., Int. Ed.*, 2006, **45**, 1; (b) P. Horcajada, C. Serre, M. Vallet-Regi, M. Sebban, F. Taulelle and G. Férey, *Angew. Chem., Int. Ed.*, 2006, **45**, 5974.
- 48 Y. Ishii, S. Sakaguchi and T. Iwahama, *Adv. Synth. Catal.*, 2001, **343**, 393.
- 49 A. Dhakshinamoorthy, M. Alvaro and H. Garcia, *Chem.–Eur. J.*, 2011, **17**, 6256.

6.1.3. Systematic Investigation of Porous Inorganic-Organic Hybrid Compounds with Photo-Switchable Properties

Die folgende Arbeit wurde in der *Zeitschrift für allgemeine und anorganische Chemie* veröffentlicht (mit freundlicher Genehmigung von Wiley).^[206]

Ziel dieser Arbeit war das Einbringen eines Azobenzolderivats in eine poröse Gerüstverbindung. Azobenzole können durch Bestrahlung mit UV-Licht von der meist stabileren *trans*-Konformation in die *cis*-Konformation überführt werden. Der Schaltvorgang kann mittels UV/Vis Spektroskopie verfolgt werden. Zum Beweis, dass der Schalter in das Gerüst eingebaut ist können Einkristallstrukturanalysen verwendet werden. Es wurden zum Aufbau neuer Metall-organischer Gerüstverbindungen die Linker 4,4'-Biphenyldicarbonsäure (H₂BPDC), 2,6-Naphthalindicarbonsäure (H₂NDC) und 4-Carboxyzimtsäure (H₂CCA) verwendet und mit 3-Azophenyl-4,4-Bipyridin (AzPy) als Coliganden umgesetzt. Die verwendeten Linker sind in Abbildung 6.2 gezeigt.

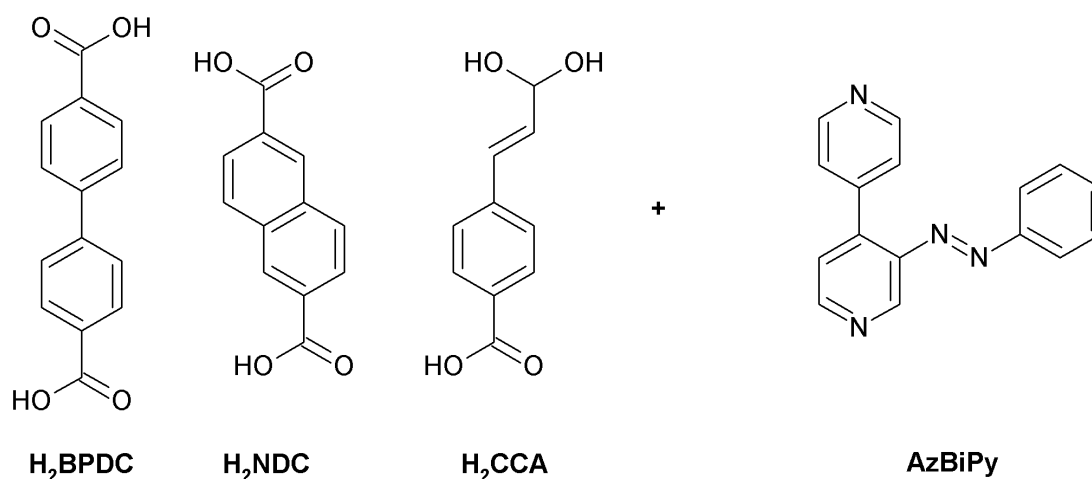


Abbildung 6.2.: 4,4'-Biphenyldicarbonsäure (H₂BPDC), 2,6-Naphthalindicarbonsäure (H₂NDC) und 4-Carboxyzimtsäure (H₂CCA) wurden in Kombination mit 3-Azophenyl-4,4-Bipyridin (AzPy) verwendet.

Es wurden die vier neuen Verbindungen mit der Zusammensetzung [Co₂(NDC)₂(AzBIPY)], [Cu₂(NDC)₂(AzBIPY)], [Zn₂(BPDC)₂(AzBIPY)] und [Zn₂(CCA)₂(AzBIPY)] erhalten. Die Kristallstrukturen von [Co₂(NDC)₂(AzBIPY)], [Zn₂(BPDC)₂(AzBIPY)] und [Zn₂(CCA)₂(AzBIPY)] wurden mittels Einkristallstrukturanalyse aufgeklärt. Die Struktur von [Cu₂(NDC)₂(AzBIPY)] wurde mittels Röntgenpulverbeugung identifiziert. Die Phenylringe der jeweiligen Linker und des Azobipyridins liegen in den Kristallstrukturen statistisch ungeordnet vor. Die Verbindungen sind aus typischen „Schauffelrad“ („Paddle Wheel“) Einheiten

aufgebaut, welche durch die Linker zu einem Netzwerk verknüpft werden. Die Kristallstrukturanalyse zeigte dass interpenetrierte Netzwerke entstanden sind. Trotzdem zeigen die Verbindungen $[\text{Co}_2(\text{NDC})_2(\text{AzBIPY})]$, $[\text{Cu}_2(\text{NDC})_2(\text{AzBIPY})]$ eine scheinbare spezifische Oberfläche von 517 und 488 m^2/g . Der Einbau der Azogruppe in die Verbindungen sollte hierbei das Einbringen eine Schaltfunktion in das Gerüst bewirken. Der Schaltvorgang konnte mittels UV/Vis Spektroskopie für $[\text{Co}_2(\text{NDC})_2(\text{AzBIPY})]$ und $[\text{Cu}_2(\text{NDC})_2(\text{AzBIPY})]$ gezeigt und verfolgt werden.

DOI: 10.1002/zaac.201200048

Systematic Investigation of Porous Inorganic-Organic Hybrid Compounds with Photo-Switchable Properties

Antje Modrow,^[a] Mark Feyand,^[a] Dordaneh Zargarani,^[b] Rainer Herges,^[b] and Norbert Stock*^[a]

Dedicated to Professor Rudolf Hoppe on the Occasion of His 90th Birthday

Keywords: Metal-organic frameworks; Paddle-wheel structure: *cis/trans*-Isomerisation; Zinc; Copper; Cobalt

Abstract. Four new compounds [Co₂(NDC)₂(AzBIPY)] (1), [Cu₂(NDC)₂(AzBIPY)] (2), [Zn₂(BPDC)₂(AzBIPY)] (3) and [Zn₂(CCA)₂(AzBIPY)] (4) (with H₂NDC: 2,6-naphthalenedicarboxylic acid, AzBIPY: 3-azo-phenyl-4,4'-bipyridine, H₂BPDC: 4,4'-biphenyldicarboxylic acid and H₂CCA: 4-carboxy-cinnamic acid) were synthesized and characterized. All compounds have paddle-wheel units and

photo switchable linker molecules in common. In all four compounds the azo group of the AzBIPY linker molecule protrudes into the pores. For compound 1 and 2 isomerization can be accomplished upon irradiation with UV light ($\lambda = 365$ nm) to switch the thermodynamically stable *trans*-isomer into the *cis*-isomer. Back switching can be achieved thermally or by irradiation with visible light ($\lambda = 455$ nm).

Introduction

Since metal organic frameworks (MOFs) were discovered in the nineties of the last century, they have attracted more and more attention mainly due to potential application such as sensing, storage, catalysis and separation which are based on their porosity and their structural diversity.^[1] The modular assembly using inorganic bricks and organic linker molecules, often leads to highly porous structures where the pore size and pore chemistry can be adjusted.^[2–4] The synthesis of these compounds can be accomplished under various reaction conditions.^[5] A common motive for metal-vertices is the so-called paddle-wheel unit which contain typically metal(II)-ions that are bridged by four dicarboxylic acid molecules.^[6] Most of the MOFs which have been reported to contain paddle-wheel units are based on the metals zinc^[7–9] and copper.^[10–12] The incorporation of other ions such as iron,^[13] cobalt,^[14,15] nickel,^[16] cadmium,^[17] and rare earth metals^[18,19] is less common. In prominent examples of stable and highly porous paddle-wheel containing MOFs such as HKUST-1,^[10] MOF-14,^[20] and PCN-14^[21] only one organic linker molecule is incorporated. The use of mixed linker systems consisting of a dicarboxylic

acid and a diamine leads to the formation of MOFs with the general composition [M₂(dicarboxylate)₂(diamine)], which is composed of two-dimensional sheets of paddle wheel units connected by the diamine ions. Pillaring of the sheets by the diamines leads to the formation of three-dimensional structures. Commonly aryl dicarboxylic acids such as terephthalic acid, naphthalenedicarboxylic acid and diamines, such as 1,4-diazabicyclo[2.2.2]octan (DABCO)^[7,16] and 4,4'-bipyridine^[7] have been used (Figure 1).

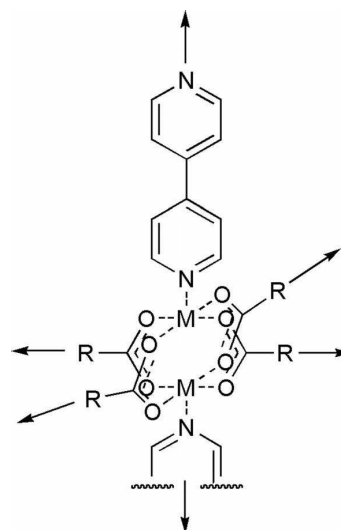


Figure 1. Schematic representation of the paddle-wheel unit and its interconnection as observed in mixed linker compounds [M₂(dicarboxylate)₂(diamine)]. M = metal ion, R = dicarboxylate.

* Prof. Dr. N. Stock
E-Mail: stock@ac.uni-kiel.de

[a] Institut für Anorganische Chemie
Christian-Albrechts Universität zu Kiel
Max-Eyth-Str. 2
24118 Kiel, Germany

[b] Otto Diels Institut für Organische Chemie
Christian-Albrechts Universität zu Kiel
Max-Eyth-Str. 2
24118 Kiel, Germany

Supporting information for this article is available on the WWW under <http://dx.doi.org/10.1002/zaac.201200048> or from the author.

Depending on the organic linker molecules multiple interpenetrating structures have been reported.^[7] Interpenetration can be suppressed by using functionalized linker molecules.^[7] In some cases the incorporated functional groups can be used for post-synthetic modification reactions and thus more complex groups can be introduced in the pore space of the MOFs.^[22–24] Another route to incorporate complex functional groups is by using the corresponding pre-functional organic linker. Thus, we have recently been able to incorporate a photo-switchable azo-bipyridine linker into such a mixed linker MOF $[\text{Zn}_2(\text{NDC})_2(\text{AzBIPY})]$ (H_2NDC = 2,6-naphthalenedicarboxylic acid, AzBIPY = 3-azo-phenyl-4,4'-bipyridine, denoted CAU-5, CAU = Christian-Albrechts-University).^[25] The azo-phenyl-group protrudes into the pore space and *trans/cis*-isomerization can be observed upon irradiation with light ($\lambda = 365$ and 455 nm). In comparison to the pure azo-linker molecule in solution the switching efficiency within in the MOF is much lower. This behavior was attributed to structural aspects. Since twofold interpenetrated networks are observed for $[\text{Zn}_2(\text{NDC})_2(\text{AzBIPY})]$, the isomerization of the azo-groups is hindered.

Here, we present the results of our investigation on the impact of the metal-ion and the size and shape of the dicarboxylic acid linker molecule on the structure of the compounds exhibiting the composition $[\text{M}_2(\text{dicarboxylate})_2(\text{AzBIPY})]$. In addition to structural aspects, the influence on the switching properties are in the focus of this study.

Results

The synthesis of mixed linker compounds $[\text{M}_2(\text{dicarboxylate})_2(\text{diamine})]$ was investigated using Cu^{2+} , Co^{2+} and Ni^{2+} in combination with the linker molecules, 2,6-naphthalenedicarboxylic acid (H_2NDC), 4,4'-biphenyl-dicarboxylic acid (H_2BPDC) and 4-carboxy-cinnamic acid (H_2CCA) (Figure 2).

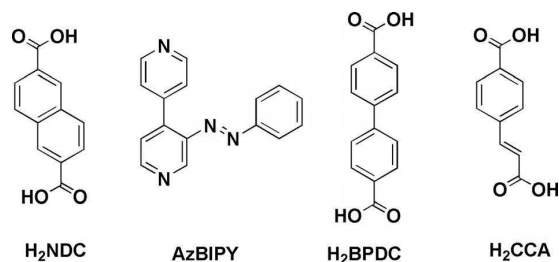


Figure 2. H_2NDC : 2,6-naphthalenedicarboxylic acid, AzBIPY: 3-azo-phenyl-4,4'-bipyridine, H_2BPDC : 4,4'-biphenyl-dicarboxylic acid, H_2CCA : 4-carboxy-cinnamic acid.

The investigations led to the four new compounds $[\text{Co}_2(\text{NDC})_2(\text{AzBIPY})]$ (**1**), $[\text{Cu}_2(\text{NDC})_2(\text{AzBIPY})]$ (**2**), $[\text{Zn}_2(\text{BPDC})_2(\text{AzBIPY})]$ (**3**) and $[\text{Zn}_2(\text{CCA})_2(\text{AzBIPY})]$ (**4**). All compounds are obtained from exactly the same synthesis procedures as previously reported for CAU-5 ($[\text{Zn}_2(\text{NDC})_2(\text{AzBIPY})]$) by just varying the metal ion or the organic linker. We were able to solve three of the four structures from single X-ray diffraction data; structure **2** was confirmed by X-

ray powder diffraction. The structures of **1–4** exhibit the same framework topology as observed for CAU-5.

Variation of the Metal Atom

By changing the metal from Zn^{2+} to Cu^{2+} or Co^{2+} the isostructural compounds of Zn-CAU-5 were obtained. This was demonstrated by XRD measurements (Table 2, Figure S1). While the use of $\text{Co}(\text{NO}_3)_2 \cdot 6\text{H}_2\text{O}$ led to single crystals of **1** suitable for a X-ray structure analysis, $\text{Cu}(\text{NO}_3)_2 \cdot 3\text{H}_2\text{O}$ gave rise a green microcrystalline powder of **2**. A Pawley fit was carried out and the following cell parameters were obtained $a = 18.795(2)$, $b = 17.969(2)$, $c = 13.947(1)$ Å, $\beta = 109.91(9)^\circ$, which are similar to the ones observed for Zn-CAU-5 ($a = 19.060(4)$, $b = 17.898(4)$, $c = 13.932(3)$ Å, $\beta = 111.66(1)^\circ$) (Figure 3)

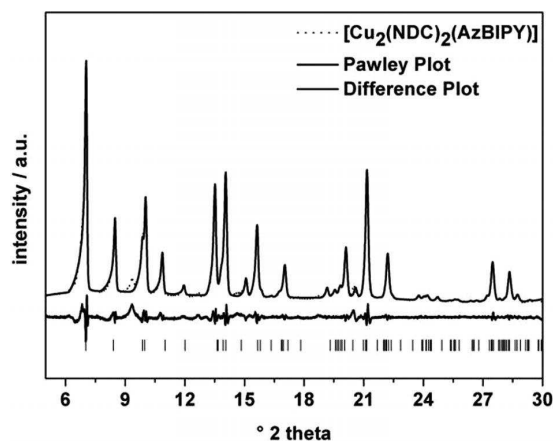


Figure 3. Collected powder pattern of $[\text{Cu}_2(\text{NDC})_2(\text{AzBIPY})]$ (dotted graph), Pawley fit (black graph) and the difference plot (below). A minor crystalline impurity exhibiting a reflection at 9.3° (2θ) is detected. For clarity, the colored figure is presented in the Supporting Information (Figure S2).

Based on the lattice parameters and the comparison of the simulated and measured XRPD patterns, **2** is isostructural to **1** and Zn-CAU-5. The compounds crystallize in the monoclinic space group $C2/c$ with one crystallographic independent metal ion one dicarboxylate ion and half an azobipyridine molecule in the asymmetric unit (Figure S3). Two metal ions are each bridged by four naphthalenedicarboxylate ions and the paddle-wheel units are formed, which are connected to a 2D net. The azobipyridine linker molecules occupy the axial sites and form a 3D network. Due to the large pore space a twofold interpenetrated structure is observed. Nevertheless, all three compounds exhibit permanent porosity after activation under vacuum (Figures S4 and S5). The calculated specific surface areas and micropore volumes for **1** and **2** are in accordance with the ones observed for Zn-CAU-5 with small variations due to the different molar masses (Table 1).

According to the results of the thermogravimetric analyses of activated **1** and **2** (Figures S6 and S7), the compounds are stable up to 350°C and 300°C , respectively. Above this tem-

Table 1. Specific surface area S_{BET} and micropore volume V_{m} of Zn-CAU-5^[25], **1** and **2**.

	$S_{\text{BET}} / \text{m}^2 \cdot \text{g}^{-1}$	$V_{\text{m}} / \text{cm}^3 \cdot \text{g}^{-1}$	$V_{\text{m,calc}} / \text{cm}^3 \cdot \text{g}^{-1}$
Zn-CAU-5 ^[25]	554	0.23	0.23
Co-CAU-5 (1)	517	0.22	0.22
Cu-CAU-5 (2)	488	0.21	–

perature thermal composition in air leads to the formation of the corresponding metal oxides CoO and CuO as established by XRPD measurements. The calculated weight losses correspond well to the observed ones (85.4 % / 85.6 % for **1** and 84.4 % / 84 % for **2**). The Raman spectra of both compounds exhibit the characteristic vibration of both, the azobipyridine linker and the naphthalenedicarboxylic acid. The intense –N=N– stretching vibration of the azo-group is clearly visible at 1449 and 1443 cm^{-1} for **1** and **2**, respectively (Figure S8).

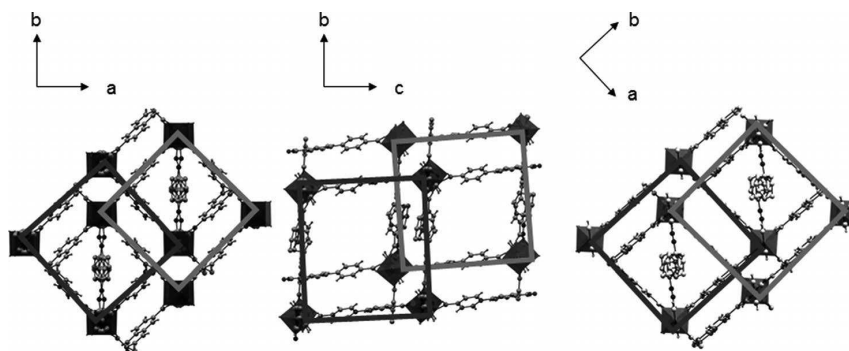
Variation of the Organic Linker Molecule

Changes of the organic linker can result in a more open or even a less-interpenetrated framework structure.^[7] Therefore, the reaction of $\text{Zn}(\text{NO}_3)_2 \cdot 6\text{H}_2\text{O}$ and AzBIPY in DMF/MeOH was carried out with 4-4'-biphenyl-dicarboxylic acid (H_2BPDC) and 4-carboxy-cinnamic acid (H_2CCA) instead of

naphthalenedicarboxylic acid, respectively. The synthesis resulted in the formation of well-developed orange crystals, which were characterized by single-crystal X-ray diffraction (Table 2). Based on the structure determination the compounds have the composition $[\text{Zn}_2(\text{BPDC})_2(\text{AzBIPY})]$ (**3**) and $[\text{Zn}_2(\text{CCA})_2(\text{AzBIPY})]$ (**4**). The structures exhibit the same composition $[\text{M}_2(\text{dicarboxylate})_2(\text{diamine})]$ and the same framework topology as the CAU-5 derivatives, but due to the different size and shape of the linker molecules the space group symmetry is reduced to $P\bar{1}$. In both compounds double interpenetrated framework structures are observed (Figure 4). The use of H_2BPDC results also in a structure with disordered AzBIPY molecules (Figure S9). The use of H_2CCA results in an even more disordered structure (Figures S10, S11). The CCA^{2-} ions are statistically incorporated which leads to partially occupied carbon atom positions and the resulting molecule resembles a naphthalenedicarboxylate ion (Figure S11). Based

Table 2. Crystal Data of $[\text{Co}_2(\text{NDC})_2(\text{AzBIPY})]$ (**1**), $[\text{Zn}_2(\text{BPDC})_2(\text{AzBIPY})]$ (**3**) and $[\text{Zn}_2(\text{CCA})_2(\text{AzBIPY})]$ (**4**).

Chemical formula	$[\text{Co}_2(\text{NDC})_2(\text{AzBIPY})]$	$[\text{Zn}_2(\text{BPDC})_2(\text{AzBIPY})]$	$[\text{Zn}_2(\text{CCA})_2(\text{AzBIPY})]$
Crystal system	monoclinic	triclinic	triclinic
Space group	$C2/c$	$P\bar{1}$	$P\bar{1}$
$a / \text{\AA}$	18.893(4)	13.912(1)	13.174(1)
$b / \text{\AA}$	18.051(4)	15.221(1)	13.219(1)
$c / \text{\AA}$	13.799(3)	15.216(1)	14.029(1)
$\alpha / ^\circ$	90	80.86(1)	82.989(9)
$\beta / ^\circ$	110.72(3)	81.06(1)	82.369(8)
$\gamma / ^\circ$	90	76.49(1)	84.054(9)
$V / \text{\AA}^3$	4401.6(17)	3069.7(5)	2393.9(3)
Z	8	2	2
Formula weight / $\text{g} \cdot \text{mol}^{-1}$	806.44	871.57	771.45
Total number of data collected	32343	33024	20691
Unique/obsd. data [$I > 2\sigma(I)$]	4578 / 4155	14418 / 10045	10033 / 6828
$R(\text{int.})$	0.1087	0.0661	0.0437
$R1, wR2$ [$I > 2\sigma(I)$]	0.0925, 0.1922	0.0642, 0.1838	0.0514, 0.1453
$R1, wR2$ (all data)	0.1018, 0.1972	0.0872, 0.1948	0.0750, 0.1546

**Figure 4.** Interpenetrated networks as observed in compound **1** (left), compound **3** (middle), and compound **4** (right).

on the structural data, the micropore volume changes with the size of the organic linker and the micropore volume of $[\text{Zn}_2(\text{BPDC})_2(\text{AzBIPY})]$ and $[\text{Zn}_2(\text{CCA})_2(\text{AzBIPY})]$ was calculated to be 0.49 and $0.37 \text{ cm}^3 \cdot \text{g}^{-1}$, respectively (Zn-CAU-5: $V_{\text{mic}} = 0.23 \text{ cm}^3 \cdot \text{g}^{-1}$). Unfortunately, the stability of both compounds is limited and no further characterization regarding the porosity and switching behavior could be performed.

UV/Vis Switching Experiments

In analogy to Zn-CAU-5,^[25] compounds **1** and **2** were further characterized by UV/Vis spectroscopy and optical switching experiments were carried out. Due to the permanent porosity of **1** and **2** and the azo-phenyl group protruding into the pore space, *cis/trans* isomerization should be feasible. Successful switching of the azo-phenyl group can be confirmed by UV/Vis spectroscopy since both isomers exhibit distinct electronic spectra which are mainly dominated by $\pi \rightarrow \pi^*$ and $n \rightarrow \pi^*$ transitions. In solution the thermodynamically stable *trans*-isomer of the free AzBIPY linker molecule exhibits two distinct maxima of the $\pi \rightarrow \pi^*$ and $n \rightarrow \pi^*$ transitions at $\lambda = 321 \text{ nm}$ and $\lambda = 460 \text{ nm}$, respectively (Figure S12). After the irradiation with UV-light the intensity of the $\pi \rightarrow \pi^*$ transition ($\lambda = 321 \text{ nm}$) of the *trans*-isomer decreases while the intensity of the $n \rightarrow \pi^*$ transition of the *cis*-isomer ($\lambda = 440 \text{ nm}$) increases. Back switching can be achieved after the irradiation with visible light.

For the solids **1** and **2** switching experiments were performed as described in reference 25. The measurements were carried out in reflection geometry using a BaSO_4 matrix. The results of the switching experiments are shown in Figure 5 and Figure 6. Upon irradiation with UV light ($\lambda = 365 \text{ nm}$) and visible light ($\lambda = 455 \text{ nm}$) small intensity changes of the $n \rightarrow \pi^*$ transition band are observed. These are due to the different concentrations of the *cis*- and *trans*-isomers in the BaSO_4 matrix. Repeated alternating irradiation with UV and

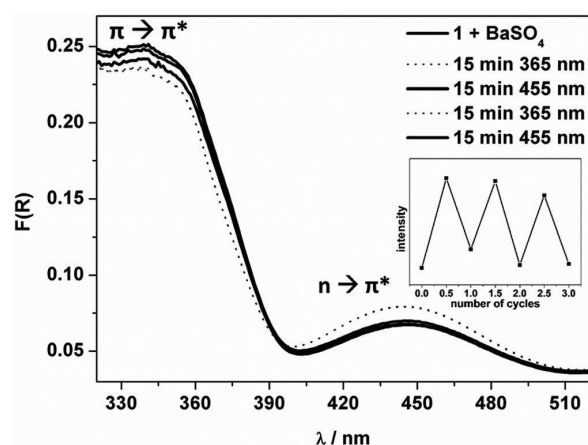


Figure 5. Results of the UV/Vis switching experiment of **1** in a BaSO_4 matrix. For clarity only two switching cycles are shown. Dotted graphs are in a line with each other. For clarity, the colored figure is presented in the Supporting Information (Figure S14).

visible light was carried out to demonstrate the partial reversibility of the *trans/cis* isomerization. In principle back switching from the *cis*- to the *trans*-isomer can also be accomplished at room temperature in the dark. The minor changes in the UV/Vis spectra after 12 h (Figures S13, S14) show that the back switching has long half-life times ($t_{1/2}$). These results are very similar to the ones observed for Zn-CAU-5.^[25]

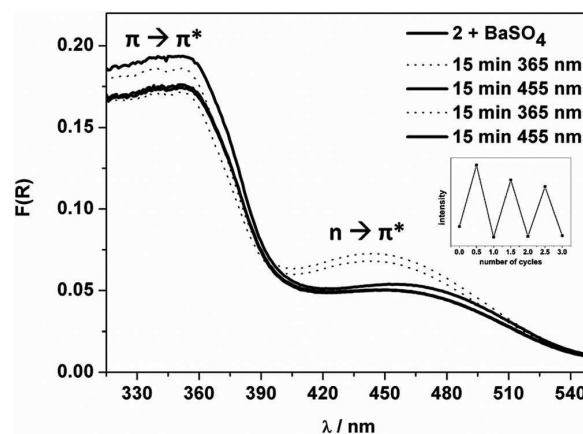


Figure 6. Results of the UV/Vis switching experiment of **2** in a BaSO_4 matrix. For clarity only two switching cycles are shown. For clarity, the colored figure is presented in the Supporting Information (Figure S15).

Discussion

So far we have been able to synthesize and characterize five compounds containing the switchable AzBIPY linker molecule. Variation of the metal ion lead to three isorecticular compounds $[\text{M}_2(\text{NDC})_2(\text{AzBIPY})]$ (M-CAU-5, M = Co, Cu, Zn). These exhibit twofold interpenetrated frameworks. Nevertheless, N_2 sorption measurements confirmed microporosity. UV/Vis switching experiments demonstrated partial reversible *trans/cis* isomerization, but only small changes were observed. This could be attributed to the limited pore space which is due to the interpenetration. Since all three compounds show very similar switching properties the metal ions seem to have little influence on the *trans/cis* isomerization.

One possibility to accomplish more pronounced switching effects could be to increase the available pore space. Different strategies have been reported to accomplish this goal. The length of the linker,^[26] the steric demand,^[7] and the number of carboxylic acid groups^[27] have been varied in order to adjust the pore size. The systematic variation of the linker length lead to the so called IRMOF-series which exhibits interpenetrating structures for IRMOF-9, -10, -13 and -15.^[26] On the other hand in mixed linker MOFs, as presented in this contribution, the steric demand can be varied using diamine or dicarboxylate derivatives. Thus, $[\text{Zn}_2(\text{NDC})_2(4,4'\text{-bipyridine})]$ forms a threefold interpenetrated network whereas $[\text{Zn}_2(\text{NDC})_2(\text{AzBIPY})]$ only shows two fold interpenetration.^[25] In the case of $[\text{Zn}_2(\text{BDC})_2(4,4'\text{-bipy})]$ and $[\text{Zn}_2(\text{TMBDC})_2(4,4'\text{-bi-}$

pyridine)] (BDC = terephthalic acid, TMBC = tetramethylterephthalic acid) the exchange of BDC²⁻ by TMBDC²⁻ molecules lead to a non-interpenetrated framework structure.^[7] Interpenetration can also be prevented by using tetracarboxylic acid molecules instead of dicarboxylic acids. *Nguyen et al.* demonstrated this for [Zn₂(TCPB)(DPG)] (TCPB = 1,2,4,5-tetrakis(4-carboxyphenyl)-benzene, DPG = meso-1,2-bis(4-pyridyl)-1,2-ethanediol).^[27]

Replacement of H₂NDC by other dicarboxylic acids have resulted in the formation of the title compounds **3** and **4** containing BPDC²⁻ and CCA²⁻ ions. Both structures exhibit two-fold interpenetrated networks. Due to the longer (BPDC²⁻) and sterically less demanding (CCA²⁻) linker molecules higher micropore volumes are expected and were in fact calculated based on the crystallographic data. Since both compounds are not stable upon removal of the guest molecules from the pores no optical switching experiments could be carried out.

Conclusions

Based on the structure of Zn-CAU-5 we investigated the influence of the metal ion and the organic linker molecule on the structure formation and the switching behavior. The variation of the metal ion has no influence on the switching behavior, whereas the replacement of NDC²⁻ by BPDC²⁻ and CCA²⁻ led to more open, but less stable structures. Current work focuses on the use of tetracarboxylic acid linker molecules in combination with AzBIPY to prevent the formation of interpenetrating structures.

Experimental Section

General

All reagents and solvents were purchased from commercial sources and were used without further purification. 2,6-Naphthalenedicarboxylic acid was synthesized by hydrolysis of dimethyl-2,6-naphthalenedicarboxylate (Sigma Aldrich). The compound H₂CCA was donated by BASF. All syntheses were carried out in 0.2–0.5 mL glass vials (Biotage). Elemental analyses were measured using a EuroVector EuroEA Elemental Analyzer. Raman spectra were recorded using a Bruker FRA 106 Raman spectrometer. UV/Vis measurements were performed with a Cary 5000 (Varian). Switching experiments were performed using two LED light sources from NICHIA ($\lambda = 365$ nm: NC4U133E and $\lambda = 455$ nm: NS6C083A). Thermogravimetric (TG) analyses were carried out in air (25 mL·min⁻¹, 25–900 °C, 4 K·min⁻¹) on a NETZSCH STA-449C thermal analyzer. Sorption measurements were realized with a BELSORP Max from Bel Japan. INC; for proper activation the samples were heated in vacuum (10⁻² kPa) for 3 h at 130 °C. XRPD measurements were carried out in transmission mode using a STOE high-throughput powder diffractometer equipped with an image-plate position-sensitive detector (IPPSD). Additional XRPD measurements were done with a PANalytical X'Pert diffractometer equipped with a PicCell semiconductor detector using Cu-K α radiation. These measurements were performed in reflection geometry.

Structure Determination and Refinement

A single crystal of **1** was isolated from the washed crystalline powder, whereas single-crystals of **3** and **4** had to be directly isolated from the

mother liquid due to their inferior stability. The single-crystal XRD measurements were performed with a STOE IPDS diffractometer. The instrument was equipped with a fine focus sealed tube (Mo-K α radiation, $\lambda = 71.073$ pm). For data reduction and absorption correction the programs X-Area, XRED and XSHAPE were used.^[28] The crystal structures were solved by direct methods and refined using the program package SHELXTL.^[29] The crystal structures of compound **3** and **4** were solved with SIR^[30] and refined using the program package SHELXTL.^[29] As-synthesized crystals were used for the single crystal measurement. These contain disordered guest (solvent) molecules in the pores of **1**, **3**, and **4** and therefore, for the final structure refinement the SQUEEZE procedure was applied as implemented in the PLATON software.^[31] Crystallographic data (excluding structure factors) for the structures in this paper have been deposited with the Cambridge Crystallographic Data Centre as supplementary publication nos. CCDC-865843, -865844, and -865845 for **1**, **3**, and **4**, respectively. Copies of the data can be obtained, free of charge, on application to CCDC, 12 Union Road, Cambridge CB2 1EZ, UK (fax: +44-1223-336033 or E-Mail: deposit@ccdc.cam.ac.uk).

Pawley-Fit

Since for Cu-CAU-5 only a microcrystalline powder was obtained, the lattice parameter refinement was done with a Pawley fit. Therefore, the powder pattern was measured in reflection geometry with a PANalytical X'Pert diffractometer equipped with a PicCell semiconductor detector using Cu-K α irradiation. The Pawley fit was carried out starting from the lattice parameters obtained from Zn-CAU-5 using TOPAS Academics^[32] in an angular range of 5–30° 2theta. In the final stage, the refinement involved 116 parameters: six background parameters, one zero point, four profile parameters, four lattice parameters, one simple axial model and 100 peak intensity parameters. The final refinement led to a satisfying fit with an r_{wp} of 5.93 %.

Switching Experiments

All UV/Vis measurements for **1** and **2** were performed in a mixture of the microcrystalline powder and BaSO₄ in reflection geometry. The Kubelka–Munk equation was used to transform the data into adsorption spectra. Prior to the switching experiments, a UV/Vis spectrum of each sample was recorded. To convert the *trans*- into the *cis*-isomer the sample was irradiated with UV light ($\lambda = 365$ nm) for a period of 15 min (time to achieve the photo stationary state, Figure S16). Back switching was achieved with visible light ($\lambda = 455$ nm). The switching process was repeated several times.

Syntheses

3-Azo-phenyl-4,4'-bipyridine (AzBIPY) was synthesized according to the procedure reported by us previously.^[25]

[Co₂(NDC)₂(AzBIPY)] (**1**): Co(NO₃)₂·6H₂O (11.0 mg, 0.037 mmol), 2,6-naphthalenedicarboxylic acid (H₂NDC) (8.1 mg, 0.037 mmol) and 3-azo-phenyl-4,4'-bipyridine (AzBIPY) (4.8 mg, 0.019 mmol), were added to a mixture of DMF (0.375 mL) and CH₃OH (0.375 mL) in a 0.2–0.5 mL glass vial (Biotage). The sealed vial was stirred for one day at room temperature and transferred to an isothermal oven heated to 120 °C. After 2 days dark red, almost black single crystals were obtained. The product was dried at room temperature in air and activated in an isothermal oven at 80 °C overnight. Elemental analysis of the activated sample [Co₂(NDC)₂(AzBIPY)] (M = 807 g·mol⁻¹) calc. (%): C 59.57, H 3.00, N 6.95; found (%): 58.67, H 3.02, N 7.05. TG/

DTA analysis of **1**: Between 350 and 500 °C, a total weight loss of 85.6 % (weight loss calc. 85.4 %) was observed in one step, which is due to the oxidative decomposition (see Figure S5). The final product was identified as CoO by X-ray powder diffraction (XRPD).

[Cu₂(NDC)₂(AzBIPY)] (2): The starting materials Cu(NO₃)₂·3H₂O (9.0 mg, 0.037 mmol), 2,6-naphthalenedicarboxylic acid (8.1 mg, 0.037 mmol) and AzBIPY (4.8 mg, 0.019 mmol) were added to a mixture of DMF (0.375 mL) and CH₃OH (0.375 mL) in a 0.2–0.5 mL glass vial (Biotage). The sealed vial was stirred for one day at room temperature and transferred to an isothermal oven heated to 120 °C. After two days the microcrystalline green product was filtered and washed three times with DMF (1 mL). The product was dried at room temperature in air and activated in an isothermal oven at 80 °C overnight. Elemental analysis of the activated sample [Cu₂(NDC)₂(AzBIPY)] (M = 816 g·mol⁻¹) calc. (%): C 58.40, H 2.97, N 6.87; found (%): C 58.24, H 2.90, N 6.82. TG/DTA analysis of **2**: Between 300 and 400 °C, a total weight loss of 84 % (weight loss calc. 84.4 %) was observed in one step, which is due to the oxidative decomposition (see Figure S6). The final product was identified as CuO by X-ray powder diffraction (XRPD).

[Zn₂(BPDC)₂(AzBIPY)] (3): The starting materials Zn(NO₃)₂·6H₂O (11.0 mg, 0.037 mmol), 4,4'-biphenyl-dicarboxylic acid (9.11 mg, 0.037 mmol) and AzBIPY (4.8 mg, 0.019 mmol) were stirred in a mixture of DMF (0.375 mL) and CH₃OH (0.375 mL) in a 0.2–0.5 mL glass vial (Biotage). The sealed vial was stirred for one day at room temperature and transferred to an isothermal oven heated to 120 °C. After two days the orange crystals were obtained. The single-crystal XRD measurement (at 200 K) was performed on a single crystal of **3**, which was directly mounted from the mother liquid. No further characterization was carried out due to the instability of the compound.

[Zn₂(CCA)₂(AzBIPY)] (4): The starting materials Zn(NO₃)₂·6H₂O (11.0 mg, 0.037 mmol), 4-carboxy-cinnamic acid (7.2 mg, 0.037 mmol) and AzBIPY (4.8 mg, 0.019 mmol) were stirred in a mixture of DMF (0.375 mL) and CH₃OH (0.375 mL) in a 0.2–0.5 mL glass vial (Biotage). The sealed vial was stirred for one day at room temperature and transferred to an isothermal oven heated to 120 °C. After two days orange crystals were obtained. The single-crystal XRD measurement (at 200 K) was performed on a single crystal of **4**, which was directly mounted from the mother liquid. No further characterization was carried out due to the instability of the compound.

Supporting Information (see footnote on the first page of this article): Sorption isotherms, results of the TG/DTA measurements, Raman- and UV/Vis spectra, XRPD patterns, results of the Rietveld refinements as well as the ORTEP presentations.

Acknowledgments

This work has been supported by the State of Schleswig-Holstein and the Deutsche Forschungsgemeinschaft (DFG) via the SFB 677 *Function by Switching*. The authors thank: *Uschi Cornelissen* and *Stephanie Pehlke* for supporting all spectroscopic measurements, *Inke Jess* and *Christian Näther* for single crystal measurements, *Adam Wutkowski* for TG/DTA measurements.

References

- [1] J. L. C. Rowsell, O. M. Yaghi, *Microporous Mesoporous Mater.* **2004**, *73*, 3.
- [2] A. Sonnauer, F. Hoffmann, M. Fröba, L. Kienle, V. Duppel, M. Thommes, C. Serre, G. Férey, N. Stock, *Angew. Chem. Int. Ed.* **2009**, *48*, 3791.
- [3] S. Biswas, T. Ahnfeldt, N. Stock, *Inorg. Chem.* **2011**, *50*, 9518.
- [4] H. Reinsch, N. Stock, *Dalton Trans.* **2012**, *41*, 4164.
- [5] N. Stock, S. Biswas, *Chem. Rev.* **2012**, *112*, 933.
- [6] S. I. Vagin, A. K. Ott, B. Rieger, *Chem. Ing. Technol.* **2007**, *79*, 767.
- [7] H. Chun, N. Dytsev, H. Kim, K. Kim, *Chem. Eur. J.* **2005**, *11*, 3521.
- [8] B. Q. Ma, K. L. Mulfort, J. T. Hupp, *Inorg. Chem.* **2005**, *44*, 4912.
- [9] E. B. Lobkovsky, O. M. Yaghi, S. Dai, *Angew. Chem. Int. Ed.* **2006**, *45*, 1390.
- [10] S. S.-Y. Chui, S. M.-F. Lo, J. P. H. Charmant, A. G. Orpen, I. D. Williams, *Science* **1999**, *283*, 1148.
- [11] M. Eddaoudi, J. Kim, M. O'Keeffe, O. M. Yaghi, *J. Am. Chem. Soc.* **2002**, *124*, 376.
- [12] B. Mu, F. Li, K. S. Walton, *Chem. Commun.* **2009**, 2493.
- [13] Y.-W. Li, J.-P. Zhao, L.-F. Wang, X.-H. Bu, *CrystEngComm* **2011**, *13*, 6002.
- [14] H. Chun, H. Jung, J. Seo, *Inorg. Chem.* **2009**, *48*, 2043.
- [15] E.-Y. Choi, K. Park, C.-M. Yang, H. Kim, J.-H. Son, S. W. Lee, Y. H. Lee, D. Min, Y.-U. Kwon, *Chem. Eur. J.* **2004**, *10*, 5535.
- [16] P. Maniam, N. Stock, *Inorg. Chem.* **2011**, *50*, 5085.
- [17] R. Wang, M. Hong, D. Yuan, Y. Sun, L. Xu, J. Luo, R. Cao, A. S. C. Chan, *Eur. J. Inorg. Chem.* **2004**, 37.
- [18] X. Guo, G. Zhu, Q. Fang, M. Xue, G. Tian, J. Sun, X. Li, S. Qiu, *Inorg. Chem.* **2005**, *44*, 3850.
- [19] T. M. Reineke, M. Eddaoudi, D. Moler, M. O'Keeffe, O. M. Yaghi, *J. Am. Chem. Soc.* **2000**, *122*, 4843.
- [20] B. Chen, M. Eddaoudi, S. T. Hyde, M. O'Keeffe, O. M. Yaghi, *Science* **2001**, *291*, 1021.
- [21] S. Ma, D. Sun, J. M. Simmons, C. D. Collier, D. Yuan, H.-C. Zhou, *J. Am. Chem. Soc.* **2008**, *130*, 1012.
- [22] T. Gadzikwa, O. K. Farha, K. L. Mulfort, J. T. Hupp, S. B. T. Nguyen, *Chem. Commun.* **2009**, 3720.
- [23] Z. Wang, K. K. Tanabe, S. M. Cohen, *Inorg. Chem.* **2009**, *48*, 296.
- [24] S. Han, Z. Ma, R. Hopson, Y. Wei, D. Budil, S. Gulla, B. Moulton, *Inorg. Chem. Commun.* **2012**, *15*, 78.
- [25] A. Modrow, D. Zargarani, R. Herges, N. Stock, *Dalton Trans.* **2011**, *40*, 4217.
- [26] M. Eddaoudi, J. Kim, N. Rosi, D. Vodak, J. Wachter, M. O'Keeffe, O. M. Yaghi, *Science* **2002**, *295*, 469.
- [27] T. Gadzikwa, O. K. Farha, K. L. Mulfort, J. T. Hupp, S. B. T. Nguyen, *Chem. Commun.* **2009**, 3720.
- [28] *X-AREA* Version 1.44, *XRED* Version 1.31, *X-SHAPE* Version 1.06/2.07, Stoe & Cie GmbH, Darmstadt, Germany, **2008**.
- [29] G. M. Sheldrick, *SHELXTL-PLUS* Crystallographic System, Siemens, Analytical X-Ray Instruments Inc. Madison, WI, **1992**.
- [30] M. C. Burla, R. Caliandro, M. Camalli, B. Carrozzini, G. L. Cascarano, L. De Caro, C. Giacovazzo, G. Polidori, D. Siliqi, R. Spagna, *J. Appl. Crystallogr.* **2007**, *40*, 609.
- [31] A. L. Spek, *PLATON*, A Multipurpose Crystallographic Tool, Utrecht University, Utrecht, The Netherlands, **2005**.
- [32] A. A. Coelho, *TOPAS*, Academic Version 4.1, Brisbane, Australia, **2007**.

Received: February 7, 2012
Published Online: May 31, 2012

6.1.4. $[\text{Zn}(\text{C}_3\text{H}_3\text{N}_2)(\text{C}_3\text{H}_2\text{N}_2\text{-N=N-C}_6\text{H}_5)]$, a Mixed-Linker ZIF Containing a Photoswitchable Phenylazo Group

Die folgende Arbeit wurde in der Zeitschrift *European Journal of Inorganic Chemistry* veröffentlicht und behandelte die Synthese und Strukturaufklärung eines neuen Zeolitic Imidazolate Frameworks (ZIFs) mit schaltbarer Azofunktion.^[207]

ZIFs sind eine weitere Klasse von MOFs. Hierbei werden Zn^{2+} - oder Co^{2+} -Ionen und verschieden modifizierte Imidazolate zum Aufbau von Gerüsten verwendet.^[208] Ist das Metallzentrum tetraedrisch koordiniert, sind die M-Imidazol-M Winkel mit 145° ähnlich dem Si-O-Si Winkel in Zeolithen. Dadurch lassen sich Netzwerktopologien erzeugen, die auch für Zeolithe beobachtet werden. Das wohl bekannteste Beispiel ist ZIF-8 ($\text{Zn}(\text{MeIm})_2$), das aus Zn^{2+} -Ionen und 2-Methylimidazol-Ionen (MeIm^-) auf gebaut ist und in der sogenannten Sodalith-Struktur kristallisiert. Die Kristallstruktur ist in Abbildung 6.3 gezeigt.

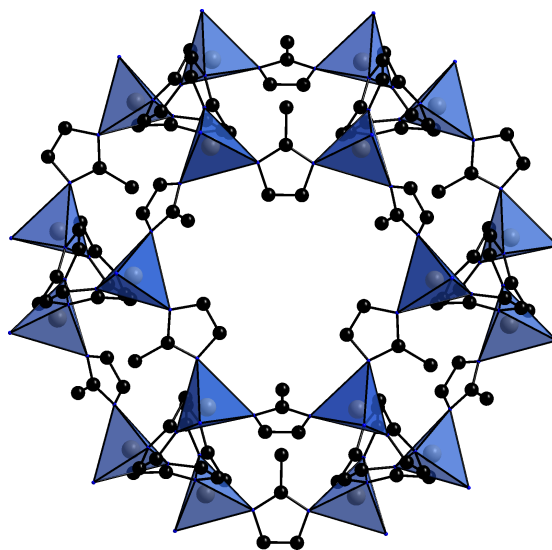


Abbildung 6.3.: Sodalit Käfig aus Zn^{2+} und Methylimidazol in ZIF-8. Die Kohlenstoffatome sind in schwarz, die Stickstoffatome in blau, die Zinkatome in grau und die ZnN_4 Polyeder sind in blau dargestellt.

Ebenso wie in Metallcarboxylaten kann eine Schaltfunktion auch in ZIFs durch Verwendung von 2-Phenylazoimidazol (HaIm) eingebracht werden. Wurde ein Gemisch von HIm/aIm von 1:1 verwendet, bildete sich das aus ZIF-8 bekannte Sodalith-Gerüst. Die Verwendeten Linker sind in Abbildung 6.4 gezeigt. Der Beweis des erfolgreichen Einbaus der Schaltfunktion geschah hierbei u.a. mittels Einkristallstrukturanalyse. ZIF-8 kristallisiert in der nicht zentrosymmetrischen Raumgruppe $I\bar{4}3m$. Versuche die Struktur in dieser

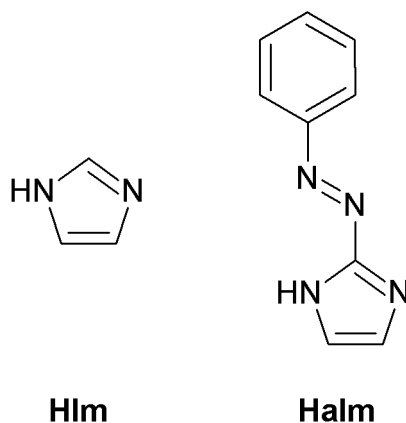


Abbildung 6.4.: Strukturformel der verwendeten Linker Imidazol (HIm) und 2-Phenylazoimidazol (Halm).

Raumgruppe zu bestimmen führten nur zur Lokalisierung der Gerüstatome und hohen Restelektronendichten in den Poren. Die Strukturlösung wurde daraufhin in der nicht-zentrosymmetrischen chiralen Untergruppe *I*23 durchgeführt, in der es möglich war, die Azophenylgruppen zu lokalisieren. Zusätzlich zu Einkristallstrukturanalytik wurde der Einbau von aIm^- auch mittels FK-NMR- und IR-Spektroskopie sowie durch UV/Vis Schalterexperimente verifiziert.

FULL PAPER

DOI: 10.1002/ejic.201100789

[Zn(C₃H₃N₂)(C₃H₂N₂-N=N-C₆H₅)], a Mixed-Linker ZIF Containing a Photoswitchable Phenylazo Group

Stephan Bernt,^[a] Mark Feyand,^[a] Antje Modrow,^[a] Julia Wack,^[b] Jürgen Senker,^[b] and Norbert Stock^{*[a]}

Keywords: Metal-organic frameworks / Microporous materials / Structure elucidation / Optical switching / High-throughput methods

We report the synthesis and characterization of the new switchable Zn-based zeolitic imidazolate framework (ZIF) [Zn(Im)(alm)] (**1**). The high-throughput investigation of the mixed linker system Zn²⁺/imidazole (HIm)/2-phenylazoimidazole (HaIm)/DMF at 85 °C led to **1**, which is isostructural to ZIF-8 and crystallizes in a sodalite (SOD)-type structure. The preparation was also studied with microwave-assisted heating and ultrasound-assisted synthesis. The crystal structure was determined from single-crystal X-ray diffraction data. Although Im⁻ and alm⁻ ions are present in a 1:1 molar ratio, no ordering of the 2-phenylazo group was observed. Incorporation of the Im⁻ and alm⁻ linkers as an integral part of the

framework structure was confirmed by elemental analysis, ¹³C and ¹⁵N MAS NMR, IR and Raman spectroscopy. In addition, the permanent porosity of **1** was demonstrated by N₂ sorption experiments and a specific surface area of S_{BET} = 580 m²g⁻¹ is observed. The photoswitching properties were investigated by UV/Vis spectroscopy as the *cis* and *trans* isomers exhibit different UV absorption spectra. Switching can be achieved by irradiation with UV light (λ = 355 nm), and back-switching using visible light (λ = 525 nm). Although changes in the UV/Vis spectra are detected, the switching process is only partially reversible.

Introduction

Metal-organic frameworks (MOFs) have gained increased attention in recent years due to their specific chemical and physical properties, such as pore size distribution, surface properties and chemical functionality.^[1–4] They constitute a class of porous compounds that bridge the gap between microporous zeolites and ordered mesoporous silica-based materials.^[5] MOFs are constructed from inorganic building units that are connected by organic linkers.^[6] The choice of the linker molecule can vary the pore size, chemical functionality and physical properties such as sorption.^[7,8] Functionality can be introduced directly by using functionalized linkers such as aminoterephthalic acid,^[9,10] by coordination of guest molecules to unsaturated metal sites^[11] or by postsynthetic covalent modification.^[12,13]

Tian et al. have reported a new class of MOFs^[14,15] called zeolitic imidazolate frameworks (ZIFs).^[16] These compounds contain Zn²⁺ or Co²⁺ ions that are tetrahedrally surrounded by imidazolate linkers, which each bridge two

Zn²⁺ or Co²⁺ ions. By employing imidazolate derivatives or mixtures thereof, various zeolitic topologies with numerous functional groups have been obtained.^[17,18,19]

One goal in our current studies on MOFs is the introduction of functionality that can be modified by external stimuli. For example, sorption properties can be changed by ion exchange,^[20] porosity can be switched by guest exchange^[21] and the opening of pores can be triggered by gas adsorption.^[22] In addition, guest-induced colour change^[23] and temperature-induced cooperative spin-crossover behaviour in a 3D coordination polymer have been observed.^[24] We are interested in the use of photoswitchable organic linker molecules for the synthesis of MOFs and have recently demonstrated the reversible switching of the mixed-linker MOF CAU-5, which contains azophenyl-4,4'-bipyridine and 2,6-naphthalenedicarboxylate ions.^[25]

Aromatic molecules that contain azo groups, such as azobenzene or arylazoimidazole derivatives, are textbook examples for photoisomerization reactions.^[26,27] In general the *trans* isomer of azobenzene is the thermodynamically more stable form^[28,29] and exhibits two distinct absorption maxima. One with a lower intensity at λ_{max} = 444 nm (*n* → π* transition) and another at λ_{max} = 316 nm (π → π* transition). The *cis* isomer exhibits an absorption maximum at λ_{max} = 437 nm (*n* → π* transition) and the π → π* transition is shifted to λ_{max} = 270 nm. The *trans* isomer can be switched to the *cis* isomer by irradiation with UV light (ca. 365 nm). The switching process is schematically shown in

[a] Institut für Anorganische Chemie, Christian-Albrechts-Universität zu Kiel, Max-Eyth-Straße 2, 24118 Kiel, Germany
Fax: +49-431-8801774
E-mail: stock@ac.uni-kiel.de

[b] Anorganische Chemie III, Universität Bayreuth, Universitätsstr. 30, 95447 Bayreuth, Germany

Supporting information for this article is available on the WWW under <http://dx.doi.org/10.1002/ejic.201100789>.

Figure 1. This is clearly visible in the UV/Vis spectra as the intensity of the band at $\lambda_{\max} = 316$ nm decreases and the intensity of the band at $\lambda_{\max} = 444$ nm increases. Therefore, both isomers have distinct UV/Vis spectra and can easily be distinguished. The reversible back-switching can be achieved by heating or irradiation (ca. 440 nm).

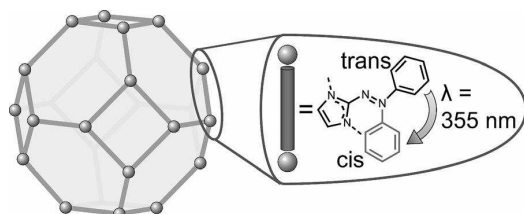


Figure 1. Schematic representation of the switching process.

MOFs containing azo groups are known in the literature.^[25,30,31,32] In most of these structures the azo groups are an integral part of the linker molecules. Thus, switching is strongly hindered and has not been demonstrated to date. In contrast, reversible switching should be feasible for linker molecules with azo groups that protrude into the pores. The structure of a 1,1'-bis[(2-phenylazo)imidazol-1-yl]methane-based MOF that contains two phenylazo groups was recently published but no switching properties were shown.^[33]

Here, we present the synthesis and detailed characterization of a switchable mixed-linker ZIF, [Zn(Im)(aIm)] (**1**), which contains imidazolate (Im^-) and 2-phenylazoimidazolate (aIm^-) ions.

Results and Discussion

The HaIm linker was synthesized from aniline and HIm^[34] and purified by column chromatography (Figure 2). It was subsequently employed in the high-throughput investigation of the $\text{Zn}(\text{NO}_3)_2 \cdot 6\text{H}_2\text{O}/\text{HIm}/\text{HaIm}/N,N$ -dimethylformamide (DMF) system. High-throughput (HT) methods allow the simultaneous investigation of different reaction parameters in solvothermal syntheses (Figure S1, Supporting Information) and are useful in the discovery of new phases and the subsequent synthesis optimization.^[35] The discovery library was set up varying the solvent (DMF and methanol) and employing the molar ratios $\text{Zn}^{2+}/\text{HaIm}/\text{HIm} = 1-3:1-4:0-3$ (Figure 3 and Table S2). The reaction products were characterized by X-ray powder diffraction (XRPD) measurements and the results are shown in Figure 3.

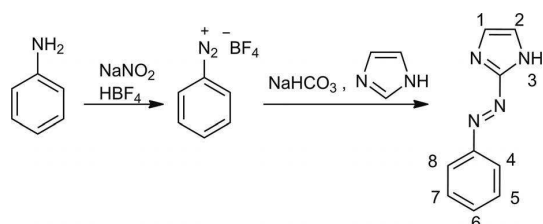


Figure 2. Synthesis of HaIm.

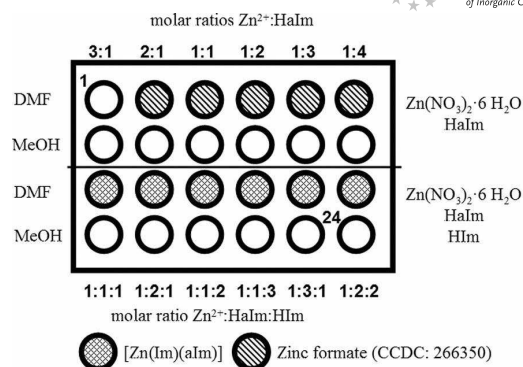


Figure 3. Discovery library of the high-throughput investigation. Empty circles denote clear solutions. The amounts used in each reactor are given in Table S2.

When HaIm was solely employed as the organic linker, reactions in methanol led exclusively to clear solutions, whereas reactions in DMF yielded zinc formate (CCDC-266350),^[36] which is due to the partial hydrolysis of DMF. The mixed-linker system **1** was obtained with DMF and orange, air-stable single crystals (Figure S3) suitable for crystal structure determination were isolated from the mixture containing $\text{Zn}(\text{NO}_3)_2 \cdot 6\text{H}_2\text{O}/\text{HIm}/\text{HaIm}/\text{DMF}$ in the molar ratio 1:3:1:97.

Compound **1** was also obtained using conventional heating (CH), microwave-assisted (MW) heating or ultrasound (US). The last two methods led to a substantially reduced reaction time (5 min). The three different synthetic methods resulted in phase-pure products. The CH synthesis led to large single crystals, whereas MW and US reactions yielded microcrystalline powders.

The orange, air stable compound was activated at 200 °C in vacuo for characterization by XRPD, thermogravimetric analysis (TGA), elemental analysis and IR, Raman, UV/Vis and solid-state NMR spectroscopy.

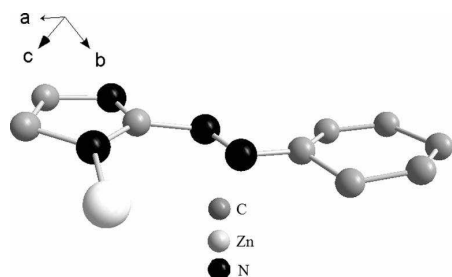
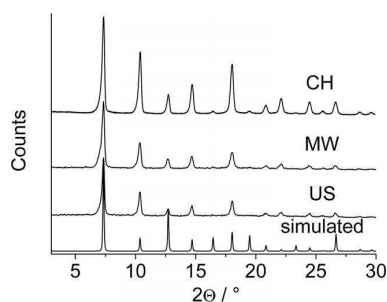
Compound **1** is isostructural to ZIF-8, which crystallizes in a sodalite (SOD)-type framework. The SOD structure has been observed in compounds that contain Zn^{2+} or Co^{2+} with 2-methyl-, 2-nitroimidazole, imidazole-2-carbaldehyde or benzimidazole (ZIF-7, -8, -9, -65, -67, -90, -91, -92).^[19,37,38] Two linkers are incorporated in **1**: Im^- and aIm^- . Based on the single crystal data, no ordering of the phenylazo groups takes place. **1** is isostructural to ZIF-8 and crystallizes in the space group $I\bar{2}3$. Thus, we were able to establish the SOD framework as well as the position of the azo group during structure refinement (see experimental section for crystallographic data, Figures 4 and S4).

Indexing the XRPD pattern (Figures 5 and S5) unequivocally demonstrated the presence of only one crystalline phase. The lattice parameter [$a = 17.009(6)$ Å] compares well with results from the single-crystal X-ray diffraction experiment [$a = 17.023(2)$ Å].

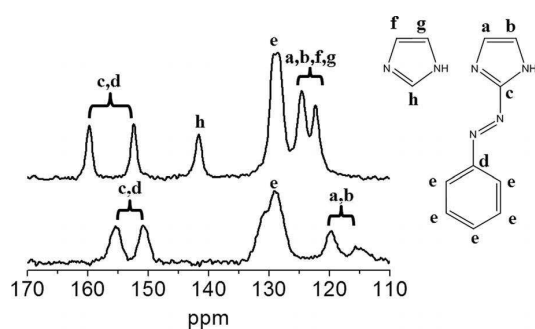
The composition of activated **1** was established by elemental analysis and TGA. The observed and calculated C, H and N values compare well, and the TGA curve shows a

FULL PAPER

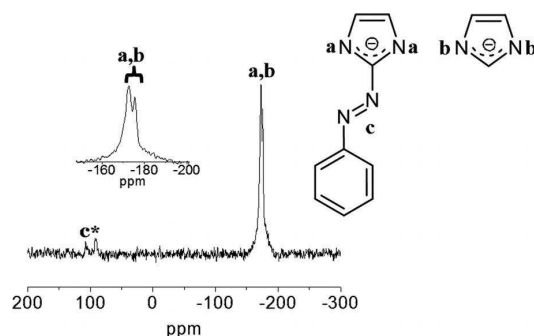
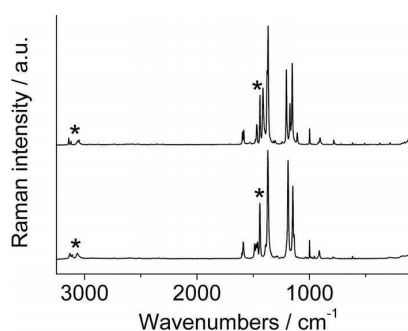
N. Stock et al.

Figure 4. Asymmetric unit of **1**.Figure 5. XRPD patterns of **1** compared to the simulated pattern, which is based on single crystal data.

weight loss of 73.14% for the CH and MW products and 66% for the US product between 340 and 700 °C (calcd. 73.54%) with ZnO as the final decomposition product (Figure S6). The incorporation of the alm linker as part of the framework was confirmed by solid-state NMR and Raman spectroscopy (Figures 6, 7 and 8). The characteristic --N=N-- asymmetric vibration band is located at 1441 cm^{-1} in the Raman spectrum, and characteristic aromatic =C--H stretching vibrations are observed between 3142 and 3047 cm^{-1} .

Figure 6. ^{13}C MAS NMR spectrum of **1** (top) and ^{13}C CP MAS NMR spectrum of pure HaIm (bottom).

The ^{13}C cross polarization (CP) magic angle spinning (MAS) NMR spectrum of the HaIm linker (Figure 6, bottom) shows five signals that can be clearly assigned. The signals of **1** can be assigned to both imidazolate linkers (Figures 6, top, and S8). Due to the deprotonation of HaIm and HIm, only two signals for a, b, f and g are observed,

Figure 7. ^{15}N CP MAS NMR spectrum of **1**. The spinning side-band is marked with an asterisk.Figure 8. Raman spectra of **1** (bottom) and HaIm (top). The trans--N=N-- vibration of **1** (1441 cm^{-1}) and the aromatic =C--H stretching vibrations ($3142\text{--}3047\text{ cm}^{-1}$) of the phenyl ring and the imidazolate ions are marked with asterisks.

which are shifted downfield. Two new signals (h and f, g) for Im^- are present.

The ^{15}N CP MAS NMR spectrum shows three signals that can be assigned to aIm and Im. The signal at 107 ppm is due to the nitrogen atoms of the azo group, and those at -172 and -175 ppm can be assigned to the nitrogen atoms of the imidazolate ions (Figure 7). A ^{15}N MAS NMR spectrum of the pure HaIm molecule cannot be recorded due to its very slow spin relaxation.

Although the aIm linker protrudes into the SOD cages, permanent porosity was demonstrated by N_2 sorption experiments at 77 K (Figure 9). The N_2 sorption isotherm of the activated sample (CH, 200 °C , 12 h , vacuum) shows a rapid increase at low p/p_0 values followed by a plateau, which is typical of type I isotherms. Evaluating the data with the Brunauer–Emmett–Teller (BET) equation resulted in a specific surface area (S_{BET}) of $580\text{ m}^2\text{ g}^{-1}$ with a micropore volume (V_p) of $0.26\text{ cm}^3\text{ g}^{-1}$. The N_2 sorption isotherms of the MW and US samples show similar behaviour but with slightly lower specific surface areas (US: $S_{\text{BET}} = 544\text{ m}^2\text{ g}^{-1}$, $V_p = 0.25\text{ cm}^3\text{ g}^{-1}$; MW: $S_{\text{BET}} = 507\text{ m}^2\text{ g}^{-1}$, $V_p = 0.26\text{ cm}^3\text{ g}^{-1}$). The specific surface area of **1** is significantly lower than ZIF-8 [$S_{\text{BET}} = 1030\text{ m}^2\text{ g}^{-1}$, $V_p = 0.49\text{ cm}^3\text{ g}^{-1}$] (calculated with PLATON as $0.54\text{ cm}^3\text{ g}^{-1}$), in which a methyl group protrudes into the SOD cages.^[12,32]

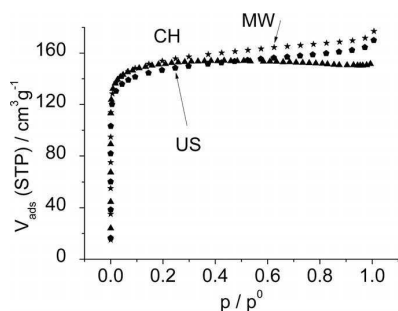


Figure 9. N_2 sorption isotherms of **1** (triangles: CH product, pentagons: US product, stars: MW product).

The switching properties of **1** were investigated using UV/Vis spectroscopy (Figures 10 and S9). Switching the azo groups from *trans* to *cis* configuration was accomplished by UV irradiation (355 nm, 150 W xenon lamp, 1 h). Back-switching was achieved by irradiation with visible light (525 nm, 150 W xenon lamp, 1 h) but not thermally (100 °C in air for 14 h). The switching of HaIm is hard to observe as fast thermal back-switching (*cis* to *trans*) takes place. In contrast, *N*-alkyl-substituted imidazolate derivatives exhibit much lower rate constants.^[24,25]

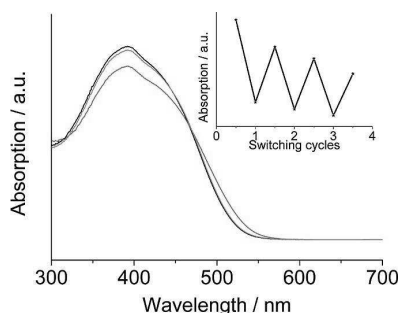


Figure 10. UV/Vis spectra of **1** before irradiation (black line), after irradiation at 355 nm for 1 h (red line) and after irradiation at 525 nm for 1 h (green line). Only one cycle is presented for clarity and more cycles are shown in Figure S9. The reversibility of the switching process (based on the $\pi \rightarrow \pi^*$ absorption band at 392 nm) is shown in the inset. Every whole number represents a cycle of switching to the *cis* product and back-switching to the *trans* product.

Based on results reported for HaIm,^[28,29] the bands can be assigned to the $\pi \rightarrow \pi^*$ (392 nm) and $n \rightarrow \pi^*$ transitions (450 nm). Upon irradiation with UV light, changes in the intensities of these bands are observed; the intensity of the $\pi \rightarrow \pi^*$ band decreases, which is accompanied by an increase in the intensity of the $n \rightarrow \pi^*$ band. Back-switching with visible light leads to an increase in the intensity of the $\pi \rightarrow \pi^*$ band and a decrease in the intensity of the $n \rightarrow \pi^*$ band. Although back-switching is not fully reversible, repeated switching and back-switching led to the corresponding changes in the UV/Vis spectra.

The partial reversibility could be due to a photobleaching effect or the steric hinderance of the switching process

(confinement effect). Repeating this procedure led to the observation of the same behaviour. After three switching cycles the initial curve cannot be reached.

Conclusions

We have synthesized the porous, air-stable ZIF [Zn(Im)(aIm)] (**1**), which contains photoswitchable azophenyl groups. This compound was formed in a solvothermal reaction using a mixed-linker system. X-ray diffraction experiments demonstrated its structural relationship with ZIF-8, and the incorporation of aIm was proven by Raman and solid-state NMR spectroscopy. Although the large phenylazo group protrudes into the cage, **1** shows permanent porosity. UV/Vis switching experiments demonstrated the *cis*-*trans* isomerization and showed partial reversibility of the switching process.

Experimental Section

General: Synthetic procedures for HaIm and **1** and selected spectroscopic data are described in this section. All chemicals were used as obtained, unless stated otherwise.

2-Phenylazoimidazole (HaIm):^[34] A mixture of aniline (10.6 mL, 116 mmol) and tetrafluoroboric acid (57.5 mL, 50%) was cooled to 0 °C. A solution of sodium nitrite in deionized water (18 mL) was slowly added. The precipitate was separated and washed with ethanol and diethyl ether to obtain benzenediazonium tetrafluoroborate (26.7 g).

Imidazole (6.8 g, 100 mmol) was added to a solution of sodium hydrogen carbonate (4.5 g, 53.6 mmol) in deionized water (45 mL). After homogenization of the solution, benzenediazonium tetrafluoroborate (19.2 g, 100 mmol) in deionized water (100 mL) was added. A brown precipitate formed immediately and the mixture was stirred for 30 min and allowed to stand for another 30 min. The precipitate was separated and washed with deionized water. The product was purified by column chromatography on basic aluminium oxide with ethyl acetate (+1% triethylamine) to give HaIm (9.8 g, 57%) as orange needles. $C_9H_8N_4$ (172.07): calcd. C 62.78, H 4.68, N 32.54; found C 62.54, H 4.64, N 32.61. 1H NMR (200 MHz, $[D_6]DMSO$, 300 K, numbering according to Figure 2): δ = 7.38 [s, 2 H, 1,2-H], 7.6 [m, 3 H, 5,6,7-H], 7.85 [m, 2 H, 4,8-H], 13.2 [br. s, 1 H, 3-H] ppm. MS-EI: m/z (%) = 172.0 $[M]^+$ (77%), 144 (100), 117 (57), 105 (10); (CI) 173 $[M + H]^+$ (65%), 144 (100), 117 (48), 105 (11).

[Zn(Im)(aIm)] (1**):** Single crystals of **1** were formed from a solvothermal reaction in 2 mL Teflon[®] autoclaves in a high-throughput reactor (see Supporting Information). Solutions of $Zn(NO_3)_2 \cdot 6H_2O$ (193 μL , 0.3 M), HaIm (193 μL , 0.3 M) and imidazole (580 μL , 0.3 M) in DMF were mixed and additional DMF (433 μL) was added. The reaction mixture was heated at 85 °C in an isothermal oven for 96 h. The crystalline orange product was collected by filtration and washed with DMF (2 mL) and acetone (5 mL). The product was dried at room temperature in air for five days followed by 12 h at 200 °C in vacuo. $C_{12}H_{10}N_6Zn$ (302.03): calcd. C 47.46, H 3.32, N 27.68; found C 46.85, H 3.64, N 27.04.

Microwave-Assisted Synthesis of **1:** In a typical reaction, solutions of $Zn(NO_3)_2 \cdot 6H_2O$ (193 μL , 0.3 M), HaIm (193 μL , 0.3 M) and imidazole (580 μL , 0.3 M) in DMF with additional DMF (433 μL)

FULL PAPER

were mixed in a 2 mL glass vial sealed with a Teflon[®]-coated cap. The reaction mixture was stirred and exposed to microwave irradiation for 5 min at 100 °C (Biotage Initiator Eight EXP). The orange solid was collected by centrifugation and redispersed in DMF (2 mL). The redispersing and centrifugation steps were repeated twice more with acetone. The product was dried at room temperature in air for five days followed by 12 h at 200 °C in vacuo. C₁₂H₁₀N₆Zn (302.03): calcd. C 47.46, H 3.32, N 27.68; found C 46.86, H 3.32, N 27.42.

Ultrasound-Assisted Synthesis of 1: In a typical reaction, solutions of Zn(NO₃)₂·6H₂O (193 μL, 0.3 M), HaIm (193 μL, 0.3 M) and imidazole (580 μL, 0.3 M) in DMF with additional DMF (433 μL) were mixed in a 2 mL glass vial. The reaction mixture was sonicated using an ultrasonic generator with sonotrode (UP200S, Hielscher-Ultrasound Technology, 200 W, 24 kHz) for 10 min. The orange solid was collected by centrifugation and redispersed in DMF (2 mL). The redispersing and centrifugation steps were repeated twice more with acetone. The product was dried at room temperature in air for five days followed by 12 h at 200 °C in vacuo. C₁₂H₁₀N₆Zn (302.03): calcd. C 47.46, H 3.32, N 27.68; found C 46.94, H 3.46, N 26.63.

Single-Crystal Structure Analysis: The crystal structure determination was performed with an imaging plate diffraction system (IPDS-1) with Mo-K_α radiation from STOE & CIE. The structure solution was carried out with direct methods using SHELXS-97 and structure refinements were performed against |F₂| using SHELXL-97. The structure solution in the space group *I*43*m* (as found for ZIF-8) did not lead to a reasonable structure model. Choosing the subgroup *I*23 allowed the azophenyl rings to be assigned by a split model. The azophenyl rings were isotropically refined and the Zn and imidazolate ions were refined anisotropically. A numerical absorption correction was applied using X-Red (version 1.31) and X-Shape (version 2.11) of the program package X-Area. All non-hydrogen atoms were refined with anisotropic displacement parameters. Refinement of the structure led to a Flack parameter of 0.50(1). The model was therefore refined as a racemic twin using the TWIN and BASF command implemented in ShelXL. All aromatic C–H hydrogen atoms were positioned with idealized geometries and were refined with fixed isotropic displacement

parameters [$U_{\text{eq}}(\text{H}) = -1.2 \cdot U_{\text{eq}}(\text{C})$] using a riding model with $d_{\text{C-H}} = 0.93 \text{ \AA}$. Details of the structure determination are given in Table 1.

CCDC-836865 contains the supplementary crystallographic data for this paper. These data can be obtained free of charge from the Cambridge Crystallographic Data Centre via <http://www.ccdc.cam.ac.uk/>.

X-ray Powder Diffraction (XRPD): XRPD experiments were performed using an X'Pert Pro PANalytical Reflection Powder Diffraction System, with Cu-K_α radiation ($\lambda = 154.0598 \text{ pm}$), equipped with a PIXcel semiconductor detector from PANalytical. Products of the HT investigations were characterized using a STOE HT X-ray powder diffractometer (Cu-K_α radiation) equipped with an image plate detector.

Supporting Information (see footnote on the first page of this article): Crystallographic data, HT methodology, the experimental data for the HT system where **1** was found and spectroscopic data.

Acknowledgments

We acknowledge funding from the Deutsche Forschungsgemeinschaft (DFG) (SFB 667, *Function by Switching*). We also thank Ursula Cornelissen for undertaking the Raman and UV/Vis measurements, Inke Jeß for the single crystal measurements, Adam Wutkowiński and Jan Boeckmann for the DTA/TG measurements and Dr. Frank Sönnichsen for recording solution ¹H NMR spectra.

Table 1. Selected crystal data and details of the structure determination of **1**.

Formula	Zn ₂ C ₁₆ H ₅ N ₁₀
<i>M</i> [g mol ⁻¹]	468.08
Crystal system	cubic
Space group	<i>I</i> 23
<i>a</i> [Å]	17.023(2)
<i>V</i> [Å ³]	4933(1)
<i>T</i> [K]	293
<i>Z</i>	6
<i>D</i> _{calcd.} [g cm ⁻³]	0.945
μ [mm ⁻¹]	1.472
θ_{max} [°]	25.3
Measured reflections	19788
Unique reflections	1496
Reflections [<i>I</i> ₀ > 4σ(<i>I</i> ₀)]	1320
<i>R</i> _{int}	0.100
<i>R</i> ₁ [all data]	0.1192
<i>R</i> ₁ [<i>I</i> ₀ > 4σ(<i>I</i> ₀)]	0.1109
<i>wR</i> ₂ [all data]	0.2717
<i>wR</i> ₂ [<i>I</i> ₀ > 4σ(<i>I</i> ₀)]	0.2706
Gof	1.25
$\Delta\rho_{\text{max}}, \Delta\rho_{\text{min}}$ [e Å ⁻³]	0.51, -0.41

- [1] P. Horcajada, C. Serre, M. Vallet-Regí, M. Sebban, F. Taulelle, G. Férey, *Angew. Chem. Int. Ed.* **2006**, *45*, 5974–5978.
- [2] M. Latroche, S. Surblé, C. Serre, C. Mellot-Daznié, P. Llewellyn, J. Lee, J. Chang, S. Jung, G. Férey, *Angew. Chem.* **2006**, *118*, 8407; *Angew. Chem. Int. Ed.* **2006**, *45*, 8227–8231.
- [3] Z. Gu, X. Yan, *Angew. Chem.* **2010**, *122*, 1519–1522; *Angew. Chem. Int. Ed.* **2011**, *49*, 1477–1480.
- [4] K. Tanabe, S. Cohen, *Angew. Chem.* **2009**, *121*, 7560; *Angew. Chem. Int. Ed.* **2009**, *48*, 7424–7427.
- [5] G. Férey, *Chem. Soc. Rev.* **2008**, *37*, 191–214.
- [6] S. James, *Chem. Soc. Rev.* **2003**, *32*, 276–288.
- [7] Z. Wang, K. Tanabe, S. Cohen, *Chem. Eur. J.* **2010**, *16*, 212–217.
- [8] A. Sonnauer, F. Hoffmann, M. Fröba, K. Kienle, V. Duppel, M. Thommes, C. Serre, G. Férey, N. Stock, *Angew. Chem.* **2009**, *121*, 3849; *Angew. Chem. Int. Ed.* **2009**, *48*, 3791–3794.
- [9] S. Bauer, C. Serre, T. Devic, P. Horcajada, J. Marrot, G. Férey, N. Stock, *Inorg. Chem.* **2008**, *47*, 7568–7576.
- [10] T. Ahnfeldt, D. Gunzelmann, T. Loiseau, D. Hirsemann, J. Senker, G. Férey, N. Stock, *Inorg. Chem.* **2009**, *48*, 3057.
- [11] D.-Y. Hong, Y. K. Hwang, C. Serre, G. Férey, J.-S. Chang, *Adv. Funct. Mater.* **2009**, *19*, 1537–1552.
- [12] K. K. Tanabe, S. M. Cohen, *Chem. Soc. Rev.* **2011**, *40*, 498–519.
- [13] S. Bernt, V. Guillermin, C. Serre, N. Stock, *Chem. Commun.* **2011**, *47*, 2838–2840.
- [14] Y.-Q. Tian, C.-X. Cai, Y. Ji, X.-Z. You, S.-M. Peng, G.-H. Lee, *Angew. Chem.* **2002**, *114*, 1442; *Angew. Chem. Int. Ed.* **2002**, *41*, 1384–1386.
- [15] X.-C. Huang, Y.-Y. Lin, J.-P. Zhang, X.-M. Chen, *Angew. Chem.* **2006**, *118*, 1587; *Angew. Chem. Int. Ed.* **2006**, *45*, 1557–1559.
- [16] A. Phan, C. Doonan, F. Uribe-Romo, C. Knobler, M. O'Keeffe, O. Yaghi, *Acc. Chem. Res.* **2010**, *43*, 58–67.
- [17] R. Banerjee, A. Phan, B. Wang, C. Knobler, H. Furukawa, M. O'Keeffe, O. Yaghi, *Science* **2008**, *319*, 939–943.
- [18] B. Wang, A. Côté, H. Furukawa, M. O'Keeffe, O. Yaghi, *Nature* **2008**, *453*, 207–211.

6. Strukturlösung von anorganisch-organischen Hybridverbindungen

Photoswitchable Metal-Organic Framework



- [19] W. Morris, C. Doonan, H. Furukawa, R. Banerjee, O. Yaghi, *J. Am. Chem. Soc.* **2008**, *130*, 12626–12627.
- [20] S. Yang, X. Lin, A. J. Blake, G. Walker, P. Hubberstey, N. Champness, M. Schröder, *Nature Chem.* **2009**, *1*, 487–493.
- [21] T. Maji, G. Mostafa, R. Matsuda, S. Kitagawa, *J. Am. Chem. Soc.* **2005**, *127*, 17152–17153.
- [22] D. Tanaka, K. Nakagawa, M. Higuchi, S. Horike, Y. Kubota, T. Kobayashi, M. Takata, S. Kitagawa, *Angew. Chem.* **2008**, *120*, 3978; *Angew. Chem. Int. Ed.* **2008**, *47*, 3914–3918.
- [23] S. Shimomura, R. Matsuda, T. Tsujino, T. Kawamura, S. Kitagawa, *J. Am. Chem. Soc.* **2006**, *128*, 16416–16417.
- [24] V. Niel, J. Martinez-Agudo, M. Muñoz, A. Gaspar, J. Real, *Inorg. Chem.* **2001**, *40*, 3838–3839.
- [25] A. Modrow, D. Zargarani, R. Herges, N. Stock, *Dalton Trans.* **2011**, *40*, 4217–4222.
- [26] J. Griffiths, *Chem. Soc. Rev.* **1972**, *1*, 481–493.
- [27] H. Dürr, H. Bouas-Laurent, in: *Photochromism*, Elsevier, Amsterdam **1990**, vol 1.
- [28] J. Otsuki, K. Suwa, K. Narutaki, C. Sinha, I. Yoshikawa, K. Araki, *J. Phys. Chem. A* **2005**, *109*, 8064–8069.
- [29] J. Otsuki, K. Suwa, K. Sarker, C. Sinha, *J. Phys. Chem. A* **2007**, *111*, 1403–1409.
- [30] T. Reineke, M. Eddaoudi, D. Moler, M. O’Keeffe, O. Yaghi, *J. Am. Chem. Soc.* **2000**, *122*, 4843–4844.
- [31] Z.-F. Chen, R.-G. Xiong, B. Abrahams, X.-Z. You, C.-M. Che, *J. Chem. Soc., Dalton Trans.* **2001**, *17*, 2453–2455.
- [32] V. Zeleňák, Z. Vargová, M. Al máši, A. Zeleňáková, J. Kuchár, *Microporous Mesoporous Mater.* **2010**, *129*, 354–359.
- [33] C.-M. Jun, Z. Zhu, Z.-F. Chen, Y.-J. Hu, X.-G. Meng, *Cryst. Growth Des.* **2010**, *10*, 2054–2056.
- [34] R. Verma, M. Aggarwal, M. Bansal, I. Kaur, *Med. Chem. Res.* **2007**, *15*, 483–491.
- [35] N. Stock, *Microporous Mesoporous Mater.* **2010**, *129*, 287–295.
- [36] H. F. Clausen, R. D. Poulsen, A. D. Bond, M.-A. S. Chevallier, B. Brummerstedt Iversen, *J. Solid State Chem.* **2005**, *178*, 3343–3351.
- [37] K. Park, Z. Ni, A. Côté, J. Choi, R. Huang, F. Uribe-Romo, H. Chae, M. O’Keeffe, O. Yaghi, *Proc. Natl. Acad. Sci. USA* **2006**, *103*, 10186–10191.
- [38] A. Phan, C. Doonan, F. Uribe-Romo, C. Knobler, M. O’Keeffe, O. Yaghi, *Acc. Chem. Res.* **2010**, *43*, 58–67.

Received: July 28, 2011

Published Online: October 26, 2011

7 | Zusammenfassung

Im Folgenden sollen die in dieser Arbeit erhaltenen Ergebnisse der *in situ* Kristallisationsuntersuchungen und der Kristallstrukturbestimmung von anorganische-organischen Hybridverbindungen zusammengefasst werden.

7.1. Zusammenfassung der *in situ* Untersuchungen

In dieser Arbeit wurde die Kristallisation von 13 anorganisch-organischen Hybridverbindungen mittels EDXRD untersucht. Die untersuchten Verbindungen sind in Tabelle 7.1 zusammengefasst. Der Fokus lag vor allem auf den *in situ* Untersuchungen von Metallphosphonaten, da im Vorfeld dieser Arbeit keine derartigen Studien publiziert worden waren.

1. Die Kristallisationsexperimente der polyfunktionalisierten Metallphosphonate haben gezeigt, dass die Kristallisationen sehr schnell binnen Minuten oder Stunden ablaufen. Dies ist besonders in Hinblick auf die üblich verwendeten Reaktionszeiten von Tagen bis Wochen überraschend. Zusätzlich treten bei sehr kurzen Reaktionszeiten oft kristalline Intermediate auf, die teilweise strukturell charakterisiert werden konnten. Bei der Kristallisation von $[\text{Cu}_2(\text{O}_3\text{P}-\text{C}_2\text{H}_4-\text{SO}_3(\text{OH})(\text{H}_2\text{O})_2)] \cdot 3\text{H}_2\text{O}$, $[\text{Cu}_2(\text{O}_3\text{P}-\text{C}_2\text{H}_4-\text{SO}_3(\text{OH})(\text{H}_2\text{O}))]$ und $\text{Ca}(\text{O}_3\text{P}-\text{C}_2\text{H}_4-\text{NH}_2)$ konnten kristalline Intermediate isoliert und deren Kristallstruktur zu bestimmt werden. Anhand der Daten konnte die möglichen Reaktionsmechanismen postuliert werden. Die Intermediate waren im Vergleich mit dem finalen Produkt stärker hydratisiert und enthielten bereits Struktur motive der Endprodukte.
2. Die *in situ* Untersuchungen der isostrukturellen Verbindungen $\text{M}((\text{HO}_3\text{P}-\text{CH}_2)_2-\text{NHCH}_2-\text{C}_6\text{H}_4-\text{COOH})_2$ ($\text{M}=\text{Mn}^{2+}, \text{Fe}^{2+}, \text{Co}^{2+}, \text{Ni}^{2+}$) zeigten, dass in Abhängigkeit des Metallions verschiedene Reaktionszeiten benötigt werden und die Reaktionen über keine bzw. verschiedene Intermediate verlaufen. Für die Verbindungen $\text{Ni}((\text{HO}_3\text{P}-\text{CH}_2)_2-\text{NHCH}_2-\text{C}_6\text{H}_4-\text{COOH})_2$ und $\text{Mn}((\text{HO}_3\text{P}-\text{CH}_2)_2-\text{NHCH}_2-\text{C}_6\text{H}_4-\text{COOH})_2$ wurden Intermediate detektiert, die jedoch nicht isoliert werden konnten.

Tabelle 7.1.: Untersuchte Verbindungen und die aus den EDXRD-Studien erhaltenen Intermediate.

Verbindung	Intermediat
$\text{Sm}(\text{O}_3\text{P}-\text{C}_4\text{H}_8-\text{SO}_3)(\text{H}_2\text{O})$	Ja / unbekannt
$[\text{Cu}_2(\text{O}_3\text{P}-\text{C}_2\text{H}_4-\text{SO}_3(\text{OH})(\text{H}_2\text{O})_2)] \cdot 3\text{H}_2\text{O}$	$[\text{Cu}_2(\text{O}_3\text{P}-\text{C}_2\text{H}_4-\text{SO}_3(\text{OH})(\text{H}_2\text{O})_2)] \cdot 4\text{H}_2\text{O}$
$[\text{Cu}_2(\text{O}_3\text{P}-\text{C}_2\text{H}_4-\text{SO}_3(\text{OH})(\text{H}_2\text{O}))]$	$[\text{Cu}_2(\text{O}_3\text{P}-\text{C}_2\text{H}_4-\text{SO}_3(\text{OH})(\text{H}_2\text{O})_2)] \cdot 3\text{H}_2\text{O}$
$\text{Mn}((\text{HO}_3\text{P}-\text{CH}_2)_2-\text{NHCH}_2-\text{C}_6\text{H}_4-\text{COOH})_2$	Ja / unbekannt
$\text{Co}((\text{HO}_3\text{P}-\text{CH}_2)_2-\text{NHCH}_2-\text{C}_6\text{H}_4-\text{COOH})_2$	nein
$\text{Fe}((\text{HO}_3\text{P}-\text{CH}_2)_2-\text{NHCH}_2-\text{C}_6\text{H}_4-\text{COOH})_2$	nein
$\text{Ni}((\text{HO}_3\text{P}-\text{CH}_2)_2-\text{NHCH}_2-\text{C}_6\text{H}_4-\text{COOH})_2$	Ja / unbekannt
$\text{Ca}(\text{O}_3\text{PC}_2\text{H}_4\text{NH}_2)$	$[\text{Ca}(\text{OH})(\text{O}_3\text{PC}_2\text{H}_4\text{NH}_3)] \cdot 2\text{H}_2\text{O}$
$[\text{Co}_2(\text{BDC})-(\text{OH})_2] \cdot 8\text{H}_2\text{O}$	keine
$[\text{Ni}_2(\text{BDC})-(\text{OH})_2] \cdot 8\text{H}_2\text{O}$	keine
$\text{Bi}(\text{HPyr})$	$\text{Bi}_2(\text{O})(\text{Pyr})(\text{H}_2\text{O})$, $\text{Bi}(\text{HPyr})$
$\text{Bi}(\text{Tri})(\text{H}_2\text{O})$	amorphes Intermediat
$\text{Bi}_2(\text{O})(\text{OH})(\text{HBTC})(\text{NO}_3)$	$[(\text{Bi}(\text{BTC})(\text{H}_2\text{O})) \cdot \text{H}_2\text{O}]$, $\text{Bi}_6\text{O}_5(\text{BTC})_2(\text{HBTC})$

- Erstmals wurde die Kristallisation von Bismutcarboxylaten mittels EDXRD verfolgt. Hierzu wurden drei Systeme unter Verwendung der Linker Pyromellitsäure (H_4Pyr), Trimellitsäure (H_3Tri) und Trimesinsäure (H_3BDC) untersucht. Es zeigte sich, dass bei der Kristallisation der Verbindung $\text{Bi}(\text{HPyr})$ und $\text{Bi}_2(\text{O})(\text{OH})(\text{HBTC})(\text{NO}_3)$ jeweils zwei Intermediate während der Reaktion auftraten. Bei der Kristallisation von $\text{Bi}(\text{Tri})(\text{H}_2\text{O})$ wurden keine Intermediate beobachtet. Drei der gefundenen Intermediate konnten strukturell mittels Röntgenpulver- bzw. Röntgeneinkristallbeugung charakterisiert werden. Die Kristallisation von $\text{Bi}(\text{HPyr})$ verläuft hierbei über ein polymorphes Intermediat.
- Neben qualitativen Betrachtungen und dem Auffinden von Intermediaten konnte gezeigt werden, dass ebenso aus EDXRD Untersuchungen kinetische Auswertungen für die Bildung von anorganisch-organischen Hybridverbindungen möglich sind. Hierzu wurden die Kristallisationsdaten der Synthese von $\text{Sm}(\text{O}_3\text{P}-\text{C}_4\text{H}_8-\text{SO}_3)(\text{H}_2\text{O})$ nach der Methode von Sharp und Hancock ausgewertet. Sowohl mikrowellenunterstützte als auch konventionelle Solvothermalsynthesen wurden hierbei temperaturabhängig untersucht. Die kinetischen Parameter wie Geschwindigkeitskonstanten und Arrhenius Aktivierungsenergien konnten daraus bestimmt und miteinander verglichen werden. Die Bestimmung der Kristallstruktur dieser Verbindung gelang aus einem nicht meroedrisch verzwilligten Einkristall.

5. Die Kristallisation von $[\text{Co}_2(\text{BDC})-(\text{O})_2]\cdot 8\text{H}_2\text{O}$ und $[\text{Ni}_2(\text{BDC})-(\text{O})_2]\cdot 8\text{H}_2\text{O}$ wurde ebenso mit dem Modell von Gualtieri ausgewertet. Dabei wurden mikrowellenunterstützten Solvothermalreaktionen sowie konventionellen Solvothermalsynthesen miteinander verglichen.

7.2. Zusammenfassung der Strukturlösung von anorganisch-organischen Hybridverbindungen

In dieser Arbeit wurden 16 neue Kristallstrukturen aus Röntgenpulverdaten gelöst und verfeinert bzw. nur verfeinert. Die Verbindungen und die verwendeten Kristallstrukturbestimmungsmethoden sind in Tabelle 7.2 zusammengefasst.

7. Zusammenfassung

Tabelle 7.2.: Kristallstrukturen die mit Hilfe von Röntgenpulverdaten bestimmt wurden.

Summenformel	Strukturbestimmungsmethoden
$[\text{Cu}_2(\text{O}_3\text{P-C}_2\text{H}_4\text{-SO}_3)(\text{OH})(\text{H}_2\text{O})_2] \cdot 4\text{H}_2\text{O}$	direkte Methoden / Rietveld-Verfeinerung an Synchrotron Röntgenpulverdaten
$[\text{Cu}_{1.5}(\text{O}_3\text{P-C}_2\text{H}_4\text{-SO}_3)(\text{H}_2\text{O})_2]$	Kraftfeldrechnungen / Rietveld-Verfeinerung
$\text{Mn}((\text{HO}_3\text{P-CH}_2)_2\text{-NHCH}_2\text{-C}_6\text{H}_4\text{-COOH})_2$	Rietveld-Verfeinerung
$\text{Fe}((\text{HO}_3\text{P-CH}_2)_2\text{-NHCH}_2\text{-C}_6\text{H}_4\text{-COOH})_2$	Rietveld-Verfeinerung
$\text{Co}((\text{HO}_3\text{P-CH}_2)_2\text{-NHCH}_2\text{-C}_6\text{H}_4\text{-COOH})_2$	Rietveld-Verfeinerung
$\text{Ni}((\text{HO}_3\text{P-CH}_2)_2\text{-NHCH}_2\text{-C}_6\text{H}_4\text{-COOH})_2$	Rietveld-Verfeinerung
$\text{Ca}(\text{O}_3\text{PC}_2\text{H}_4\text{NH}_2)$	direkte Methoden / Rietveld-Verfeinerung
$\text{Ca}(\text{OH})(\text{O}_3\text{PC}_2\text{H}_4\text{NH}_3) \cdot 2\text{H}_2\text{O}$	direkte Methoden / Rietveld-Verfeinerung
$[\text{Ni}(m\text{-}[(\text{HO}_3\text{PCH}_2)_2\text{-NHCH}_2]_2\text{C}_6\text{H}_4)] \cdot \text{H}_2\text{O}$	direkte Methoden / Rietveld-Verfeinerung an Synchrotron Röntgenpulverdaten
$[\text{Zn}(p\text{-}[(\text{HO}_3\text{PCH}_2)_2\text{-NHCH}_2]_2\text{C}_6\text{H}_4)\text{H}_2\text{O}]$	Modellerstellung / Rietveld-Verfeinerung an Synchrotron Röntgenpulverdaten
$[\text{Cd}(p\text{-}[(\text{HO}_3\text{PCH}_2)_2\text{-NHCH}_2]_2\text{C}_6\text{H}_4)]$	direkte Methoden / Rietveld-Verfeinerung an Röntgenpulverdaten
Bi(BTB) (CAU-7)	Strukturlösung aus Elektronenbeugungsdaten (simulated annealing) / Rietveld-Verfeinerung / DFT Rechnungen
Bi(HPyr)	parallel tempering / Rietveld-Verfeinerung
$[(\text{Bi}(\text{BTC})(\text{H}_2\text{O})) \cdot \text{H}_2\text{O}]$	parallel tempering / Rietveld-Verfeinerung an Synchrotron Röntgenpulverdaten
$[\text{Al}_2(\text{OCH}_3)_4\text{BDC}]$	direkte Methoden / Rietveld-Verfeinerung
$[\text{Al}_2(\text{OCH}_3)_4\text{BDC-NH}_2]$	Kraftfeldrechnungen / Rietveld-Verfeinerung
$[\text{Al}_2(\text{OCH}_3)_4\text{NDC}]$	Kraftfeldrechnungen / Rietveld-Verfeinerung

1. **Kupferphosphonatosulfonate:** Die Kristallstruktur des metastabilen Intermediats $[\text{Cu}_2(\text{O}_3\text{P-C}_2\text{H}_4\text{-SO}_3)(\text{OH})(\text{H}_2\text{O})_2] \cdot 4\text{H}_2\text{O}$ konnte aus Röntgenpulverdaten mittels direkter Methoden bestimmt werden. Dies führte zur Aufstellung eines potentiellen Kristallisationsmechanismus für die Bildung von $[\text{Cu}_2(\text{O}_3\text{P-C}_2\text{H}_4\text{-SO}_3(\text{OH})(\text{H}_2\text{O})_2)] \cdot 3\text{H}_2\text{O}$. Durch Einkristallstrukturanalyse und der Kombination aus Kraftfeldrechnungen und Rietveld-Verfeinerung konnten die Kristallstrukturen von $[\text{NaCu}(\text{O}_3\text{P-C}_2\text{H}_4\text{-SO}_3)(\text{H}_2\text{O})_2]$ und $[\text{Cu}_{1.5}(\text{O}_3\text{P-C}_2\text{H}_4\text{-SO}_3)(\text{H}_2\text{O})_2]$. Die Kenntnis dieser Strukturen erlaubte die Struktur-Synthese Beziehungen des pH-Wertes zu ermitteln.

2. **Aminofunktionalisierte Metallphosphonate:** Die *in situ* EDXRD Untersuchung von $\text{Ca}(\text{O}_3\text{P-C}_2\text{H}_4\text{-NH}_2)$ zeigte, dass während der Kristallisation das Intermediat

$\text{Ca}(\text{OH})(\text{O}_3\text{P}-\text{C}_2\text{H}_4-\text{NH}_3)\cdot 2\text{H}_2\text{O}$ auftritt. Beide Kristallstrukturen konnten aus Röntgenpulverdaten gelöst werden.

3. Mikrowellenunterstützte Hochdurchsatzsynthesen wurden verwendet um systematisch die Abhängigkeit der Linkergeometrie, des Ionenradiuses und des eingesetzten Gegenions auf die Produktbildung zu untersuchen. Dies führte zu den Verbindungen $[\text{Ni}(m-[(\text{HO}_3\text{PCH}_2)_2-\text{NHCH}_2]_2\text{C}_6\text{H}_4)] \cdot \text{H}_2\text{O}$, $[\text{Cd}(p-[(\text{HO}_3\text{PCH}_2)_2-\text{NHCH}_2]_2\text{C}_6\text{H}_4)]$ und $[\text{Zn}(p-[(\text{HO}_3\text{PCH}_2)_2-\text{NHCH}_2]_2\text{C}_6\text{H}_4)\text{H}_2\text{O}]$. Die Kristallstrukturen der ersten beiden Verbindungen wurden aus Labor bzw. Synchrotron Röntgenpulverdaten gelöst. Für die Kristallstruktur der dritten Verbindung wurde aus kristallographischen Zusammenhängen von Zellvolumen und Raumgruppe, in Verbindung mit der aus den Charakterisierung gewonnenen Summenformel, ein Strukturmodell hergeleitet und mittels Rietveld-Methode verfeinert.
4. **Aluminiumcarboxylate:** Die Verwendung von direkten Methoden, Kraftfeldrechnungen, und Rietveld-Verfeinerungen führte zu der Strukturaufklärung einer Familie an neuen aluminiumbasierenden hochporösen Gerüstverbindungen $[\text{Al}_2(\text{OCH}_3)_4\text{BDC}]$, $[\text{Al}_2(\text{OCH}_3)_4\text{BDC}-\text{NH}_2]$ und $[\text{Al}_2(\text{OCH}_3)_4\text{NDC}]$.
5. **Bismutcarboxylate:** In einer systematischen Hochdurchsatzstudie wurde der Einfluss von Linkergeometrie und der Anzahl an funktionellen Gruppen auf die Bildung von Bismutcarboxylaten unter Verwendung von Pyromellitsäure (H_4Pyr), Trimellitsäure (H_3Tri) und Trimesinsäure (H_3BTC) untersucht. Die Kristallstrukturen der erhaltenen Verbindungen $\text{Bi}_2(\text{O})(\text{Pyr})(\text{H}_2\text{O})$, $\text{Bi}(\text{HPyr})$, $\text{Bi}(\text{Tri})(\text{H}_2\text{O})$, $\text{Bi}_2(\text{O})(\text{OH})(\text{HBTC})(\text{NO}_3)$, $\text{Bi}_6\text{O}_5(\text{BTC})_2(\text{HBTC})_4$ wurden aus Einkristallstrukturanalysen bestimmt. Die Kristallisation von $\text{Bi}(\text{HPyr})$, $\text{Bi}(\text{Tri})(\text{H}_2\text{O})$ und $\text{Bi}_2(\text{O})(\text{OH})(\text{HBTC})(\text{NO}_3)$ wurde mittels EDXRD untersucht. Hierbei wurden die Kristallstrukturen der gefundenen Intermediate $\text{Bi}(\text{HPyr})$ und $[(\text{Bi}(\text{BTC})(\text{H}_2\text{O}))\cdot \text{H}_2\text{O}]$ mittels Realraummethoden unter Verwendung des Algorithmus „parallel tempering“ gelöst und anschließend erfolgreich mittels Rietveld-Methode verfeinert. Die Kristallstruktur des Intermediats $\text{Bi}_2(\text{O})(\text{Pyr})(\text{H}_2\text{O})$ war bereits aus Einkristallstrukturanalyse bekannt.
6. Die Verwendung von 1,3,5-Benzoltrisbenzoesäure führte zu dem ersten hoch porösen Bismutcarboxylat $\text{Bi}(\text{BTB})$. Die Verbindung zeigt eine scheinbare spezifische Oberfläche von $1150 \text{ m}^2/\text{g}$ und ist für die Hydroxymethylierung von Furan katalytisch aktiv. Die Kristallstruktur von $\text{Bi}(\text{BTB})$ wurde aus Elektronenbeugungsdaten, gewonnen mittels Automated Diffraction Tomography Messungen, durch Verwendung

von „simulated annealing“ gelöst. Anschließend wurde das Strukturmodell durch eine Kombination von Rietveld-Methode und DFT Rechnungen verfeinert. Insbesondere die Kombination von Methoden erwies sich als sehr hilfreich um Strukturmodelle zu erstellen oder zu vervollständigen.

- 7. Metalltetrazolate:** Die Kristallstrukturen von $[\text{Co}(\text{DMA})_6]_3[(\text{Co}_4\text{Cl})_3(\text{BTT})_8(\text{H}_2\text{O})_{12}]_2 \cdot 12\text{H}_2\text{O}$ und $[\text{Cd}(\text{DMF})_6]_3[(\text{Cd}_4\text{Cl})_3(\text{BTT})_8(\text{H}_2\text{O})_{12}]_2 \cdot 14\text{H}_2\text{O} \cdot 4\text{DMF}$ konnten mittels Einkristallstrukturanalyse aufgeklärt werden und die Verbindung $[\text{Co}(\text{DMA})_6]_3[(\text{Co}_4\text{Cl})_3(\text{BTT})_8(\text{H}_2\text{O})_{12}]_2 \cdot 12\text{H}_2\text{O}$ hinsichtlich ihrer katalytischen Eigenschaften zur Benzinentschwefelung, der oxidativen Ringöffnung von Styroloxid und der Oxidation von Benzyl- und Cyclohexylverbindungen untersucht werden.
- 8. Schaltbare Metallcarboxylate:** Unter anderem mittels Einkristallstrukturanalyse konnte der erfolgreiche Einbau einer schaltbaren Azofunktion in die Metall-organischen Gerüstverbindungen $[\text{Co}_2(\text{NDC})_2(\text{AzBIPY})]$, $[\text{Cu}_2(\text{NDC})_2(\text{AzBIPY})]$, $[\text{Zn}_2(\text{BPDC})_2(\text{AzBIPY})]$ und $[\text{Zn}_2(\text{CCA})_2(\text{AzBIPY})]$ und $(\text{Zn}(\text{Im})(\text{aIm}))$ bewiesen werden.

7.3. Ausblick

Die *in situ* Untersuchungen der polyfunktionalisierten Phosphonate hat gezeigt, dass sich oft kristalline Intermediate bilden können und daher weitergehende Untersuchungen an neuen Metallphosphonaten notwendig sind. Das grundlegende Verständnis für die notwendigen Bedingungen zur Bildung von Intermediaten und ihren Eigenschaften könnten daraus erhalten werden. Die Verwendung von aromatischen, starren Phosphonosulfonsäuren (wie z.B. die 1,4-Phosphonophenylsulfonsäure) oder aminofunktionalisierten Phosphonsäuren könnten zu neuen Intermediaten führen, da auf Grund der geringeren Flexibilität Struktur motive der bisher beobachteten Intermediate nicht möglich sind. Ebenso könnte der Einsatz flexibler Phosphonocarbonsäuren wie z.B. 1,2-Phosphonoethancarbonsäure untersucht werden, die auf Grund ihrer höheren Flexibilität zur Bildung von kristallinen Intermediaten führen sollten. Mögliche Linker sind in Abbildung 7.1 gezeigt. Ebenso bietet sich die Synthese neuer polyfunktionalisierter Linker wie z.B. Nitrophosphonsäuren, Thiophosphonsäuren oder Boronophosphonsäuren an, die potentiell zur Synthese von neuen porösen Gerüstverbindungen geeignet sein sollten.

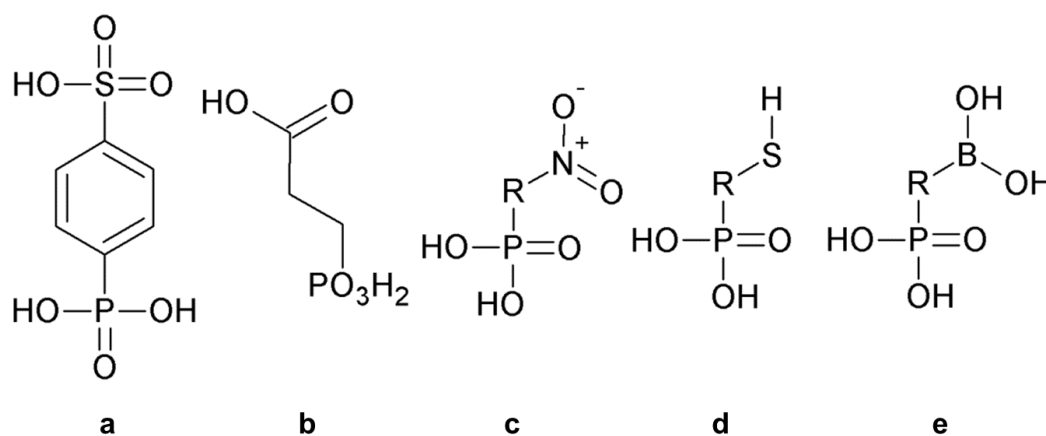


Abbildung 7.1.: Mögliche Linker zur Synthese neuer anorganisch-organischer Hybridverbindungen **a:** 1,4-Phosphonophenylsulfonsäure, **b:** 1,2-Phosphonoethancarbonsäure, **c:** Nitrophosphonsäure, **d:** Thiophosphonsäure und **e:** Boronophosphonsäure.

Weiterhin müssen in Zukunft *in situ* Röntgenbeugungsmethoden an neue Synchrotronstrahlungsquellen adaptiert werden, die höhere Zeit- und Reflexauflösungen ermöglichen. Die hohen Energien der neuen Synchrotrons erlauben den Übergang zu winkeldispersiven Messungen und mittels Pawley oder LeBail-Methoden können parallel zur Detektion von kristallinen Verbindungen, Teilchengrößen bestimmt werden. Da Röntgenbeugung alleine

nur Informationen über kristalline Stoffe liefert, müssen in Zukunft weitere Methoden mit den *in situ* Röntgenbeugungsexperimenten kombiniert werden. Hierbei bieten sich vor allem IR- und Raman-Spektroskopie oder auch Röntgen-Kleinwinkelstreuung an. Zusätzlich ermöglichen *in situ* EXAFS und PDF Studien Informationen über die in Lösung befindlichen Spezies oder amorphen Vorstufen zu erhalten und könnten zusätzlich Informationen über lokale Strukturen liefern.

Zur Zeit sind immer noch sehr wenige Strukturen von Bismutcarboxylaten publiziert, sodass noch viele Linker für die Synthese dieser Verbindungen untersucht werden können. Eine Auswahl an möglichen Linkern ist in Abbildung 7.2 gezeigt.

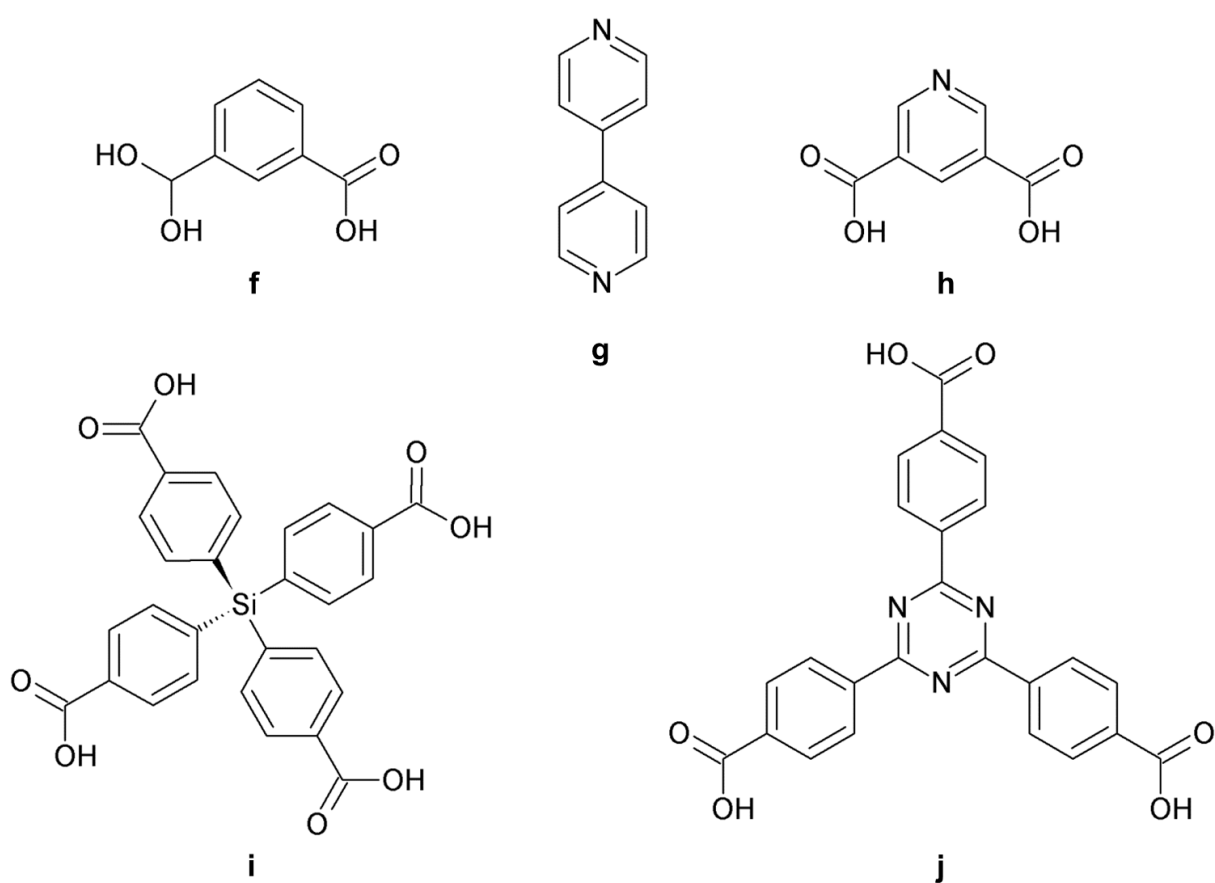


Abbildung 7.2.: Mögliche carboxylatbasierende Linker zur Synthese neuer Bismutcarboxylate. **f:** Isophthalsäure, **g:** 4,4'-Bipyridin, **h:** 3,5-Pyridindicarbonsäure, **i:** Tetrakis(4-carboxyphenyl)silan, **j:** 2,4,6-(1,3,5-Triazin)trisbenzoesäure.

Da weder die Synthese noch die Struktur von Bismutisophthalaten publiziert wurden, bietet sich die Verwendung von Isophthalsäure in Anlehnung an die in dieser Arbeit vorgestellten Ergebnisse an. In der Literatur wurden bereits durch Umsetzung von Salicylsäure

und 1,10-Phenanthrolin mit Bismut diskrete Cluster erhalten.^[209,210] Durch die Kombination von Poly- oder auch Monocarboxylaten mit pyridinbasierenden Linkern wie 4,4'-Bipyridin könnten Mischligandenverbindungen erzeugt werden, die auf solchen Clustern basieren und zur Darstellung poröser Strukturen führen könnten. Weiterhin bietet sich 3,5-Pyridindicarbonsäure als Linker an, da bereits gezeigt werden konnte, dass die substituierten Pyridine 2,5- und 2,6-Pyridindicarbonsäure zu Synthese von bismuthaltigen Verbindungen genutzt werden können. Über den Einsatz von 3,5-Pyridindicarbonsäure wurde in der Literatur noch nichts in Bezug auf bismutbasierenden Verbindungen berichtet.

Zur Erzeugung neuer poröser Strukturen können die Linker 2,4,6-(1,3,5-Triazin)trisbenzoesäure und Tetrakis(4-carboxyphenyl)silan verwendet werden um die Bildung zu hoch kondensierter anorganischer Einheiten durch die Sterik des gewählten Linkers zu unterbinden. Der Linker Tetrakis(4-carboxyphenyl)silan konnte bereits erfolgreich zur Synthese von metall-organischen Gerüstverbindungen eingesetzt werden und die Synthese dieses Linkers ist etabliert.^[211-215] Der Linker 2,4,6-(1,3,5-Triazin)trisbenzoesäure könnte zur Bildung von CAU-7 analogen oder eng verwandten Netzwerken führen.

Neben Carbonsäuren könnten ebenfalls Sulfonsäuren zur Synthese neuer bismuthaltiger Gerüstverbindungen verwendet werden. Für Bismut wurden bisher diskrete 6, 22 oder 38-kernige Bismutoxido-Cluster beobachtet, die durch endständige Sulfonatgruppen stabilisiert werden.^[187,216-219] Das Verknüpfen dieser Cluster über Polysulfonate könnte zu dreidimensionalen porösen Gerüststrukturen führen. Mögliche Linker sind in Abbildung 7.3 gezeigt.

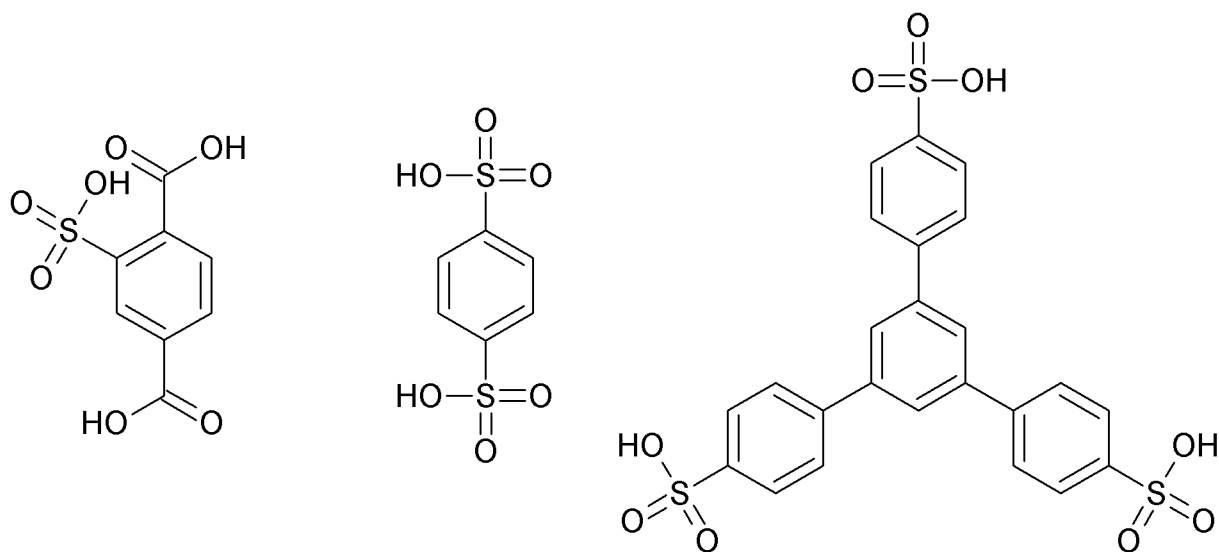


Abbildung 7.3.: Mögliche sulfonsäurebasierende Linker zur Synthese neuer bismuthaltiger Gerüstverbindungen. **links:** 2-Sulfoterephthalsäure, **mitte:** 1,4-Benzoldisulfonsäure, **rechts:** 1,3,5-Benzoltrisbenzolsulfonsäure.

Anfangs könnten hierbei sulfonsäurefunktionalisierte Carbonsäuren wie die 2-Sulfoterephthalsäure untersucht werden, aber auch reine Sulfonsäuren wie 1,4-Benzoldisulfonsäure oder 1,3,5-Benzol(trisbenzolsulfonsäure) könnten zur Synthese neuer Bismutsulfonate dienen. Die *in situ* Untersuchungen der Bismutcarboxylate zeigten, dass die Kristallisation oft über Intermediate verläuft. Die neu erhaltenen Bismuthsulfonate und Bismutcarboxylate sollten ebenfalls mit *in situ* Röntgenbeugungsexperimenten untersucht werden, um neue mögliche kristalline Intermediate zu finden und die Reaktionsverläufe aufzuklären.

Teil III.

Anhang

Supporting Information

Systematic and *in-situ* EDXRD investigations on the formation of lanthanide phosphonatobutanesulfonates $-\text{Ln}(\text{O}_3\text{P}-\text{C}_4\text{H}_8-\text{SO}_3)(\text{H}_2\text{O})$ (Ln = La-Gd)

*Mark Feyand,^a Christian Näther,^a André Rothkirch,^b and Norbert Stock^{*a}*

^a Institute für Anorganische Chemie, Christian-Albrechts-Universität, Max-Eyth Straße 2, D 24118 Kiel, Germany

^b HASYLAB, DESY Hamburg, Notkestraße 85, 22607 Hamburg, Germany

- (1) High-throughput synthesis
- (2) XRPD patterns and lattice parameters of $\text{Ln}(\text{O}_3\text{P}-\text{C}_4\text{H}_8-\text{SO}_3)(\text{H}_2\text{O})$ (Ln = La-Gd)
- (3) Selected bond lengths of compounds 1 and 2
- (4) Characterization of $\text{Sm}(\text{O}_3\text{P}-\text{C}_4\text{H}_8-\text{SO}_3)(\text{H}_2\text{O})$ by TG analysis and IR- and Raman-spectroscopy
- (5) Results of the *in-situ* EDXRD studies

1) High-throughput synthesis

Table S1. Exact amounts of reactants for the high throughput investigations of the system SmCl₃ / H₃L / NaOH in water.

Nr.	H ₃ L (15mg) 4 mol/l	M 2 mol/l	NaOH 4 mol/l	H ₃ L ₂ [μl]	H ₂ O [μl]	SmCl ₃ [μl]	NaOH [μl]	pH	Product
1	1	1	0	14.6	166.3	29.1	0.0	1	no precipitate
2	1	1	0.5	14.6	159.1	29.1	7.3	1	no precipitate
3	1	1	1	14.6	151.8	29.1	14.6	2	compound 1
4	1	1	2	14.6	137.2	29.1	29.1	3	compound 1
5	1	1	3	14.6	122.7	29.1	43.7	5	compound 1
6	1	1	4	14.6	108.1	29.1	58.2	8	compound 1 / Sm(OH) ₃
7	1	1	6	14.6	79.0	29.1	87.3	8	Sm(OH) ₃
8	1	1	8	14.6	49.9	29.1	116.4	11	Sm(OH) ₃
9	2	1	0	14.6	180.9	14.6	0.0	1	no precipitate
10	2	1	1	14.6	173.6	14.6	7.3	1	compound 1
11	2	1	2	14.6	166.3	14.6	14.6	3	compound 1
12	2	1	3	14.6	159.1	14.6	21.8	5	compound 1
13	2	1	4	14.6	151.8	14.6	29.1	8	Sm(OH) ₃
14	2	1	5	14.6	144.5	14.6	36.4	9	Sm(OH) ₃
15	2	1	6	14.6	137.2	14.6	43.7	9	Sm(OH) ₃
16	2	1	8	14.6	122.7	14.6	58.2	11	Sm(OH) ₃
17	3	1	0	14.6	185.7	9.7	0.0	1	compound 1
18	3	1	2	14.6	176.0	9.7	9.7	2	compound 1
19	3	1	3	14.6	171.2	9.7	14.6	5	compound 1
20	3	1	5	14.6	161.5	9.7	24.3	8	compound 1 / Sm(OH) ₃
21	3	1	6	14.6	156.6	9.7	29.1	9	Sm(OH) ₃
22	3	1	7	14.6	151.8	9.7	34.0	11	Sm(OH) ₃
23	4	1	0	14.6	188.2	7.3	0.0	1	compound 1
24	4	1	2	14.6	180.9	7.3	7.3	2	compound 1
25	4	1	4	14.6	173.6	7.3	14.6	7	compound 1
26	4	1	6	14.6	166.3	7.3	21.8	9	Sm(OH) ₃
27	4	1	8	14.6	159.1	7.3	29.1	9	Sm(OH) ₃
28	4	1	10	14.6	151.8	7.3	36.4	11	Sm(OH) ₃
29	1	2	0	14.6	137.2	58.2	0.0	1	no precipitate
30	1	2	1	14.6	122.7	58.2	14.6	2	compound 1
31	1	2	2	14.6	108.1	58.2	29.1	4	compound 1
32	1	2	3	14.6	93.6	58.2	43.7	4	compound 1
33	1	2	4	14.6	79.0	58.2	58.2	7	compound 1
34	1	2	5	14.6	64.4	58.2	72.8	9	Sm(OH) ₃
35	1	2	6	14.6	49.9	58.2	87.3	11	Sm(OH) ₃
36	1	2	8	14.6	20.8	58.2	116.4	13	Sm(OH) ₃
37	1	3	0	14.6	108.1	87.3	0.0	2	no precipitate
38	1	3	2	14.6	79.0	87.3	29.1	4	no precipitate
39	1	3	3	14.6	64.4	87.3	43.7	7	no precipitate
40	1	3	5	14.6	35.3	87.3	72.8	8	compound 1 / Sm(OH) ₃
41	1	3	6	14.6	20.8	87.3	87.3	10	Sm(OH) ₃
42	1	3	7	14.6	6.2	87.3	101.9	11	Sm(OH) ₃
43	1	4	0	14.6	79.0	116.4	0.0	1	no precipitate
44	1	4	2	14.6	49.9	116.4	29.1	3	compound 1
45	1	4	4	14.6	20.8	116.4	58.2	5	compound 1
46	1	5	2	14.6	20.8	145.6	29.1	8	compound 1 / Sm(OH) ₃
47	1	5	2	14.6	20.8	145.6	29.1	9	Sm(OH) ₃
48	1	5	3	14.6	6.2	145.6	43.7	9	Sm(OH) ₃

Temperature 150 °C total volume: 210 μL

2.) X-ray powder diffraction patterns of $\text{Ln}(\text{O}_3\text{P-C}_4\text{H}_8\text{-SO}_3)(\text{H}_2\text{O})$
(Ln = La-Gd)

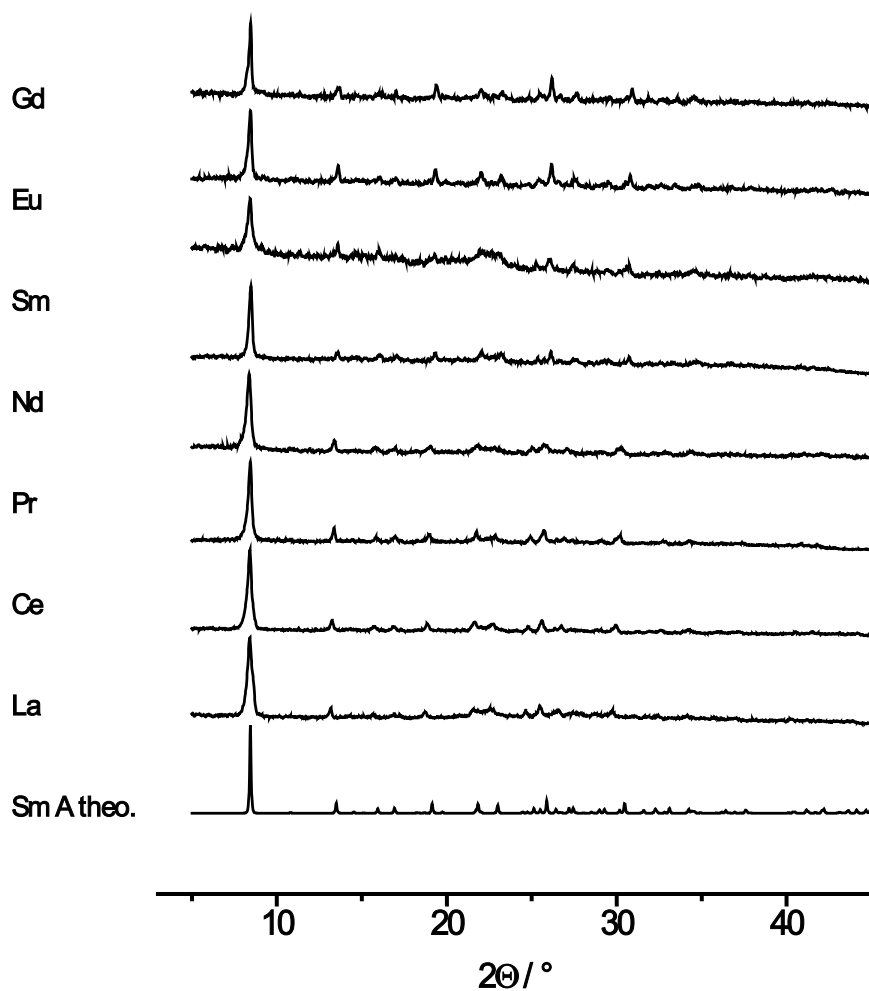


Figure S 1. XRPD patterns of $\text{Ln}(\text{O}_3\text{P-C}_4\text{H}_8\text{-SO}_3)(\text{H}_2\text{O})$ (Ln = La-Gd).

Table S2. Determined lattice constants

<i>Ln</i>	<i>a</i> / pm	<i>b</i> / pm	<i>c</i> / pm	β / °
La	1054(1)	1344(2)	698(1)	104.8(1)
Ce	1053(1)	1336(3)	694(1)	104.6(1)
Nd	1059(5)	1322(6)	692(1)	104.6(1)
Eu	1051(3)	1302(6)	682(2)	104.4(1)
Gd	1052(3)	1300(4)	680(1)	104.4(1)

3.) Selected Bond distances of compounds 1 and 2.

Table S3. Selected bond lengths of compound 1 (left) and compound 2 (right).

Atom 1	Atom 2	d / Å	Atom 1	Atom 2	d / Å
Sm1	O1	2.25(1)	Pr1	O1	2.29(1)
--	O2	2.43(1)	--	O2	2.48(1)
--	O3	2.454(4)	--	O3	2.500(5)
--	O5	2.47(3)	--	O5	2.501(5)
--	O6	2.45(1)	--	O6	2.503(5)
--	OW	2.404(5)	--	OW	2.460(6)
P1	O1	1.510(4)	P1	O1	1.49(1)
--	O2	1.552(4)	--	O2	1.532(4)
--	O3	1.545(4)	--	O3	1.52(1)
--	C1	1.811(7)	--	C1	1.800(7)
S1	O4	1.454(4)	S1	O4	1.45(1)
--	O5	1.454(4)	--	O5	1.45(1)
--	O6	1.473(5)	--	O6	1.46(1)
--	C4	1.76(1)	--	C4	1.76(1)
C1	C2	1.53(1)	C1	C2	1.52(1)
C2	C3	1.52(1)	C2	C3	1.54(1)
C3	C4	1.52(1)	C3	C4	1.50(1)

Table S4. H-bonding distances and angles of compound 1.

	d / pm	Acceptor	Angle / °	d (Donor-Acceptor)
OW-HW1	0.88(1)	O4	139.7(1)	2.75(1)
OW-HW2	0.89(1)	O4	159.5(1)	2.69(1)

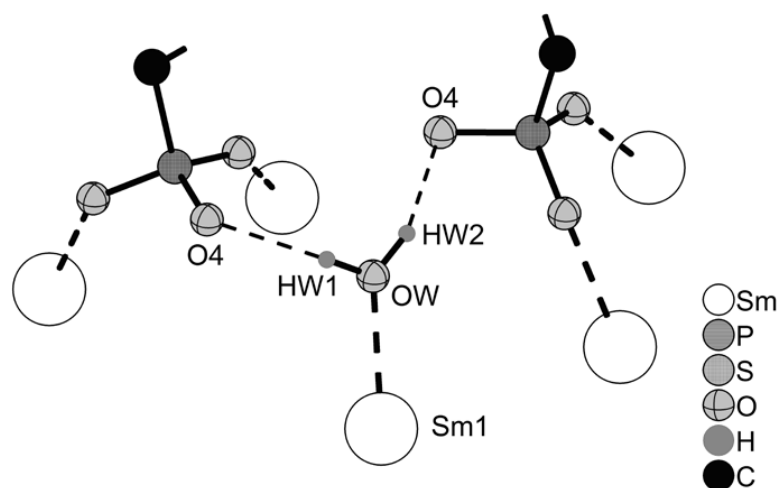


Figure S3. H-bonding theme of compound 1.

4.) Characterization of compound 1

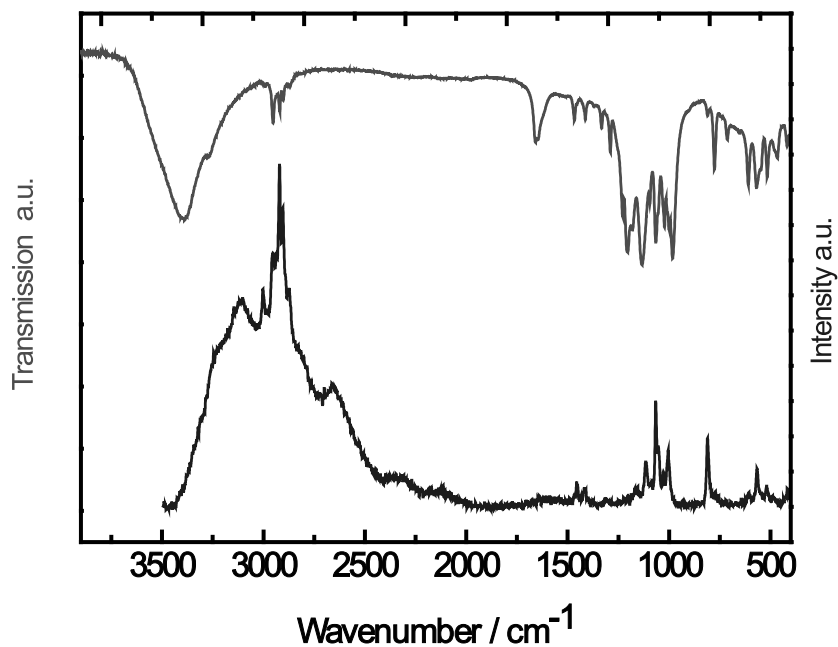


Figure S 4. IR- and Raman Spectra of compound 1.

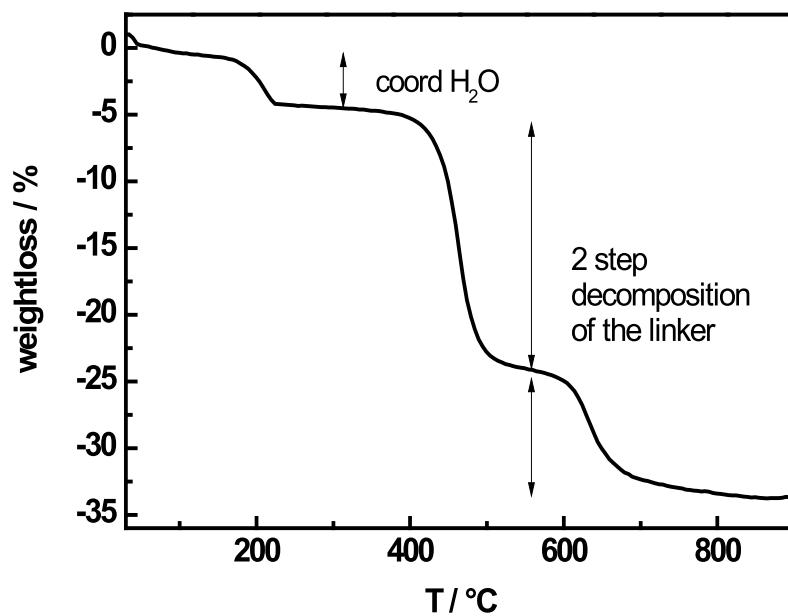


Figure S 5. Thermogravimetric analysis of compound 1.

5.) Results of the *in-situ* EDXRD studies

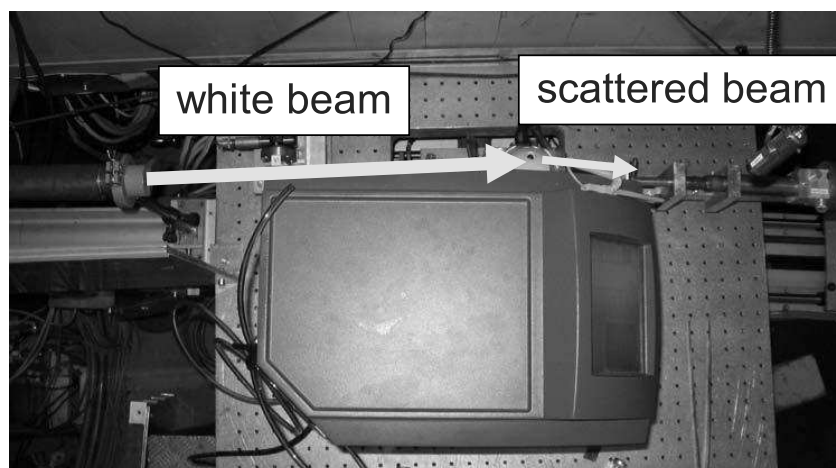


Figure S6. Picture of the implemented microwave reactor for the *in-situ* experiments.

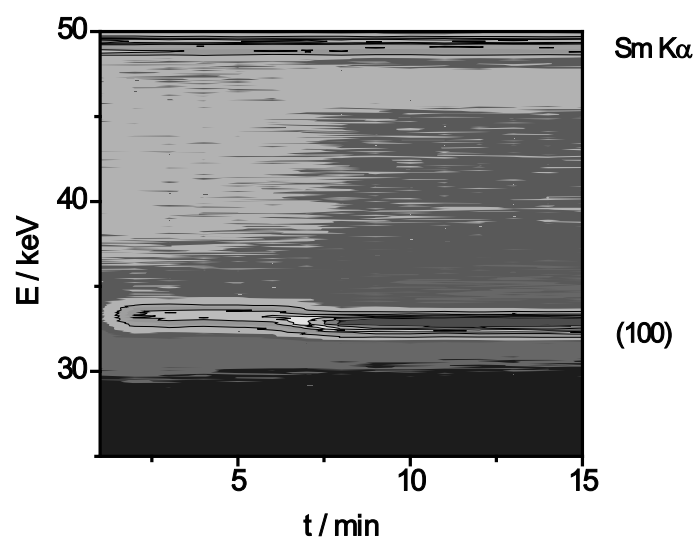


Figure S7. Contour plot illustrating the formation of compound 1 at 150 °C (conventional heating).

Table S5. Kinetic analyses of the reactions using microwave heating. The results were obtained by analyses of Sharp-Hancock plots (see figure S8-S12).

T [°C]	early reaction			late reaction		
	m	b = m lnk	k [s ⁻¹]	m	b = m lnk	k [s ⁻¹]
110	2.9(1)	-16.1(3)	4.40 · 10 ⁻³ (4)	0.29(1)	-1.1(1)	1.74 · 10 ⁻² (5)
120	2.0(2)	-10.6(1)	5.44 · 10 ⁻³ (4)	0.3(1)	-1.1(1)	2.25 · 10 ⁻² (4)
130	2.80(1)	-14.8(6)	5.5 · 10 ⁻³ (1)	0.3(1)	-0.8(4)	4.65 · 10 ⁻² (3)
140	2.2(2)	-11(1)	8.33 · 10 ⁻³ (5)	0.31(4)	-0.8(2)	7.41 · 10 ⁻² (5)
150	2.11(7)	-9.2(2)	1.26 · 10 ⁻² (4)	0.23(7)	-0.5(4)	9.6 · 10 ⁻² (1)

a) Sharp Hancock plots for microwave synthesis

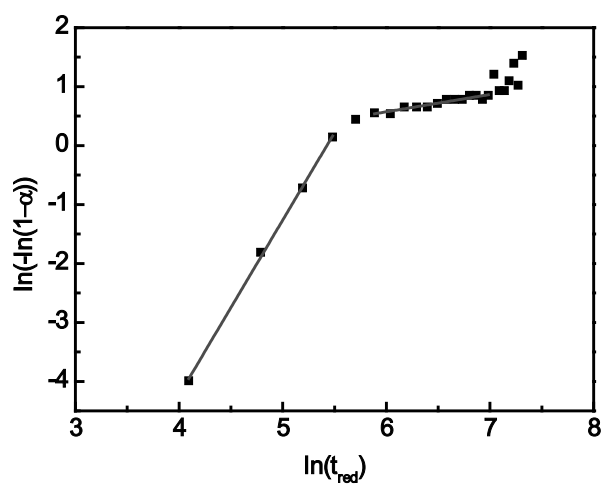


Figure S8: Sharp Hancock plot of the formation of compound 1 at 110 °C (microwave heating).

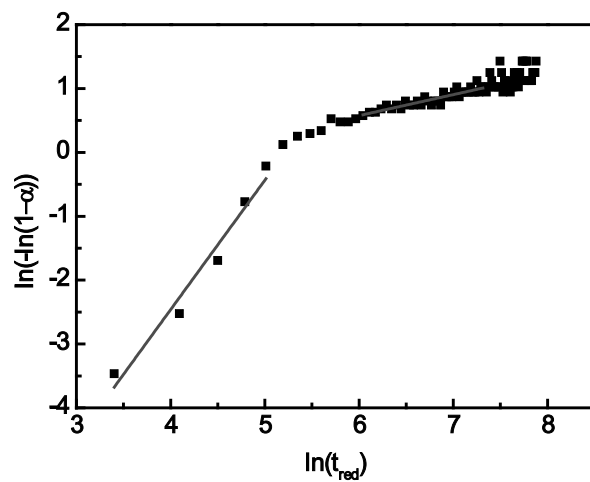


Figure S9: Sharp Hancock plot of the formation of compound 1 at 120 °C (microwave heating).

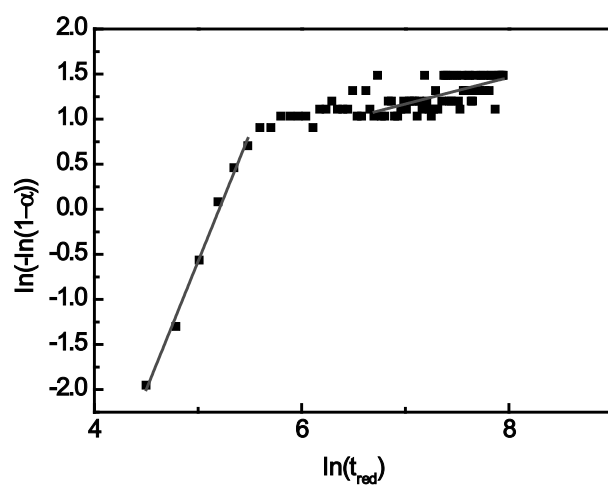


Figure S10: Sharp Hancock plot of the formation of compound 1 at 130 °C (microwave heating).

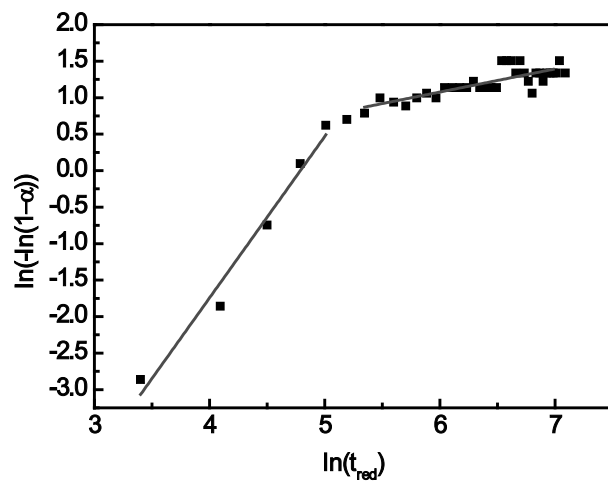


Figure S11: Sharp Hancock plot of the formation of compound 1 at 140 °C (microwave heating).

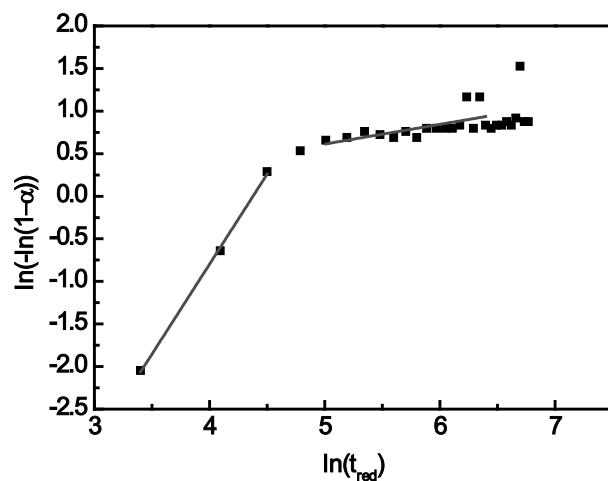


Figure S12: Sharp Hancock plot of the formation of compound 1 at 150 °C (microwave heating).

b) Syntheses under conventional heating

Table S6. Kinetic analysis of the reactions using conventional heating. The results were taken from the Sharp-Hancock analyses (Figure S13-S17).

T [°C]	early reaction			late reaction		
	m	b = m lnk	k [s ⁻¹]	m	b = m lnk	k [s ⁻¹]
110	2.3(1)	-14(1)	2.49·10 ⁻³ (1)	0.68(1)	-4.3(1)	1.97·10 ⁻³ (1)
120	2.21(4)	-12.6(2)	3.34·10 ⁻³ (5)	0.60(2)	-3.2(1)	4.74·10 ⁻³ (4)
130	3.1(1)	-16(1)	5.40·10 ⁻³ (4)	0.34(3)	-1.5(2)	1.08·10 ⁻³ (5)
140	2.1(1)	-11(1)	4.70·10 ⁻³ (6)	0.3(2)	-0.8(2)	9.05·10 ⁻² (4)
150	3.0(1)	-14(1)	9.9·10 ⁻³ (1)	0.37(3)	-1.1(2)	5.02·10 ⁻² (6)

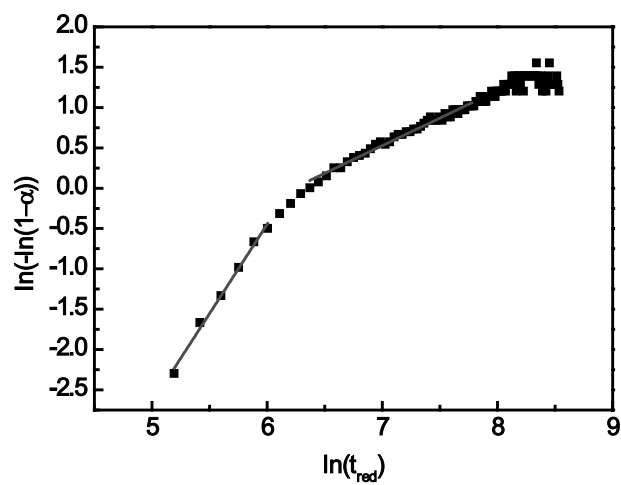
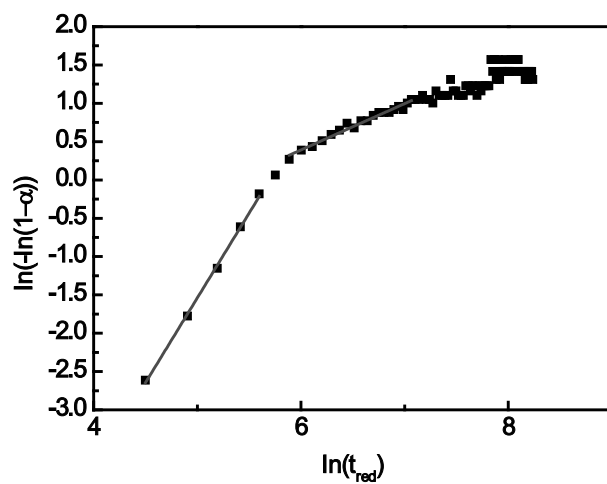


Figure S13: Sharp Hancock plot of the formation of compound **1** at 110 °C (conventional heating).



?

Figure S14: Sharp Hancock plot of the formation of compound 1 at 120 °C (conventional heating).

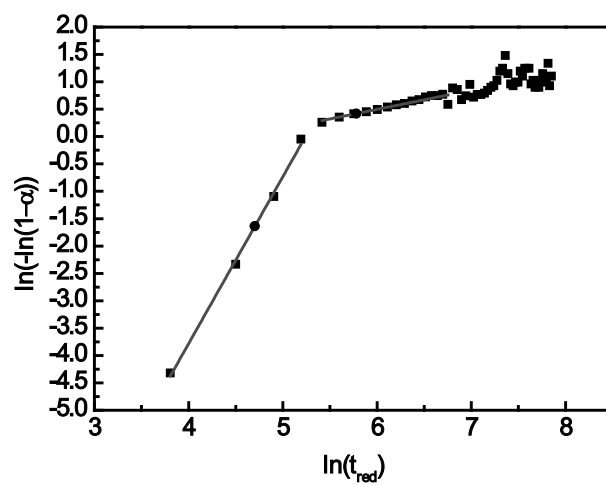


Figure S15: Sharp Hancock plot of the formation of compound 1 at 130 °C (conventional heating).

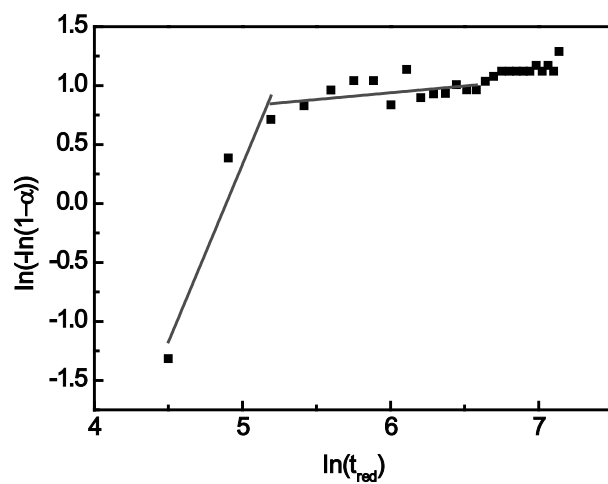


Figure S16: Sharp Hancock plot of the formation of compound 1 at 140 °C (conventional heating).

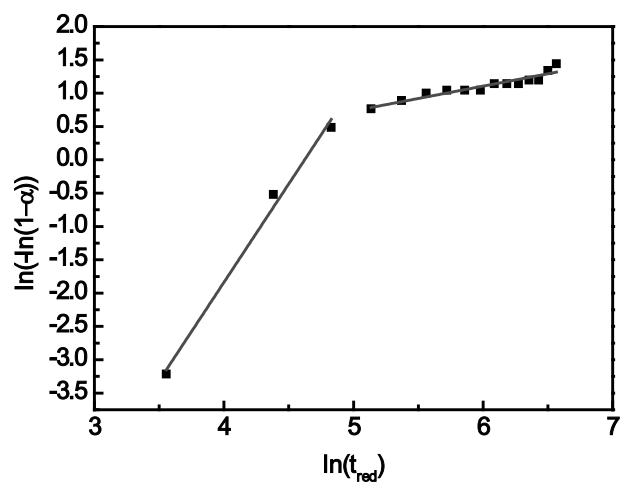


Figure S17: Sharp Hancock plot of the formation of compound 1 at 150 °C (conventional heating).

c) Determination of the Arrhenius Activation Energy

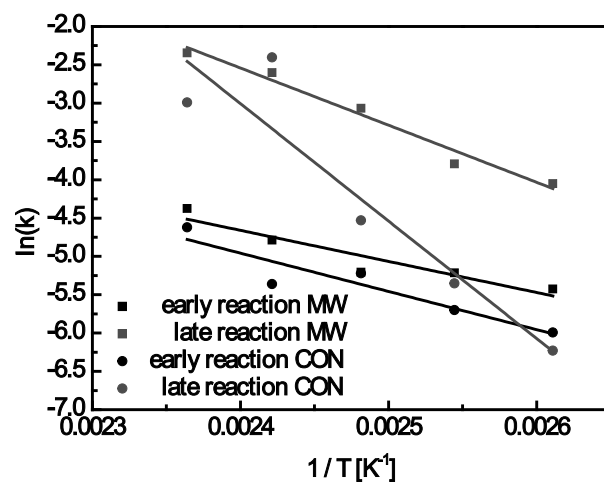


Figure S18. Determination of Arrhenius activation energy for the conventional and microwave heating.

Table S6. Results of the determination of the Arrhenius activation energy.

	early reaction [KJ/mol]	error [KJ/mol]	late reaction [KJ/mol]	error [KJ/mol]
MW	33.71	6.82	61.99	5.80
CON	41.48	9.00	127.42	27.46

Supporting Information

***In-situ* EDXRD investigation on the formation of copper phosphonatoethanesulfonates**

*Mark Feyand,^a , Annika Hübner,^a André Rothkirch,^b David Wragg,^c and Norbert
Stock^{*a}*

^a Institute für Anorganische Chemie, Christian-Albrechts-Universität, Max-Eyth Straße
2, D 24118 Kiel, Germany

^b HASYLAB, DESY Hamburg, Notkestraße 85, 22607 Hamburg, Germany

Centre for Materials Science and Nanotechnology/InGAP/Department of Chemistry,
University of Oslo, Postbox 1033, Blindern, 0315 Oslo, Norway

1. Crystal Structure of compound $[\text{Cu}_2 (\text{O}_3\text{P}-\text{C}_2\text{H}_4-\text{SO}_3) (\text{H}_2\text{O})_2(\text{OH})] \cdot 4\text{H}_2\text{O}$ (**6**).....2
2. Characterization of compound $[\text{Cu}_2 (\text{O}_3\text{P}-\text{C}_2\text{H}_4-\text{SO}_3) (\text{H}_2\text{O})_2(\text{OH})] \cdot 4\text{H}_2\text{O}$ (**6**).4
3. Crystal structure of $[\text{Cu}_{1.5}((\text{O}_3\text{P}-\text{C}_2\text{H}_4-\text{SO})(\text{H}_2\text{O})) \cdot (\text{H}_2\text{O})]$ (**3**).....6
4. Crystal structure of $[\text{NaCu}(\text{O}_3\text{P}-\text{C}_2\text{H}_4-\text{SO}_3) (\text{H}_2\text{O})_2]$ (**5**)9

1. Crystal Structure of compound $[\text{Cu}_2 (\text{O}_3\text{P-C}_2\text{H}_4\text{-SO}_3) (\text{H}_2\text{O})_2(\text{OH})] \cdot 4\text{H}_2\text{O}$ (6)

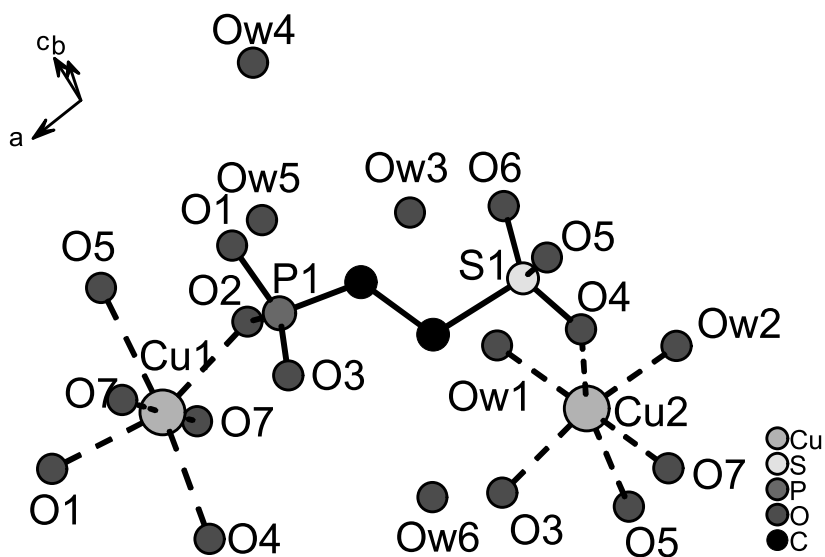


Figure S1. Asymmetric unit of compound 6.

Table S1 Selected bond lengths of $[\text{Cu}_2 (\text{O}_3\text{P-C}_2\text{H}_4\text{-SO}_3) (\text{H}_2\text{O})_2(\text{OH})]\cdot 4\text{H}_2\text{O}$ (6).

Atom 1	Atom 2	bond lengths / Å
Cu1	O7	1.9233(4)
	O1	2.1406(6)
	O2	2.1980(5)
	O7	2.2462(5)
	O5	2.5361(7)
	O4	2.7116(7)
Cu2	O3	2.0473(6)
	Ow2	2.0693(6)
	O7	2.0701(6)
	Ow1	2.2054(6)
	O4	2.2906(6)
S1	O5	2.5388(7)
	O5	1.4106(3)
	O6	1.4245(4)
	O4	1.4648(3)
P1	C2	1.8235(5)
	O3	1.5183(4)
	O1	1.5345(3)
	O2	1.5605(3)
O2	C1	1.8560(5)
	Ow5	2.6487(6)
	Ow2	2.6178(5)
Ow2	Ow5	2.6178(5)
	Ow4	2.8237(6)
	Ow1	2.4497(6)
Ow1	Ow6	2.4497(6)
	Ow3	2.7876(6)
	Ow3	2.7876(6)
C1	C2	1.5711(4)
C2	S1	1.8235(5)
Ow3	Ow5	2.6055(6)
	O6	2.6946(5)
	Ow1	2.7876(6)
Ow4	Ow6	2.6796(6)
	Ow2	2.8237(6)
	O6	2.8723(7)
Ow5	Ow3	2.6055(6)
	Ow2	2.6178(5)
	O2	2.6487(6)

2. Characterization of compound $[\text{Cu}_2 (\text{O}_3\text{P-C}_2\text{H}_4\text{-SO}_3) (\text{H}_2\text{O})_2(\text{OH})]\cdot 4\text{H}_2\text{O}$ (**6**).

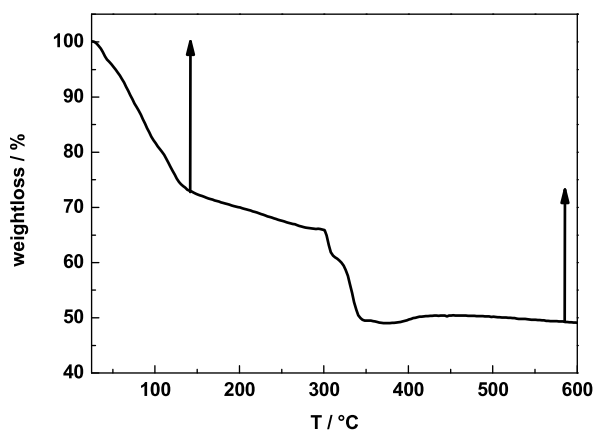


Figure S2. Results of the thermogravimetric analysis of compound **6**.

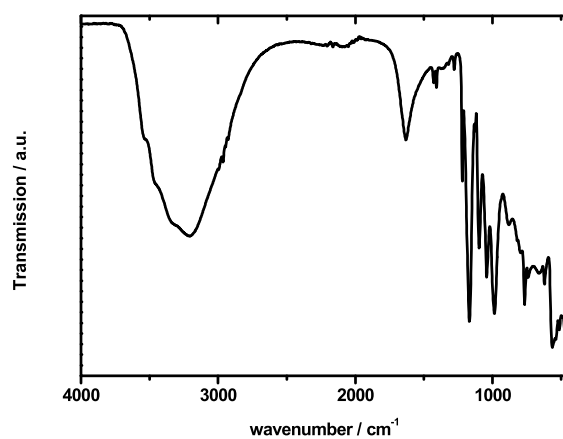


Figure S3. IR spectrum of compound **6**.

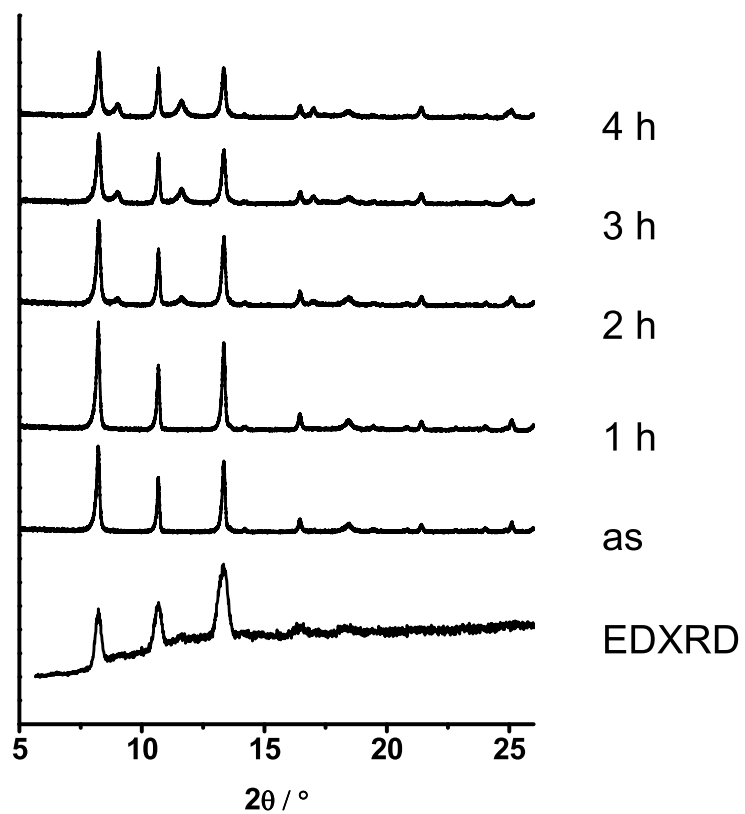


Figure S4. EDXRD spectra and experimental XRPD pattern of compound 6 as synthesized (as) and after storage at air after 1h, 2 h 3h and 4h.

3. Crystal structure of $[\text{Cu}_{1.5}((\text{O}_3\text{P}-\text{C}_2\text{H}_4-\text{SO})(\text{H}_2\text{O}))^+(\text{H}_2\text{O})] (\text{3})$

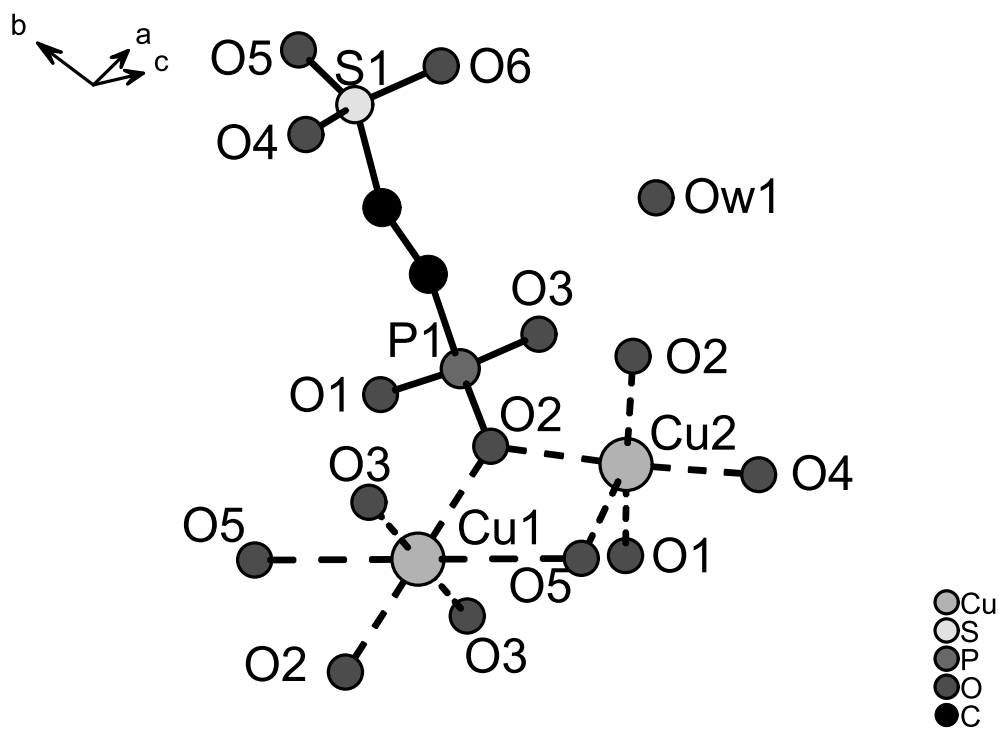


Figure S5. Asymmetric unit of compound 3.

Table S2. Selected bond lengths (Å) of $[\text{Cu}_{1.5}((\text{O}_3\text{P}-\text{C}_2\text{H}_4-\text{SO})(\text{H}_2\text{O}))\cdot(\text{H}_2\text{O})]$ (**3**).

Atom 1	Atom 2	bond lengths / Å
Cu1	O1	1.9598(60)
	O3	1.9744(135)
	O2	2.0358(98)
	O4	2.0374(108)
	O7	2.2420(69)
	O7	2.9641(72)
	Cu2	O5
O5		1.9236(64)
O4		2.0176(65)
O4		2.0176(65)
O7		2.8510(68)
O7		2.8510(68)
S1		O6
	O7	1.4371(75)
	O3	1.4723(65)
	C1	1.8448(123)
P1	O1	1.5109(78)
	O5	1.5208(67)
	O4	1.5585(87)
	C2	1.8255(139)
C2	C	1.5369(242)
	P1	1.8255(139)
	O5	2.6633(155)
	O1	2.7195(176)
	O4	2.7200(146)
	S1	2.7433(141)
C1	C2	1.5369(242)

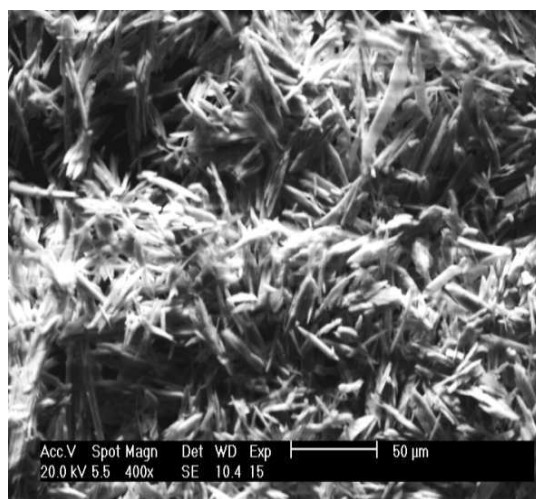


Figure S6. Scanning electron micrograph of compound **3**.

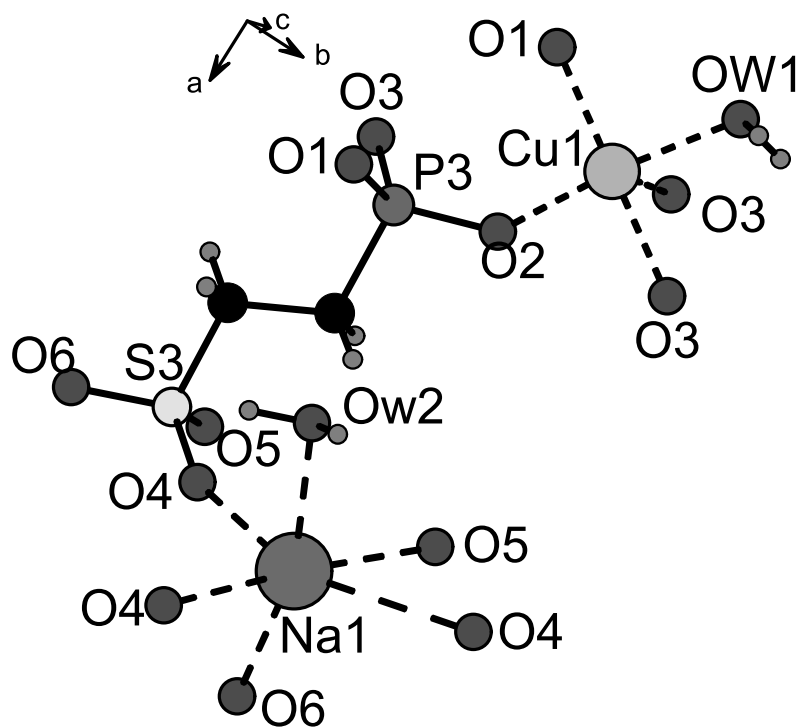
4. Crystal structure of $[\text{NaCu}(\text{O}_3\text{P}-\text{C}_2\text{H}_4-\text{SO}_3)(\text{H}_2\text{O})_2]$ (5)

Figure S7. Asymmetric unit of compound 5.

Table S3. Bond lengths [Å] of [NaCu(O₃P-C₂H₄-SO₃)(H₂O)₂] (5).

Atom 1	Atom 2	bond lengths / Å
Cu1	O3	1.9392(27)
	O2	1.9427(24)
	O4	1.9844(24)
	O1	1.9996(24)
	O4	2.3651(23)
P3	O2	1.5316(24)
	O3	1.5347(26)
	O4	1.5397(24)
	C1	1.7915(32)
S3	O6	1.4299(43)
	O5	1.4622(37)
	O7	1.4636(43)
	C2	1.7659(34)
	C1	1.5335(53)
C1	H2A	2.0682(38)
	H2B	2.0683(38)
	C2	2.0656(41)
C2	H1A	2.0660(38)
	H1B	2.0660(38)
	Na1	O6
Na1	O8	2.3457(50)
	O5	2.3546(44)
	O7	2.3953(52)
	O5	2.4059(41)
	O5	2.8675(44)

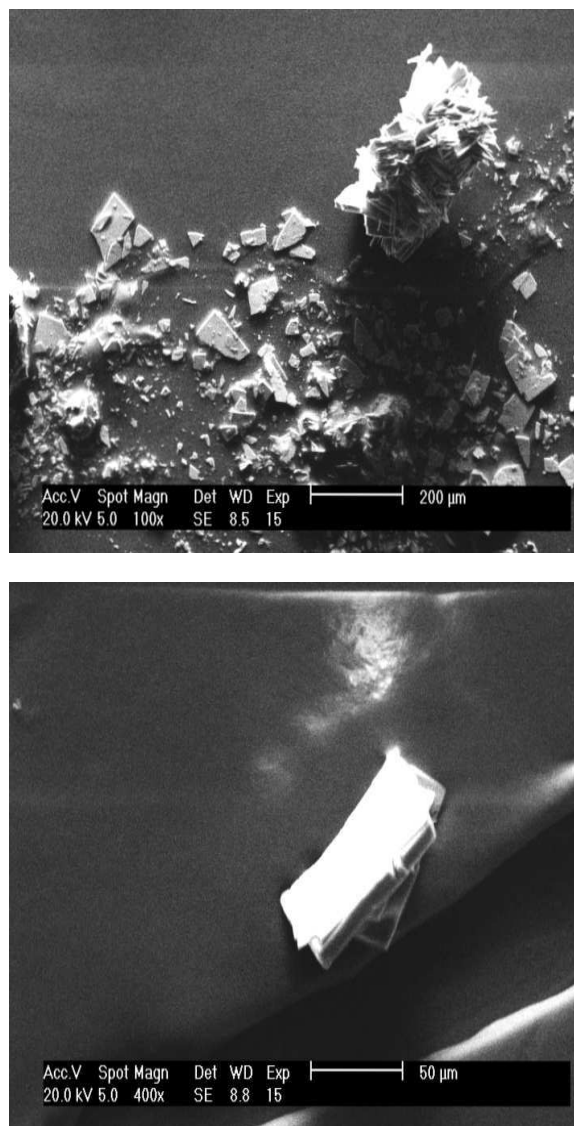


Figure S8. Scanning electron micrographs of compound 5.

Supporting Information

High-throughput and in situ EDXRD investigation on the formation of two new metal aminoethylphosphonates – $\text{Ca}(\text{O}_3\text{PC}_2\text{H}_4\text{NH}_2)$ and $\text{Ca}(\text{OH})(\text{O}_3\text{PC}_2\text{H}_4\text{NH}_3)\cdot 2\text{H}_2\text{O}$

Corinna Schmidt,^a Mark Feyand,^a André Rothkirch,^b and Norbert Stock^{*,a}

^a Institut für Anorganische Chemie, Christian-Albrechts-Universität, Max-Eyth Straße 2, D
24118 Kiel, Germany

^b HASYLAB, DESY Hamburg, Notkestraße 85, 22607 Hamburg, Germany

- 1) Amounts of reagents applied in high throughput synthesis
- 2) Parameters obtained from Rietveld refinement of compounds 1 and 2
- 3) Selected bond lengths and angles of compounds 1 and 2
- 4) IR- and Raman spectroscopic investigation
- 5) Thermal investigation
- 6) *In-situ* EDXRD study

1) Amounts of reagents applied in high-throughput synthesis

All compounds were applied as aqueous solutions: AEPA (1 mol/L), $\text{Ca}(\text{NO}_3)_2 \cdot 4\text{H}_2\text{O}$ (2 mol/L), NaOH (4 mol/L). The total amount of AEPA was kept constant at 40 μmol . The filling level of the PTFE vessels amounted to 200 μL . Table S1 gives the exact amounts of starting materials that were used in the HT experiment, the final pH of the reaction mixtures as well as the products formed.

Table S1. Molar ratios and exact amounts of the reactants for the high-throughput investigation of the system AEPA / $\text{Ca}(\text{NO}_3)_2 \cdot 4\text{H}_2\text{O}$ / NaOH.

No.	AEPA	$\text{Ca}(\text{NO}_3)_2 \cdot 4\text{H}_2\text{O}$	NaOH	AEPA [μl]	H_2O [μl]	$\text{Ca}(\text{NO}_3)_2 \cdot 4\text{H}_2\text{O}$ [μl]	NaOH [μl]	pH	product
	molar ratios			exact amounts					
1	1	1	0.25	40.0	138	20.0	2.5	6	no precipitate
2	1	1	0.5	40.0	135	20.0	5.0	6	no precipitate
3	1	1	1	40.0	130	20.0	10.0	7.5	no precipitate
4	1	1	1.5	40.0	125	20.0	15.0	8	$\text{Ca}(\text{O}_3\text{PC}_2\text{H}_4\text{NH}_2)$
5	1	1	2	40.0	120	20.0	20.0	10	$\text{Ca}(\text{O}_3\text{PC}_2\text{H}_4\text{NH}_2)$
6	1	1	3	40.0	110	20.0	30.0	12	$\text{Ca}(\text{O}_3\text{PC}_2\text{H}_4\text{NH}_2)$
7	1	1	4	40.0	100	20.0	40.0	13	$\text{Ca}(\text{O}_3\text{PC}_2\text{H}_4\text{NH}_2)$
8	1	1	6	40.0	80	20.0	60.0	14	X-ray amorphous
9	1	2	0.25	40.0	118	40.0	2.5	6	no precipitate
10	1	2	0.5	40.0	115	40.0	5.0	6	no precipitate
11	1	2	1	40.0	110	40.0	10.0	8	no precipitate
12	1	2	1.5	40.0	105	40.0	15.0	8.5	$\text{Ca}(\text{O}_3\text{PC}_2\text{H}_4\text{NH}_2)$
13	1	2	2	40.0	100	40.0	20.0	9	$\text{Ca}(\text{O}_3\text{PC}_2\text{H}_4\text{NH}_2)$
14	1	2	3	40.0	90	40.0	30.0	12	$\text{Ca}(\text{O}_3\text{PC}_2\text{H}_4\text{NH}_2)$
15	1	2	4	40.0	80	40.0	40.0	13	$\text{Ca}(\text{O}_3\text{PC}_2\text{H}_4\text{NH}_2)$
16	1	2	6	40.0	60	40.0	60.0	14	X-ray amorphous
17	1	3	0.5	40.0	95	60.0	5.0	6	no precipitate
18	1	3	1	40.0	90	60.0	10.0	6	no precipitate
19	1	3	2	40.0	80	60.0	20.0	9	$\text{Ca}(\text{O}_3\text{PC}_2\text{H}_4\text{NH}_2)$
20	1	3	3	40.0	70	60.0	30.0	12	$\text{Ca}(\text{O}_3\text{PC}_2\text{H}_4\text{NH}_2)$
21	1	3	4	40.0	60	60.0	40.0	13	$\text{Ca}(\text{O}_3\text{PC}_2\text{H}_4\text{NH}_2)$
22	1	4	0.5	40.0	75	80.0	5.0	6	no precipitate
23	1	4	1	40.0	70	80.0	10.0	6	no precipitate
24	1	4	2	40.0	60	80.0	20.0	9	$\text{Ca}(\text{O}_3\text{PC}_2\text{H}_4\text{NH}_2)$
25	1	4	3	40.0	50	80.0	30.0	12	$\text{Ca}(\text{O}_3\text{PC}_2\text{H}_4\text{NH}_2)$
26	1	6.5	1	40.0	20	130.0	10.0	6	no precipitate
27	1	6.5	2	40.0	10	130.0	20.0	9	$\text{Ca}(\text{O}_3\text{PC}_2\text{H}_4\text{NH}_2)$
28	1	6.5	3	40.0	0	130.0	30.0	12	$\text{Ca}(\text{O}_3\text{PC}_2\text{H}_4\text{NH}_2)$
29	1	0.5	0.25	40.0	148	10.0	2.5	6	no precipitate
30	1	0.5	0.5	40.0	145	10.0	5.0	6	no precipitate
31	1	0.5	1	40.0	140	10.0	10.0	7	no precipitate
32	1	0.5	1.5	40.0	135	10.0	15.0	9	$\text{Ca}(\text{O}_3\text{PC}_2\text{H}_4\text{NH}_2)$
33	1	1.5	0.5	40.0	125	30.0	5.0	6	no precipitate
34	1	1.5	1	40.0	120	30.0	10.0	7	no precipitate
35	1	1.5	1.5	40.0	115	30.0	15.0	9	$\text{Ca}(\text{O}_3\text{PC}_2\text{H}_4\text{NH}_2)$
36	1	2.5	0.25	40.0	108	50.0	2.5	6	no precipitate
37	1	2.5	0.5	40.0	105	50.0	5.0	6	no precipitate
38	1	2.5	1	40.0	100	50.0	10.0	7	no precipitate
39	1	2.5	1.5	40.0	95	50.0	15.0	9	$\text{Ca}(\text{O}_3\text{PC}_2\text{H}_4\text{NH}_2)$
40	1	0.33	0.17	40.0	152	6.6	1.7	6	no precipitate
41	1	0.33	0.33	40.0	150	6.6	3.3	6	no precipitate
42	1	0.33	0.67	40.0	147	6.6	6.7	6	no precipitate
43	1	0.33	1	40.0	143	6.6	10.0	8	no precipitate
44	1	0.67	0.33	40.0	143	13.4	3.3	6	no precipitate
45	1	0.67	0.67	40.0	140	13.4	6.7	6	no precipitate
46	1	0.67	1	40.0	137	13.4	10.0	7	no precipitate
47	1	0.17	0.17	40.0	155	3.4	1.7	6	no precipitate
48	1	0.17	0.33	40.0	153	3.4	3.3	6	no precipitate

2) Parameters obtained from Rietveld refinement of compounds 1 and 2

Table S2. Atomic coordinates for non-hydrogen atoms of $\text{Ca}(\text{O}_3\text{PC}_2\text{H}_4\text{NH}_2)$ (**1**) obtained from the Rietveld refinement.

Atom	x	y	z
Ca1	-0.06385(46)	0.13182(73)	0.16344(47)
P1	-0.16836(38)	-0.15168(65)	0.49879(46)
O1	-0.1348(11)	0.0011(13)	0.64207(99)
O2	-0.0529(12)	-0.2012(15)	0.0484(12)
O3	-0.17694(60)	-0.0379(11)	0.3446(12)
C1	-0.39075(79)	-0.4068(12)	0.37608(83)
C2	-0.34798(96)	-0.22189(97)	0.51331(73)
N1	-0.3166(11)	-0.6371(16)	0.45854(95)

Table S3. Atomic coordinates for non-hydrogen atoms of $\text{Ca}(\text{OH})(\text{O}_3\text{PC}_2\text{H}_4\text{NH}_3) \cdot 2\text{H}_2\text{O}$ (**2**) obtained from the Rietveld refinement.

Atom	x	y	z
Ca1	1.00000	-1/2	0
OH	1.1348(12)	-1/4	0.124(3)
P1	0.82778(66)	-1/4	0.4308(14)
O1	0.84561(82)	-0.42540(69)	0.2699(19)
O2	0.9268(14)	-1/4	-0.3528(29)
C1	0.6733(11)	-1/4	0.4924(26)
C2	0.5948(15)	-1/4	0.2066(26)
N1	0.4689(14)	-1/4	0.2661(28)

3) Selected bond lengths and angles of compounds 1 and 2

Table S4. Selected bond lengths [pm] and angles [°] of Ca(O₃PC₂H₄NH₂) (1).

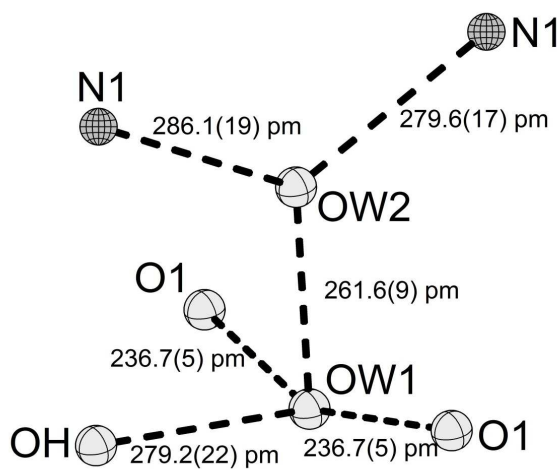
Atoms	Distance [pm]	Atoms	Angle [°]
Ca1-O1	232.5(9)	O1-Ca1-O3	85.7(4)
Ca1-O1	247.5(9)	O2-Ca1-O3	79.8(3)
Ca1-O2	238.5(11)	O3-Ca1-N1	84.7(3)
Ca1-O2	242.2(13)	O1-Ca1-N1	157.9(4)
Ca1-O2	261.3(9)	O2-Ca1-N1	93.7(4)
Ca1-O3	239.6(10)		
Ca1-N1	258.4(9)		
P1-O1	152.7(9)	O1-P1-O2	108.6(5)
P1-O2	144.7(11)	O2-P1-O3	115.5(6)
P1-O3	147.9(10)	O2-P1-C2	95.9(5)
P1-C2	185.1(10)	O3-P1-C2	111.3(3)
C2-C1	163.9(9)	P1-C2-C1	100.6(5)
C1-N1	172.1(12)	C2-C1-N1	102.9(4)

Table S5. Selected bond lengths and angles of Ca(OH)(O₃PC₂H₄NH₃)·2H₂O (2).

Atoms	Distance [pm]	Atoms	Angle [°]
Ca1-O1 (2 X)	244.6(10)	O1-Ca1-O2	86.2(4)
Ca1-O2 (2 X)	255.8(9)	O1-Ca1-OH	99.8(4)
Ca1-OH (2 X)	235.4(9)	O2-Ca1-OH	93.8(4)
P1-O1 (2 X)	152.8(8)	O1-P1-O1	104.7(6)
P1-O2	141.7(16)	O1-P1-O2	110.4(8)
P1-C1	181.5(15)	O2-P1-C1	108.1(5)
C1-C2	155.6(17)	P1-C1-C2	103.9(9)
C2-N1	149.5(23)	C1-C2-N1	102.3(11)

Table S6. Hydrogen bonding scheme of the anticipated hydrogen bonds in $\text{Ca}(\text{OH})(\text{O}_3\text{PC}_2\text{H}_4\text{NH}_3)\cdot 2\text{H}_2\text{O}$ (**2**).

D...A	D...A [pm]
N1 ...OW2	286.1(19)
N1...OW2	279.6(17)
OW2 ...OW1	261.6(9)
OH ...OW1	279.2(22)
OW1 ...O1	236.75(5)
OW1 ...O1	236.75(5)

**Figure S1.** Proposed H-bonding scheme in $\text{Ca}(\text{OH})(\text{O}_3\text{PC}_2\text{H}_4\text{NH}_3)\cdot 2\text{H}_2\text{O}$ (**2**).

4) IR- and Raman spectroscopic investigations

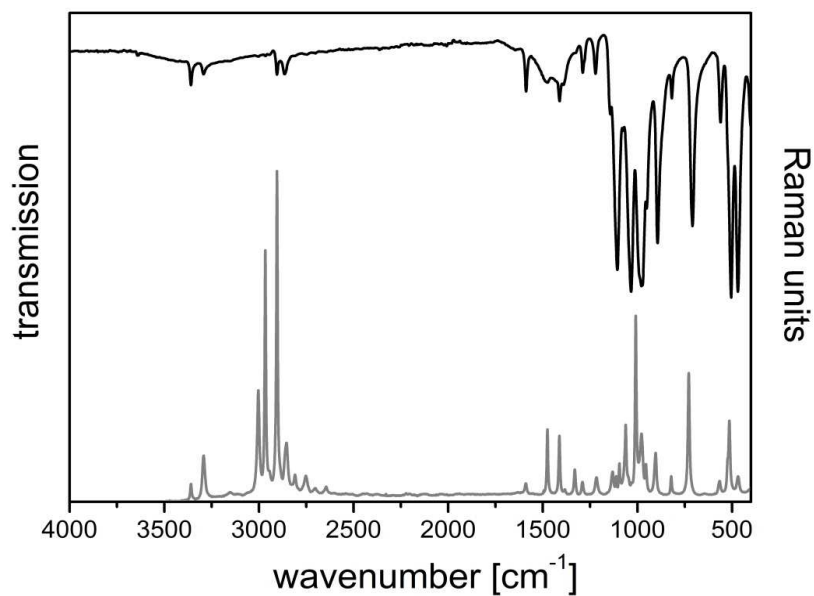


Figure S2. IR- (black) and Raman (gray) spectrum of $\text{Ca}(\text{O}_3\text{PC}_2\text{H}_4\text{NH}_2)$ (1).

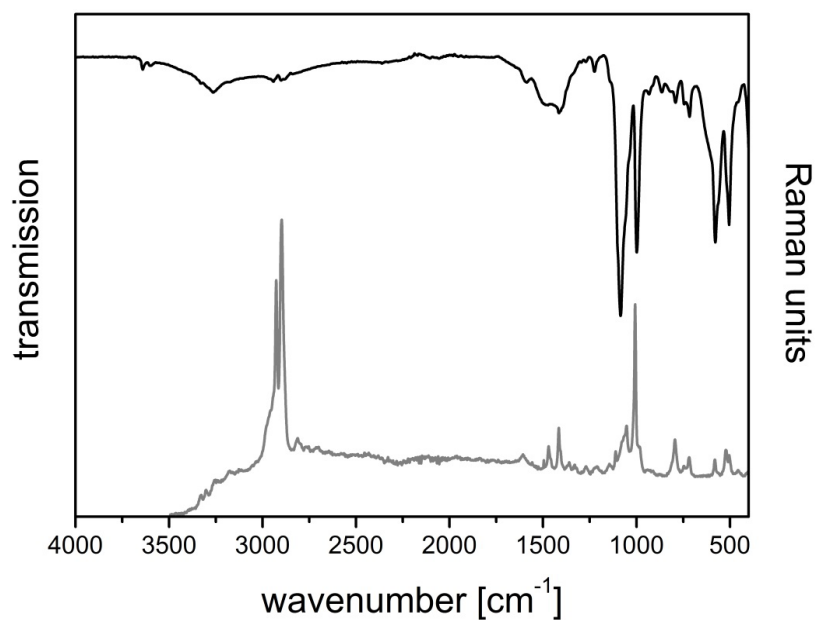


Figure S3. IR- (black) and Raman (gray) spectrum of $\text{Ca}(\text{OH})(\text{O}_3\text{PC}_2\text{H}_4\text{NH}_3) \cdot 2\text{H}_2\text{O}$ (2).

5) Thermogravimetric investigations

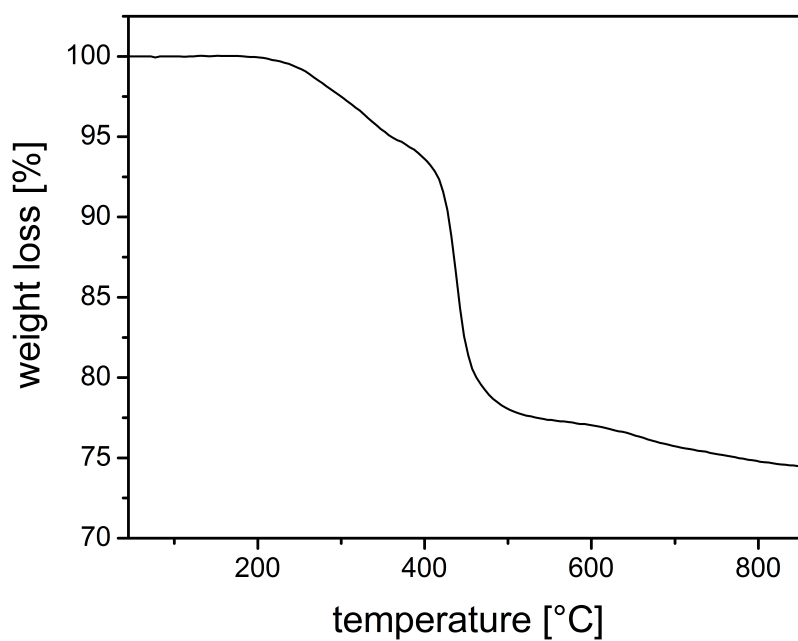


Figure S4. Thermal decomposition of $\text{Ca}(\text{O}_3\text{PC}_2\text{H}_4\text{NH}_2)$ (1).

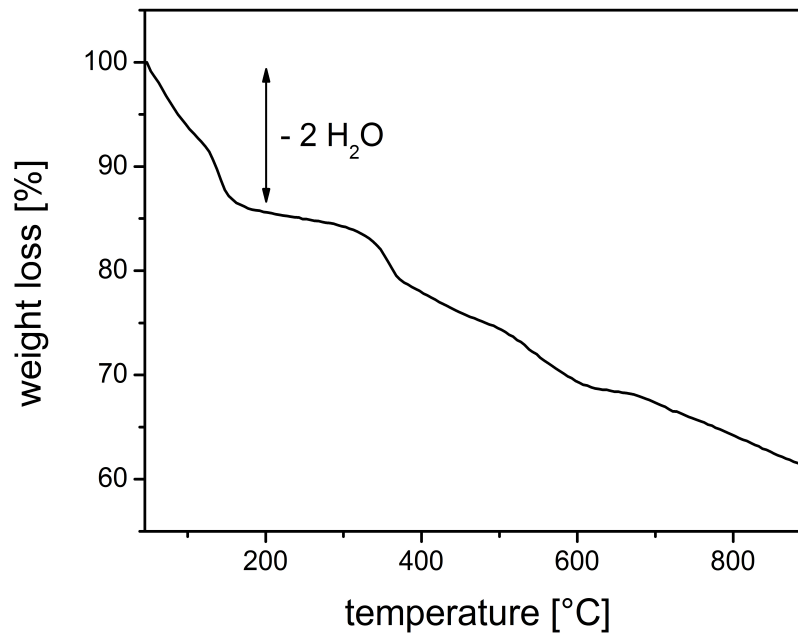


Figure S5. Thermal decomposition of $\text{Ca}(\text{OH})(\text{O}_3\text{PC}_2\text{H}_4\text{NH}_3) \cdot 2\text{H}_2\text{O}$ (2).

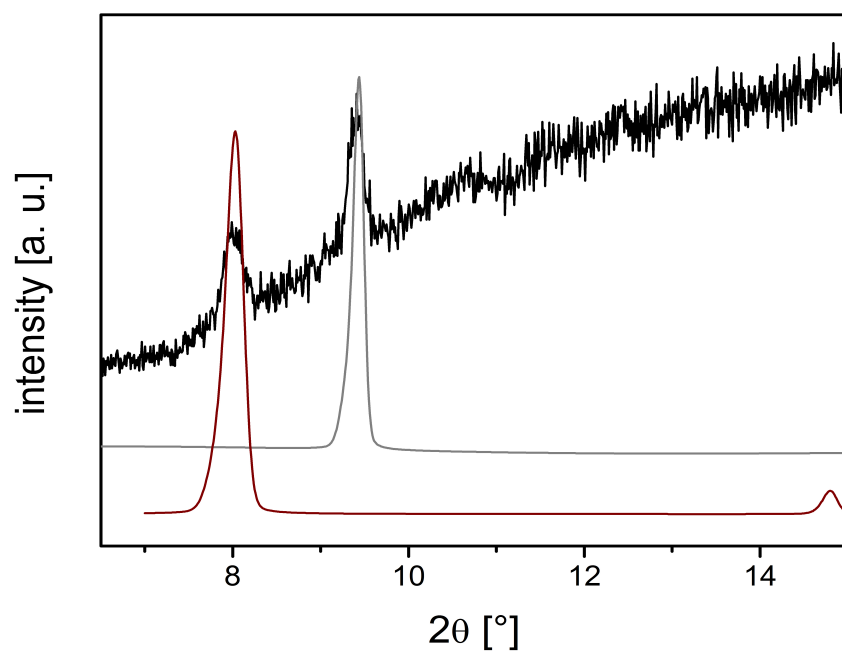
6) *In-situ* EDXRD study

Figure S6. Comparison of a section of the EDXRD spectrum monitored after 3 min (black) and the XRPD patterns of $\text{Ca}(\text{O}_3\text{PC}_2\text{H}_4\text{NH}_2)$ (**1**) (gray) and $\text{Ca}(\text{OH})(\text{O}_3\text{PC}_2\text{H}_4\text{NH}_3)\cdot 2\text{H}_2\text{O}$ (**2**) (dark red) between 6.5 and 15 °(2θ). The first peak in the EDXRD spectrum corresponds to the 100 reflection of compound **2** and the second peak corresponds to the 100 reflection of compound **1**.

Supporting information

High-throughput microwave-assisted discovery of new metal phosphonates

Mark Feyand,^a Christopher F. Seidler^d, Carsten Deiter,^b Andre Rothkirch,^b Alexandra Lieb^c,
Michael Wark^d and Norbert Stock^{a,*}

a Institut für Anorganische Chemie, Christian-Albrechts-Universität, Max-Eyth Straße 2, 24118
Kiel, Germany E-mail: stock@ac.uni-kiel.de

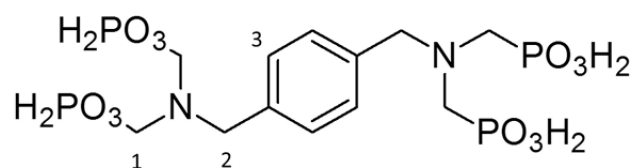
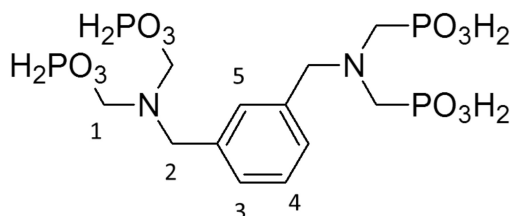
b HASYLAB, DESY Hamburg, Notkestraße 85, 22607 Hamburg, Germany.

c Institut für Chemie, Otto von Guericke Universität, Universitätsplatz 2, 39106, Magdeburg,
Germany.

d Lehrstuhl für Technische Chemie, Ruhr-Universität Bochum, Universitätsstr. 150, D44801,
Bochum, Germany.

NMR Spectroscopy.....	2
Structure Determination of 2.	5
Crystal Structures.....	7
IR Spectroscopy.....	10
Thermogravimetric Analyse	11
Proton Conductivity	12
Literature.....	13

NMR SPECTROSCOPY

a) $p\text{-(H}_2\text{O}_3\text{PCH}_2)_2\text{N-C}_6\text{H}_4\text{-N(CH}_2\text{PO}_3\text{H}_2)_2$ ($p\text{-H}_8\text{L}$) $^1\text{H-NMR}$ (500 MHz, NaOD/D₂O 10 %, TMS): = 7.11 (s, 4H, C3-H), 3.54 (s, 4H, C2-H), 2.34 (d, 8H, $^3J_{\text{P-H}} = 11.8$ Hz, C1-H) ppm. $^{31}\text{P-NMR}$ (500 MHz, NaOD/D₂O 10 %, H₃PO₄): = 17.06 ppm (s).b) $m\text{-(H}_2\text{O}_3\text{PCH}_2)_2\text{N-C}_6\text{H}_4\text{-N(CH}_2\text{PO}_3\text{H}_2)_2$ ($m\text{-H}_8\text{L}$) $^1\text{H-NMR}$ (500 MHz, NaOD/D₂O 10 %, TMS): = 6.80-6.70 (s, 4H, C3-H, C4-H, C5-H), 3.24 (s, 4H, C2-H), 1.90 (d, 8H, $^3J_{\text{P-H}} = 11.5$ Hz, C1-H) ppm. $^{31}\text{P-NMR}$ (500 MHz, NaOD/D₂O 10 %, H₃PO₄): = 17.06 ppm (s).

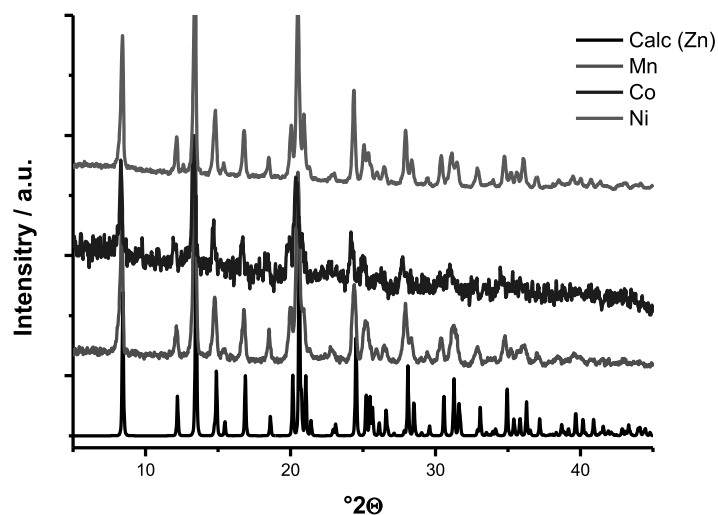


Fig. S2 X-ray powder diffraction patterns of $M[p-(\text{HO}_3\text{PCH}_2)_2\text{N}(\text{H})-\text{CH}_2-\text{C}_6\text{H}_4-\text{CH}_2-\text{N}(\text{H})(\text{CH}_2\text{PO}_3\text{H})_2(\text{H}_2\text{O})]$ ($M = \text{Mn}^{2+}$, Co^{2+} , Ni^{2+}) (**2**). The structure determination was carried out using XRD pattern of **2** (Zn).

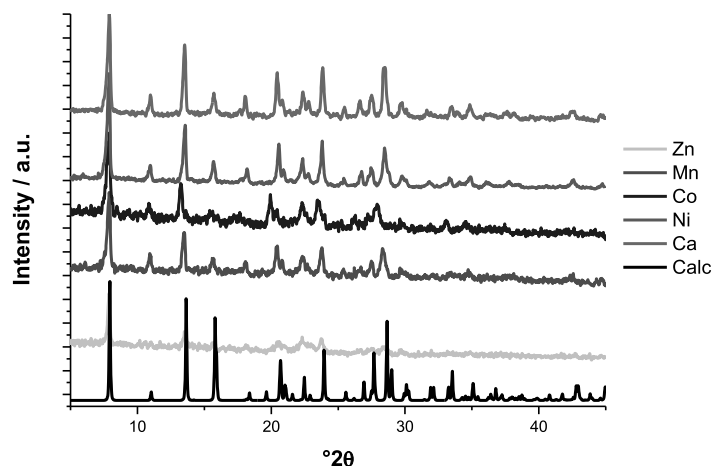


Fig. S3 X-ray powder diffraction patterns of $M[m-(\text{HO}_3\text{PCH}_2)_2\text{N}(\text{H})-\text{CH}_2-\text{C}_6\text{H}_4-\text{CH}_2-\text{N}(\text{H})(\text{CH}_2\text{PO}_3\text{H})_2]$ (H_2O) ($M = \text{Ca}^{2+}$, Mn^{2+} , Co^{2+} , Ni^{2+} , Zn^{2+}) (**3**). The calculated powder pattern is shown in black below. The structure determination was carried out using XRD pattern of **3** (Ni).

7. Anhang

Electronic Supplementary Material (ESI) for Dalton Transactions
This journal is © The Royal Society of Chemistry 2013

Exact reaction condition

Table S1. Exact amounts of the educts used in the high-throughput reactions. The following metal salts were used: $\text{Ca}(\text{NO}_3)_2 \cdot 4\text{H}_2\text{O}$, $\text{Mn}(\text{NO}_3)_2 \cdot 6\text{H}_2\text{O}$, $\text{Co}(\text{NO}_3)_2 \cdot 6\text{H}_2\text{O}$, $\text{Ni}(\text{NO}_3)_2 \cdot 6\text{H}_2\text{O}$, $\text{Zn}(\text{NO}_3)_2 \cdot 6\text{H}_2\text{O}$, $\text{Cd}(\text{NO}_3)_2 \cdot 4\text{H}_2\text{O}$, $\text{CaCl}_2 \cdot 4\text{H}_2\text{O}$, $\text{MnCl}_2 \cdot 2\text{H}_2\text{O}$, $\text{CoCl}_2 \cdot 2\text{H}_2\text{O}$, $\text{NiCl}_2 \cdot 6\text{H}_2\text{O}$, ZnCl_2 , CdCl_2

Metall	Count erion	Nr.	H ₈ L	M		H ₈ L [mg]	H ₂ O [μl]	2M M ²⁺ [μl]	Nr.	Result (identified by XRPD)
Ca^{2+}	NO_3^{2-}	1	1	1		50	2000	49	1	X-ray amorphous
Mn^{2+}	NO_3^{2-}	2	1	1		50	2000	49	2	X-ray amorphous
Co^{2+}	NO_3^{2-}	3	1	1	R	50	2000	49	3	X-ray amorphous
Ni^{2+}	NO_3^{2-}	4	1	1	1	50	2000	49	4	X-ray amorphous
Zn^{2+}	NO_3^{2-}	5	1	1		50	2000	49	5	X-ray amorphous
Cd^{2+}	NO_3^{2-}	6	1	1	1	50	2000	49	6	1
Ca^{2+}	Cl^-	7	1	1		50	2000	49	7	$[\text{Ca}(\text{p-H}_6\text{L})] \cdot 2\text{H}_2\text{O}^1$
Mn^{2+}	Cl^-	8	1	1		50	2000	49	8	2
Co^{2+}	Cl^-	9	1	1	R	50	2000	49	9	2
Ni^{2+}	Cl^-	10	1	1	2	50	2000	49	10	2
Zn^{2+}	Cl^-	11	1	1		50	2000	49	11	2
Cd^{2+}	Cl^-	12	1	1		50	2000	49	12	X-ray amorphous
Ca^{2+}	NO_3^{2-}	13	1	1		50	2000	49	13	3
Mn^{2+}	NO_3^{2-}	14	1	1		50	2000	49	14	3
Co^{2+}	NO_3^{2-}	15	1	1	R	50	2000	49	15	3
Ni^{2+}	NO_3^{2-}	16	1	1	3	50	2000	49	16	3
Zn^{2+}	NO_3^{2-}	17	1	1		50	2000	49	17	3
Cd^{2+}	NO_3^{2-}	18	1	1		50	2000	49	18	X-ray amorphous
Ca^{2+}	Cl^-	19	1	1		50	2000	49	19	X-ray amorphous
Mn^{2+}	Cl^-	20	1	1		50	2000	49	20	X-ray amorphous
Co^{2+}	Cl^-	21	1	1	R	50	2000	49	21	X-ray amorphous
Ni^{2+}	Cl^-	22	1	1	4	50	2000	49	22	X-ray amorphous
Zn^{2+}	Cl^-	23	1	1		50	2000	49	23	X-ray amorphous
Cd^{2+}	Cl^-	24	1	1		50	2000	49	24	X-ray amorphous

STRUCTURE DETERMINATION OF 2.

The crystal structure was solved by molecular modeling techniques using Materials Studio 5.5. The results of the elemental analysis and the indexing procedure need to be taken into account. The elemental analysis lead to the molar ratio Zn^{2+} : linker = 1 : 1. Taking the unit cell volume of 527 \AA^3 into account and a volume of 18 \AA^3 per non-hydrogen atom only 30 non-hydrogen atoms fit into the unit cell. According to the chemical formula only one Zn^{2+} ion and one tetraphosponate linker molecule can be present in the unit cell. Thus, in the space group *P*-1 the Zn ion and the linker must be located on special positions. The, for developing the structural model, important inversion centers in the space group *P*-1 are given in Figure 3 (top). The Zn ion was placed on 0.5/0.5/0.5 and the phenyl ring around 0/0/0 as shown in Figure 3 middle. The phenyl ring was connected by the $\text{CH}_2\text{-NH-(CH}_2\text{-PO}_3\text{H)}_2$ groups with the Zn ion and the coordination sphere was completed by adding a water molecule (Figure 3 bottom). The obtained model was used for further Rietveld refinements.

7. Anhang

Electronic Supplementary Material (ESI) for Dalton Transactions
This journal is © The Royal Society of Chemistry 2013

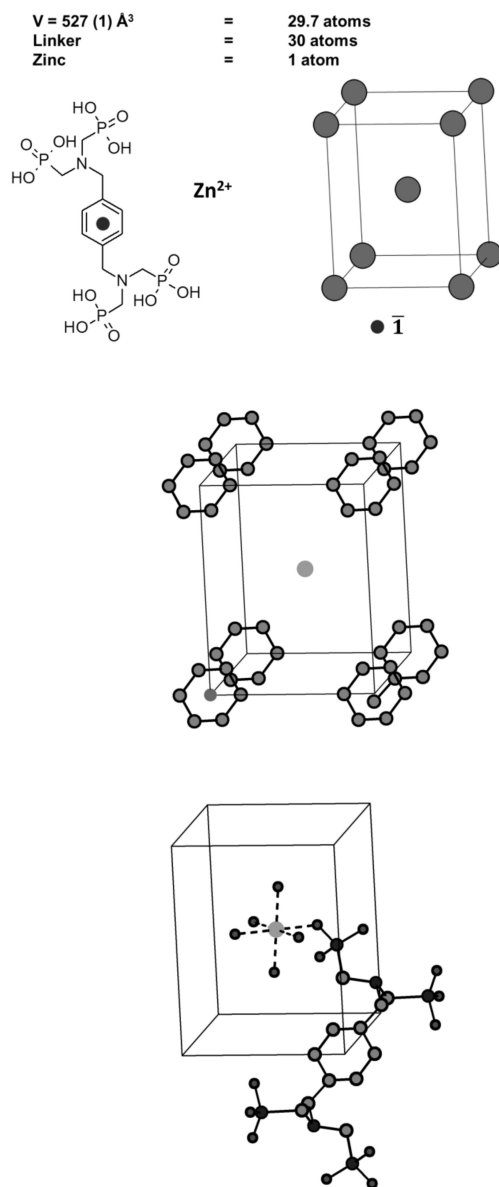


Fig. S4. Important inversion centers in the space group P-1 for deriving the structural model and the inversion center of the linker molecule (top); Initial model by placing the phenylring and the Zn ion on/ around the inversion center (middle) and final starting model for the Rietveld refinement (bottom).

CRYSTAL STRUCTURES

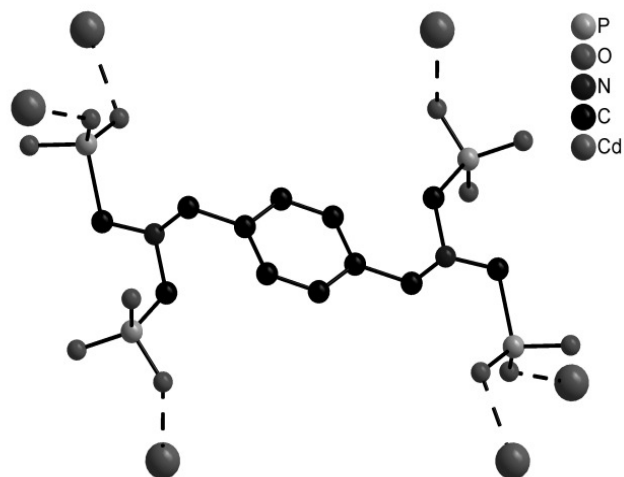


Fig. S5. Interconnection of the Cd^{2+} ions by the linker molecule in the structure of $\text{Cd}[p\text{-}(\text{HO}_3\text{PCH}_2)_2\text{N}(\text{H})\text{-CH}_2\text{-C}_6\text{H}_4\text{-CH}_2\text{-N}(\text{H})(\text{CH}_2\text{PO}_3\text{H})_2]$ (**1**). Fragmented lines represent Cd-O bonds.

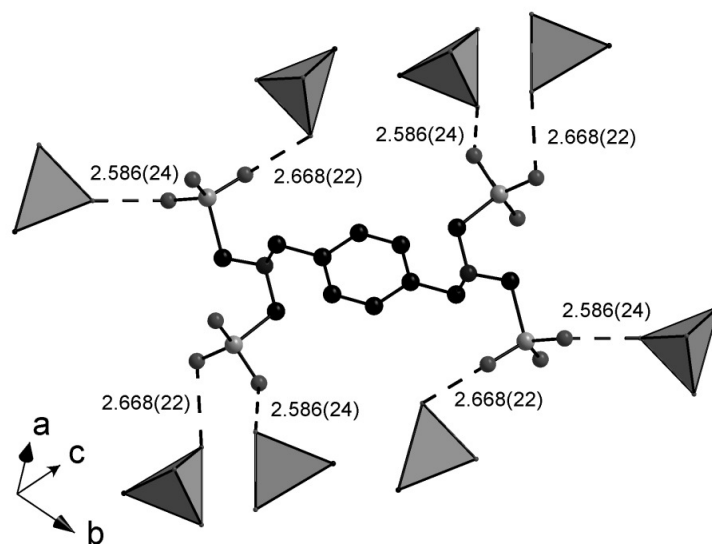


Fig. S6. Hydrogen bonds of the phosphonate groups in compound of $\text{Cd}[p\text{-}(\text{HO}_3\text{PCH}_2)_2\text{N}(\text{H})\text{-CH}_2\text{-C}_6\text{H}_4\text{-CH}_2\text{-N}(\text{H})(\text{CH}_2\text{PO}_3\text{H})_2]$ (**1**) and their bond lengths.

7. Anhang

Electronic Supplementary Material (ESI) for Dalton Transactions
This journal is © The Royal Society of Chemistry 2013

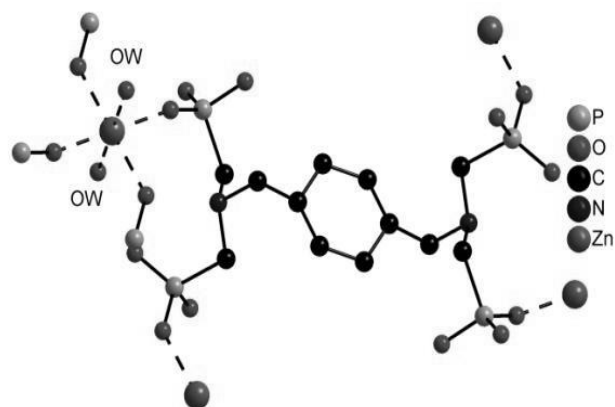


Fig. S7. Interconnection of the metal ions by the linker molecules in the structure of $M[p-(\text{HO}_3\text{PCH}_2)_2\text{N}(\text{H})-\text{CH}_2-\text{C}_6\text{H}_4-\text{CH}_2-\text{N}(\text{H})(\text{CH}_2\text{PO}_3\text{H})_2(\text{H}_2\text{O})]$ ($M=\text{Ca}, \text{Mn}, \text{Co}, \text{Ni}, \text{Zn}$) (**2**) Fragmented lines represent M-O bonds.

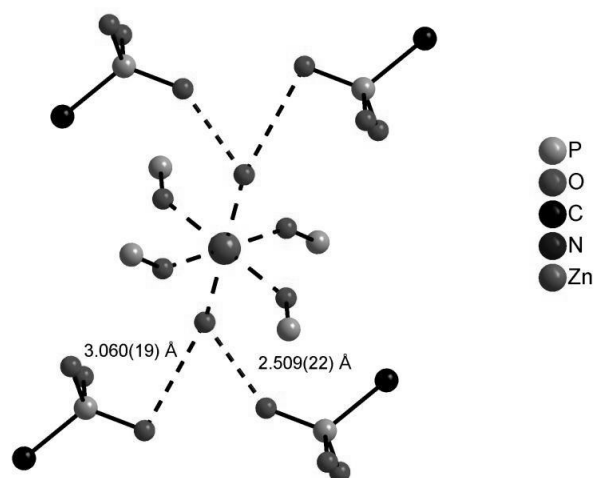


Fig. S8. Possible hydrogen bonds of the coordinated water molecule in the structure of $\text{Zn}[p-(\text{HO}_3\text{PCH}_2)_2\text{N}(\text{H})-\text{CH}_2-\text{C}_6\text{H}_4-\text{CH}_2-\text{N}(\text{H})(\text{CH}_2\text{PO}_3\text{H})_2(\text{H}_2\text{O})]$ (**2**)

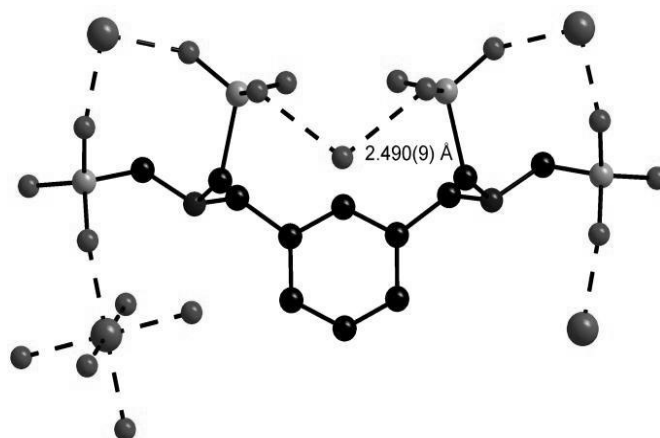


Fig. S9. Interconnection of the metal ions by the linker molecule and possible hydrogen bonds of the water molecule in the structure of $M[m\text{-(HO}_3\text{PCH}_2)_2\text{N(H)-CH}_2\text{-C}_6\text{H}_4\text{-CH}_2\text{-N(H)(CH}_2\text{PO}_3\text{H)}_2\text{]}\cdot\text{H}_2\text{O}$ ($M=\text{Ca, Mn, Co, Ni, Zn}$) (**3**).

7. Anhang

Electronic Supplementary Material (ESI) for Dalton Transactions
This journal is © The Royal Society of Chemistry 2013

IR SPECTROSCOPY

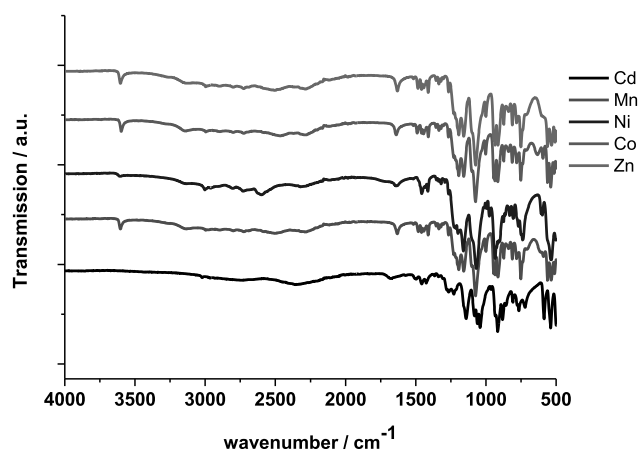


Fig. S10. IR spectra of the title compounds $M[p\text{-(HO}_3\text{PCH}_2)_2\text{N(H)-CH}_2\text{-C}_6\text{H}_4\text{-CH}_2\text{-N(H)(CH}_2\text{PO}_3\text{H)}_2\text{(H}_2\text{O)}]$ (M=Cd, Mn, Co, Ni, Zn) (**1,2**).

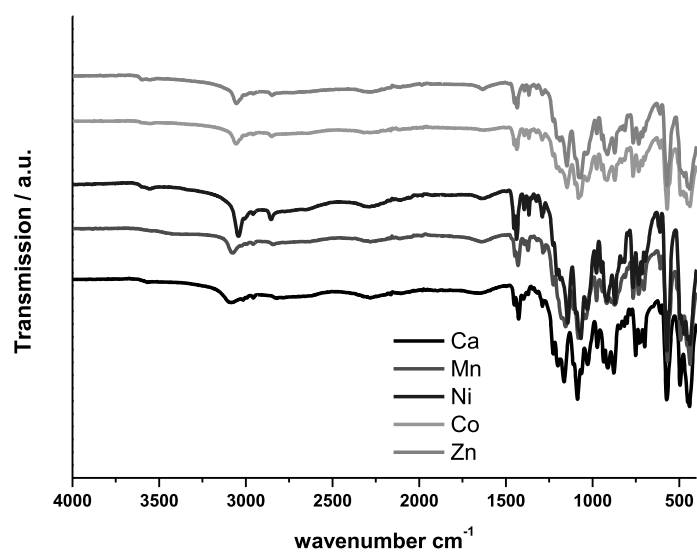


Fig. S11. IR spectra of the title compounds $M[m\text{-(HO}_3\text{PCH}_2)_2\text{N(H)-CH}_2\text{-C}_6\text{H}_4\text{-CH}_2\text{-N(H)(CH}_2\text{PO}_3\text{H)}_2\text{]}\cdot\text{H}_2\text{O}$ (M=Ca, Mn, Co, Ni, Zn) (**3**).

THERMOGRAVIMETRIC ANALYSE

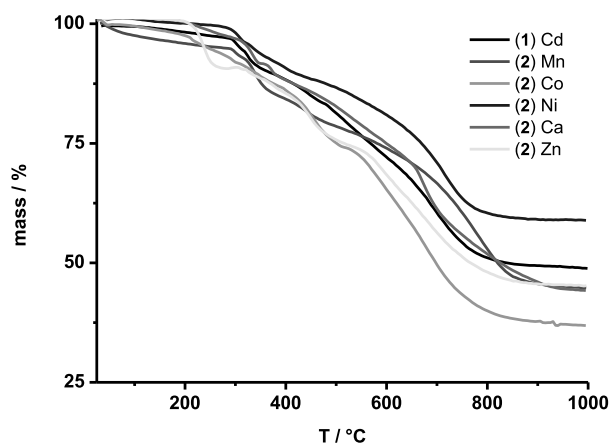


Fig. S12. Results of the thermogravimetric analyses of $M[p\text{-(HO}_3\text{PCH}_2)_2\text{N(H)-CH}_2\text{-C}_6\text{H}_4\text{-CH}_2\text{-N(H)(CH}_2\text{PO}_3\text{H)}_2\text{(H}_2\text{O)}]$ (M=Cd, Ca, Mn, Co, Ni, Zn) (**1,2**).

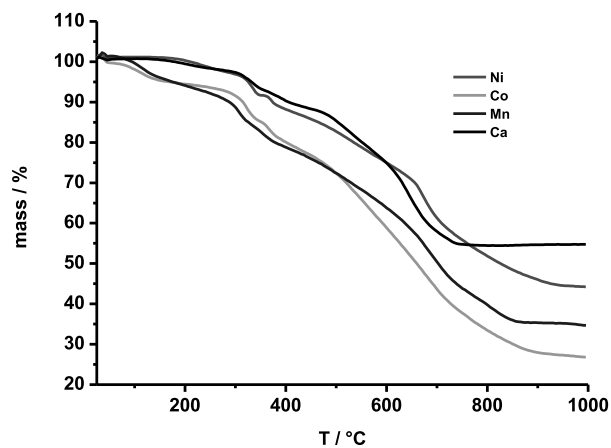


Fig. S13. Results of the thermogravimetric analyses of $M[m\text{-(HO}_3\text{PCH}_2)_2\text{N(H)-CH}_2\text{-C}_6\text{H}_4\text{-CH}_2\text{-N(H)(CH}_2\text{PO}_3\text{H)}_2\text{]}\cdot\text{H}_2\text{O}$ (M=Ca, Mn, Co, Ni, Zn) (**3**).

PROTON CONDUCTIVITY

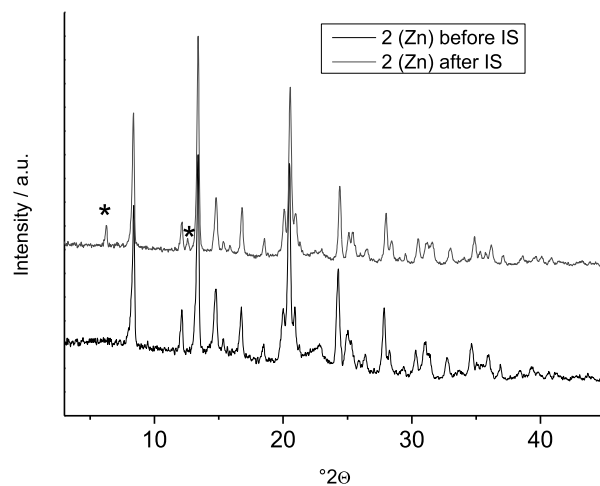


Fig. S14 . X-ray powder patterns before (black) and after (red) impedance spectroscopy measurements of **2** (Zn). The impurities are marked with a star.

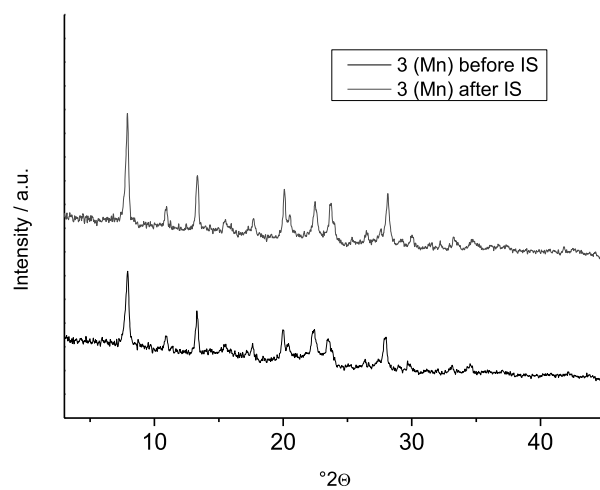


Fig. S15 . X-ray powder patterns before (black) and after (red) impedance spectroscopy measurements of **3** (Mn).

LITERATURE

1. Stock, N.; Stoll, A.; Bein, T., *Microporous and Mesoporous Materials* **2004**, 69 (1–2), 65.



Supporting Information

© Wiley-VCH 2012

69451 Weinheim, Germany

Automated Diffraction Tomography for the Structure Elucidation of Twinned, Sub-micrometer Crystals of a Highly Porous, Catalytically Active Bismuth–Metal–Organic Framework**

Mark Feyand, Enrico Mugnaioli, Frederik Vermoortele, Bart Bueken, Johannes M. Dieterich, Tim Reimer, Ute Kolb, Dirk de Vos, and Norbert Stock**

ange_201204963_sm_miscellaneous_information.pdf

1. Synthesis of CAU-7	2
2. Electron microscopy	4
3. Rietveld Refinement	11
4. DFT Calculation	14
5. Sorption Experiments	15
6. Thermal Stability	19
7. IR Spectroscopy	21
8. Catalytic experiments	22
9. References	27



1. Synthesis of CAU-7

Different heating methods and solvent systems were used for the synthesis of CAU-7. This leads to changes in crystal size, purity and reaction time. All chemicals were used as obtained.

Bi(NO₃)₃·5H₂O (Merck)

DMF 99 % (ABCR)

Methanol pure (Aldrich)

(H₃BTB) (BASF)

a) Conventional solvothermal reaction

1,3,5-benzenetrisbenzoic acid (H₃BTB) (200 mg, 0.46 mmol) and Bi(NO₃)₃·5H₂O (148 mg, 0.31 mmol) were mixed in a 23 ml Teflon lined steel reactor, to which methanol (99.8%) (10 ml) was added. The reactor was then sealed, the reaction mixture homogenized and heated to 120 °C for 12 h. The yellow precipitated was filtered, washed with methanol, dimethylformamide (DMF) and methanol again. The product was identified by X-ray powder diffraction as pure CAU-7. (yield 67% based on H₃BTB) (Figure S1)

b) Conventional solvothermal reaction for larger crystals suitable for electron diffraction

1,3,5-benzenetrisbenzoic acid (H₃BTB) (200 mg, 0.46 mmol) of and Bi(NO₃)₃·5H₂O (148 mg, 0.31 mmol) were added into a 23 ml Teflon lined steel reactor, to which methanol (99.8%) (7.5 ml) and DMF (2.5 ml) were added. The reactor was then sealed, the reaction mixture homogenized and heated to 120 °C for 12 h. The yellow precipitated was filtered, washed with methanol, DMF and methanol again. The product was identified as CAU-7 with a minor impurities (marked with * in Figure S1) by X-ray powder diffraction. (yield 73% based on H₃BTB)

c) Synthesis under microwave assisted heating

1,3,5-benzenetrisbenzoic acid (H₃BTB) (200 mg, 0.46 mmol) and Bi(NO₃)₃·5H₂O (148 mg, 0.31 mmol) were mixed into 30 ml microwave glass reaction vessel (Biotage) to which methanol (99.8%) (20 ml) methanol was added. The reactor was sealed with a septum, the reaction mixture homogenized and heated to 120 °C for 20 min in a Biotage Initiator microwave synthesizer. The mixture was stirred with a magnetic stirring bar during the reaction. The yellow precipitated was filtered, washed with methanol, DMF

and methanol again. The product was identified as pure CAU-7 by X-ray powder diffraction. (Figure S1) (yield 72 % based on H₃BTB)

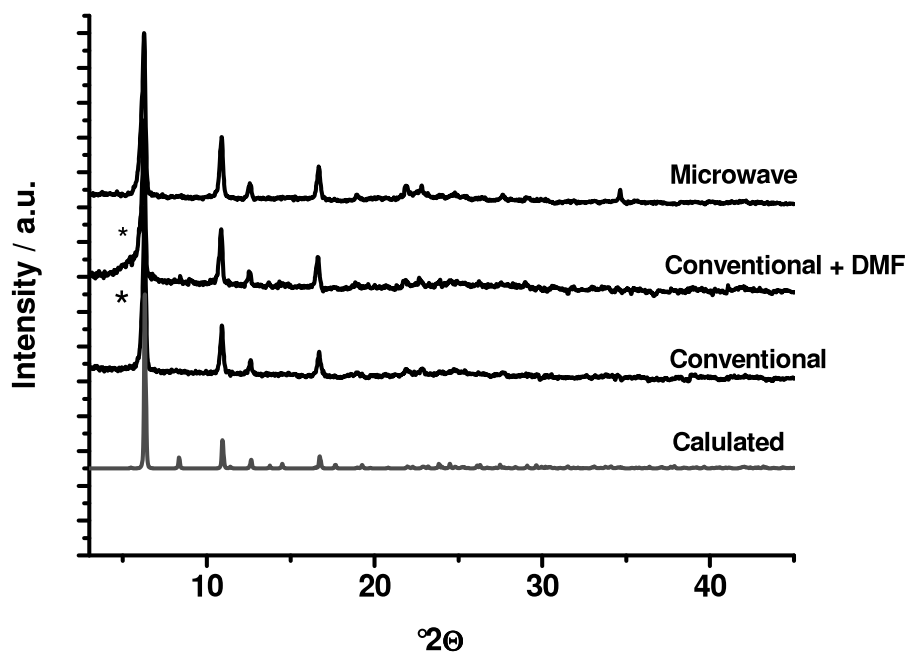


Figure S1. Experimental and calculated X-ray powder pattern obtained from different synthesis methods

2. Electron microscopy

SEM

High Resolution Scanning Electron Microscopy studies were carried out on a JEOL JSM-6500F hot cathode scanning electron microscope.

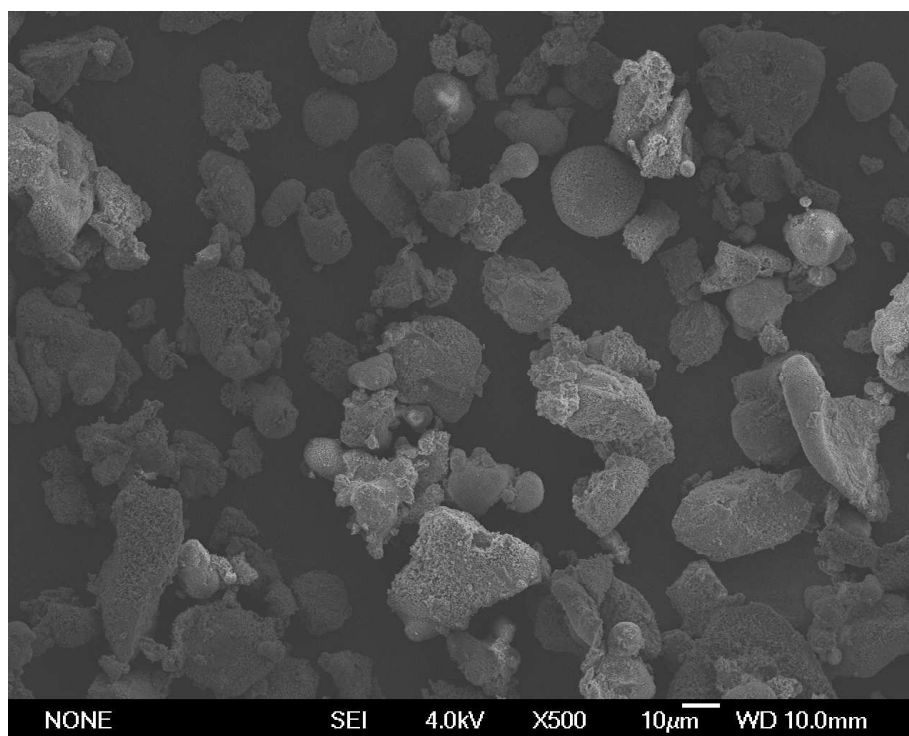


Figure S2. HRSEM micrograph of CAU-7 synthesized in methanol using microwave assisted heating.

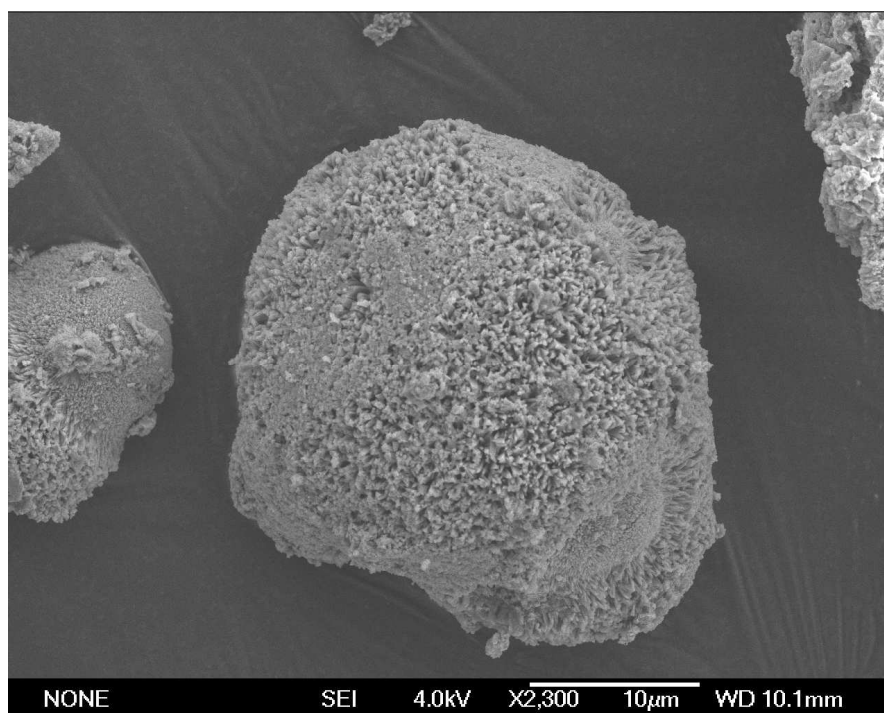


Figure S3. HRREM micrograph of CAU-7 synthesized in methanol using microwave assisted heating.

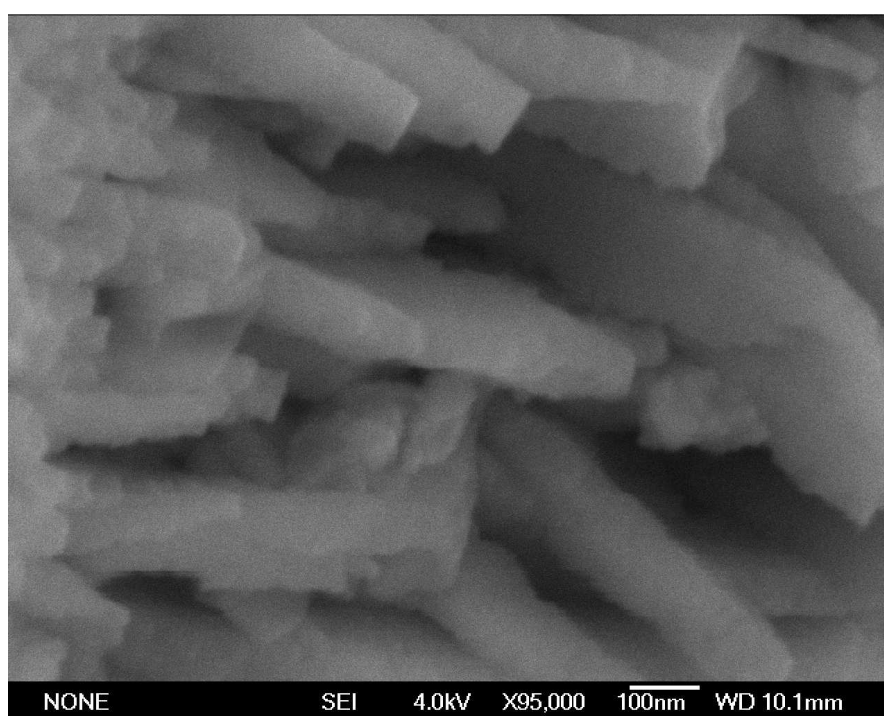


Figure S4. HRREM micrograph of CAU-7 synthesized in methanol using microwave assisted heating.

TEM

TEM investigations were carried out with an FEI Tecnai F30 working at 300 kV and equipped with field emission gun and super-twin objective lenses. A dry CAU-7 sample was gently crushed in an agate mortar, distributed on a carbon-coated Cu-grid and mounted on a GATAN cryo single-tilt holder able of a tilt range up to 50°. The holder was cooled down to approximately 120 K and an anti-contaminator trap cooled to about 80 K was inserted close to the holder tip. TEM micrographs were recorded by a CCD camera (14-bit GATAN 794MSC, 1024×1024 pixels).

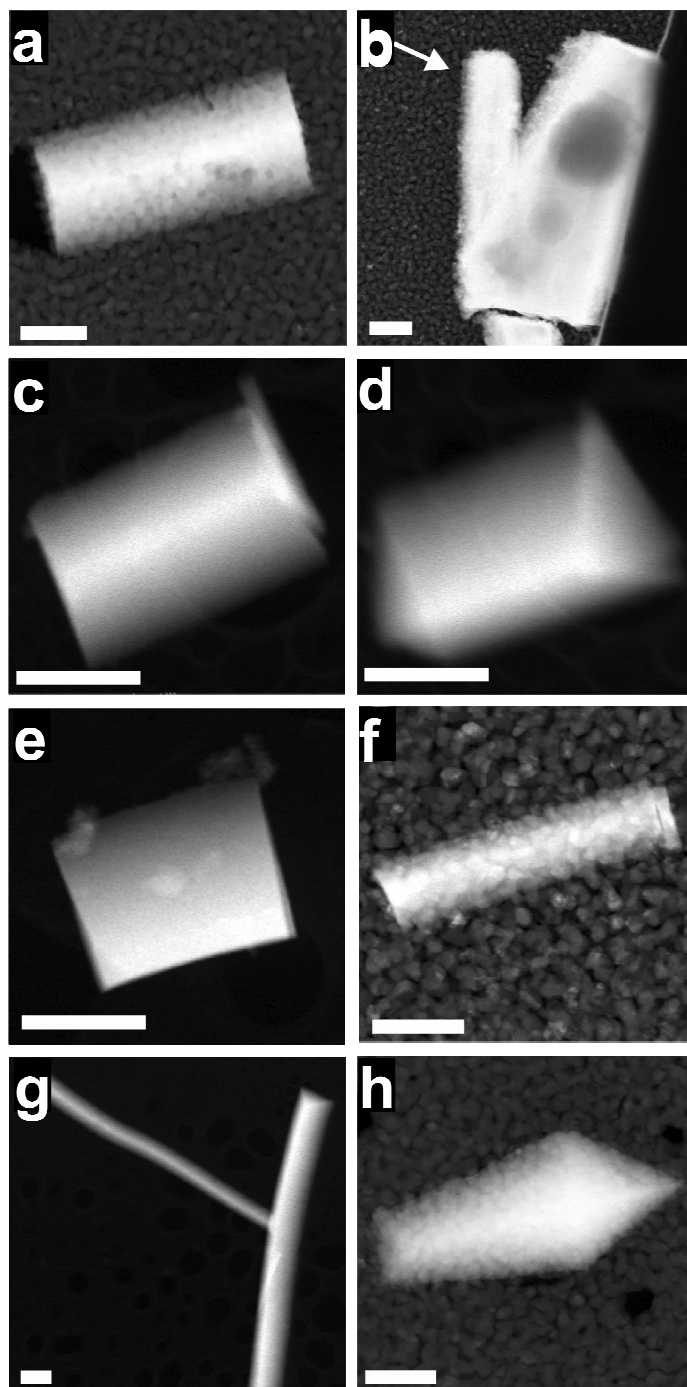


Figure S5. TEM micrographs of exemplary CAU-7 rods of different shape and dimension synthesized under conventional heating with DMF as additive. Rods in a) and b) were used for ADT acquisition. Rod in c) and in d) is the same rod shown in Figure 1, before and after tilting. In d) the triangular base of the rod is evident. e), f), g) and h) show further crystals used for ADT which were not used for the structure determination. Small ice crystals are visible on the background of some images. Scale bar = 500 nm.

Automated Diffraction Tomography (ADT), structure solution and twinning

For the ADT investigation the same experimental setting as described for TEM measurements was used. ADT data was collected with steps of 1° with precession of the beam (precession angle = 1.2°). Precession was performed using a NanoMEGAS DigiStar unit. For tracking the crystal position during the tilt scanning transmission electron microscopy (STEM) images were acquired with a high angular dark field detector (HAADF). Nano electron diffraction was performed with a mild illumination using high gun lens current and spot size and inserting a C2 condenser aperture of $10\ \mu\text{m}$. The ADT3D package was used for data processing, including 3D diffraction volume reconstruction, cell parameter determination and intensity integration.

From the crystal shown in Figure S5a a tilt series in a range $-40^\circ/+48^\circ$ was acquired. The tilt axis is horizontal. The range $-40^\circ/-6^\circ$ was acquired on the upper-left part of the rod (first crystalline individual). The range $-5^\circ/+48^\circ$ was acquired on the bottom-right part of the crystal (second crystalline individual). The three-dimensional reconstruction of the full acquisition is shown in Figure S6. Only the reflections coming from the second individual were used for intensity extraction.

From the crystal indicated by the arrow in Figure S5b a tilt series in the range $-20^\circ/+35^\circ$ was acquired. The tilt axis is horizontal. As the whole tilt was acquired on the same side of the rod, only one crystalline individual was sampled.

Intensities coming from the two acquisitions were merged in a single data set with a scale factor of 2.2 calculated on the basis of the common 121, 131 and 141 reflection families. The scale factor take into account the different size of the crystal, and therefore of the diffractive volume. Important data set parameters are reported in table S1.

Table S1. Important parameters of the ADT data set used for CAU-7 structure solution.

Tilt range (°)	53 + 55
Total sampled reflections	4268
Independent reflections	1158
Resolution, Å	1.15
Independent reflection coverage, %	67
Rsym, %	22.1
Overall U, Å ²	0.041

A first trial of structure determination by classic direct methods was able only to deliver the position of the bismuth atom. Therefore simulated annealing (SA) as implemented in SIR2011 were used. A single bismuth atom and a single BTB³⁻ molecule were used as cell content. All the six rotation angles of the BTB³⁻ molecule were kept free to rotate. The problem is therefore restricted in the determination of 15 geometrical parameters (Bi translation, BTB³⁻ translations and global rotation and 6 torsion angles). SA converged nicely to a final solution with an optimal function value of 511.12. Remarkably, this is the first time ADT data were used in a SA routine.

Three-dimensional diffraction reconstruction of the ADT tilt series collected on the rod of Figure S5a, as well as on other rods, reveals that the two side of each rod are in fact two distinctive crystalline individua (Figure S6). The central part of the rod is in general too thick to deliver any diffraction pattern, and their measured patterns are hard to be interpreted. Nevertheless the triangular shape of the rod bases (Figure 1 and S5d) and the mutual orientation of the crystalline individua, suggest that each rod is a trilling composed by three individual sharing the [001] axis (that is also the main growth direction of the rod) and mutually rotated by 120°. In this arrangement the [010] direction of first crystalline individuum is almost parallel to the [2-10] and [-2-10] directions of the other two individua, in fact crystallochemically closely related (Figure S7). The [100] direction of the first crystalline individuum has an angular difference with [-120] and [-1-20] directions of the other two individua of 6.4° (Figure S6b).

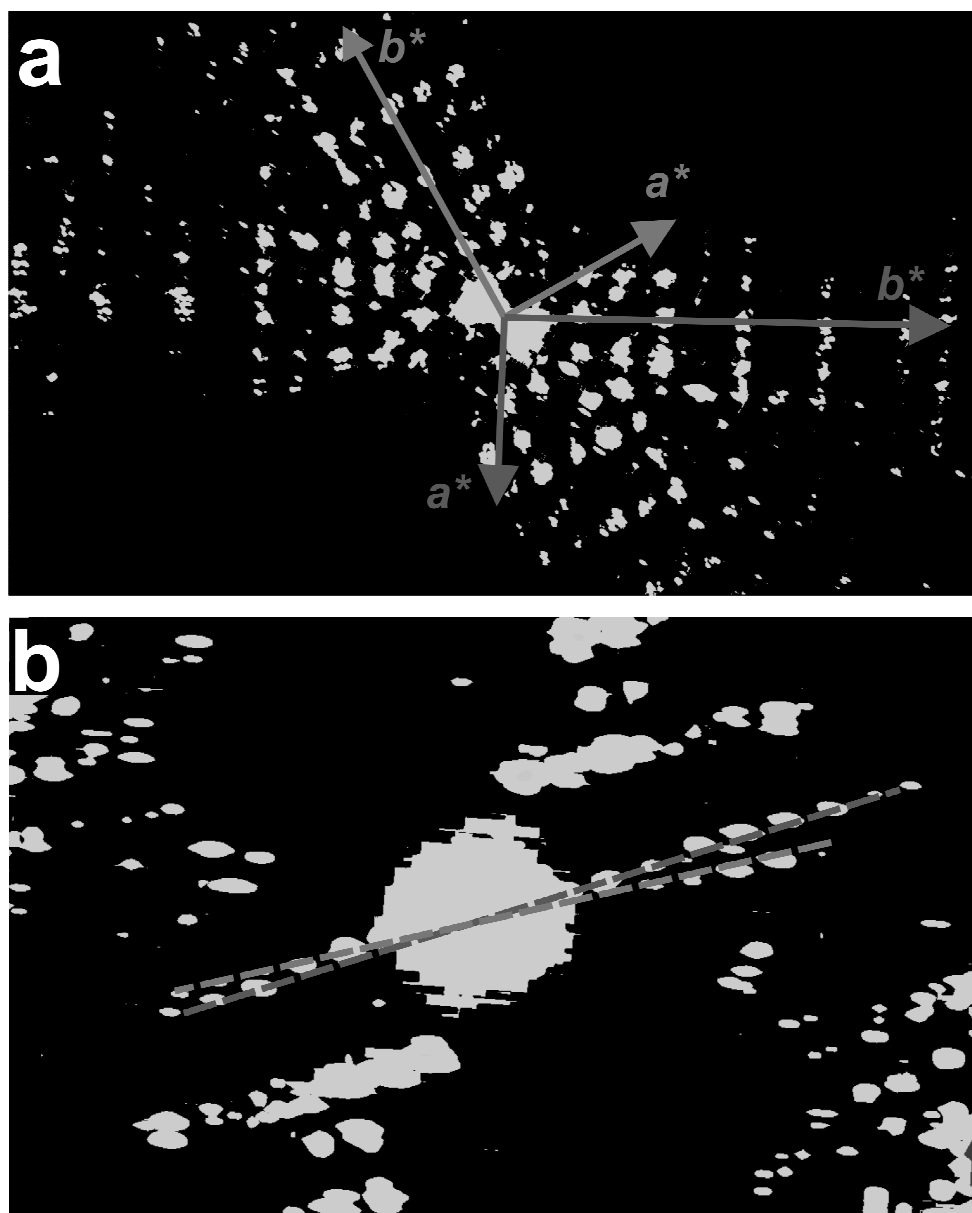


Figure S6. Three-dimensional diffraction space reconstruction of the rod shown in figure S5a. A) Projection along [001] showing two overlapping lattices, respectively rotated 120°. B) Particular showing the [100] direction of the first domain almost overlapping with the [-120] direction of the second domain.

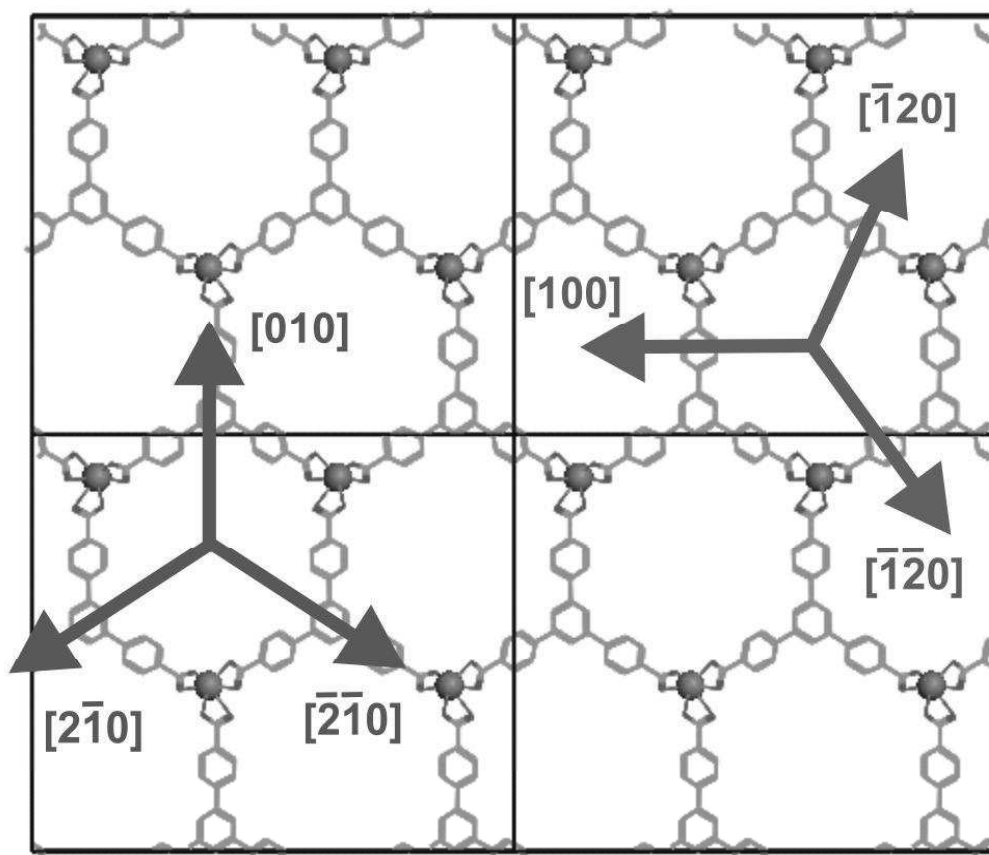


Figure S7. Projection of CAU-7 structure along $[001]$. In this projection the structure show a marked hexagonal pseudo-symmetry.

3. Rietveld Refinement

X-ray powder diffraction measurements were performed on a Stoe Stadi P diffractometer equipped with a linear PSD detector system and a Germanium (111) monochromator with Copper $K\alpha$ radiation. The Rietveld refinement was carried out using Topas Academics 4.1 in a range of 5 to 70 $^{\circ}2\theta$. (resolution 1.33 Å). The refinement includes 6 background points, on scaling factor, four profile parameters (Thompson-Cox-Hastings function) and two isotropic temperature factors (one for the Bi^{3+} ion and one for the organic linker molecule). Peak asymmetry and anisotropic peak broadening were modeled by a simple axial model and a spherical harmonics series, respectively. The BTB^{3-} molecule was refined as four sub rigid bodies (RB) to allow rotation around the torsion angles between the phenyl rings. (compare Figure S3). The final Rietveld plot is given in Figure S4 and the parameters of the refinement in Table S1. The Fourier map is shown in Figure S5.

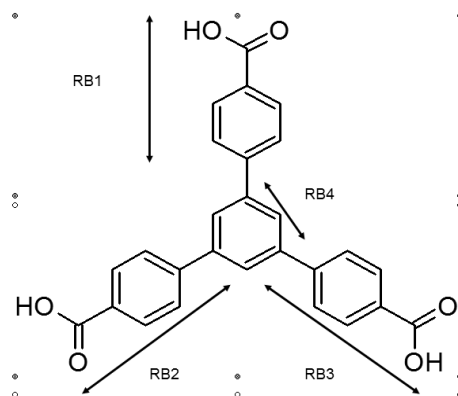


Figure S8. Rigid bodies (RB) used for the Rietveld refinement.

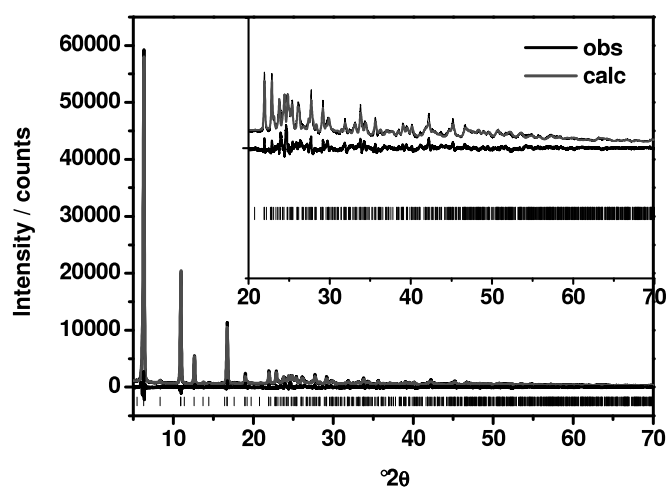


Figure S9. Final Rietveld plot of CAU-7. The observed powder pattern is shown in black the calculated pattern is shown in red and the difference is shown in black below. The allowed Bragg positions are given as ticks.

Table S1. Final parameters of the Rietveld Refinement.

<i>parameter</i>	<i>value</i>
R_{wp}	9.43
R_{Bragg}	3.17
GOF	2.85
a	32.36(1)
b	28.084(7)
c	3.9132(9)
<i>space group</i>	$Pb2_1a$

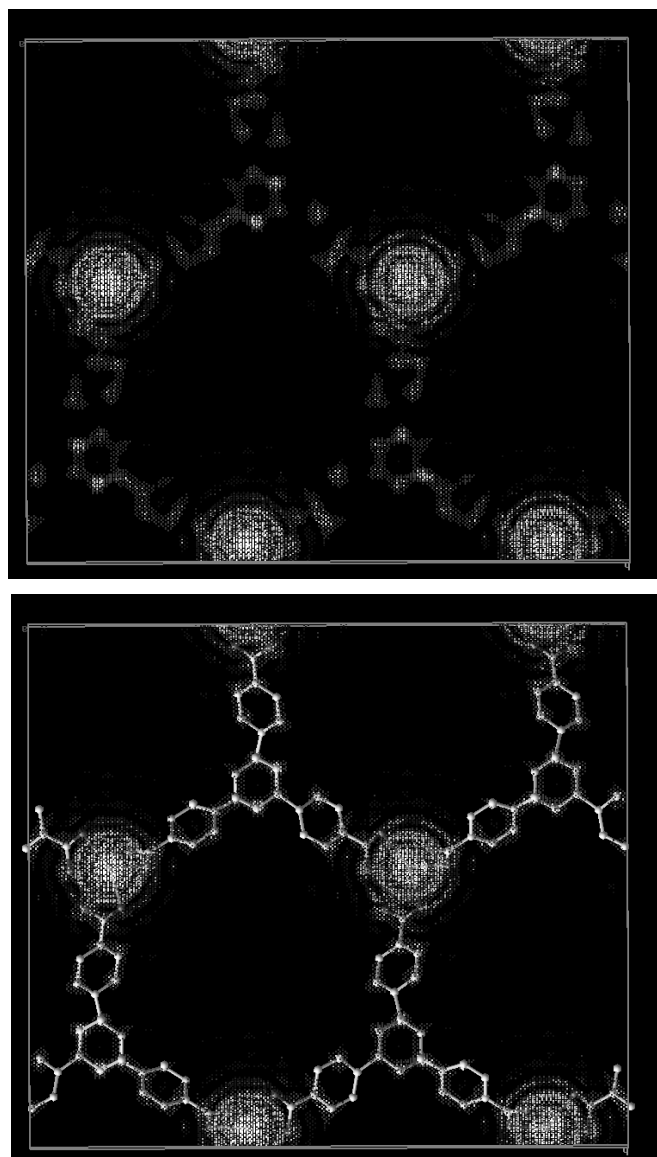


Figure S10. Fourier map of CAU-7 without model (top) and with model. (bottom)

4. DFT Calculation

Density functional theory (DFT)-based calculations of the CAU-7 crystal structure were carried out to further support the experimental observations. The geometric optimization included 196 Atoms (4 Bismuth atoms, 108 Carbon atoms, 60 H atoms and 24 Oxygen Atoms) without taking any symmetry into account. A plane-wave approach as implemented in the CPMD program package was employed, using the PBE functional together with Goedecker-Teter-Hutter-pseudopotentials. The model structure obtained from the electron diffraction experiments was optimized with an initial wavefunction cutoff of 70 Rydberg (density cutoff 280 Ry), followed by a final optimization using a wavefunction cutoff of 100 Ry (density cutoff 400 Ry)[1-5]. In both cases, the experimental lattice parameters were used and default convergence thresholds (wavefunction optimization $1.0\text{E-}5 E_h$, geometry optimization $5.0\text{E-}4 E_h$) were employed. The optimized structural model was checked for symmetry using Materials Studio resulting in the space group $Pb2_1a$. [6] Also, the optimized structure reflects the geometrical stress imposed on the crystal structure through distortions in the phenyl ring. Wannier-localized orbitals of the relevant coordination environment of the Bi atom can be found in Fig S11. The orbitals are regularly shaped and clearly show that all oxygen atoms have an attractive interaction with the Bismuth atom

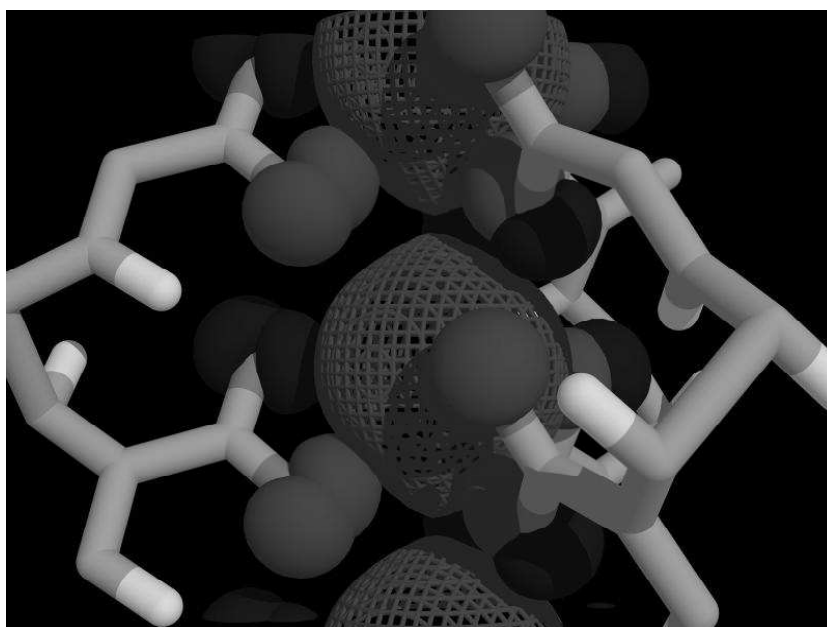


Figure S11. Wannier-localized orbitals of CAU-7.

To confirm the optimized structure as a minimum, a vibrational analysis was carried out using the same level of theory with a tighter convergence threshold of $1.0\text{E-}7 E_h$ for the wavefunction optimization. The analysis revealed only minor imaginary frequencies for two Bi-O stretch vibrations which is understandable considering the geometrical stress imposed on the crystal structure by the small experimental unit cell size. A plot of the line spectrum can be found in Fig. S12.

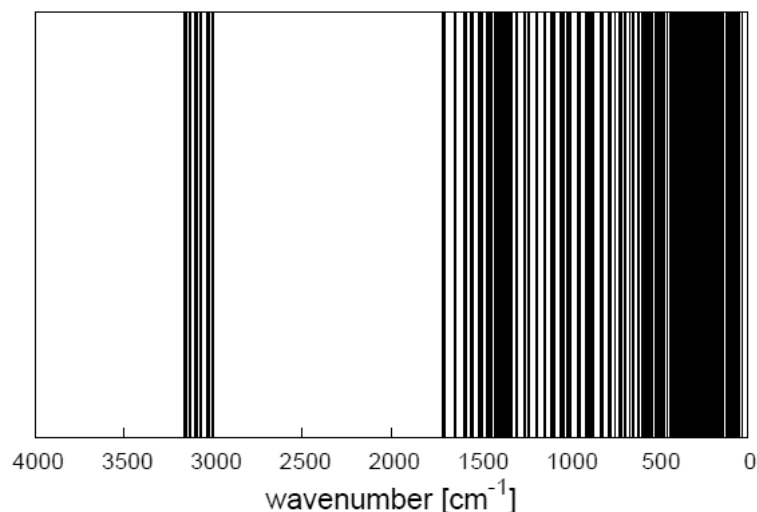


Figure S12 Calculated IR Spectrum

5. Sorption Experiments

To confirm the successful activation an elemental analysis was carried out.

Table S2. Elemental analysis after nitrogen sorption experiments

	C	H	N	S
obs.	51.23%	2.56%	0%	0%
calc.	50.33%	2.35%	0%	0%

Sorption experiments using H_2 , H_2O , N_2 , CO_2 were carried out on a BelsorpMax at 77 K and 298 K respectively. The sample was treated with in a ultrasonic bath in methanol for 30 min and subsequently activated at 160°C in vacuum for 12 h at 0.01 kPas. A calculated and experimental powder pattern after sorption measurements is shown in Figure S13.

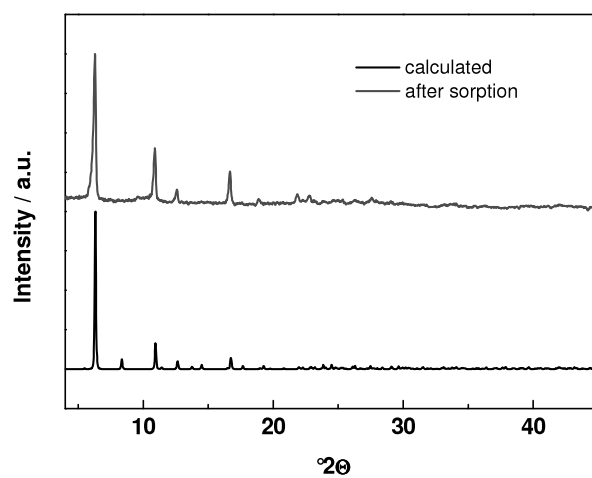


Figure S13. Calculated and observed powder pattern of CAU-7 after sorption (Nitrogen) measurement.

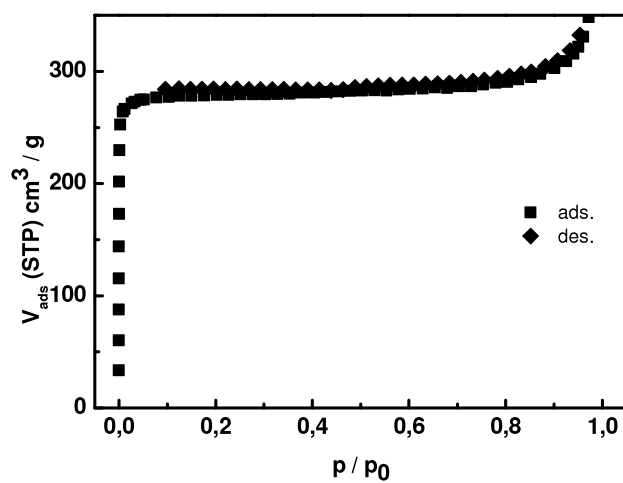
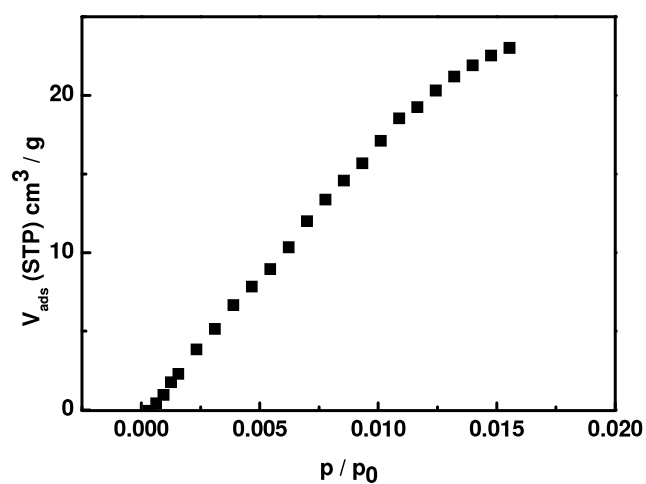
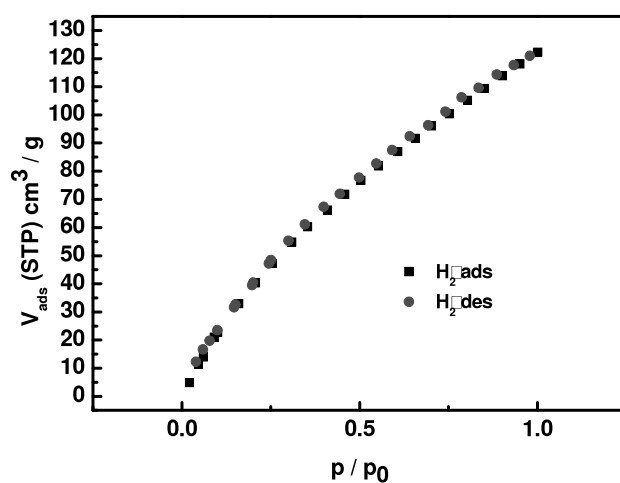


Figure S14. Nitrogen adsorption isotherm measured at 77 K.

Figure S15. CO₂ adsorption isotherm measured at 298 K. (4.31 wght%)Figure S16. H₂ adsorption isotherm measured at 77 K. The adsorption is shown in black the desorption in red. of (1.07 wght%)

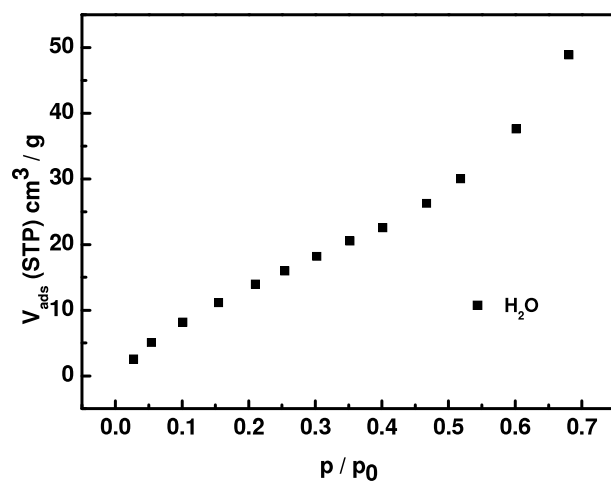


Figure S17. H_2O adsorption isotherm measured at 289 K. (2.62 wght%)

6. Thermal Stability

For the thermogravimetric analysis under air atmosphere a NETSCH STA 409 CD analyzer was used with a flow rate of 75 ml/min and a heating rate of 4 K/min. To determine the thermal stability of the compound and to verify its chemical composition, thermogravimetric (TG) measurements were performed. The results of the investigation show two steps of weight loss for CAU-7, of which the first (-14.23%) can be attributed to solvent molecules that leave the compound up to a temperature of 100°C. Beyond 350°C the organic molecules begin to decompose, leaving a residue of Bi_2O_3 as determined by XRPD measurements (observed: -52.08 %, calculated: 51.12 %).

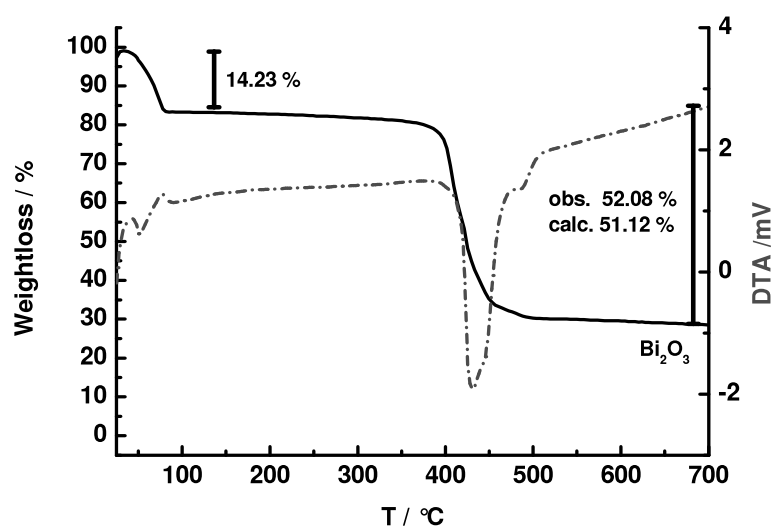


Figure S18. Thermogravimetric analysis (black) and difference thermo analysis (red) of CAU-7.

Temperature dependent X-ray powder diffraction was carried out on a Stoe Stadi P equipped with a image plate detector system using copper $K\alpha$ radiation. The temperature was adjusted using a Stoe capillary oven. The compound is stable up to 380 °C. Above this temperature a X-ray amorphous residue is obtained. (red)

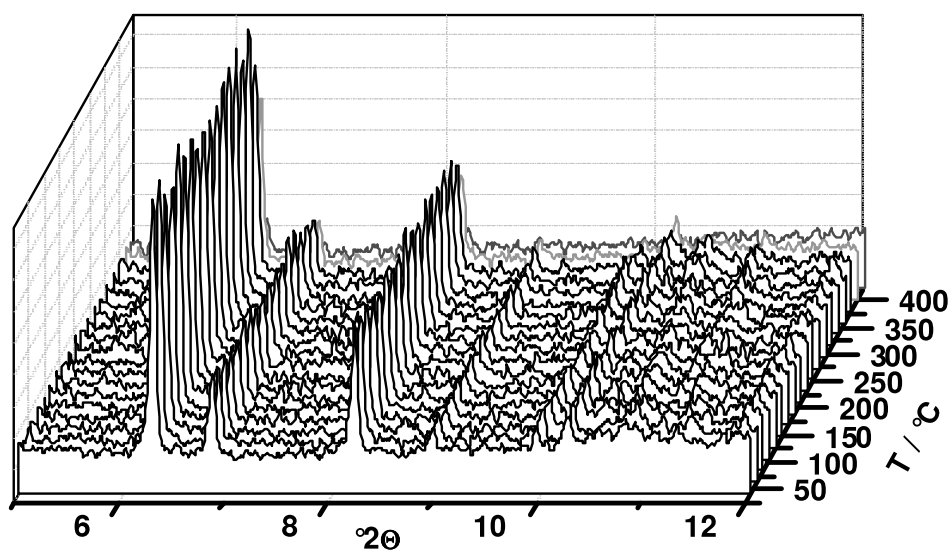


Figure S19. Temperature dependent X-ray diffraction of CAU-7.

7. IR Spectroscopy

IR spectras of H₃BTB and CAU-7 are shown in Figure S20. H₃BTB shows a broad band in the region of 1800 – 3200 cm⁻¹, characteristic for carboxylic acid groups; the band at 1690 cm⁻¹ can be assigned to the C=O stretching vibration of aromatic carboxylic acids. The bands ranging from 1605 – 1507 cm⁻¹ can be assigned to C-H and ring C-C stretching vibrations. The bands from 1422 – 1106 cm⁻¹ are the result of C-O stretching and O-H deformation vibrations of the carboxylic acid groups, with the exception of the bands at 1278 and 1180 cm⁻¹; these two bands, together with the band at 1015 cm⁻¹, result from aromatic -C-H in-plane deformation vibrations of 1,3,5-trisubstituted benzene. The bands in the fingerprint area below 1000 cm⁻¹ can be assigned to out-of-plane deformation vibrations of 1,3,5-trisubstituted benzene. The desired, but unpurified product (CAU-7 as synthesized), shows a very similar spectrum.

The persistent presence of bands characteristic for carboxylic acid groups suggests that some unreacted BTB entered the pores of the product during synthesis and could not be removed by washing with methanol. The spectrum of the activated product (Bi(BTB) washed), after being thoroughly washed with DMF and methanol, shows significant differences to the previous two spectra. The previously observed broad band from 3200 – 1800 cm⁻¹ has disappeared. The bands at 1690 cm⁻¹ and 1422 – 1106 cm⁻¹, also assigned to the carboxylic acid groups, have lost most of their intensity. New bands can be observed at 1653 cm⁻¹, 1530 cm⁻¹ and 1390 cm⁻¹, which we attribute to DMF in the pores of the compound.

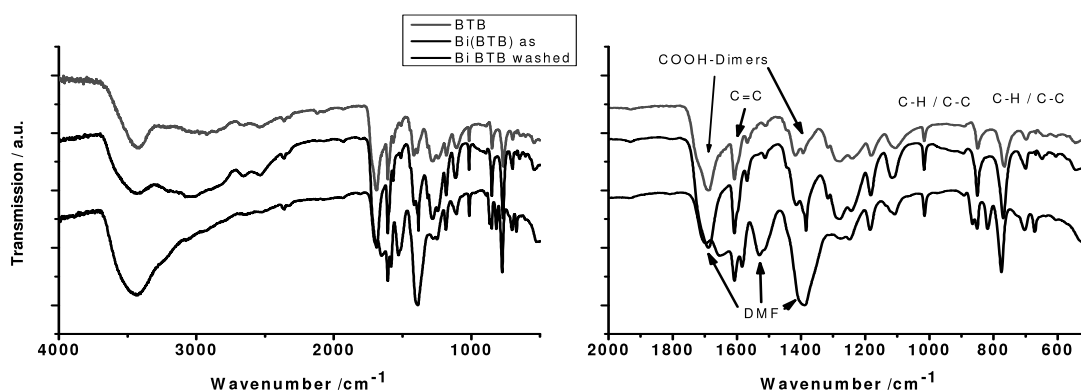


Figure S20. IR spectrum of BTB (red), Bi(BTB) as synthesized (blue) and the washed sample (black).

8. Catalytic experiments

Experimental

Chemisorption

IR acetonitrile chemisorption data were obtained using a Thermo Nicolet FTIR spectrometer. Measurements were performed on a self-supporting wafer of CAU-7. The spectra were recorded in the transmission mode in an in situ cell. Prior to the measurements, the sample was activated at 423 K for 2 hours.

Catalytic reactions

The hydroxymethylation of 2-methylfuran was carried out in a batch reactor setup at 373 K. A mixture of para-formaldehyde and 2-methylfuran in a 2:1 ratio was added to 5 wt % of the dried catalyst. The MOF catalysts were pretreated overnight at 150°C before reaction. As paraformaldehyde does not dissolve well in methylfuran, a mixture of 70 wt % paraformaldehyde in methanol was used. After introduction of the reaction mixture, the reactors were placed in a copper heating block placed on a stirrer. Reaction slurry samples were immediately cooled with an icebath and filtered through a 0.2 µm HPLC filter. The analysis was carried out using a Shimadzu 2010 GC equipped with a FID-detector and a CP-SIL-5 CB column.

Conversions were calculated based on the amount of methylfuran left in the reaction mixture, using nonane as an internal standard.

Catalytic results

The catalytic activity was probed in the solvent-free hydroxymethylation of 2-methylfuran to 5-methylfurfuryl alcohol (Figure S21).

CAU-7 was compared to other MOFs with reported Lewis or Brønsted acidity, like the Zr-terephthalate UiO-66 or the Ga-terephthalate MIL-53(Ga). The best result is obtained with CAU-7, leading to 75% yield at 90% conversion (Figure S22). While UiO-66 is much more active (Figure S23), it catalyzes further condensations, leading to a tarry resin. MIL-53(Ga) has lower activity and selectivity. Such data prove that CAU-7 must contain acid sites of moderate strength. Moreover, the hydrophobic nature of the material promotes the fast desorption of the polar alcohol reaction product, thus reducing the risk of consecutive condensation reactions.

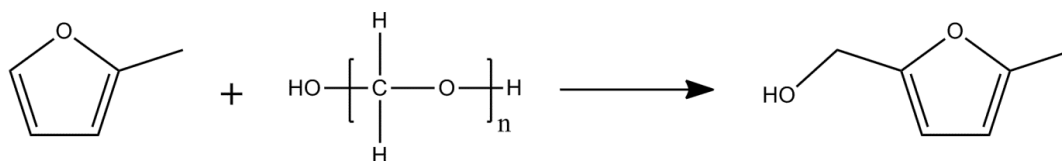


Figure S21. Hydroxymethylation of 2-methylfuran with paraformaldehyde.

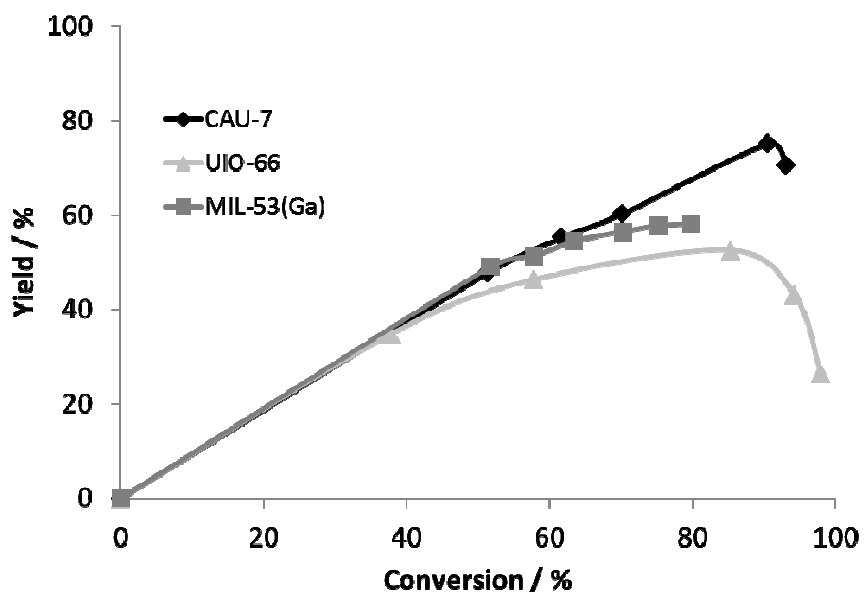
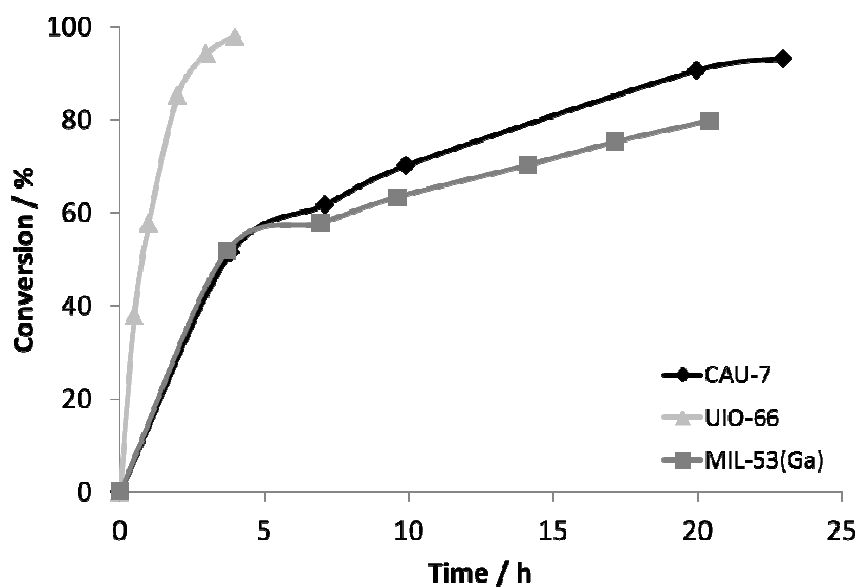


Figure S22. Yield vs conversion in the solventless hydroxymethylation of methylfuran with paraformaldehyde (5 wt % catalyst, 373 K).



7. Anhang

Figure S23. Conversion in function of time for the solventless hydroxymethylation of methylfuran with para-formaldehyde (5 wt% catalyst, 373 K).

Acetonitrile chemisorption

Acetonitrile chemisorption was used to determine the presence of Lewis acid sites. While the structure shows no evidence for open metal sites or catalytic –OH groups, the IR spectra of acetonitrile adsorbed on CAU-7 (Figure S24) reveal weak Lewis acid sites in the framework, as evidenced by the C≡N stretching vibration at 2292 cm⁻¹ of chemisorbed acetonitrile.

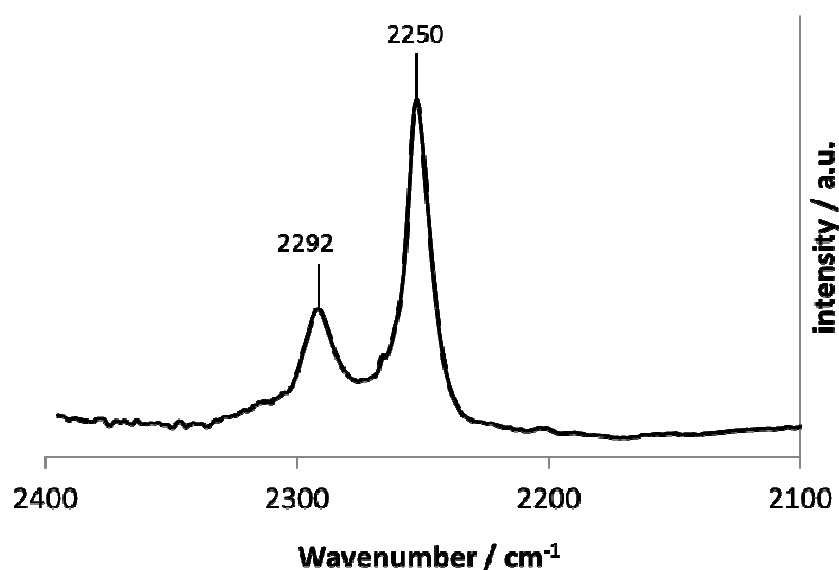


Figure S24. IR spectra of CAU-7 after exposure to 25 mbar of acetonitrile at 298K. The peak at 2292 cm⁻¹ is characteristic for the C-N stretching vibration of chemisorbed acetonitrile. The peak at 2250 cm⁻¹ corresponds to physisorbed acetonitrile.

Comparison with homogeneous catalysts

A comparison with a homogeneous Bi³⁺ catalyst results in a similar yield vs. conversion plot for the Bi salt as for CAU-7 (Figure S25). With the free carboxylic acid BTB, a lower yield is obtained at high conversion. All data together allow to identify open Bi³⁺ sites in the material as the catalytic sites; the large size of the Bi³⁺ cation corresponds well to the mild acidity observed.

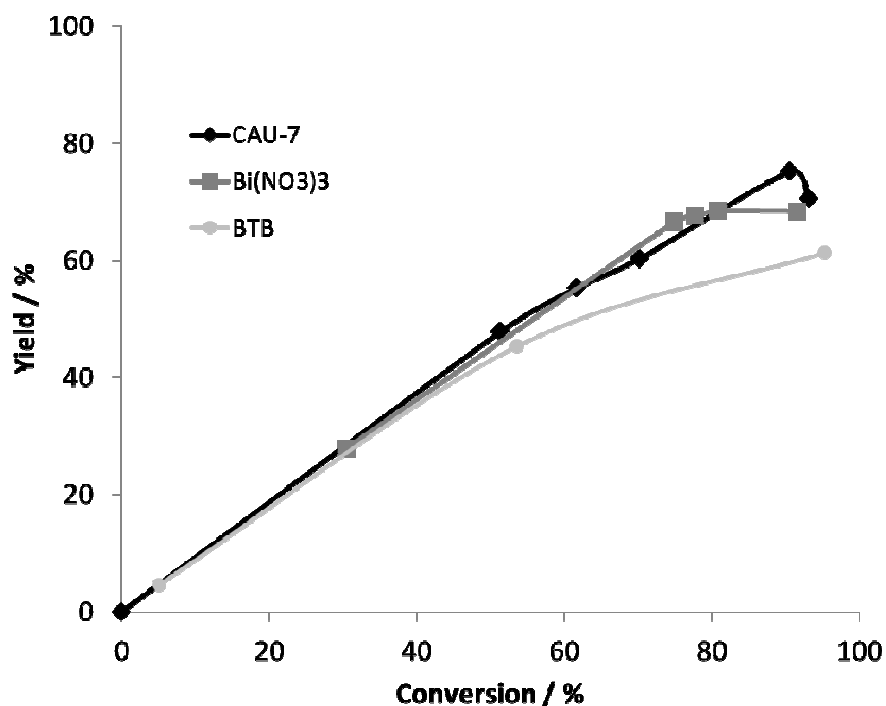


Figure S25. Yield vs conversion of the hydroxymethylation of methylfuran. The amount of catalyst used for the homogeneous salts was calculated as 10% of the amount of each compound present in CAU-7.

Heterogeneity and reusability

To prove the heterogeneity of the catalyst; a filtration test was performed and ICP-AES analysis was carried out on the reaction mixture after removal of the catalyst.

The volatile organic components were removed and the residue was dissolved in 2.5 ml H₂O.

The amount of Bi³⁺ present in the filtrate after reaction was determined by ICP-AES. The sample was analyzed on an *Ultima* apparatus equipped with a *Burgener* atomizer and a radial optic detector. Argon was used as carrier gas and as plasma.

0.15 ppm Bi³⁺ was found in the reaction mixture from a reaction with 50 mg CAU-7. This means that a negligible portion (0.0023%) of the total amount of Bi³⁺ leached proving the truly heterogeneous nature of the catalyst.

For the filtration test, part of the reaction suspension was withdrawn after 2 hours at reaction temperature. The catalyst was removed with a 0.2µm HPLC filter, and the supernatant was allowed to react further in a separate vial.

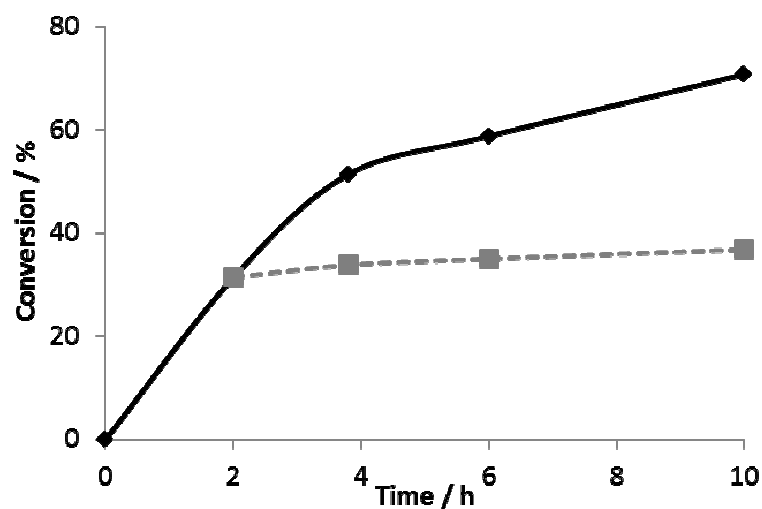


Figure S26. Filtration experiment for CAU-7. Conversions are given in function of time. The full line represents the reaction with CAU-7 as a catalyst. The dashed line represents the reaction course after withdrawing the catalyst.

For the recycling tests, the same procedure was used as in the catalytic tests. In each run, the reaction was stopped after 20 hours (at maximum yield) by placing the reaction vial in an ice bath. The MOF-catalyst was recovered by centrifugation and a sample was taken for GC-analysis. The powder was thoroughly washed with THF and methanol and dried at 150°C after which the reaction was repeated with the same amount of reactants as in the first run.

The reusability of the catalyst was also assessed. The data in Table S3 indicate that the catalyst can be reused as no decrease in activity or selectivity was observed in 2 consecutive runs.

Table S3. Conversion and selectivity for the recycling test of CAU-7 in the hydroxymethylation of 2-methylfuran.

	conversion (%) ¹	selectivity (%) ¹
run 1	90	83.2
run 2	90	83.6

¹: conversion and selectivity after a reaction of 20 hours

9. References

- [1] CPMD v3.15.1, <http://www.cpmc.org>, Copyright IBM Corp **1990-2008**, Copyright MPI für Festkörperforschung **1997-2001**.
- [2] S.Goedecker, J.Hutter, M.Teter, *Phys. Rev. B* **1996**, 54, 1703.
- [3] J.P. Perdew, K. Burke and M. Ernzerhof *Phys. Rev. Lett.* **1996**, 77, 3865.
- [4] C. Hartwigsen, S. Goedecker, and J. Hutter, *Phys. Rev.* **1998**, B 58, 3641.
- [5] M. Krack, *Theor. Chem. Acc.* **2005**, 114, 145.
- [6] Materials Studio 5.3, Accelrys 2011.

Supporting Information

High-Throughput and *in situ* EDXRD Investigations on Bismuth Carboxylates

Mark Feyand,^a Milan Köppen,^a Gernot Friedrichs^b and Norbert Stock^{a*}

a) Institut für Anorganische Chemie

Christian-Albrechts-Universität zu Kiel

Max-Eyth Straße 2, 24118 Kiel (Germany)

b) Institut für Physikalische Chemie

Christian-Albrechts-Universität zu Kiel

Max-Eyth Straße 1, 24118 Kiel (Germany)

1. The system $\text{Bi}(\text{NO}_3)_2$ / pyromellitic acid (H_4Pyr) / H_2O	2
Crystal structure of $\text{Bi}_2\text{O}(\text{Pyr})(\text{H}_2\text{O})$ (1).....	2
Crystal structure of $\text{Bi}(\text{HPyr})$ (2).....	5
Crystal structure of $\text{Bi}(\text{HPyr})$ (3).....	8
Thermogravimetric analyses of 1-3.....	12
IR-spectra of compound 1-3.....	14
2. The system $\text{Bi}(\text{NO}_3)_2$ / trimellitic acid (H_3Tri) / H_2O	16
Crystal structure of $\text{Bi}(\text{Tri})(\text{H}_2\text{O})$ (4).....	16
Thermogravimetric analysis of compound 4.....	22
IR-spectra of compound 4 and 5.....	22
3. The system $\text{Bi}(\text{NO}_3)_2$ / trimesic acid (H_3BTC) / H_2O	24
Crystal structure of $\text{Bi}_6\text{O}_5(\text{BTC})_2(\text{HBTC})$ (7).....	27
Crystal structure of $\text{Bi}_2(\text{O})(\text{OH})(\text{HBTC})(\text{NO}_3)$ (8).....	31
Thermogravimetric analyses of compound 6 and 8.....	37
IR-spectra of 6 and 8.....	38
4. Results of luminescence measurements.....	40

1. The system $\text{Bi}(\text{NO}_3)_2$ / pyromellitic acid (H_4Pyr) / H_2O

Crystal structure of $\text{Bi}_2\text{O}(\text{Pyr})(\text{H}_2\text{O})$ (1)

The crystal structure is build up from two crystallographically independent Bi^{3+} ions which are eight fold coordinated by oxygen atoms. The atom Bi1 is surrounded by six carboxylate groups, one water molecule and one O^{2-} ion and Bi2 is surrounded by seven carboxylate groups and one O^{2-} ion . Face-sharing of BiO_8 polyhedra through O^{2-} ions leads to the formation of Bi_4O_{12} units. Edge-sharing of these units through oxygen atoms of the carboxylate groups leads to Bi-O-layers in the a,b -plane (Fig. S1). The so formed layers are connected by the aromatic rings of the organic linker molecules. The final crystallographic parameters are summarized in table S1.

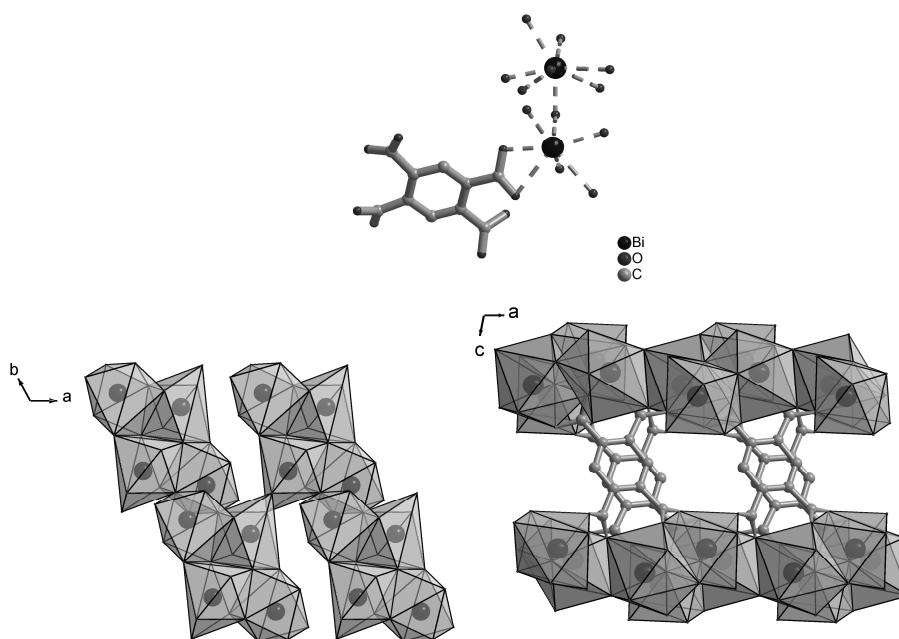


Fig. S1. Section of the crystal structure of $\text{Bi}_2\text{O}(\text{Pyr})(\text{H}_2\text{O})$ (1). **Top left:** asymmetric unit and first coordination sphere of compound 1. **Top, right:** Layers along the a,b -plane formed by Bi_4O_{12} units. **Bottom:** Connection of these layers along the c -axis (bottom) by the aromatic rings of the pyromellate ions. The BiO_8 polyhedra are given in grey.

Table S1. Final crystallographic parameters of the refinement of Bi₂(O)(Pyr)(H₂O) (1).

Empirical formula	C ₁₀ H ₄ Bi ₂ O ₁₀	
Formula weight	1157.16 g/mol	
Temperature	293(2) K	
Wavelength	0.71073 Å	
Crystal system	Monoclinic	
Space group	C2/c	
Unit cell dimensions	a = 21.838(4) Å	α = 90°
	b = 7.5788(15) Å	β = 121.17(3)°
	c = 19.748(4) Å	γ = 90°
Volume	2796.4(10) Å ³	
Z	4	
Density (calculated)	2.749 g/cm ³	
Absorption coefficient	18.912 mm ⁻¹	
F(000)	2060	
Crystal size	0.125 x 0.882 x 0.623 mm ³	
Theta range for data collection	2.18 to 27.96°.	
Index ranges	-28 ≤ h ≤ 28, -10 ≤ k ≤ 9, -25 ≤ l ≤ 25	
Reflections collected	21193	
Independent reflections	3344 [R _(int) = 0.0622]	
Completeness to theta = 27.96°	99.7 %	
Refinement method	Full-matrix least-squares on F ²	
Data / restraints / parameters	3344 / 0 / 190	
Goodness-of-fit on F ²	1.031	
Final R indices [I > 2σ(I)]	R ₁ = 0.0460, wR ₂ = 0.1232	
R indices (all data)	R ₁ = 0.0584, wR ₂ = 0.1326	
Largest diff. peak and hole	5.028 and -4.296 e.Å ⁻³	

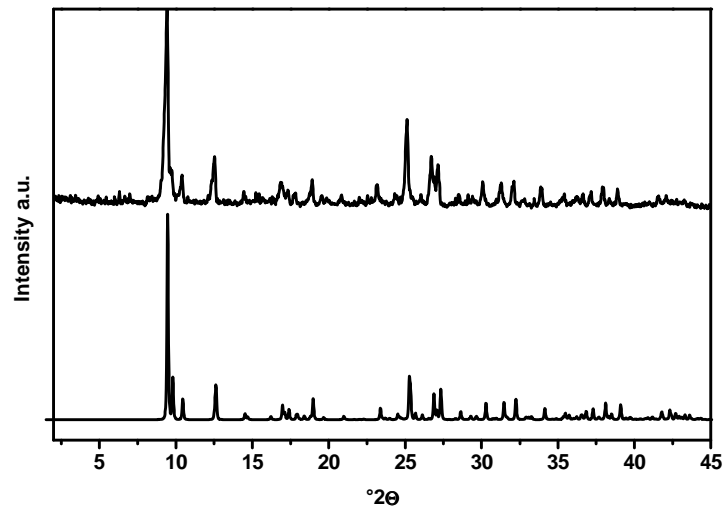


Fig. S2. Calculated (bottom) and experimental (top) powder pattern of $\text{Bi}_2(\text{O})(\text{Pyr})(\text{H}_2\text{O})$ (1).

Crystal structure of Bi(HPyr) (2).

The asymmetric unit and the coordination environment of the Bi^{3+} ion of compound **2** is shown in Fig. S3. The crystal structure of **2** is build up from one crystallographically independent Bi^{3+} ion and one single protonated pyromellate ion. In compound **2** edge-sharing BiO_9 polyhedra are connected to zigzag chains (Fig. S4). All oxygen atoms coordinated to the Bi^{3+} ion stem from carboxylate groups. The Bi-O-chains are interconnected by the aromatic rings of the pyromellate ions to form a three-dimensional network. The protonated carboxylic acid can be assigned to the O6 atom and it does not coordinate. Based on the refined atomic distances the OH group seems to be involved in hydrogen bonding with another carboxylate group. The proposed hydrogen bonds and the bond lengths are given in Fig. S5. The final crystallographic parameters of the Rietveld refinement are given in Table S2.

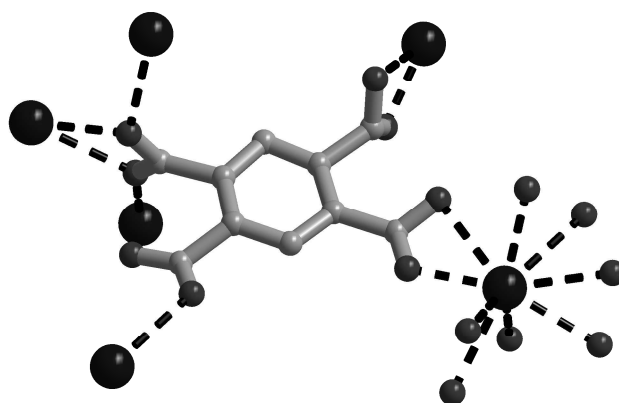


Fig. S3. Interconnection of Bi^{3+} ions by HPyr^{3-} and coordination environment of one Bi^{3+} ion in compound **2**. Bismuth atoms are given as blue, carbon atoms as grey and oxygen atoms as red spheres.

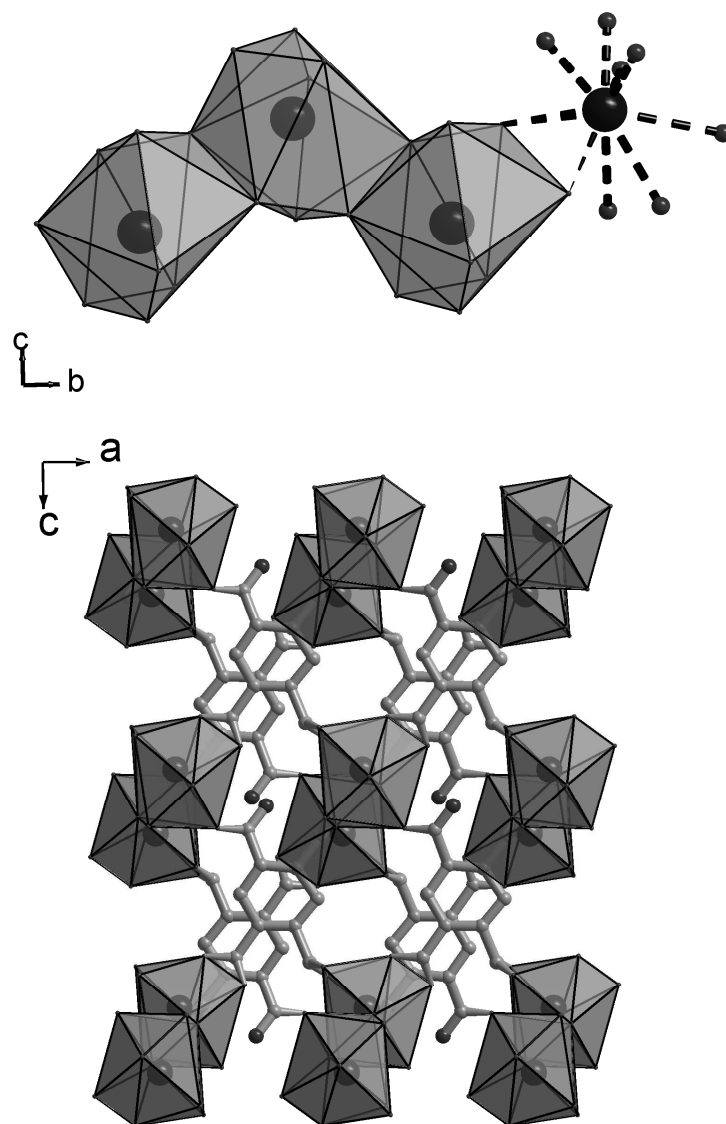


Fig.S4. Section of the crystal structure of Bi(HPyr) (**2**). **Top:** Zig-Zag chains along the *b*-axis. **Bottom:** Formation of a three-dimensional network by the interconnection of these chains along the *a*- and *c*-axis. The bismuth atoms are given as blue, the carbon atoms are given as grey and the oxygen atoms are given as red spheres. The BiO₈ polyhedra are given in grey.

Table S2. Final crystallographic parameters of the refinement of Bi(HPy) (**2**).

Lattice parameters	$a = 14.5379(2) \text{ \AA}$	$\alpha = 90.0^\circ$
	$b = 7.0295(1) \text{ \AA}$	$\beta = 89.004(1)^\circ$
	$c = 9.3130(2) \text{ \AA}$	$\gamma = 90.0^\circ$
Space Group	$P2_1/a$	
$R_{wp} = 10.34$	$R_{Bragg} = 2.64$	GoF = 1.43

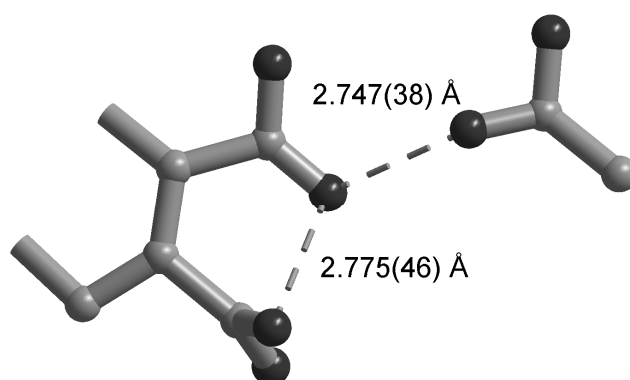


Fig. S5. Proposed hydrogen bonds and donor-acceptor distances (thin dotted lines) between CO_2^- and COOH groups in compound **2**. Carbon atoms are given as grey and oxygen atoms as red spheres.

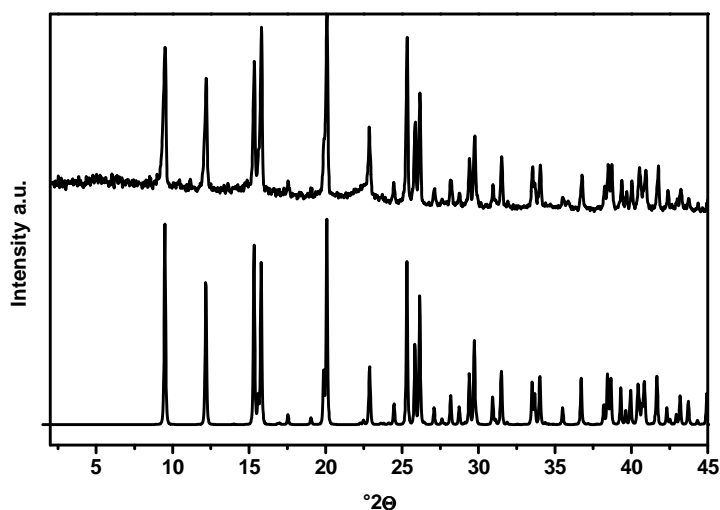


Fig. S6. Calculated and experimental powder pattern of Bi(Hpyr)(**2**).

Crystal structure of *Bi(HPyr)* (**3**).

The final crystallographic parameters of the crystal structure refinement are summarized in Table S4. The connectivity of the HPyr^{3-} and the Bi^{3+} ions is shown in Figure S7. The crystal structure is built up by one crystallographically independent Bi^{3+} ion and one single protonated pyromellate ion. Edge-sharing of BiO_9 polyhedra along [010] leads to the formation of Bi-O-chains (Fig. S8). These chains are interconnected by the pyromellate ions. The protonated oxygen atom of the $-\text{COOH}$ group can be assigned to the non-coordinating oxygen atom O6. This is in good agreement with the determined bond length C9 - O6 of 1.264(15) Å and C9 - O7 of 1.208(13) Å. The oxygen atom O6 is involved in the formation of a hydrogen bond to a second carboxylate group. The proposed hydrogen bonding schemes with donor-acceptor distances are given in Fig. S9.

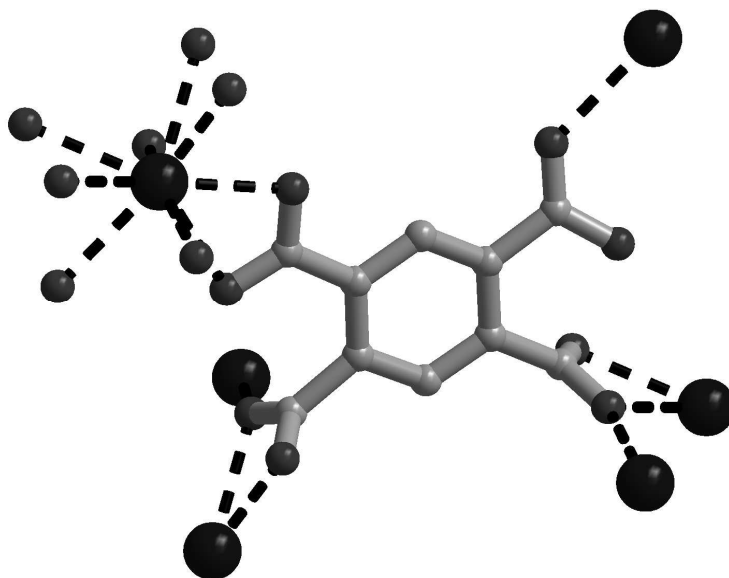


Fig. S7. Interconnection of Bi^{3+} ions by HPyr^{3-} and coordination environment of one Bi^{3+} ion in compound **3**. Bismuth atoms are given as blue, carbon atoms as grey and oxygen atoms as red spheres.

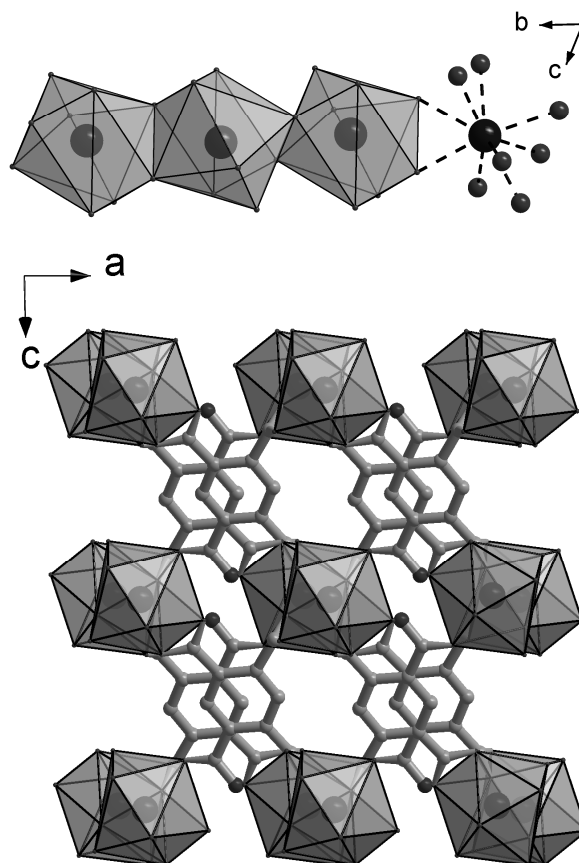


Fig. S8. Section of the crystal structure of Bi(HPyr) (**3**). **Top:** Edge-sharing of BiO_9 polyhedra leads to the formation of chains along the a -axis. **Bottom:** Interconnection of these chains along the a - and c -axis (bottom). The bismuth atoms are blue, the carbon atoms are given as grey balls and the oxygen atoms are given as red balls. The BiO_9 polyhedra are given in grey.

Table S3. Final crystallographic parameters of the refinement of Bi(HPyr) (**3**).

Empirical formula	C ₁₀ H ₂ Bi ₂ O ₈	
Formula weight	684.08	
Temperature	293(2) K	
Wavelength	0.71073 Å	
Crystal system	Triclinic	
Space group	P-1	
Unit cell dimensions	a = 7.8825(16) Å	α = 108.96(3)°
	b = 8.4482(17) Å	β = 90.93(3)°
	c = 9.890(2) Å	γ = 116.25(3)°
Volume	548.57(19) Å ³	
Z	2	
Density (calculated)	4.141 g/cm ³	
Absorption coefficient	32.087 mm ⁻¹	
F(000)	600	
Crystal size	0.123 x 0.103 x 0.088 mm ³	
Theta range for data collection	2.22 to 29.16°.	
Index ranges	-10 ≤ h ≤ 10, -11 ≤ k ≤ 10, 0 ≤ l ≤ 13	
Reflections collected	2912	
Independent reflections	2912 [R _(int) = 0.13]	
Completeness to theta = 29.16°	98.3 %	
Refinement method	Full-matrix least-squares on F ²	
Data / restraints / parameters	2912 / 0 / 185	
Goodness-of-fit on F ²	4.163	
Final R indices [I > 2σ(I)]	R ₁ = 0.0870, wR ₂ = 0.1592	
R indices (all data)	R ₁ = 0.1172, wR ₂ = 0.1599	
Largest diff. peak and hole	6.392 and -8.774 e.Å ⁻³	

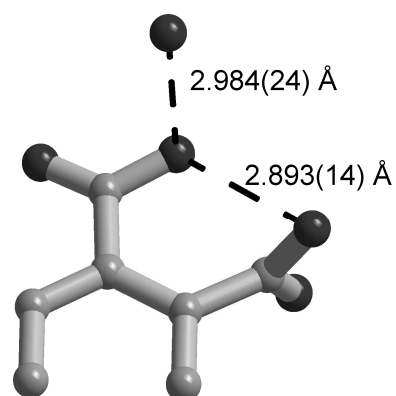


Fig. S9. Proposed hydrogen bonds and donor-acceptor distances (thin dotted lines) between CO_2^- and COOH groups in compound **3**. Carbon atoms are given as grey and oxygen atoms as red spheres.

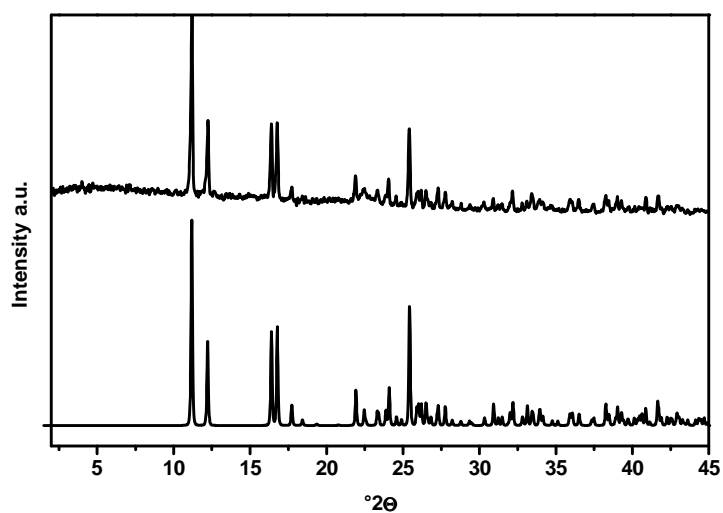


Fig. S10. Calculated (bottom) and experimental (top) powder pattern of $\text{Bi}(\text{Hpyr})(\mathbf{3})$.

Thermogravimetric analyses of 1-3

All three compounds exhibit similar thermal behavior (Fig. S11 - S13). The TG curve of compound **1** shows two steps of weight loss. The first weight loss of 7.6 % between 20 and 150 °C is due to the loss of adsorbed and coordinated water molecules (calc. 7.3 % for 3 H₂O molecules per formula unit). The second weight loss above 320 °C is due to the decomposition of the linker molecules (obs. 29.4 % calc. 29.6 %). The decomposition results in the formation of Bi₂O₃. Compound **2** and **3** show only one step of weight loss. For compound **2** a weight loss of 49.1 % (390-440 °C) and for compound **3** a weight loss of 48.5 % (370-480 °C) is observed. Both results are in good agreement with the theoretical value of 49.4 %. The decomposition results in the formation of Bi₂O₃.

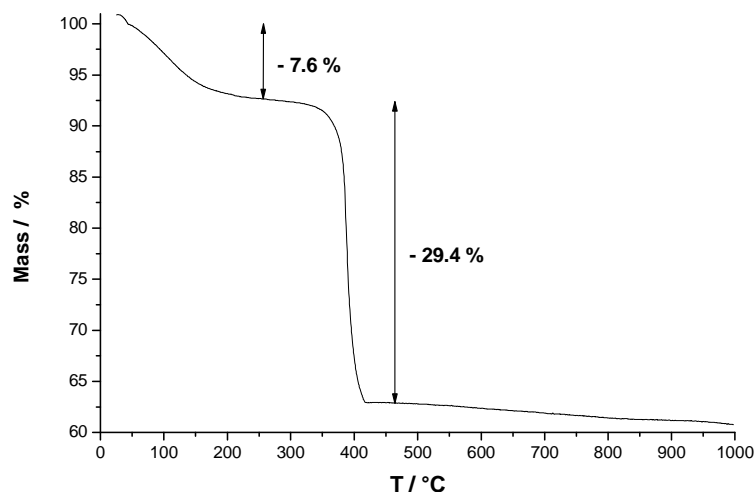


Fig. S11. Results of the thermogravimetric analysis of Bi₂(O)(Pyr)(H₂O) (**1**). The decomposition leads to the formation of Bi₂O₃.

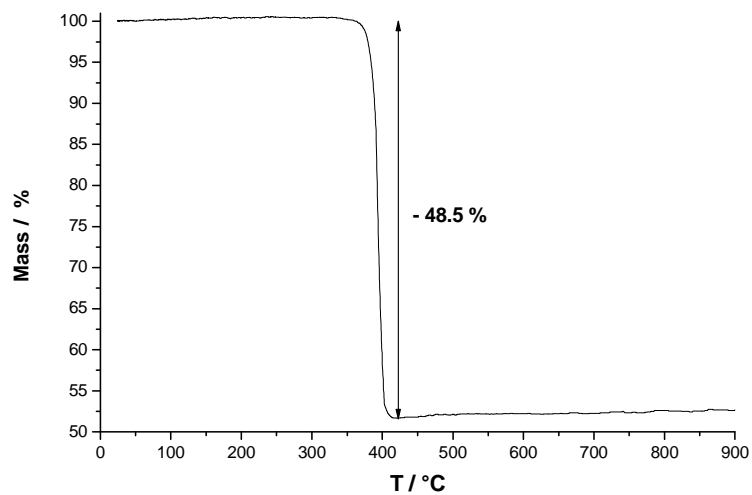


Fig. S12. Result of the thermogravimetric analysis of Bi(HPyr) (**2**). The decomposition leads to the formation of Bi_2O_3 .

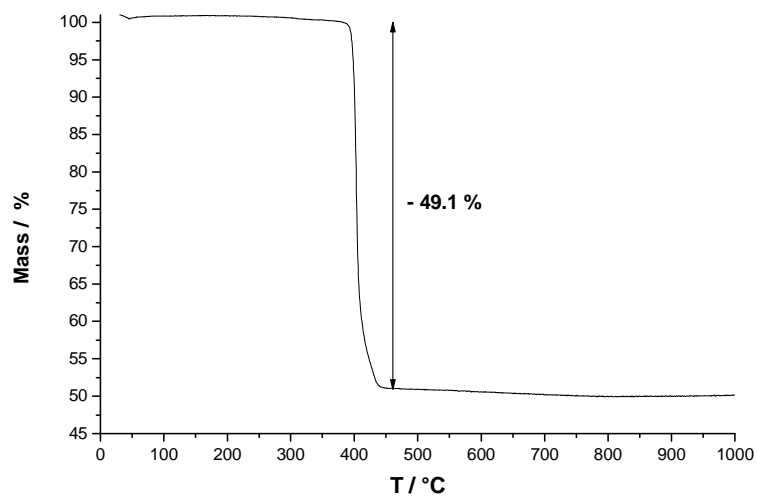


Fig. S13. Result of the thermogravimetric analysis of Bi(HPyr) (**2**). The decomposition leads to the formation of Bi_2O_3 .

IR-spectra of compound 1-3

The IR-spectra of compound 1-3 are shown in Fig. S14-S16. Compound 1 shows broad bands in the region of 3400-2500 cm^{-1} which can be assigned to O-H vibrations of the water molecules. Compound 1-3 show at 1550 to 1560 cm^{-1} the asymmetric stretching vibrations of the carboxylate groups and in the range of 1420-1483 cm^{-1} the symmetric stretching vibration are observed. The aromatic C-C stretching vibrations are observed in the range of 1514-1483 cm^{-1} and the aromatic C-H deformation vibrations are observed in the range between 873-761 cm^{-1} .

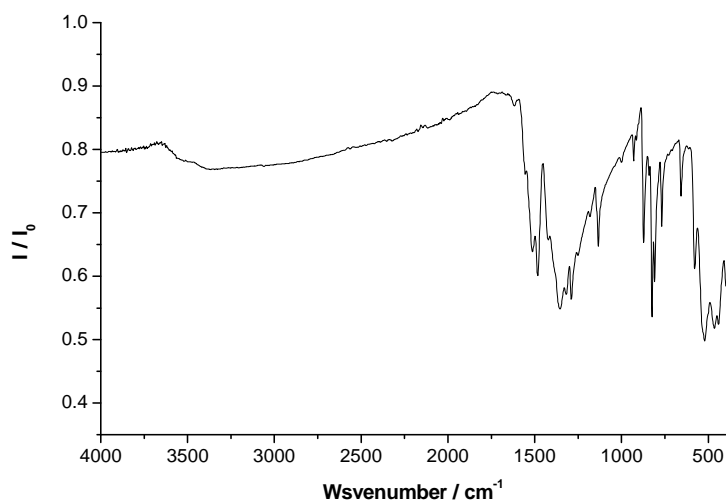


Fig. S14. IR-spectrum of $\text{Bi}_2(\text{O})(\text{Pyr})(\text{H}_2\text{O})$ (1).

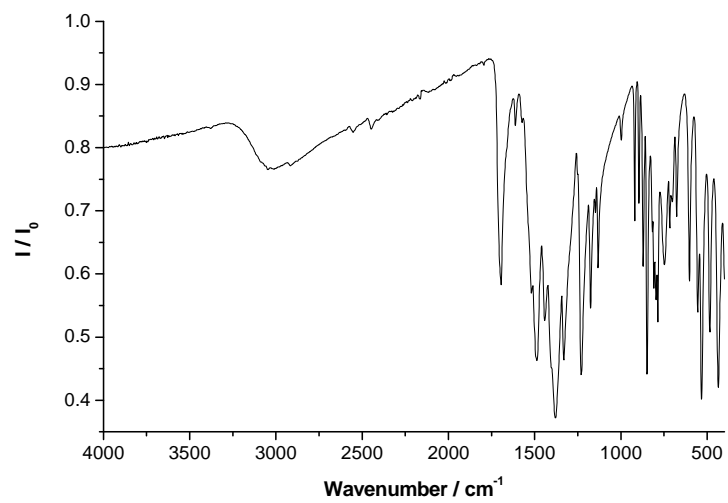


Fig. S15. IR-spectrum of Bi(HPyr) (2).

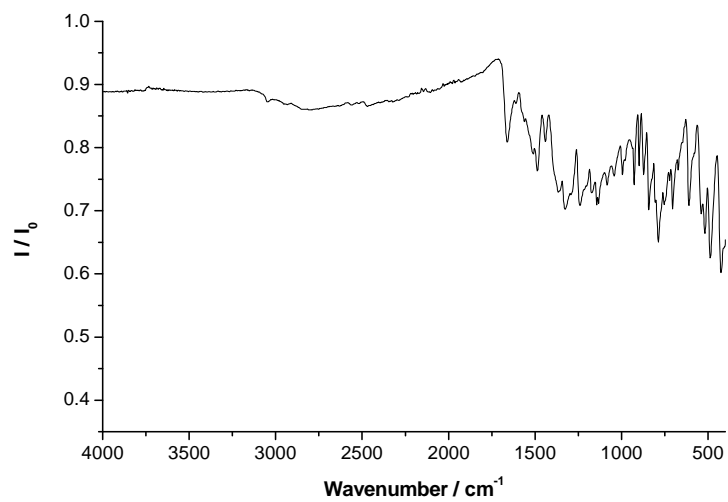


Fig. S16. IR-Spectrum of Bi(HPyr) (3).

2. The system $\text{Bi}(\text{NO}_3)_2$ / trimellitic acid (H_3Tri) / H_2O

Crystal structure of $\text{Bi}(\text{Tri})(\text{H}_2\text{O})$ (4)

The coordination property of the trimellate ion Tri^{3-} and the coordination environment of the Bi^{3+} ion in $\text{Bi}(\text{Tri})(\text{H}_2\text{O})$ (4) are shown in Fig. S17. The coordination environment of Bi^{3+} ions results from seven carboxylates oxygen atoms and one water molecule. Edge-sharing of the BiO_8 polyhedra along [010] leads to the formation of chains (Fig. S18). These chains are connected by the aromatic rings of the trimellate ions in the a,c -plane. The water molecules are involved in the formation of hydrogen bonds (Fig. 19) with the carboxylate groups of the trimellate ions.

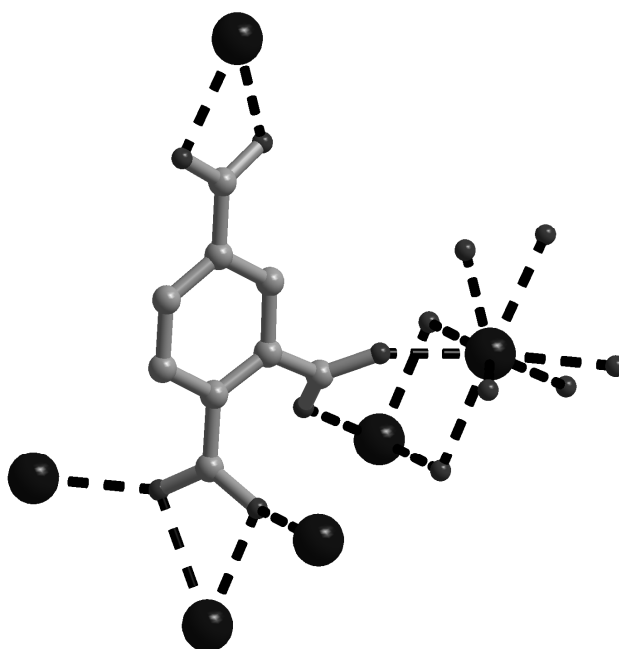


Fig. S17. Interconnection of Bi^{3+} ions by Tri^{3-} and coordination environment of one Bi^{3+} ion in $\text{Bi}(\text{Tri})(\text{H}_2\text{O})$ (4). Bismuth atoms are given as blue, carbon atoms as grey and oxygen atoms as red spheres.

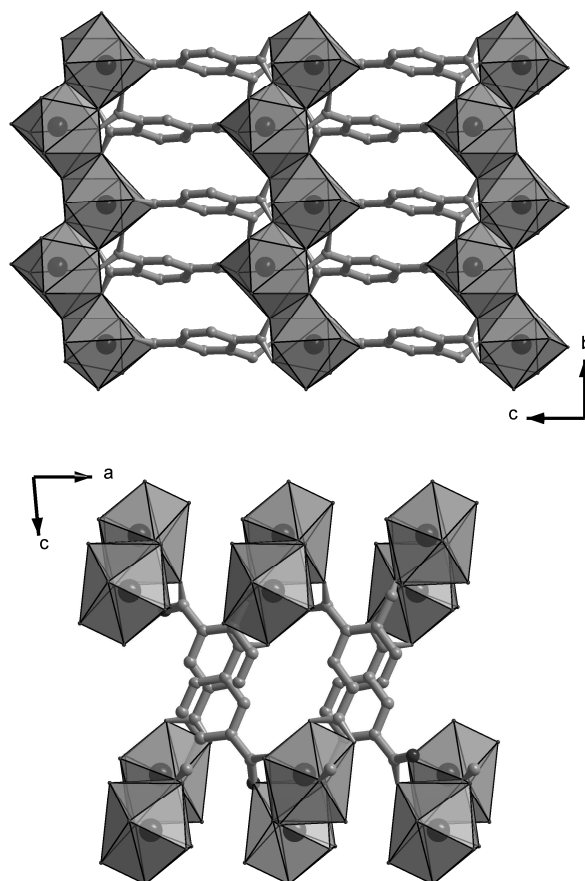


Fig. S18. Section of the crystal structure of Bi(Tri)(H₂O) (**4**). **Top:** Zig-zag chains of edge-sharing BiO₉ polyhedra along the *b*-axis. **Bottom:** The interconnection of these chains along the *a*- and *c*-axis. The bismuth atoms are given as blue, the carbon atoms as grey and the oxygen atoms as red spheres. The BiO₈ polyhedra are shown in grey.

Table S4. Final crystallographic parameters of the refinement of (Bi(Tri)(H₂O) (4).

Empirical formula	C ₉ H ₃ Bi O ₇	
Formula weight	431.09	
Temperature	293(2) K	
Wavelength	0.71073 Å	
Crystal system	Triclinic	
Space group	P-1	
Unit cell dimensions	$a = 6.2249(12)$ Å	$\alpha = 89.99(3)^\circ$.
	$b = 6.9903(14)$ Å	$\beta = 84.93(3)^\circ$.
	$c = 10.404(2)$ Å	$\gamma = 89.99(3)^\circ$.
Volume	450.95(15) Å ³	
Z	2	
Density (calculated)	3.175 g/cm ³	
Absorption coefficient	19.573 mm ⁻¹	
F(000)	390	
Crystal size	0.151 x 0.113 x 0.054 mm ³	
Theta range for data collection	1.97 to 29.20°.	
Index ranges	-8<=h<=6, -9<=k<=9, -14<=l<=14	
Reflections collected	4136	
Independent reflections	2288 [R(int) = 0.0690]	
Completeness to theta = 29.20°	94.00%	
Refinement method	Full-matrix least-squares on F ²	
Data / restraints / parameters	2288 / 0 / 155	
Goodness-of-fit on F ²	1.329	
Final R indices [I>2sigma(I)]	R ₁ = 0.0702, wR ₂ = 0.1821	
R indices (all data)	R ₁ = 0.0789, wR ₂ = 0.1901	
Largest diff. peak and hole	3.424 and -4.731 e.Å ⁻³	
BASF / TWIN	0.46 / -1 0 0 0 1 0 0 0 -1	

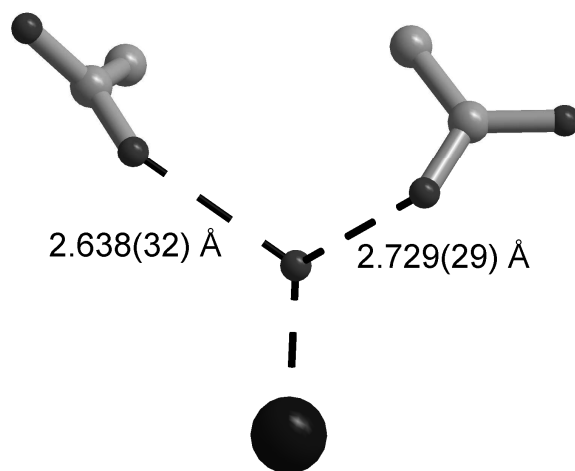


Fig. S19. Proposed hydrogen bonds and donor-acceptor distances (thin dotted lines) between CO_2^- groups and one H_2O molecule in compound **4**. Bismuth atoms are given as blue, carbon atoms as grey and oxygen atoms as red spheres.

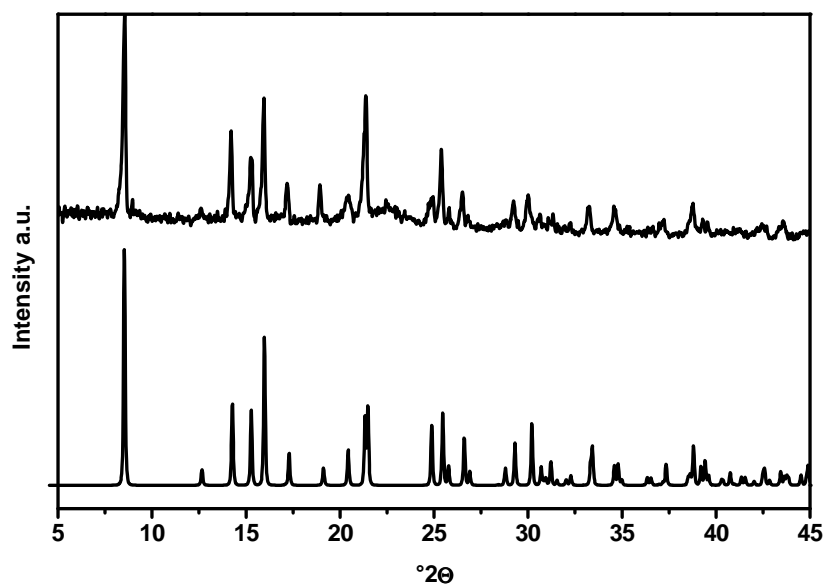


Fig. S20. Calculated (top) and experimental (bottom) powder pattern of $\text{Bi}(\text{Tri})(\text{H}_2\text{O})$ (**4**).

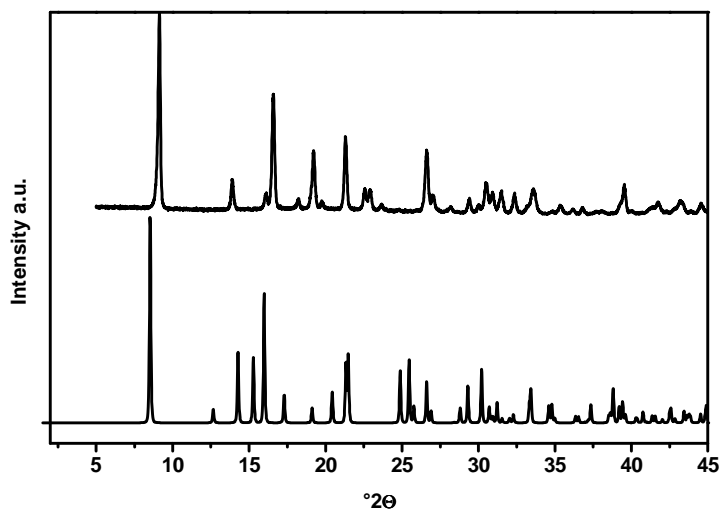


Fig. S21. Experimental powder pattern of Bi(Tri) (**5**) (top) compared with the calculated pattern of Bi(Tri)(H₂O)(**4**) (bottom).

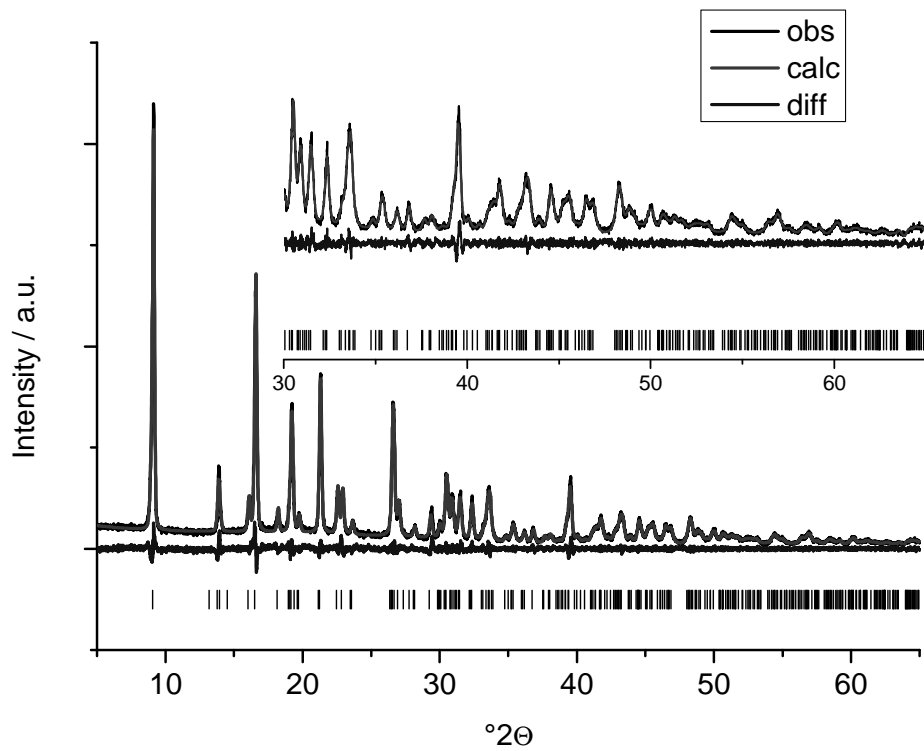


Fig. S22. Final Pawley plot of the lattice parameter refinement of compound Bi(Tri) (5).

Thermogravimetric analysis of compound **4**.

The TG curve of compound **4** shows two steps of weight loss (Fig. S23). The first weight loss of 4.3 % between 130 and 160 °C is due to the loss of the coordinated water molecule (calc. 4.1 % for one H₂O per formula unit). The second weight loss between 350 - 450 °C is due to the decomposition of the linker molecule (obs. 41.2 / calc. 42.2 %). The decomposition results in the formation of Bi₂O₃.

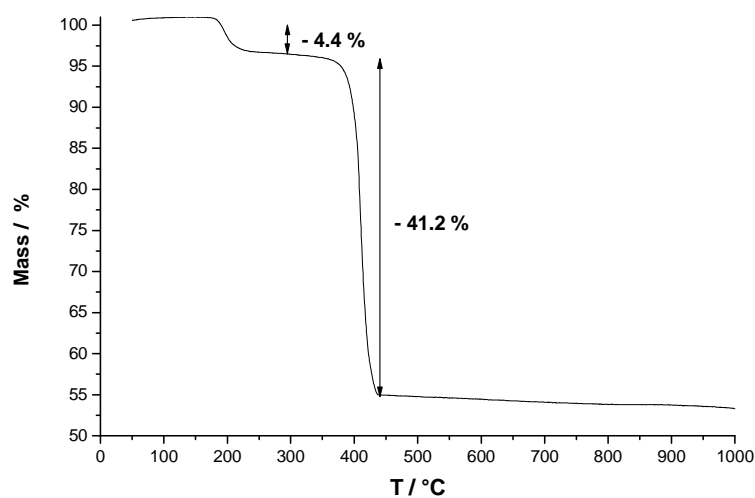


Fig. S23. Thermogravimetric analysis Bi(Tri)(H₂O) (**4**). The decomposition leads to the formation of Bi₂O₃.

IR-spectra of compound **4** and **5**.

The IR-spectra of compound **4** and **5** are shown in Fig. S24. Both spectra are very similar. Compound **4** shows broad bands in the region of 3400-2500 cm⁻¹ which can be assigned to O-H vibrations of the coordinated water molecules involved in hydrogen bonding. Compound **4** and **5** show at 1550-1560 cm⁻¹ the asymmetric stretching vibrations of the carboxylate groups and in the range of 1420-1483 cm⁻¹ the symmetric stretching vibration are observed. The aromatic C-C stretching vibrations are observed in the range of 1483-1514cm⁻¹ and the C-H deformation vibrations are found between 761-873 cm⁻¹.

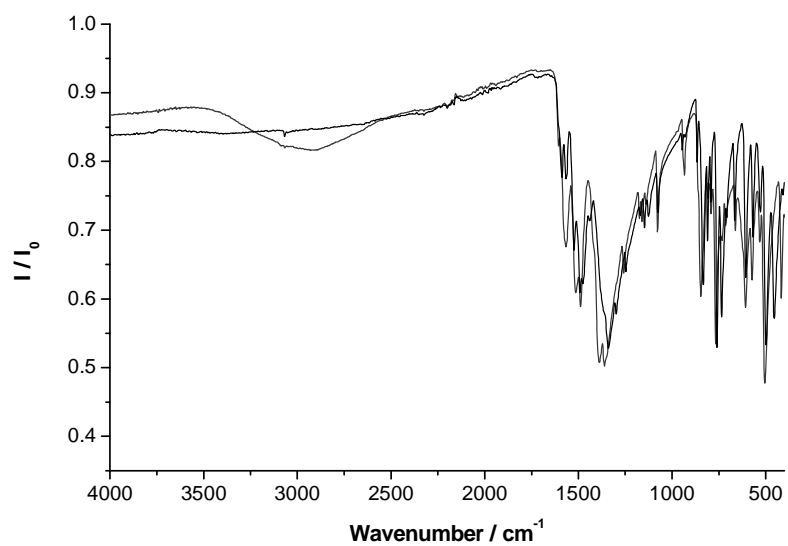


Fig. S24. IR-spectrum of Bi(Tri)(H₂O) (4, red) and Bi(Tri) (5, black).

3. The system $\text{Bi}(\text{NO}_3)_2$ / trimesic acid (H_3BTC) / H_2O

The coordination property of the trimesate ion BTC^{3-} and the coordination environment of the Bi^{3+} ion of compound **6** is shown in Fig. S25. The crystal structure is build up from one crystallographic independent Bi^{3+} ion, one BTC^{3-} ion, one coordinated (Ow1) and one uncoordinated (Ow2) water molecule. The Bi^{3+} ion is eightfold coordinated. Edge-sharing of two BiO_8 polyhedra leads to Bi_2O_{14} dimers (Fig. S26). Twelve of the oxygen atoms stem from carboxylate groups and the last two oxygen atoms from coordinated water molecules. The dimers are connected by the aromatic ring of the trimesate ions along the *b*-axis which lead to the formation of a three-dimensional network. The coordinated and uncoordinated water molecules are involved in hydrogen bonds with carboxylate groups (Fig. S27).

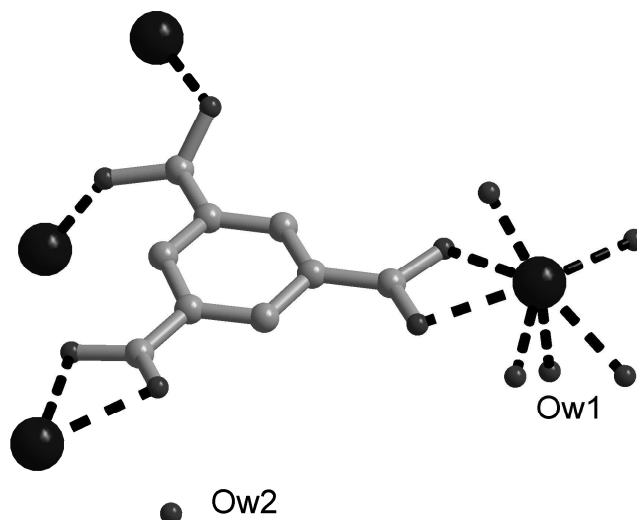


Fig. S25. Interconnection of Bi^{3+} ions by BTC^{3-} and coordination environment of one Bi^{3+} ion in $[\text{Bi}(\text{BTC})(\text{H}_2\text{O})]\cdot\text{H}_2\text{O}$ (**6**). Bismuth atoms are given as blue, carbon atoms as grey and oxygen atoms as red spheres.

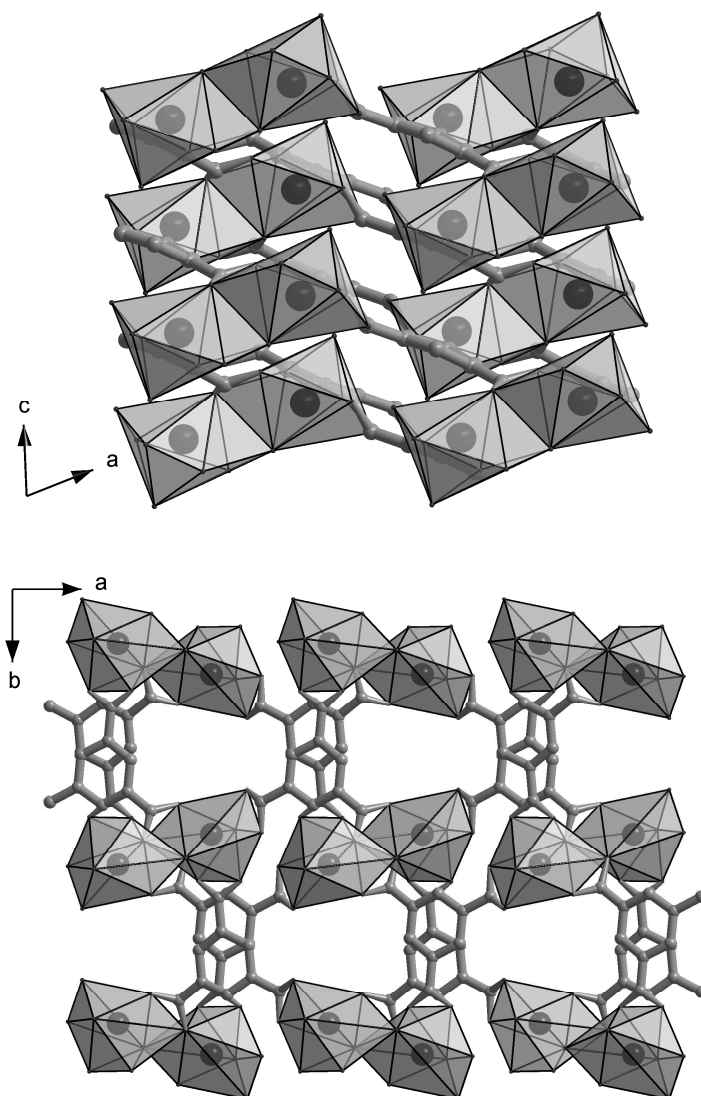


Fig. S26. Section of the crystal structure of [Bi(BTC)(H₂O)]·H₂O (**6**). **Top:** Bi₂O₁₄ units connected by the aromatic rings of the trimesate ions. **Bottom:** further interconnection to a three-dimensional structure. The uncoordinated water molecules are localized in the pores but they are not shown for clarity. The bismuth atoms are given as blue, the carbon atoms as grey and the oxygen atoms are given as red spheres. The BiO₈ polyhedra are shown in grey.

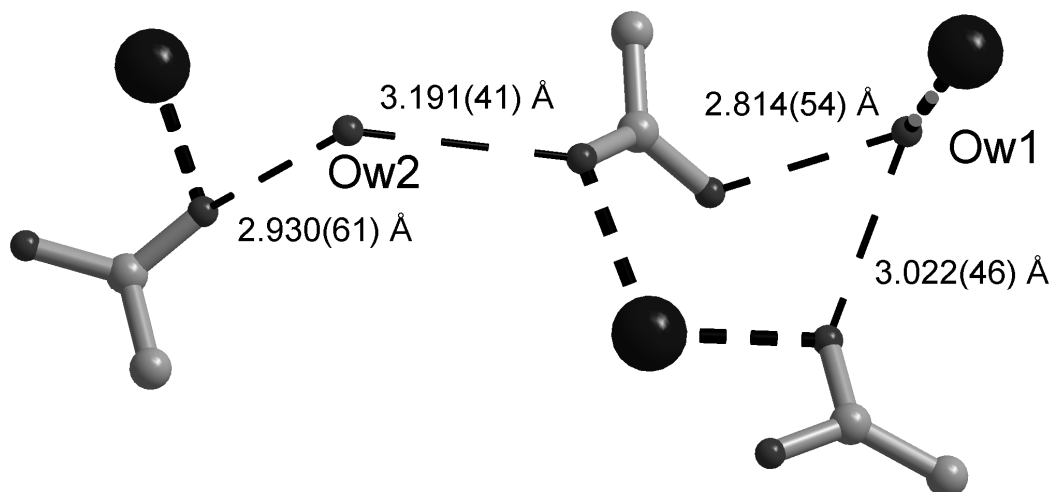


Fig. S27. Proposed hydrogen bonds and donor-acceptor distances (thin dotted lines) between CO₂⁻ groups and coordinated (Ow1) and uncoordinated (Ow2) water molecules in compound **6**. Bismuth atoms are given as blue, carbon atoms as grey and oxygen atoms as red spheres.

Table S5. Final crystallographic parameters of the refinement of [(Bi(BTC)(H₂O)]·H₂O (**6**).

Lattice parameters	$a = 9.8909(6) \text{ \AA}$	$\alpha = 90.0^\circ$
	$b = 16.8706(8) \text{ \AA}$	$\beta = 70.71(2)^\circ$
	$c = 7.20305(2) \text{ \AA}$	$\gamma = 90.0^\circ$
Space Group	$P2_1/c$	
$R_{\text{wp}} = 3.95$	$R_{\text{Bragg}} = 2.70$	GoF = 1.23

Crystal structure of $\text{Bi}_6\text{O}_5(\text{BTC})_2(\text{HBTC})$ (7).

The crystal structure of **7** is build up from six crystallographic independent Bi^{3+} ions five O^{2-} ions and two fully deprotonated and one single protonated BTC^{3-} ion. The coordination property of the HBTC^{3-} and the BTC^{3-} ions as well as the coordination environment of the Bi^{3+} ions are shown in Figure S28. The Bi^{3+} ions exhibit coordination numbers between 7 and 9. They are surrounded by oxygen atoms from carboxylates groups and O^{2-} ions. Thus Bi_6O_{31} units are formed (Fig. S29) which are connected to chains along the *a*-axis. The latter are connected by the aromatic rings of the trimesate ions and a pseudo hexagonal arrangement of the chains is observed. The HBTC^{2-} ion is involved in the formation of hydrogen bonds Fig. S30.

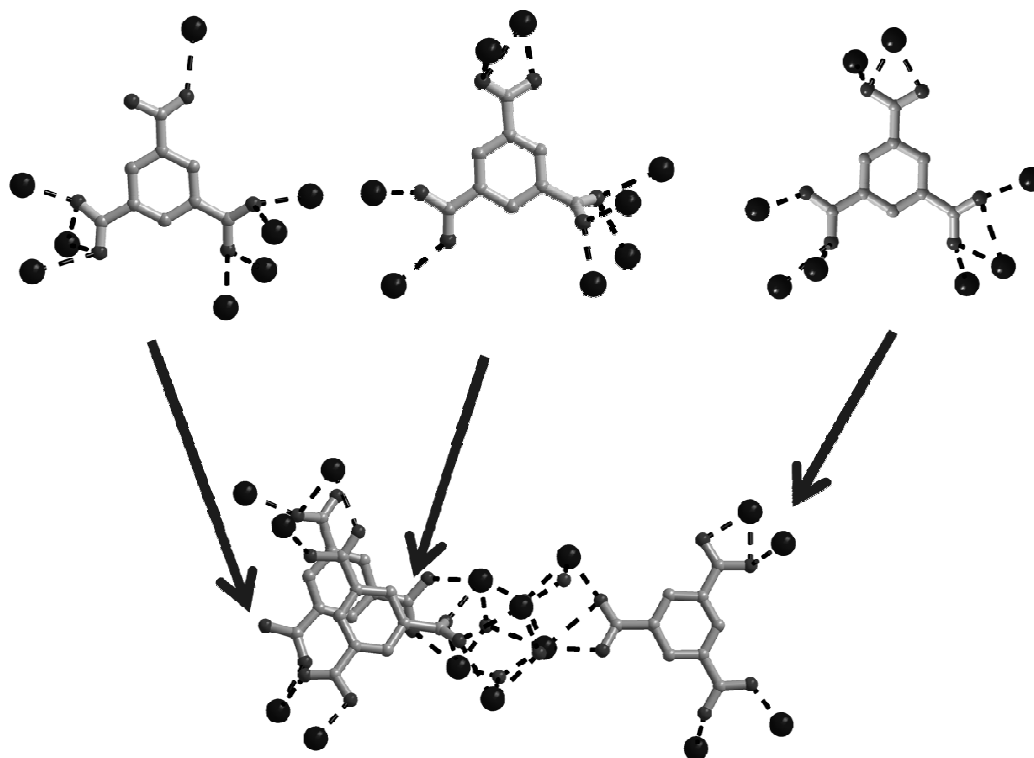


Fig. S28 Interconnection of Bi^{3+} ions by BTC^{3-} and HBTC^{2-} ions and coordination environment of Bi^{3+} ions in compound **7**. Bismuth atoms are given as blue, carbon atoms as grey and oxygen atoms as red spheres.

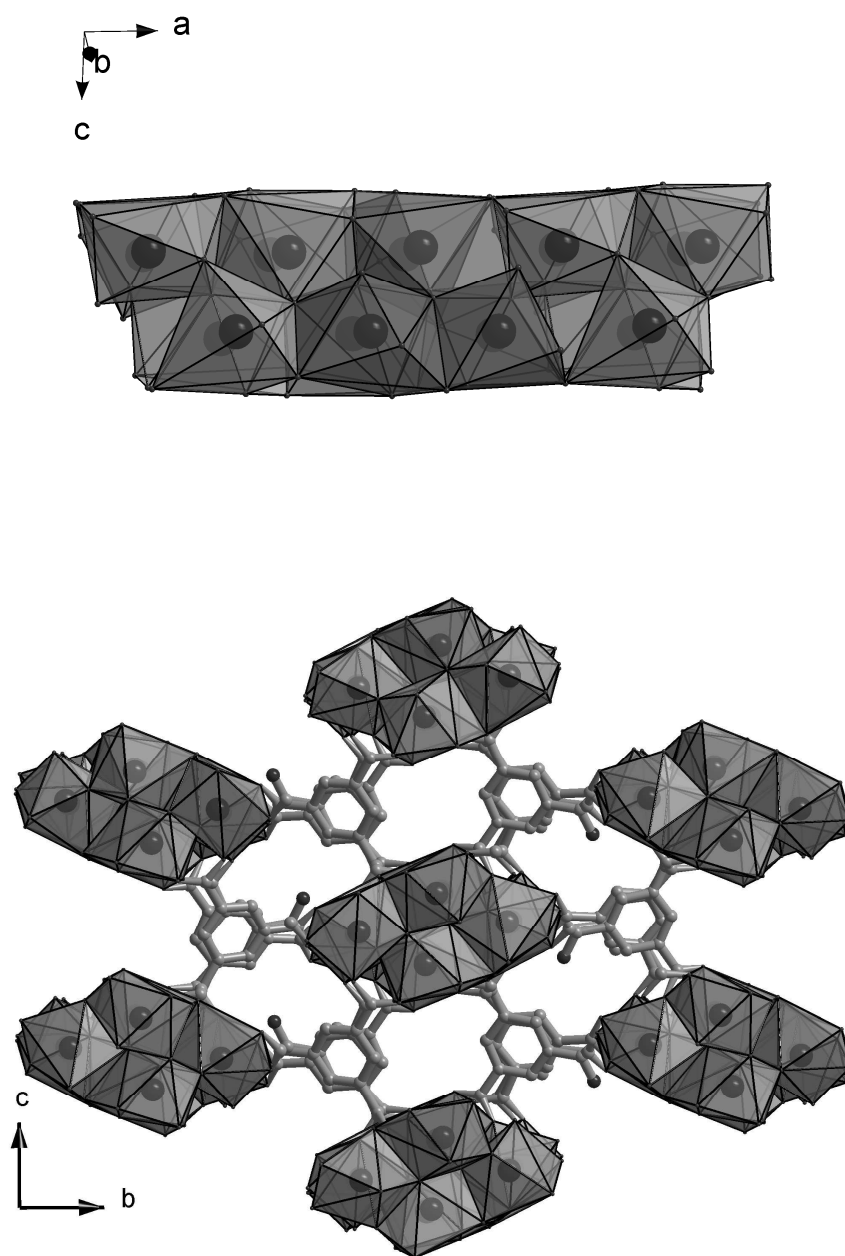


Fig. S29. Sections of the crystal structure of $\text{Bi}_6\text{O}_5(\text{BTC})_2(\text{HBTC})$ (**7**). **Top:** Connection of the Bi_6O_{31} units which are shown in blue and grey lead to the formation of chains along the *a*-axis. **Bottom:** These chains connected by the BTC^{3-} and HBTC^{2-} ions.

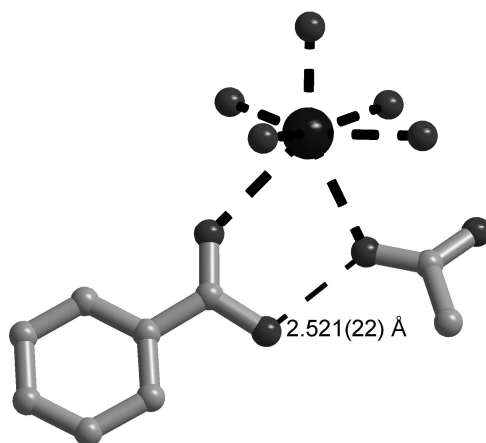


Fig. 30. Proposed hydrogen bonds and donor-acceptor distance (thin dotted lines) between -COOH and CO_2^- groups in compound **7**. Bismuth atoms are given as blue, carbon atoms as grey and oxygen atoms as red spheres, Bi-O bonds are given as thick dotted lines.

Table S6. Final crystallographic parameters of the refinement of $\text{Bi}_6\text{O}_5(\text{BTC})_2(\text{HBTC})$ (7).

Empirical formula	$\text{C}_{27} \text{H}_9 \text{Bi}_6 \text{O}_{23}$	
Formula weight	1955.22	
Temperature	293(2) K	
Wavelength	0.71073 Å	
Crystal system	Monoclinic	
Space group	$P2_1/c$	
Unit cell dimensions	$a = 12.127(2)$ Å	$\alpha = 90^\circ$
	$b = 25.055(5)$ Å	$\beta = 90.23(3)^\circ$
	$c = 10.628(2)$ Å	$\gamma = 90^\circ$
Volume	$3229.2(10)$ Å ³	
Z	4	
Density (calculated)	4.022 g/cm ³	
Absorption coefficient	32.68 mm ⁻¹	
F(000)	3412	
Crystal size	$0.070 \times 0.040 \times 0.056$ mm ³	
Theta range for data collection	1.63 to 28.03°.	
Index ranges	$-16 \leq h \leq 15, -32 \leq k \leq 32, -13 \leq l \leq 14$	
Reflections collected	37012	
Independent reflections	7705 [$R_{\text{int}} = 0.0699$]	
Completeness to theta = 28.03°	98.70%	
Refinement method	Full-matrix least-squares on F^2	
Data / restraints / parameters	7705 / 0 / 506	
Goodness-of-fit on F^2	1.095	
Final R indices [$ I > 2\sigma(I)$]	$R_1 = 0.0657, wR_2 = 0.1418$	
R indices (all data)	$R_1 = 0.0757, wR_2 = 0.1465$	
Largest diff. peak and hole	3.257 and -2.967 e Å ⁻³	
BASF / TWIN	0.20443 / 1 0 0 0 -1 0 0 0 -1	

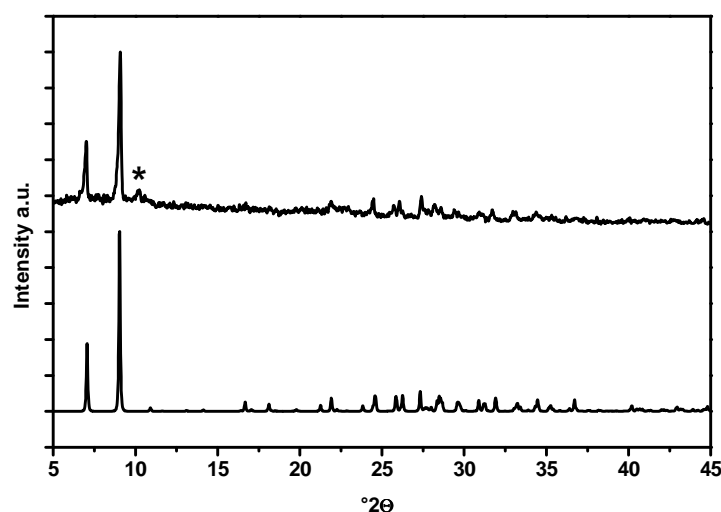


Fig. S31. Experimental (top) and calculated (bottom) powder pattern $\text{Bi}_6\text{O}_5(\text{BTC})_2(\text{HBTC})$ (**7**). The minor impurity is marked with a star.

Crystal structure of $\text{Bi}_2(\text{O})(\text{OH})(\text{HBTC})(\text{NO}_3)$ (**8**)

The coordination environment of Bi^{3+} ions and their connectivity by the HBTC^{2-} ions in $\text{Bi}_2(\text{O})(\text{OH})(\text{HBTC})(\text{NO}_3)$ (**8**) is shown in Figure S32. Sections of the crystal structure are given in Fig. S33. The crystal structure is built up from two crystallographically independent Bi^{3+} ions, one nitrate ion, one O^{2-} ion, one hydroxide ion and one single protonated linker ion. The Bi^{3+} ions form BiO_6 and one BiO_8 polyhedra which are connected to zig-zag double chains. These chains are interconnected by the nitrate ions and two-dimensional layers are formed in the a,c -plane. The electron pair of the BiO_6 polyhedra is sterically active. The layers are connected by the aromatic rings of the trimesate ion along the b -axis to form a three-dimensional network. The $-\text{COOH}$ group of the HBTC^{2-} ion is involved in the formation of hydrogen bonds to two carboxylate groups. The bond lengths and the proposed hydrogen bonding scheme are shown in Fig. S34. The observed C-O bond lengths are 1.201(9) and 1.320(9) Å for C5-O4 and C5-O5, respectively. Thus, it can be assumed that O5 is protonated.

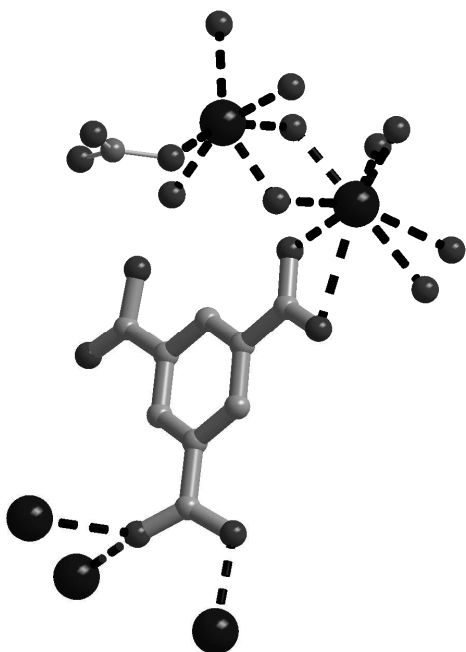


Fig. S32. Interconnection of Bi³⁺ ions by BTC³⁻ and coordination environment of two Bi³⁺ ions in Bi₂(O)(OH)(HBTC)(NO₃) (**8**). Bismuth atoms are given as blue, carbon atoms as grey and oxygen atoms as red spheres.

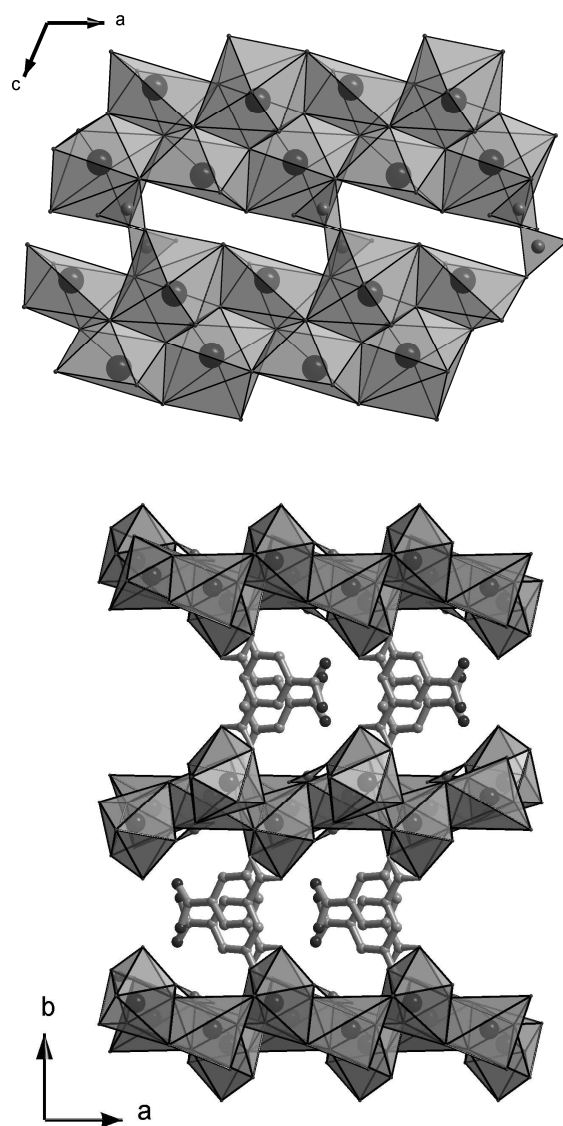


Fig. S33. Section of the crystal structure of $\text{Bi}_2(\text{O})(\text{OH})(\text{HBTC})(\text{NO}_3)$ (**8**). **Top**: View onto the layers by the interconnection of Bi-O-chains through nitrate ions (green triangles). **Bottom**: The connection of these layers along the b -axis. The bismuth atoms are given as blue, the carbon atoms as grey, the oxygen atoms as red and the nitrogen atoms as green spheres. The BiO_x polyhedra are shown in grey and the NO_3^- ions are presented as green triangles.

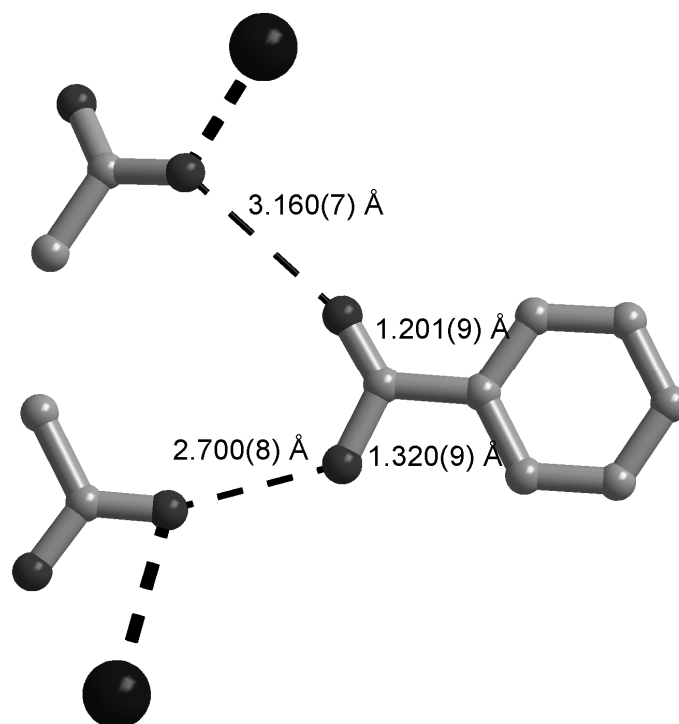


Fig. S34. Proposed hydrogen bonds and donor-acceptor distances (thin dotted lines) between -COOH and CO_2^- groups in compound **8**. Bismuth atoms are given as blue, carbon atoms as grey and oxygen atoms as red spheres, Bi-O bonds are given as thick dotted lines.

Table S7. Final crystallographic parameters of the crystal structure refinement of $(\text{Bi}_2(\text{O})(\text{OH})(\text{HBTC})(\text{NO}_3))$ (**8**).

Empirical formula	$\text{C}_9 \text{H}_6 \text{Bi}_2 \text{N O}_9$	
Formula weight	690.11 g/mol	
Temperature	293(2) K	
Wavelength	0.71073 Å	
Crystal system	Monoclinic	
Space group	$P2_1/c$	
Unit cell dimensions	$a = 7.7377(15)$ Å	$\alpha = 90^\circ$.
	$b = 22.285(5)$ Å	$\beta = 113.92(3)^\circ$.
	$c = 8.1491(16)$ Å	$\gamma = 90^\circ$.
Volume	$1284.5(4)$ Å ³	
Z	4	
Density (calculated)	3.569 g/cm ³	
Absorption coefficient	27.410 mm ⁻¹	
F(000)	1220	
Crystal size	$0.117 \times 0.074 \times 0.093$ mm ³	
Theta range for data collection	1.83 to 27.93°.	
Index ranges	$-10 \leq h \leq 9, 0 \leq k \leq 29, 0 \leq l \leq 10$	
Reflections collected	3081	
Independent reflections	3081 [$R_{\text{(int)}} = 0.086$]	
Completeness to theta = 27.93°	99.60%	
Refinement method	Full-matrix least-squares on F^2	
Data / restraints / parameters	3081 / 0 / 208	
Goodness-of-fit on F^2	0.842	
Final R indices [$I > 2\sigma(I)$]	$R_1 = 0.0237, wR_2 = 0.0479$	
R indices (all data)	$R_1 = 0.0375, wR_2 = 0.0496$	
Largest diff. peak and hole	0.894 and -1.175 e.Å ⁻³	

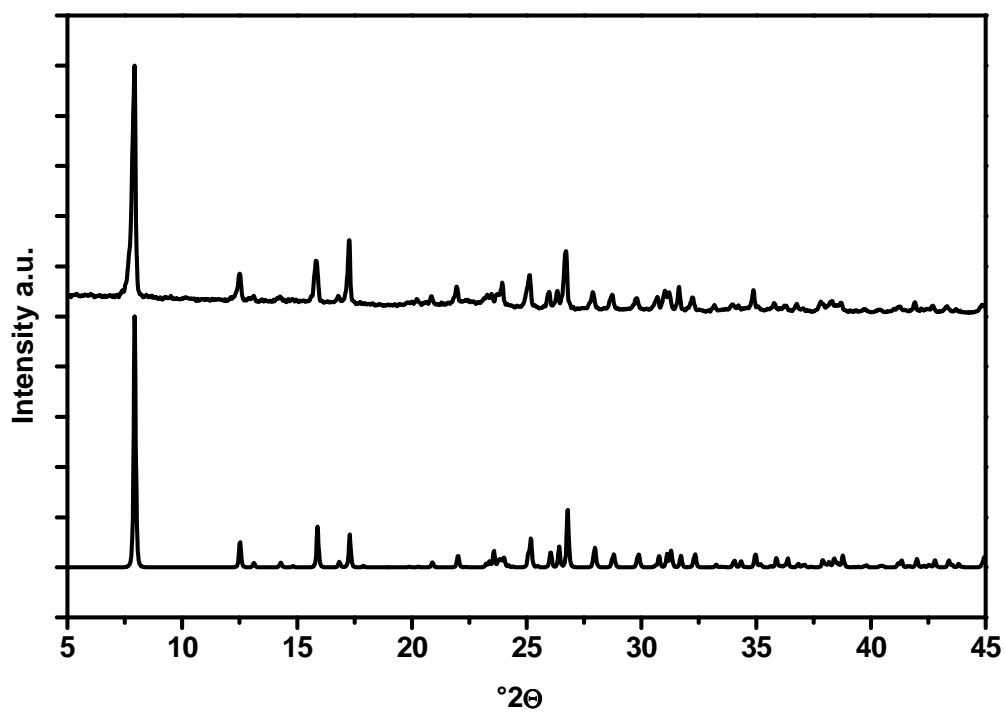


Fig. S35. Experimental (top) and calculated (bottom) powder pattern of $(\text{Bi}_2(\text{O})(\text{OH})(\text{HBTC})(\text{NO}_3))$ (**8**).

Thermogravimetric analyses of compound **6** and **8**

The TG curve of compound **6** (Fig. S36) shows two steps of weight loss. The first step between 90 and 150°C can be assigned to loss of the coordinated and uncoordinated water molecules (obs. 10.6 %, calc. 7.9 % for two H₂O molecules per formula unit). The second step at between 300 and 420 °C can be attributed to the decomposition of the linker molecule (calc. 38.7, obs. 40.7 %). The observed weight loss of 34.4 % for compound **8** (Fig. 37) can be assigned to the decomposition of the organic species and the decomposition of the nitrate ions (calc. 35.4 %, one NO₃⁻ and BTC³⁻ per formula unit).

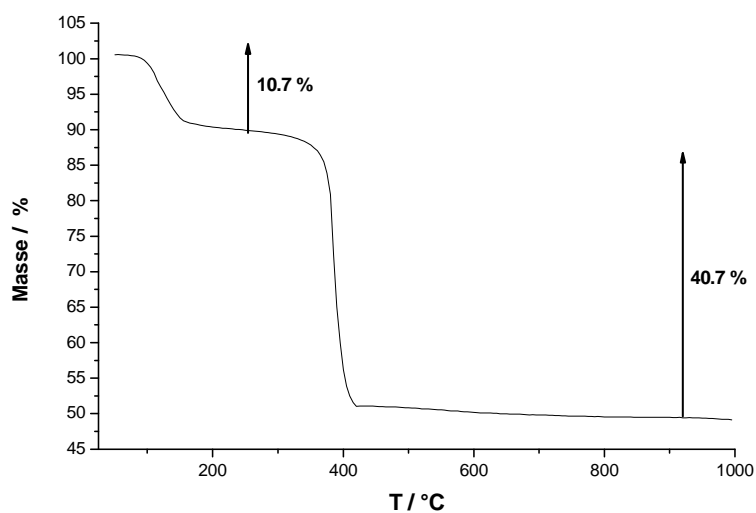


Fig. S36. Results of the thermogravimetric analysis of [Bi(BTC)(H₂O)]·H₂O (**6**). The decomposition leads to the formation of Bi₂O₃.

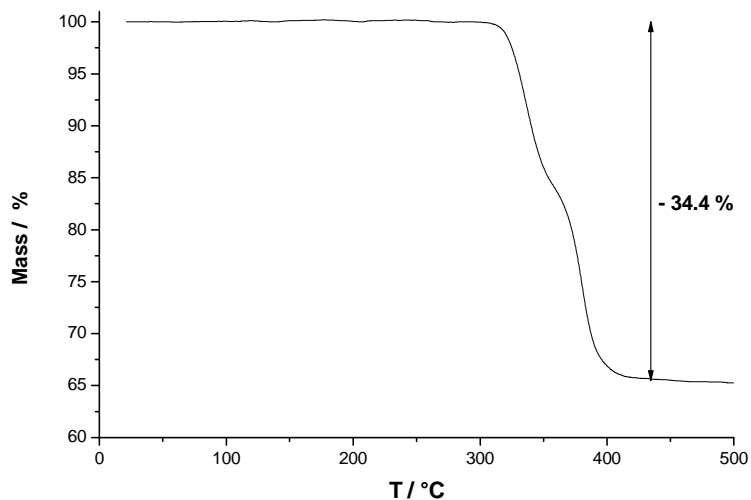


Fig. S37. Results of the thermogravimetric analysis of $\text{Bi}_2(\text{O})(\text{OH})(\text{HBTC})(\text{NO}_3)$ (**8**). The decomposition leads to the formation of Bi_2O_3 .

IR-spectra of 6 and 8

The IR-spectra of compound **6** and **8** are given Fig. S38-S39. The spectrum of compound **6** shows broad bands in the region of $2500\text{-}3400\text{ cm}^{-1}$ which can be assigned to O-H stretching vibrations of the water molecules involved in hydrogen bonds. Both spectra shows bands in the range of $1550\text{ - }1560\text{ cm}^{-1}$ and $1421\text{ - }1495\text{ cm}^{-1}$ which are characteristic for asymmetric and symmetric stretching vibrations of the carboxylate groups. The aromatic C-C stretching vibrations are observed in the range of $1490\text{-}1510\text{ cm}^{-1}$ and the C-H deformation vibrations are observe between $766\text{-}873\text{ cm}^{-1}$.

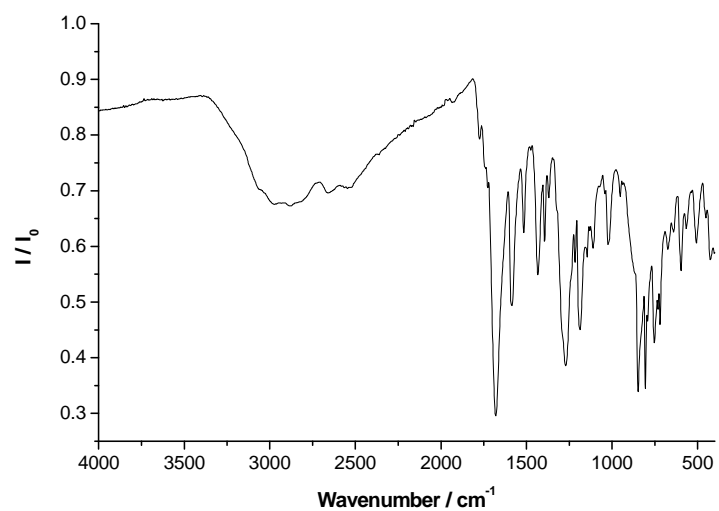


Fig. S38. IR-spectrum of $[\text{Bi}(\text{BTC})(\text{H}_2\text{O})]\cdot\text{H}_2\text{O}$ (**6**).

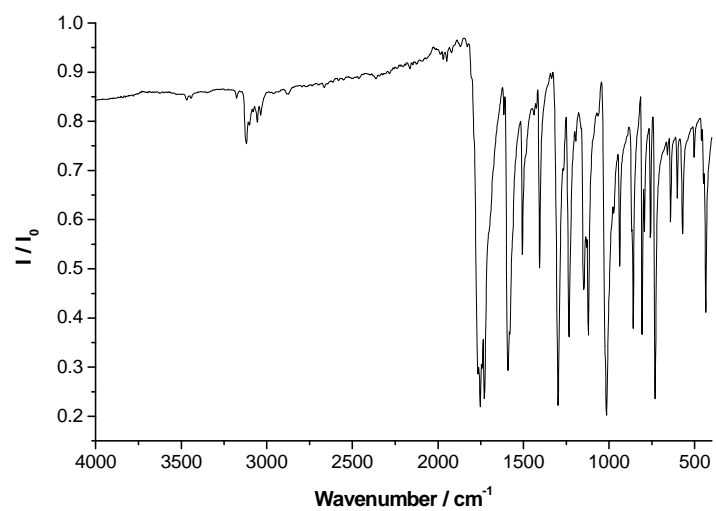
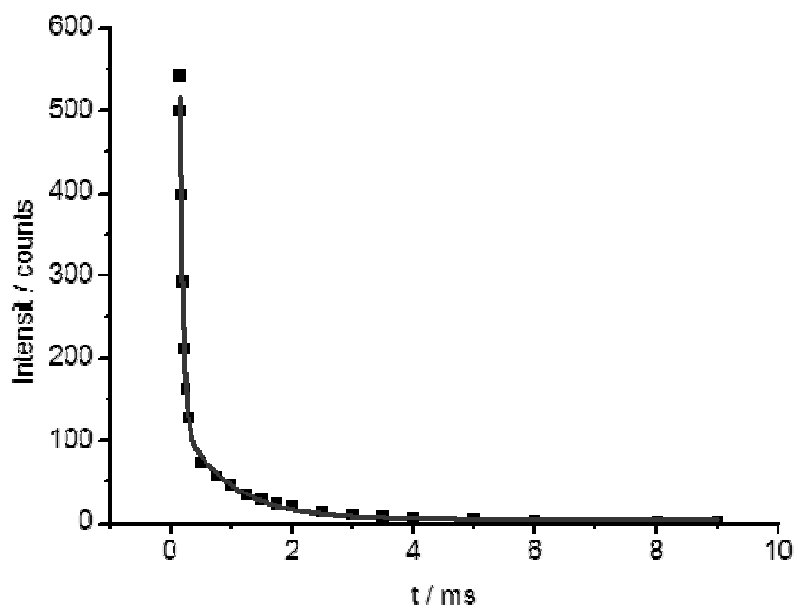


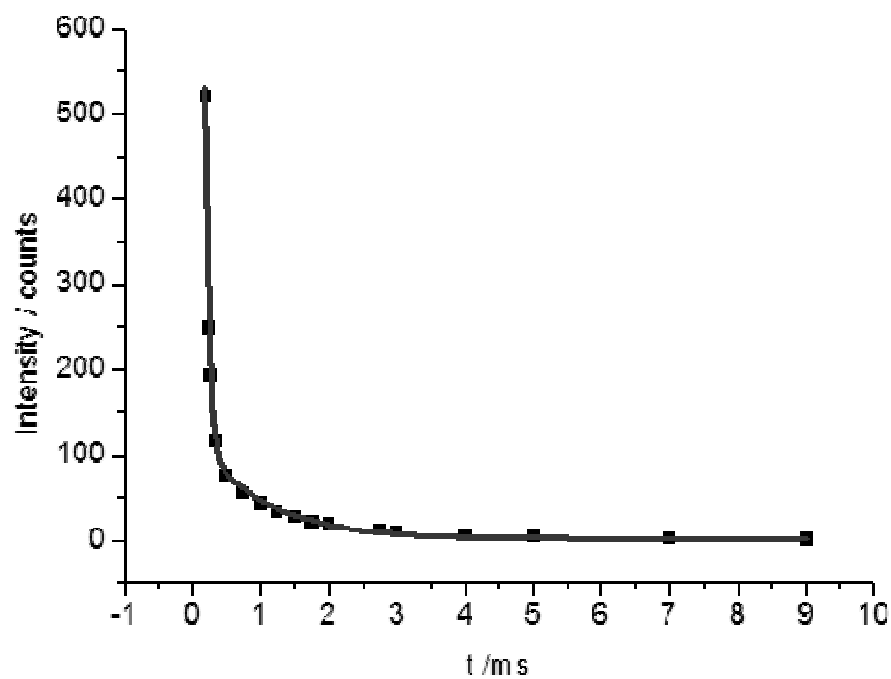
Fig. S39. IR-spectrum of $\text{Bi}_2(\text{O})(\text{OH})(\text{HBTC})(\text{NO}_3)$ (**8**).

4. Results of luminescence measurements



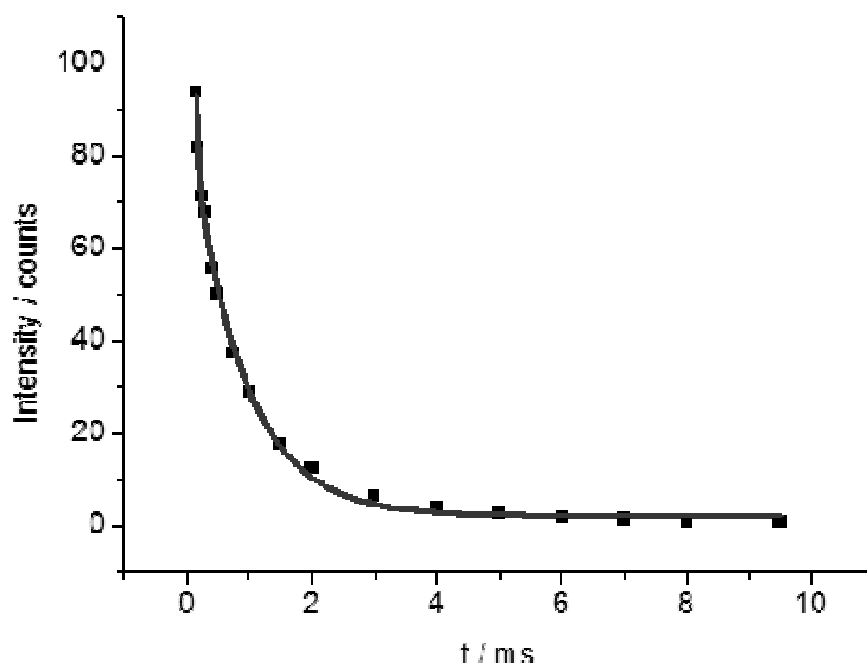
Equation	$y = y_0 + A_1 \cdot \exp(-(x-x_0)/t_1) + A_2 \cdot \exp(-(x-x_0)/t_2)$		
Reduced Chi-Sqr		74.86654	
Adj. R-Square		0.99718	
		Value	
	y0		4.67242
	x0		0.03599
	A1		4022.48266
	t1		0.04909
	A2		135.96368
	t2		0.80688

Fig. 40. Exponential fit of the time dependent decay at 550 nm of compound 1.



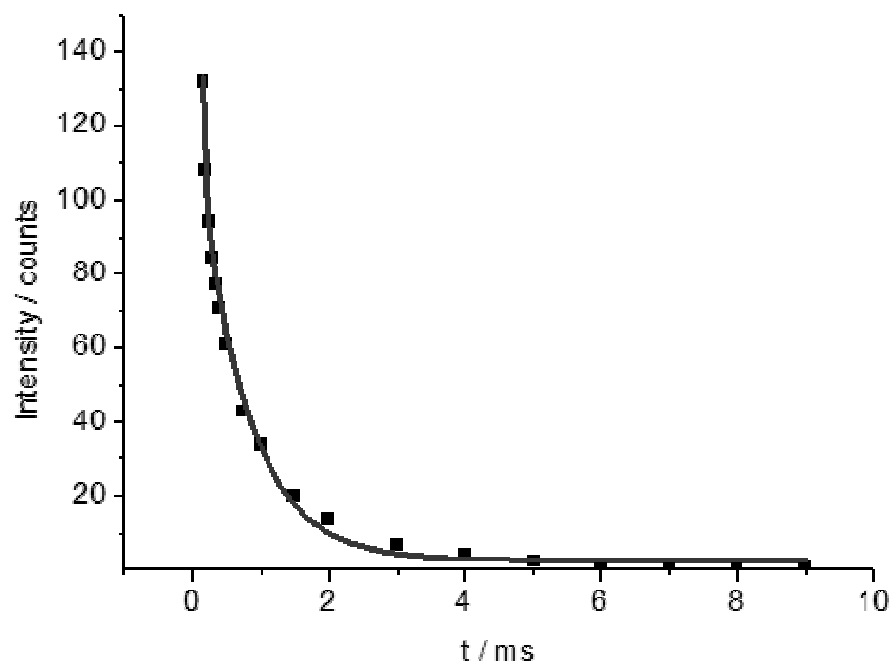
Equation	$y = y_0 + A_1 \cdot \exp(-(x-x_0)/t_1) + A_2 \cdot \exp(-(x-x_0)/t_2)$		
Reduced Chi-Sqr		7.76749	
Adj. R-Square		0.99954	
		Value	
	y0		3.52095
	x0		0.03597
	A1		124.28341
	t1		0.86546
	A2		10879.0115
	t2		0.05014

Fig. 41. Exponential fit of the time dependent decay at 510 nm of compound **1**.



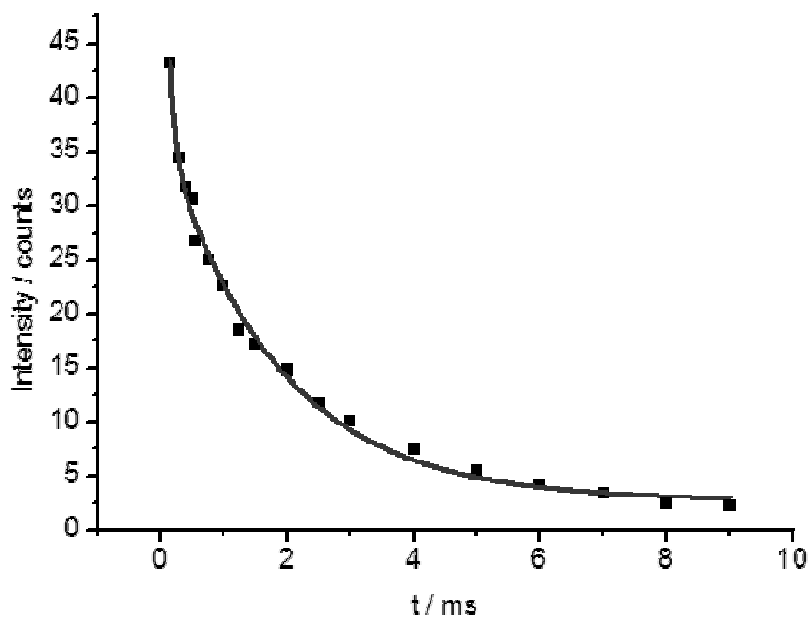
Equation	$y = y_0 + A_1 \cdot \exp(-(x-x_0)/t_1) + A_2 \cdot \exp(-(x-x_0)/t_2)$		
Reduced Chi-Sqr		2.71914	
Adj. R-Square		0.99741	
		Value	
	y0		1.63743
	x0		0.05717
	A1		74.2619
	t1		0.96543
	A2		50.7612
	t2		0.11395

Fig. 42. Exponential fit of the time dependent decay at 550 nm of compound 2.



Equation	$y = y_0 + A_1 \cdot \exp(-(x-x_0)/t_1) + A_2 \cdot \exp(-(x-x_0)/t_2)$		
Reduced Chi-Sqr		1.61614	
Adj. R-Square		0.99913	
		Value	
	y0		1.74577
	x0		0.03914
	A1		126.87563
	t1		0.10898
	A2		94.37752
	t2		0.90427

Fig. 43. Exponential fit of the time dependent decay at 510 nm of compound 2.



Model	ExpDecay2		
Equation	$y = y_0 + A_1 \cdot \exp(-(x-x_0)/t_1) + A_2 \cdot \exp(-(x-x_0)/t_2)$		
Reduced Chi-Sqr		0.94536	
Adj. R-Square		0.99399	
		Value	
	y0		2.74767
	x0		0.05
	A1		30.26109
	t1		0.08
	A2		33.85672
	t2		1.79531

Fig. 44. Exponential fit of the time dependent decay at 540 nm of compound **3**.

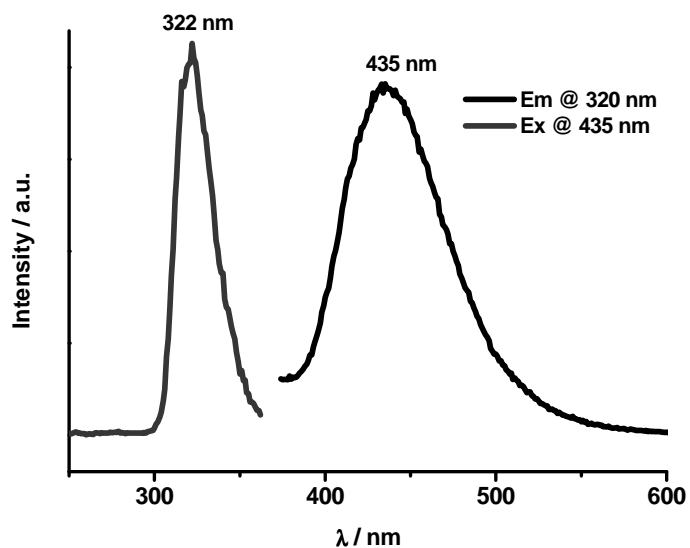


Fig. S45. Luminescence spectra of pyromellitic acid in a 2 M NaOH solution.

Table S8. Energies, assigned hkl values, observed and calculated d spacings of the EDXRD spectra.

Compound	energy/keV	hkl	$d_{\text{obs}}/\text{\AA}$	$d_{\text{calc}}/\text{\AA}$
1	29.54	001	9.35	9.19
	37.52	010	7.23	7.03
2	37.68	001	9.31	9.23
	38.12	200	7.36	7.26
	48.64	201/011	5.72	5.77 /5.60
		(not resolved)		(not resolved)
4	33.42	001	10.20	12.36
6	34.42	020	8.32	8.44
	45.02	111	6.01	6.17
7	22.42	020	12.35	12.52
	27.21	011	9.70	9.78

Supporting Information

**CAU-3: A new family of porous MOFs with a novel Al-based
brick: $[\text{Al}_2(\text{OCH}_3)_4(\text{O}_2\text{C-X-CO}_2)]$ (X=aryl)**

Helge Reinsch, Mark Feyand, Tim Ahnfeldt and Norbert Stock

Institute of Inorganic Chemistry, Christian-Albrechts-Universität, Max-Eyth-Straße 2, 24118
Kiel, Germany

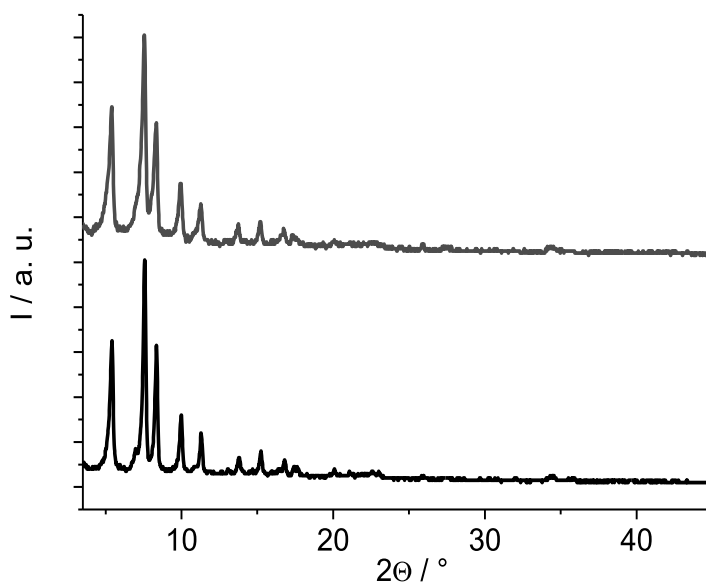


Figure S1: Powder pattern of an “as”-sample of CAU-3-BDC (black), and a sample after activation procedure and sorption measurement (red).

7. Anhang

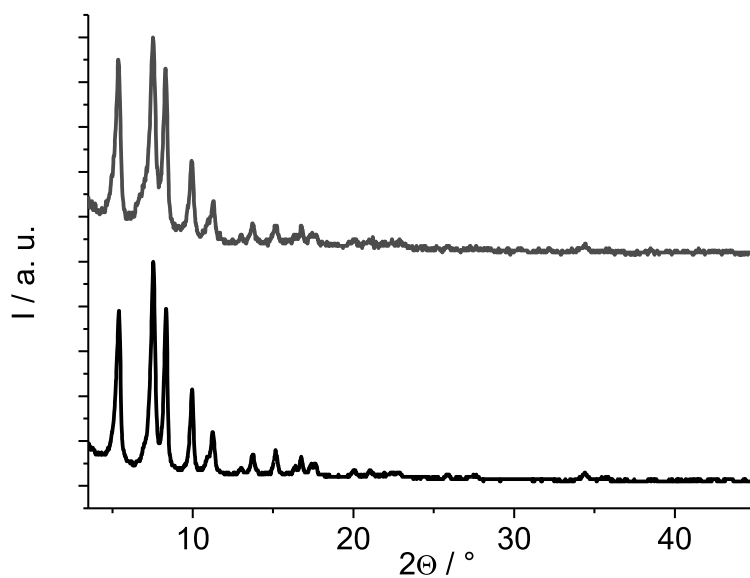


Figure S2: Powder pattern of an “as”-sample of CAU-3-BDC-NH₂ (black), and a sample after activation procedure and sorption measurement (red).

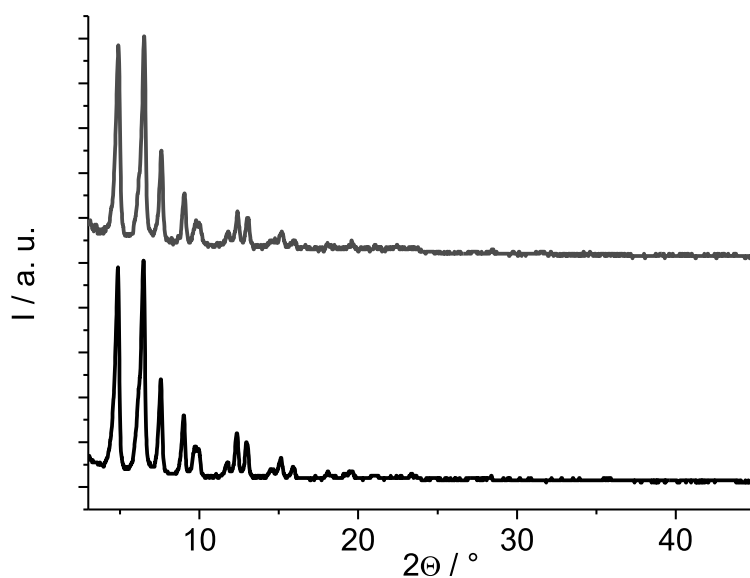


Figure S3: Powder pattern of an “as”-sample of CAU-3-NDC (black), and a sample after activation procedure and sorption measurement (red).

7.10. Kristallstrukturbestimmung von CAU-3

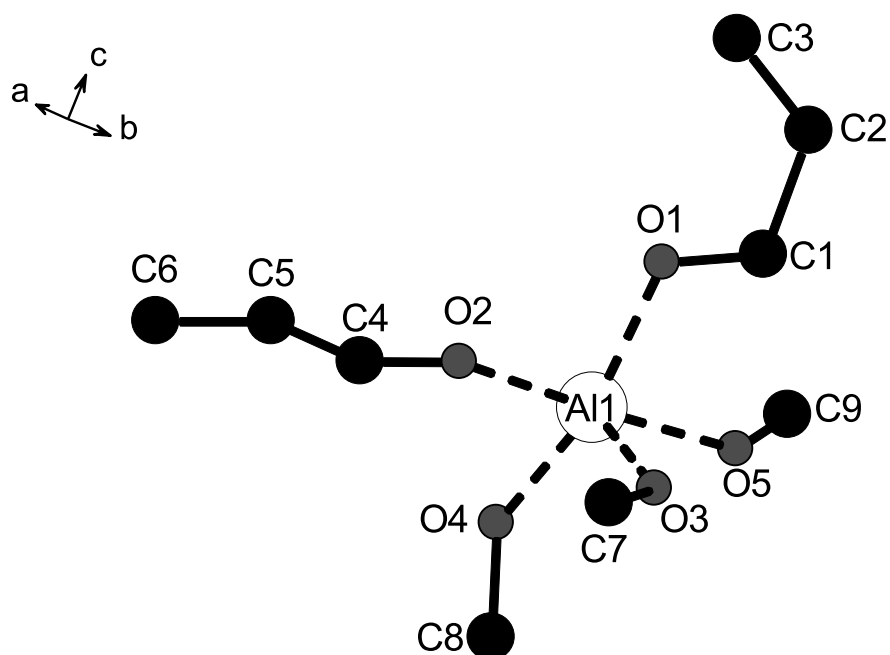


Figure S4: Asymmetric unit of CAU-3-BDC with numbering scheme.

Table S1: Selected bond lengths in CAU-3-BDC [Å].

<i>Atom 1</i>	<i>Atom 2</i>	<i>d / Å</i>			
Al1	O1	1.96(1)	C2	C3	1.39(1)
	O2	1.98(2)	O2	C4	1.23(1)
	O3	1.92(1)	C5	C6	1.37(1)
	O4	1.83(1)	O3	C7	1.47(3)
	O5	1.89(2)	O4	C8	1.46(2)
O1	C1	1.22(2)	O5	C9	1.51(3)
C1	C2	1.54(1)	C9	O5	1.51(3)

7. Anhang

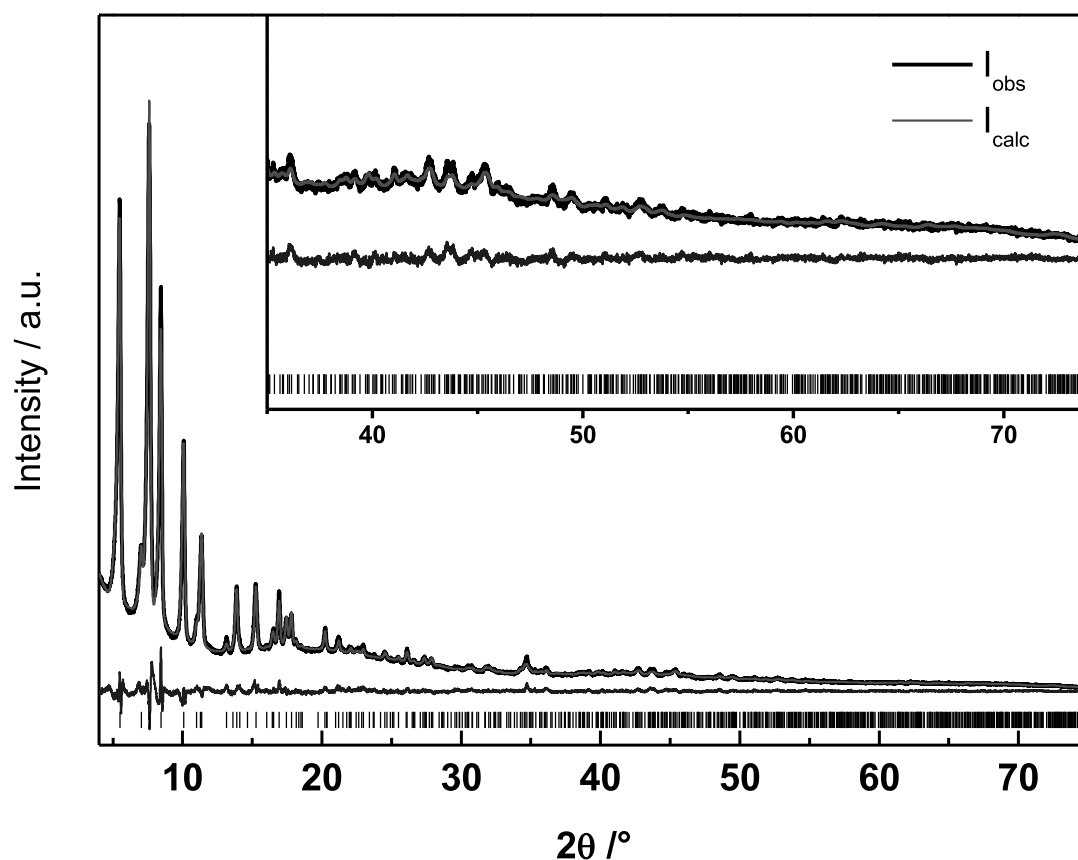


Figure S5: Final Rietveld plot of the refinement of CAU-3-BDC-NH₂. The observed intensities are shown in black, the calculated intensities are shown in red. The difference curve is shown below in blue, vertical bars mark the Bragg positions. The insert shows a plot enlargement from 35 -75 °2θ.

Table S2: Selected bond lengths in CAU-3-BDC-NH₂ [Å].

<i>Atom 1</i>	<i>Atom 2</i>	<i>d / Å</i>				
Al1	O1	1.99(2)	C3	C3	1.39(3)	
	O2	1.80(2)		O2	C4	1.39(5)
	O3	1.74(2)		C4	O2	1.39(3)
	O4	1.87(3)			C5	1.53(9)
	O5	1.99(4)		C5	C6	1.33(5)
O1	C1	1.23(5)	N1	C3	1.5 (1)	
C1	C2	1.60 (2)	N2	C6	1.5(1)	
C2	C3	1.38 (6)				

7.10. Kristallstrukturbestimmung von CAU-3

Table S3: Atomic coordinates of CAU-3-NDC obtained from the force field calculations using Materials Studio 5.0.

<i>Symbol</i>	<i>x/a</i>	<i>y/b</i>	<i>z/c</i>				
Fe1	0.25217	0.05104	0.51501	C23	0.34838	0.16804	0.47475
O2	0.27995	0.07593	0.55811	O24	0.18921	0.08691	0.51862
O3	0.32005	0.02894	0.51211	C25	0.15431	0.07905	0.54788
O4	0.21924	0.01434	0.47145	C26	0.31919	0.97871	0.49943
C5	0.26741	0.0306	0.44692	H27	0.31796	0.05445	0.456
C6	0.24497	0.90175	0.2889	H28	0.26201	0.06152	0.42827
C7	0.24115	0.91213	0.32179	H29	0.26215	0.9876	0.43382
C8	0.19049	0.86321	0.34061	H30	0.28504	0.94023	0.27504
C9	0.14677	0.7935	0.29296	H31	0.27804	0.9583	0.33253
C10	0.19805	0.84234	0.27414	H32	0.11043	0.7473	0.28205
Fe11	0.0794	0.26015	0.48371	H33	0.10738	0.20825	0.54132
O12	0.11136	0.28559	0.44055	H34	0.03412	0.14329	0.52646
O13	0.06741	0.33477	0.4861	H35	0.04152	0.18272	0.56665
O14	0.04232	0.23563	0.52706	H36	0.54135	0.665	0.47882
C15	0.05494	0.18882	0.54084	H37	0.43518	0.56247	0.47513
C16	0.5384	0.61932	0.48658	H38	0.63177	0.55735	0.51734
C17	0.47766	0.56072	0.48441	H39	0.31608	0.15723	0.45372
C18	0.47197	0.50052	0.49396	H40	0.3848	0.15121	0.47182
C19	0.58885	0.55858	0.50829	H41	0.3791	0.22248	0.47602
C20	0.59464	0.61894	0.49844	H42	0.1003	0.04938	0.54346
C21	0.29241	0.12878	0.57297	H43	0.16228	0.12602	0.55768
O22	0.31378	0.14379	0.50389	H44	0.16881	0.05767	0.56752

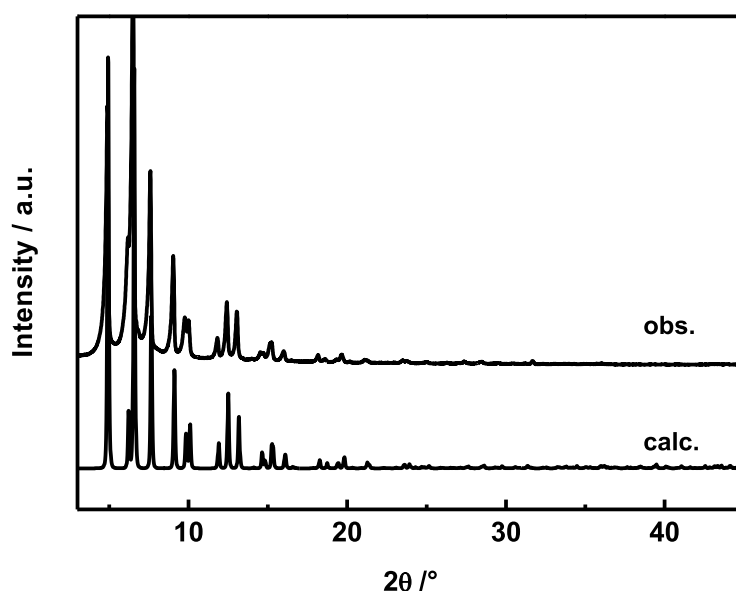


Figure S6: Calculated and observed powder pattern obtained from force field calculation.

7. Anhang

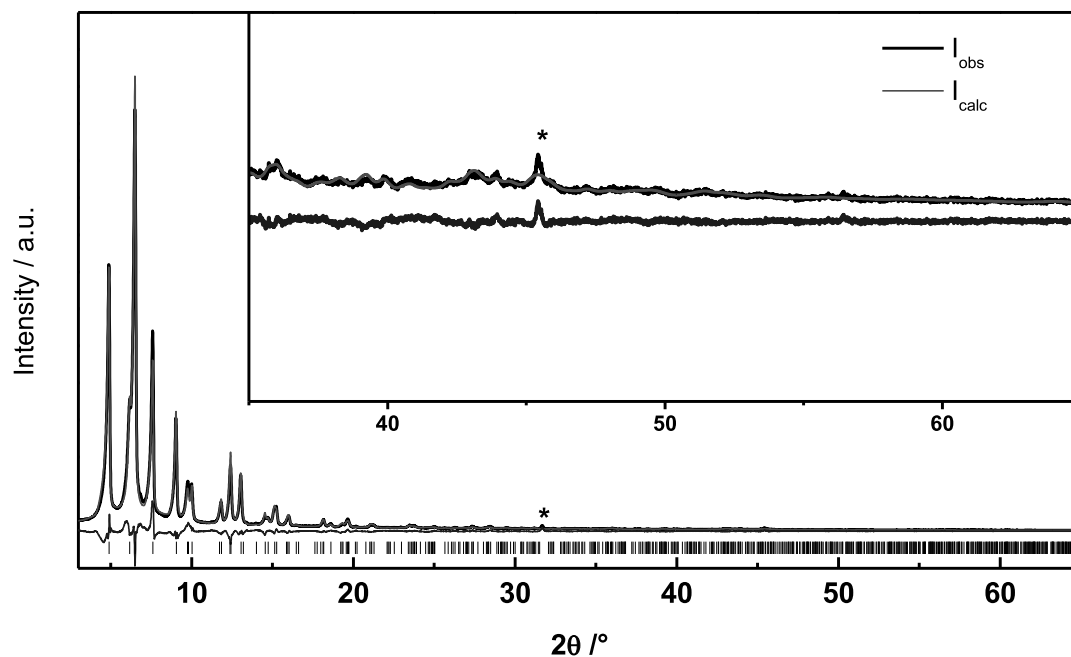


Figure S7: Final Rietveld plot of CAU-3-NDC. The asterisks correspond to NaCl as a by-product. The observed intensities are shown in black, the calculated intensities are shown in red. The difference curve is shown below in blue, vertical bars mark the Bragg positions. The insert shows a plot enlargement from 35 -65 °2θ.

Table S4: Selected bond lengths of CAU-3-NDC [Å]

Atom 1	Atom 2	d /				
Al1	O1	1.8(2)	C3	C4	1.4(3)	
	O4	1.8(2)	C4	C5	1.3(3)	
	O5	1.9(2)	C5	C5	1.3(4)	
	O6	1.9(2)		C6	1.5(6)	
	O7	1.8(1)	O3	C7	1.2(3)	
	O8	2.0(3)	O4	C7	1.2(2)	
	Al2	O2	1.8(2)	C7	C8	1.5(2)
		O3	1.8(1)	C8	C9	1.3(6)
O5		2.0(3)		C12	1.4(6)	
O6		1.9(3)		C7	1.5(2)	
O7		1.9(2)	C9	C10	1.3(4)	
O8		2.0(2)	C10	C11	1.3(7)	
O1		C1	1.2(4)	C11	C12	1.3(4)
O2		C1	1.2(4)	O5	C13	1.4(2)
C1	C2	1.4(3)	O6	C16	1.3(4)	
C2	C3	1.4(1)	O7	C14	1.3(2)	
	C6	1.4(4)	O8	C15	1.4(2)	

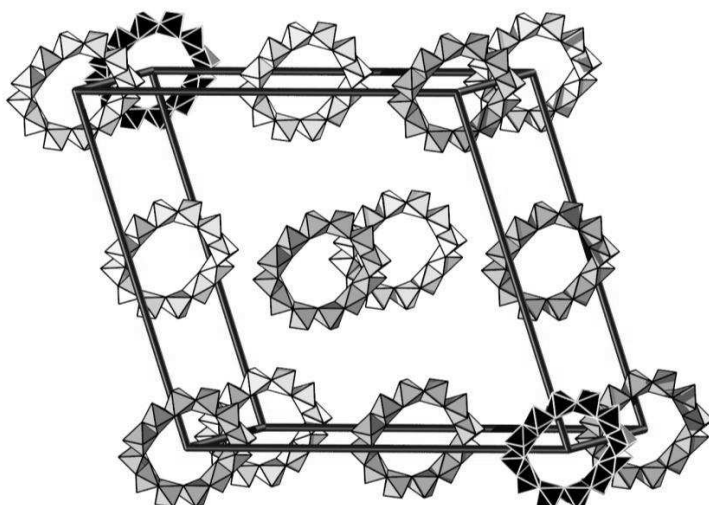


Figure S8: Pseudo-fcc-arrangement of the inorganic units. The colours emphasize the ABC-stacking,

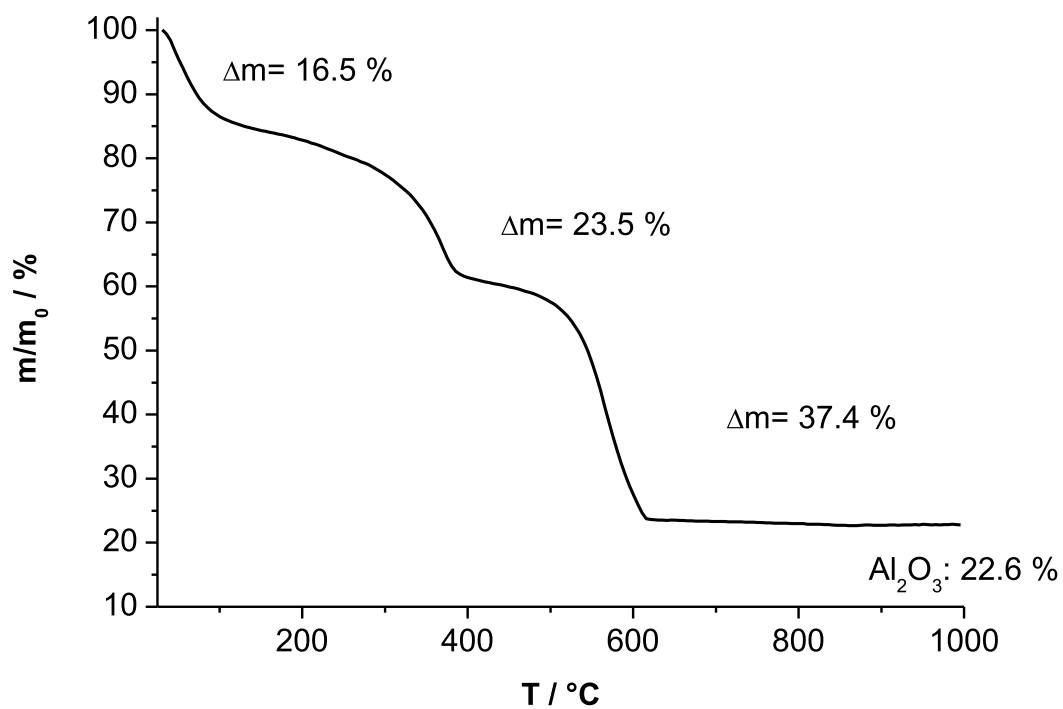


Fig. S9: TG-curve for CAU-3-BDC (1).

7. Anhang

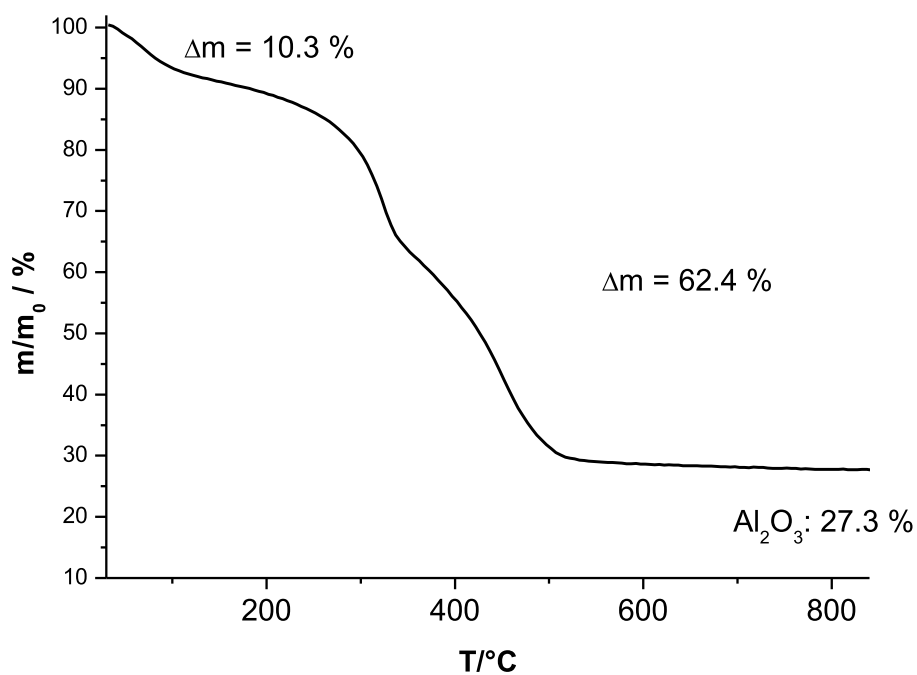


Figure S10. TG-diagram of the decomposition of CAU-3-BDC-NH₂ (2).

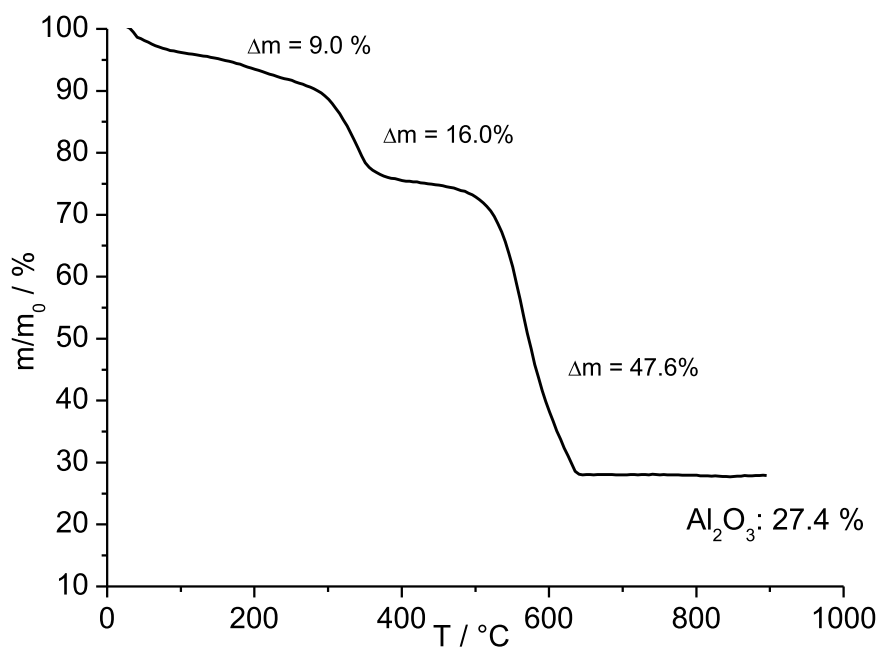


Figure S11. TG-diagram of the decomposition of CAU-3-NDC (3).

Table S5: Exact amounts of starting materials used in the discovery of CAU-3-BDC.

Reaktor No.	molar ratio		molar ratio		amount		amount		mass		volume	
	H ₂ BDC	AlCl ₃ *6H ₂ O	H ₂ BDC	NaOH	H ₂ BDC	AlCl ₃ *6H ₂ O	NaOH	AlCl ₃ *6H ₂ O	H ₂ BDC	AlCl ₃ *6H ₂ O	NaOH [μL]	MeOH [μL]
1	0,25	1	32	0,5	128	64	5	31	32	1368		
2	0,25	1	32	0,75	128	96	5	31	48	1352		
3	0,25	1	32	1,25	128	160	5	31	80	1320		
4	0,25	1	32	1,5	128	192	5	31	96	1304		
5	0,25	1	32	1,75	128	224	5	31	112	1288		
6	0,25	1	32	2	128	256	5	31	128	1272		
7	0,25	1	32	1	128	130	5	31	65	935		
8	0,25	1	32	1	128	130	5	31	65	1185		
9	0,25	1	32	1	128	130	5	31	65	1435		
10	0,50	2	64	2	256	260	11	62	130	870		
11	0,50	2	64	2	256	260	11	62	130	1120		
12	0,50	2	64	2	256	260	11	62	130	1370		
13	0,50	2	64	1	256	128	11	62	64	1336		
14	0,50	2	64	1,25	256	160	11	62	80	1320		
15	0,50	2	64	1,50	256	192	11	62	96	1304		
16	0,50	2	64	1,75	256	224	11	62	112	1288		
17	0,50	2	64	2	256	256	11	62	128	1272		
18	0,50	2	64	2,5	256	320	11	62	160	1240		
19	1	4	128	1,55	512	198	21	124	99	1301		
20	1	4	128	2,18	512	279	21	124	140	1260		
21	1	4	128	2,81	512	360	21	124	180	1220		
22	1	4	128	3,43	512	439	21	124	220	1180		
23	1	4	128	4,06	512	520	21	124	260	1140		
24	1	4	128	4,68	512	599	21	124	300	1100		

7. Anhang

Supporting Information For

Fuel purification, Lewis acid and aerobic oxidation catalysis performed by a microporous Co-BTT (BTT³⁻ = 1,3,5-benzenetristetrazolate) framework having coordinatively unsaturated sites

Shyam Biswas,^a Michael Maes,^b Amarajothi Dhakshinamoorthy,^c Mark Feyand,^a Dirk E. De Vos,^b Hermenegildo Garcia,^c and Norbert Stock^{*a}

^a *Institut für Anorganische Chemie, Christian-Albrechts-Universität, Max-Eyth-Strasse 2, 24118 Kiel, Germany. E-mail: stock@ac.uni-kiel.de; Tel: +49-4318801675; Fax: +49-4318801775*

^b *Centre for Surface Chemistry and Catalysis, Katholieke Universiteit Leuven, Kasteelpark Arenberg 23, 3001 Leuven, Belgium*

^c *Instituto Universitario de Tecnología Química CSIC-UPV and Departamento de Química, Universidad Politécnica de Valencia, Av. De los Naranjos s/n, 46022 Valencia, Spain*

Table of Contents:

Fig. S1 View of the (3,8)-connected topological net of 1	Page S2
Fig. S2 Theoretical and experimental XRPD patterns of 1	Page S3
Fig. S3 Theoretical and experimental XRPD patterns of 2	Page S4
Fig. S4 XRPD patterns of 1 in different forms	Page S5
Fig. S5 XRPD patterns of 2 in different forms	Page S6
Fig. S6 FT-IR spectra of as-synthesized 1 and 2	Page S7
Fig. S7 FT-IR spectra of methanol-exchanged 1 and 2	Page S7
Fig. S8 TG analysis of methanol-exchanged 1	Page S8
Fig. S9 TG analysis of hydrated 1	Page S8
Fig. S10 TG analysis of methanol-exchanged 2	Page S9
Fig. S11 TG analysis of hydrated 2	Page S9
Fig. S12 Fluorescence spectra of as-synthesized 2 and free H ₃ BTT	Page S10
Fig. S13 UV-Vis spectra of as-synthesized and thermally activated 1	Page S10
Fig. S14 Photos of 1 showing colour changes in different forms	Page S11
Fig. S15 Reusability test for ring opening of epoxide with 1	Page S11
Table S1 Elemental analyses of the compounds in different forms	Page S12
Table S2 Bond lengths for 1	Page S12
Table S3 Bond lengths for 2	Page S13

7. Anhang

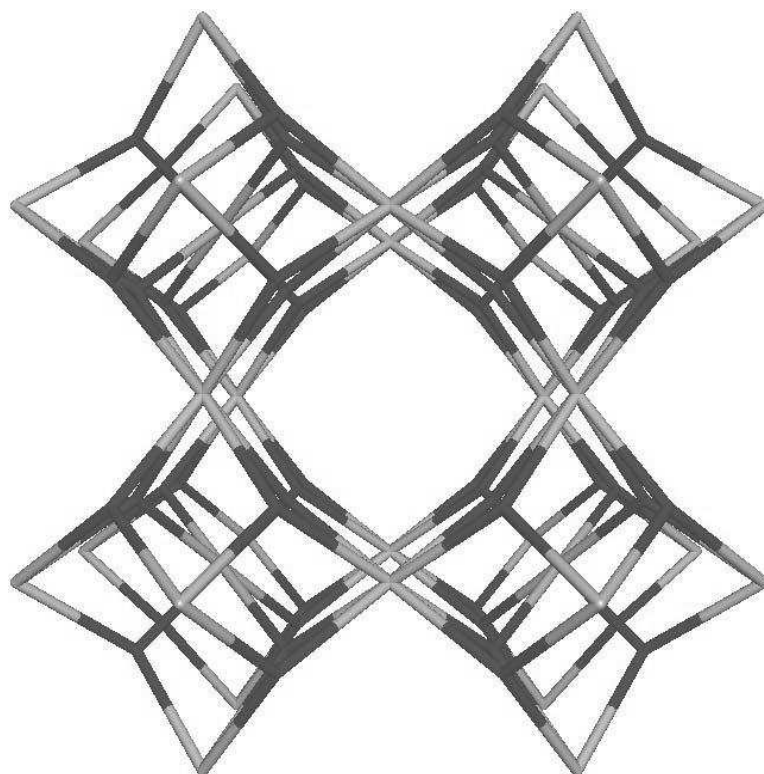


Fig. S1. Wire representation of a portion of the framework of **1** (or **2**) showing its 3D topological connectivity considering BTT ligands and square-planar $[M_4Cl]^{7+}$ units ($M = Co$, **1**; Cd , **2**) as 3 (blue) and 8 (grey) – connected nodes, respectively, to form the (3,8)-connected “Moravia” net.

7.11. Kristallstrukturbestimmung von Co-BTT und Cd-BTT

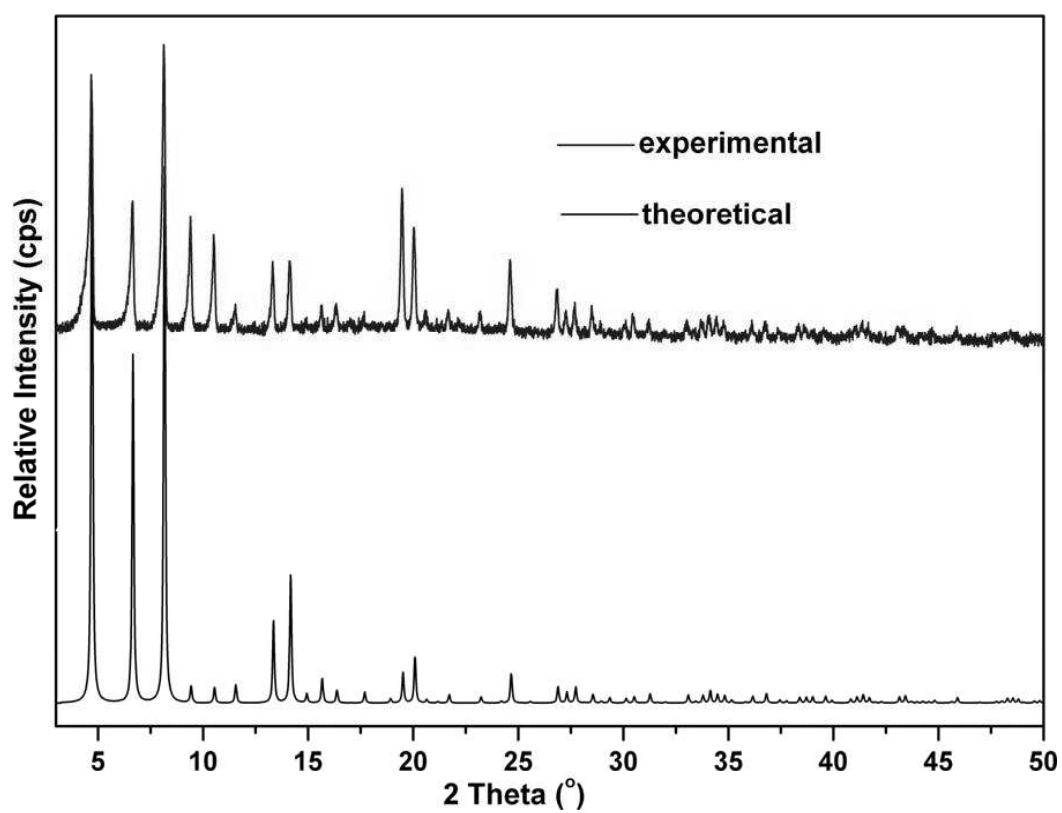


Fig. S2. Theoretical (black) and experimental (blue) XRPD patterns of 1.

7. Anhang

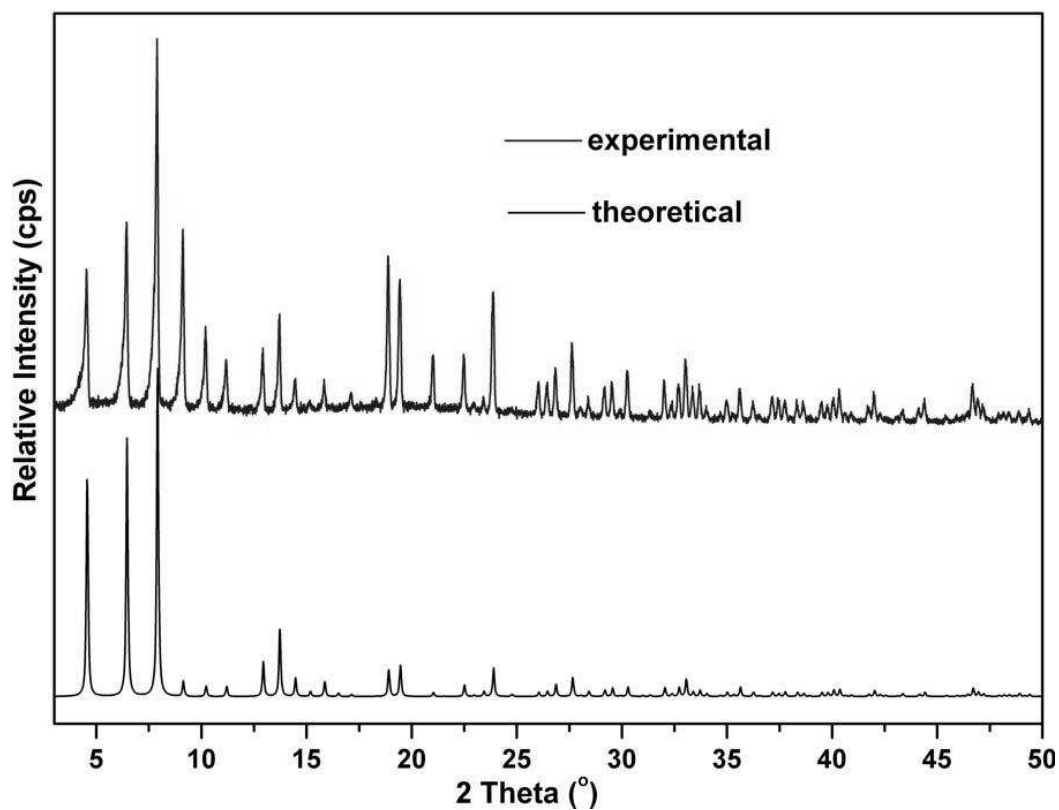


Fig. S3. Theoretical (black) and experimental (blue) XRPD patterns of 2.

7.11. Kristallstrukturbestimmung von Co-BTT und Cd-BTT

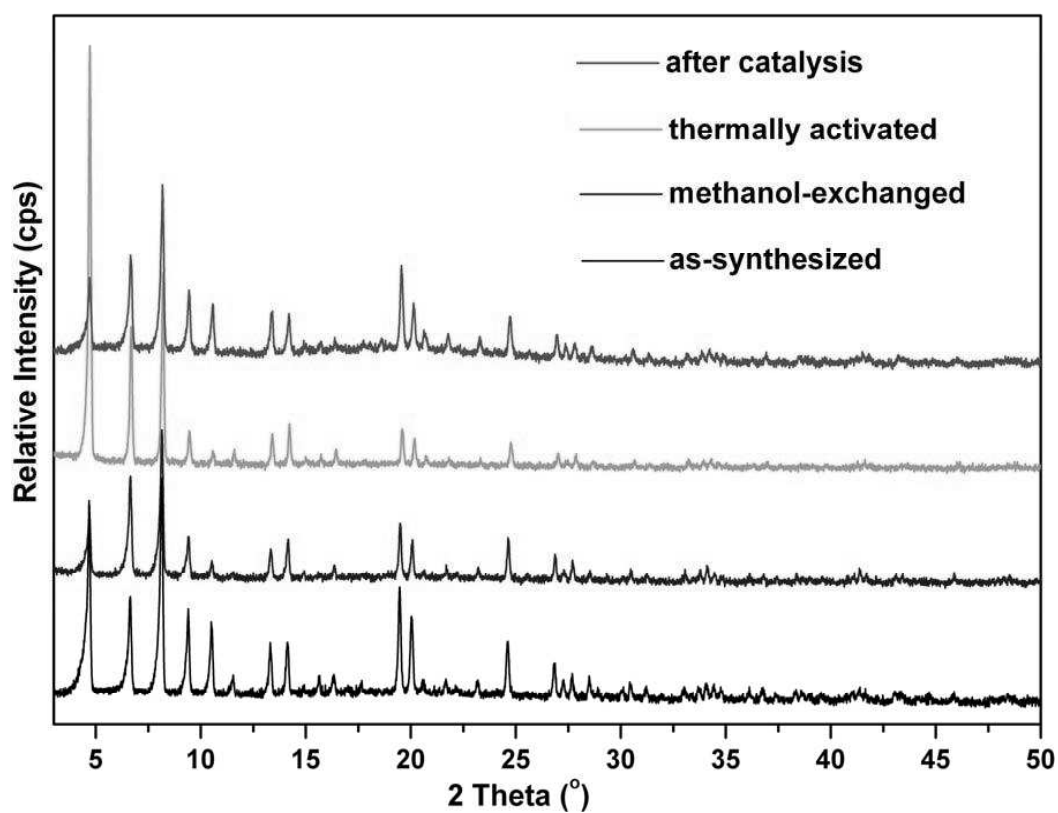


Fig. S4. XRPD patterns of **1** in different forms: as-synthesized (black), methanol-exchanged (blue), thermally activated (green), and after use in ring-opening of styrene oxide with methanol for thrice (red).

7. Anhang

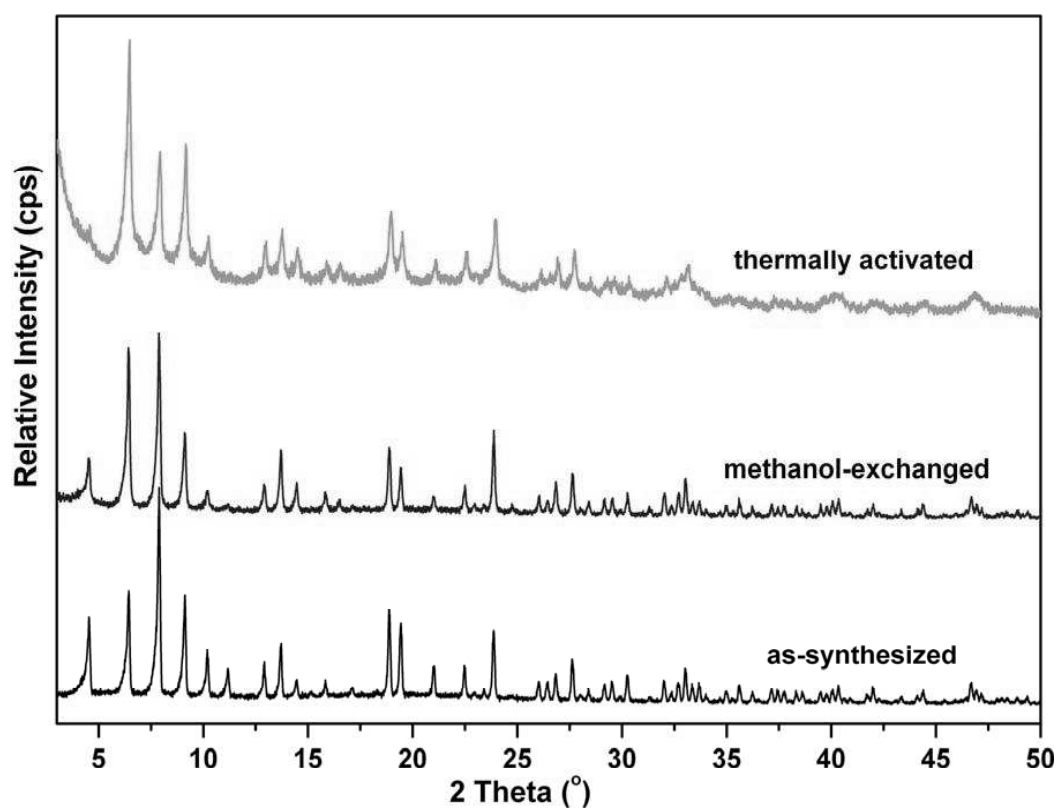


Fig. S5. XRPD patterns of **2** in different forms: as-synthesized (black), methanol-exchanged (blue), and thermally activated (green).

7.11. Kristallstrukturbestimmung von Co-BTT und Cd-BTT

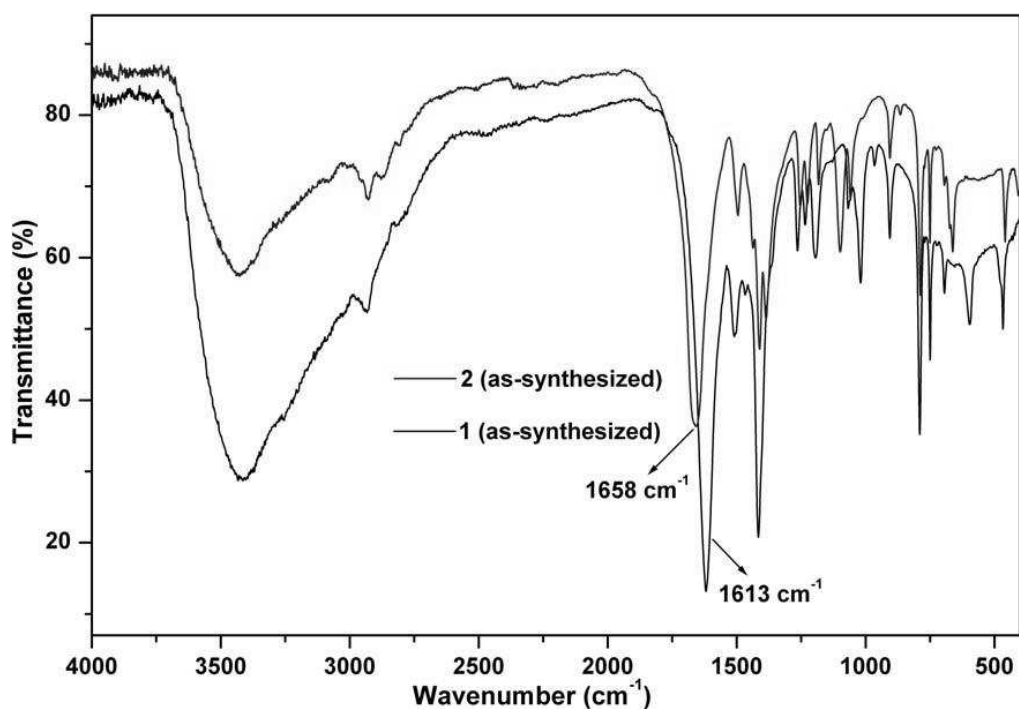


Fig. S6. Comparison between the FT-IR spectra of as-synthesized **1** (black) and **2** (blue).

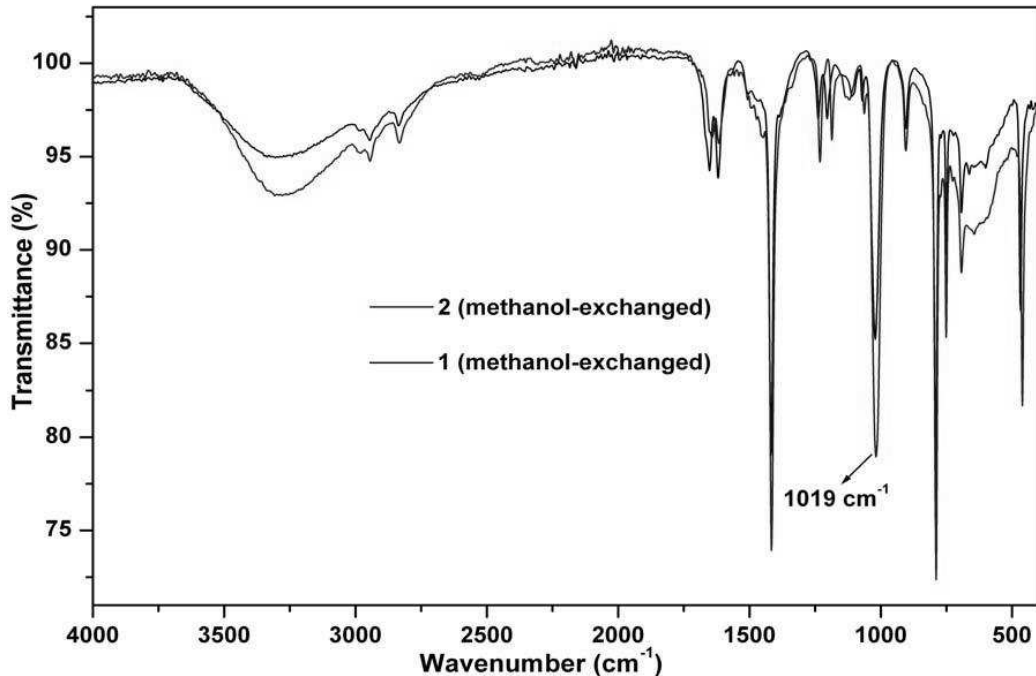


Fig. S7. Comparison between the FT-IR spectra of methanol-exchanged **1** (black) and **2** (blue).

7. Anhang

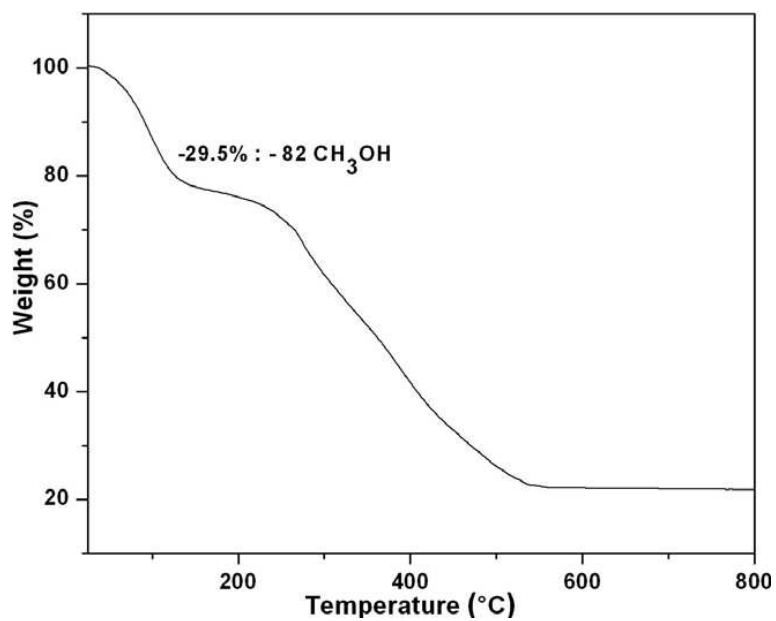


Fig. S8. TG analysis of methanol-exchanged 1.

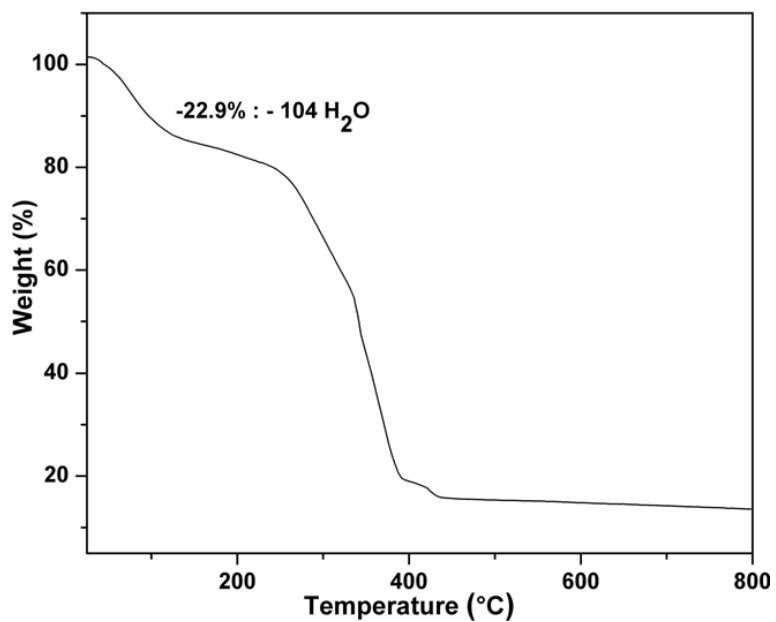


Fig. S9. TG analysis of hydrated 1.

7.11. Kristallstrukturbestimmung von Co-BTT und Cd-BTT

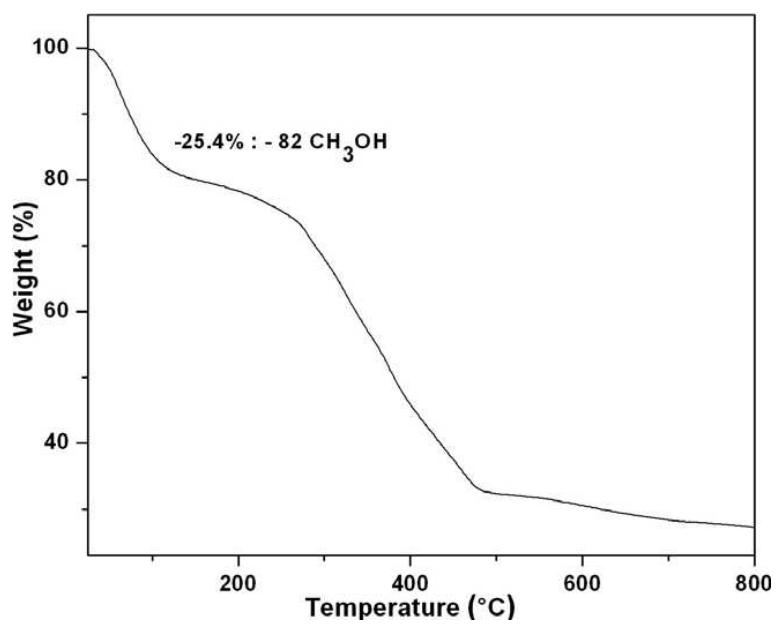


Fig. S10. TG analysis of methanol-exchanged 2.

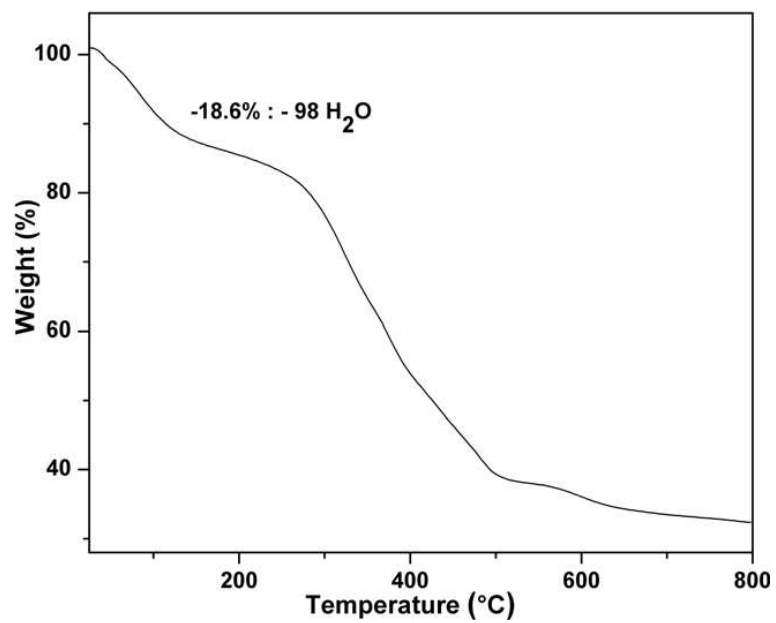


Fig. S11. TG analysis of hydrated 2.

7. Anhang

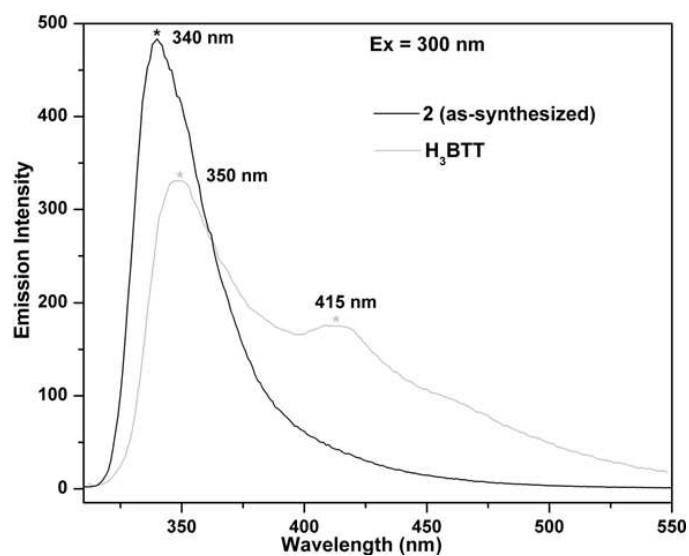


Fig. S12. Solid-state photoluminescence spectra of as-synthesized **2** and free H₃BTT ligand.

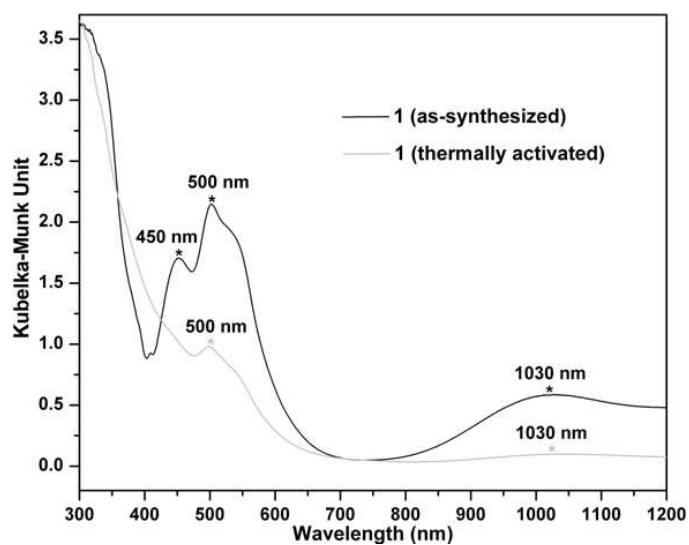


Fig. S13. Solid-state UV-Vis spectra of as-synthesized and thermally activated **1**.

7.11. Kristallstrukturbestimmung von Co-BTT und Cd-BTT

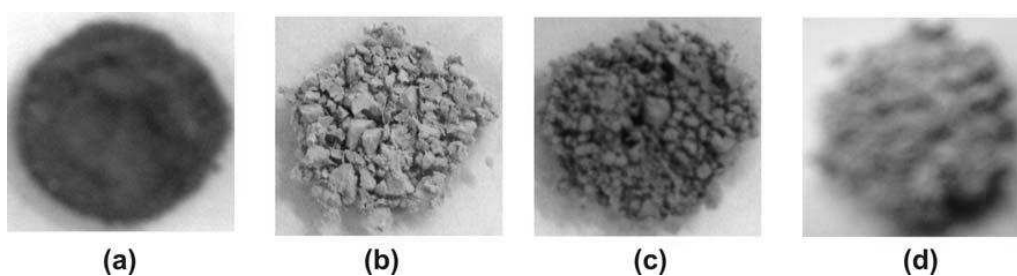


Fig. S14. Photos of **1** showing colour changes in different forms: (a) as-synthesized, (b) methanol-exchanged, (c) thermally activated and (d) after catalysis.

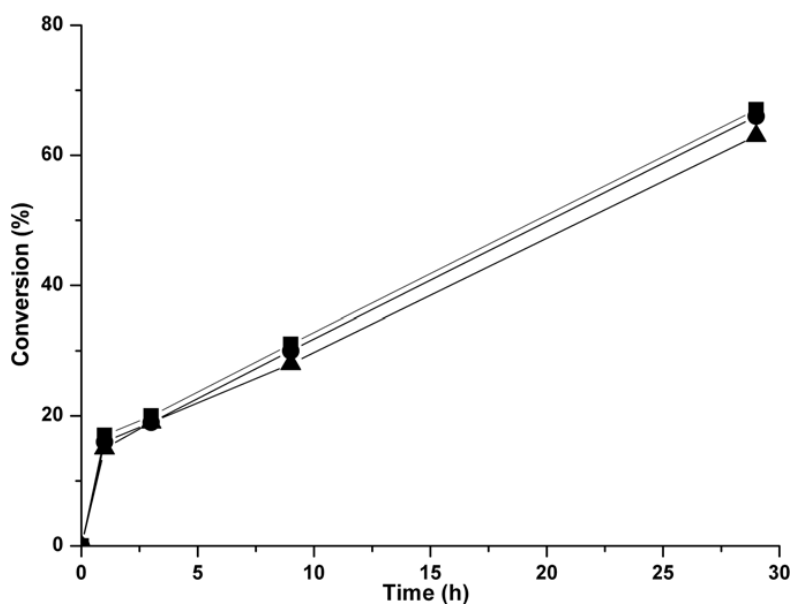


Fig. S15. Reusability test for ring opening of epoxide with methanol using thermally activated **1** as catalyst. Squares, circles and triangles correspond to the first, second and third cycle, respectively. Reaction conditions: (a) styrene oxide (0.1 mL), thermally activated **1** (20 mg), methanol (5 mL), 50 °C.

7. Anhang

Table S1. Elemental analyses of the compounds in different forms.

Compound	Molecular Formula	C _{obs.} / C _{cal.} (%)	H _{obs.} / H _{cal.} (%)	N _{obs.} / N _{cal.} (%)
1-as-synthesized	[Co(C ₄ H ₉ NO) ₆] ₃ [(Co ₄ Cl) ₃ (C ₉ H ₃ N ₁₂) ₈ (H ₂ O) ₁₂] ₂ ·12H ₂ O	30.34 / 30.56	3.21 / 3.34	34.27 / 34.65
1-methanol-exchanged	[Co(CH ₃ OH) ₆] ₃ [(Co ₄ Cl) ₃ (C ₉ H ₃ N ₁₂) ₈ (CH ₃ OH) ₁₂] ₂ ·40(CH ₃ OH)	30.63 / 30.50	3.97 / 4.25	30.29 / 30.22
1-hydrated	[Co(H ₂ O) ₆] ₃ [(Co ₄ Cl) ₃ (C ₉ H ₃ N ₁₂) ₈ (H ₂ O) ₁₂] ₂ ·62(H ₂ O)	21.53 / 21.23	3.51 / 3.16	32.97 / 33.01
2-as-synthesized	[Cd(C ₃ H ₇ NO) ₆] ₃ [(Cd ₄ Cl) ₃ (C ₉ H ₃ N ₁₂) ₈ (H ₂ O) ₁₂] ₂ ·14(H ₂ O)·4(C ₃ H ₇ NO)	25.17 / 25.20	2.63 / 2.79	29.64 / 29.95
2-methanol-exchanged	[Cd(CH ₃ OH) ₆] ₃ [(Cd ₄ Cl) ₃ (C ₉ H ₃ N ₁₂) ₈ (CH ₃ OH) ₁₂] ₂ ·40(CH ₃ OH)	25.96 / 26.24	3.43 / 3.66	26.12 / 26.00
2-hydrated	[Cd(H ₂ O) ₆] ₃ [(Cd ₄ Cl) ₃ (C ₉ H ₃ N ₁₂) ₈ (H ₂ O) ₁₂] ₂ ·56(H ₂ O)	18.05 / 18.24	2.73 / 2.59	28.15 / 28.36

Table S2. Bond lengths (Å) for **1**.

Co(1)-O(1)	2.082(7)	N(2)-N(2)#6	1.317(7)
Co(1)-N(2)#1	2.098(3)	N(2)-N(1)	1.337(4)
Co(1)-N(2)	2.098(3)	N(1)-C(1)	1.348(4)
Co(1)-N(2)#2	2.098(3)	C(2)-C(3)#7	1.390(4)
Co(1)-N(2)#3	2.098(3)	C(2)-C(3)	1.390(4)
Co(1)-Cl(1)	2.6007(12)	C(2)-C(1)	1.448(7)
Cl(1)-Co(1)#1	2.6007(12)	C(1)-N(1)#6	1.348(4)
Cl(1)-Co(1)#4	2.6007(12)	C(3)-C(2)#8	1.390(4)
Cl(1)-Co(1)#5	2.6007(12)		

Symmetry operators used to generate equivalent atoms are #1: -x, y, -z+1; #2: -x, y, z; #3: x, y, -z+1; #4: x, z, -y+1; #5: -x, -y+1, -z+1; #6: x, -z+1, -y+1; #7: y, -z+1, -x+1; #8: -z+1, x, -y+1.

7.11. Kristallstrukturbestimmung von Co-BTT und Cd-BTT

Table S3. Bond lengths (Å) for **2**.

Cd(1)-O(1)	2.301(8)	C(1)-N(1)#6	1.335(4)
Cd(1)-N(2)#1	2.329(3)	C(1)-N(1)	1.335(4)
Cd(1)-N(2)#2	2.329(3)	C(1)-C(2)	1.476(7)
Cd(1)-N(2)	2.329(3)	N(1)-N(2)	1.326(4)
Cd(1)-N(2)#3	2.329(3)	N(2)-N(2)#6	1.295(6)
Cd(1)-Cl(1)	2.8032(6)	C(3)-C(2)#7	1.385(4)
Cl(1)-Cd(1)#4	2.8032(6)	C(3)-C(2)	1.385(4)
Cl(1)-Cd(1)#5	2.8032(6)	C(2)-C(3)#8	1.385(4)
Cl(1)-Cd(1)#2	2.8032(6)		

Symmetry operators used to generate equivalent atoms are #1: x, -y, z; #2: -x+1, y, z; #3: -x+1, -y, z; #4: -z+1, -y, x; #5: -x+1, -y, -z+1; #6: -z+1, y, -x+1; #7: y+1, -z, -x+1; #8: -z+1, x-1, -y.

SUPPORTING INFORMATION

Title: Systematic Investigation of Porous Inorganic-Organic Hybrid Compounds with Photo-Switchable Properties

Author(s): A. Modrow, M. Feyand, D. Zargarani, R. Herges, N. Stock*

Ref. No.: Z201200048

Supplementary Material

Systematic investigation of porous inorganic-organic hybrid compounds with photo switchable properties

Antje Modrow, Mark Feyand, Dordaneh Zargarani, Rainer Herges, Norbert Stock

Institut für Anorganische Chemie, Christian-Albrechts-Universität, Max-Eyth-Straße 2, D-24118 Kiel (Germany)

Fax: (+49) 0431-880-1775

E-mail: stock@ac.uni-kiel.de

^bOtto-Diels-Institut für Organische Chemie, Christian-Albrechts-Universität, Otto-Hahn-Platz 4, D-24098 Kiel (Germany)

- (1) XRPD pattern of Zn-CAU-5, Co-CAU-5 and Cu-CAU-5
- (2) Colored Figure 3
- (3) ORTEP presentation of the asymmetric unit of [Co₂(NDC)₂(AzBIPY)]
- (4) N₂ adsorption isotherm of [Co₂(NDC)₂(AzBIPY)]
- (5) N₂ adsorption isotherm of [Cu₂(NDC)₂(AzBIPY)]
- (6) Results of the TG/DTA investigation of [Co₂(NDC)₂(AzBIPY)]
- (7) Results of the TG/DTA investigation of [Cu₂(NDC)₂(AzBIPY)]
- (8) Raman spectra of [Co₂(NDC)₂(AzBIPY)] and [Cu₂(NDC)₂(AzBIPY)]
- (9) ORTEP presentation of the asymmetric unit of [Zn₂(BPDC)₂(AzBIPY)]
- (10) ORTEP presentation of the asymmetric unit of [Zn₂(CCA)₂(AzBIPY)]
- (11) Crystallographic results of the CAA linker in [Zn₂(CCA)₂(AzBIPY)]
- (12) UV/Vis spectra of 3-azo-phenyl-4,4'-bipyridine in EtOH
- (13) UV/Vis spectra of the thermal relaxation of [Co₂(NDC)₂(AzBIPY)]
- (14) UV/Vis spectra of the thermal relaxation of [Cu₂(NDC)₂(AzBIPY)]
- (15) colored Figure 5
- (16) colored Figure 6
- (17) UV/Vis spectra of the thermal relaxation of [Cu₂(NDC)₂(AzBIPY)]

(18) UV/Vis spectra to investigate the photo stationary equilibrium of $[\text{Cu}_2(\text{NDC})_2(\text{AzBIPY})]$

(1) XRPD pattern of Zn-CAU-5, Co-CAU-5 and Cu-CAU-5

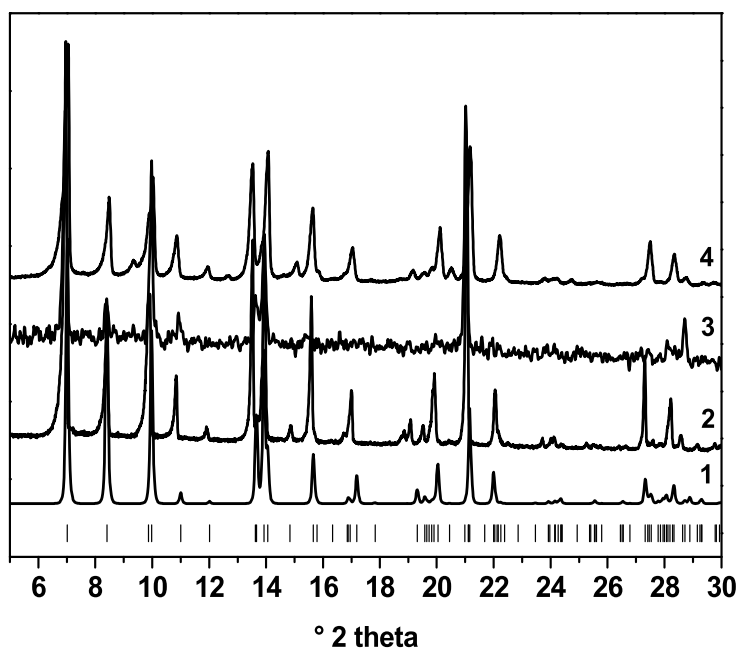


Fig. S1: XRPD-pattern of CAU-5 derivates: theoretical pattern of Zn-CAU-5 (1) and measured patterns of Zn-CAU-5 (2), Co-CAU-5 (3) and Cu-CAU-5 (4).

(2) Colored Figure 3

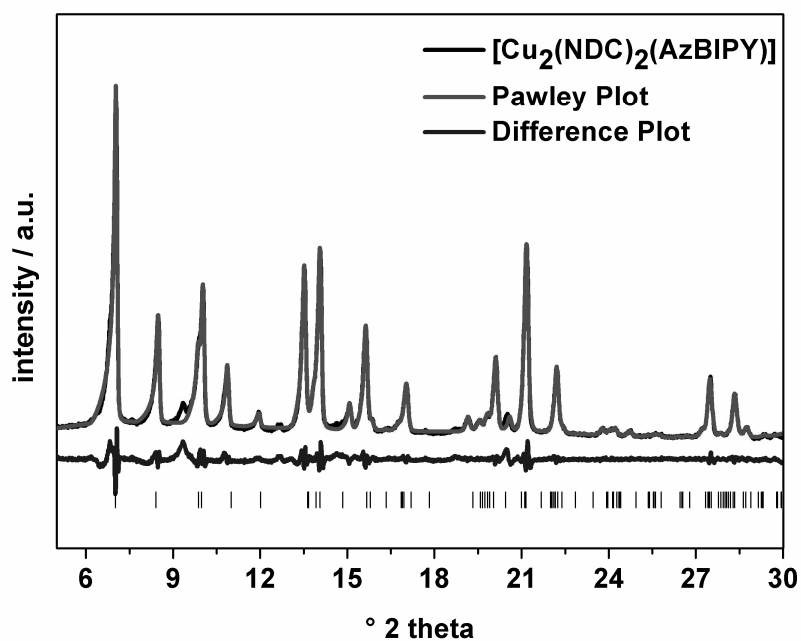


Figure 3. Collected powder pattern of $[\text{Cu}_2(\text{NDC})_2(\text{AzBIPY})]$ (black graph), Pawley fit (red graph) and the difference plot (blue graph). A minor crystalline impurity exhibiting a reflection at 9.3° (2θ) is detected.

(3) ORTEP presentation of the asymmetric unit of $[\text{Co}_2(\text{NDC})_2(\text{AzBIPY})]$

ORTEP presentation of **1**. The azo-bipyridine, is disordered. Therefore the 4,4'-bipyridine group is represented by the atoms N1, C13, C13A, C14, C14A, C15, C16, C16A, C17 and C17 A. The atoms N2, N3, C18, C18A, C19, C19A, C20 and C20A are part of the azo-phenyl moiety. Hydrogen atoms are omitted for clarity; thermal ellipsoids are shown at 65 % probability.

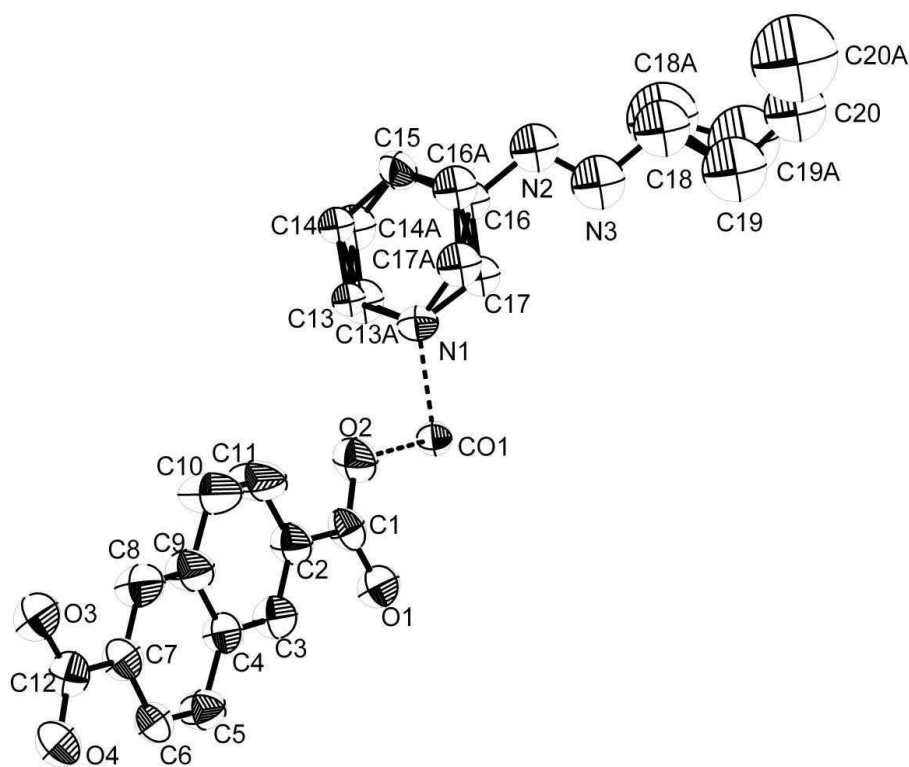


Fig. S3: Asymmetric unit of $[\text{Co}_2(\text{NDC})_2(\text{AzBIPY})]$.

(4) N₂ sorption isotherms of [Co₂(NDC)₂(AzBIPY)]

Figure S4 shows the N₂-sorption isotherm of [Co₂(NDC)₂(AzBIPY)] at 77 K. Evaluation of the data with the Brunauer-Emmett-Teller (BET) equation results in a specific surface area of $S_{\text{BET}} = 517 \text{ m}^2/\text{g}$. The micropore volume of $V_m = 0.22 \text{ cm}^3/\text{g}$ was determined at $p/p_0 = 0.5$.

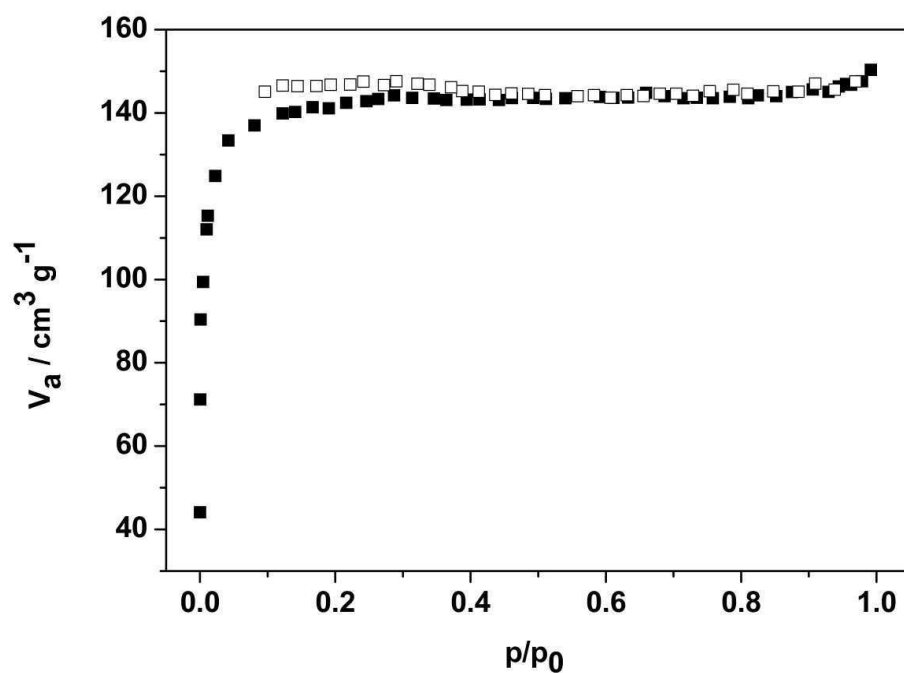


Fig. S4: N₂ adsorption (filled squares) and desorption (open squares) isotherm at 77 K of 1.

(5) N₂ adsorption isotherm of [Cu₂(NDC)₂(AzBIPY)]

Figure S5 shows the N₂-sorption and desorption isotherm of [Cu₂(NDC)₂(AzBIPY)]. With the BET equation a specific surface area of $S_{\text{BET}} = 488 \text{ m}^2/\text{g}$ was calculated. A micro pore volume (at $p/p_0 = 0.5$) of $V_m = 0.21 \text{ cm}^3/\text{g}$ was determined.

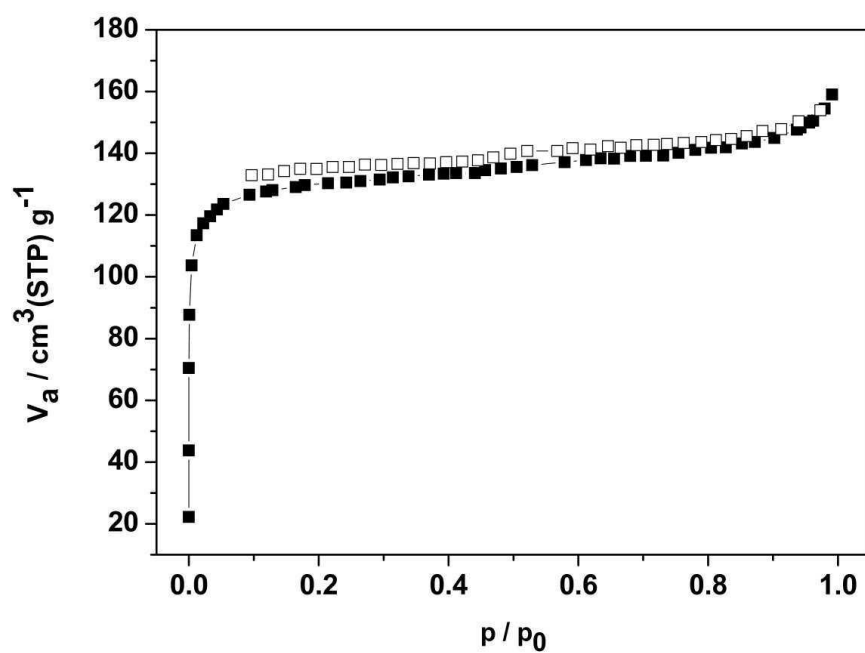


Fig. S5: N₂ adsorption (filled squares) and desorption (open squares) isotherm of 2.

(6) Results of the TG/DTA investigation of $[\text{Co}_2(\text{NDC})_2(\text{AzBIPY})]$

Figure S6 shows the results of the TG/DTA experiment of $[\text{Co}_2(\text{NDC})_2(\text{AzBIPY})]$: Between 350 and 500 °C a total weight loss of 85.6 % (weight loss calc. 85.4 %) is observed in one step, which is due to the oxidative decomposition. The final product was identified as CoO by X-ray powder diffraction (XRPD).

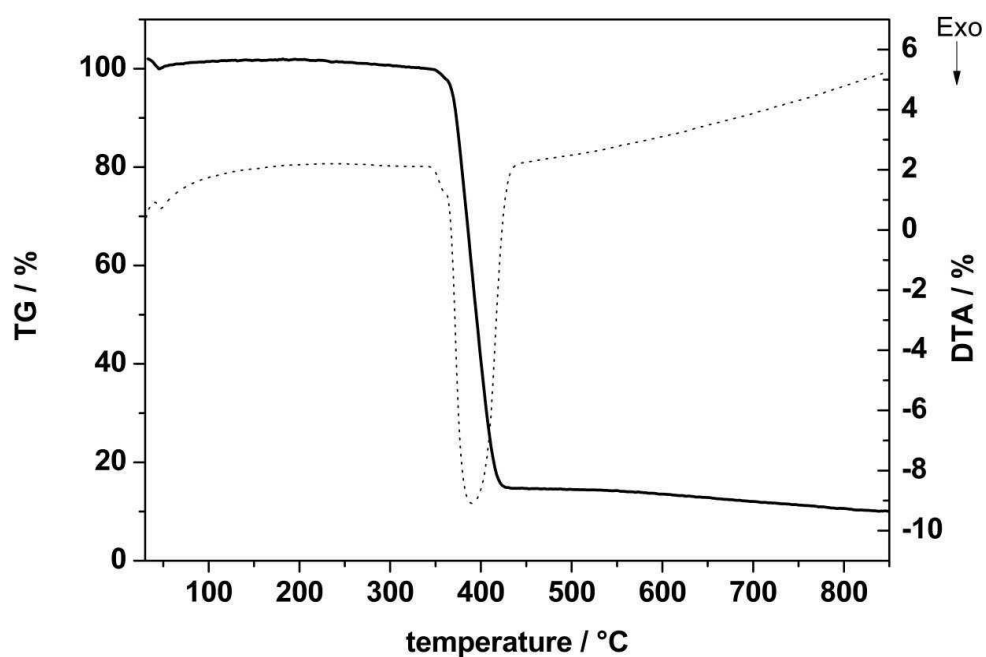


Fig. S6. TG and DTA curve of the thermal decomposition of $[\text{Co}_2(\text{NDC})_2(\text{AzBIPY})]$

(7) Results of the TG/DTA investigation of $[\text{Cu}_2(\text{NDC})_2(\text{AzBIPY})]$

Figure S7 shows the results of the TG/DTA experiment of $[\text{Cu}_2(\text{NDC})_2(\text{AzBIPY})]$: Between 300 and 400 °C a total weight loss of 84 % (weight loss calc. 84.4 %) is observed in one step, which is due to the oxidative decomposition. The final product was identified as CuO by X-ray powder diffraction (XRPD).

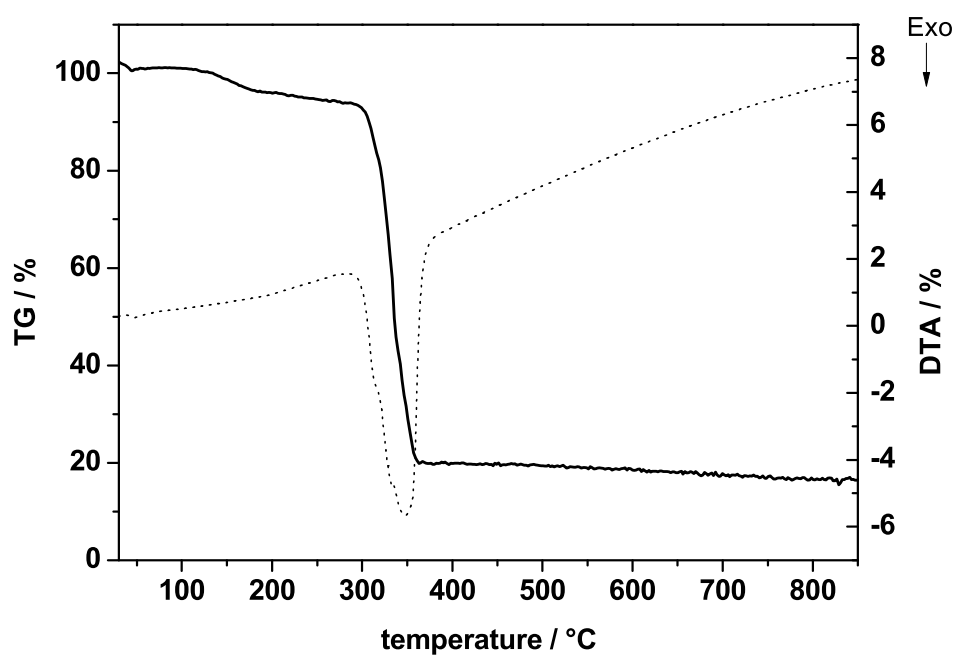


Fig. S7:

TG and DTA curve of the thermal decomposition of 2.

(8) Raman spectrum of $[\text{Co}_2(\text{NDC})_2(\text{AzBIPY})]$ and $[\text{Cu}_2(\text{NDC})_2(\text{AzBIPY})]$

Figure S8 shows the Raman spectrum of $[\text{Co}_2(\text{NDC})_2(\text{AzBIPY})]$, $[\text{Cu}_2(\text{NDC})_2(\text{AzBIPY})]$, AzBIPY and H_2NDC . The characteristic -N=N- stretching vibration at 1449 cm^{-1} / 1443 cm^{-1} is marked with an asterisks. All other characteristic vibration are listed in the table below (Tab. S1).

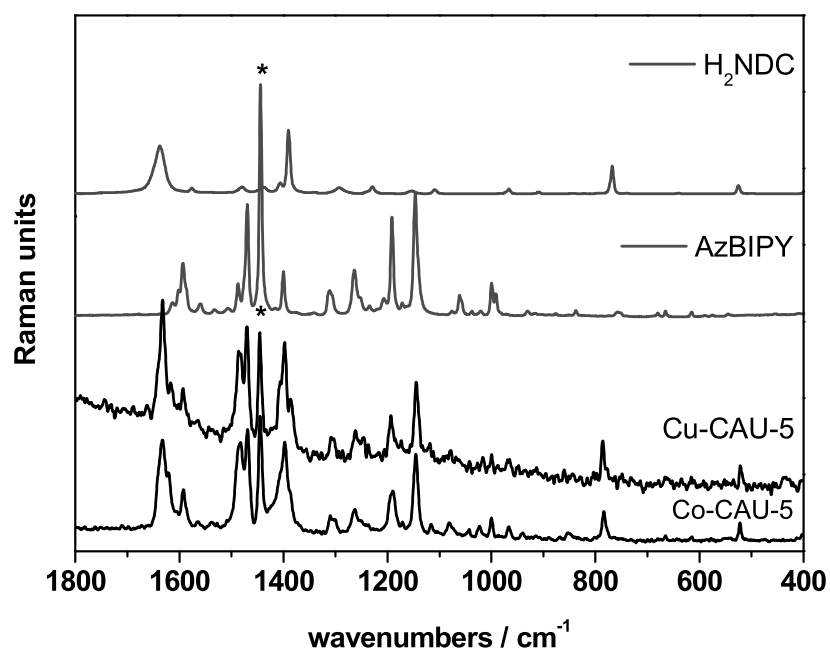


Fig. S8: Raman-spectra of Co-CAU-5, Cu-CAU-5, AzBIPY and H_2NDC .

Tab. S1: Assignment of Raman-signals of 1 and 2.

AzBIPY	NDC	[Co ₂ (NDC) ₂ (AzBIPY)]	[Cu ₂ (NDC) ₂ (AzBIPY)]	assignment
	1636	1633		C=C str. vib.
1594	1577	1591	1592	C=C str. vib.
1485	1479	1482	1486	s-m, C=C, C=N in plane vib. or C-H sym. def. vib.
1469		1469	1470	s-m, C=C, C=N in plane vib. or C-H sym. def. vib.
1443		1449	1443	<i>trans</i> N=N vib.
	1407			s-m, C=C, C=N in plane vib.
1398	1390	1397	1398	arom. ring vibration
		1309	1307	arom. ring vibration
1261		1264	1261	arom. C-H in plane def.
1199		1190	1194	arom. C-H in plane def.
1142		1146	1143	arom. C-H in plane def. vib.
		1024		C-O str. vib. or arom. C-H in plane. def. vib.
998		1000		s-m, C=C, C=N in plane vib. or arom. C-H in plane. def. vib.
	966	966		out-of-plane def. vib. (3 neigh. H)
		940		out-of-plane def. vib. (1 isolated H)
		852		naphthalene rings out-of plane vib.

(9) ORTEP presentation of the asymmetric unit of $[\text{Zn}_2(\text{BPDC})_2(\text{AzBIPY})]$

The ORTEP presentation of **3**. The azo-bipyridine, is disordered. Therefore the 4,4'-bipyridine consist of N1, C29, C30, C31, C32, C32A, C33, C33A, C34, C35, C36, C37, C38 and N4. The atoms N2A, N2B, N3, C39A, C39B, C40, C41, C42A, C42B, C43A, C43B, C44A, C44B are part of the azo-phenyl moiety. Hydrogen atoms are omitted for clarity; thermal ellipsoids are shown at 65 % probability.

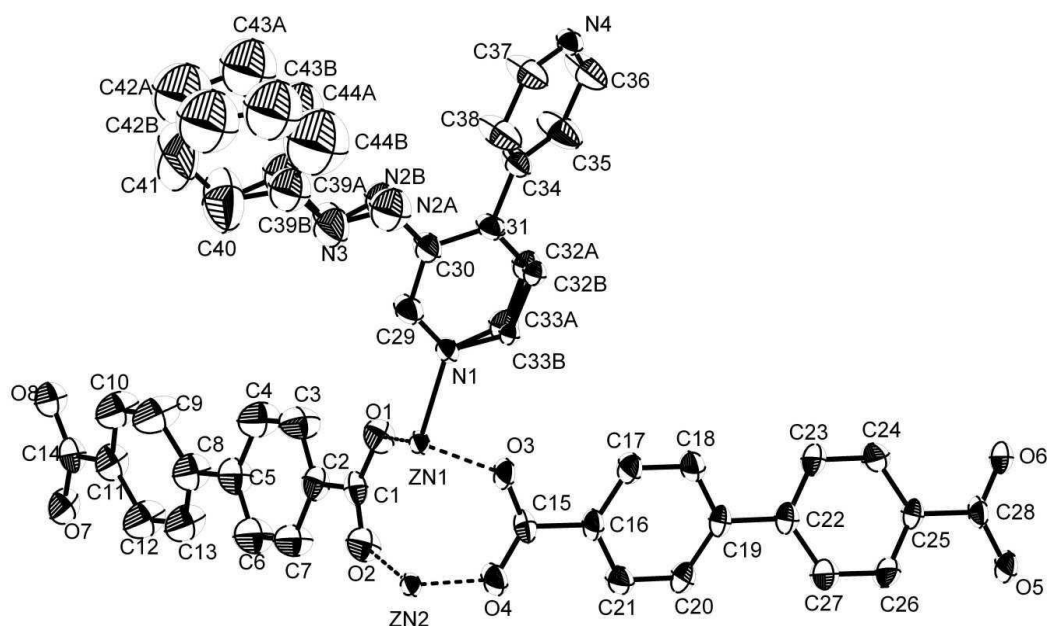


Fig. S9: Asymmetric unit of $[\text{Zn}_2(\text{BPDC})_2(\text{AzBIPY})]$.

(10) ORTEP presentation of the asymmetric unit of $[\text{Zn}_2(\text{CCA})_2(\text{AzBIPY})]$

ORTEP presentation of **4**. The azo-bipyridine, is disordered. Therefore the 4,4'-bipyridine consist of N1, C21, C22, C23, C24, C25, C26, C27, C28, C29, C30 and N4. The atoms N2, N3, C31, C32A, C32B, C33A, C33B, C34, C35A, C35B, C36A, and C36B are part of the azo-phenyl moiety. Hydrogen atoms are omitted for clarity; thermal ellipsoids are shown at 35 % probability.

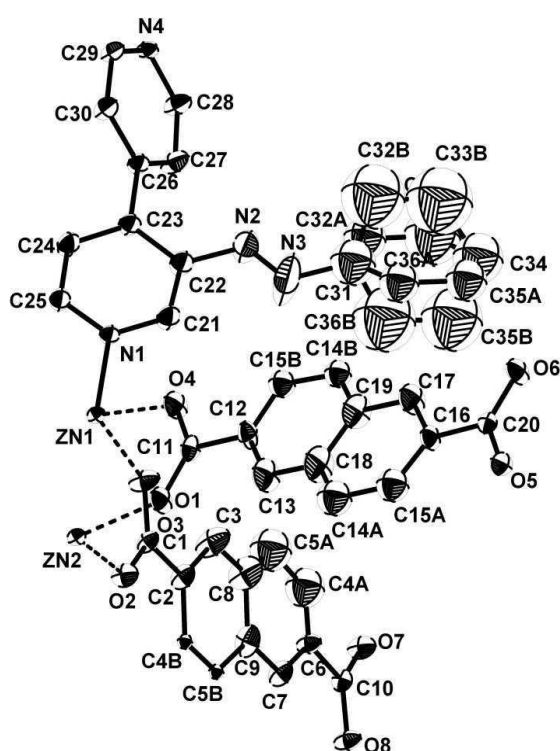


Fig. S10: Asymmetric unit of $[\text{Zn}_2(\text{CCA})_2(\text{AzBIPY})]$.

(11) Crystallographic results of the CAA linker in $[\text{Zn}_2(\text{CCA})_2(\text{AzBIPY})]$

Figure S11 explains the crystallographic results of the linker molecule CCA in $[\text{Zn}_2(\text{CCA})_2(\text{AzBIPY})]$. The carbon atoms C4A, C5A, C4B and C5B of the linker molecule 4-carboxy-cinnamic acid are dislocated in $[\text{Zn}_2(\text{CCA})_2(\text{AzBIPY})]$. The distinction between the double bond and the aromatic ring of the linker molecule is not possible to symmetry effects.

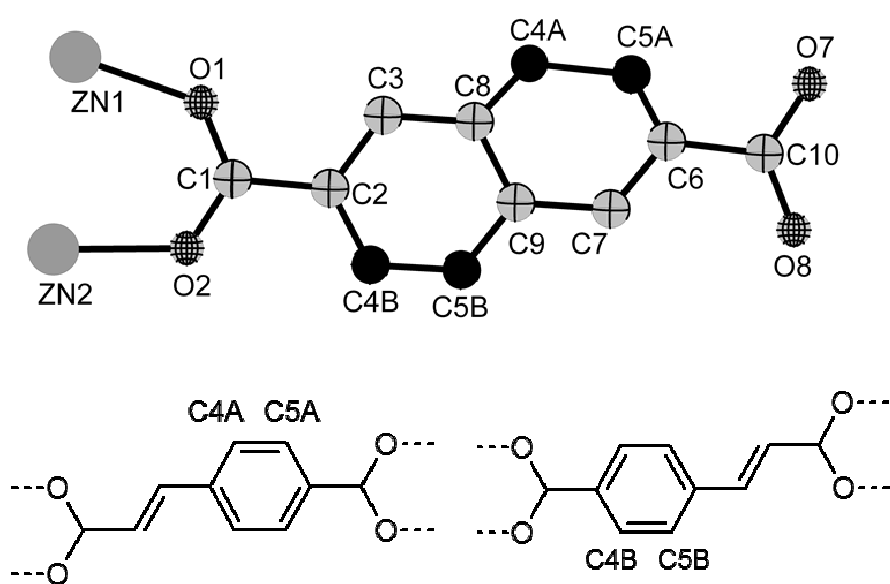


Fig. S11: 4-carboxy-cinnamic acid: crystallographic results of the linker molecule CCA in $[\text{Zn}_2(\text{CCA})_2(\text{AzBIPY})]$.

(12) UV/Vis spectra of 3-azo-phenyl-4,4'-bipyridine in EtOH

Fig. S12 shows the UV/Vis spectra of the switching experiment of 3-azo-phenyl-4,4'-bipyridine in EtOH. The blue, gray and green graphs were collected after the sample was irradiated for 1 h with UV-light. The orange, red and violet graphs were collected after the sample was irradiated for 1 h with visible light.

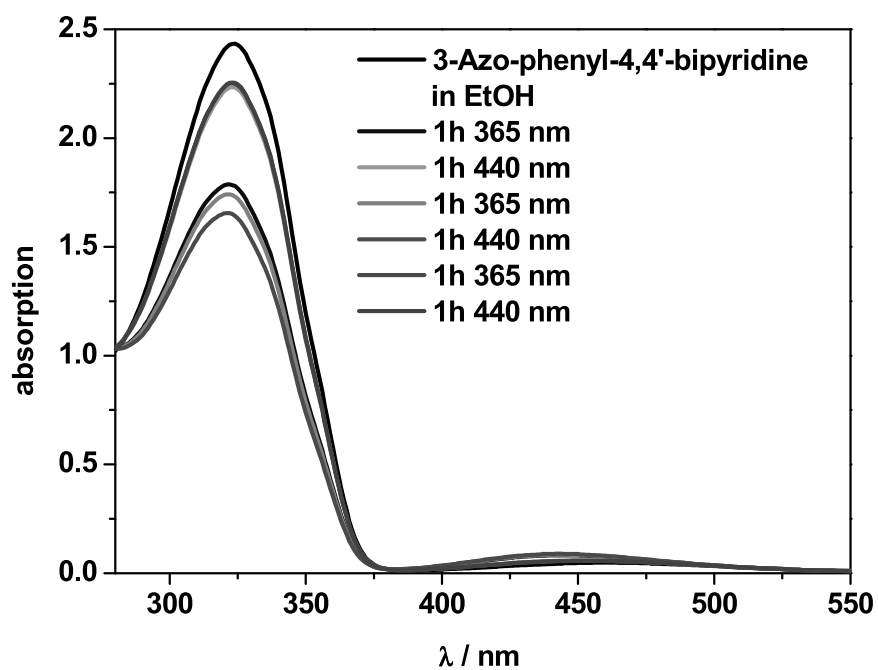


Fig. S12: UV/Vis spectra of 3-azo-phenyl-4,4'-bipyridine in EtOH.

(13) UV/Vis spectra of the thermal relaxation of [Co₂(NDC)₂(AzBIPY)]

Figure S13 shows the UV/Vis spectra of **1** in a BaSO₄ matrix (black graph), the irradiated sample (green graph) and after the sample was placed in the dark at room temperature for 12 h (red graph). After 12 h in the dark at room temperature only a small amount of the *cis* isomers are switched back to the *trans* isomers.

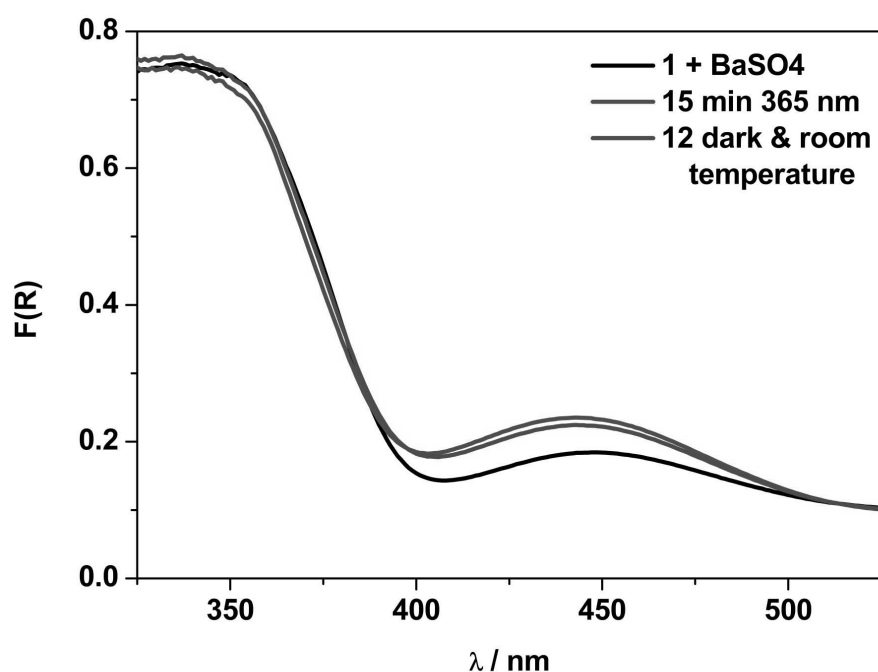


Fig. S13: UV/Vis spectra of **1** in a BaSO₄ matrix (black graph), the irradiated sample (green graph) and after the sample was placed in the dark at room temperature for 12 h (red graph).

(14) UV/Vis spectra of the thermal relaxation of [Cu₂(NDC)₂(AzBIPY)]

Figure S14 shows the UV/Vis spectra of **2** in a BaSO₄ matrix (black graph), the irradiated sample (green graph) and after the sample was placed in the dark at room temperature for 12 h (red graph). After 12 h in the dark at room temperature no cis isomer could be detected anymore, therefore the complete back switching was achieved.

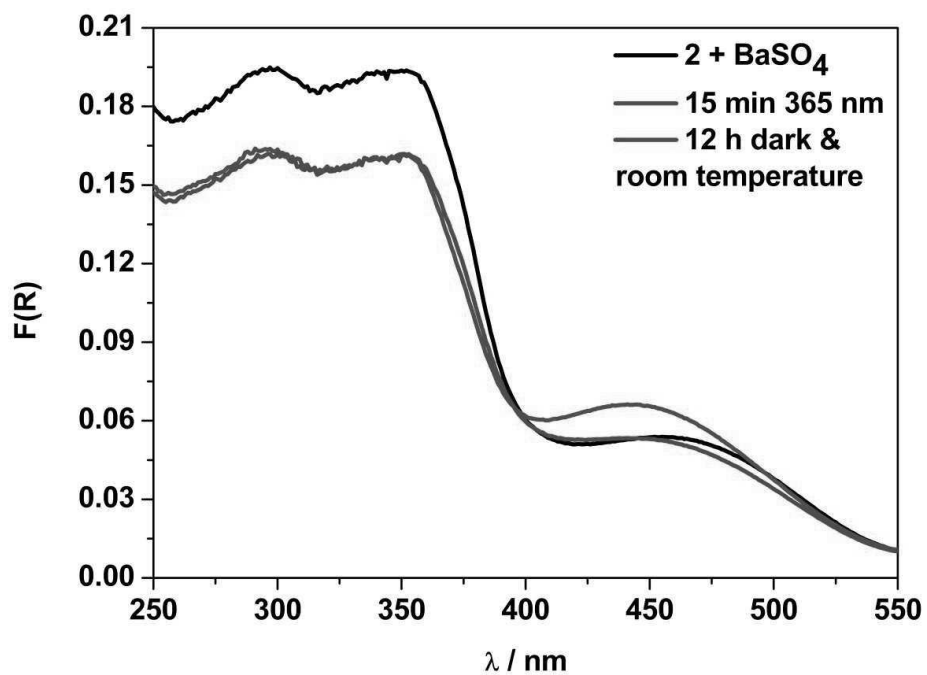


Fig. S14: UV/Vis spectra of **2** in a BaSO₄ matrix (black graph), the irradiated sample (green graph) and after the sample was placed in the dark at room temperature for 12 h (red graph).

(15) Colored Figure 5

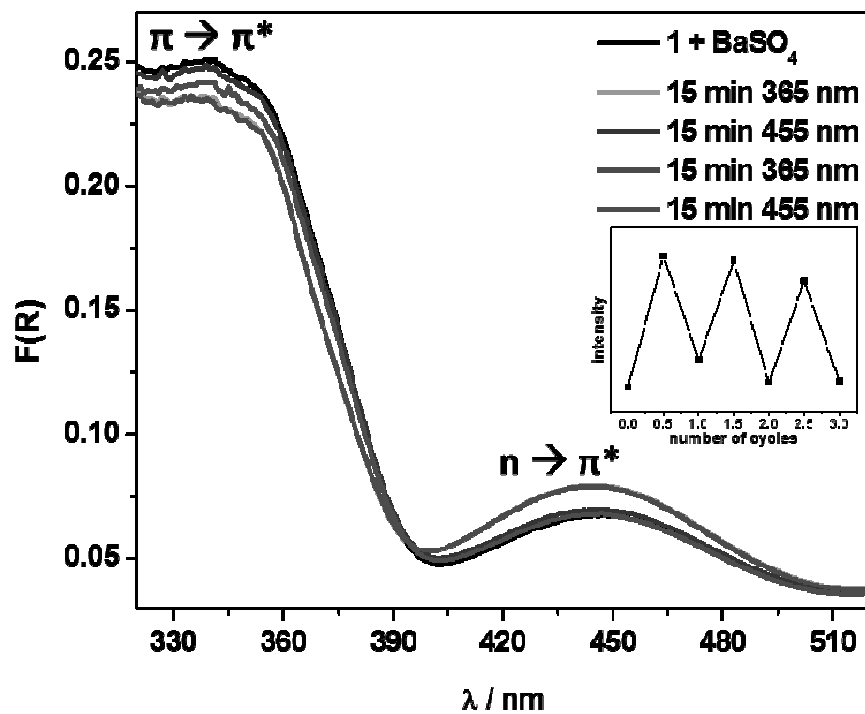


Figure S15. Results of the UV/Vis switching experiment of **1** in a BaSO₄ matrix. For clarity only two switching cycles are shown. Orange and green graphs are in a line with each other.

(16) Colored Figure 5

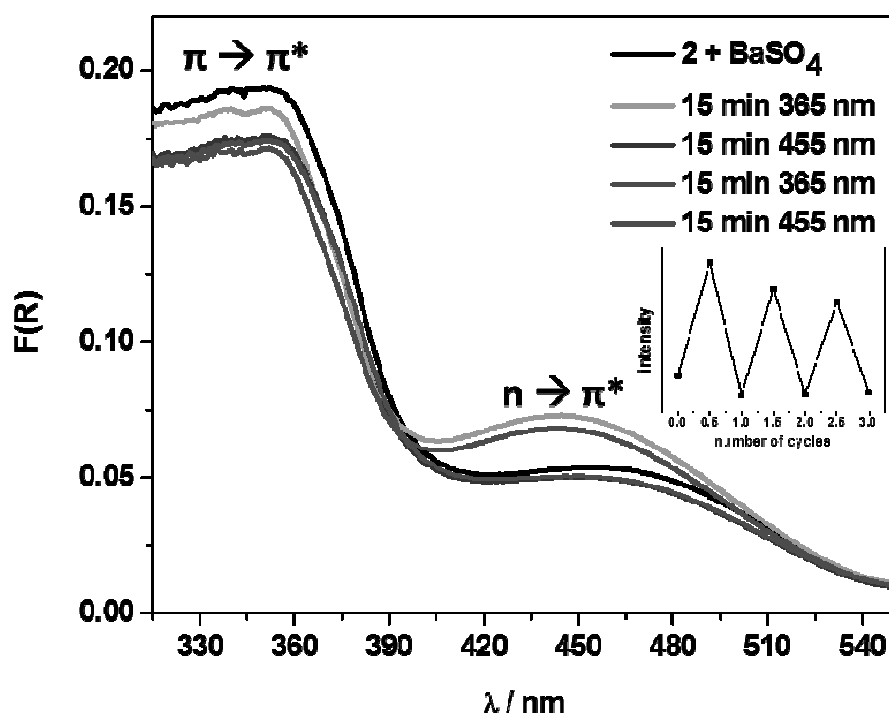


Figure S16. Results of the UV/Vis switching experiment of **2** in a BaSO₄ matrix. For clarity only two switching cycles are shown.

(17) UV/Vis spectra to investigate the photo stationary equilibrium of $[\text{Cu}_2(\text{NDC})_2(\text{AzBIPY})]$

In figure S17 the UV/Vis spectrum of $[\text{Cu}_2(\text{NDC})_2(\text{AzBIPY})]$ is shown. The photo stationary equilibrium is reached after 30 min, since no changes of the adsorption maximum at 455 nm are visible.

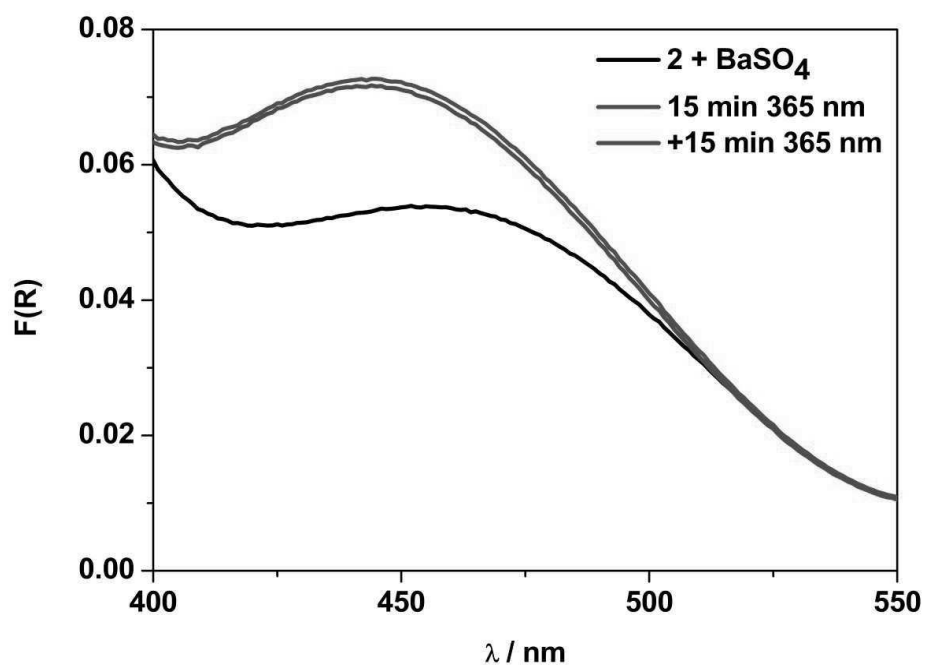


Fig. S17: UV/Vis spectrum of $[\text{Cu}_2(\text{NDC})_2(\text{AzBIPY})]$ for the investigation of the photo stationary equilibrium.

7.13. Kristallstrukturbestimmung von photoschaltbaren ZIF-8 analogen Verbindungen

Eur. J. Inorg. Chem. **2011** · © WILEY-VCH Verlag GmbH & Co. KGaA, 69451 Weinheim, 2011 · ISSN 1434-1948

SUPPORTING INFORMATION

DOI: 10.1002/ejic.201100789

Title: $[\text{Zn}(\text{C}_3\text{H}_3\text{N}_2)(\text{C}_3\text{H}_2\text{N}_2\text{-N=N-C}_6\text{H}_5)]$, a Mixed-Linker ZIF Containing a Photoswitchable Phenylazo Group

Author(s): Stephan Bernt, Mark Feyand, Antje Modrow, Julia Wack, Jürgen Senker, Norbert Stock*

(S1) High-throughput synthesis

[Zn(lm)(alm)] was discovered using our high-throughput (HT) methodology.^[1] Our high-throughput reactors are based on the 96 well plate format and contain 24 or 48 teflon inserts. Thus a total volume of 200 μ L (48 reactor block) and 2 mL (24 reactor block) is used.

For the systematic investigation a 24 reactor block was used. Methanol and DMF were chosen since numerous ZIFs have been synthesized in these solvents. A 0.3 M solution of imidazole, a 0.3 M solution of 2-phenylazoimidazole and a 0.3 M solution of $\text{Zn}(\text{NO}_3)_2 \cdot 6 \text{H}_2\text{O}$ in DMF and methanol were used as stock solutions. The exact amounts of starting materials are given in table S2. The reactants were mixed without stirring in the following order: 2-phenylazoimidazole, imidazole, $\text{Zn}(\text{NO}_3)_2 \cdot 6 \text{H}_2\text{O}$ and solvent. The reaction block was covered with a teflon foil, sealed with the top plate of the reactor and heated in an oven at 85 °C for 96 h. A cooling ramp of 12 h was chosen to form highly crystalline material. After the reaction the crystals were filtered, washed with 2 mL DMF, twice with 5 mL acetone and dried at 200 °C in vacuo. The samples were automatically characterized using a STOE HT X-ray powder diffractometer (Cu $K_{\alpha 1}$ radiation) equipped with an image plate detector.

[1] N. Stock, *Microporous Mesoporous Mater.* **2010**, *129*, 287-295.

7.13. Kristallstrukturbestimmung von photoschaltbaren ZIF-8 analogen Verbindungen

(S2) Discovery library where **1** was found

The following stock solutions were prepared:

Zn(NO₃)₂·6 H₂O: 0.3 M in DMF / MeOH

2-Phenylazoimidazole: 0.3 M in DMF / MeOH

Imidazole: 0.3 M in DMF / MeOH

These solutions were directly used in the HT synthesis. The exact amounts are given in table S2:

Table S2: Amounts of reactants used in the high-throughput study (**1** = title compound).

#	molar ratios			dispensed amounts (μL)					result
	Zn(NO ₃) ₂ ·6H ₂ O	HaIm	HIIm	Zn(NO ₃) ₂ ·6 H ₂ O	HaIm	Him	DMF	EtOH	
1	3	1	-	656	219	-	525	-	clear solution
2	2	1	-	545.5	274	-	580.5	-	Zn-formate*
3	1	1	-	438	438	-	524.5	-	Zn-formate*
4	1	2	-	328	657	-	415	-	Zn-formate*
5	1	3	-	284.5	854	-	261.5	-	Zn-formate*
6	1	4	-	219	876	-	305	-	Zn-formate*
7	3	1	-	656	219	-	-	525	clear solution
8	2	1	-	545.5	274	-	-	580.5	clear solution
9	1	1	-	438	438	-	-	524.5	clear solution
10	1	2	-	328	657	-	-	415	clear solution
11	1	3	-	284.5	854	-	-	261.5	clear solution
12	1	4	-	219	876	-	-	305	clear solution
13	1	1	1	193.3	193.3	193.3	820	-	1
14	1	2	1	193.3	386.7	193.3	626.7	-	1
15	1	1	2	193.3	193.3	386.7	626.7	-	1
16	1	1	3	193.3	193.3	580	433.7	-	1
17	1	3	1	193.3	580	193.3	433.7	-	1
18	1	2	2	193.3	386.7	386.7	433.7	-	1
19	1	1	1	193.3	193.3	193.3	-	820	clear solution
20	1	2	1	193.3	386.7	193.3	-	626.7	clear solution
21	1	1	2	193.3	193.3	386.7	-	626.7	clear solution
22	1	1	3	193.3	193.3	580	-	433.7	clear solution
23	1	3	1	193.3	580	193.3	-	433.7	clear solution
24	1	2	2	193.3	386.7	386.7	-	433.7	clear solution

* Zn-formate was obtained as described in the literature^[2] (CCDC: 266350).

[2] H. F. Clausen, R. D. Poulsen, A. D. Bond, M.-A. S. Chevallier, B. Brummerstedt Iversen, *J. Solid State Chem.* **2005**, *178*, 3343-3351.

(S3) SEM-picture of single crystals of the title compound

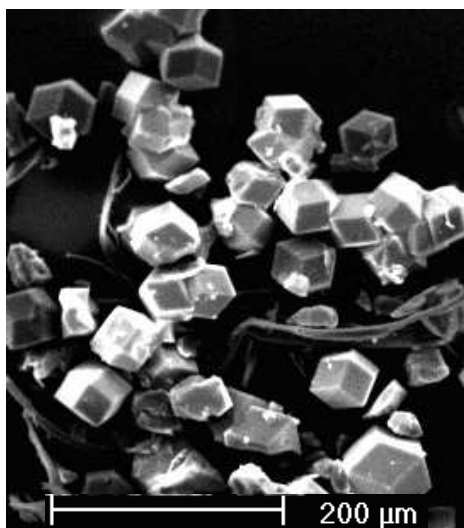


Fig. S3. SEM image of single crystals of the compound Zn(Im)(alm).

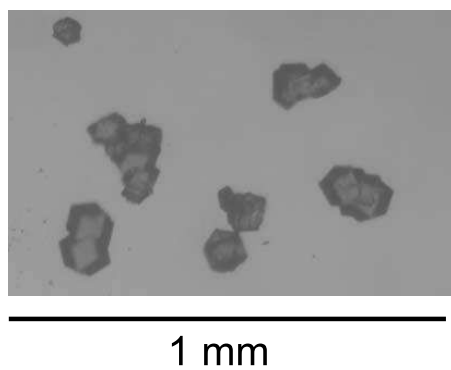


Fig. S3b. Optical micrograph of the title compound.

(S4) Crystal structure of [Zn(Im)(alm)]

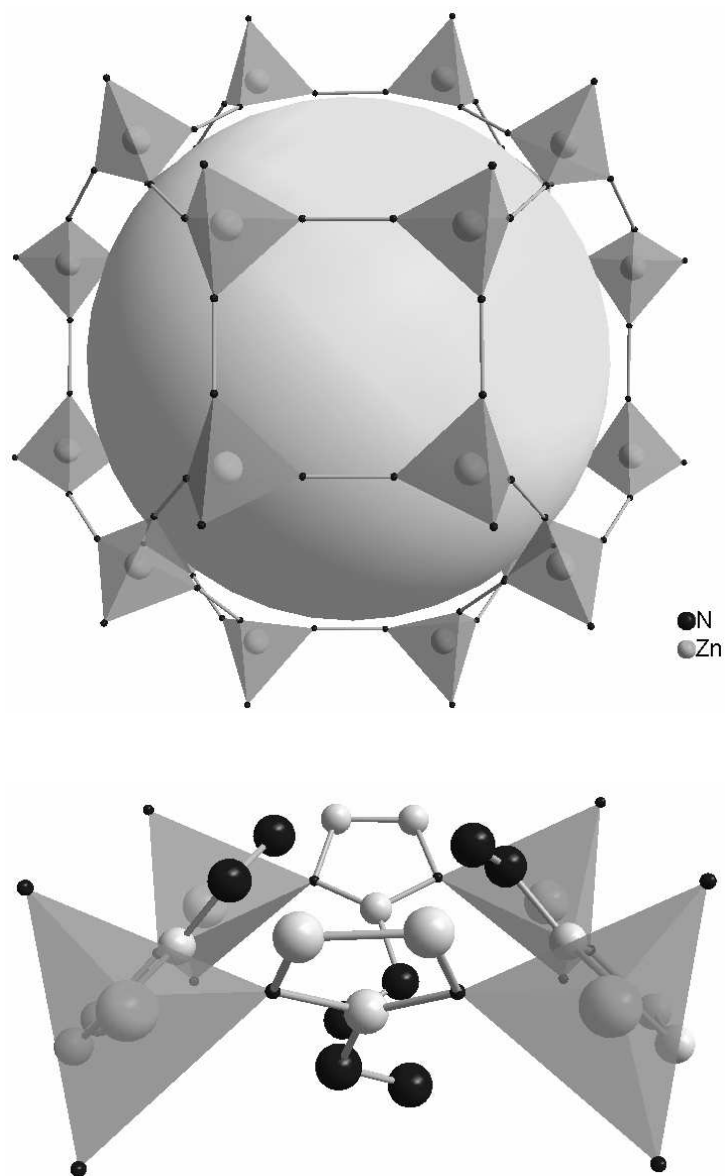


Fig. S4a. Top: SOD cage of [Zn(Im)(alm)] with a view at a four ring which is composed of four Zn^{2+} and four imidazolate ions (for clarity the imidazolate ions are replaced by a line between the two coordinating N atoms); bottom: four ring with imidazolate linkers. Due to the statistical disorder only every second imidazolate ion is connected to the azophenyl group. Phenyl rings are omitted for clarity.

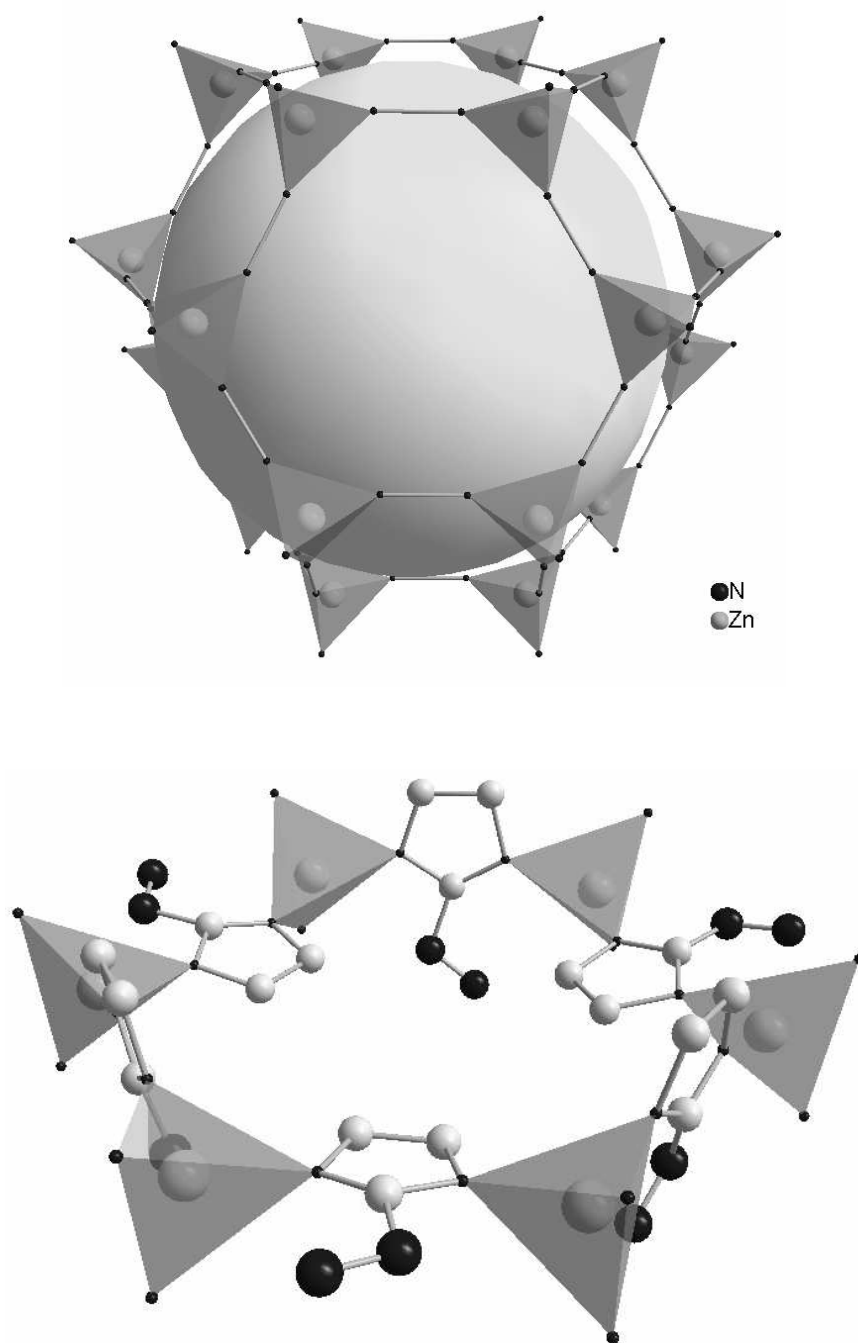


Fig. S4b. Top: SOD cage of $[\text{Zn}(\text{Im})(\text{alm})]$ with a view at a six ring which is composed of six Zn^{2+} and six imidazolate ions (for clarity the imidazolate ions are replaced by a line between the two coordinating N atoms); bottom: six ring with imidazolate linkers. Due to the statistical disorder only every second imidazolate ion is connected to the azophenyl group. Phenyl rings are omitted for clarity.

7.13. Kristallstrukturbestimmung von photoschaltbaren ZIF-8 analogen Verbindungen

(S5) Crystallographic data from the XRPD

X-ray powder diffraction data for indexing were collected in reflection mode employing a X'Pert Pro PANalytical diffractometer with Cu K $_{\alpha 1}$ radiation ($\lambda = 1.5418$) equipped with a PIXcel detector.

Wavelength: 1.540598

Number of accepted peaks: 31

Symmetry: Cubic I

Refined cell parameters:

Cell_A: 17.009(6)

Cell_Volume: 4921.1(28)

Number of single indexed lines: 31

Number of unindexed lines: 0

2Theta zeropoint: 0.024(11)

Final 2Theta window: 0.0600

N	2Th[obs]	H	K	L	2Th[calc]	obs-calc	Int.	d[obs]	d[calc]
1	7.343	1	1	0	7.344	-0.0013	100.0	12.0295	12.0274
2	10.391	2	0	0	10.393	-0.0026	36.5	8.5068	8.5046
3	12.738	2	1	1	12.738	0.0006	11.4	6.9437	6.9440
4	14.719	2	2	0	14.719	-0.0001	16.6	6.0137	6.0137
5	16.458	3	1	0	16.467	-0.0089	3.5	5.3817	5.3788
6	18.050	2	2	2	18.052	-0.0018	23.1	4.9106	4.9102
7	19.508	3	2	1	19.511	-0.0038	3.8	4.5468	4.5459
8	20.882	4	0	0	20.873	0.0089	5.9	4.2505	4.2523
9	22.154	3	3	0	22.155	-0.0014	7.5	4.0094	4.0091
10	23.419	4	2	0	23.370	0.0490	2.9	3.7955	3.8034
11	24.521	3	3	2	24.528	-0.0064	6.3	3.6273	3.6264
12	25.606	4	2	2	25.637	-0.0303	3.2	3.4760	3.4720
13	26.698	5	1	0	26.702	-0.0042	5.9	3.3363	3.3358

7. Anhang

14	28.722	5	2	1	28.724	-0.0020	2.3	3.1057	3.1055
15	29.672	4	4	0	29.687	-0.0151	2.4	3.0083	3.0068
16	30.600	5	3	0	30.623	-0.0228	2.8	2.9192	2.9171
17	31.528	6	0	0	31.534	-0.0053	2.6	2.8353	2.8349
18	32.434	6	1	1	32.421	0.0131	3.2	2.7582	2.7593
19	33.340	6	2	0	33.287	0.0526	1.7	2.6853	2.6894
20	34.158	5	4	1	34.134	0.0233	1.8	2.6229	2.6246
21	34.953	6	2	2	34.963	-0.0101	3.0	2.5650	2.5642
22	36.585	4	4	4	36.572	0.0134	2.1	2.4542	2.4551
23	37.314	7	1	0	37.353	-0.0391	1.9	2.4079	2.4055
24	38.861	7	2	1	38.876	-0.0154	1.4	2.3156	2.3147
25	41.800	6	5	1	41.782	0.0180	1.6	2.1593	2.1602
26	43.170	8	1	1	43.174	-0.0041	1.8	2.0939	2.0937
27	44.562	6	5	3	44.531	0.0310	1.6	2.0317	2.0330
28	45.821	7	5	0	45.856	-0.0345	1.6	1.9787	1.9773
29	49.644	9	2	1	49.666	-0.0219	1.4	1.8349	1.8342
30	50.910	9	3	0	50.888	0.0215	1.4	1.7922	1.7929
31	56.124	10	2	2	56.151	-0.0268	1.1	1.6374	1.6367

Average delta(2Theta) = 0.016

Maximum delta(2Theta) = 0.053 (peak 19) = 3.3 * average

Figure of Merit F(30) = 44.2 (0.015, 44)

Durbin-Watson serial correlation = 2.056 (not significant)

Sqrt[sum(w * delta(q)^2) / (Nobs - Nvar)] = 0.00016027

(S6) TG analysis of [Zn(Im)(alm)]

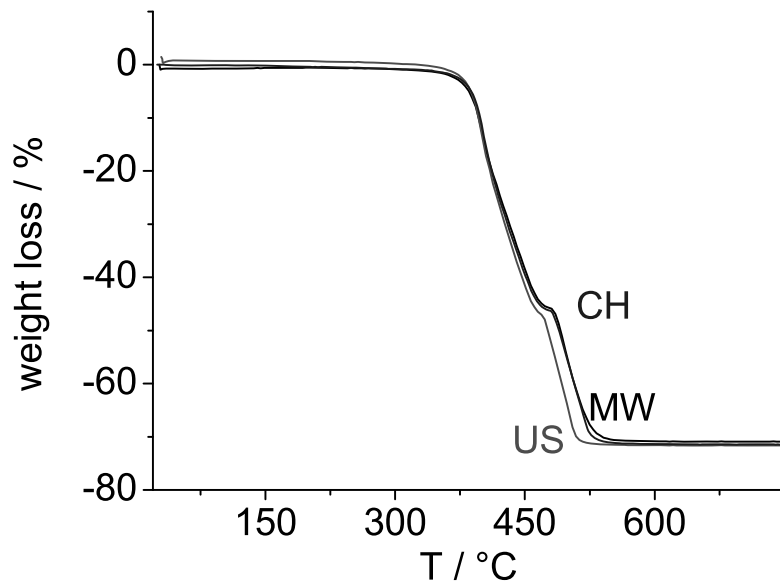


Fig. S6. The TG analyses of the samples synthesized by conventional heating (CH, blue), microwave-assisted heating (MW, black) and by applying ultrasound (US, red) demonstrate the high thermal stability of the title compound. The mass losses of 72.14% for CH, 71.68% for MW and 71.25% for US are in good agreement with the calculated value (73.05 %) where only ZnO remains as decomposition product (verified by X-ray powder diffraction). The difference between the graphs for US (above 400 °C) and CH/MW are due to differences in the particle sizes of the samples.

(S7) FTIR spectrum of the title compound

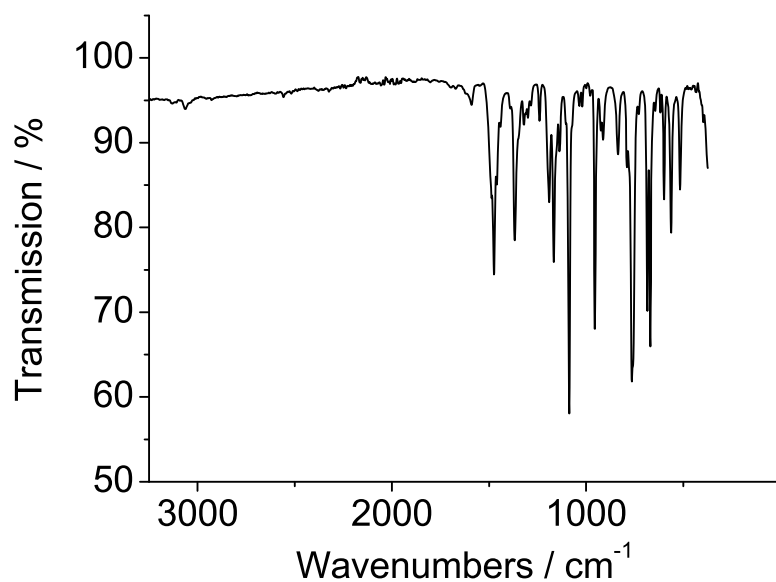


Fig. S7. FTIR spectrum of [Zn(Im)(alm)].

The signal at 3057 cm^{-1} can be assigned to aromatic =C-H stretching vibrations. Due to the reflection geometry in the measurement (ATR unit), the =C-H stretching signal is very weak. The ring -C=C- stretching vibrations of the phenylgroup are of variable intensity and occur in the region of 1625 cm^{-1} and 1430 cm^{-1} . The ring -C=C- and -C=N- stretching vibrations of the imidazolate groups occur in the region of 1670 cm^{-1} and 1320 cm^{-1} .

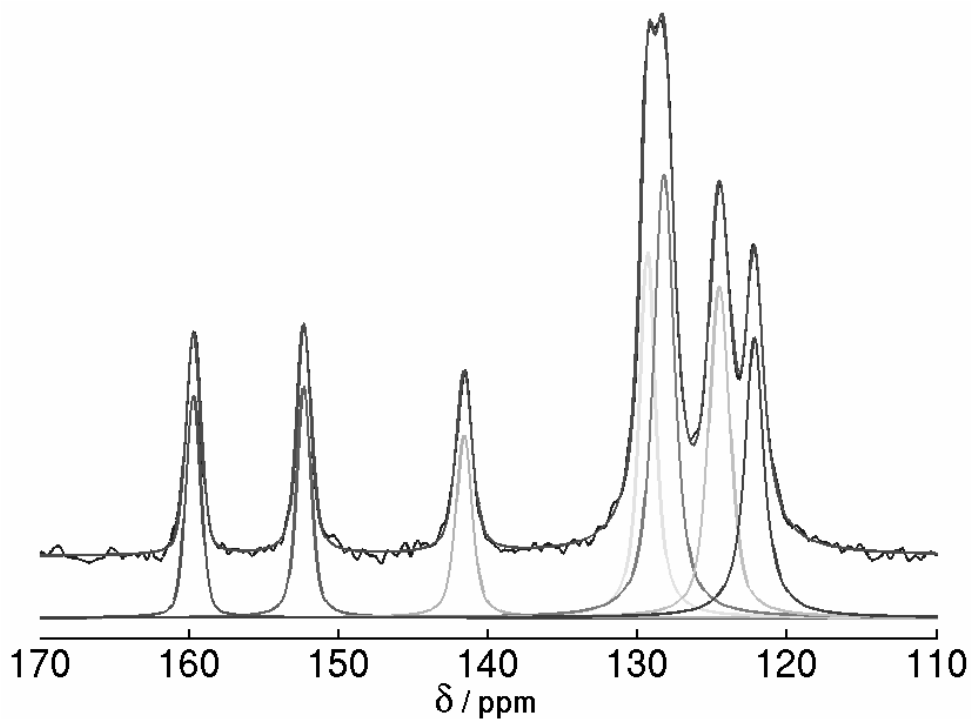
(S8) ^{13}C -MAS NMR spectrum with integrals

Fig. S8. ^{13}C -MAS-NMR (see also Fig. 3 for assignments) spectrum of the title compound $[\text{Zn}(\text{Im})(\text{alm})]$. The corresponding integrals are given in table S8.

Table S8. Expected and observed (calculated from the ^{13}C -MAS spectrum) integrals of the ^{13}C -MAS spectrum.

signal	expected integral (amount of C atoms)	observed integral (amount of C atoms)
159.6	1	1.0
152.3	1	1.1
141.5	1	1
129.1	2	2.1
128.5	3	3.3
124.5	2	2.4
122.2	2	2.0

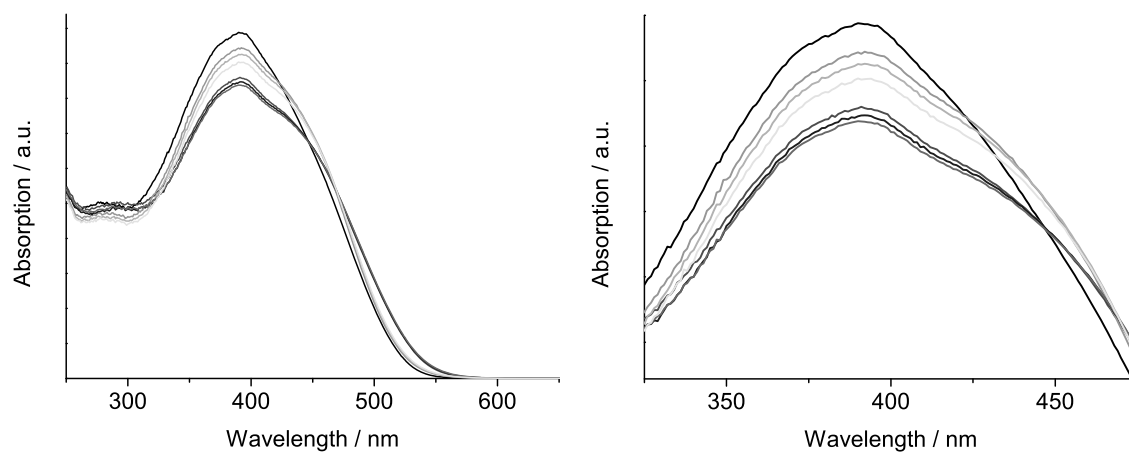
(S9) UV/Vis spectra of the (*trans-cis* and *cis-trans*) isomerization of all cycles

Fig. S9. Results of the UV/vis switching experiments of [Zn(Im)(alm)]. Left UV/vis spectra recorded from 250–600 nm; right: detailed view from 325–475 nm ($\pi \rightarrow \pi^*$ transition of the *trans* isomer at 392 nm). The assignments of the graphs are given in the table below.

color	isomer	switching cycle
black (initial curve)	-	-
purple	<i>cis</i>	1 (355 nm irradiation)
green	<i>trans</i>	1 (525 nm irradiation)
blue	<i>cis</i>	2 (355 nm irradiation)
turquoise	<i>trans</i>	2 (525 nm irradiation)
red	<i>cis</i>	3 (355 nm irradiation)
yellow	<i>trans</i>	3 (525 nm irradiation)

Literaturverzeichnis

- [1] N. Pienack, W. Bensch, *Angew. Chem.* **2011**, *123*(9), 2062–2083.
- [2] G. Sanda, R. E. Winans, S. Seifert, K. A. Carrado, *Chem. Mater.* **2002**, *14*(2), 739–742.
- [3] J. Morell, C. V. Teixeira, M. Cornelius, V. Rebbin, M. Tiemann, H. Amenitsch, M. Fröba, M. Lindan, *Chem. Mater.* **2004**, *16*(26), 5564–5566.
- [4] K. Flodström, C. V. Teixeira, H. Amenitsch, V. Alfredsson, M. Lindön, *Langmuir* **2004**, *20*(12), 4885–4891.
- [5] C.-H. Cheng, D. F. Shantz, *J. Phys. Chem. B* **2005**, *109*(29), 13912–13920.
- [6] R. Kiebach, N. Pienack, M.-E. Ordolff, F. Studt, W. Bensch, *Chem. Mater.* **2006**, *18*(5), 1196–1205.
- [7] T. Ressler, *Anal. Bioanal. Chem.* **2003**, *376*, 584–593.
- [8] R. I. Walton, D. O’Hare, *Chem. Commun.* **2000**, (23), 2283–2291.
- [9] A. Christensen, P. Norby, J. Hanson, *J. Solid State Chem.* **1995**, *114*(2), 556–559.
- [10] M. G. O’Brien, A. M. Beale, C. R. A. Catlow, B. M. Weckhuysen, *J. Am. Chem. Soc.* **2006**, *128*(36), 11744–11745.
- [11] E. Boccaleri, F. Carniato, G. Croce, D. Viterbo, W. van Beek, H. Emerich, M. Milanesio, *J. Appl. Crystallogr.* **2007**, *40*(4), 684–693.
- [12] O. B. Vistad, D. E. Akporiaye, F. Taulelle, K. P. Lillerud, *Chem. Mater.* **2003**, *15*(8), 1639–1649.
- [13] J. Shi, M. W. Anderson, S. W. Carr, *Chem. Mater.* **1996**, *8*(2), 369–375.
- [14] P. Bussian, F. Sobott, B. Brutschy, W. Schrader, F. Schüth, *Angew. Chem.* **2000**, *112*(21), 4065–4069.

- [15] S. A. Pelster, W. Schrader, F. Schüth, *J. Am. Chem. Soc.* **2006**, *128*(13), 4310–4317.
- [16] S. Xu, C. A. Melendres, J. H. Park, M. A. Kamrath, *J. Electrochem. Soc.* **1999**, *146*(9), 3315–3323.
- [17] T. Tanigaki, K. Ito, Y. Nagakubo, T. Asakawa, T. Kanemura, *J. Electron Microsc.* **2009**, *58*(5), 281–287.
- [18] P. W. Sutter, E. A. Sutter, *Nat. Mater.* **2007**, *6*(5), 363–366.
- [19] H. Putz, J. C. Schön, M. Jansen, *Ber. Bunsenges. Phys. Chem.* **1995**, *99*, 1148–1153.
- [20] M. D. Foster, M. M. J. Treacy, J. B. Higgins, I. Rivin, E. Balkovsky, K. H. Randall, *J. Appl. Crystallogr.* **2005**, *38*(6), 1028–1030.
- [21] J. L. Rowsell, O. M. Yaghi, *Microporous Mesoporous Mater.* **2004**, *73*(1–2), 3 – 14.
- [22] A. R. Millward, O. M. Yaghi, *J. Am. Chem. Soc.* **2005**, *127*(51), 17998–17999.
- [23] L. J. Murray, M. Dinca, J. R. Long, *Chem. Soc. Rev.* **2009**, *38*(5), 1294–1314.
- [24] M. T. Wharmby, J. P. S. Mowat, S. P. Thompson, P. A. Wright, *J. Am. Chem. Soc.* **2011**, *133*(5), 1266–1269.
- [25] K. J. Gagnon, H. P. Perry, A. Clearfield, *Chem. Rev.* **2011**, *112*(2), 1034–1054.
- [26] J. Lee, O. K. Farha, J. Roberts, K. A. Scheidt, S. T. Nguyen, J. T. Hupp, *Chem. Soc. Rev.* **2009**, *38*(5), 1450–1459.
- [27] P. Horcajada, C. Serre, M. Vallet-Regí, M. Sebban, F. Taulelle, G. Férey, *Angew. Chem. Int. Ed.* **2006**, *45*(36), 5974–5978.
- [28] P. Horcajada, T. Chalati, C. Serre, B. Gillet, C. Sebrie, T. Baati, J. F. Eubank, D. Heurtaux, P. Clayette, C. Kreuz, J.-S. Chang, Y. K. Hwang, V. Marsaud, P.-N. Bories, L. Cynober, S. Gil, G. Férey, P. Couvreur, R. Gref, *Nat. Mater.* **2010**, *9*(2), 172–178.
- [29] P. Horcajada, R. Gref, T. Baati, P. K. Allan, G. Maurin, P. Couvreur, G. Férey, R. E. Morris, C. Serre, *Chem. Rev.* **2011**, *112*(2), 1232–1268.
- [30] M. D. Allendorf, C. A. Bauer, R. K. Bhakta, R. J. T. Houk, *Chem. Soc. Rev.* **2009**, *38*(5), 1330–1352.

- [31] M. Kurmoo, *Chem. Soc. Rev.* **2009**, *38*(5), 1353–1379.
- [32] G. K. H. Shimizu, R. Vaidhyanathan, J. M. Taylor, *Chem. Soc. Rev.* **2009**, *38*(5), 1430–1449.
- [33] G. Férey, *J. Solid State Chem.* **2000**, *152*(1), 37 – 48.
- [34] O. M. Yaghi, M. O’Keeffe, N. W. Ockwig, H. K. Chae, M. Eddaoudi, J. Kim, *Nature* **2003**, *423*(6941), 705–714.
- [35] R. El Osta, M. Frigoli, J. Marrot, M. E. Medina, R. I. Walton, F. Millange, *Cryst. Growth Des.* **2012**, *12*(3), 1531–1537.
- [36] F. Millange, R. El Osta, M. E. Medina, R. I. Walton, *CrystEngComm* **2011**, *13*(1), 103–108.
- [37] F. Millange, M. Medina, N. Guillou, G. Férey, K. M. Golden, R. Walton, *Angew. Chem.* **2010**, *122*(4), 775–778.
- [38] T. Ahnfeldt, N. Stock, *CrystEngComm* **2012**, *14*(2), 505–511.
- [39] T. Ahnfeldt, J. Moellmer, V. Guillerm, R. Staudt, C. Serre, N. Stock, *Chem. Eur. J.* **2011**, *17*(23), 6462–6468.
- [40] S. Surblé, F. Millange, C. Serre, G. Férey, R. I. Walton, *Chem. Commun.* **2006**, *0*(14), 1518–1520.
- [41] S. Hermes, T. Witte, T. Hikov, D. Zacher, S. Bahn Müller, G. Langstein, K. Huber, R. A. Fischer, *J. Am. Chem. Soc.* **2007**, *129*(17), 5324–5325.
- [42] J. Cravillon, C. A. Schröder, R. Nayuk, J. Gummel, K. Huber, M. Wiebcke, *Angew. Chem.* **2011**, *123*(35), 8217–8221.
- [43] U. Kolb, T. E. Gorelik, E. Mugnaioli, A. Stewart, *Polym. Rev.* **2010**, *50*(3), 385–409.
- [44] U. Kolb, E. Mugnaioli, T. Gorelik, *Cryst. Res. Technology* **2011**, *46*, 542–554.
- [45] J. Jiang, J. L. Jorda, J. Yu, L. A. Baumes, E. Mugnaioli, M. J. Diaz-Cabanas, U. Kolb, A. Corma, *Science* **2011**, *333*(6046), 1131–1134.
- [46] K. Shankland, W. I. F. David, T. Csoka, *Z. Kristallogr.* **1997**, *212*(8), 550–552.

- [47] R. Černý, V. Favre-Nicolin, *Z. Kristallogr.* **2007**, *222*(3-4), 105–113.
- [48] C. J. Gilmore, K. Shankland, G. Bricogne, *Proc. R. Soc. London, Ser. A* **1993**, *442*(1914), 97–111.
- [49] M. Sakata, M. Sato, *Acta Crystallogr. Sect. A* **1990**, *46*(4), 263–270.
- [50] C. Baerlocher, F. Gramm, L. Massüger, L. B. McCusker, Z. He, S. Hovmöller, X. Zou, *Science* **2007**, *315*(5815), 1113–1116.
- [51] C. Baerlocher, L. B. McCusker, L. Palatinus, *Z. Kristallogr.* **2007**, *222*(2), 47–53.
- [52] C. Baerlocher, D. Xie, L. B. McCusker, S.-J. Hwang, I. Y. Chan, K. Ong, A. W. Burton, S. I. Zones, *Nat. Mater.* **2008**, *7*(8), 631–635.
- [53] A. Rabenau, *Angew. Chem.* **1985**, *97*(12), 1017–1032.
- [54] P. Lidström, J. Tierney, B. Wathey, J. Westman, *Tetrahedron* **2001**, *57*(45), 9225 – 9283.
- [55] C. O. Kappe, *Chem. Soc. Rev.* **2008**, *37*, 1127–1139.
- [56] H. Bux, F. Liang, Y. Li, J. Cravillon, M. Wiebcke, J. Caro, *J. Am. Chem. Soc.* **2009**, *131*(44), 16000–16001.
- [57] Z. Ni, R. I. Masel, *J. Am. Chem. Soc.* **2006**, *128*(38), 12394–12395.
- [58] A. V. Murugan, T. Muraliganth, A. Manthiram, *The Journal of Physical Chemistry C* **2008**, *112*(37), 14665–14671.
- [59] M. Zawadzki, *J. Alloys Compd.* **2008**, *454*(1–2), 347 – 351.
- [60] C. S. Cundy, P. A. Cox, *Chem. Rev.* **2003**, *103*(3), 663–702.
- [61] N. Stock, S. Biswas, *Chem. Rev.* **2011**, *112*(2), 933–969.
- [62] S. H. Jhung, J.-H. Lee, J.-S. Bull, *Bull. Korean Chem. Soc.* **2005**, *26*, 88.
- [63] Z. Ni, R. I. Masel, *J. Am. Chem. Soc.* **2006**, *128*(38), 12394–12395.
- [64] S. Jhung, J.-H. Lee, J. Yoon, C. Serre, G. Férey, J.-S. Chang, *Adv. Mater.* **2007**, *19*(1), 121–124.

-
- [65] J.-S. Choi, W.-J. Son, J. Kim, W.-S. Ahn, *Microporous Mesoporous Mater.* **2008**, *116*(1–3), 727 – 731.
- [66] N. A. Khan, E. Haque, S. H. Jung, *Phys. Chem. Chem. Phys.* **2010**, *12*(11), 2625–2631.
- [67] S. Bauer, N. Stock, *Chem. unserer Zeit* **2007**, *41*(5), 390–398.
- [68] N. Stock, *Microporous Mesoporous Mater.* **2010**, *129*(3), 287–295.
- [69] T. Ahnfeldt, N. Guillou, D. Gunzelmann, I. Margiolaki, T. Loiseau, G. Férey, J. Senker, N. Stock, *Angew. Chem.* **2009**, *121*(28), 5265–5268.
- [70] P. Maniam, C. Näther, N. Stock, *Eur. J. Inorg. Chem.* **2010**, *2010*(24), 3866–3874.
- [71] P. Maniam, N. Stock, *Inorg. Chem.* **2011**, *50*(11), 5085–5097.
- [72] M. Feyand, Diplomarbeit, CAU Kiel, **2008**.
- [73] S. Bauer, T. Bein, N. Stock, *J. Solid State Chem.* **2006**, *179*(1), 145–155.
- [74] A. Sonnauer, N. Stock, *J. Solid State Chem.* **2008**, *181*(11), 3065–3070.
- [75] A. Sonnauer, N. Stock, *Eur. J. Inorg. Chem.* **2008**, *2008*(32), 5038–5045.
- [76] C. Schmidt, N. Stock, *Inorg. Chem.* **2012**, *51*(5), 3108–3118.
- [77] S. Bauer, N. Stock, *Angew. Chem. Int. Ed.* **2007**, *46*(36), 6857–6860.
- [78] N. Reimer, B. Gil, B. Marszalek, N. Stock, *CrystEngComm* **2012**, *14*(12), 4119–4125.
- [79] W. Massa, *Einkristallstrukturanalyse*, 5. überarbeitete Aufl., Teubner, **2007**.
- [80] G. Taylor, *Acta Crystallogr. Sect. D* **2003**, *59*(11), 1881–1890.
- [81] A. L. Patterson, *Phys. Rev.* **1934**, *46*(5), 372–376.
- [82] A. L. Patterson, *Z. Krist.* **1935**, (A)90, 517–542.
- [83] I. L. Karle, H. Hauptman, J. Karle, A. B. Wing, *Acta Cryst.* **1958**, *11*(4), 257–263.
- [84] G. Oszlányi, A. Süto, *Acta Crystallogr. Sect. A* **2004**, *60*(2), 134–141.

- [85] G. Oszlányi, A. Sütö, *Acta Crystallogr. Sect. A* **2005**, *61*(1), 147–152.
- [86] G. Oszlányi, A. Sütö, *Acta Crystallogr. Sect. A* **2007**, *63*(2), 156–163.
- [87] D. Harker, J. S. Kasper, *Acta Cryst.* **1948**, *1*(2), 70–75.
- [88] G. M. Sheldrick, *ShelX 97 Software Suite* **1997**.
- [89] M. C. Burla, R. Caliendo, M. C. B. Carrozzini, G. L. Casciarano, C. Giacovazzo, M. Mallamo, A. Mazzone, G. Polidori, R. Spagna, *J. Appl. Cryst.* **2012**, *45*, 357–361.
- [90] A. Altomare, R. Caliendo, M. Camalli, C. Cuocci, C. Giacovazzo, A. G. G. Moliterni, R. Rizzi, *J. Appl. Crystallogr.* **2004**, *37*(6), 1025–1028.
- [91] A. Altomare, M. Camalli, C. Cuocci, C. Giacovazzo, A. Moliterni, R. Rizzi, *J. Appl. Crystallogr.* **2009**, *42*(6), 1197–1202.
- [92] A. Altomare, C. Cuocci, C. Giacovazzo, A. Moliterni, R. Rizzi, *J. Appl. Crystallogr.* **2012**, *45*(4), 789–797.
- [93] V. Favre-Nicolin, R. Černý, *J. Appl. Crystallogr.* **2002**, *35*(6), 734–743.
- [94] V. Favre-Nicolin, R. Černý, *Z. Kristallogr.* **2004**, *219*(12-2004), 847–856.
- [95] R. Černý, V. Favre-Nicolin, *Powder Diffr.* **2005**, *20*(04), 359–365.
- [96] T. ITO, *Nature* **1949**, *164*, 755–756.
- [97] J. W. Visser, *J. Appl. Crystallogr.* **1969**, *2*(3), 89–95.
- [98] A. Boultif, D. Louër, *J. Appl. Crystallogr.* **1991**, *24*(6), 987–993.
- [99] A. Boultif, D. Louër, *J. Appl. Crystallogr.* **2004**, *37*(5), 724–731.
- [100] P.-E. Werner, L. Eriksson, M. Westdahl, *J. Appl. Crystallogr.* **1985**, *18*(5), 367–370.
- [101] A. A. Coelho, *J. Appl. Crystallogr.* **2003**, *36*(1), 86–95.
- [102] W. David, K. Shankland, L. McCusker, C. Baerlocher, *Structure Determination from Powder Diffraction Data*, Oxford Science Publications, **2002**.
- [103] V. Favre-Nicolin, R. Černý, *Fox 1.9.7.1* **2012**.

-
- [104] A. A. Coelho, *Topas Academic 4.1* **2007**.
- [105] R. A. Young, *The Rietveld Method*, International Union of Crystallography Monographs on Crystallography, **1995**.
- [106] R. E. Dinnebier, S. J. L. Billinge, *Powder Diffraction: Theory and Practice*, RSC publishing, **2008**.
- [107] L. Spieß, R. Schwarzer, H. Behnken, G. Teichert, *Moderne Röntgenbeugung*, Teubner Studienbücher, **2009**.
- [108] M. Avrami, *The Journal of Chemical Physics* **1939**, 7(12), 1103–1112.
- [109] M. Avrami, *The Journal of Chemical Physics* **1940**, 8(2), 212–224.
- [110] M. Avrami, *The Journal of Chemical Physics* **1941**, 9(2), 177–184.
- [111] J. D. Hancock, J. H. Sharp, *J. Am. Ceram. Soc.* **1972**, 55(2), 74–77.
- [112] L. Engelke, M. Schaefer, M. Schur, W. Bensch, *Chem. Mater.* **2001**, 13(4), 1383–1390.
- [113] D. S. Wragg, P. J. Byrne, G. Giriat, B. L. Ouay, R. Gyepes, A. Harrison, A. G. Whittaker, R. E. Morris, *J. Phys. Chem. C* **2009**, 113(48), 20553–20558.
- [114] A. K. Cheetham, C. F. Mellot, *Chem. Mater.* **1997**, 9(11), 2269–2279.
- [115] J. N. Hay, *Brit. Poly. J.* **1971**, 3(2), 74–82.
- [116] G. R. Williams, D. O'Hare, *J. Phys. Chem. B* **2006**, 110(22), 10619–10629.
- [117] A. Marangoni, *J. Am. Oil Chem. Soc.* **1998**, 75(10), 1465–1467.
- [118] A. F. Gualtieri, *Phys. Chem. Miner.* **2001**, 28(10), 719–728.
- [119] J. Cravillon, C. A. Schroder, H. Bux, A. Rothkirch, J. Caro, M. Wiebecke, *CrystEngComm* **2012**, 14(2), 492–498.
- [120] M. T. Wharmby, G. M. Pearce, J. P. Mowat, J. M. Griffin, S. E. Ashbrook, P. A. Wright, L.-H. Schilling, A. Lieb, N. Stock, S. Chavan, S. Bordiga, E. Garcia, G. D. Pirngruber, M. Vreeke, L. Gora, *Microporous Mesoporous Mater.* **2012**, 157(0), 3–17.

- [121] S.-F. Tang, J.-L. Song, J.-G. Mao, *Eur. J. Inorg. Chem.* **2006**, 2006(10), 2011–2019.
- [122] J.-G. Mao, *Coord. Chem. Rev.* **2007**, 251(11–12), 1493–1520.
- [123] Y. Ji, X. Ma, X. Wu, N. Wang, Q. Wang, X. Zhou, *Catalysis Letters* **2007**, 118(3–4), 187–194.
- [124] M. Deng, Y. Ling, B. Xia, Z. Chen, Y. Zhou, X. Liu, B. Yue, H. He, *Chem. Eur. J.* **2011**, 17(37), 10323–10328.
- [125] M. J. Beier, W. Kleist, M. T. Wharmby, R. Kissner, B. Kimmerle, P. A. Wright, J.-D. Grunwaldt, A. Baiker, *Chem. Eur. J.* **2012**, 18(3), 887–898.
- [126] D. M. Poojary, B. L. Zhang, P. Bellinghausen, A. Clearfield, *Inorg. Chem.* **1996**, 35(17), 4942–4949.
- [127] J. G. Mao, Z. K. Wang, A. Clearfield, *Inorg. Chem.* **2002**, 41(9), 2334–2340.
- [128] J. L. Song, J. G. Mao, *Chem. Eur. J.* **2005**, 11(5), 1417–1424.
- [129] S. J. Langley, M. Helliwell, R. Sessoli, P. Rosa, W. Wernsdorfer, R. E. P. Winpenny, *Chem. Comm.* **2005**, (40), 5029–5031.
- [130] Z.-Y. Du, H.-B. Xu, J.-G. Mao, *Inorg. Chem.* **2006**, 45(24), 9780–9788.
- [131] B.-P. Yang, A. V. Prosvirin, Y.-Q. Guo, J.-G. Mao, *Inorg. Chem.* **2008**, 47(5), 1453–1459.
- [132] A. Clearfield, in *Progress in Inorganic Chemistry*, John Wiley & Sons, Inc., **2007**, 371–510.
- [133] V. Zima, J. Svoboda, Y.-C. Yang, S.-L. Wang, *CrystEngComm* **2012**, 14(10), 3469–3477.
- [134] P. Maniam, N. Stock, *Z. Anorg. Allg. Chem.* **2011**, 637(9), 1145–1151.
- [135] P. Maniam, N. Stock, *Acta Crystallogr. Sect. C* **2011**, 67(3), m73–m76.
- [136] Z.-Y. Du, H.-B. Xu, J.-G. Mao, *Inorg. Chem.* **2006**, 45(16), 6424–6430.
- [137] Z.-Y. Du, X.-L. Li, Q.-Y. Liu, J.-G. Mao, *Cryst. Growth Des.* **2007**, 7(8), 1501–1507.

- [138] Z.-Y. Du, A. V. Prosvirin, J.-G. Mao, *Inorg. Chem.* **2007**, *46*(23), 9884–9894.
- [139] Z.-Y. Du, J.-J. Huang, Y.-R. Xie, H.-R. Wen, *J. Mol. Struct.* **2009**, *919*(1–3), 112–116.
- [140] Z.-Y. Du, H.-B. Xu, X.-L. Li, J.-G. Mao, *Eur. J. Inorg. Chem.* **2007**, *2007*(28), 4520–4529.
- [141] A. Sonnauer, C. Näther, H. Höpfe, J. Senker, N. Stock, *Inorg. Chem.* **2007**, *46*, 9968–9974.
- [142] A. Sonnauer, N. Stock, *J. Solid State Chem.* **2008**, *181*, 3065–3070.
- [143] A. Sonnauer, N. Stock, *Acta Crystallogr. Sect. E* **2008**, *E64*, m1433.
- [144] A. Sonnauer, N. Stock, *J. Solid State Chem.* **2008**, *181*, 473–479.
- [145] A. Sonnauer, N. Stock, *Solid State Sci.* **2009**, *11*, 358–363.
- [146] A. Sonnauer, N. Stock, *Eur. J. Inorg. Chem.* **2008**, 5038–5045.
- [147] A. Sonnauer, A. Lieb, N. Stock, *Acta Crystallogr. Sect. E* **2008**, *E64*, m1417–m1418.
- [148] Z.-Y. Du, H.-R. Wen, Y.-R. Xie, *J. Mol. Struct.* **2008**, *891*(1–3), 272–277.
- [149] A. Sonnauer, M. Feyand, N. Stock, *Cryst. Growth Des.* **2008**, *9*, 586–592.
- [150] T.-B. Liao, Y. Ling, Z.-X. Chen, Y.-M. Zhou, L.-H. Weng, *Chem. Commun.* **2010**, *46*(7), 1100–1102.
- [151] S. Bauer, J. Marrot, T. Devic, G. Férey, N. Stock, *Inorg. Chem.* **2007**, *46*(23), 9998–10002.
- [152] J.-L. Song, A. Prosvirin, H.-H. Zhao, J.-G. Mao, *Eur. J. Inorg. Chem.* **2004**, *2004*(18), 3706–3711.
- [153] S. Bauer, T. Bein, N. Stock, *Inorg. Chem.* **2005**, *44*(16), 5882–5889.
- [154] J. K. Stalick, C. O. Quicksall, *Inorg. Chem.* **1976**, *15*(7), 1577–1584.
- [155] N. Zakowsky, P. S. Wheatley, I. Bull, M. P. Attfield, R. E. Morris, *J. Chem. Soc., Dalton Trans.* **2001**, (19), 2899–2902.

- [156] E. M. Bauer, C. Bellitto, M. Colapietro, G. Portalone, G. Righini, *Inorg. Chem.* **2003**, *42*(20), 6345–6351.
- [157] W. R. Gemmill, M. D. Smith, B. A. Reisner, *J. Solid State Chem.* **2005**, *178*(9), 2658–2662.
- [158] S. R. Miller, G. M. Pearce, P. A. Wright, F. Bonino, S. Chavan, S. Bordiga, I. Margiolaki, N. Guillou, G. Férey, S. Bourrelly, P. L. Llewellyn, *J. Am. Chem. Soc.* **2008**, *130*(47), 15967–15981.
- [159] N. Stock, T. Bein, *Angew. Chem.* **2004**, *116*, 767–770.
- [160] S.-M. Ying, J.-G. Mao, *Cryst. Growth Des.* **2006**, *6*(4), 964–968.
- [161] F. Costantino, A. Ienco, P. L. Gentili, F. Presciutti, *Cryst. Growth Des.* **2010**, *10*(11), 4831–4838.
- [162] F. Costantino, T. Bataille, N. Audebrand, E. Le Fur, C. Sangregorio, *Cryst. Growth Des.* **2007**, *7*(9), 1881–1888.
- [163] N. Stock, A. Stoll, T. Bein, *Microporous and Mesoporous Materials* **2004**, *69*(1–2), 65–69.
- [164] B. Seidlhofer, E. Antonova, J. Wang, D. Schinkel, W. Bensch, *Z. Anorg. Allg. Chem.* **2012**, *638*, 2555–2564.
- [165] E. Antonova, B. Seidlhofer, J. Wang, M. Hinz, W. Bensch, *Chem. Eur. J.* **2012**, *18*(48), 15316–15322.
- [166] A. M. Fogg, J. S. Dunn, D. O'Hare, *Chem. Mater.* **1998**, *10*(1), 356–360.
- [167] A. T. Davies, G. Sankar, C. R. A. Catlow, S. M. Clark, *J. Phys. Chem. B* **1997**, *101*(48), 10115–10120.
- [168] A. M. Beale, G. Sankar, *Nucl. Instrum. Meth. B* **2003**, *199*(0), 504–508.
- [169] R. I. Walton, D. O'Hare, *J. Phys. Chem. B* **2000**, *105*(1), 91–96.
- [170] E. Stavitski, M. Goesten, J. Juan-Alcañiz, A. Martinez-Joaristi, P. Serra-Crespo, A. V. Petukhov, J. Gascon, F. Kapteijn, *Angew. Chem.* **2011**, *123*(41), 9798–9802.

- [171] H. Reinsch, N. Stock, *CrystEngComm* **2013**, –.
- [172] R. I. Walton, A. S. Munn, N. Guillou, F. Millange, *Chem. Eur. J.* **2011**, *17*(25), 7069–7079.
- [173] M. Feyand, C. Näther, A. Rothkirch, N. Stock, *Inorg. Chem.* **2010**, *49*(23), 11158–11163.
- [174] M. Feyand, A. Hübner, A. Rothkirch, D. Wragg, N. Stock, *Inorg. Chem.* **2012**, *51*(22), 12540–12547.
- [175] K. Moedritzer, R. R. Irani, *J. Org. Chem.* **1966**, *31*(5), 1603–1607.
- [176] SPP-1415, *Kristalline Nichtgleichgewichtsphasen* **2012**.
- [177] A. F. Holleman, E. Wiberg, *Lehrbuch der Anorganischen Chemie 101., verb. u. stark erw. A.*, Gruyter, **1995**.
- [178] C. Schmidt, M. Feyand, R. A. N. Stock, *J. Solid State Chem.* **2012**, *188*(0), 44 – 49.
- [179] N. M. Leonard, L. C. Wieland, R. S. Mohan, *Tetrahedron* **2002**, *58*(42), 8373–8397.
- [180] J. M. Bothwell, S. W. Krabbe, R. S. Mohan, *Chem. Soc. Rev.* **2011**, *40*(9), 4649–4707.
- [181] S. Horike, M. Dincâ, K. Tamaki, J. R. Long, *J. Am. Chem. Soc.* **2008**, *130*(18), 5854–5855.
- [182] G. Férey, C. Mellot-Draznieks, C. Serre, F. Millange, J. Dutour, S. Surblé, I. Margiolaki, *Science* **2005**, *309*(5743), 2040–2042.
- [183] J. H. Cavka, S. Jakobsen, U. Olsbye, N. Guillou, C. Lamberti, S. Bordiga, K. P. Lillerud, *J. Am. Chem. Soc.* **2008**, *130*(42), 13850–13851.
- [184] H. Sun, L. Zhang, K. Szeto, *Metal Ions in Biological Systems*, Marcel Dekker Inc., **2003**.
- [185] N. A. Tumanov, E. V. Timakova, E. V. Boldyreva, *Acta Crystallogr. Sect. E* **2010**, *66*(10), m1248.
- [186] C.-I. Stalhandske, *Acta. Chem. Scand.* **1969**, 1525–1533.

- [187] L. Miersch, T. Ruffer, M. Mehring, *Chem. Commun.* **2011**, 47(22), 6353–6355.
- [188] V. Andre, A. Hardeman, I. Halasz, R. S. Stein, G. J. Jackson, D. G. Reid, M. J. Duer, C. Curfs, M. T. Duarte, T. Friscic, *Angew. Chem.* **2011**, 123(34), 8004–8007.
- [189] A. C. Wibowo, M. D. Smith, H.-C. zur Loye, *Chem. Commun.* **2011**, 47(26), 7371–7373.
- [190] A. C. Wibowo, M. D. Smith, H.-C. zur Loye, *Cryst. Growth Des.* **2011**, 11(10), 4449–4457.
- [191] V. Stavila, K. H. Whitmire, I. Rusakova, *Chem. Mater.* **2009**, 21(22), 5456–5465.
- [192] V. Stavila, I. Bulimestru, A. Gulea, A. C. Colson, K. H. Whitmire, *Acta Crystallogr. Sect. C* **2011**, 67(3), m65–m68.
- [193] M. Ranjbar, H. Aghabozorg, A. Moghimi, *Z. Kristallogr.-New Cryst. Struct.* **2003**, 218, 432.
- [194] S. Sheshmani, P. D. Kheirollahi, H. Aghabozorg, A. Shokrollahi, G. Kickelbick, M. Shamsipur, F. Ramezanipour, A. Moghimi, *Z. Anorg. Allg. Chem.* **2005**, 631(15), 3058–3065.
- [195] M. Ranjbar, H. Aghabozorg, A. Moghimi, A. Yanovsky, *Anal. Sci.* **2001**, 17(12), 1469–1470.
- [196] H. Aghabozorg, S. Kazemi, A. A. Agah, M. Mirzaei, B. Notash, *Acta Crystallogr. Sect. E* **2011**, 67(3), m360–m361.
- [197] O. Anjaneyulu, T. K. Prasad, K. C. K. Swamy, *Dalton Trans.* **2010**, 39(8), 1935–1940.
- [198] A. Thirumurugan, W. Li, A. K. Cheetham, *Dalton Trans.* **2012**, 41(14), 4126–4134.
- [199] A. Thirumurugan, J.-C. Tan, A. K. Cheetham, *Cryst. Growth Des.* **2009**, 10(4), 1736–1741.
- [200] A. Thirumurugan, A. K. Cheetham, *Eur. J. Inorg. Chem.* **2010**, 2010(24), 3823–3828.

- [201] H. Pasdar, M. Namegh, H. Aghabozorg, B. Notash, *Acta Crystallogr. Sect. E* **2011**, *67*(3), m353–m354.
- [202] M. Feyand, E. Mugnaioli, F. Vermoortele, B. Bueken, J. M. Dieterich, T. Reimer, U. Kolb, D. de Vos, N. Stock, *Angew. Chem.* **2012**, *124*(41), 10519–10522.
- [203] H. Reinsch, M. Feyand, T. Ahnfeldt, N. Stock, *Dalton Trans.* **2012**, *41*(14), 4164–4171.
- [204] S. Biswas, M. Maes, A. Dhakshinamoorthy, M. Feyand, D. E. De Vos, H. Garcia, N. Stock, *J. Mater. Chem.* **2012**, *22*(20), 10200–10209.
- [205] Y. Ishii, S. Sakaguchi, T. Iwahama, *Adv. Synth. Catal.* **2001**, *343*(5), 393–427.
- [206] A. Modrow, M. Feyand, D. Zargarani, R. Herges, N. Stock, *Z. Anorg. Allg. Chem.* **2012**, *638*(12-13), 2138–2143.
- [207] S. Bernt, M. Feyand, A. Modrow, J. Wack, J. Senker, N. Stock, *Eur. J. Inorg. Chem.* **2011**, *2011*(35), 5378–5383.
- [208] R. Banerjee, A. Phan, B. Wang, C. Knobler, H. Furukawa, M. O’Keeffe, O. M. Yaghi, *Science* **2008**, *319*(5865), 939–943.
- [209] J. H. Thurston, E. M. Marlier, K. H. Whitmire, *Chem. Commun.* **2002**, *0*(23), 2834–2835.
- [210] Y.-J. Wang, J. Zhao, Z.-H. Dang, L. Xu, *Acta Crystallogr. Sect. E* **2007**, *63*(6), m1770–m1771.
- [211] J. B. Lambert, Z. Liu, C. Liu, *Organometallics* **2008**, *27*(7), 1464–1469.
- [212] J. M. Gotthardt, K. F. White, B. F. Abrahams, C. Ritchie, C. Boskovic, *Cryst. Growth Des.* **2012**, *12*(9), 4425–4430.
- [213] R. P. Davies, P. D. Lickiss, K. Robertson, A. J. P. White, *Aust. J. Chem.* **2011**, *64*(9), 1237–1244.
- [214] R. P. Davies, R. Less, P. D. Lickiss, K. Robertson, A. J. P. White, *Cryst. Growth Des.* **2010**, *10*(10), 4571–4581.

- [215] R. P. Davies, A. Jumabekov, R. J. Less, P. D. Lickiss, K. Robertson, K. G. Sandeman, A. J. P. White, in *Nanotech Conf. Expo 2010*, Bd. 2, CRC Press, Bd. 2, 103–106.
- [216] D. Mansfeld, L. Miersch, T. Ruffer, D. Schaarschmidt, H. Lang, T. Böhle, R. W. Troff, C. A. Schalley, J. Müller, M. Mehring, *Chem. Eur. J.* **2011**, *17*(52), 14805–14810.
- [217] L. Miersch, T. Ruffer, M. Schlesinger, H. Lang, M. Mehring, *Inorg. Chem.* **2012**, *51*(17), 9376–9384.
- [218] L. Miersch, T. Ruffer, H. Lang, S. Schulze, M. Hietschold, D. Zahn, M. Mehring, *Eur. J. Inorg. Chem.* **2010**, *2010*(30), 4763–4769.
- [219] L. Miersch, M. Schlesinger, R. W. Troff, C. A. Schalley, T. Ruffer, H. Lang, D. Zahn, M. Mehring, *Chem. Eur. J.* **2011**, *17*(25), 6985–6990.

Eidesstattliche Erklärung

Hiermit versichere ich an Eides statt, dass ich die vorliegende Arbeit selbständig – abgesehen von der wissenschaftlichen Betreuung durch meinen Lehrer – und nur unter Verwendung der angegebenen Hilfsmittel angefertigt habe. Die Dissertation wird ausschließlich an dieser Stelle zur Promotion vorgelegt. Teile der Arbeit wurden in den genannten Journalen als wissenschaftliche Beiträge bereits veröffentlicht oder wurden zur Veröffentlichung eingereicht. Ich erkläre hiermit, dass ich noch keinen Promotionsversuch unternommen habe und dass die Arbeit unter Einhaltung der Regeln guter wissenschaftlicher Praxis der Deutschen Forschungsgesellschaft entstanden ist.

Kiel, März 2013

(Mark Feyand)

Curriculum Vitae

Persönliche Details

Mark Feyand

Geburtstag 01.11.1983
Geburtsort Helmstedt
Staatsangehörigkeit Deutsch

Ausbildung

Seit Oktober 2009 **Promotion, Institut für Anorganische Chemie, Kiel**

„Synthese und *in situ* Untersuchungen von anorganisch-organischen Hybridverbindungen auf Basis von Metall-Phosphonaten und Bismutcarboxylaten“
.

Dezember 2008 -
Mai 2009 **Diplomarbeit, Institut für Anorganische Chemie, Kiel**

„*In-situ* Untersuchungen, Synthese und ausführliche Charakterisierung von Metall-Phosphonatoalkylsulfonaten.“

Oktober 2004 -
Mai 2009 **Chemie Studium, Christian Albrechts Universität zu Kiel**

Mai 2003 **Abitur, Gymnasium Julianum Helmstedt, Germany**